MARTIN MARIETTA ENERGY SYSTEMS LIBRARIES
3 4456 0049180 3

CD

ORNL-5274

Cy. 1

GAS-COOLED REACTOR PROGRAMS

HIGH-TEMPERATURE GAS-COOLED REACTOR BASE-TECHNOLOGY PROGRAM PROGRESS REPORT

July 1, 1975 - December 31, 1976

F. J. Homan

Paul R. Kasten

OAK RIDGE NATIONAL LABORATORY
CENTRAL RESEARCH LIBRARY
DOCUMENT COLLECTION
LIBRARY LOAN COPY
DO NOT TRANSFER TO ANOTHER PERSON
If you wish someone else to see this
document, send in name with document
and the library will arrange a loan.
UCN-7969
(3-67)

OAK RIDGE NATIONAL LABORATORY
OPERATED BY UNION CARBIDE CORPORATION FOR THE ENERGY RESEARCH AND DEVELOPMENT ADMINISTRATION

Printed in the United States of America. Available from
National Technical Information Service
U.S. Department of Commerce
5285 Port Royal Road, Springfield, Virginia 22161
Price: Printed Copy $14.00; Microfiche $3.00

This report was prepared as an account of work sponsored by the United States Government. Neither the United States nor the Energy Research and Development Administration/United States Nuclear Regulatory Commission, nor any of their employees, nor any of their contractors, subcontractors, or their employees, makes any warranty, express or implied, or assumes any legal liability or responsibility for the accuracy, completeness or usefulness of any information, apparatus, product or process disclosed, or represents that its use would not infringe privately owned rights.

ORNL-5274
Distribution
Category UC-77

Contract No. W-7405-eng-26

GAS-COOLED REACTOR PROGRAMS

HIGH-TEMPERATURE GAS-COOLED REACTOR BASE-TECHNOLOGY PROGRAM PROGRESS REPORT FOR JULY 1, 1975, THROUGH DECEMBER 31, 1976

F. J. Homan, Program Manager

Paul R. Kasten, Program Director

Edited by Sigfred Peterson

Date Published: November 1977

OAK RIDGE NATIONAL LABORATORY
Oak Ridge, Tennessee 37830
operated by
UNION CARBIDE CORPORATION
for the
DEPARTMENT OF ENERGY

MARTIN MARIETTA ENERGY SYSTEMS LIBRARIES
3 4456 0049180 3

CONTENTS

SUMMARY . . . . . .

1. PRESTRESSED CONCRETE PRESSURE VESSEL DEVELOPMENT 1

1.1 INTRODUCTION 1

1.2 PCRV ANALYTICAL STUDIES 2

1.2.1 Analysis of Elastic Response 2

1.2.1.1 Description of the Ohbayashi-Gumi Test Vessel 2

1.2.1.2 Analysis of Ohbayashi-Gumi Multicavity Vessel 4

1.2.2 Analysis Methods Development 13

1.3 HEAD FAILURE STUDIES 15

1.3.1 Analytical Studies 18

1.3.2 Experimental Studies 18

1.4 INSTRUMENTATION EVALUATION AND DEVELOPMENT 22

1.4.1 Concrete Embedment Strain Instrumentation Evaluation 22

1.4.1.1 General Gage Performance Characteristics . 22

1.4.1.2 Gage Performance in Representative PCRV Environment 30

1.4.1.3 Gage Performance in Extreme Environments . 34

1.4.2 Acoustic Emission Study 38

1.5 CONCRETE STRUCTURAL MODEL TESTS 40

1.5.1 Background: Grouted and Nongrouted Tendons 41

1.5.2 Experimental Investigation 42

1.5.2.1 Structural Behavior 42

1.5.2.2 New Materials 49

1.5.2.3 Corrosion Behavior 52

1.5.2.4 Tendon Monitoring Techniques 55

1.6 LINER AND PENETRATION STUDIES 55

1.7 LONG-TERM CREEP AND MOISTURE MIGRATION STUDIES 65

1.8 REFERENCES 67

2. STRUCTURAL MATERIALS 69

2.1 INTRODUCTION 69

2.2 MECHANICAL PROPERTIES 69

2.2.1 Tensile Testing 69
2.2.2 Creep Testing 73
2.2.2.1 Environmental Test Facilities 73
2.2.2.2 Environmental Creep Tests 79
2.2.3 Low-Cycle Fatigue 88
2.2.3.1 Description of 2 1/4 Cr-1 Mo Steel Tested 89
2.2.3.2 Continuous Cycling Fatigue Behavior of 2 1/4 Cr-1 Mo Steel 94
2.2.3.3 Creep-Fatigue Behavior of 2 1/4 Cr-1 Mo Steel 99
2.2.3.4 Description of Hastelloy X 106
2.2.3.5 Continuous Cycling Fatigue Behavior of Hastelloy X 107
2.2.3.6 Creep-Fatigue Behavior of Hastelloy X . . 114
2.2.4 Crack Growth Studies 120
2.2.4.1 Hastelloy X 120
2.2.4.2 2 1/4 Cr-1 Mo Steel 123
2.3 WELDING DEVELOPMENT 133
2.3.1 Hot Cracking Tests 133
2.3.2 Hastelloy X and Dissimilar-Metal Weldment Studies . 136
2.4 STEAM CORROSION 140
2.4.1 Injection Loops 141
2.4.2 Inconel 617 Test Loop 142
2.4.3 The Heat-Transfer Corrosion Test Loop 144
2.5 REFERENCES 145
3. FISSION PRODUCT TECHNOLOGY 151
3.1 INTRODUCTION 151
3.2 FISSION PRODUCT RELEASE FROM COATED PARTICLE FUELS 151
3.2.1 Coated Failure Determinations 151
3.2.2 Fission Product Release During Irradiation 153
3.2.3 Cesium, Antimony, and Europium Release from Bare Kernels During Postirradiation Anneal Experiments . 155
3.2.4 Cesium Concentration Profiles in Pyrocarbon Coatings 156
3.3 FEASIBILITY STUDY OF THE DESIGN OF FUEL STABILITY AND FISSION PRODUCT RELEASE IN-REACTOR EXPERIMENTS 158

3.3.1 High-Temperature Materials 159
3.3.2 Temperature Measurement 159
3.3.3 Fuel Stability Irradiation Experiment 161
3.3.4 In-Reactor Studies of Fission Product Release from Intact Fuel Particles 162
3.4 FISSION PRODUCT SURVEILLANCE OF THE PEACH BOTTOM HTGR PRIMARY CIRCUIT 162
3.4.1 Surveillance of the Primary Duct 163
3.4.2 The Coolant Sampler Experiment 164
3.4.3 Measurement of Xenon and Krypton Levels 165
3.4.4 Primary System Dust Levels 166
3.5 POSTIRRADIATION EXAMINATION OF PEACH BOTTOM HTGR FUEL ELEMENTS 167
3.5.1 Physical Appearance and Dimensional Change of Fuel Element Components 168
3.5.2 Nuclide Inventories in Fuel Compacts 168
3.5.3 Axial Distribution of Fission Products in the Graphite Sleeve and Spine 172
3.5.4 Radial Distributions of Radionuclides in Graphite Fuel Element Components 176
3.6 REFERENCES 179
4. HTGR KERNEL MIGRATION AND IRRADIATED FUEL CHEMISTRY 181
4.1 INTRODUCTION 181
4.2 KERNEL MIGRATION STUDIES 181
4.3 GAS PRESSURE MEASUREMENTS 182
4.4 THE CHEMICAL BEHAVIOR OF HTGR FISSILE FUELS 182
4.5 LOSS OF UC_2 FROM WAR KERNELS 183
4.6 INTERACTION OF SiC WITH LANTHANIDE DICARBIDES 184
4.7 REFERENCES . . . . . .
5. COOLANT CHEMISTRY: THE STEAM-GRAPHITE REACTION 187
5.1 INTRODUCTION 187
5.2 ANALYSIS OF COOLANT IMPURITY COMPOSITION DATA OBTAINED DURING FORT ST. VRAIN HTGR START-UP 187
5.3 GAS TRANSPORT PROPERTIES OF HTGR GRAPHITES 190
5.3.1 Description of the Bulk Source Graphites 192
5.3.2 Procedures and Results 193
5.3.2.1 Porosity and Surface Area 193

5.3.2.2 Gas Transport Characterization 194
5.4 REFERENCES 198
6. HTGR FUEL QUALIFICATION 199
6.1 INTRODUCTION 199
6.2 FUEL PARTICLE PROCESS DEVELOPMENT AND QUALIFICATION . . . 199
6.2.1 Resin Kernel Property Control 200
6.2.2 Carbon Coating Development 203
6.3 FUEL ROD FABRICATION DEVELOPMENT AND QUALIFICATION 204
6.3.1 Studies of Quick-Cure Resin Materials 204
6.3.2 Determination of Low-Level Lithium in Graphite by Isotope Dilution Mass Spectrometry 206
6.4 CHARACTERIZATION OF PYROCARBON COATINGS 207
6.4.1 OPTAF Techniques 208
6.4.2 X-Ray Diffraction Determination of BAF 209
6.4.3 Permeability of Pyrocarbon Coatings 210
6.5 IRRADIATION TESTS IN THE HFIR TARGET FACILITY 216
6.5.1 Postirradiation Examination of HT-17, -18, -19 . . 216
6.5.2 Capsules HT-20 Through -23 221
6.5.3 Irradiation Experiments HT-28, -29, and -30 227
6.5.3.1 Operating History 227
6.5.3.2 Postirradiation Examination 229
6.5.3.3 Chlorine Leach Analysis 233
6.5.3.4 Fission-Gas Release Measurements on HT-30 Fuel Compacts 235
6.5.3.5 Permeability of LTI Coatings in HT-30 . . 239
6.5.3.6 Other Materials 240
6.5.4 Irradiation of Capsule HT-31 240
6.5.4.1 Description of Experiment 241
6.5.4.2 Operating Conditions 247
6.5.4.3 Postirradiation Examination 249
6.5.5 Irradiation Experiment HT-32 250
6.5.5.1 Description of Experiment and Operating Conditions 254
6.5.6 Capsule HT-33 257
6.5.6.1 Operating Conditions 259

6.5.6.2 Fabrication of Specimens 259
6.5.6.3 Postirradiation Examination 264
6.6 IRRADIATION TESTS IN HFIR REMOVABLE BERYLLIUM FACILITY . . 271
6.6.1 Capsules HRB-7 and -8 271
6.6.2 Capsules HRB-9 and -10 272
6.6.3 Capsules HRB-11 and -12 272
6.6.3.1 Capsule Design 273
6.6.3.2 Preparation of Test Specimens 276
6.6.3.3 Capsule Operation 283
6.6.3.4 Postirradiation Examination 287
6.6.4 Capsule HRB-13 289
6.6.4.1 Capsule Design 290
6.6.4.2 Preparation of Test Specimens 292
6.6.4.3 Capsule Operation 299
6.7 IRRADIATION TESTS IN THE ORR 299
6.7.1 OF-1 Capsule 299
6.7.2 Capsule OF-2 300
6.7.2.1 Capsule Operation 300
6.7.2.2 Postirradiation Examination 305
6.8 CAPSULE THERMOMETRY 309
6.8.1 Thermometer Development 309
6.8.1.1 Johnson Noise Power Thermometer Development 309
6.8.1.2 Development of Platinum-Base Thermocouples 313
6.8.1.3 Sensor Sheath Compatibility with Coated Fuel Particles 316
6.8.2 Thermometry in HRB Capsules 320
6.8.3 Thermometry in ORR Capsules 323
6.8.4 The Effect of Transmutation Alloying on the EMF of W-Re Thermocouples 323
6.9 NUCLEAR ANALYSIS IN SUPPORT OF IRRADIATIONS 325
6.9.1 HFIR Flux Map Experiment 326
6.9.1.1 Description of the Flux Capsules 327
6.9.1.2 Presentation of Results 327
6.9.1.3 Analysis of Results 327

6.9.1.4 Conclusions 334
6.9.1.5 Future Efforts 335
6.9.2 Sensitivity Study of HRB Neutronics Parameters . . 336
6.9.2.1 Results 336
6.9.2.2 Conclusions 336
6.9.2.3 Future Efforts 338
6.9.3 Development of a Coupled Neutron-Gamma Cross Section Library for Calculation of Nuclear Heating Rates 339
6.9.4 Performance of In-Core Nuclear Heating Instruments in the ORR 339
6.9.5 MONUHRIH Experiment (Measurement of Nuclear Heating Rates in the HFIR 344
6.9.5.1 Scope of the Experiment 344
6.9.5.2 Design Considerations 344
6.9.6 Status of OC-1 and OF-2 Analysis 345
6.10 POSTIRRADIATION PERFORMANCE ASSESSMENT 346
6.10.1 Thermal Analysis of Irradiation Capsules 347
6.10.2 Microprobe Analysis of WAR Particles 347
6.10.3 Irradiated-Microsphere Gamma Analyzer 351
6.10.4 Defective Particle Fraction Measurement 358
6.10.5 Burnup Analysis of HTGR Fuel Particles 358
6.10.6 Fuel Rod Deconsolidation 359
6.11 REFERENCES 369
7. CHARACTERIZATION AND STANDARDIZATION OF GRAPHITE 373
7.2 INTRODUCTION 373
7.2.1 Experiment Design 373
7.2.2 Capsule Operation and Initial Results 377
7.2.3 Summary 377
7.2.4 Specimen Temperature Control 379
7.2.5 Movable Thermocouples Operation and Use 381
7.2.6 Fixed Thermocouples 383
7.2.7 Heaters 383
7.2.8 Pressure Systems 384
7.2.9 Linear Variable Differential Transformer Load Cell Transducers 384

7.2.10 Computer Operation 385
7.2.11 Postirradiation Examination 385
7.3 RESULTS FROM CAPSULE OC-1 — GRAPHITE SPECIMENS EVALUATION 390
7.3.1 Specimen Material Evaluation 390
7.3.2 Examination of Creep Specimens 390
7.3.3 Dimensional Changes 390
7.3.4 Elastic Properties 398
7.3.5 Electrical Resistivity 399
7.3.6 Coefficient of Thermal Expansion 401
7.3.7 Discussion 402
7.4 STATUS OF FUTURE GRAPHITE CREEP EXPERIMENTS 403
7.5 REFERENCES 404

SUMMARY

1. PRESTRESSED CONCRETE PRESSURE VESSEL DEVELOPMENT

Analyses of elastic response of a Japanese PCRV model have been conducted to verify capability to analyze a large multicavity PCRV designed for a commercial HTGR power plant. Results obtained using the NØNSAP and STATIC SAP three-dimensional finite element codes demonstrated the need for using a code such as STATIC SAP having an out-of-core solution routine that permitted modeling of the full depth vertical section of the vessel using higher order 20-node elements.

Constitutive laws were developed at Northwestern University using the endochronic theory to accurately describe concrete stress versus strain relationships and modes of failure. The resulting equations, which are intended for use in three-dimensional finite element codes, were verified in part by comparing calculated results with published data for reinforced concrete structural members.

At the University of Illinois, ten small-scale pressure vessels were pressurized to failure to provide understanding of the effects of inside-diameter-to-head-depth ratios, head penetration arrangements, and concrete strengths on head failure. An interactive computer program, ISA, based on a linear axisymmetric model was developed for eventual expansion to include nonlinear analysis options and predictions of crack development in vessel heads. A three-dimensional code, FINITE, was used to confirm capability of modified axisymmetric analytical models to determine strains in the vicinity of penetrations. The vessel tests showed that the failure mechanism is a function of head diameter-to-depth ratio and size of penetrations. The penetrations also affect mode of failure.

Experimental studies are being conducted at ORNL to evaluate long-term stability and overall performance of representative commercial concrete embedment strain gages under environments simulating PCRV operating conditions as well as possibly more severe environments. The gages are monitored periodically while immersed in water baths and while embedded in concrete cylinders of various sizes both at room temperature and at elevated temperatures. The potentials of acoustic emission systems for monitoring PCRV structural components are also being investigated.

Post-tensioned concrete flexural elements are being tested to demonstrate the structural advantages of grouted tendons over nongrouted tendons. Studies are also being conducted to evaluate corrosion protection, new materials for tendon grouting and structural applications, and tendon monitoring techniques.

The fracture toughness properties of representative PCRV liner and forging materials are being obtained on Charpy V-notch specimens. Instrumented precracked Charpy specimens are tested under impact and

slow-bend conditions. These specimens are obtained from various locations within forgings to evaluate effects of quenched edges and orientation. Compact tensile specimen tests have also been performed on both forging and plate materials.

The final reports of the concrete creep tests conducted at the University of Texas and U.S. Army Engineers Waterways Experiment Station (WES) have been published. The WES study involved concretes having three different moduli of elasticity, while the University of Texas study was a more extensive investigation of a single widely used limestone aggregate concrete.

2. STRUCTURAL MATERIALS

The principal objective of the structural materials program is to provide the data base for construction of high-temperature components of an HTGR. Mechanical properties studies are being conducted in prototypical helium environments. In addition, steam corrosion, weldability, and structural stability are being studied on the principal high-temperature materials in the primary circuit and the steam generator.

Tensile tests were conducted in air on Inconel 617 up to 982°C. Above 593°C ultimate tensile strength and ductility decreased rapidly. Yield strength decreased rapidly above 816°C.

Significant modifications were made in the helium gas analysis system to improve the accuracy of impurity monitoring.

No significant differences in the stress-rupture behavior in air and helium have been found for 2 1/4 Cr-1 Mo steel under the temperature-stress-time conditions tested thus far. In helium the rate of attack at 593°C decreased with increasing time. The behavior of Hastelloy X in air and helium was similar at temperatures of 760°C or lower.

Fatigue testing of 2 1/4 Cr-1 Mo steel and Hastelloy X in air has been conducted from room temperature to 593 and 871°C, respectively. Under the test conditions components of total strain range can be expressed as a power function of the cycles to failure. Heat-to-heat variations in the continuous cycling behavior of 2 1/4 Cr-1 Mo steel suggest that dynamic strain aging may be a factor in fatigue behavior. Tensile or compressive hold periods decreased the fatigue life (cycles to failure) of both materials. Compressive hold periods were the more damaging. The strain range partitioning method was used to analyze the creep fatigue data generated thus far. An environmental chamber for fatigue testing in helium and vacuum has been designed and constructed.

The crack growth behavior of 2 1/4 Cr-1 Mo steel and Hastelloy X is being investigated. The effects of stress intensity, temperature, frequency, environment, thermal aging, and heat-to-heat variations on the behavior of 2 1/4 Cr-1 Mo steel were studied. At temperatures

above 510°C crack growth rate increased with decreasing test frequency. At 510 and 593°C the crack growth rate was significantly lower in helium and steam compared with air, but it was higher than in vacuum. In tests from room temperature to 649°C no difference in crack growth rate of Hastelloy X was observed in HTGR helium compared with air. Crack growth rate increased with increasing temperature.

Welding development studies were conducted to investigate the weldability and metallurgical stability of Hastelloy X similar- and dissimilar-metal joints. Two heats of Hastelloy X showed different susceptibilities to hot cracking as measured by the spot Varestraint test. In thermal stability studies weldments were found to exhibit significant losses in ductility after aging at 649, 700, and 871°C.

The corrosion behavior of selected steam generator materials is being investigated in test facilities at the Florida Power Corporation. Constant-stress specimens of 2 1/4 Cr-1 Mo steel, 9 Cr-1 Mo steel, alloy 800, types 304 and 304L stainless steel, Inconel 600, and Inconel 625 exposed to steam containing chloride additions showed no tendency toward stress-corrosion cracking. Specimens have been exposed to pure superheated steam at 482 and 538°C in an Inconel 617 loop for 5000 hr. Corrosion product scales on the specimens appear to be adherent, and weight increases in the specimens show a near-parabolic relation with time. Tests of 2 1/4 Cr-1 Mo steel exposed to superheated steam at 510 and 541°C under heat flux conditions indicate an increased rate of attack compared with isothermal test conditions. Cracking and porosity of the oxide were noted after 500 hr, and exfoliation of the oxide began after 2000 hr.

3. FISSION PRODUCT TECHNOLOGY

Coating failure characteristics and fission product releases from whole particles and bare kernels were determined for Biso-coated ThO_2 particles that were irradiated in the HT-12 through -15 capsule experiment. The coating failure studies showed that visual inspection is inadequate for determining coating integrity. That hot chlorine leaching and consequent measurement of leached cesium, cerium, or thorium may be used as an accurate measure of failed particle fraction was found by comparing leach results with internal gas pressure measurements on a series of particles.

Fission product losses during irradiation were determined by comparing the average amounts of fission products in the coated particles, as measured by gamma-ray spectroscopy after irradiation, with the corresponding calculated inventories. Loss of cesium was insignificant to a burnup of about 2% FIMA at either 1200 or 1500°C. At 1200°C, no loss is apparent until a burnup of 4.5% FIMA is exceeded. At 1500°C, the release of up to 20% cesium at 6% FIMA indicates that losses occur earlier at the higher temperature and increase with burnup, as would be expected.

Fission product release from bare ThO_2 kernels was determined in annealing experiments conducted at 1400°C. Fractional release rates of ^{125}Sb, ^{154}Eu, and ^{137}Cs were determined, the latter being used for estimation of the effective diffusion coefficient of cesium in the kernel material. Diffusivities of cesium in ThO_2 ranging from 1.9×10^{-19} to 9.1×10^{-23} m^2/s were observed in a series of eight determinations.

A series of measurements regarding the distribution and levels of radioactivity in the primary circuit of the Peach Bottom HTGR was undertaken throughout the course of Core 2 operation, from July 1970 to final shutdown in October 1974. Four types of observation were conducted in this phase of the Peach Bottom Surveillance Program: (1) the cold duct of the primary circuit was scanned axially for gamma-emitting nuclides on four occasions, the last soon after final shutdown; (2) the primary coolant was sampled upstream and downstream from the steam generator through diffusion tubes and filters to differentitate between gaseous and particulate-borne activity; (3) the primary coolant and fuel element purge flow were sampled for fission gas measurement; and (4) dust samples collected by use of the cyclone separators in the primary loops were examined for size distribution, chemical makeup, and contained activity.

A series of six Peach Bottom driver fuel elements are being examined: these include one element that had experienced 384 equivalent full power days (EFPD) of operation, one irradiated to 700 EFPDs, and four end-of-life elements experiencing 900 EFPDs service in the Peach Bottom HTGR second core. Of these, the examinations of first two elements and one end-of-life element are complete.

Inventories of the radionuclides ^{95}Zr, ^{103}Ru, ^{106}Ru, ^{110m}Ag, ^{125}Sb, ^{134}Cs, ^{137}Cs, ^{141}Ce, ^{144}Ce, ^{154}Eu, and ^{233}Pa in each of the 30 fuel compacts at end of life are obtained as a part of the postirradiation examination. Inspection of these inventory distributions indicates that some elements, such as cesium and europium, may show gross shifts in axial location, while others, such as zirconium and cerium, seem fixed in location.

4. HTGR KERNEL MIGRATION AND IRRADIATED FUEL CHEMISTRY

A theoretical analysis of in-reactor kernel migration data indicates that a solid-state diffusion process controls the migration rate in particles containing $Th_{0.84}U_{0.16}C_2$, UO_2, ThO_2, PuO_{2-x}, or $Th_{0.8}U_{0.2}O_2$ fuel kernels. Moreover, results obtained in laboratory tests are consistent with data obtained from in-reactor experiments. Measurements of gas pressure in irradiated ThO_2 and $Th_{0.81}U_{0.19}O_2$ fuel particles yielded data that could be described by the relation $O/f = 74.6F \exp(-7400/T)$, where O/f is the moles of oxygen (as CO) released per mole of fissioned actinide, F is fractional fissions per initial heavy-metal atom, and T is the equilibration temperature. The equation is applicable over the temperature range 1325–2270 K.

At 1900°C, Biso-coated weak-acid-resin UC_2 and UC_2-UO_2 kernels lost a significant amount of uranium over a several hundred hour period. The rate of escape of the uranium depends upon temperature and surface area of the kernel. However, calculations indicate that this phenomenon is unimportant at current HTGR design temperatures.

5. COOLANT CHEMISTRY: THE STEAM-GRAPHITE REACTION

Comparisons of measured coolant gas compositions during rise to power in the Fort St. Vrain HTGR with values predicted by the computational program GOP (Graphite Oxidation Program) indicate that radiolytic processes rather than thermally induced reactions are controlling the system at core outlet temperatures below 500°C. However, at the 19.5 and 27% power levels, corresponding to core outlet temperatures of 450 and 500°C, respectively, GOP appears to be overestimating the rates of the radiolytic processes.

Gas flow characterization parameters were determined for samples of ATJ and Stackpole 2020 graphites. Although ATJ is about 10 times as permeable to gases (under forced flow) as Stackpole 2020, the porosity-tortuosity ratios of the two graphites are sensibly identical.

6. HTGR FUEL QUALIFICATION

Fuel Particle Process Development and Qualification

Studies on resin kernel conversion and control of stoichiometry for uranium oxide-carbide were completed and a topical report was issued. The effect of oxygen and chloride ion on weak-acid-resin kernels was studied because both species are known to alter the course of polymer carbonization. The coating process was reviewed in view of the increased heavy metal loading required to achieve higher conversion ratios. In particular, acetylene-produced buffer layers are known to have high standard deviations in thickness and to be difficult to handle because of soot formation. Studies were initiated using MAPP gas in an attempt to produce high-density, highly reproducible buffer layers. Studies were also initiated to react the thoria kernel with the buffer layer to produce both the required void volume and a reduced oxygen potential within the kernel. This approach appears promising.

Fuel Rod Fabrication Development and Qualification

Early in the reporting period a small effort on development of thermosetting resins was initiated. This work sought an alternative to in-block carbonization of fuel rods because of the complexity of the in-block carbonization process and because of the inability to inspect and characterize the rods after carbonization. The thermosetting resin program was terminated in July 1976 without finding a suitable material or process. The work was terminated because of insufficient funding and a change in program guidance.

An analytical technique for low concentrations of lithium in graphite was developed. It uses a mass spectrometric comparison of normal lithium to a ^{6}Li spike, and can detect levels below 1 ppm. Apparently lithium exists in nuclear graphite at levels below 5 ppb and thus does not contribute significant tritium to the reactor system.

Characterization of Pyrocarbon Coatings

Work on the ORNL OPTAF equipment was abandoned because of the rapid progress at General Atomic with the Synchronous Micro-Polarimeter. The GA device uses the same measurement technique as the ORNL system but avoids the problem of sample rotation by rotating the plane of polarization of the incident light ray. The most significant accomplishment of the ORNL OPTAF work was recognition of sample polishing as a large source of error, which always leads to too high a value of the anisotropy. Work continued during the reporting period to develop a direct x-ray determination of the anisotropy (BAF) as a means of avoiding the polishing of specimens entirely.

Recent awareness that Biso particles can become permeable during irradiation has prompted considerable effort to determine permeability of coatings and its relationship to microstructure. A technique is being developed at ORNL to compare the flow of helium and neon through the LTI and into the buffer layer and kernel at high temperatures and fixed times. The most interesting result to date is that the flow does not obey gas laws but is an activated process with relatively high activation energies. Work is continuing to evaluate coating permeability both before and after irradiation, and to identify the mechanisms involved.

Irradiation Tests in HFIR Target Facility

Data on capsules HT-17 through -19 were analyzed. These capsules were designed to test the influence of different coating conditions on the irradiation performance of Biso particles. Postirradiation examination (PIE) also progressed on capsules HT-20 through -23, which contained specimens for measurement of the influence of irradiation on physical properties of fuel rods. The fuel rods contained unfueled particles so that thermal conductivity and thermal expansion after irradiation could be measured in conventional equipment. Several fuel rods were broken during disassembly of the HT-20 through -23 capsules, and replacement rods were irradiated in capsules HT-31 and -32. Capsule HT-33 contained only General Atomic fuel, although some ORNL experiments were conducted in driver rods. On capsules HT-28 through -30 PIE was done during the reporting period but not completed. These capsules were designed to test the influence on irradiation performance of subtle microstructural changes due to slight variations in coating conditions.

Irradiation Tests in HFIR Removable Beryllium Facility

Final reports were prepared on HFIR Capsules HRB-7 through -10. Capsule HRB-11 was being examined at the end of the reporting period, and capsules HRB-12 and -13 were in reactor. The HRB-7 and -8 capsules were designed as a comprehensive test of mixed thorium-uranium oxide

fissile particles for HTGR recycle application. In addition, testing of weak-acid-resin-derived (WAR) fissile particles as a potential backup fissile particle for HTGR recycle was also included in the capsule objectives. This was the first systematic test of the WAR fissile fuel. Several other minor objectives were also accomplished in HRB-7 and -8. The two capsules were designed identically; HRB-8 was operated at a design fuel centerline temperature of 1250°C and HRB-7 at 1500°C.

Capsules HRB-9 and -10 were designed to test the influence of initial O/U ratio on the performance of WAR fissile kernels. Kernels with conversion levels of 0% (WAR UO_2), 15%, 50%, 75%, and 100% (WAR UC_2) were compared. The partially converted kernels performed better than WAR UO_2 or WAR UC_2. A WAR UC_xN_y kernel was also tested, and it performed poorly. As with HRB-7 and -8, the capsules were designed identically, with HRB-9 operating at a design fuel centerline temperature of 1250°C and HRB-10 at 1500°C.

The HRB-7 through -10 experience revealed that testing of identical capsules at two operating temperatures was providing no more information on relative performance of candidate HTGR fuels than testing at one temperature would have provided. Therefore, the use of identically designed capsules operated at 1250 and 1500°C was abandoned. The next two capsules in the HRB series (HRB-11 and -12) were operated at a design fuel centerline temperature of 1300°C and contained different fuel specimens in support of seven overall objectives for the two capsules. The objectives are the following: (1) extend the study of WAR kernel performance as a function of initial O/U ratio, (2) obtain performance data on a second resin material, (3) study the influence of buffer layer thickness on fissile particle performance, (4) study the influence of SiC layer deposition rate on fission product retention in fissile particles, (5) compare the performance of fuel coated in the 0.13-m coating furnace with a frit gas distributor with that produced with a conical gas distributor, (6) test GA fuel fabricated with thermosetting matrix materials, and (7) test ZrC-coated particles fabricated by LASL. At the end of the reporting period HRB-11 was being examined, and HRB-12 was still in reactor.

The HRB-13 experiment was designed primarily to test the kernel shape specification for recycle fuel. The specific objectives are: (1) determine the extent to which small satellites attached to Amberlite IRC-72 resin influence irradiation performance, (2) determine the influence of numerous satellites attached to IRC-72 resin on irradiation performance, (3) obtain irradiation performance data on irregularly shaped fuel kernels or clusters of small fuel particles derived from IRC-72 resin, (4) determine the influence of slight eccentricity of fuel kernels derived from Duolite C-464 resin, (5) evaluate the importance of gross eccentricity of C-464 resin kernels relative to irradiation performance, and (6) determine the influence of very irregular shapes on irradiation performance of C-464 resin kernels. This capsule was in the reactor at the end of the reporting period.

Irradiation Tests in the ORR

Work on two OF-type capsules was accomplished during the reporting period. At the end of the reporting period a final report on the OF-1 capsule had been completed and was being reviewed. Postirradiation examination was in progress on the OF-2 capsule.

The OF-2 capsule had a number of objectives: (1) test fissile and fertile fuel fabricated in the 0.13-m-diam coating furnace, (2) continue testing the matrix-particle interaction phenomenon, (3) determine the influence on performance of coating microstructure, which is in turn influenced by numerous coating parameters, (4) determine the influence of kernel stoichiometry and density on irradiation performance, (5) verify the adequate performance of fissile fuel that would later be irradiated in the Fort St. Vrain Reactor, (6) compare the performance of fuels fabricated in the 0.13-m coating furnace using a frit gas distribution system with the performance of fuels fabricated in the same furnace with a conical gas distributor, and (7) determine the removability of fuel rods from the graphite holder after full-life irradiation, particularly for in-block carbonized rods.

On the basis of the OF-2 experience the batch of particles fabricated with the conical gas distributor (0.13-m-diam coating furnace) was eliminated from the test matirx for the FSVR Test Element Program.

Capsule Thermometry

The performance of fuel centerline thermometers in Capsules HRB-9 through -12 and OF-2 is reviewed. The Johnson Noise Thermometer was marginally successful. It operated in HRB-9 for most of the irradiation, and then failed at the beginning of the last cycle of irradiation. Interference from external electrical noise and from irradiation effects on cable insulators influenced accuracy, as did transmutation from rhenium to osmium in the temperature sensing element. Performance of the JNT in HRB-10 was even less successful. In addition to the problems encountered in HRB-9 there was the additional problem of a chemical reaction between the fuel rods and the Mo-Re sheath.

In HRB-11 a platinum-molybdenum thermocouple was used. This thermocouple exhibited progressive degradation of the loop resistance, and the indicated temperature was about 200°C low at the end of the irradiation, based on in-pool thermocouple calibration measurements. This thermocouple was wrapped in rhenium foil, which reacted severely with the fuel.

In HRB-12 a dual-element JNT was used. Large nonthermal noises from the HFIR water pumps introduced considerable error. The errors were several hundred degrees Celsius above the calculated fuel centerline temperatures. Both rhenium resistors failed at the beginning of the eighth cycle of irradiation. As a result of the poor performance of JNTs in HRB-9, -10, and -12, these temperature sensors are no longer considered for use in future HRB capsules.

In OF-2 two platinum-molybdenum thermocouples were used, with the same compositions as the thermocouple used in HRB-11. In OF-2 the couple performed very well. The measured temperatures agreed well with calculated temperatures (indicating little decalibration) and the platinum sheaths showed moderate grain growth, but there was no evidence of swelling, intergranular rupture, or reaction with the graphite.

Nuclear Analysis in Support of Irradiations

The areas of work reported include: (1) flux mapping experiments, (2) neutronic parameter study, (3) gamma heating rate experiments with GAFI (GAmma and FIssion calorimeter), (4) neutron-gamma cross section library compilations, (5) capsule design for measurement of heating rates in RB and VXF facilities and (6) retrieval and analysis of OF-2 flux monitors.

During FY 1976 the beryllium reflector of the HFIR was replaced, and it was important to determine whether the neutron fluxes had been changed. The flux map experiment determined that there was no change, a very important result because of the need to compare results from capsules irradiated before and after the change in reflector.

With the HRB-7 and -8 capsules, which included tests of fully enriched fissile particles, it was necessary to "preirradiate" the fuel in the VXF-13 facility, where the thermal fluxes are about half the RB facility levels. The purpose of the "preirradiation" is to burn out about half the ^{235}U before operation in the RB facility, and thus avoid excessive power generation rates in the coated fissile particles. The irradiation conditions in the VXF-13 facility are not well known. The neutron fluxes are not as well known as the PB facility fluxes, and the gamma heating characteristics are unknown. Characterization of the VXF-13 facility was an important activity during the reporting period.

Postirradiation Performance Assessment

Work in the area of performance assessment includes: (1) thermal analysis of irradiation capsules, (2) microprobe analysis of irradiated fuels, (3) development of the IMGA system (irradiated microsphere gamma analyzer), (4) chlorine leaching analysis for measurement of defective particle fraction, (5) burnup analyses, and (6) fuel rod deconsolidation.

Very little work was done on thermal analysis. The techniques and computer codes were fully developed at the beginning of the reporting period and were applied in a production mode during the year to analyze specific irradiation capsules. Extensive work was done during the reporting period on microprobe analysis of WAR fissile fuels. Fission product distributions within the coated particles were determined as a function of initial kernel composition. This work has been extremely useful in interpreting the irradiation behavior of the WAR fuel.

Development work on the IMGA system was completed during the reporting period. This device was developed to measure fission product inventories in individual coated particles and to permit statistically accurate determinations of failed particle fractions. The system is now installed in the ORNL hot cells and is being used for post-irradiation examination of capsule irradiation experiments. Work on chlorine leaching and burnup measurements continued during the reporting period. Development work in both areas is essentially complete, and the techniques are being applied on a routine basis during PIE.

Electrolytic disintegration of HTGR fuel rods is part of the procedure for IMGA analysis. The rods are deconsolidated to recover the individual coated particles. During the reporting period the deconsolidation processes were developed; they are now being applied routinely.

7. CHARACTERIZATION AND STANDARDIZATION OF GRAPHITE

The graphite irradiation creep experiment OC-1 operated successfully in the ORR. The capsule operated at 900°C for 1140 hr at 30-MW reactor power to a peak fluence of 1.1×10^{25} n/m^2 (equivalent fission fluence). The specimens were removed and examined to determine the effect of compressive creep strain on the physical properties. The creep characteristics are in good agreement with the literature; however, the creep deformation caused significant alterations in the physical properties of the graphites. The coefficient of thermal expansion was increased, the moduli and Poisson's ratio were both reduced, while the electrical conductivity was unchanged by the creep strain. These results indicate core structure regions with high shutdown thermal stresses should be reexamined.

1. PRESTRESSED CONCRETE PRESSURE VESSEL DEVELOPMENT

J. P. Callahan

1.1 INTRODUCTION

The prestressed concrete reactor vessel (PCRV) research and development efforts at ORNL are directed towards analysis, structural behavior, and materials properties for the basic elements of these vessels consisting primarily of concrete, liner, and prestressing tendons. The Program is divided into the following eight technical task areas:

1. analysis methods,
2. head failure,
3. concrete properties in nuclear environments,
4. long-term concrete creep and moisture migration,
5. prestressing tendons,
6. liners and penetrations,
7. instrumentation,
8. structural models.

Sections 1.2 through 1.7 summarize the accomplishments during the present reporting period under the various task areas. Included are discussions of analytical elastic response studies of a multicavity PCRV model, a constitutive equation for describing nonlinear response of concrete, model studies of the influence of penetrations on PCRV head failures, calibration and performance tests of concrete embedment strain gages, structural model studies of grouted and nongrouted tendon systems, and fracture toughness tests of liner and forging materials. The final reports for the two investigations of concrete creep behavior that were published during the present reporting period are also described.

In formulating the various studies undertaken under this program, every effort has been made to ensure that the work addresses problems relevant to the ongoing development of PCRVs for commercial HTGRs and

that the resulting information will be in a form useful both for design and for providing technical support for development of understanding and acceptance of PCRVs.

1.2 PCRV ANALYTICAL STUDIES

1.2.1 Analysis of Elastic Response — D. N. Fanning

A three-dimensional finite element analysis of a commercial HTGR is to be made with a finite element code. The analysis is preceded by an evaluation of candidate computer codes using comparisons of experimental data with analytical results for the Ohbayashi-Gumi multicavity PCRV model. The Ohbayashi-Gumi vessel was chosen as our basis for comparison because of its geometrical similarity to the large multicavity PCRV and the anticipated availability of a complete set of the original experimental data. Although we were unable to obtain a copy of the original data, sufficient data have been published in the open literature[1] to permit limited but meaningful comparisons. The three-dimensional finite element codes NONSAP and STATIC-SAP were employed for the analysis of the Ohbayashi-Gumi vessel.

1.2.1.1 Description of the Ohbayashi-Gumi Test Vessel

The Ohbayashi-Gumi multicavity test vessel shown in Figs. 1.1 and 1.2 is a 1/20 scale model of a 1000-MW(e) HTGR. It has six steam generator cavities arranged symmetrically about the central cavity as shown in Sect. A and C of Figs. 1.1 and 1.2. A star-like support structure (Sect. D of Figs. 1.1 and 1.2) was connected rigidly beneath the bottom slab. The concrete had an ultimate strength of 44.6 MPa (6500 psi). A 2.3-mm-thick (0.09-in.) liner served as the pressure boundary. Vertical prestressing was applied by 60 axial tendons. Circumferential prestressing was applied by winding wire under tension around the outside of the vessel. The vessel was instrumented with embedded-type gages for measuring concrete strains.

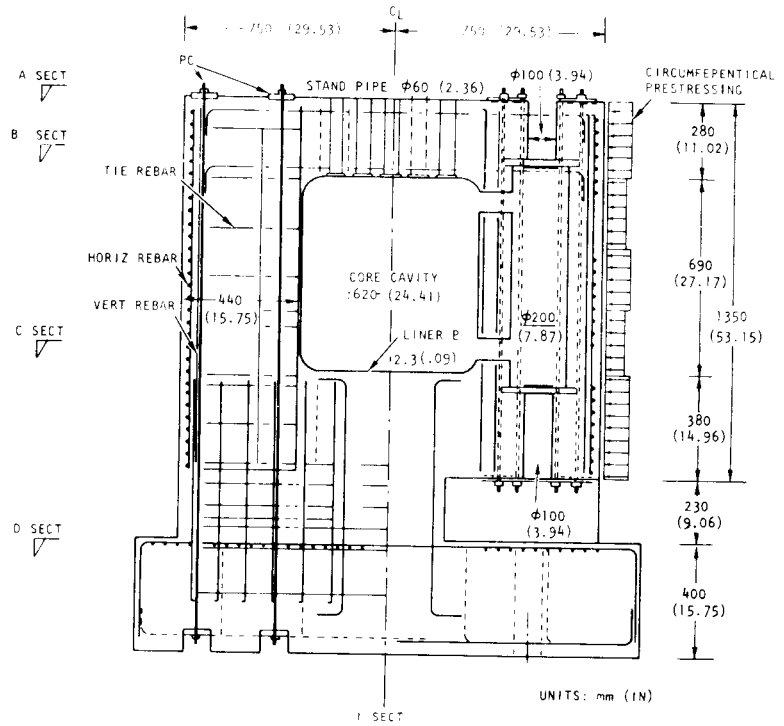

Fig. 1.1. Vertical Section of the 1/20th Scale Ohbayashi-Gumi PCRV Model. From K. C. Cheung, GA-A-12821-A (October 1975).

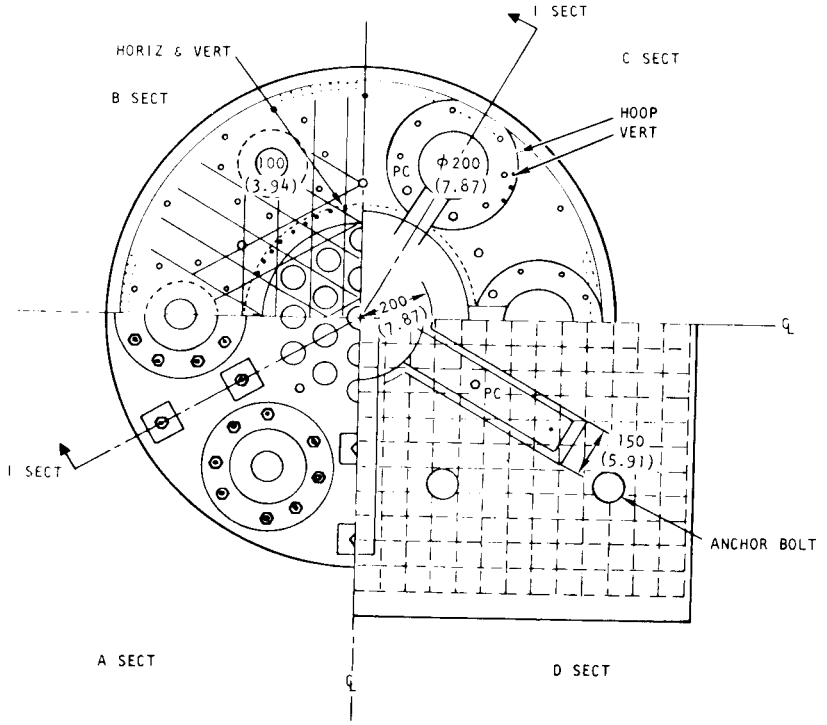

Fig. 1.2. Cross Sections of the 1/20th Scale Ohbayashi-Gumi PCRV Model. From K. C. Cheung, GA-A-12821-A (October 1975).

1.2.1.2 Analysis of Ohbayashi-Gumi Multicavity Vessel

The first analytical model of the Ohbayashi-Gumi vessel was generated by use of 20-node elements for the NONSAP code. This particular type of element was selected since it offers advantages in modeling curved boundaries such as the vessel outer wall and also for economic reasons. Since the edges of the 20-node element are described quadratically fewer elements are required to represent curved surfaces than when linear elements are employed. The in-core solution routine of NONSAP severely limited the number of elements that could be used, forcing the omission of the steel closures and bearing pads. Figure 1.3 shows the resulting analytical model. Curved edges of the elements are represented in the figure by two straight lines. The analytical model consists of a 30° sector of the vessel region above midheight of the reactor cavity. The midheight symmetry assumed for this model represents an approximation of the actual vessel since the bottom head of the actual vessel is one-third thicker than the top head and is further stiffened by the support structure.

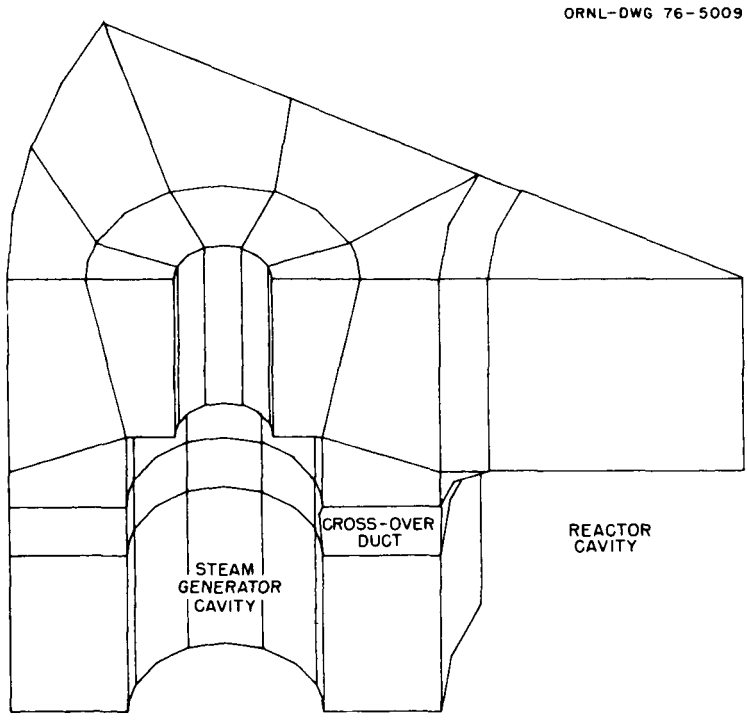

Fig. 1.3. Initial Finite Element Representation of the Ohbayashi-Gumi PCRV Model.

The analytical results and the experimental data are compared for three loads: (1) vertical prestressing, (2) circumferential prestressing, and (3) operating pressure of 4.9 MPa (711 psi). The comparisons are presented in Fig. 1.4 for the vertical cross section midway between steam generator cavities (left half of Sect. I of Fig. 1.1).

The calculated axial strains due to vertical prestressing shown in Fig. 1.4(a) are slightly larger than the corresponding experimental values. This discrepancy is likely due to the use of too small a modulus of elasticity or too large a value of prestressing for the analytical calculations. Good agreement relative to the experimental data is shown in Fig. 1.4(b) for the calculated radial strains due to the circumferential prestress. The hoop strains produced by the circumferential prestressing are presented in Fig. 1.4(c). The analysis agrees fairly well with the experimental results except in the wall of the vessel near the reactor cavity, where the analytical results are approximately double the experimental results. The correctness of the experimental data is questionable, however, since the hoop strains measured in the walls between steam generator cavities are larger than the strains in the wall sections where the concrete is continuous in the hoop direction. The radial strains due to internal pressure are presented in Fig. 1.4(d). The agreement between the experimental values and the analytical values is reasonable. The comparison between the experimental and analytical values for hoop strain due to pressure is not good [see Fig. 1.4(e)]. In general, the analytical values are about 50×10^{-6} greater in tension than the experimental values. Unfortunately the gages are not located in the regions of highest strain.

In an attempt to assess the magnitude of error introduced by failure to model the steel closures and bearing pads, we included these features in a second analytical model for the NONSAP code. As with the first analytical model, only the portion of the vessel above midheight of the reactor cavity was modeled (see Fig. 1.5). The greater geometric detail of this model, as compared with the first model, prevented the use of 20-node elements. Eight-node elements were used to model most of the vessel; midside nodes were added where the geometry of the vessel

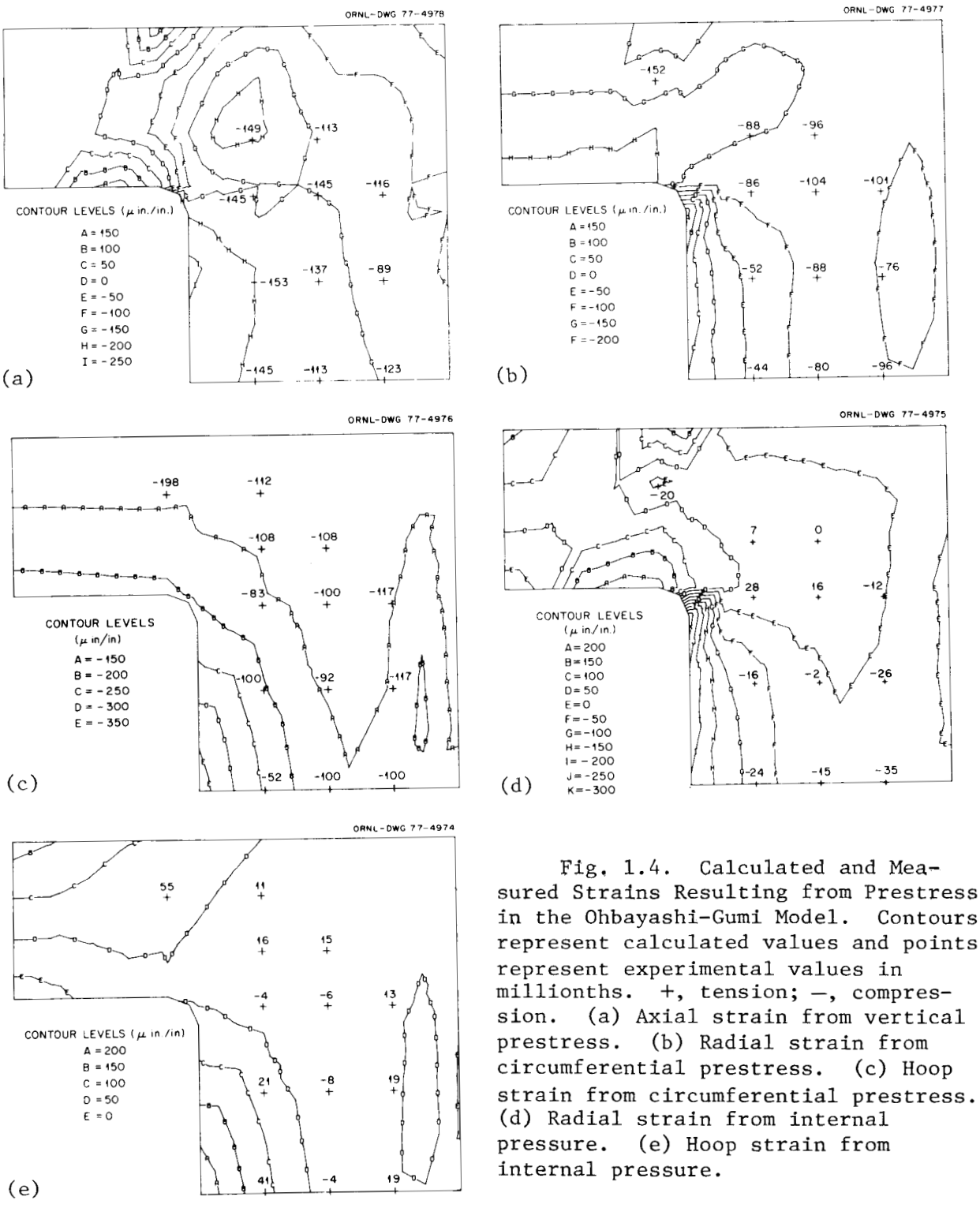

Fig. 1.4. Calculated and Measured Strains Resulting from Prestress in the Ohbayashi-Gumi Model. Contours represent calculated values and points represent experimental values in millionths. +, tension; —, compression. (a) Axial strain from vertical prestress. (b) Radial strain from circumferential prestress. (c) Hoop strain from circumferential prestress. (d) Radial strain from internal pressure. (e) Hoop strain from internal pressure.

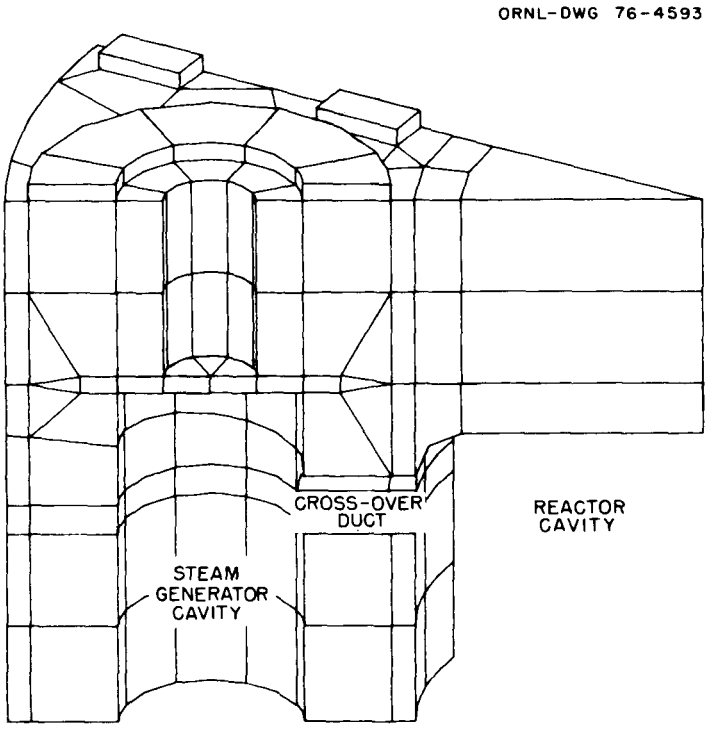

Fig. 1.5. Second Finite Element Representation of the Ohbayashi-Gumi PCRV Model.

required curved edges. The use of the lower order elements was dictated by limitations imposed by the NONSAP in-core solution routine. The results of the second analysis are presented in Fig. 1.6.

In Fig. 1.6(a) the contour lines showing calculated axial strains due to vertical prestressing differ appreciably from those of the first analysis [Fig. 1.4(a)]. This is particularly evident in the top slab region and at the haunch. However, there is little significant difference between the results for the two analyses in the instrumented region of the vessel wall.

In the case of the radial strains due to circumferential prestress, model 1 [Fig. 1.4(b)] exhibited a much higher concentration at the haunch than model 2 [Fig. 1.6(b)]. This difference can be explained by characteristics of the elements employed in the two analytical models. The higher order 20-node element used for the first analysis is more capable of identifying regions subjected to steep strain gradients than is the eight-node element used for the second analysis.

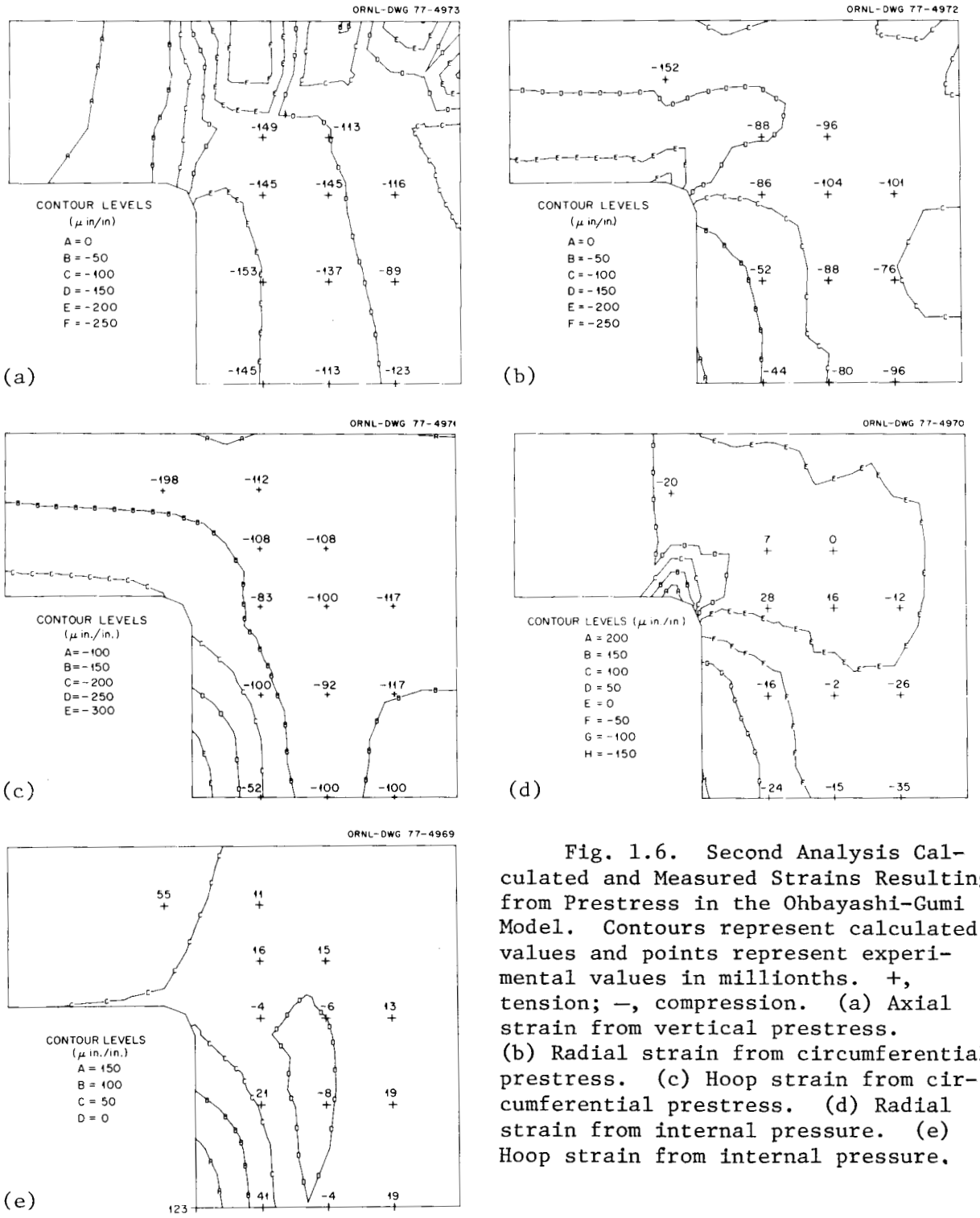

Fig. 1.6. Second Analysis Calculated and Measured Strains Resulting from Prestress in the Ohbayashi-Gumi Model. Contours represent calculated values and points represent experimental values in millionths. +, tension; —, compression. (a) Axial strain from vertical prestress. (b) Radial strain from circumferential prestress. (c) Hoop strain from circumferential prestress. (d) Radial strain from internal pressure. (e) Hoop strain from internal pressure.

The contour lines for hoop strain due to circumferential prestressing shown in Fig. 1.6(c) for the second analysis are essentially identical with those of the first model [Fig. 1.4(c)]. The same differences in stress concentrations previously discussed with respect to radial strains resulting from circumferential prestress can be seen when comparing the radial strains due to internal pressure for the first [Fig. 1.4(d)] and second [Fig. 1.6(d)] analyses; however, the values in the instrumented region of the vessel for the two analyses give virtually the same values. In both analyses, the central portion of the top slab has a tensile radial strain but, whereas Fig. 1.4(d) shows a linear variation in strain through the thickness of the slab, Fig. 1.6(d) indicates a constant strain through the thickness. This is probably related to the fact that 20-node elements used in model 1 can accommodate linear strains while the eight-node elements of model 2 can have only constant strains on any given edge. The only case where model 2 appears to be clearly superior to model 1 is the hoop strain due to pressure. The results for model 2 [Fig. 1.6(e)] show a compressive hoop strain in the wall of the vessel between steam generator cavities as do the experimental data; model 1 [Fig. 1.4(e)] showed no compressive strains in this region.

The results of the Ohbayashi-Gumi multicavity PCRV model analytical studies conducted thus far with NONSAP have indicated that the geometric representations used in the analytical model were too crude to accurately represent the actual physical model. Consequently, the three-dimensional finite element code STATIC-SAP was used to conduct a final analysis of the Ohbayashi-Gumi model before analyzing the proposed multicavity PCRV for a commercial HTGR. STATIC-SAP has an out-of-core solution routine that enables it to accommodate a much larger problem than NONSAP. The finite element model of the Ohbayashi-Gumi vessel developed for use with STATIC-SAP is shown in Fig. 1.7. It represents a 30° sector of the vessel as did the previous models, but it also models the full height, thereby eliminating the previous assumption of midheight symmetry. The model uses 20-node elements throughout except for the two layers of elements designated by cross-hatching in Fig. 1.7. There, 16-node elements are used to significantly reduce the bandwidth of the structural stiffness

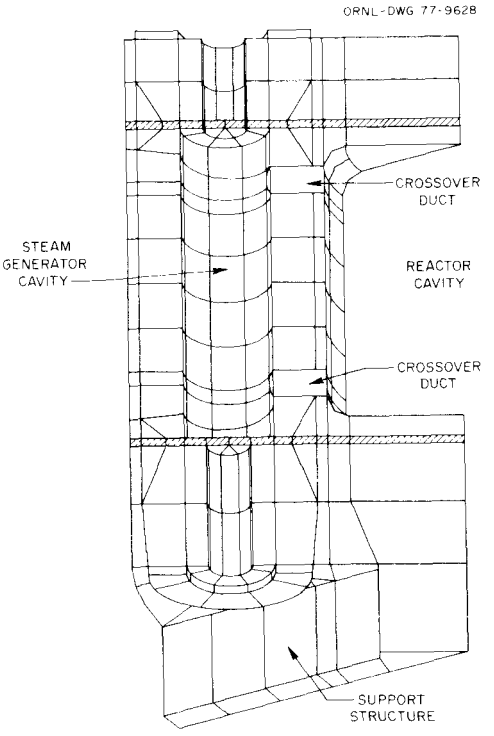

Fig. 1.7. Finite-Element Model of the Ohbayashi-Gumi Vessel for the Third Analysis Made by Use of STATIC-SAP.

matrix. The bearing pads for the vertical prestressing cables, the steel plate pressure boundaries above the steam-generator cavities, and the support structure were included in the analytical model.

In Fig. 1.8 the contour lines showing calculated axial strains due to vertical prestressing are essentially identical to those of the second analysis [Fig. 1.6(a)], indicating that for this loading condition the higher order elements are not needed. This conclusion is not surprising since the vertical prestress does not cause appreciable bending. Comparing the axial strains due to prestress for the last two analytical models with the first model shows the importance of modeling the bearing pads for the vertical prestressing tendons if accurate results are desired in the region of the top slab near the prestressing tendons.

The radial strains resulting from circumferential prestress, presented in Fig. 1.9, show tension along the inner surface of the vessel wall as in Fig. 1.4(b) for model 1. As mentioned previously, the use of lower order elements in the second model is probably reasonable for the tensile zone of Fig. 1.6(b) not extending to the haunch. To accurately calculate

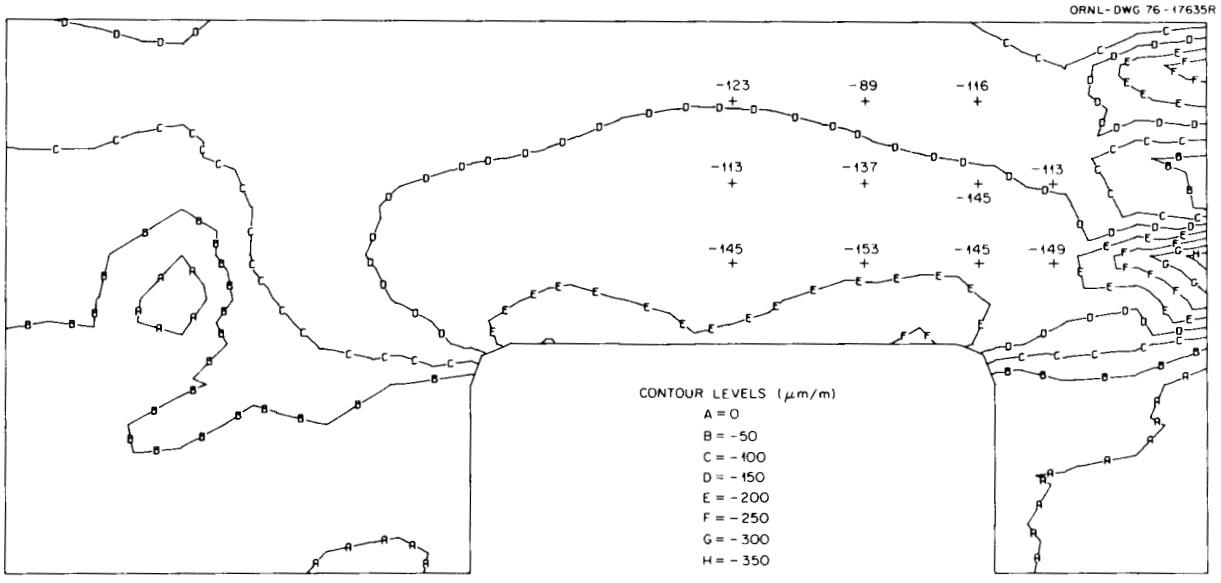

Fig. 1.8. Third Analysis Calculated and Measured Axial Strains Due to Vertical Prestress in the Ohbayashi-Gumi PCRV Model. (Contours represent calculated values; points represent experimental values in millionths). The top of the vessel is represented on the left of the drawing.

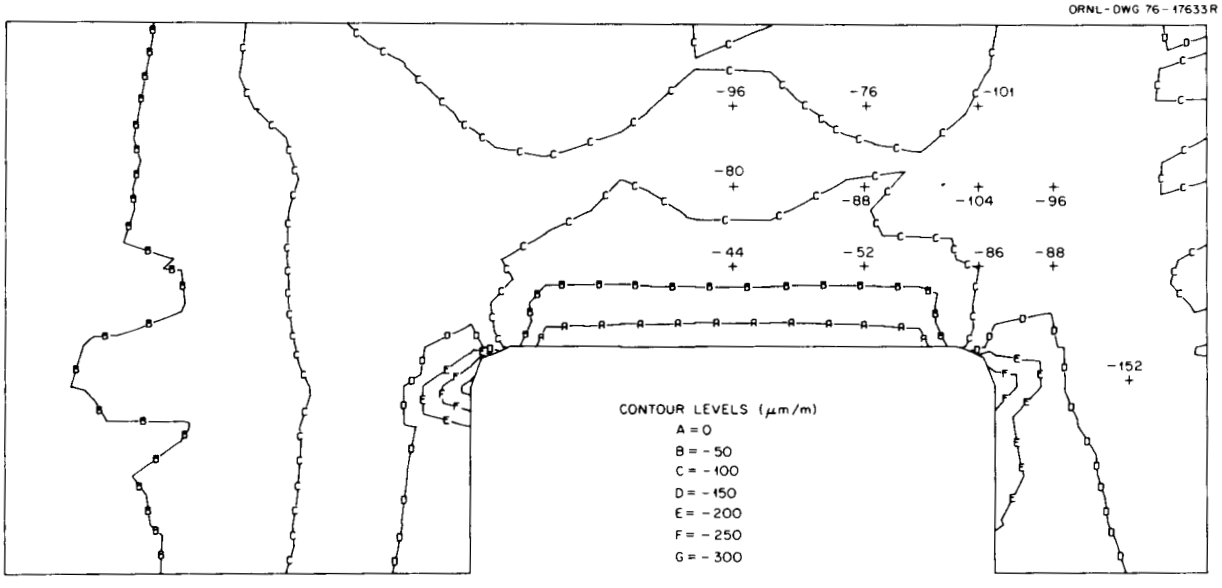

Fig. 1.9. Third Analysis Calculated and Measured Radial Strains Due to Circumferential Prestress in the Ohbayashi-Gumi PCRV Model. (Contours represent calculated values; points represent experimental values in millionths). The top of the vessel is represented on the left of the drawing.

the radial strains due to this loading apparently requires the higher order elements. The hoop strains due to circumferential prestressing shown in Fig. 1.10 are almost identical to those presented in Figs. 1.4(c) and 1.6(c).

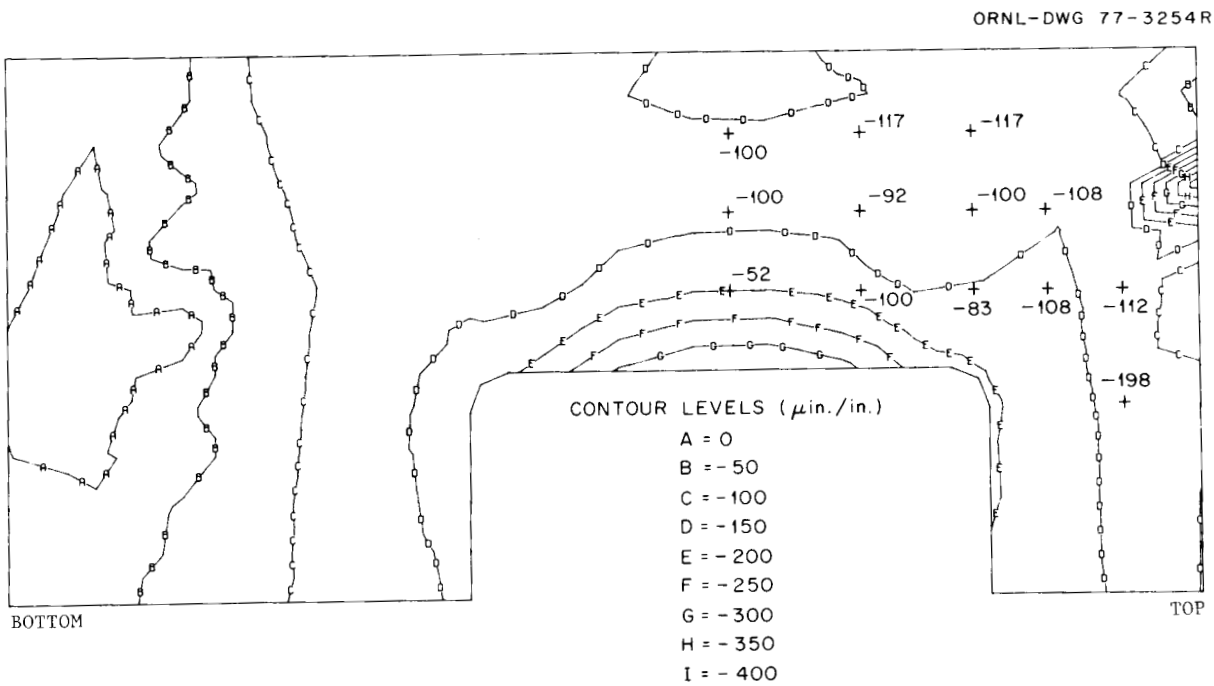

Fig. 1.10. Third Analysis Calculated and Measured Hoop Strains Due to Circumferential Prestress in the Ohbayashi-Gumi PCRV Model. (Contours represent calculated values and points represent experimental values in millionths).

The hoop strains due to internal pressure shown in Fig. 1.11 agree as well with the experimental data as the results for model 2 [Fig. 1.6(e)]. Figure 1.11 also shows a linear variation in strain through the thickness of the central portion of the top slab similar to the analytical results of model 1 [Fig. 1.4(e)].

Because the experimental data was restricted to regions where the strains varied relatively slowly, the relative merits of the three models had to be evaluated with little regard for the actual experimental-analytical comparisons; fortunately, the results of all the models were reasonable and essentially the same in the instrumented region of the vessel. Examining other regions of the vessel, however, such as under the vertical

ORNL-DWG 77-3253R

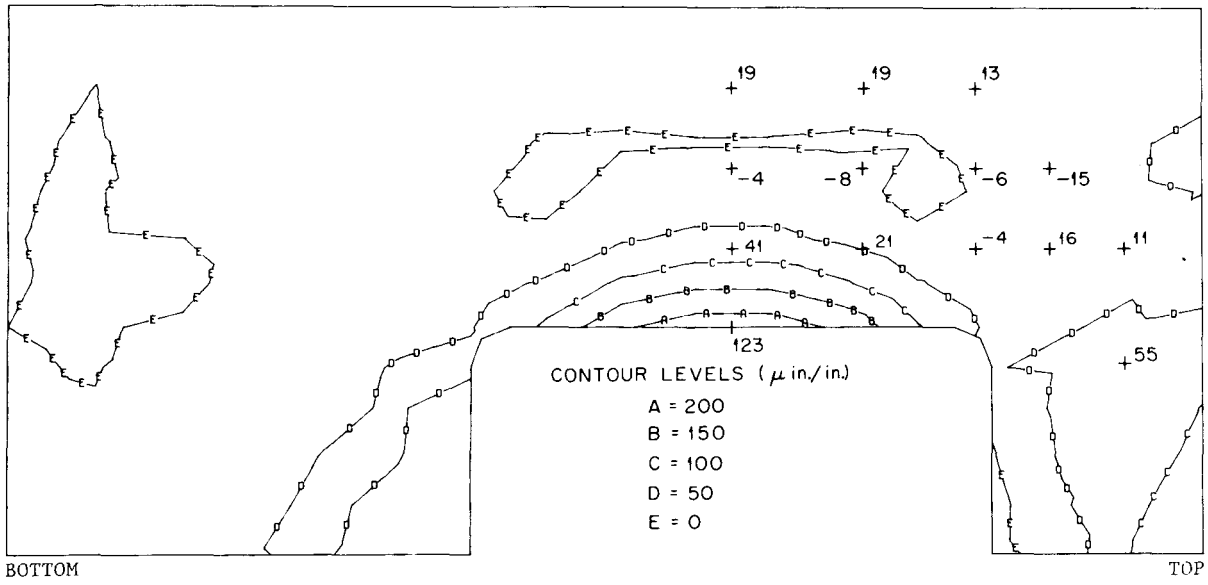

Fig. 1.11. Third Analysis Calculated and Measured Hoop Strains Due to Internal Pressure in the Ohbayashi-Gumi PCRV Model. (Contours represent calculated values and points represent experimental values in millionths).

prestressing bearing pads, showed that model 1 lacked sufficient geometric detail. Also, looking at the radial strains along the inner surface of the vessel wall indicated that the lower order elements of model 2 could not give a good representation of the complete vessel behavior. Some of the results of model 3 showed a distinct lack of symmetrical behavior above and below midheight of the reactor cavity. For the above reasons we elected to model the full height of the vessel using the more desirable 20-node elements for subsequent analytical studies of a PCRV of a commercial HTGR.

1.2.2 Analysis Methods Development — J. P. Callahan and W. G. Dodge

The development of an inelastic analytical model of concrete using the endochronic theory has been completed. The work was performed under subcontract by Prof. Z. P. Bazant at Northwestern University. The objective was to develop accurate constitutive laws describing the stress versus strain relationships and failure of concrete. This work was

undertaken since the existing constitutive relations and failure criteria are limited to specific loading conditions, and further generalization appears to be impractical if not impossible.

The application of endochronic theory to concrete is a relatively recent development, although it has been used for metals for some time. This method does not attempt to describe a failure surface. Instead, the inelastic strain is characterized by an independent scalar parameter called "intrinsic time," whose increment is a function of strain increments. The required material parameters were developed by use of data from tests of plain concrete, and a computer program was developed to simulate the response of the concrete to various loading conditions.

The resulting constitutive equations were then implemented in a computer program, which can consider inelastic behavior of both steel and concrete. This program was used to predict moment-curvature relations for reinforced concrete structural members that were subjected to cyclic loading. The endochronic theory appears to correctly predict the structural response without needing adjustment of any values of the material parameters determined previously from tests of plain concrete.

The inelastic model based on the endochronic theory has been programmed at ORNL. Independent verification studies will be conducted for different test results.

Work was also undertaken at Northwestern University to further refine the endochronic theory for concrete by taking into account (1) inelastic strains due to hydrostatic compression, (2) improved descriptions of strain softening behavior, (3) cyclic loading and volume changes in the strain-softening range, (4) type of triaxial test and resulting failure envelopes, and (5) dependence of material parameters on strength. The resulting formulation consists of fully continuous functions containing no inequalities. Unfortunately, these refined expressions are quite complicated and contain many parameters. The final report[2] on this work is in the publication process.

1.3 HEAD FAILURE STUDIES — M. A. Sozen and W. C. Schnobrich (University of Illinois)

The overall objective of the current studies is to develop a design (or safety-analysis) procedure to determine the strength of end slabs of prestressed-concrete pressure vessels. The project included experiments with end slabs having span-depth ratios and penetration arrangements which reflected the geometry of slabs covering the main cavity for the current generation of vessel designs.

Ten small-scale pressure vessels (Figs. 1.12 and 1.13) were tested to failure by increasing the internal pressure until structural failure was obtained in the end slab. The three variables in the experimental program were (1) the ratio of clear span to depth of slab, which was 2.5 for three and 2.0 for seven test vessels, (2) size and arrangement of penetrations (Fig. 1.13), and (3) concrete strength, which was nominally 38 MPa (5500 psi) for eight and 17 MPa (2500 psi) for two test vessels. Properties of the individual test vessels are listed in Table 1.1.

Tensile forces generated by the internal prestress were resisted by the circumferential (provided by five bands of continuously wound 2-mm-diam wire) and longitudinal (provided by sixty 20-mm-diam stressteel rods) prestressing reinforcement. Each circumferential band was made up of approximately 290 turns of wire at an effective prestress of 830 MPa (120 ksi). The total prestressing force provided by the longitudinal reinforcement was approximately 12 MN (2700 kips). No reinforcing sleeves were used in the penetrations, which were closed by steel plates on the pressurized surface of the slab. There was no bonded reinforcement within the end slab.

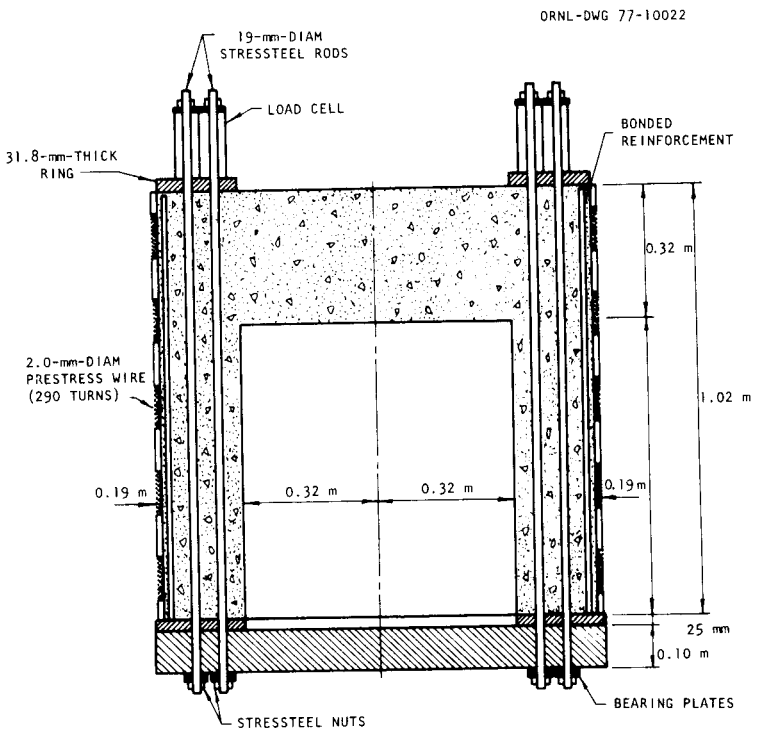

Fig. 1.12. Cross Section of Unpenetrated Head Failure Test Model.

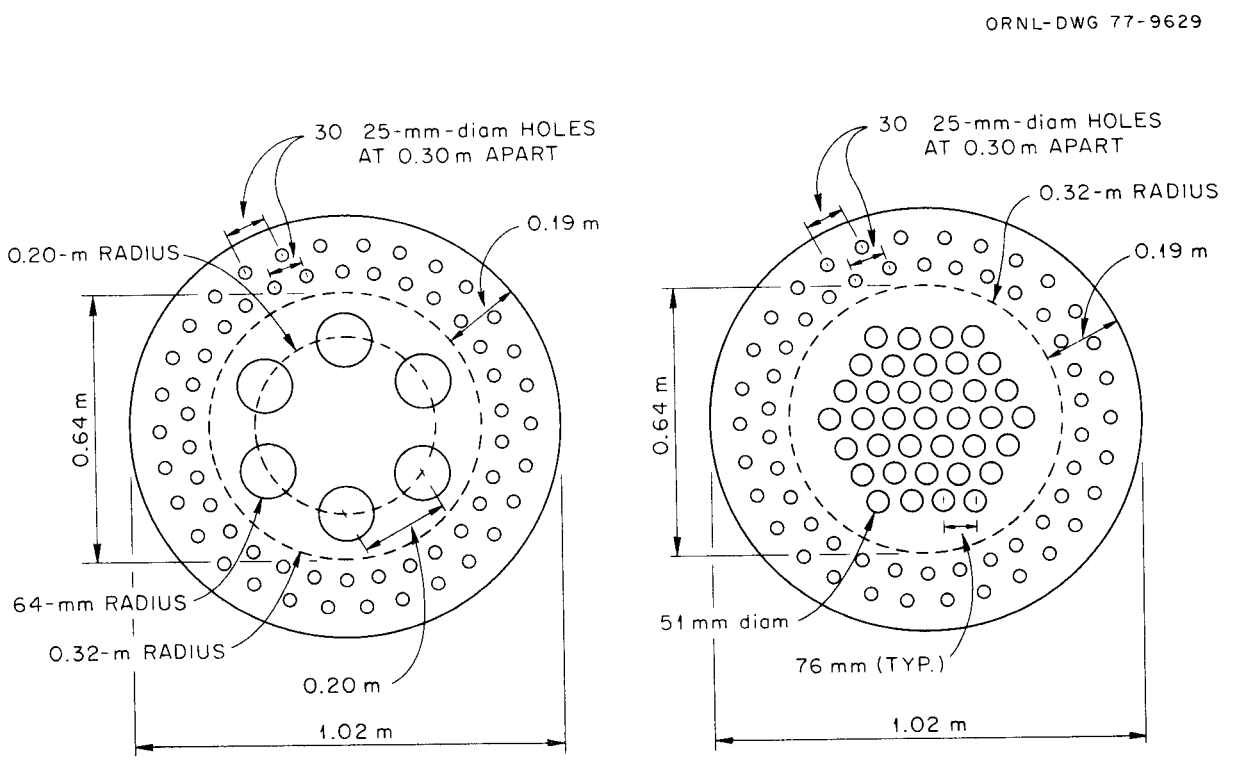

Fig. 1.13. Basic Penetration Patterns Used in Head Failure Models.

Table 1.1. Summary of PCRV Head Failure Model Tests

Mark	Nominal Slab Thickness		Concrete Compressive Strength		Penetrations			Prestress Index, MPa (psi)		Failure Pressure		Failure Mode[c]
					Number	diameter		long.[a]	circum.[b]			
	(m)	(in.)	(MPa)	(psi)		(mm)	(in.)			(MPa)	(ksi)	
PV26	0.25	10	46.3	6710				34.5(5010)	10.8(1560)	18.0	2610	SD
PV27	0.25	10	47.2	6845	6	127	5	36.8(5340)	10.8(1560)	16.6	2400	SD
PV29	0.25	10	37.8	5480	37	51	2	36.8(5330)	11.8(1710)	16.6	2400	SD
PV28	0.32	12.5	44.3	6420				39.7(5760)	11.7(1700)	26.0	3765	SD
PV30	0.32	12.5	43.4	6300	37	51	2	36.8(5340)	11.7(1690)	22.1	3210	SP
PV31	0.32	12.5	34.3	4970	37	51	2	37.9(5500)	11.6(1680)	19.3	2800	SP
PV32	0.32	12.5	39.4	5720	6	127	5	38.2(5540)	12.3(1780)	21.2	3075	SP
PV33	0.32	12.5	33.6	4875	6	127	5	37.2(5400)	12.3(1780)	21.4	3100	SP
PV34	0.32	12.5	16.8	2440	37	51	2	35.7(5180)		12.4	1800	SP
PV35	0.32	12.5	21.7	3150	6	127	5	36.1(5240)		13.1	1900	SP

[a]Total effective prestress force divided by horizontal cross-sectional area of cavity.

[b]Mean effective prestress force in prestressing bands 1 and 2 divided by vertical tributary area of cavity.

[c]SD = Shear failure after complete formation of cryptodome. SP = Shear failure by punching.

1.3.1 Analytical Studies

The ultimate goal of the study is the development of a generally applicable analytical model to simulate the response of the end slab. The model is intended to reproduce the entire range of response, automatically differentiating between failure mechanisms under increasing internal pressure. To develop such a model demands two different levels of analytical capability. The necessity for a large number of parametric studies to establish sensitivity to variations in physical properties, for design as well as data interpretation, requires a computer program that is easily accessible and produces solutions at moderate cost. On the other hand, the necessity for investigating three-dimensional nonlinear discontinuous phenomena in order to study local forces and deformations in the perforated end slab requires a rather extensive computer program.

To satisfy the first requirement, an interactive computer program, ISA, based on a linear axisymmetric model was developed. ISA is also suitable for problems of plane stress or strain and has been designed to include options for nonlinear analysis as well as analysis of crack development within the end slab. The linear-response version of ISA has been documented in a report[3] scheduled for distribution during the next reporting period. The current version of ISA has been expanded to handle nonlinear response.

Linear three-dimensional analyses of the end slab, in intact and cracked conditions, have been made with the use of a general-purpose program, FINITE.[4] Comparisons of results obtained from the axisymmetric and three-dimensional models have confirmed the feasibility of using modified axisymmetric models to determine strains around the penetrations in the linear range of response.

1.3.2 Experimental Studies

All ten test vessels failed as a result of shear stresses in the end slab, but in different modes. Despite the use of fluid as the loading medium, the structural failures were violent as contrasted with rather gentle leakage failures in initial pressurizations, which could not be carried through to structural failure because of cracks in the cavity liner. Maximum pressures ranged from 16.6 to 26.0 MPa (2400–3765 psi).

The shear failures in the end slab occurred through two different mechanisms. In test vessels identified by the letters "SD" in the last column of Table 1.1, the internal inclined cracks carved a complete "cryptodome" out of the end slab (Fig. 1.14) before failure occurred. In perforated end slabs having a clear span-to-depth ratio of 2, the shear failure occurred substantially along vertical lines, as illustrated in Fig. 1.15.

In the case of the cryptodome failures, the test results indicated an insensitivity to the presence of the penetrations. In the case of the "shear-proper" failures, the strength of the end slab was affected by the presence of the penetrations as indicated in Table 1.2.

In the linear range of response, deflections of the perforated end slabs as well as strains measured on the walls of the penetrations were

ORNL-DWG 77-9630

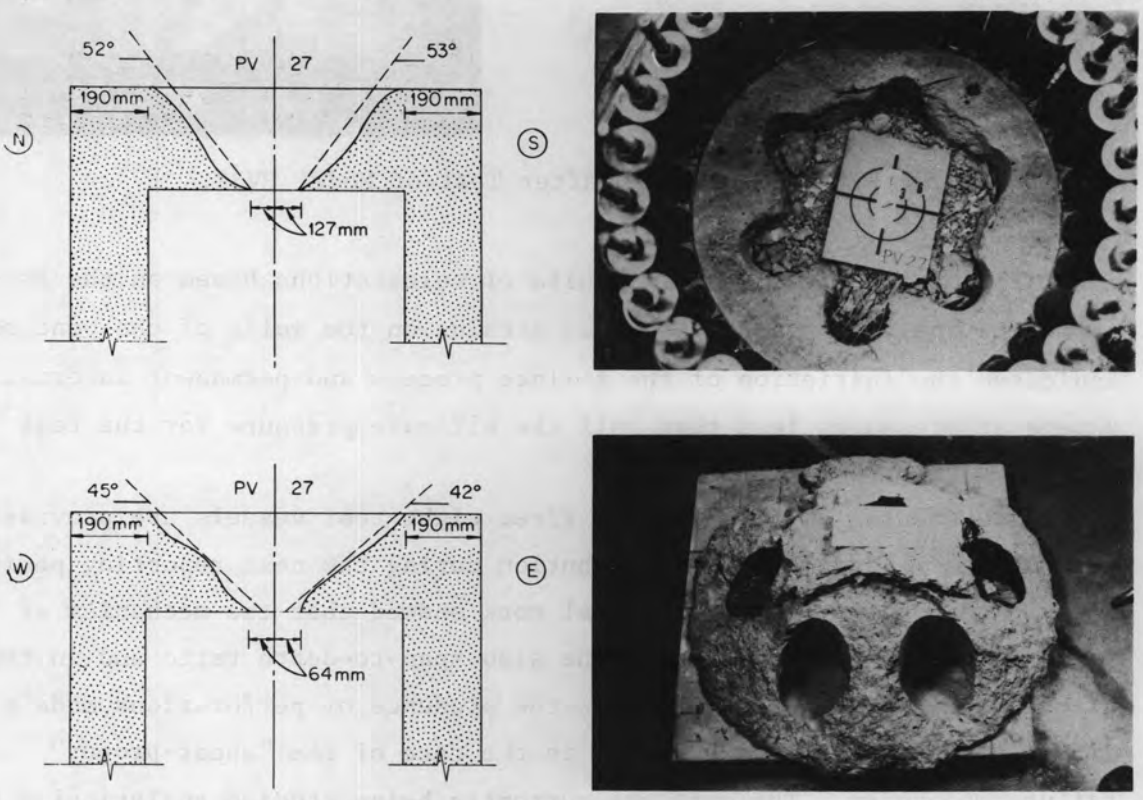

Fig. 1.14. End Slab After Test of Model PV27.

ORNL-DWG 77-9631

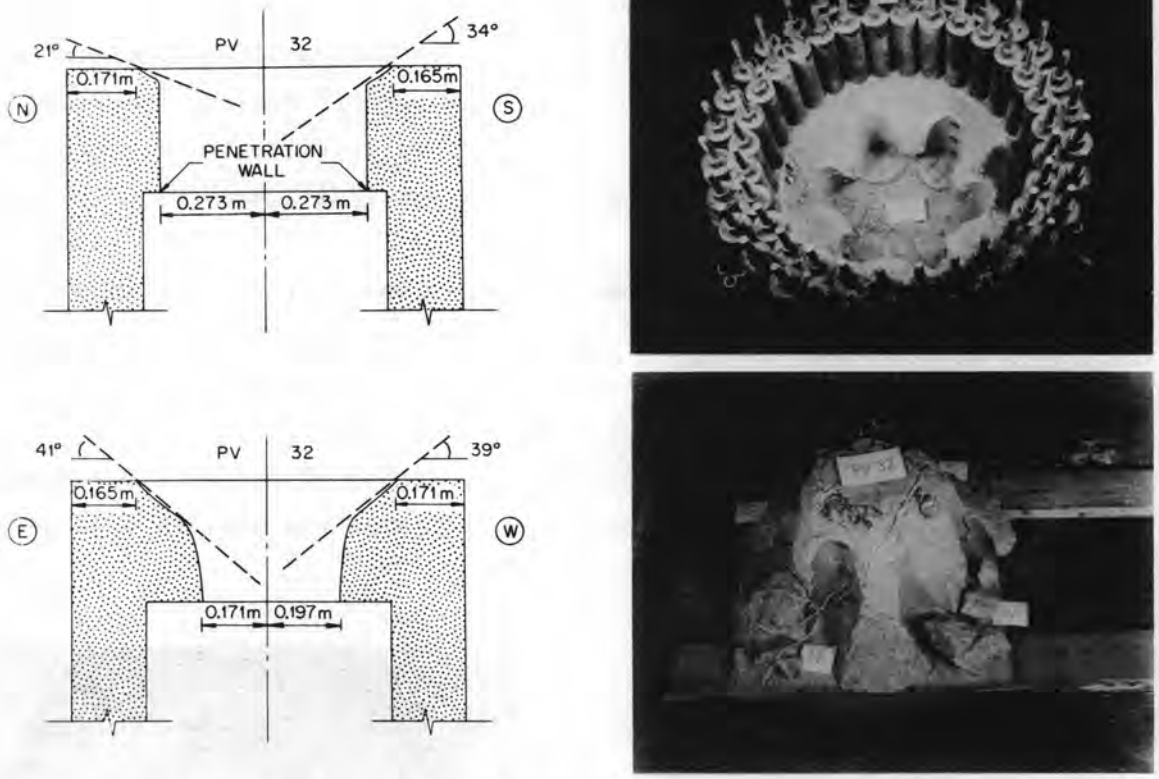

Fig. 1.15. End Slab After Test of Model PV32.

generally consistent with the results of calculations based on the axisymmetric analysis model. Measured strains on the walls of the penetrations indicated the initiation of the failure process and permanent internal damage at pressures less than half the ultimate pressure for the test vessels with 0.05-m openings.

Experimental details for the first eight test vessels are provided in a report[5] scheduled for distribution during the next reporting period.

On the whole, the experimental work showed that the mechanism of failure changed with changes in the slab span-to-depth ratio and in the size of the perforations, and that the presence of perforations made a difference for slab strength only in the case of the "shear-proper" failure mechanism. The data are currently being studied analytically to identify the critical parameters controlling the mode of failure and formulate them to enable their use in a conceptual model of the end slab.

Table 1.2. Nominal Shear Stresses in End Slab of PCRV Head Failure Models

Mark	Meas. Slab Thickness		Penetrations			Maximum Pressure		Shear Stress at Slab Edge[a,b]				Maximum Shear Stress[b,c]			
			Number	Size				v		$v/\sqrt{f'_c}$		v_m		$v_m/\sqrt{f'_c}$	
	(mm)	(in.)		(mm)	(in.)	(MPa)	(psi)	(MPa)	(psi)	($\sqrt{MPa}$)	($\sqrt{psi}$)	(MPa)	(psi)	($\sqrt{MPa}$)	($\sqrt{psi}$)
PV26	249.2	9.81				18.0	2610	11.4	1660	1.69	20.3				
PV27	255.5	10.06	6	127	5	16.5	2400	10.3	1490	1.49	18.0	16.3	2370	2.39	28.8
PV29	252.5	9.94	37	51	2	16.5	2400	10.4	1510	10.41	20.4	19.4	2820	3.16	38.1
PV28	314.5	12.38				26.0	3765	13.1	1900	1.97	23.7				
PV30	310.4	12.22	37	51	2	22.1	3210	11.3	1640	1.72	20.7	21.2	3070	3.21	38.7
PV31	305.3	12.02	37	51	2	19.3	2800	10.1	1460	1.72	20.7	18.8	2720	3.21	38.6
PV32	312.4	12.30	6	127	5	21.2	3075	10.8	1560	1.72	20.7	17.2	2490	2.74	33.0
PV33	316.2	12.45	6	127	5	21.4	3100	10.8	1560	1.85	22.3	17.1	2480	2.96	35.6
PV34	309.6	12.19	37	51	2	12.4	1800	6.4	930	1.56	18.8	11.9	1730	2.91	35.0
PV25	312.7	12.31	6	127	5	13.1	1900	6.6	960	1.42	17.1	10.5	1530	2.27	27.3

[a]Nominal shear stress at the slab-wall interface.

[b]f'_c = compressive strength of the concrete.

[c]Nominal shear stress at the net section through the penetrations.

1.4 INSTRUMENTATION EVALUATION AND DEVELOPMENT — D. J. Naus and C. C. Hurtt

Unique types of instrumentation are used in PCRVs. Their primary objective is to provide a means for monitoring these complex structures during initial proof testing and to provide continuing assurance of reliability and safety. The data obtained by the instrumentation are also used to evaluate the original design calculations and to confirm concrete properties.

Numerous commercial concrete embedment instruments are presently available for measurement of strain, stress, and moisture. According to the above criteria, these instruments must be capable of providing reliable data for extended periods of time in hostile environments. To provide insight into concrete embedment instrumentation, laboratory investigations are being conducted under this task. The initial phase of the investigation includes an evaluation of concrete embedment strain instrumentation and development of an acoustic emission monitoring capability.

1.4.1 Concrete Embedment Strain Instrumentation Evaluation

Commercially available concrete embedment strain indicating devices and associated readout instrumentation have been procured for evaluation. Table 1.3 presents these instruments and summarizes characteristics of the individual gages. These gages are being evaluated relative to general performance, performance in a representative PCRV environment, and performance in extreme environments.

1.4.1.1 General Gage Performance Characteristics

The general gage characteristics of the strain instrumentation listed in Table 1.3 are being evaluated. Characteristics considered include: range, sensitivity, accuracy, response, data acquisition requirements, cost factors, adequacy of calibration data supplied by manufacturers, and resistance of gage to damage during construction. The range, sensitivity, accuracy, response, data acquisition requirements, cost factors, and gage

Table 1.3. Strain Gage Instrumentation Included in Evaluation Study

Type	Gage Length (mm)	Strain[a] Range	Temperature Range (°C)	Sensitivity[a]	Gage Factor	Stability	Direct Concrete Embedment Recommended	Readout Requirements	Approximate Cost/Gage ($)	Comments
Electrical Resistance										
Unbonded wire Type A	100–500	1050–2100	65	2–6		Fair	Yes	Carlson Meter	35–75	Proven reliability
Unbonded wire Type B	100–250	+500 to −1000	−30 to +70	4–7		Fair	Yes	Carlson Meter	35–40	Proven reliability
Unbonded wire Type C	50–100	±5000	−20 to +100	5–10	∿2.5	Good	Yes	Strain indicator	50–70	Temperature compensated
Polyester encapsulated	10–130	−20,000 to ±15,000	−20 to +60	10	2.11	Poor	Yes	Strain indicator	5–20	Stability in moist environment questionable, volume change of plastic
Single wire	50–150	±20,000	−200 to >600	5–10	2	Good	No	Strain indicator	55–150	High-temperature use, small cross section requires careful placement
Acoustic										
Vibrating wire Type A	70–140	>1000	80	0.5	0.96×10^{-3}	Good	Yes	Period Meter	85–95	Used extensively, requires sealing
Vibrating wire Type B	140	>1000	80	0.5	3.00×10^{-3}	Good	Yes	Period Meter	75	Used extensively, requires sealing
Vibrating wire Type C	127	4000	−40 to +66	1.0	b	Good	Yes	Period Meter	150	Wire tension easily adjusted, temperature measurement capability
Vibrating wire Type D	130	3000		0.5	2.60×10^{-3}	Good	Yes	Period Meter	160	Temperature measurement capability
Vibrating wire Type E	100	3000	−40 to +80	0.1	2.01×10^{-3}	Good	Yes	Period Meter	150	Temperature measurement capability
Vibrating wire Type F	88	1000	−10 to +70	1	1.20×10^{-3}	Good	Yes	Period Meter	125	Temperature measurement capability
Vibrating wire Type G	133	2000	−10 to +70[c]	1	3.00×10^{-3}	Good	Yes	Period Meter	125–200	Temperature measurement capability

[a]"Microstrain" units: fractional strain × 10^6.

[b]Strain determined from table supplied with gages.

[c]May be specified for temperature range −30 to +200°C.

ruggedness* were obtained primarily from manufacturer's data and are summarized in Table 1.3. The adequacy of manufacturer's calibration data has been evaluated by laboratory testing. Separate studies have also been conducted to determine the effect on gage performance of size of specimen used for calibration, concrete strength, and maximum aggregate size.

Before the test series to evaluate calibration data supplied by the manufacturer, a limited laboratory study was conducted to select a test specimen geometry. Three sets of four test specimens each were cast. Each set of specimens consisted of concrete cylinders having diameters of 51, 76, 102, and 152 mm and each having a length-to-diameter ratio of 3.54.† Embedded in each specimen was an unbonded-wire type A gage, which was aligned with the specimen axis. The mix design for each set of specimens consisted of a 20-mm maximum size aggregate, a gravel-to-cement ratio of 2.64, and a sand-to-cement ratio of 2.04. The only difference between sets of specimens was the water-to-cement ratios employed, which were 0.575, 0.500, and 0.424. Thus, each set of specimens represented a different strength concrete in order to indicate the effect of concrete strength on gage performance.

After the specimens had cured in the laboratory environment for approximately six months, two electrical-resistance strain gages (having 0.1 m gage length) were bonded to the surface of each specimen at 180° intervals and were connected in series to compensate for specimen bending effects. The specimens were loaded in uniaxial compression to failure with surface and embedded strain gage readings taken at specified load intervals. Figure 1.16 presents stress vs strain plots obtained from the surface strain gages and embedded strain gages. It can be noted from the figure that surface strains were always less than embedded gage strains at the same stress level. This was probably due to a superimposed surface tensile strain resulting from the slight specimen bulging that

---

*Identified by whether or not the gage can be directly embedded in the concrete or casting in a mortar briquette before placement is required.

†The length-to-diameter ratio was limited by the clearance between loading platens of the testing machine. To minimize end effects the longest specimen possible was used.

ORNL-DWG 77-3951

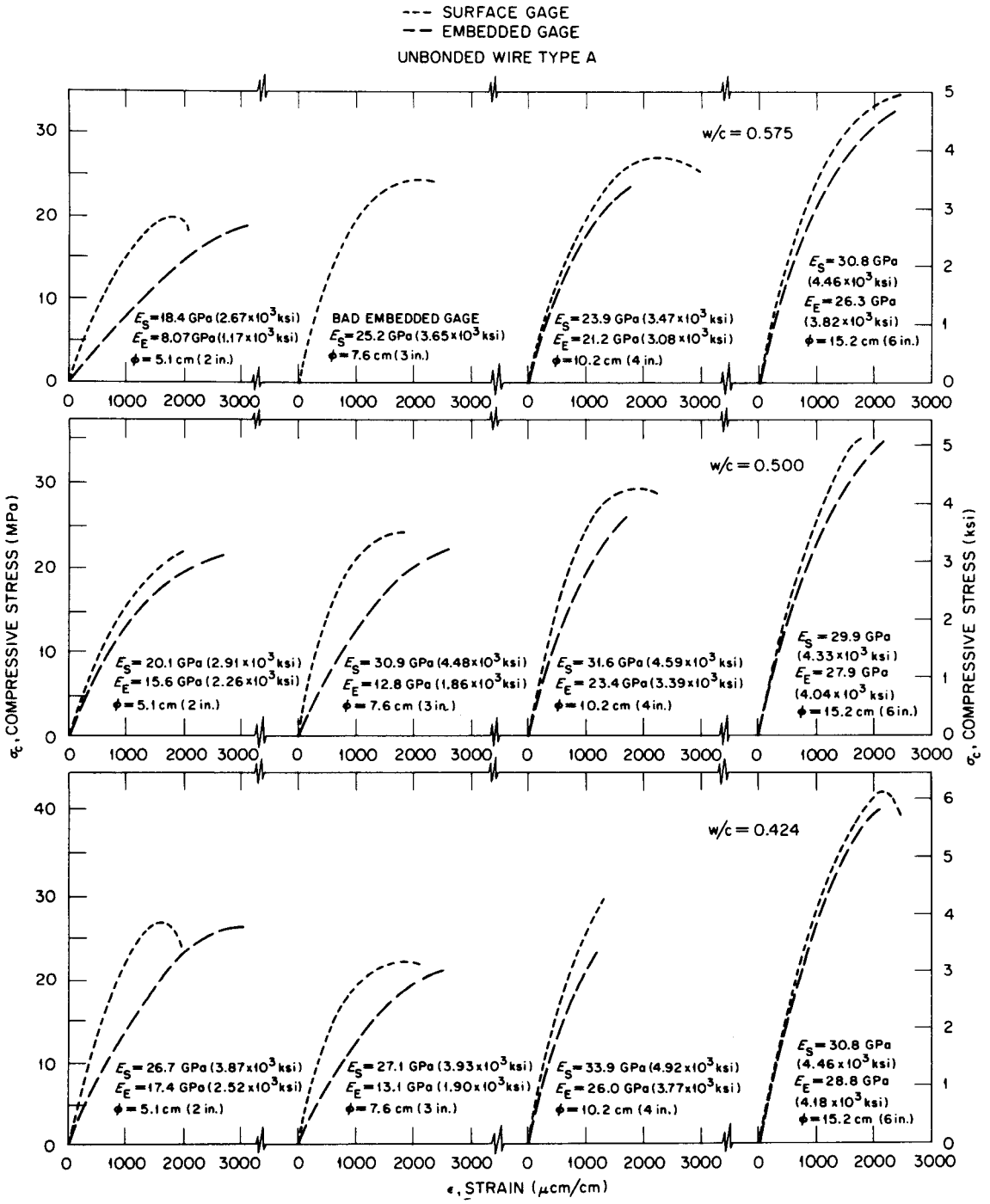

Fig. 1.16. Effect of Specimen Size and Concrete Strength on Embedded Base Performance. w/c = water-to-cement ratio by weight. E_S = Young's modulus obtained from surface strain gages. E_E = Young's modulus obtained from embedded strain gages. ϕ = specimen diameter.

occurred under compressive loading. No significant difference between embedded and surface strain gage results was noted when strength effects were compared between data sets, but it appears that a cylindrical test specimen 0.152 m diam by 0.53 m long provided the best results. Consequently, this specimen size was selected for subsequent gage calibration studies.

The accuracy of calibration data (generally the gage factor) supplied with each gage by the manufacturer has been evaluated for each gage listed in Table 1.3. Embedment strain meters were cast, one per specimen, in the 0.15-m-diam by 0.53-m-long cylindrical concrete test specimens* with the gages aligned with the cylinder axis. After the concrete was cured (>28 days), three sets of mechanical gage points with 0.20-m gage lengths were placed at 120° intervals around each specimen's circumference, and two 0.2-m electrical resistance strain gages were placed at 180° intervals on the cylinders and connected in series to eliminate bending effects. Results from the mechanical gage points and the surface strain gages were used as references for the output from the embedded gages. Figure 1.17 presents the test setup for the calibration tests.

At least two calibration specimens were tested for each of the 12 types of strain meters under investigation. The test procedure consisted of: calibrating load and strain gage responses, taking zero readings, loading the specimen in compression to 50 to 67% of its ultimate load in 22.2-kN increments with readings (mechanical, surface, and embedded gages) taken at each load increment, unloading in 22.2-kN increments with readings taken at each increment, rechecking of load and strain calibrations, and reloading the specimen in compression to specimen failure with strain readings (surface and embedded gages) taken at 22.2-kN load intervals. Figures 1.18 and 1.19 present typical stress vs strain responses for a polyester-encapsulated electrical-resistance strain gage for the initial load cycle and reloading to specimen failure, respectively. Results obtained for the different gages are summarized in Table 1.4, which lists

---

*The standard concrete mix used Type II cement, had 20-mm maximum size aggregate, had a gravel-to-cement ratio of 1.85, a sand-to-cement ratio of 2.84, and a water-to-cement ratio of 0.56.

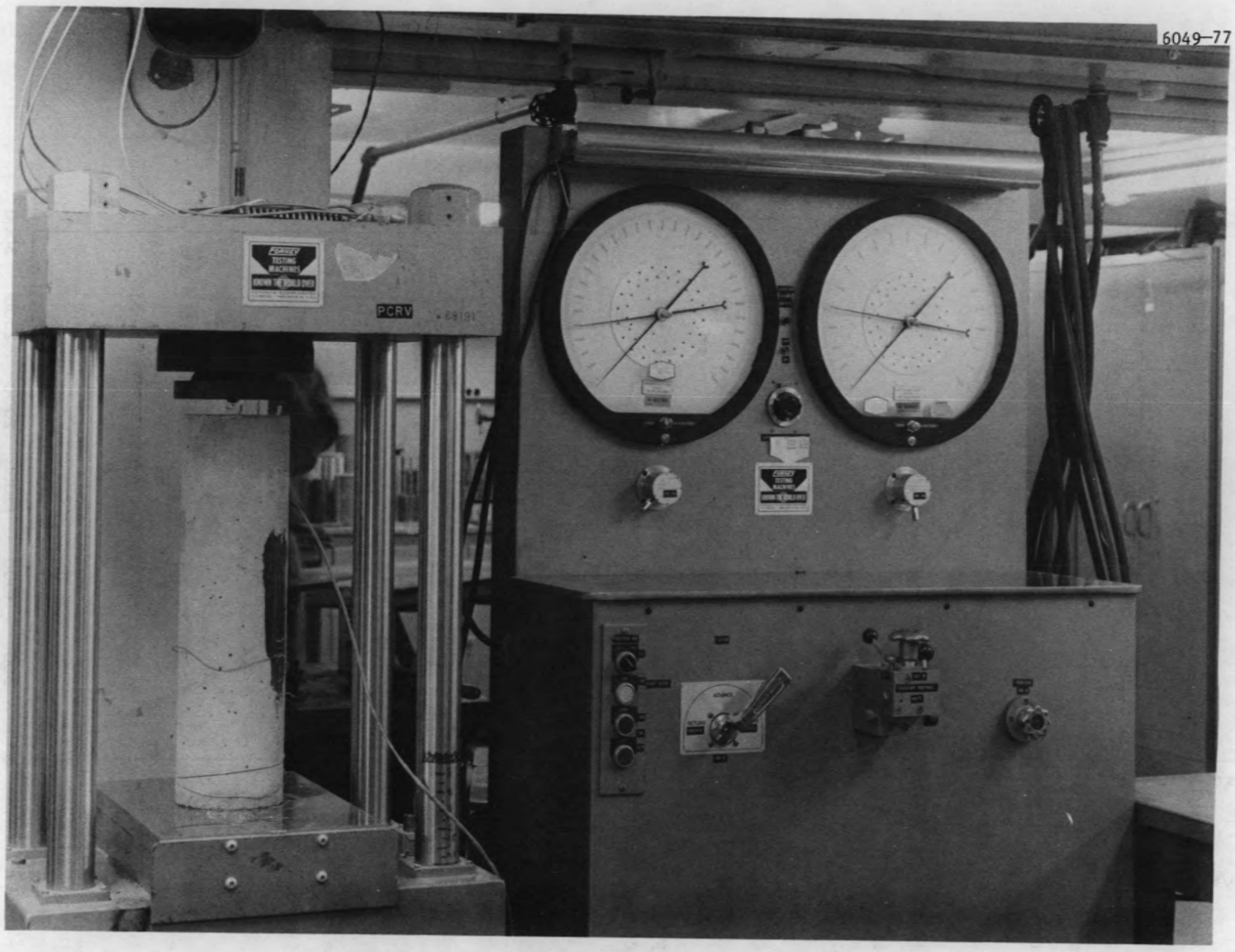

Fig. 1.17. Gage Calibration Test Setup.

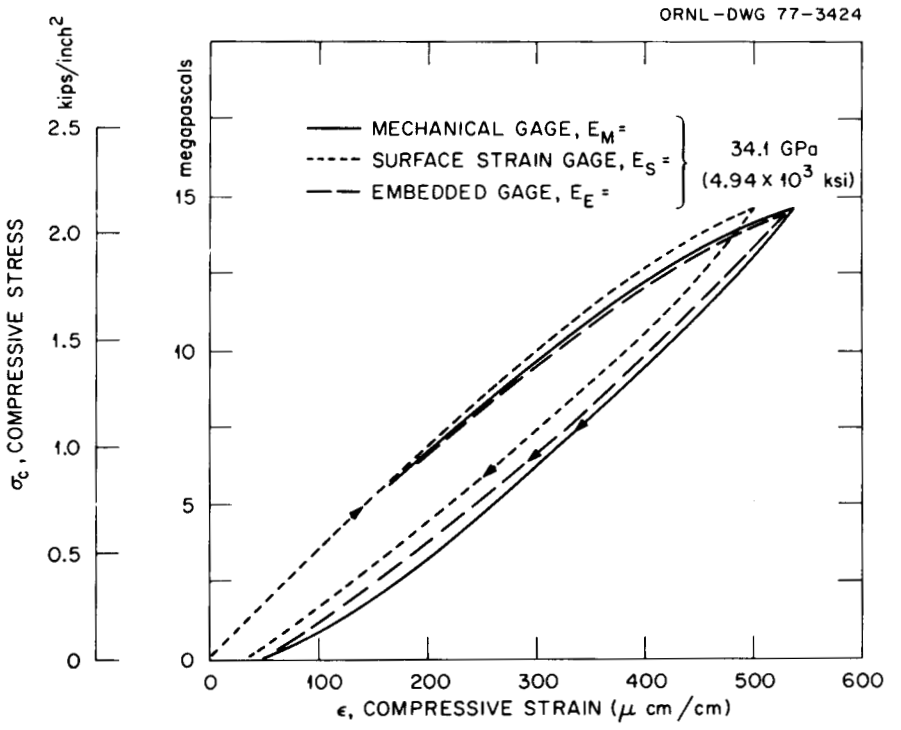

Fig. 1.18. Calibration Test Results for Initial Load Cycle: Electrical Resistance Encapsulated-Wire Strain Gage.

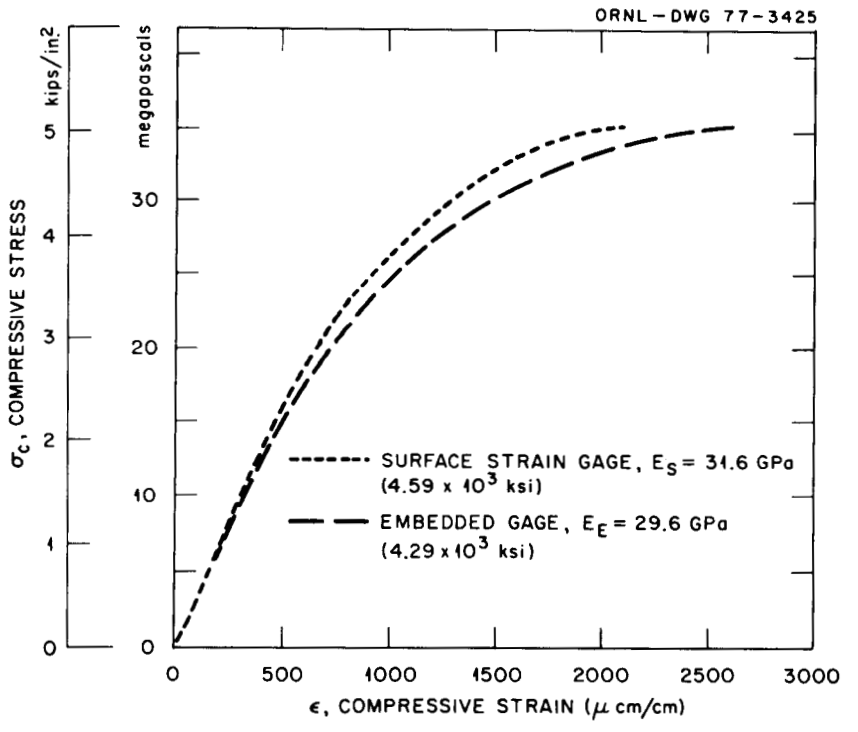

Fig. 1.19. Calibration Test Results for Loading to Failure: Electrical Resistance Encapsulated-Wire Strain Gage.

Table 1.4. Preliminary Gage Calibration Test Results

Type Gage	Difference, %, Embedded vs Surface Strain Gage	
	Range	Average
Unbonded wire Type A	−6.5 to −17.1	−13.2
Unbonded wire Type B	−9.9 to −16.9	−13.4
Unbonded wire Type C		−9.5
Polyester encapsulated	0 to −35.1	−13.9
Single wire	+19.5 to +21.2	+20.4
Vibrating wire Type A	−14.6 to −36.5	−24.4
Vibrating wire Type B	−11.6 to −12.0	−11.8
Vibrating wire Type C	−18.0 to −31.4	−24.7
Vibrating wire Type D	+10.8 to +17.2	+14.0
Vibrating wire Type E	− 2.6 to −18.5	−10.6
Vibrating wire Type F	− 4.3 to −14.6	−9.0
Vibrating wire Type G	−19.6 to −28.0	−23.6

differences between modulus of elasticity determined from the reference gage, surface strain gages, and the embedded gage. It should be noted that these results are only preliminary, with embedded gage responses calculated with manufacturer's approximate gage factors. Analyses will be conducted later to determine gage factors that give best fit to the data:

Because of the inconclusive results on the effect of concrete strength on embedded gage performance obtained from the preliminary test series to establish a calibration specimen size, three additional sets of specimens corresponding to low-, medium-, and high-strength concretes were cast. Standard 0.15-m-diam by 0.53-m-long cylindrical test specimens were used. The low- and medium-strength concrete specimen sets consisted of a total of six cylinders. One embedded gage having its axis aligned with the cylinder axis was contained in each specimen. Embedded gages used were two vibrating-wire type G, two unbonded-wire type A, and two single-wire electrical resistance gages. The specimen set made with medium-strength concrete consisted of four cylinders. Two unbonded-wire type A and two single-wire electrical-resistance embedded gages were used. Testing of the specimens followed the same procedure outlined under the section on gage calibration testing. The strengths of the concretes

corresponding to the low-, medium-, and high-strength mixes were 20.4, 29.4, and 41.8 MPa, respectively. Data reduction and analyses have not been completed.

It is generally recommended that the gage length of the embedded gages should be at least 3 to 5 times the size of the largest maximum size aggregate particles in the concrete. To provide background on the influence of the maximum aggregate size on embedded gage performance, two additional sets of cylindrical specimens 0.15 m diam by 0.53 m long were cast to complement the standard 20-mm maximum aggregate size (fineness modulus = 4.34) used throughout the investigation. The first set contained a 10-mm maximum size aggregate (fineness modulus = 4.07) and the second a 40-mm maximum size aggregate (fineness modulus = 4.63). The mix design used a sand-to-cement ratio of 2.83, a gravel-to-cement ratio of 1.85, and a water-to-cement ratio of 0.56. Embedded gages used for each mix included two unbonded-wire type A, two vibrating-wire type G, and two single-wire electrical-resistance type. The gages were cast one per specimen and the gages were aligned with the cylinder axis. Testing of the specimens followed the same procedure outlined under the section on gage calibration. The specimens have been tested, but data reduction and analysis have not been completed.

1.4.1.2 Gage Performance in Representative PCRV Environment

With the exception of the vibrating-wire strain gage type C, which was obtained too late to be included in this test phase, each of the gages listed in Table 1.3 is being evaluated for accuracy and stability in a "representative" PCRV environment. Three cylindrical test specimens 0.41 m diam by 1.02 m long were cast in a copper-jacket-lined cardboard mold (Sonotube). A representative PCRV concrete mix design (gravel-to-cement ratio of 2.60, sand-to-cement ratio of 2.02, and water-to-cement ratio of 0.48) was used. The specimen's open upper surfaces were temporarily sealed with polyethylene sheeting immediately after casting. Two days later the polyethylene was removed, and the cylinders were permanently sealed with a soldered copper lid. The specimens were then cured in the laboratory environment until they were loaded either thermally or by pressure.

Cylinder 1, Fig. 1.20, is being subjected to both thermal and pressure loadings. Contained within the cylinder and aligned with the cylinder axis are 12 concrete embedment strain gages (one unbonded-wire type A, one unbonded-wire type B, one unbonded-wire type C, one polyester-encapsulated, one single-wire electrical-resistance, one vibrating-wire type A, one vibrating-wire type B, one vibrating-wire type D, one vibrating-wire type E, two vibrating-wire type F, and one vibrating-wire type G), three weldable strain gages attached to steel reinforcing bars at 120° intervals around the cylinder circumference and placed in the concrete to aid in gage positioning, one stress meter, and two thermocouples used to provide and maintain desired temperatures. Two sets of 0.20-m-gage-length mechanical gage points were attached to bolt studs, which penetrated approximately 50 mm into the concrete. The mechanical gage points and the weldable gages are used as reference strains. To date (130 days after start of heat up) the loading on the cylinder has primarily been thermal, with the cylinder temperature maintained at 61 ± 5°C by an insulated heating blanket wrapped around the cylinder. Strain, stress, and temperature readings have been obtained before and periodically throughout the heating cycle. With the exception of one vibrating-wire type D gage (failure probably due to a temperature excursion to 74°C, which occurred during initial temperature regulation), and one polyester-encapsulated gage (due to apparent excessive strains) all gages are performing satisfactorily. Pressure loading superimposed on the thermal loading has just begun. The procedure being followed is to load the cylinder in 3.5-MPa increments to a maximum of 45% of the ultimate concrete compressive strength. Readings will be obtained throughout the loading intervals. The load will be maintained at each increment for a minimum of one week with the exception of the final load increment, during which the cylinder loading will be maintained for a two- to three-month interval before unloading.

Cylinder 2, Fig. 1.21, is being subjected to thermal loading only. Contained within the concrete cylinder and aligned with the cylinder axis are six embedment strain gages (one unbonded-wire type A, one polyester-encapsulated, one single-wire electrical-resistance, one vibrating-wire type A, one vibrating-wire type F, and one vibrating-wire type G), three weldable strain gages attached to the steel reinforcement, and two

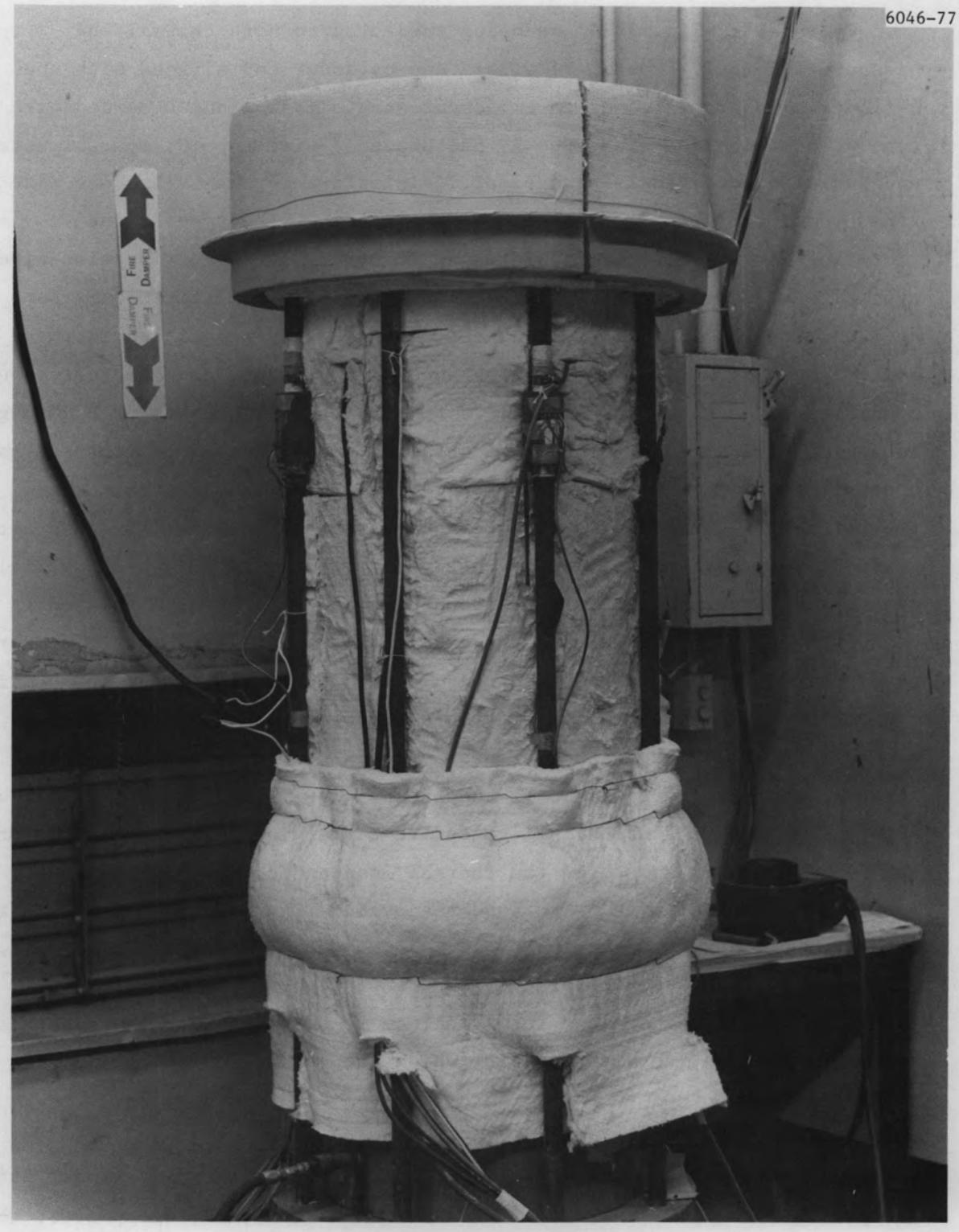

Fig. 1.20. Cylinder 1 in Insulated Loading Frame.

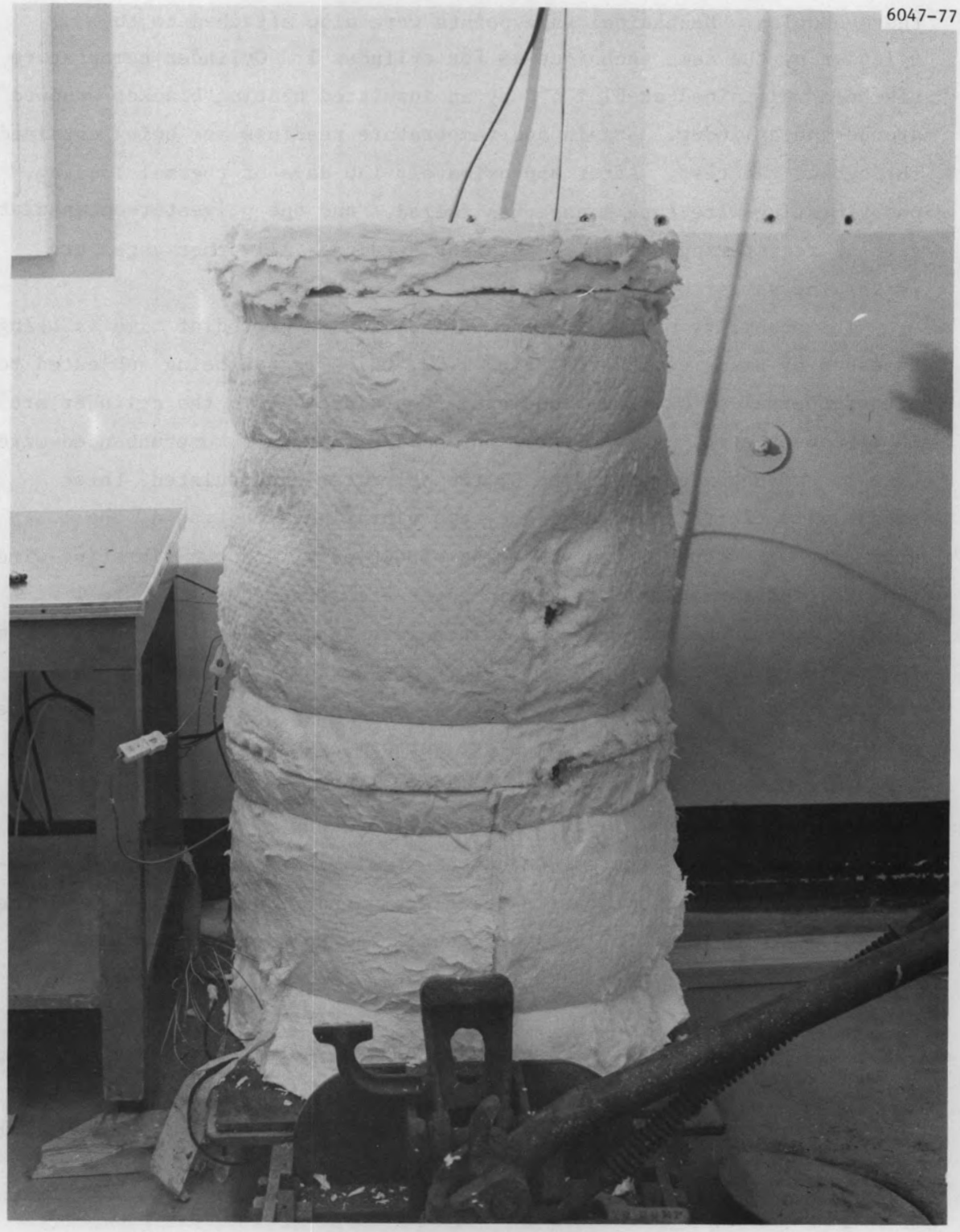

Fig. 1.21. Cylinder 2 Shown in Insulated Heating Jacket.

thermocouples. Mechanical gage points were also attached to the cylinder by the same technique as for cylinder 1. Cylinder temperature has been maintained at 61 ± 5°C by an insulated heating blanket wrapped around the cylinder. Strain and temperature readings are being obtained throughout the test. After approximately 130 days of thermal loading, one vibrating-wire type A gage has failed,* and one polyester-encapsulated gage is registering excessive apparent strains. All other gages are performing satisfactorily.

The stability of the gages over an extended period of time is being assessed by using cylinder 3, Fig. 1.22, which is not being subjected to either thermal or pressure loadings. Contained within the cylinder are 18 embedment strain gages (three unbonded-wire type A, one unbonded-wire type B, two unbonded-wire type C, two polyester-encapsulated, three single-wire electrical-resistance, two vibrating-wire type A, one vibrating-wire type B, two vibrating-wire type F, and two vibrating-wire type G), and three weldable strain gages are attached to the steel reinforcement. Mechanical gage points were attached as for the previous two cylinders. Strain and temperature are periodically being read throughout the test. After 150 days of testing, one vibrating-wire type F gage has failed; all other gages are performing satisfactorily.

1.4.1.3 Gage Performance in Extreme Environments

Performance of concrete embedment strain instrumentation under non-typical operating conditions is being evaluated. Samples of each of the gages listed in Table 1.3 have been subjected to room-temperature and elevated-temperature water immersion tests. After completion of the gage evaluations in a representative PCRV environment, the cylinder in Fig. 1.20 will be subjected to thermal and pressure loadings in excess of design.

The test setup for the room-temperature (21°C) water immersion test series is shown in Fig. 1.23. Cement has been added to the water to

---

*This could be the result of a temperature excursion during initial temperature regulation; however, another cause could be water penetration into the gage. We learned after embedment that the gage manufacturer recommends that the gage not be used directly in the as-received condition, but additional sealing precautions should be taken.

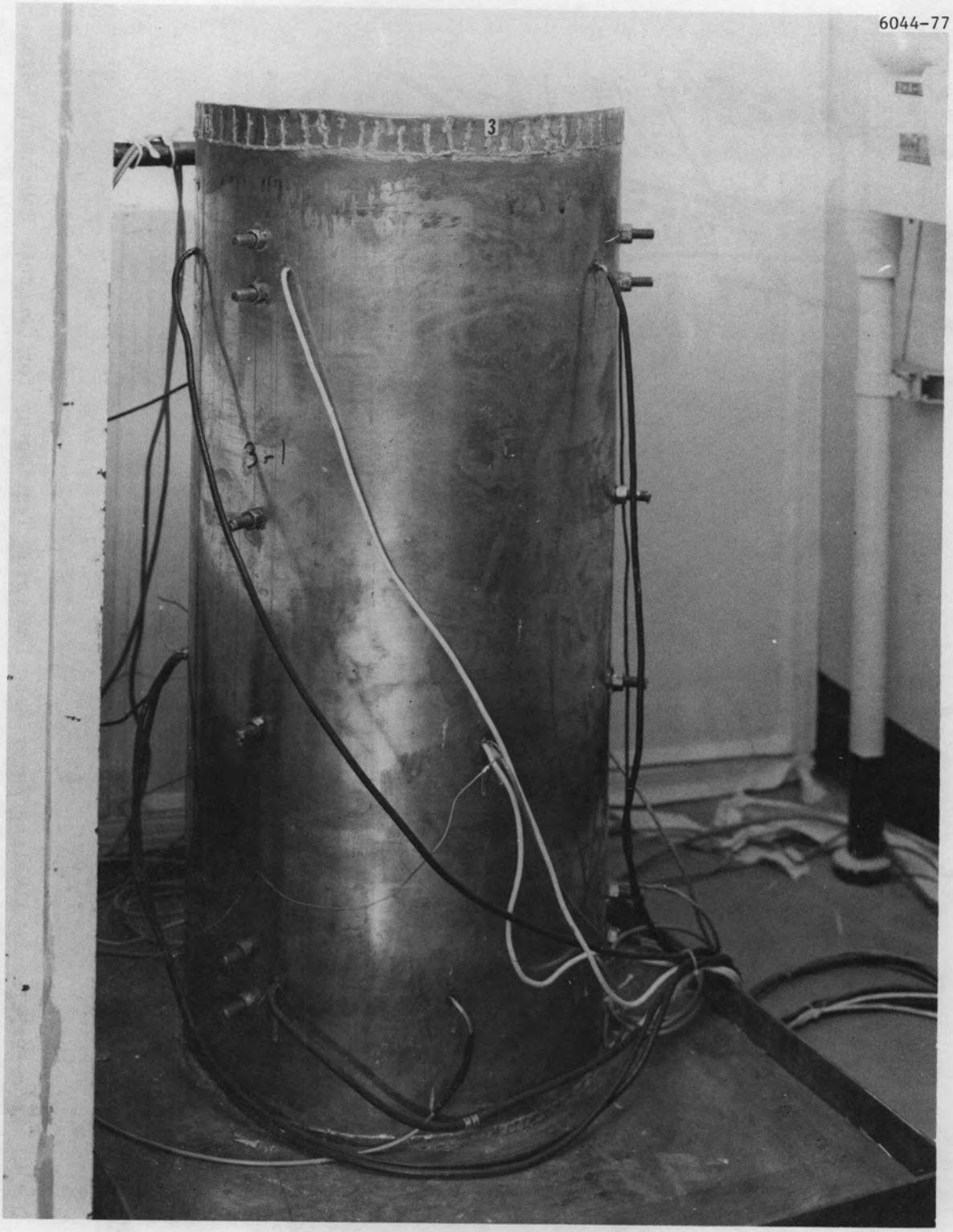

Fig. 1.22. Unstressed and Unheated Cylinder 3.

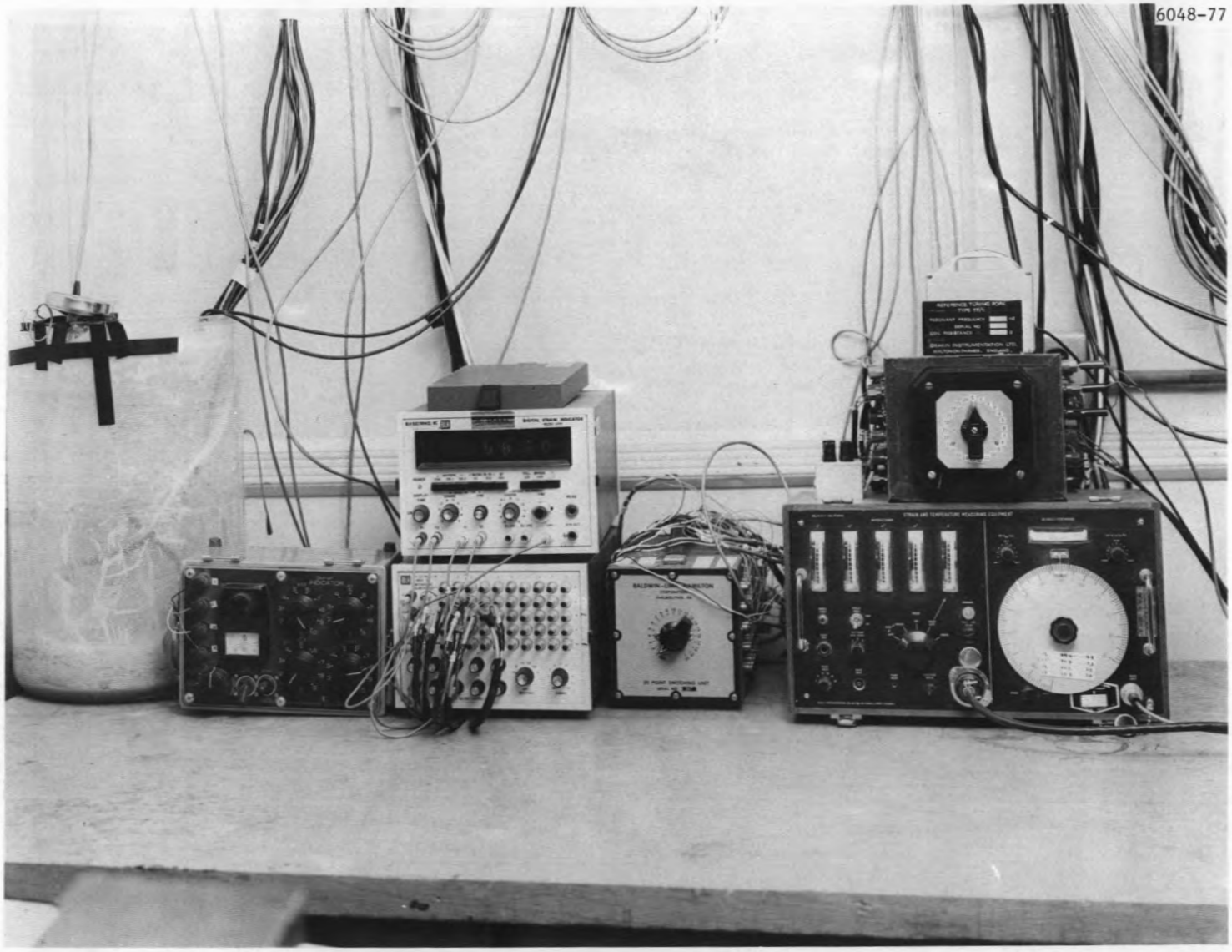

Fig. 1.23. Room-Temperature Alkaline Water Bath Immersion Test Setup for Concrete Embedment Gages.

increase the pH to 10 to simulate the pH of concrete. After samples of each of the gage types are placed in the solution, readings were periodically monitored throughout the test. Results for all gages are too voluminous for presentation in this report; however, a sample result for a polyester-encapsulated electrical-resistance strain gage is presented in Fig. 1.24. This test has recently been terminated after a duration over 425 days. Gage failures, during the life of the test, as defined by breakdown of gage resistance to ground, excessively high apparent strain readings, or inability to obtain a reading, were quite extensive, with almost all types of gages experiencing at least one failure.

The elevated-temperature alkaline water immersion test was similar to the room-temperature test except the temperature was maintained at

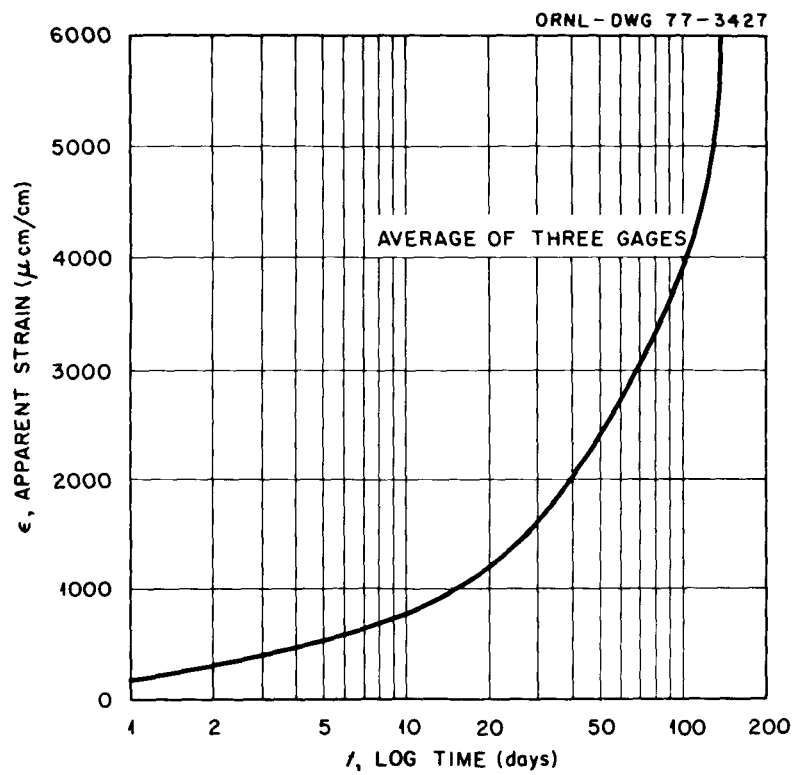

Fig. 1.24. Electrical Resistance Encapsulated Wire Strain Gage Apparent Strain vs Time of Exposure: Room-Temperature Alkaline Water Bath.

65.6°C by an immersion heater. The test setup is shown in Fig. 1.25. The test procedure included placement of the gages in the solution, taking of zero readings, slowly raising the water temperature to 65.6°C, maintaining the water temperature, and periodically taking readings. The elevated-temperature portion of the test has recently been terminated and the alkaline solution permitted to cool to room temperature. Readings are being taken periodically, and after one month the water will be removed and the gages permitted to air dry. Readings also will be obtained periodically during this phase of the investigation until the readings stabilize; then the test will be terminated.

1.4.2 Acoustic Emission Study

The ability of acoustic emission to monitor structural test members, specifically PCRVs, is being evaluated under this task. The general approach followed can be divided into three sections: feasibility assessment, equipment procurement, and test program development. The preliminary feasibility assessment indicating that the use of acoustic emission for PCRV structural monitoring is potentially promising was described in the previous report.[6] Emphasis during this reporting period was on the development of equipment performance specifications and the procurement of equipment. Development of a program to systematically evaluate acoustic emission for application to PCRVs has not been initiated.

Performance specifications for a multichannel acoustic emission source location system have been developed. The ten-channel flaw detection and location system has been procured and acceptance testing completed. Basic components of the system include transducers (50, 250, and 500 kHz resonant frequency), preamplifiers, amplifiers, detector modules, processor module, floppy disk, minicomputer, paper-tape reader, cathode-ray tube with both graphic and alpha-numeric presentation capability, hard-copy output device, and software for data assemblage and processing. Recently the capability of the system has been expanded to 12 channels, and a frequency distribution analyzer has been added.

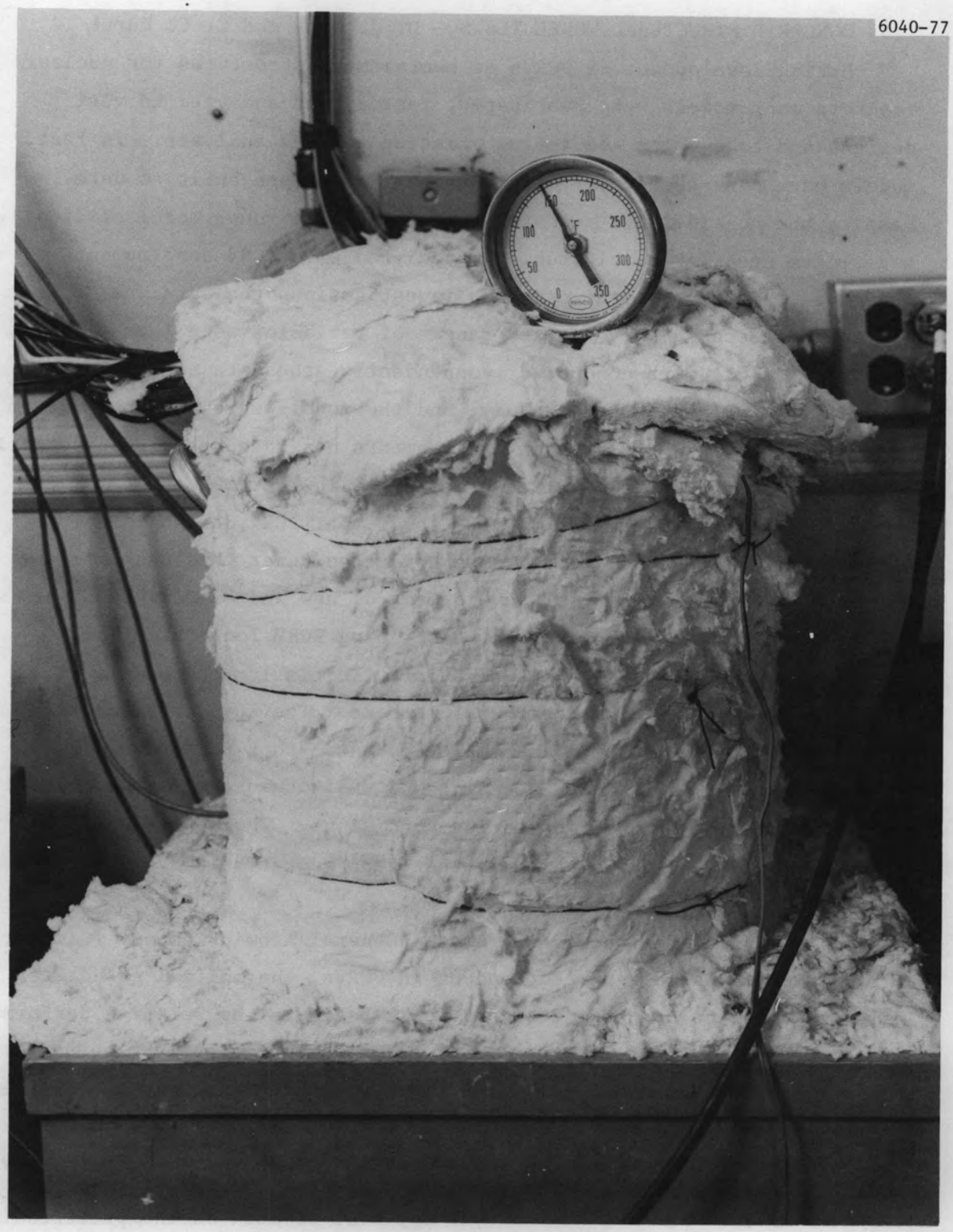

Fig. 1.25. Elevated Temperature Water Bath Immersion Test Setup for Concrete Embedment Gages.

1.5 CONCRETE STRUCTURAL MODEL TESTS — D. J. Naus and C. C. Hurtt

During development of PCRVs as containment structures for nuclear reactors many models were fabricated, tested, and analyzed to verify designs and to develop and refine existing failure analyses. In fact, models have been tested for all PCRVs that have been built to date. Despite the considerable research data obtained through model studies, a definite need for model studies associated with PCRV development continues. In many of the previous investigations the data are of limited use because only limited ranges of variables were investigated, research efforts were conducted independently, the data are applicable only to the particular model study, and the models were fabricated from "model" concretes and tested in environments not adequately representative of the aging-type material state of concrete in the PCRV (that is, the results cannot be related to the 20- to 30-year PCRV design life).

The series of model tests to be conducted under this task will be designed to provide input for development of new and/or refinement of existing analytical techniques for describing PCRV long-term time, temperature, and load-dependent behavior. Initially, the models will involve relatively simple structural members. The structural models will then increase stepwise in complexity until they represent a PCRV or major portions of a PCRV. Loading and environments will be designed to simulate long-term PCRV operating conditions. The models will generally be of sufficient size so that representative PCRV materials may be used.

As a result of a request[7] from the General Atomic Company (GA) for information on use of grouted tendons in PCRVs, the initial structural model test series has been designed to investigate the relative performance of grouted vs nongrouted tendons. If grouted tendons perform adequately in PCRVs, reduced overall costs and improved performance may be attained.*

---

*Initial costs of grouted and nongrouted tendons are approximately equal, but the surveillance costs for nongrouted tendons over the 20- to 30-year design life of the structure may cost as much as the prestressing system itself.

1.5.1 Background: Grouted and Nongrouted Tendons

Current practice in construction of PCRVs is to use post-tensioned nongrouted steel tendons. The philosophy behind this approach is that since the tendons are not grouted they may be inspected, retensioned to eliminate losses resulting from creep and shrinkage of the concrete and relaxation of the steel, and replaced, if necessary. Corrosion protection of ungrouted tendons during their service life is generally provided by application of a petroleum or wax-based material. The structural integrity of the tendons is monitored through a surveillance contract, which over the 20- to 30-year design life of the structure may cost as much as the prestressing steel system itself, which with labor, materials, and equipment may account for 60 to 70% of the PCRV cost.

Alternate measures have been attempted to prevent or significantly reduce tendon corrosion. Included in these attempts has been the use of organic and inorganic coatings, cathodic protection, galvanized steel, and stainless steel. These measures, however, have been only moderately successful. Organic and inorganic protective coatings may be removed from the tendons during placement through friction with the conduit. Cathodic protection is impractical economically because of the extensive amount and types of steel. Galvanized reinforcement is more expensive because of both the additional cost of the galvanizing (adds ∿10%) and the increased steel contents required to compensate for the strength reduction (∿15%) that occurs with galvanizing. Also, the efficiency of anchorages tends to be reduced since slippage is more apt to occur. Material costs of stainless steel tendons are much greater (∿1200%) than those of conventional tendons.

An alternate approach for corrosion protection of tendons, which has successfully been used in bridge deck construction for many years, is grouting of the tendons. Grouting of the post-tensioned tendons is believed to provide superior corrosion protection at significantly reduced costs. In addition, grouted tendons provide increased ultimate moment capacity, better crack control (increased number of cracks but of reduced width), improved anchorage efficiency of tendons, and significant reduction of dynamic effects resulting if a tendon fractures. Before accepting

a priori the use of grouted tendons, a modest test program was developed to evaluate the behavior of grouted tendons, especially in aggressive environments.

1.5.2 Experimental Investigation

A test program is being conducted to assess the relative behavior of grouted and nongrouted post-tensioned tendons. The investigation has been divided into four separate studies: (1) structural behavior, (2) new materials, (3) corrosion behavior, and (4) tendon monitoring techniques.

1.5.2.1 Structural Behavior

To simplify the testing and analysis requirements, beam structural elements were selected as the primary members to be used in the investigation. Beam geometries of 0.15 m and 0.30 m wide by 0.30 m deep by 3.1 m long were selected according to criteria that the beams be of sufficient size to accurately model flexural members and that the beam and material property specimens be cast from one mix.* The 20-mm maximum aggregate size concrete mix presented in Table 1.5 has been used for specimen fabrication. Design properties of the mix are compressive strength ⩾ 34.5 MPa, modulus of elasticity ⩾ 31 GPa, and Poisson's ratio 0.15–0.25. Type II portland cement has been used throughout the investigation. Seven-wire 10-mm-diam Lo-Lax grade 270 strand has been used as the post-tensioning reinforcement.

Specimens cast from each mix included one beam test specimen, three 0.15-m-diam by 0.30-m compression test cylinders, three 0.15-m-diam by 0.30-m splitting tensile test cylinders, and three 0.08 by 0.10 by 0.46-m modulus of rupture test prisms. Slump, air content, and unit weights were determined for each mix. The beam structural elements were cast in steel molds and the procedure followed included: placement of shear reinforcement and tendon (also conduit for grouted beams) in the mold, concrete placement, compaction by vibration, leveling of exposed surface, and covering with wet absorbent paper and plastic to minimize

---

*Two mixes are required for the 0.30-m-wide specimen.

Table 1.5. Concrete Mix Design for Grouted and Nongrouted Tendon Study

Material	Size Range	Mix Proportion (wt %)
Cement		16.37
Sand	<No. 4	33.55
Gravel	No. 4 to 20 mm	43.12
Water		6.97

moisture loss. Companion control specimens were cast by use of appropriate ASTM standards. The specimens were removed from their molds 24 to 48 hr after casting. The specimens were cured in the laboratory environment (Fig. 1.26) before post-tensioning. After specimen curing, the strand reinforcement was post-tensioned to the desired prestressing level, taking into account losses due to anchorage seating. The procedure used to grout tendons slated for grouting was as follows: excess moisture was removed and grout was pumped into conduit with the apparatus in Fig. 1.27 until it flowed freely and uniformly from opposite end. The grout was permitted to cure a minimum of two weeks before testing.

Table 1.6 summarizes the variables to be investigated to indicate relative behavior of grouted and nongrouted tendon beams (i.e., load rate, post-tensioning level, and fatigue). Beams pertaining to the particular variable are also noted in the table. Table 1.7 summarizes mix design data, plastic concrete properties, and level of post-tensioning obtained for the grouted and nongrouted beams respectively.

Static, dynamic, and cyclic flexure testing of the beams is being conducted with the test fixture presented in Fig. 1.28. The static flexure tests were conducted by loading the beams at a rate of 74 N/s until first cracking occurred. Then the load was held constant and cracks were measured and marked. Loading then proceeded in 4.45-kN increments until failure occurred, with cracks measured and marked at each load increment. Centerline deflections were monitiored throughout

Fig. 1.26. Tendon Study Specimens in Storage Before Testing.

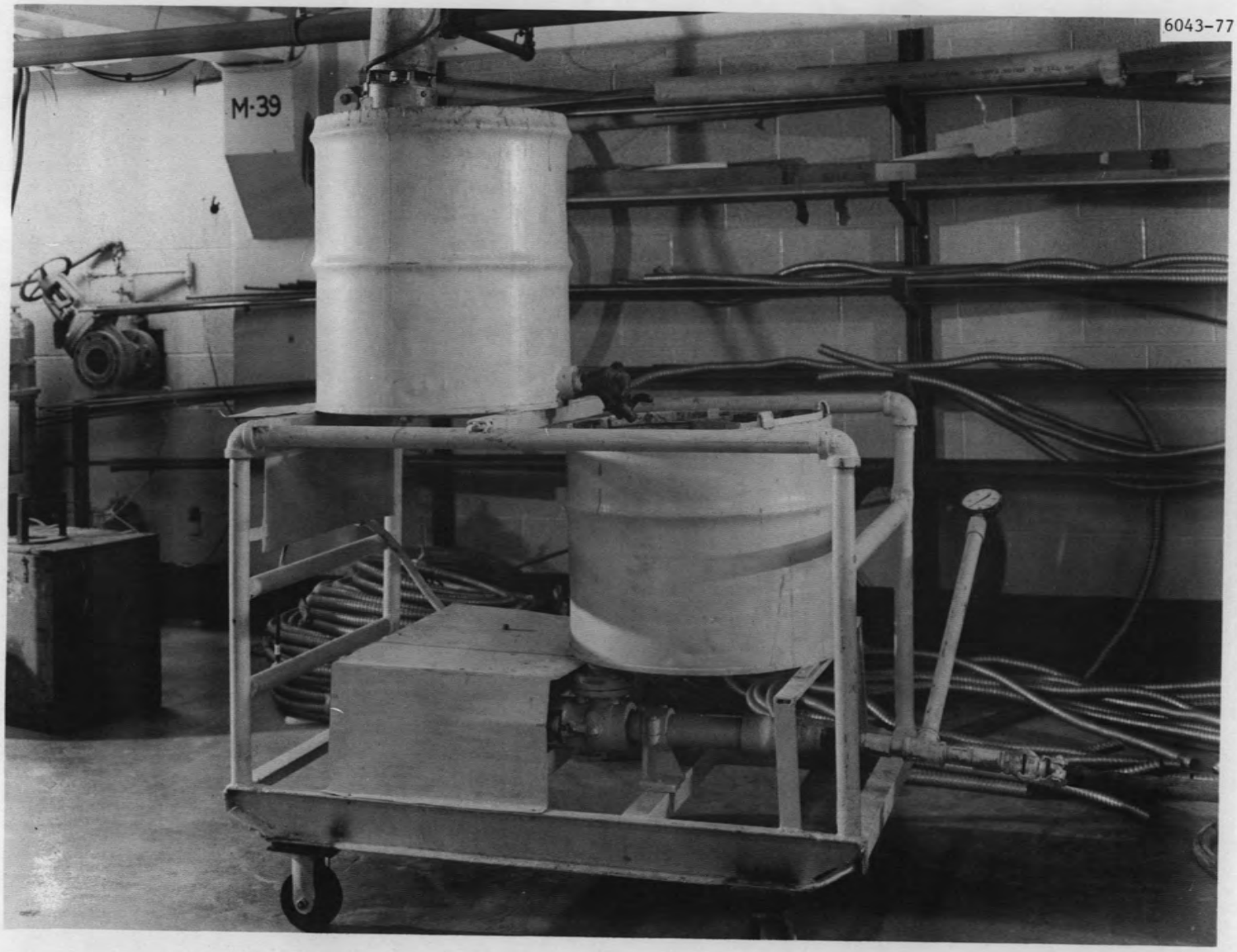

Fig. 1.27. Mixer and Pump Used to Grout Tendons.

Table 1.6. Grouted and Nongrouted Tendon Test Variables

Variable	Test Parameter	Relevant Test Specimen	
		Grouted	Nongrouted
1. Load rate	74 N/s	G4	NG15
	0.74 kN/s	G10	
	7.4 kN/s	G5	NG12
	74 kN/s	G15	NG11
2. Prestressing level[a]	$0.5f'_s$	G1	NG14
	$0.6f'_s$	G4	NG15
	$0.7f'_s$	G2	NG16
3. Fatigue[b]	0.10 to 0.45 P_u	G6	NG9
	0.10 to 0.60 P_u	G7	NG10
	0.10 to 0.75 P_u	G8	NG13

[a] f'_s = ultimate tensile strength of the tendon.

[b] P_u = static failure load.

Table 1.7. Grouted and Nongrouted Tendon Study Concrete Mix Data,[a] Plastic Concrete Properties, and Post-Tensioning Level

Beam Designation	Plastic Concrete Properties			Post-Tensioning Level (% of f'_s)[b]
	Air Content (vol %)	Slump (mm)	Unit Weight (kg/m^3)	
		Grouted Tendons		
G1	2.30	64	2425	50
G2	2.20	70	2425	69
G3	2.40	48	2438	59
G4	2.20	83	2435	65
G5	2.30	70	2428	59
G6	2.00	89	2428	59
G7	2.40	64	2428	59
G8	2.00	95	2428	54
G9	2.00	76	2444	63
G10	2.40	76	2409	62
G11	2.75	76	2403	61
G12	2.70	51	2406	69
G13	2.90	44	2416	69
G14	2.90	32	2412	60
G15	2.75	44	2422	58
G16	2.50	38	2428	49
G17	2.65	25	2435	58
G18	2.35	32	2419	59
G19	1.85	89	2428	50
		Nongrouted Tendons		
NG9	2.40	38	2435	50
NG10	2.30	38	2416	62
NG11	2.55	38	2438	62
NG12	2.25	32	2435	61
NG13	2.30	32	2428	59
NG14	2.55	32	2435	49
NG15	2.55	64	2393	61
NG16	2.65	38	2419	66

[a] The concrete batch weights for cement, sand (SSD), gravel (SSD), and water were 79.4, 162.7, 209.1, and 33.8 kg, respectively.

[b] f'_s = Ultimate tensile strength of the tendon.

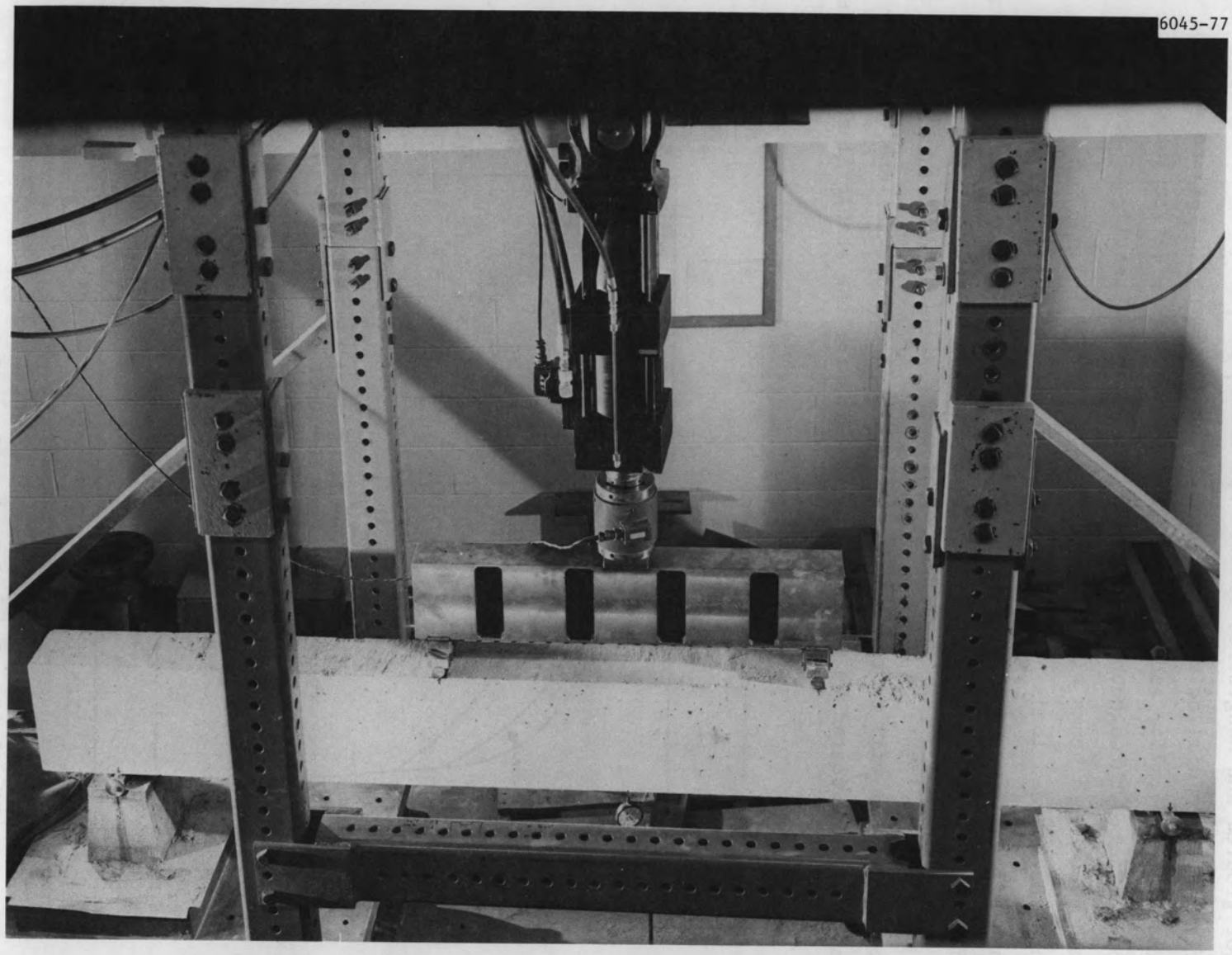

Fig. 1.28. Flexural Test Fixture for Prestressed Concrete Beams.

the test. Figures. 1.29 and 1.30 present load vs deflection results for grouted and nongrouted flexure specimens, respectively. Dynamic flexure tests will be conducted by loading specimens to failure at rates of 0.74, 7.4, and 74 kN/s. Load vs centerline deflection will be monitored throughout the test. Flexure fatigue testing of grouted and nongrouted beams will be conducted by cycling the beams at a rate of 1 Hz between loads corresponding to 10% static flexure failure load and different percentages (45, 60, and 75) of beam failure load. Each fatigue test will be terminated when either the beam fails or 10^6 cycles have been applied. One additional flexure test is planned in which one end anchorage will be removed to simulate an anchorage failure. The beam will be tested by the same procedure as for the static flexure tests.

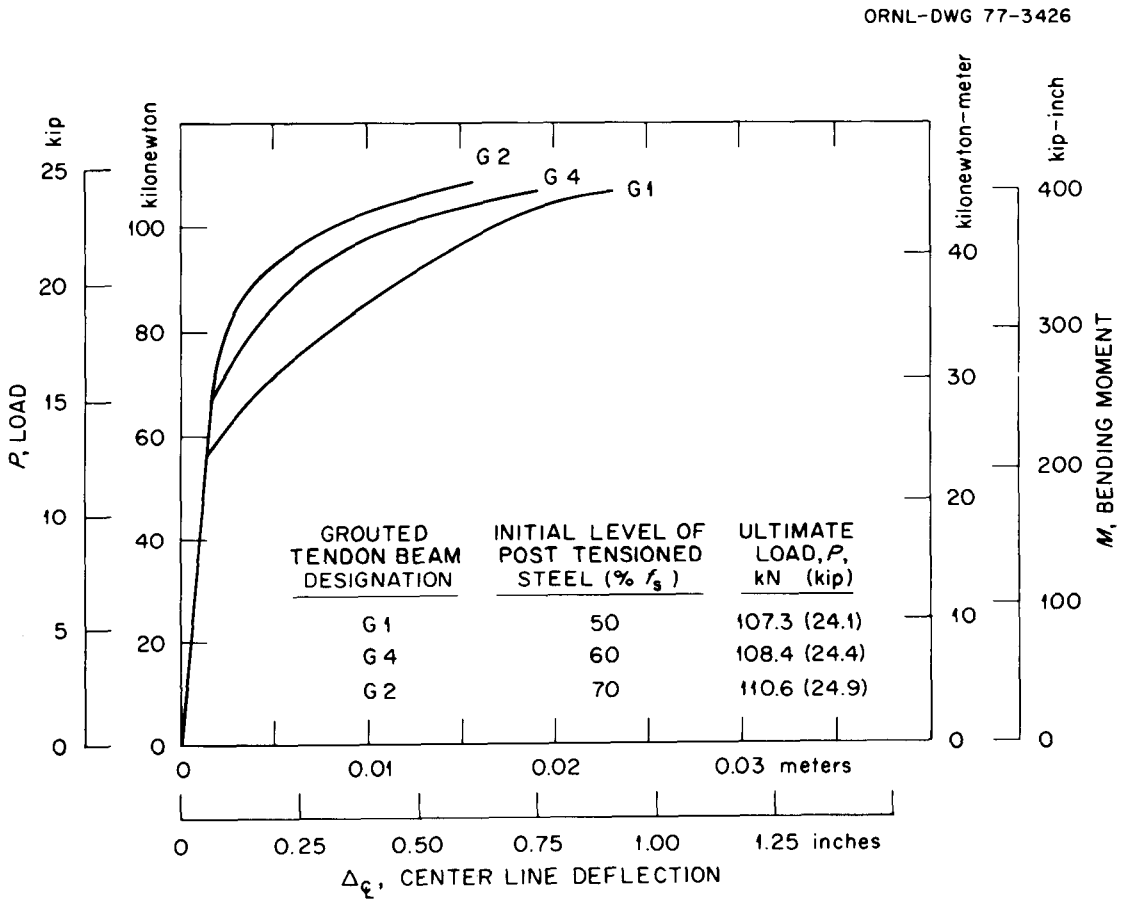

Fig. 1.29. Grouted Tendon Flexural Test Results.

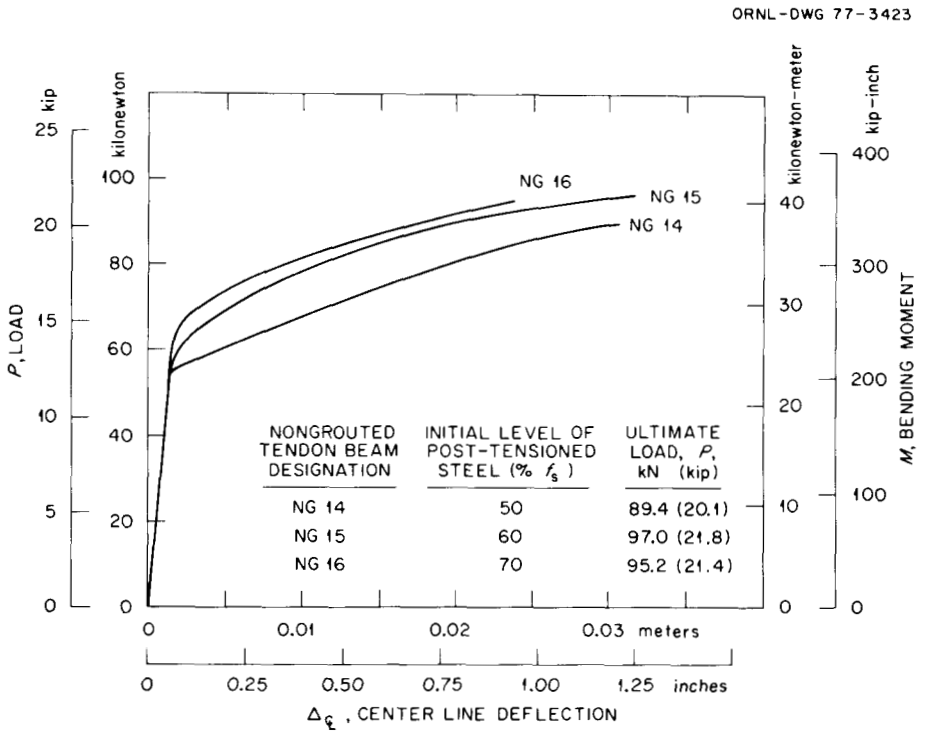

Fig. 1.30. Nongrouted Tendon Flexural Test Results.

1.5.2.2 New Materials

Potential new materials for tendon grouting and structural applications are being briefly investigated. The material systems include polymer silica and fast-setting refractory cements developed at Southwest Research Institute; steel-fiber-reinforced concrete, which has been used extensively for pavement applications where flexure stresses are high; and expansive shrinkage-compensating cements. Table 1.8 summarizes the test variables for the study of new materials.

Polymer silica materials react at predetermined activation temperatures to produce material systems that can withstand service temperatures of 538 to 1093°C, obtain compressive strengths of 70 to 140 MPa, and develop excellent adhesion to metals. The fast-setting refractory cements cure at room temperature, develop 40 MPa compressive strength in 24 hr, resist heat cycling and continuous exposure to 1093°C, and develop excellent adhesion to metals. The materials are being evaluated in this study primarily as grouting materials. Tests to be conducted include: (1) volume change and bleeding as determined by placing the materials in

Table 1.8. Test Variables for the Study of New Materials

Variable	Test Parameter[a]	Relevant Test Specimen	
		Grouted	Nongrouted
1. Prestressing level	$0.5f_s'$ – PS	G19	
	$0.5f_s'$ – SC	G16	
	$0.5f_s'$ – CG	G1	
	$0.5f_s'$ – CNG		NG14
	$0.6f_s'$ – PS	G11	
	$0.6f_s'$ – SC	G18	
	$0.6f_s'$ – CG	G4	
	$0.6f_s'$ – NCG		NG15
	$0.7f_s'$ – PS	G12	
	$0.7f_s'$ – SC	G13	
	$0.7f_s'$ – CG	G2	
	$0.7f_s'$ – NCG		NG16
2. Structural material	$0.6f_s'$ – FC	FC5	FC7
	$0.6f_s'$ – CG	G4	
	$0.6f_s'$ – CNG		NG15
	$0.7f_s'$ – FC	FC6	FC8
	$0.7f_s'$ – CG	G2	
	$0.7f_s'$ – CNG		NG16
3. Bond development length – failed anchorage	PS	G14	
	SC	G17	
	CG	G9	

[a]PS = polymer silica cements; SC = shrinkage-compensating cement; CG = control grouted; CNG = control nongrouted; FC = fibrous concrete. f_s' = ultimate tensile strength of the tendon.

a cylindrical mold 0.10 m diam by 0.25 m high and measuring bleed water and shrinkage (or expansion) on curing, (2) compressive strengths and rate of strength gain determined by testing 50-mm cube specimens, (3) tensile strengths measured by conducting splitting-tensile strength tests on 50-mm cubes and modulus of rupture tests on 50 by 50 by 300-mm prisms, (4) bond strengths evaluated by the "pull-out" test setup presented in Fig. 1.31, (5) pumpability and performance evaluated by grouting and testing of flexure specimens, and (6) bond development length* evaluated by releasing the anchorage at one end of a grouted tendon flexure specimen 0.15 m wide by 0.30 m deep by 3.1 m long and measuring with mechanical and strain gages the concrete surface strains at the level of the prestressing.

*Bond development length will be defined as the length required for a tendon to develop maximum stress when the anchorage is released.

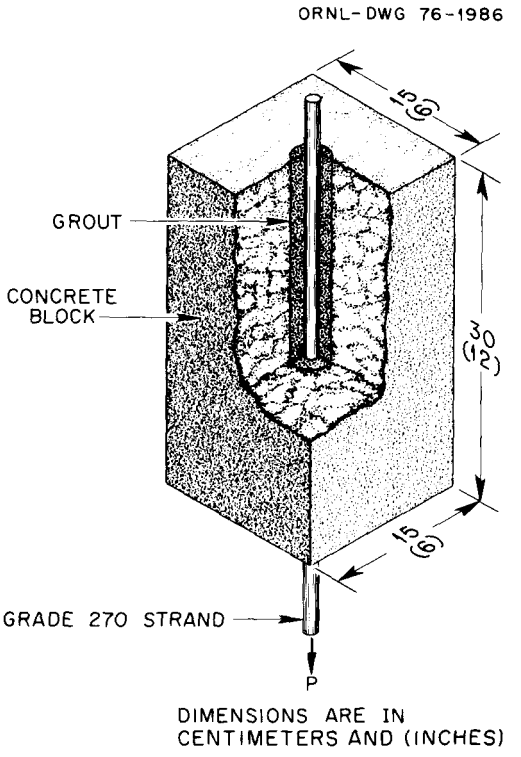

Fig. 1.31. Tendon Bond Strength Test Specimen.

Fiber-reinforced concrete consists of hydraulic cements containing fine aggregate or fine and coarse aggregates and discontinuous, discrete fibers, which are blended into concrete during the mixing cycle. The addition of fibers increases its strength, ductility, and resistance to dynamic loadings. An indication of the performance of fibrous concrete as a prestressed member will be assessed by casting four fibrous concrete beams 0.15 m wide by 0.30 m deep by 3.1 m long. Two grouted and two nongrouted beams will be tested with effective prestressing levels of $0.6f'_s$, and $0.7f'_s$ (where f'_s is the ultimate tensile strength) for each type beam. Grouting and testing procedures will be identical to those used for the grouted-nongrouted tendon behavior tests. The relative performance of the fibrous concrete flexure members will be determined by comparing the results with those obtained in the grouted-nongrouted tendon behavior tests.

Shrinkage-compensating expansive cements are designed to compensate for the tensile stresses produced during drying shrinkage of concrete.

These materials possess the ability to eliminate or reduce drying shrinkage cracks if proper design, construction, and quality control procedures are exercised. A commercially available shrinkage-compensating cement has been obtained for evaluation as a grouting material. Three flexure beams 0.15 m wide by 0.30 m deep by 3.1 m long having steel tendons post-tensioned to levels of 0.5, 0.6, and 0.7 times f_s' have been grouted with the shrinkage-compensating cement and are being cured before testing.

1.5.2.3 Corrosion Behavior

The corrosion protection provided by grouting of tendons is currently under investigation. The test procedure outlined in the previous report has been modified so that the investigation will complement a corrosion study currently being conducted in the Metals and Ceramics Division, and the time required for the study will be greatly reduced. Performance of flexure members containing a simulated corrosion-induced failed tendon is also being evaluated.

Only the center, straight wire of a seven-wire nongrouted strand is being tested. The test specimens are prepared by degreasing the wire with acetone, inspecting it for flaws, applying, if required for the particular test, the corrosion-inhibiting compound* to the wire surface within the gage length, placing the gage length of the wire in a polyethylene bottle, filling the bottle with demineralized water, bubbling hydrogen sulfide gas for 10 to 15 min through the water, sealing the bottle with a rubber stopper, placing the specimen in the testing machine, loading the specimen to the desired load level of $0.5f_s'$ to $0.8f_s'$ (where f_s' was determined for control tests),† and maintaining the load at this level until either the wire failed or six days lapsed. Figure 1.32 presents an untested specimen. Table 1.9 summarizes the results for specimens tested.

---

*Commercially available corrosion-inhibiting compounds such as would be used for protection of circumferential prestressing of an HTGR and protection in secondary containments in PWRs.

†Preliminary testing of the center wire established the wire ultimate strength, yield strength, and modulus of elasticity values as 1.92, 1.78, and 206.2 GPa, respectively.

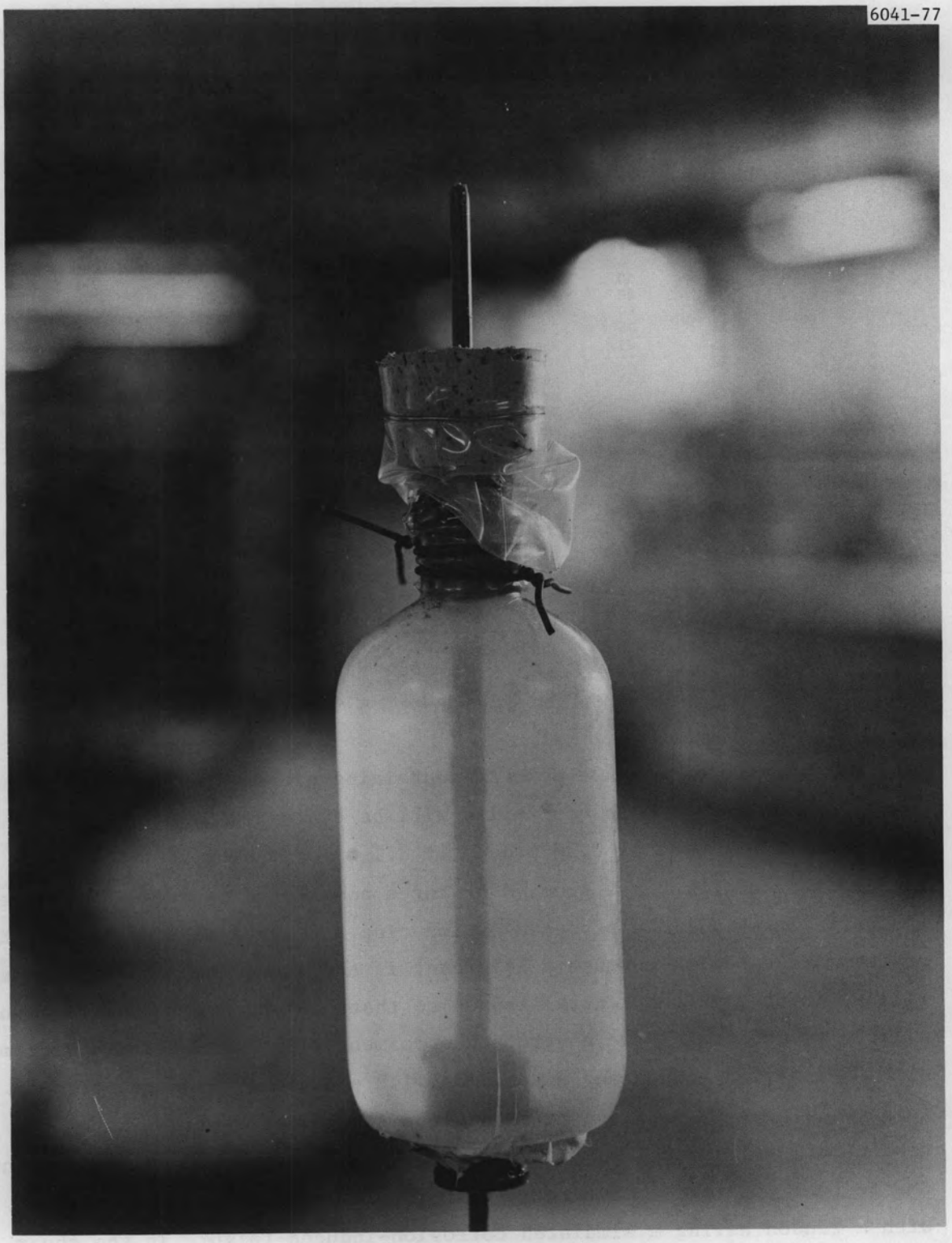

Fig. 1.32. Tendon Corrosion Test Specimen.

Table 1.9. Tendon Corrosion Test Summary

Specimen	Load (% of Ultimate)	Corrosion Inhibiting Compound	Corrosive Solution	Failure Time (min)	Failure Load (kN)
5	a	None	None		28.64
7	a	None	None		28.47
8	a	None	None		28.91
9	a	None	None		28.58
10	a	None	None		28.80
12	a	None	None		28.80
13	a	None	None		28.87
31	80	None	$H_2S + H_2O$	117	22.82
32	80	None	$H_2S + H_2O$	152	22.82
33	80	None	$H_2S + H_2O$	108	22.82
14	75	None	$H_2S + H_2O$	143	21.35
15	75	None	$H_2S + H_2O$	43	21.35
17	75	None	$H_2S + H_2O$	47	21.35
18	75	None	$H_2S + H_2O$	40	21.35
19	70	None	$H_2S + H_2O$	143	20.02
20	70	None	$H_2S + H_2O$	102	20.02
29	70	None	$H_2S + H_2O$	72	20.02
36	60	None	$H_2S + H_2O$	124	17.13
37	60	None	$H_2S + H_2O$	71	17.13
38	60	None	$H_2S + H_2O$	78	17.13
39	60	None	$H_2S + H_2O$	126	17.13
26	70	2889[b]	$H_2S + H_2O$	8640[c]	27.36
28	70	2090-P4[b]	$H_2S + H_2O$	9630[c]	27.58
34	80	1601 Amber[b]	$H_2S + H_2O$	8580[c]	29.36
35	80	2090-P4[b]	$H_2S + H_2O$	8230[c]	29.67
41	60	2889[b]	$H_2S + H_2O$	9600[c]	29.98
43	60	Grout	$H_2S + H_2O$	9144	17.13
44	60	None	0.2 *M* NH_4NO_3	10440[c]	30.92

[a]Not applicable, control specimen.

[b]Viscosity Oil Company.

[c]No failure within six days; specimen then loaded to failure.

Performance of flexure members containing either grouted or nongrouted tendons in which a tendon has failed will be evaluated by tests using specimens 0.30 m wide by 0.30 m deep by 3.1 m long. The test specimens each contain either three grouted or three nongrouted tendons. Simulated tendon failures will be produced by inducing a failure in a small length of the middle tendon through a hole cast in the specimen. These failures will be induced in the central tendon so that beam behavior under loading will be symmetrical. Two nongrouted specimens will be tested: a specimen without a failed tendon and a specimen with a corrosion-induced tendon failure. Three grouted specimens will be tested: a specimen without a tendon failure, a specimen with a simulated corrosion-induced failure in the central constant-moment region of the test specimen, and a specimen with a tendon having a simulated corrosion-induced failure in the shear region of the beam. Relative performance of the specimens will be evaluated through load-deformation behavior, cracking, and load transfer just after a tendon failure.

1.5.2.4 Tendon Monitoring Techniques

Associated with Task 7 (Instrumentation Evaluation and Development) of the PCRV Base Program, a phase of this investigation will be conducted to provide input on an assessment of acoustic emission as a technique for monitoring the structural integrity of PCRVs, in particular the grouted tendons. Basic tests will be conducted to identify concrete microcracking and fracture, prestressing tendon fracture, and tendon slippage. The ability of the technique to detect and locate flaws in more complex concrete composite members will also be investigated. Work to date has been concerned with procurement of a multichannel acoustic emission source location system and has been reported in Sect. 1.4.2.

1.6 LINER AND PENETRATION STUDIES — R. K. Nanstad and D. A. Canonico

The prestressed concrete reactor vessel (PCRV) for the High-Temperature Gas-Cooled Reactor (HTGR) is designed according to the rules of Sect. III, Division 2 of the *ASME Boiler and Pressure Vessel Code.*[8] However, for several steel penetrations and closures of the PCRV Division 2 of the Code refers to the rules of Division 1.[9] Appendix G (Protection Against Nonductile Failure), Subsection NA of Division 1 provides certain requirements regarding material fracture toughness. The steels used for PCRV penetrations and closures are different from the light-water reactor (LWR) pressure vessel steels that were used to establish these fracture toughness requirements. Thus, the purpose of this task is to develop a technically consistent fracture toughness position for PCRV liner and penetration steels. The bulk of the program involves obtaining fracture toughness data for representative heats of those steels. Additionally, other mechanical property tests and metallographic examinations are conducted for supportive material data.

The requirement for fracture toughness is manifested in the reference fracture toughness curve, commonly called the K_{IR} curve, shown in Fig. 1.33. The K_{IR} curve was developed with static, dynamic and crack arrest fracture toughness data of LWR steels. The curve is plotted relative to the reference nil-ductility temperature (RT_{NDT}) for each particular material. The RT_{NDT} of a material is determined by first performing a drop-weight test to determine the nil-ductility temperature (NDT). Charpy V-notch

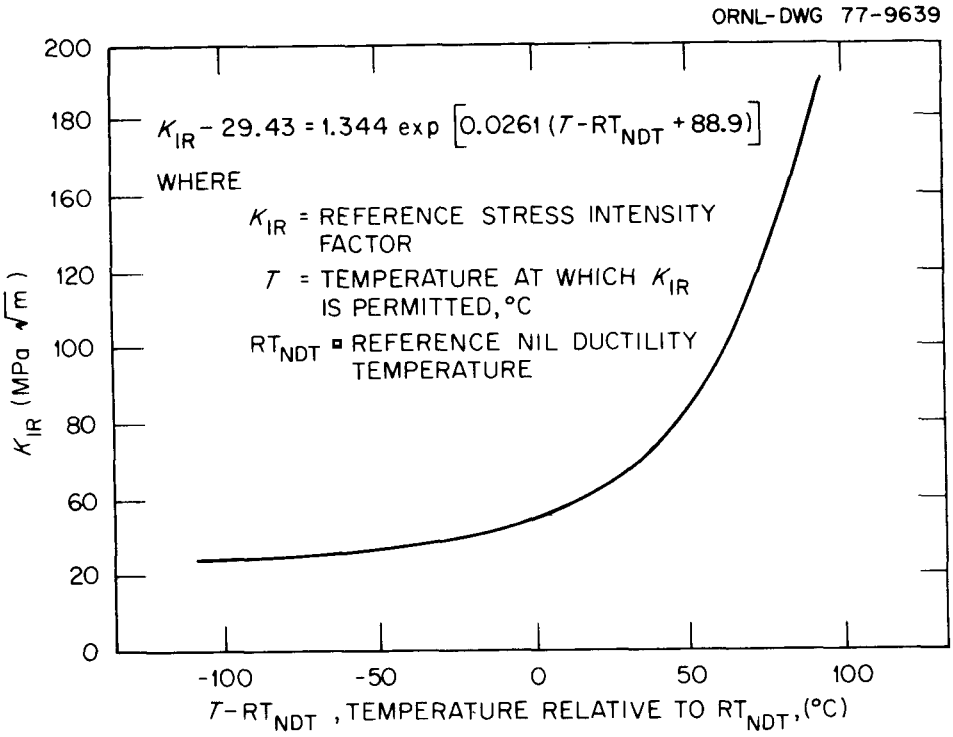

Fig. 1.33. Fracture Toughness K_{IR} Curve.

specimens are then tested at the NDT + 33°C (60°F) and must result in the attainment of at least 70 J (50 ft-lb) absorbed energy and 0.899 mm (0.035 in.) lateral expansion. If those requirements are met, the RT_{NDT} is equal to the NDT. If they are not met, the test temperature is increased in increments of 5.6°C (10°F) until the energy absorption and lateral expansion requirements are met. The excess temperature needed for compliance is then added to the NDT to define the RT_{NDT}. Since the K_{IR} curve is plotted relative to the function, $T - RT_{NDT}$, it provides a normalization procedure for comparing materials with different values of RT_{NDT}. At any selected test temperature, then, the fracture toughness data for the steel must be greater than the point on the K_{IR} curve at that test temperature. Further details concerning the genesis of the K_{IR} curve can be found in ref. 10. The equations are given below for construction of the K_{IR} curve in metric or English units.

$$K_{IR} = 29.43 + 1.344 \exp[0.0261(T - RT_{NDT} + 88.9)] \ , \qquad (1)$$

where T and RT_{NDT} are in °C and K_{IR} is in MPa$\sqrt{m}$.

$$K_{IR} = 26.78 + 1.223 \exp[0.0145(T - RT_{NDT} + 160)] , \qquad (2)$$

where T and RT_{NDT} are in °F and K_{IR} is in ksi$\sqrt{in.}$.

The materials of interest to the PCRV liner study are given in Table 1.10 along with a summary of material specifications. In addition to the base materials, tests will be conducted with weldments, both weld metal and heat affected zone (HAZ), of various configurations (plate to plate, plate to forging, and forging to forging) and welding procedures (submerged arc and manual arc). Additionally, the high-temperature alloy (1 1/4 Cr-1/2 Mo) will be thermally aged up to 10,000 hr at 343°C (650°F). The tests to be conducted and the specimens to be used are given in Table 1.11. Applicable test procedures of the ASTM are used in all cases for which they exist.[11–14] In the case of static fracture toughness tests that do not exhibit plane strain behavior, and for dynamic fracture toughness tests, state-of-the-art procedures, such as the equivalent energy and J-integral approaches, will be used to interpret test results.[15–16]

The previous annual report[17] discussed interpretation of the ASME Code with regard to location of test coupon removal in forgings. Hardness measurements throughout a cross-section of an A 508 Class 1 forging showed only small differences in hardness levels from the 38 by 19 mm (1.5 by 3/4 in.) location to the (1/4)t by t (t is thickness) location. However, the hardness plots did show that material located at the 38 by 19 mm location were in an area of the forging where hardness varied more than that at the (1/4)t by t location. Tensile tests of circumferentially oriented specimens showed that, whereas material from the 19 by 38 mm location gave an average ultimate tensile strength of about 517 MPa (75 ksi), material from the (1/4)t by t location averaged about 496 MPa (72 ksi) with some specimens as low as 486 MPa (70.6 ksi). The specification for A 508 Class 1 requires a minimum tensile strength of 483 MPa (70 ksi). Thus, all circumferential specimens met the tensile requirements but the (1/4)t by t material was very close to the minimum.

Table 1.10. Summary of PCRV Liner Materials Study
Material Specifications and Properties

Steel Identification[a]	Grade (Class)	Chemical Composition (wt %)										Tensile Requirements,[b] MPa(ksi)		Elongation (%)	Reduction of Area (%)
		C	Mn	P	S	Si	Mo	Ni	Cr	V	Cu	UTS	Yield Strength		
SA-508 (A 508)	(1)[c]	0.35	0.40/0.90	0.025	0.025	0.15/0.35	0.10	0.40	0.25	0.05		485–655 (70–95)	240 (35)	20	38
ORNL (F1)		0.17	1.27	0.010	0.006	0.30	0.12	0.40	0.20	0.003	0.05	496 (72)	344 (50)	(30)	(78)
SA-182	F11	0.10/0.20	0.30/0.80	0.040	0.040	0.50/1.00	0.44/0.65		1.00/1.50			483 (70)	276 (40)	20	30
SA-537 (A 537)	(1)	0.24	0.95/1.65	0.035	0.040	0.13/0.55	0.08	0.25	0.25		0.35	483–621 (70–90)	345 (50)	22	
ORNL (P1)		0.21	1.45	0.009	0.006	0.23	0.08	0.16	0.21		0.06	551 (80)	351 (51)	25	70
ORNL (P2)		0.22	1.56	0.007	0.006	0.16	0.08	0.25	0.06		0.06	551 (80)	365 (53)	25	74
SA-537 (A 537)	(2)	0.24	0.95/1.65	0.035	0.040	0.13/0.55	0.08	0.25	0.25		0.35	552–689 (80–100)	414 (60)	22	
ORNL (P4)		0.22	1.58	0.009	0.001	0.27	0.05	0.25	0.10		0.07	564 (82)	400 (58)	24	73

[a]Specifications have been taken from the *ASME Boiler and Pressure Vessel Code, Section II Part A* (1974 Addenda through Winter 1975).

[b]Tensile properties obtained to date with F1, P1, P2, and P4 were obtained with a subsize tensile specimen of 4.52 mm (0.178 in.) diameter and 31.75 mm (1.25 in.) gage length.

[c]Code Case 1332-6 allows an Mn content up to 1.35% providing that C is limited to 0.30% max. Forging F1 was produced according to Code Case 1332-6.

Table 1.11. Summary of PCRV Liner Study Testing Program

Test	Analysis	Specimens Used
Tensile	Yield strength Ultimate tensile strength Fracture strength Elongation Reduction of area	Round tensile specimens of 4.47 and 12.83 mm diam (0.176 and 0.505 in.)
Impact toughness	Absorbed energy Lateral contraction Instrumented behavior	Charpy V-notch
Drop-weight	Nil-ductility temperature (NDT)	15.9 mm (5/8 in.) P3
Fracture toughness	Static (K_{Ic}, K_{Icd}, J_{Ic}) Dynamic (K_{Id}, K_{Idd}, J_{Id}) Instrumented behavior	Precracked Charpy, compact tension (various thicknesses)

Charpy V-notch impact specimens from various locations within the forging were tested to determine any significant difference in toughness behavior as a function of distance from a quenched edge and orientation within the forging. We previously[17] reported initial impact toughness results with an unexplained difference between ORNL and Japan Steel Works (JSW) data. It was believed that JSW data reflected the LT orientation (circumferential specimen with an axial crack). Subsequent testing of TL oriented specimens (axial specimens with circumferential cracks) showed data comparable to that from JSW. Figure 1.34 shows the C_V energy data for $(1/4)t$ by t specimens. The TL orientation results in less toughness above the NDT. The NDT was determined with the drop weight test and is given on the curve at −57°C (−70°F). Regarding the question of specimen location within the forging, Fig. 1.35 shows the C_V data for TL-oriented specimens from both the $(1/4)t$ by t and 38 by 19 mm locations. There appears to be no significant difference in impact toughness over the temperature range examined.

A cross section of the forging was sectioned into C_V specimens with the LT orientation, and test results showed substantial differences in toughness for neighboring specimens tested at the same temperature.

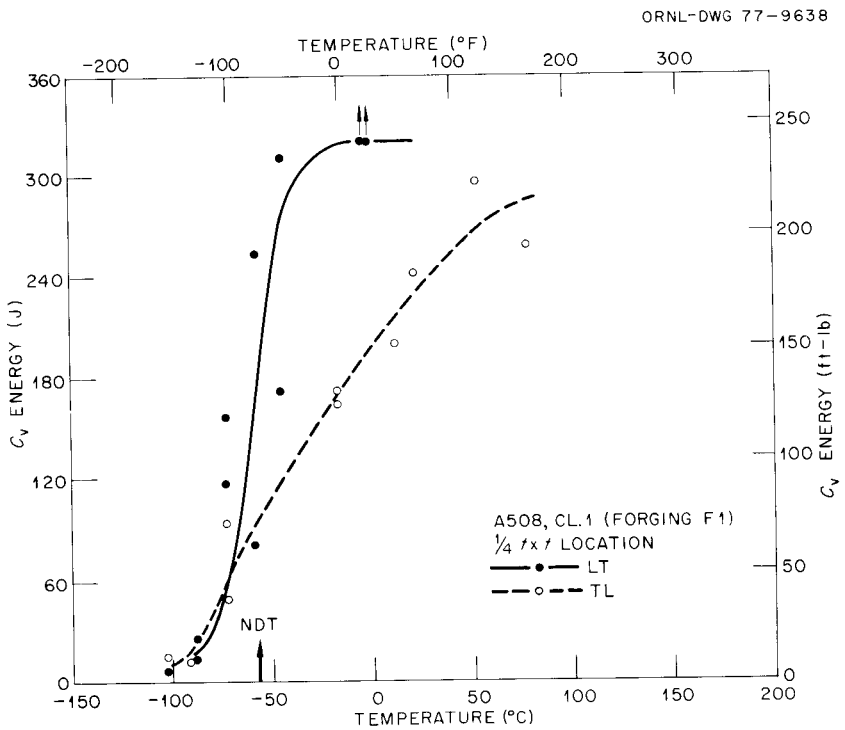

Fig. 1.34. Charpy Energy Data for (1/4)t by t Specimens.

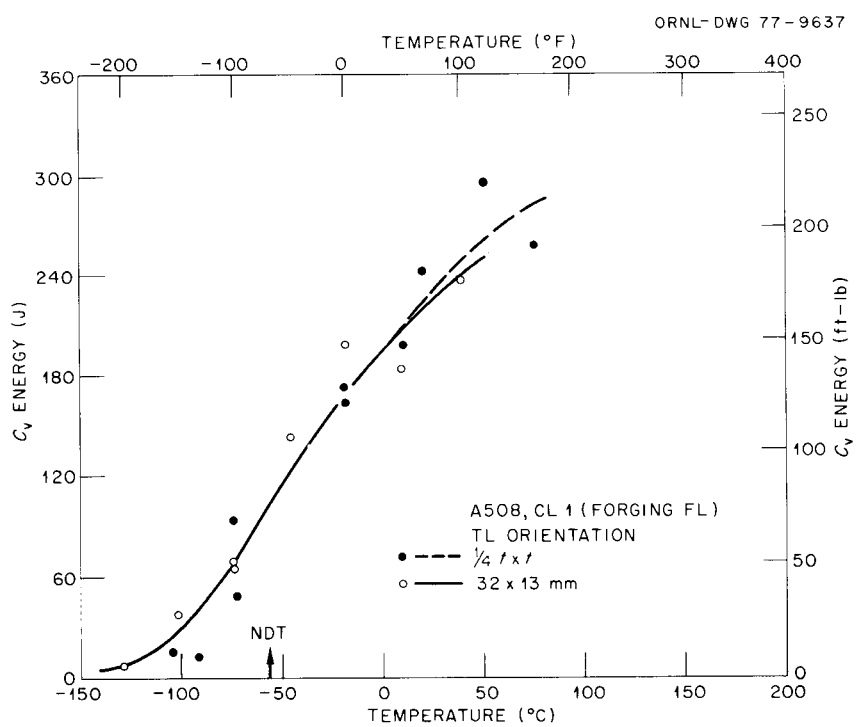

Fig. 1.35. Charpy Energy Data for TL-Oriented Specimens from (1/4)t by t and 38 by 19 mm Locations.

However, as Fig. 1.35 showed, the C_V toughness curve for the LT orientation is very steep, and much variation in the elastic-plastic region of the curve is not unexpected.

The A 537 plate materials were tested for impact toughness also. The two heats of A 537 Class 1, designated P1 and P2, have drop-weight NDT values of −40°C (−40°F) and −46°C (−50°F), respectively. The A 537 Class 2 plate has an NDT of −51°C (−60°F). C_V specimens were removed with both the LT and TL orientations. In all three cases the C_V curves for the TL orientation lie at higher temperatures than those for the LT specimens. Figure 1.36 graphically compares the C_V toughness of the A 537 plate materials and the A 508 Class 1 forging. The TL orientation and (1/4)*t* by *t* location are represented in each case. The forging and the A 537 Class 2 (P4) plate are very similar in their C_V toughness behavior. Both were quenched and tempered, while the A 537 Class 1 plates are normalized and tempered. All materials have excellent toughness, in excess of normal specifications.

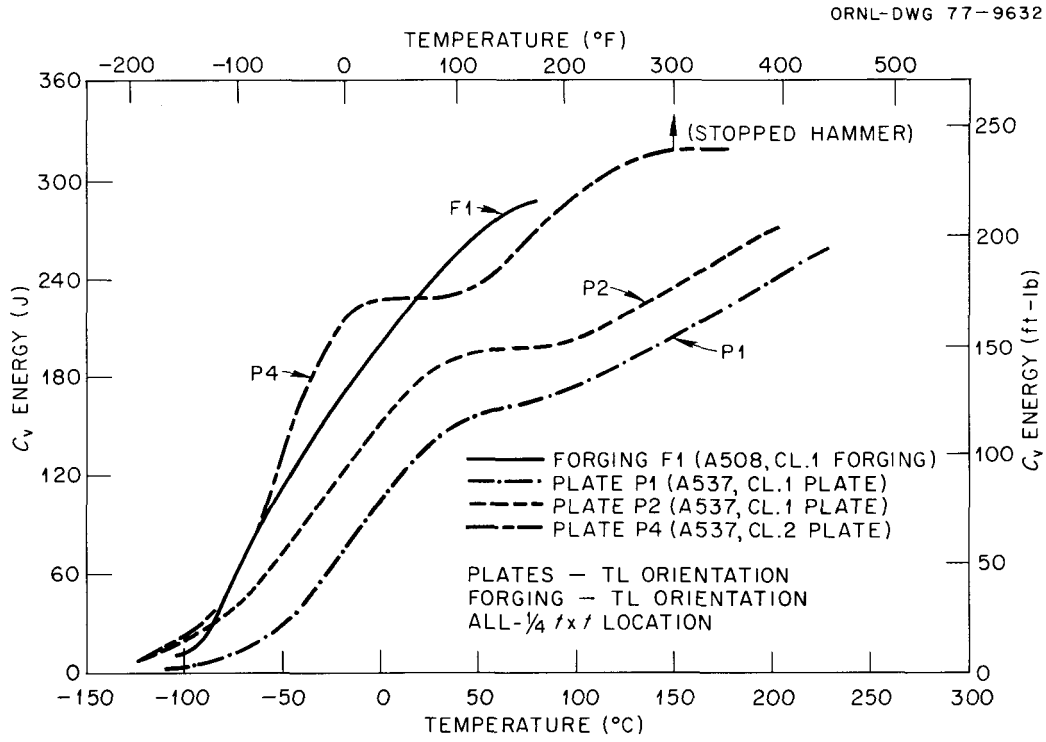

Fig. 1.36. Comparison of C_V Energy Values for A 537 Plate and A 508 Class 1 Forging.

We also tensile tested the A 508 Class 1 forging and A 537 plates. Yield strength, ultimate tensile strength, fracture strength, and deformation properties (such as elongation and reduction of area) have been measured at various temperatures. For example, Fig. 1.37 compares the yield strengths of the tested materials. The forging and plates meet the minimum room-temperature specifications. Although the minimum specified yield strength for the forging is 241 MPa (35 ksi), its actual yield strength is almost as high as the A 537 Class 1 plate at about 344 MPa (50 ksi). The other tensile properties show no unexpected behavior and adequately satisfy specifications.

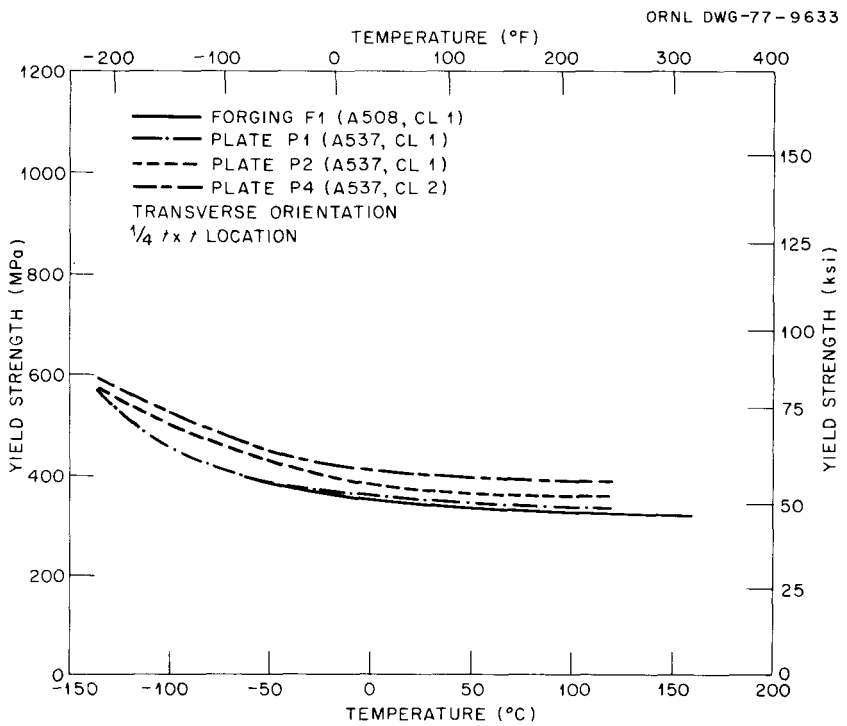

Fig. 1.37. Comparison of Yield Strengths of Pressure-Vessel Steels.

As mentioned previously, fracture toughness is being analyzed through the use of instrumented pre-cracked Charpy specimens, tested under impact and slow-bend conditions, and with compact tension specimens. Initial results for the A 508 Class 1 forging are shown in Fig. 1.38. Both slow-bend (K_{Icd}) and impact (K_{Idd}) fracture toughness data are shown for pre-cracked Charpy specimens. The dynamic curve is shifted from the

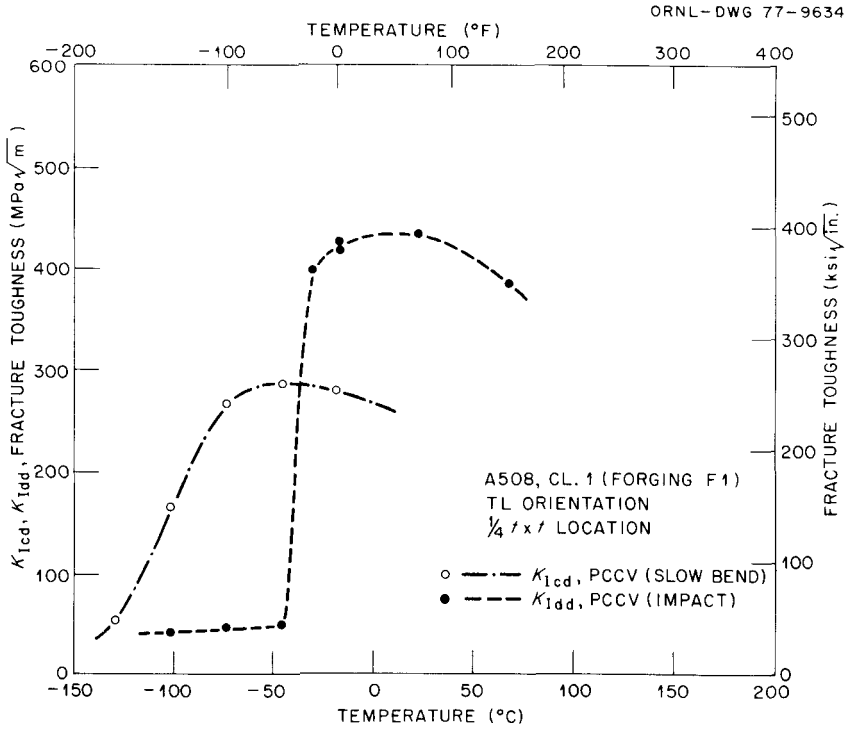

Fig. 1.38. Initial Fracture Toughness Test Results for the A 508 Class 1 Forging.

slow-bend curve toward higher temperatures. It should be noted also that the dynamic results show a very dramatic increase from low to high fracture toughness in a very small temperature regime, about 12°C (20°F), and the upper-shelf toughness level is higher in the dynamic situation.

Figure 1.39 shows the results from slow-bend pre-cracked Charpy tests with the A 537 plate steels. With the limited number of data points shown, plates P1 and P2 (both A 537 Class 1) give similar fracture toughness results over the range of test temperatures shown. Plate P4 (A 537 Class 2) shows a 200-MPa $\sqrt{m}$ transition (arbitrarily chosen near the center of the toughness range) 40–50°C (72–90°F) lower than the Class 1 material. The Class 2 plate is quenched and tempered, which accounts for the greater degree of toughness compared with the normalized and tempered Class 1 steel.

Initial compact tension tests, with specimens of the same thickness as a Charpy specimen (0.394T), provide equivalent energy data that agrees well with the pre-cracked Charpy slow-bend data for the forging and plates.

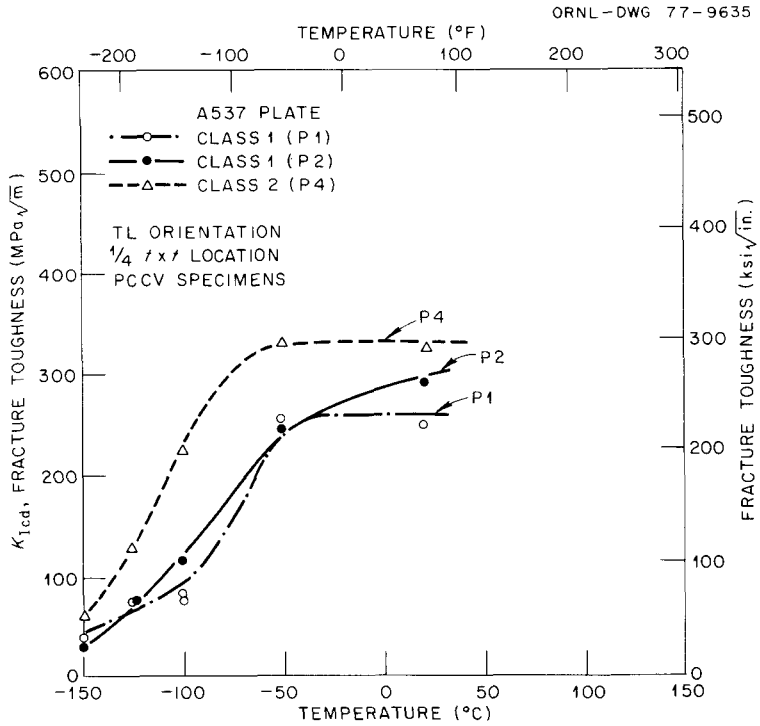

Fig. 1.39. Results of Slow-Bend Pre-Cracked Charpy Tests of A 537 Plate Steels.

Shown in Fig. 1.40 is a plot of pre-cracked Charpy fracture toughness data, relative to $T - \mathrm{RT}_{\mathrm{NDT}}$, for A 508 Class 1 and A 537 Classes 1 and 2. The K_{IR} curve discussed previously is depicted for comparison. The data represent specimens from the (1/4)t by t location and both the LT and TL orientations. The dynamic fracture toughness $K_{\mathrm{I}dd}$ results from the forging material are seen to be near or on the K_{IR} curve where $T - \mathrm{RT}_{\mathrm{NDT}}$ is from −50 to 0°C. Those same data points were plotted in Fig. 1.38 without the K_{IR} curve. Those dynamic data are the only fracture toughness values that are not very conservative with regard to the K_{IR} requirements so far in the program. It must be kept in mind, however, that Fig. 1.40 is plotted relative to $T - \mathrm{RT}_{\mathrm{NDT}}$. A material with a very low NDT can be unsatisfactory regarding the K_{IR} curve but yet be very tough at very low temperatures. For the case of the A 508 Class 1 forging, the data point that appears on the K_{IR} curve at a $T - \mathrm{RT}_{\mathrm{NDT}}$ of 10°C (18°F) occurs at an actual temperature (Fig. 1.38) of −46°C (−50°F). The test at −32°C (−25°F) shows a dramatic increase in toughness, which illustrates the excellent toughness of the material. The point to be emphasized is that

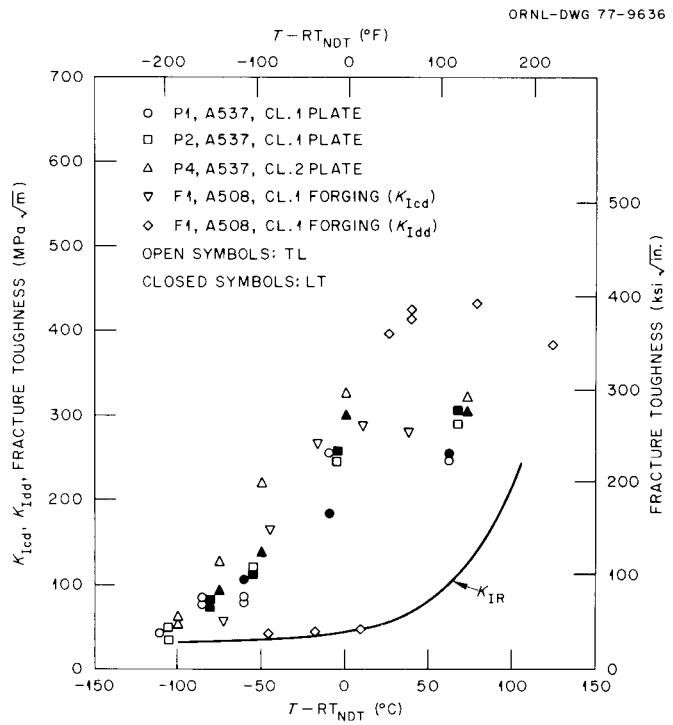

Fig. 1.40. Pre-Cracked Charpy Fracture Toughness Relative to $T - RT_{NDT}$ for A 508 Class 1 and A 537 Classes 1 and 2 Steels.

the fracture toughness capability of a material cannot necessarily be judged solely on the basis of satisfaction of the existing K_{IR} curve. Additional testing of larger compact tension specimens is under way on the same materials discussed herein as well as on other materials and weldments.

1.7 LONG-TERM CREEP AND MOISTURE MIGRATION STUDIES — J. P. Callahan

We have completed the investigation of creep behavior of concrete subjected to various uniaxial, biaxial, and triaxial states of stress and temperatures of 24.0 and 65.6°C (297.2 and 338.8 K). The experimental studies were divided into two phases. One phase was conducted at the U.S. Army Engineers Waterways Experiment Station [Interagency Agreement A T-(40-1)-3636]. Concretes having three different moduli of elasticity were investigated. The second phase was conducted at the University of Texas at Austin (Subcontract 2864). This phase consisted of an extensive investigation of a single limestone aggregate concrete. The test matrices of the two independent investigations were designed

to overlap sufficiently to provide an evaluation of the degree of agreement of creep data obtained by different investigators testing the same concrete. The final reports of both investigations were published during the current reporting period.[18,19]

The following summarizes the report[18] of the Waterways Experiment Station Study. It describes an investigation to develop information on the time-dependent deformation behavior of concrete in the presence of temperature, moisture, and loading conditions similar to those encountered in a PCRV. This particular investigation encompassed one concrete strength [41 MPa (6000 psi) at 28 days], three aggregate types (chert, limestone, and graywacke), one cement (Type II), two types of specimens (as-cast and air-dried), two temperatures during test [23 and 66°C (73 and 150°F)], and four types of loading (uniaxial, hydrostatic, biaxial, and triaxial). The report was intended primarily as a data report; therefore, the experimental procedures and results are presented in detail. A comprehensive evaluation of the effects of various parameters and their interactions on the behavior of concrete was not included. However, a number of general comparisons were made concerning the effect of the various test conditions on concrete behavior. Based on this limited evaluation of the data, general conclusions and recommendations for additional work were formulated.

The following is a summary of the final report[19] of the University of Texas study: The creep behavior of concrete subjected to multiaxial compressive stresses and elevated temperatures was studied experimentally. Strains were measured in cylindrical specimens subjected to 58 test conditions involving a variety of multiaxial loading conditions [compressive stresses ranging from zero to 25 MPa (3600 psi)], three curing times (90, 183 and 365 days), two curing histories (air-dried and as cast) and two temperatures [24 and 66°C (75 and 150°F)]. Specimens cured for 90 days were subjected to a prescribed load and temperature for 12 months, followed by a five-month unloaded recovery period at the prescribed temperature. Specimens cured for 183 or 365 days were subjected to uniaxial stresses of 4.1 or 17 MPa (600 or 2400 psi) for approximately 5.25 or 4.75 years at 24°C (75°F), followed by a 77-day recovery period. Strain was measured periodically during the loaded and unloaded periods

to evaluate the creep and creep recovery behavior of concrete. The report describes and evaluates the procedures and equipment used in the study and summarizes the test results; the overall program is evaluated and conclusions and recommendations are presented.

A report will be prepared at ORNL to compare the results of the two investigations.

1.8 REFERENCES

1. T. Takeda et al. "Pressure Tests of PCRV Models," paper presented at the Seventh Congress of the Fédération Internationale de la Précontrainte, New York, 1974.
2. Z. P. Bazant, P. D. Bhat, and C. Shiek, *Endochronic Theory for Inelasticity and Failure Analysis of Concrete Structures,* ORNL/SUB/4403-1, Northwestern University, Evanston, Ill. (to be published).
3. H. O. Abdulrahman, *ISA, Interactive Stress Analysis, a Program for Plane Stress, Plane Strain and Axisymmetric Analysis of Structural Continua-Users Manual,* ORNL/SUB/4164-2, University of Illinois, Urbana, Ill. (July 1976).
4. T. A. Lopez, J. Urzua, R. H. Dodds, and D. R. Rehak *FINITE, A POLO II Subsystem for Structural Mechanics,* Civil Engineering Systems Laboratory, University of Illinois, Urbana, Ill. October 1976.
5. J. D. Reins, J. L. Quiros Jr., W. C. Schnobrick, and M. A. Sozen *Shear Strength of End Slabs of Prestressed Concrete Nuclear Reactor Vessels,* ORNL/SUB/4164-1, University of Illinois, Urbana, Ill. (July 1976).
6. D. J. Naus, "Instrumentation Evaluation and Development" *HTGR Base Technology Program Prog. Rep. Jan. 1, 1974—June 30, 1975,* ORNL-5108, pp. 48—59.
7. F. S. Ople, General Atomic Company, private communication to J. P. Callahan, Oak Ridge National Laboratory, January 22, 1975.
8. *ASME Boiler and Pressure Vessel Code, Sect. III, Div. 2, Code for Concrete Reactor Vessels and Containments,* American Society of Mechanical Engineers, New York, 1975 plus addenda; this document is also American Concrete Institute Standard 359—74.

9. *ASME Boiler and Pressure Vessel Code, Sect. III, Div. 1, Rules for Construction of Nuclear Power Plant Components,* American Society of Mechanical Engineers, New York, 1975 plus addenda.

10. *PCRV Recommendations on Toughness Requirements for Ferritic Materials, PCRV Ad Hoc Task Group on Toughness Requirements,* WRC Bulletin 175, Welding Research Council, August 1972.

11. "Tension Testing of Metallic Materials," ASTM Designation: E 8-69, *1976 Annual Book of ASTM Standards, Part 10,* American Society for Testing and Materials, Philadelphia, 1976.

12. "Conducting Drop-Weight Test to Determine Nil-Ductility Transition Temperature of Ferritic Steels," ASTM Designation: E 208-69 (Reapproved 1975), *Annual Book of ASTM Standards, Part 10,* American Society for Testing and Materials, Philadelphia, 1976.

13. "Notched Bar Impact Testing of Metallic Materials," ASTM Designation: E 23-72, *Annual Book of ASTM Standards, Part 10,* American Society for Testing and Materials, Philadelphia, 1976.

14. "Plane-Strain Fracture Toughness of Metallic Materials," ASTM Designation: E 399-74, *Annual Book of ASTM Standards,* American Society for Testing and Materials, Philadelphia, 1976.

15. F. J. Witt, *Equivalent Energy Procedures for Predicting Gross Plastic Fracture,* ORNL, unpublished manuscripts.

16. J. D. Landes and J. A. Begley, "Test Results from J-Integral Studies: An Attempt to Establish a J_{Ic} Testing Procedure," pp. 170–86 *Fracture Analysis,* ASTM Spec. Tech. Publ. 560, American Society for Testing and Materials, Philadelphia, 1974.

17. R. K. Nanstad and D. A. Canonico, "Liner and Penetration Studies," HTGR Base-Technology Program Prog. Rep. *Jan. 1, 1974–June 30, 1975,* ORNL-5108, pp. 38–43.

18. J. E. McDonald, *Time-Dependent Deformation of Concrete Under Multiaxial Stress Conditions,* ORNL-TM-5052 (October 1975).

19. T. W. Kennedy, *An Evaluation and Summary of a Study of the Long Term Multiaxial Creep Behavior of Concrete,* ORNL/TM-5300 (December 1975).

2. STRUCTURAL MATERIALS

J. R. DiStefano

2.1 INTRODUCTION

One of the most important factors affecting the development of gas-cooled reactor systems is the availability of satisfactory materials. Components of an HTGR must be designed for very long lives at temperatures where properties of materials are time dependent. Thus, detailed data on the behavior of HTGR materials under reactor design conditions are needed to utilize improved and more accurate design methods and to satisfy safety requirements.

The main objective of this task then is to provide adequate data upon which the selection and justification of materials for high-temperature components can be based. Emphasis has been placed on obtaining prototypical environmental data on mechanical properties, corrosion resistance, and structural stability. Task areas, as reported below, include tensile, creep, fatigue, crack growth, weldments, and steam corrosion.

2.2 MECHANICAL PROPERTIES — C. R. Brinkman

2.2.1 Tensile Testing — A. Lystrup*

Tensile tests have been performed on Inconel 617 (Heat XX01A3US). Background data on the material are given in Table 2.1 and the results of the tensile tests are reported on Table 2.2. The rod-type specimens had a gage length of 31.8 mm (1.25 in.) and a gage diameter of 6.35 mm (0.25 in.). All the tests were run to failure at a strain rate of 0.4%/min. Ultimate tensile strengths were calculated from the load-crosshead movement curves, and the yield strengths were calculated from load-strain curves obtained by an extensometer attached to a 25.4 mm (1 in.) gage length.

---

*On assignment from Risö, Denmark; now returned.

Table 2.1. Data on Inconel 617 Used for Tensile Tests

Heat	XX01A3US
Source	The International Nickel Company, Inc. Huntington Alloy Products Division
Product form	12.7-mm (0.5-in.) plate
Heat treatment	Solution annealed
Hardness	Rockwell B 83
Chemical Composition, wt %	
Ni	57.35
Cr	20.30
Co	11.72
Mo	8.58
Fe	1.01
Al	0.76
Si	0.16
C	0.07
Mn	0.05
S	0.004

Yield strength of this material appeared to be very little affected by the temperature in the range 288 to 816°C (550–1500°F). Above 816°C (1500°F) the yield strength dropped very fast. Also, ultimate tensile strength decreased with increasing temperature; above 593°C (1100°F) the strength and amount of uniform elongation dropped rapidly.

For comparison the tensile properties of Hastelloy X (Heat 2600-3-4936), Hastelloy S (Heat 8635T), and Inconel 617 (Heat XX01A3US) are shown in Fig. 2.1. (The tensile properties of Hastelloy X and Hastelloy S were reported previously.[1]) The strength properties of Hastelloy X and Inconel 617 differ little; however, the yield strength of Hastelloy S is much higher up to 871°C (1600°F), and the ultimate tensile strength of Hastelloy S is higher up to 760°C (1400°F). Reduction of area is lower for Inconel 617 than for both Hastelloy X and Hastelloy S when the temperature is below 426°C (800°F). Above 600°C (1110°F) the reduction of area for Hastelloy S is higher than for the two other materials; however, all three materials show a minimum value of approximately 38% somewhere in the temperature range 538 to 704°C (1000–1300°F).

Table 2.2 Tensile Properties of Inconel 617 (Heat XX01A3US)

Test	Temperature		Yield Strength (0.2%)		Ultimate Tensile Strength		Elongation in 31.8 mm (1.25 in.)		Reduction of Area (%)	Remarks[a]
	(°C)	(°F)	(MPa)	(ksi)	(MPa)	(ksi)	Uniform (%)	Total (%)		
16545	22	72	303	43.9	747	108.3	54.1	54.3	36.2	
16546	22	72	301	43.7	757	109.8	59.6	60.9	40.7	
16547	22	72	305	44.3	754	109.3	57.4	57.9	38.4	
16548	149	300	260	37.7	698	101.2	61.3	61.7	40.9	
16549	149	300	251	36.4	698	101.2	60.2	61.4	44.0	
16550	288	550	225	32.6	671	97.3	63.2	64.8	46.0	
16551	288	550	221	32.0	663	96.2	66.7	68.7	49.6	
16552	288	550	217	31.5	665	96.5	60.7	61.9	44.0	
16553	427	800	222	32.2	640	92.8	63.1	65.4	45.7	
16554	427	800	223	32.3	635	92.1	62.3	64.2	40.1	BGM
16654	482	900	216	31.3	626	90.8	65.0	67.5	47.0	
16655	482	900	217	31.5	634	91.9	63.6	64.9	44.5	
16656	482	900	225	32.7	625	90.7	63.1	64.9	47.7	
16657	538	1000	216	31.3	610	88.5	64.7	67.3	49.8	
16658	538	1000	207	30.0	606	87.9	61.1	64.4	46.1	
16659	593	1100	201	29.1	589	85.4	59.3	60.4	43.1	BGM, SBY
16660	593	1100	203	29.5	589	85.4	57.6	58.7	42.3	SBY
16661	593	1100	206	29.9	596	86.4	61.3	62.6	39.2	BGM, SBY
16662	649	1200	210	30.4	539	78.2	51.6	59.2	39.2	BGM
16663	649	1200	210	30.4	545	79.1	53.7	62.4	39.8	BGM
16664	704	1300	199	28.8	466	67.6	29.3	68.0	49.3	
16665	704	1300	196	28.4	443	64.2	25.9	69.9	53.1	
16666	704	1300	196	28.4	454	65.9	29.9	74.7	52.5	
16667	760	1400	210	30.5	368	53.4	10.3	86.3	69.1	SBY
16668	760	1400	208	30.2	370	53.6	11.0	86.2	68.9	BGM, SBY
16669	816	1500	210	30.4	263	28.1	4.6	111.1	87.0	BGM, SBY
16670	816	1500	210	30.5	269	39.0	4.9	108.4	82.6	SBY
16671	816	1500	211	30.6	270	39.1	5.8	95.8	82.6	BGM, SBY
16672	871	1600	181	26.3	194	28.1	3.2	88.0	87.8	BGM
16673	871	1600	189	27.4	194	28.1	3.2	91.6	86.0	
16674	927	1700	127	18.4	139	20.2	2.2	99.2	88.8	
16675	927	1700	125	18.1	136	19.7	2.1	110.3	90.3	BGM
16676	927	1700	123	17.9	134	19.5	3.2	96.4	89.1	BGM
16677	982	1800	97	14.0	101	14.7	1.9	75.0	73.9	
16678	982	1800	89	12.9	99	14.3	3.2	91.5	83.0	BGM

[a]BGM = Broke at Gage Mark. SBY = Serration Occurred Before 0.2% Yield.

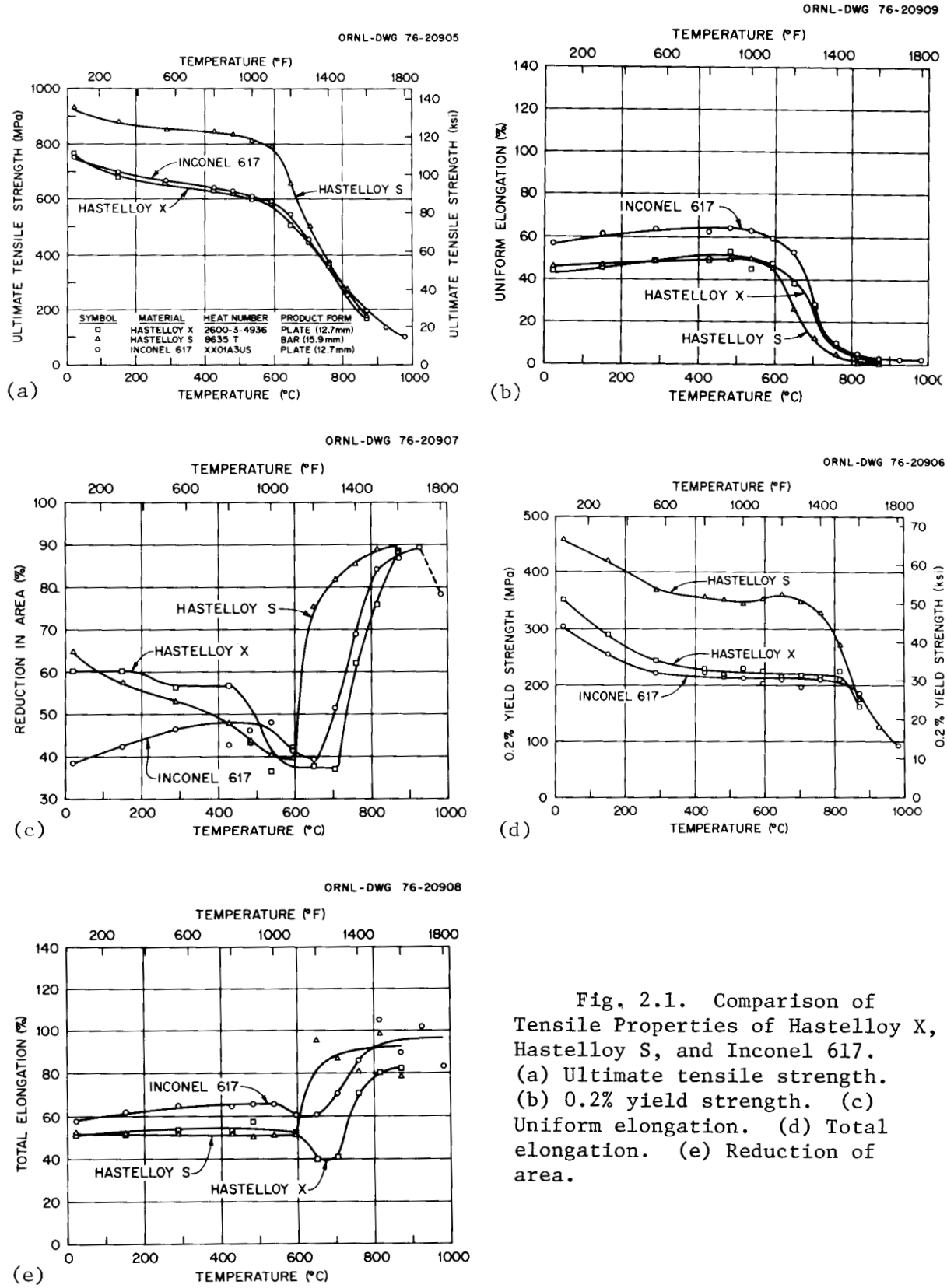

Fig. 2.1. Comparison of Tensile Properties of Hastelloy X, Hastelloy S, and Inconel 617. (a) Ultimate tensile strength. (b) 0.2% yield strength. (c) Uniform elongation. (d) Total elongation. (e) Reduction of area.

Uniform elongations are similar for all three materials, although it is a little higher for Inconel 617. The total elongations of Inconel 617 and Hastelloy X have minima at 649°C (1200°F) of 60% and 40%, respectively. Total elongation of Hastelloy S is fairly constant (51%) from room temperature up to 593°C (1100°F), but there it suddenly increases to approximately 90%.

2.2.2 Creep Testing — A. Lystrup

2.2.2.1 Environmental Test Facilities

Ten environmental creep frames have operated continuously through the year, and six new air creep machines for comparison tests were put into operation in December 1975. Simulated HTGR primary coolant helium for the environmental tests is supplied from premixed tanks containing nominal impurity contents of 250 ppm H_2, 25 ppm CH_4, and 15 ppm CO. The once-through dynamic-mix gas system has been reconstructed and modified, but it has not been tested yet.

Modifications and improvements in the gas analysis system were made during the year, and the status of the system is described below.

The H_2, CH_4, and CO concentrations in the helium are analyzed by a gas chromatograph. It is a Bendix series 2110 laboratory chromatograph with a Micro Cross Section Detector (MCSD) that uses ultrapure helium (99.9999%) as a carrier gas. This combination gives a very sensitive cell, but to obtain satisfactory and reproducible results, the system must be leaktight. The N_2 and O_2 concentrations in the gas, which can also be determined by the chromatograph, can give an indication of leaks in the system.

Results indicated by a chromatogram depend, among many other things, upon the size of the sample that is injected into the column. In order to duplicate the same sample size each time, both the pressure and volume of the sample must be controlled carefully. Volume is controlled by diverting the sample to be analyzed into a fixed-volume sample loop. At the same time, the pressure in the sample line must be checked to be sure it is maintained at the desired value.

Because of the complexity of the gas (high H_2 contents and small concentrations of CH_4 and CO), two sample volumes are needed to obtain accurate results. This was accomplished by the addition of a second fixed-volume sample loop. One of the sample valves diverts the helium to be analyzed into a large-volume sample loop [3-m-long, 3.2-mm-diam (10-ft by 1/8-in.) tube] to analyze the CH_4, CO, N_2, and O_2 contents, and the other sample valve opens to a small sample loop [1.5-m-long, 3.2-mm-diam (5 ft by 1/8-in.) tube] to analyze the H_2 content. A valve programmer automatically and serially injects the large and small samples. A typical chromatogram is shown in Fig. 2.2. To get the actual concentration of each component, the area under the peak is compared with the area under the corresponding peak obtained from a cylinder with a known gas composition.

Water vapor is analyzed by a Beckman model 340 trace moisture analyzer, in which the determination is based on the simultaneous absorption and electrolysis of water. The moisture analyzer is hooked up in series with but downstream from the gas chromatograph (see Fig. 2.3).

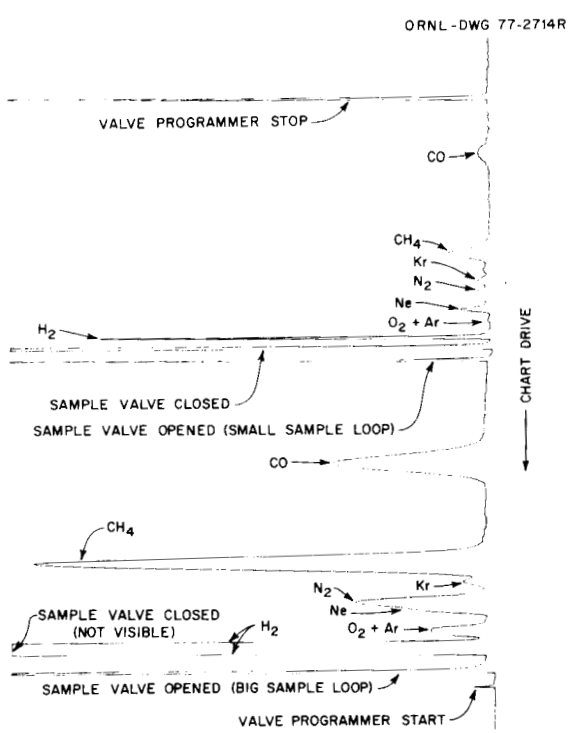

Fig. 2.2. Typical Gas Chromatogram Obtained from Entrance Gas.

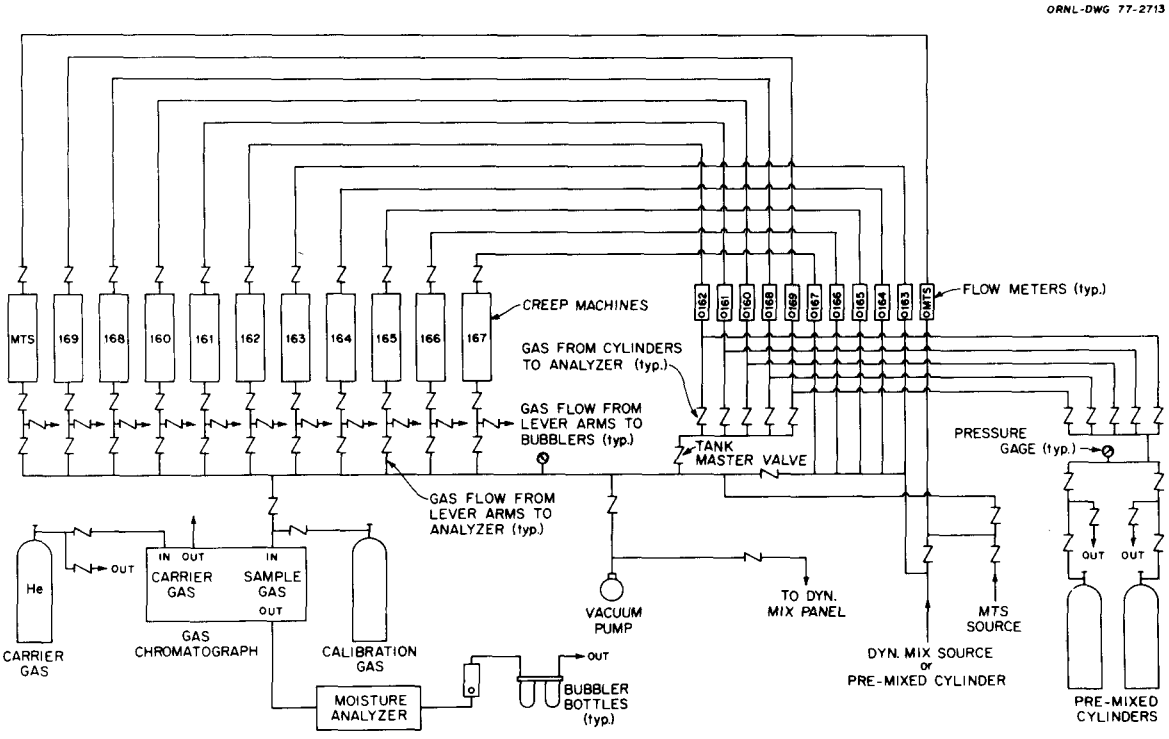

Fig. 2.3. Schematic Diagram of the HTGR Environment Test Facility.

The gas flow rate through both instruments is the same as the flow rate through each of the creep machines. In that way exit gas can be analyzed by the gas chromatograph and the moisture analyzer at the same time without changing the flow rate through the environmental creep chamber. An experiment showed that the composition of the gas (and, in particular, the moisture content) did not change when the gas was passed through the 65°C oven in the gas chromatograph. However, the moisture analyzer is very flow sensitive, and a flow-rate calibration curve was needed because the flow rate through the system is lower than that at which the moisture analyzer had been calibrated by the manufacturer.

For all tests completed thus far, the flow rate through the environmental creep machines has been 10 to 15 cm^3/min, and the pressure inside the chamber 0.12 MPa (1.2 atm).

To compare chromatograms from entrance and exit gas samples, it has been necessary to increase the pressure in the furnaces to 0.18 MPa (1.8 atm, the pressure of the entrance gas sample) during the period

that the exit gas is being analyzed. To eliminate this requirement, pressure in the furnaces has been raised to 0.18 MPa (1.8 atm). Besides the obvious advantage of not having to periodically change the test conditions, it is both simpler and faster to obtain an analysis of the exit gas. The impurity contents in our entrance and exit gases are shown in Table 2.3 together with the analyses of impurities in the environments of other test facilities and reactors.

The oxygen content in the entrance gas as determined by the gas chromatograph is not necessarily the oxygen level at which the creep specimen is exposed. Since the HTGR helium is a reducing gas mixture, the oxygen concentration is determined by equilibria among the species present when the gas enters the creep furnace. Among others, the two following reactions will occur:

$$H_2 + 1/2\ O_2 \rightleftharpoons H_2O\ ,$$

$$CO + 1/2\ O_2 \rightleftharpoons CO_2\ .$$

The first of those reactions generally determines the oxygen partial pressure.[9] Therefore,

$$P_{O_2} = (P_{H_2O}/KP_{H_2})^2\ ,$$

where K is the equilibrium constant. A typical value of the ratio P_{H_2O}/P_{H_2} in an exit gas is 0.073. At 750°C the equilibrium constant $K = 5.75 \times 10^9$, which gives an oxygen partial pressure of 1.6×10^{-17} Pa (1.6×10^{-22} atm) if equilibrium is reached. This low value cannot be detected on the gas chromatograph, but a chromatogram from the exit gas generally shows a negative response where the oxygen should appear. This means that the exit gas contains less oxygen than the carrier gas[10] (99.9999% He).

Since the gas in an HTGR is flowing and is probably equilibrated, the oxygen concentration will be very small [$<10^{-15}$ Pa (10^{-20} atm)]. Low

Table 2.3. HTGR Primary Coolant Compositions

Facility	Ref.	Condition	Impurity Partial Pressure, μatm[a]							Pressure	
			H_2	CH_4	CO	CO_2	H_2O	$O_2 + Ar$[b]	N_2	(MPa)	(atm)
					Test Facilities						
ORNL		Entrance gas	275–300	30–35	15–25		4–9	1–5	4–7	0.12	1.2
		Exit gas	250–280	25–35	10–20		15–25	<1	4–15	0.12	1.2
GA	2		1500	50	500		50				
CIIR (Oslo)	3,4	Wet	400		400		90			0.18	1.8
		Dry	100		100		20			0.18	1.8
		Ultradry	50–100	3–8	25–50		0.5–3	c	≤11	0.18	1.8
FIAT (Italy)	5	Period 1	1500	34	470	35	51			0.18	1.8
		Period 2	550	16	167	3	3			0.18	1.8
		Period 3	150	10	40	35	16			0.18	1.8
					Reactors						
Peach Bottom	6	Core 1		11–34	11–34	<11		23–68	23–160	2.31	22.8
		Core 2	114–456	11–34	11–23	<11		<2	11–68	2.31	22.8
Fort St. Vrain	7	2% Power		20	<3	59	2350		1370	3.31	32.7
		11.4% Power	1630	122	92	109	884	211	255	3.44	34.0
		20.5% Power	3830	237	178	395	3240	213	316	4.00	39.5
		26.0% Power	1690	165	220	388	1600	236	295	4.28	42.2
Dragon (England)	8	Normal	10	1	8	0.4	1		12	2.03	20.0
		During H_2O injection experiment	160–220	16	160–240	34–40	16–22		2–3	2.03	20.0
AVR (Germany)	8	Normal	445–510	2–5	1700–1900	5	1			0.94	9.3

[a]Parts per million times total pressure in atmospheres. 1 atm = 0.10132 Pa

[b]Oxygen and argon are normally not chromatographically separated.

[c]Below detection limit.

values of oxygen can be better simulated at the specimen surfaces in the creep machines by heating the premixed gas before it goes into the creep furnaces, thereby letting it reach equilibrium before it is exposed to the specimen. To eliminate leaks in the piping system between the preheating furnace and the creep furnace the gas should be preheated as close as possible to the creep machine or, even better, inside the creep furnace itself. This can be done by extending the entrance gas line inside the furnace, (Fig. 2.4). The gas is forced to go through the loop and is preheated just before it is released to the environmental chamber. In the future this loop will be mounted in the creep furnaces as tests are completed.

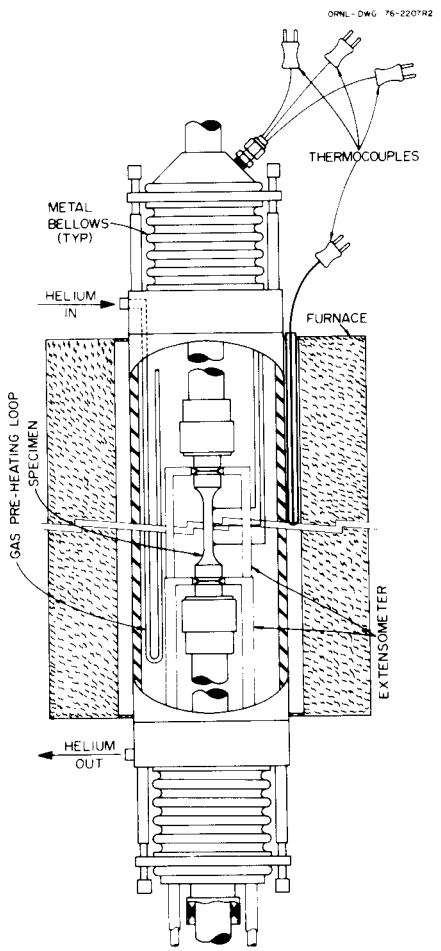

Fig. 2.4. Schematic of Environmental Creep Furnace with a Gas Preheating Loop.

2.2.2.2 Environmental Creep Tests

We have completed 17 tests of isothermally annealed 2 1/4 Cr-1 Mo steel and 14 tests of solution annealed Hastelloy X, and the results are shown in Tables 2.4 and 2.5, respectively. Also included in these tables are the tests in progress.

Stress-rupture data from our tests and those of GA in simulated HTGR primary coolant helium[2] are compared with data from air tests of 2 1/4 Cr-1 Mo steel[11] and Hastelloy X (ref. 12) in Figs. 2.5 and 2.6, respectively. In both figures the solid lines represent the average of many air tests and the points are data from the HTGR environment tests. No significant differences appear between the stress-rupture data from the helium environmental tests and from the air tests at the indicated temperature-stress-time conditions (max 15,000 hr), except for the three 2 1/4 Cr-1 Mo steel tests conducted at GA at 482°C (900°F), which had a rupture life much longer than the average air tests.

Under three different test conditions (Fig. 2.7) the time to tertiary creep for 2 1/4 Cr-1 Mo steel was much longer in air than in HTGR helium at 482°C (900°F) and 207 MPa (30 ksi) (although the minimum creep rate was the same). However, at 593°C (1100°F) and 69 MPa (10 ksi) the minimum creep rate in air was twice as high as in HTGR helium. At 593°C (1100°F) and 103 MPa (15 ksi) the creep curve for 2 1/4 Cr-1 Mo steel tested in air coincided with two creep curves for HTGR-helium tests. However, in two other tests conducted in HTGR helium 2 1/4 Cr-1 Mo steel had a lower minimum creep rate and a longer time to rupture compared with the air test data. Inexplicably, Test 16882 (Table 2.4) showed a different behavior. The minimum creep rate was one-tenth that of Test 17377, which was otherwise identical.

Creep curves for Hastelloy X (Fig. 2.8) showed no difference whether the test was conducted in air or in HTGR helium as long as the test temperature was 760°C (1400°F) or below. At 816°C (1500°F) the minimum creep rate was more than twice as high in air compared with that measured in HTGR-helium tests.

Table 2.4. Results of Creep Tests on Chromium-Molybdenum Steels

Test	Heat	Temperature (°C)	Temperature (°F)	Stress (MPa)	Stress (ksi)	Environment	Time to Indicated Creep Strain, hr (1%)	(2%)	(5%)	Steady State Creep Rate (hr^{-1})	Time to Tertiary Creep (hr)	Rupture Life (hr)	Elongation (%)
							9 Cr-1 Mo Steel						
15363	316381-1A	538	1000	103	15	HTGR-He[a]	2700	4294	7444	0.028×10^{-4}	3020	In Progress	
15377	316381-1A	482	900	172	25	HTGR-He						1317[b]	1.9[b]
							2 1/4 Cr-1 Mo Steel						
17495	72768	649	1200	69	10	HTGR-He	28	59	137	3.1×10^{-4}	100	288	47.2
17948	36202	649	1200	69	10	HTGR-He						In Progress	
17864	X-6216	649	1200	69	10	HTGR-He	167	248	370	0.39	140	513	29.1
17333	X-6216	593	1100	138	20	HTGR-He	5	11	34	13	42	89.5	42.1
16882	72768	593	1100	103	15	HTGR-He	0.8	3	81	0.44	600	1337	51.3
17377	72768	593	1100	103	15	HTGR-He	13	30	92	4.9	130	328	50.8
16883	36202	593	1100	103	15	HTGR-He	17	48	144	3.1	188	436	46.8
17334	X-6216	593	1100	103	15	HTGR-He	39	105	306	1.4	365	793	44.5
16266	72768	593	1100	103	15	Air	10	26	90	4.8	175	388	52.5
15023	X-6216	593	1100	69	10	HTGR-He	3186	4930	7380	0.024	3750	9660	38.9
15047	X-6216	593	1100	69	10	HTGR-He	3132	4660	6540	0.025	3150	7784	26.6
15045	X-6216	593	1100	69	10	HTGR-He				0.022		3186[b]	2.8[b]
16360	72768	593	1100	69	10	Air	971	2115	4435	0.054	1004	6698	27.3
17876	X-6216	593	1100	69	10	Air						In Progress	
17918	X-6216	538	1000	138	20	HTGR-He						In Progress	
15369	36202	538	1000	103	15	HTGR-He	842	2047	6144	0.072	6800	In Progress	
15046	X-6216	538	1000	103	15	HTGR-He	1122	2850	7660	0.059	8100	14957	38.2
16264	36202	538	1000	103	15	Air	1050	2700				In Progress	
17947	72768	482	900	207	30	HTGR-He						In Progress	
15373	36202	482	900	207	30	HTGR-He	349	787	1660	0.11	500	3494	35.7
17494	X-6216	482	900	207	30	HTGR-He	215	685	1885	0.22	1650	In Progress	
16263	36202	482	900	207	30	Air	204	620	1800	0.25	2030	6611	45.3
15374	36202	482	900	172	25	HTGR-He	1500	2705	5200	0.039	1300	13509	40.2
17849	36202	482	900	172	25	Air						In Progress	

[a]Helium with impurities: 275 μatm H_2, 30 μatm CH_4, 20 μatm CO, 20 μatm H_2O (1 μatm = 0.101 Pa).

[b]Terminated short of rupture.

Table 2.5. Results of Creep Tests on Hastelloy X

Test	Heat	Temperature (°C)	Temperature (°F)	Stress (MPa)	Stress (ksi)	Environment	Time to Indicated Creep Strain, hr (1%)	(2%)	(5%)	Steady State Creep Rate (hr^{-1})	Time to Tertiary Creep (hr)	Rupture Life (hr)	Elongation (%)
16054	2600-3-2792	871	1600	62	9	HTGR-He[a]	93	197	327	0.93×10^{-4}	205	554	34.8
16126	2600-3-4936	871	1600	34	5	HTGR-He	3414	4000	5400	0.010	2350	6527	14.2
17850	2600-3-4936	871	1600	34	5	Air						In Progress	
17332	2600-3-4936	816	1500	69	10	HTGR-He	253	887	1745	0.14	900	2790	25.8
16269	2600-3-4936	816	1500	69	10	Air	600[b]	940[b]	1720[b]	0.1	650[b]	3453	18.8
17375	2600-3-4936	816	1500	69	10	Air	119	400	970	0.34	690	1905	43.7
16031	2600-3-2792	760	1400	152	22	HTGR-He	7	15	38	12.0	44	159	57.5
16125	2600-3-4936	760	1400	138	20	HTGR-He	16	30	103	4.0	142	305	38.9
17330	2600-3-4936	760	1400	138	20	Air	18	35	95	4.6	113	297	52.4
16490	2600-3-4936	760	1400	103	15	HTGR-He	377	1110	2180	0.12	1480	2690	18.7
17875	2600-3-4936	760	1400	69	10	HTGR-He						In Progress	
15771	2600-3-4936	704	1300	172	25	HTGR-He	49	104	321	1.4	510	1007	35.4
15058	2600-3-4936	704	1300	138	20	HTGR-He	113	344	1920	0.17	1950	4045	21.4
15792	2600-3-4936	704	1300	138	20	HTGR-He	148	500	2590	0.11	2000	4588	23.0
16268	2600-3-4936	704	1300	138	20	Air	98	297	2139	0.12	1950	4504	18.3
17328	2600-3-4936	704	1300	103	15	HTGR-He	550					In Progress	
17376	2600-3-4936	704	1300	103	15	Air	96	423				In Progress	
17863	2600-3-4936	649	1200	207	30	HTGR-He	291	560				In Progress	
15772	2600-3-4936	649	1200	172	25	HTGR-He	471	850	2170	0.17	3950	6466	34.9
16267	2600-3-4936	649	1200	172	25	Air	385	946	4512			In Progress	
17329	2600-3-4936	649	1200	138	20	HTGR-He	805	3163				In Progress	

[a]Helium with impurities: 275 μatm H_2, 30 μatm CH_4, 20 μatm CO, 20 μatm H_2O (1 μatm = 0.101 Pa).

[b]Estimated value. Bad extensometer readings through the whole test.

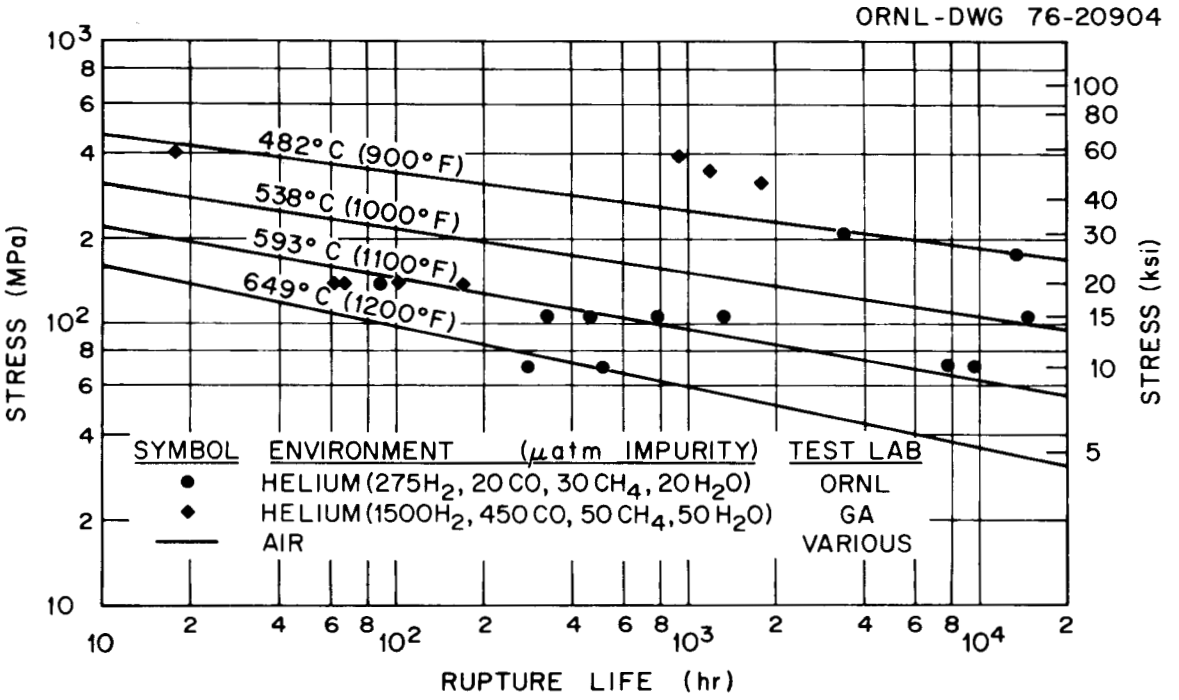

Fig. 2.5. Stress-Rupture Properties of 2 1/4 Cr-1 Mo Steel Tested in Air and HTGR Helium.

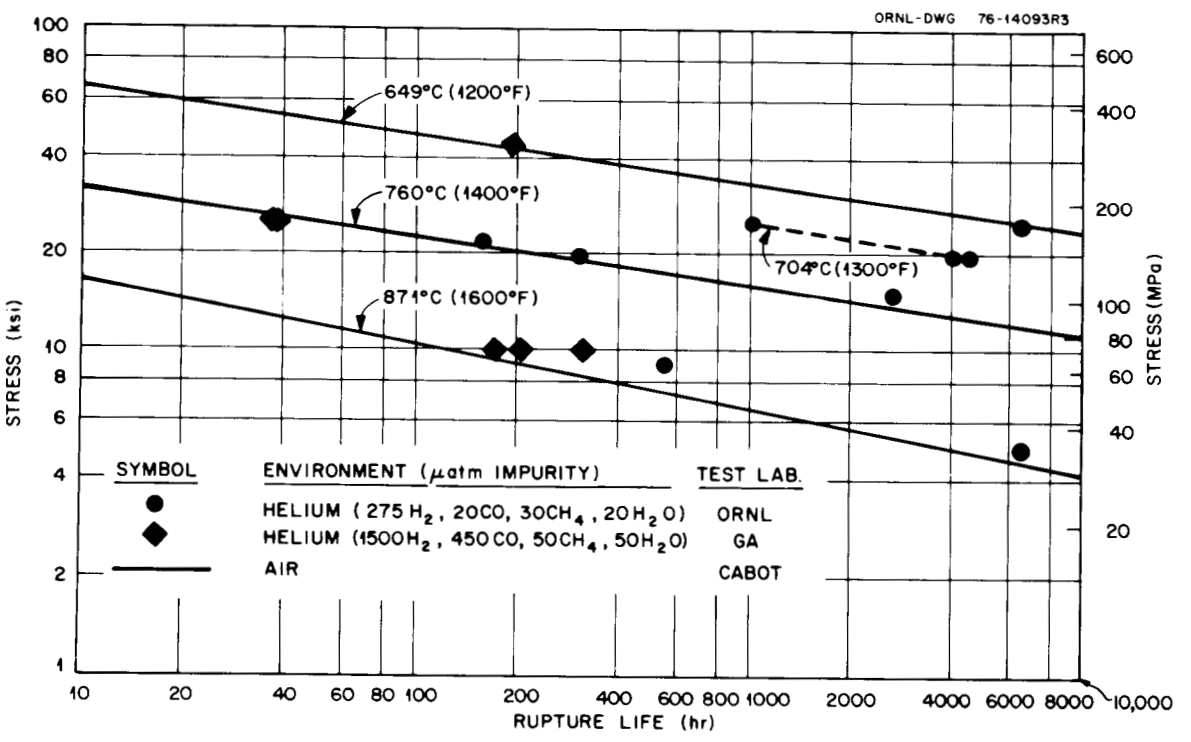

Fig. 2.6. Stress-Rupture Properties of Hastelloy X Tested in Air and HTGR Helium.

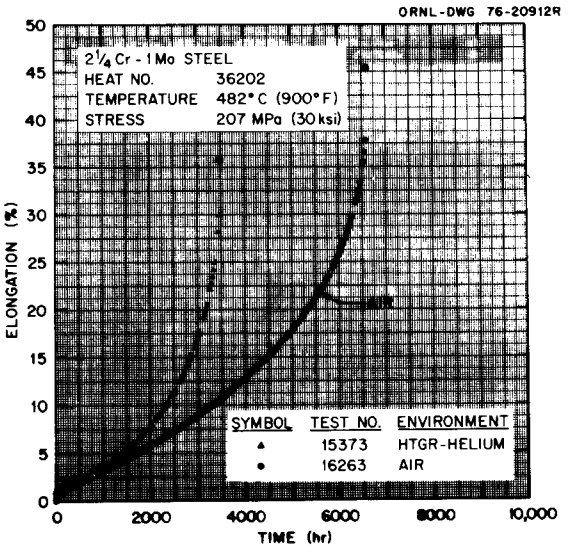

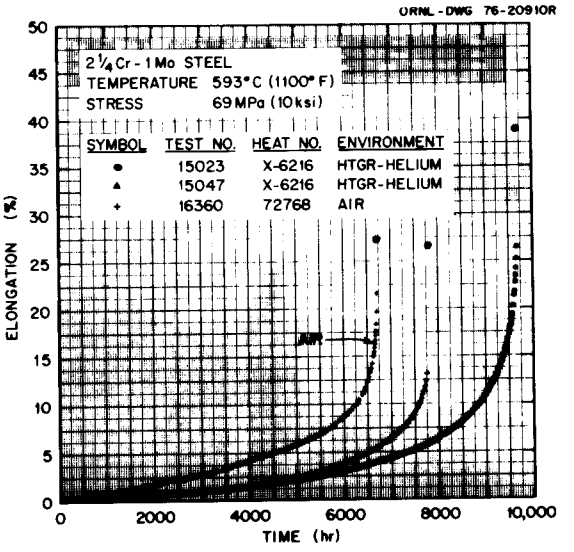

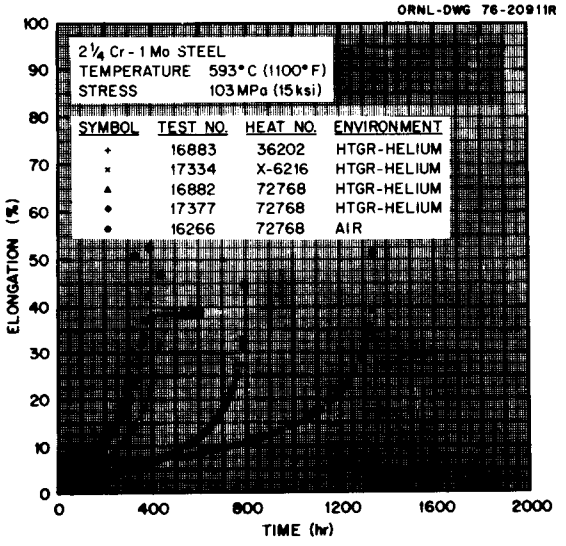

Fig. 2.7. Comparison of Creep Curves for 2 1/4 Cr-1 Mo Steel Conducted in Simulated HTGR-Helium Environment and Air.

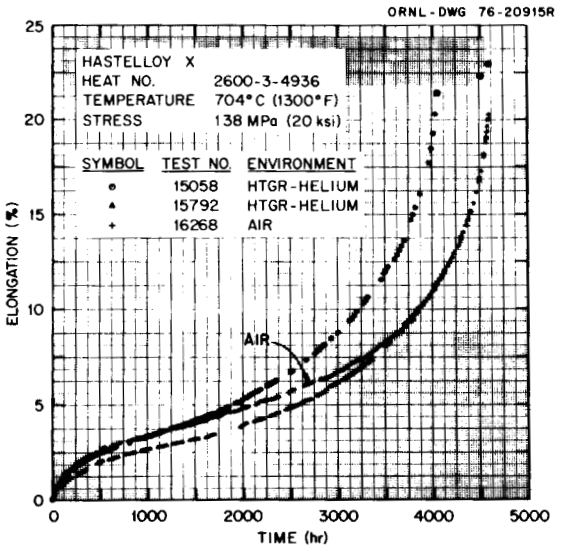

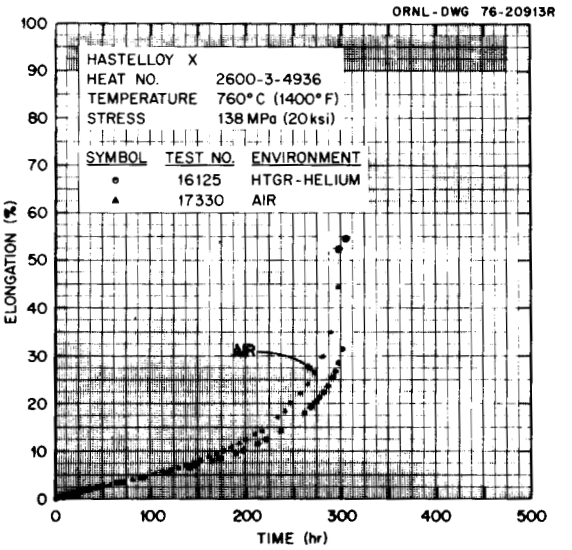

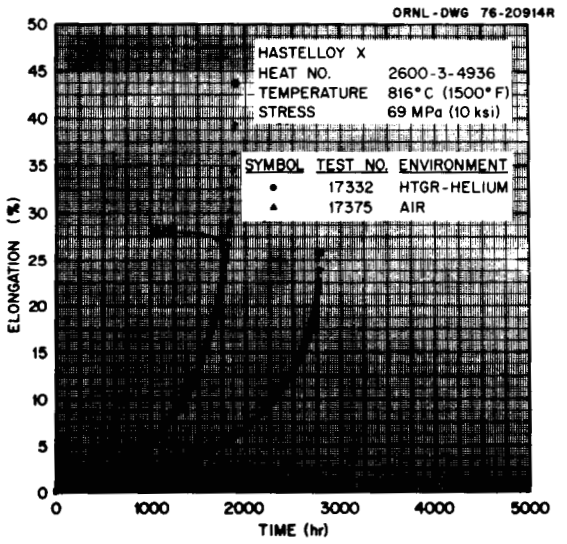

Fig. 2.8. Comparison of Creep Curves for Hastelloy X Conducted in Simulated HTGR-Helium Environment and Air.

In order to study the effect of stress on gas-metal reactions in HTGR helium, small plate specimens [31.8 by 9.52 by 1.588 mm (1.25 by 0.375 by 0.0625 in.)] of both 2 1/4 Cr-1 Mo steel and Hastelloy X were fabricated and are now being exposed in an unstressed condition inside the environmental creep machines.

Small samples have been cut from the gage section of tested 2 1/4 Cr-1 Mo steel and Hastelloy X specimens and analyzed for C, H, O, and N. The results are shown in Table 2.6 with the data from the as-received material. The increase in oxygen contents in the tested specimens (both 2 1/4 Cr-1 Mo steel and Hastelloy X) may derive from the thin oxide layer that was formed during the test. Apparently 2 1/4 Cr-1 Mo steel was decarburized and Hastelloy X increased its carbon content under these conditions.

Table 2.6. Analysis of Specimens Tested in HTGR Helium

Test	Material	Heat	Test Conditions			Results of Analysis, ppm			
			Temperature		Time (hr)	C	H	O	N
			(°C)	(°F)					
	2 1/4 Cr-1 Mo	X-6216	as-received			1216	9	40	125
15023	2 1/4 Cr-1 Mo	X-6216	593	1100	9660	729	7	547	127
	Hastelloy X	2600-3-4936	as-received			792	11	21	545
16126	Hastelloy X	2600-3-4936	871	1600	6527	1334	8	555	545

Metallographic samples have been examined from all completed tests. Corrosion rates were measured at the edge of a cross section of the shoulder (where the stress was one-fourth that at the gage section). The corrosion rate of 2 1/4 Cr-1 Mo steel decreased with increasing time at 593°C (1100°F) in the HTGR-helium environment. This is shown on the curve in Fig. 2.9 together with micrographs of specimens from five different tests. One of the tests was conducted in air, and the corrosion resistance of 2 1/4 Cr-1 Mo steel at 593°C (1100°F) appears to be much better in HTGR helium than in air. The depth of attack in air reached 24 μm in 388 hr and 200 μm in 9660 hr, whereas it reached only 20 μm in 9660 hr in HTGR helium.

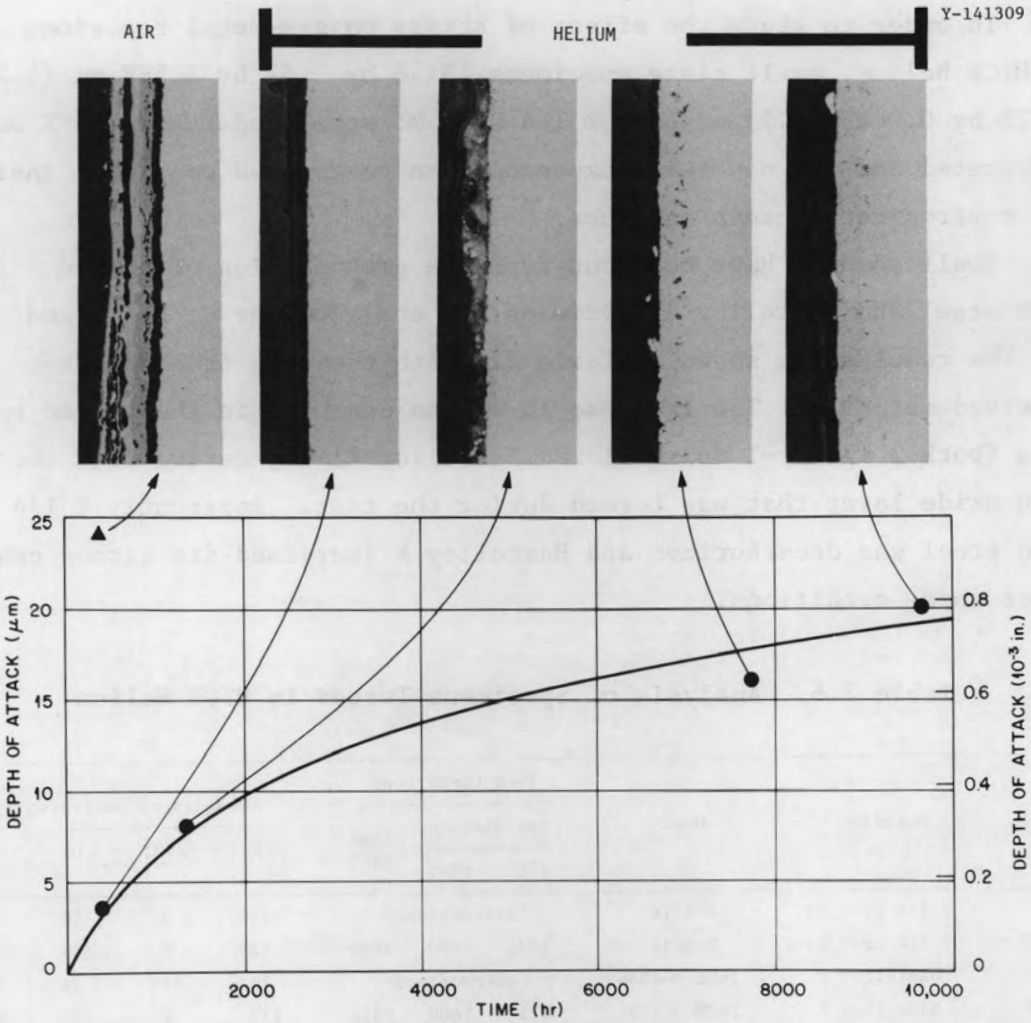

Fig. 2.9. Corrosion Behavior of 2 1/4 Cr-1 Mo Steel at 593°C (1100°F) in HTGR-Helium Environment and Air. The micrographs are from the following tests (from left to right): 16266, 16883, 16882, 15047, and 15023.

The corrosion behavior of Hastelloy X in HTGR-helium environment differed only slightly when compared with air at 704°C (1300°F). At this temperature Hastelloy X has excellent oxidation resistance, and in these test time periods no large difference was expected. At the higher temperatures a difference between air and HTGR helium is more apparent. Figures 2.10 through 2.12 show no difference in the HTGR-helium exposed specimens at the three temperatures, but the rate of attack in air increased with increasing temperature.

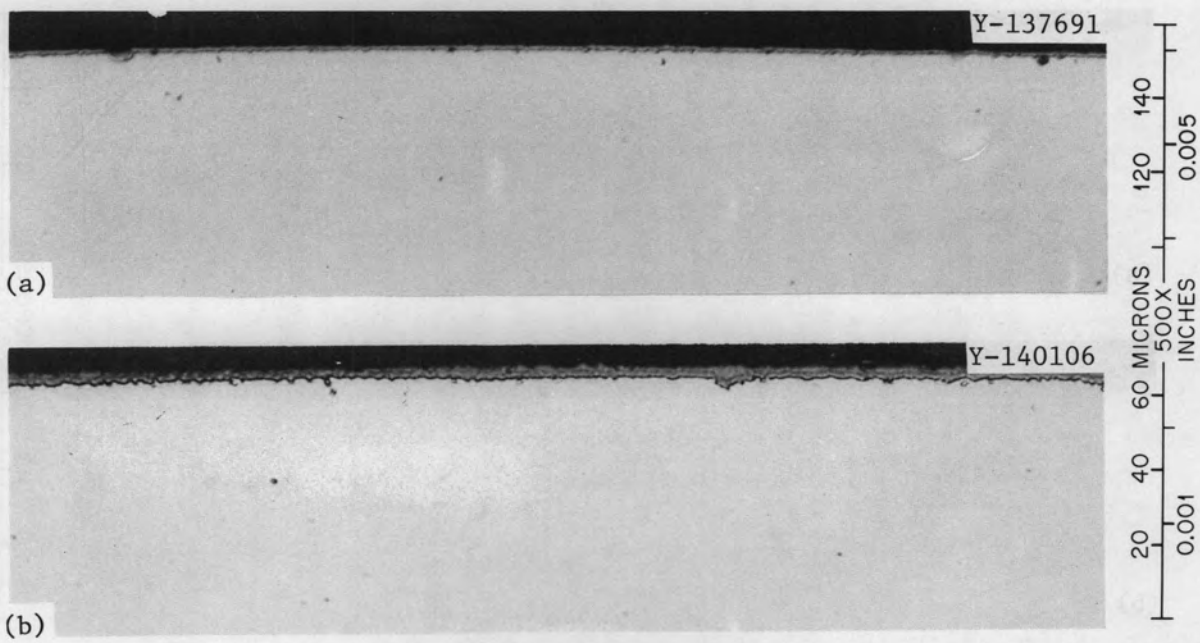

Fig. 2.10. Edge of Cross Section of the Shoulders of Hastelloy X Creep Specimens. (a) Test 15792, HTGR-helium exposed for 4588 hr at 704°C (1300°F). (b) Test 16268, air exposed for 4504 hr at 704°C (1300°F).

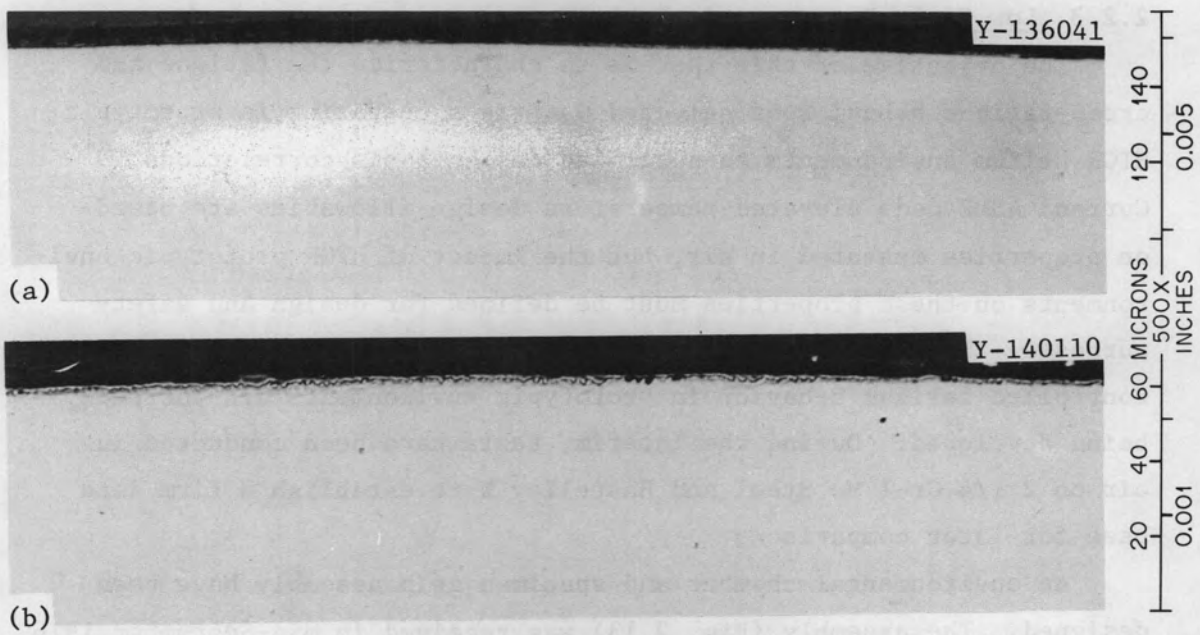

Fig. 2.11. Edge of Cross Section of the Shoulders of Hastelloy X Creep Specimens. (a) Test 16125, HTGR-helium exposed for 305 hr at 760°C (1400°F). (b) Test 17330, air exposed for 297 hr at 760°C (1400°F).

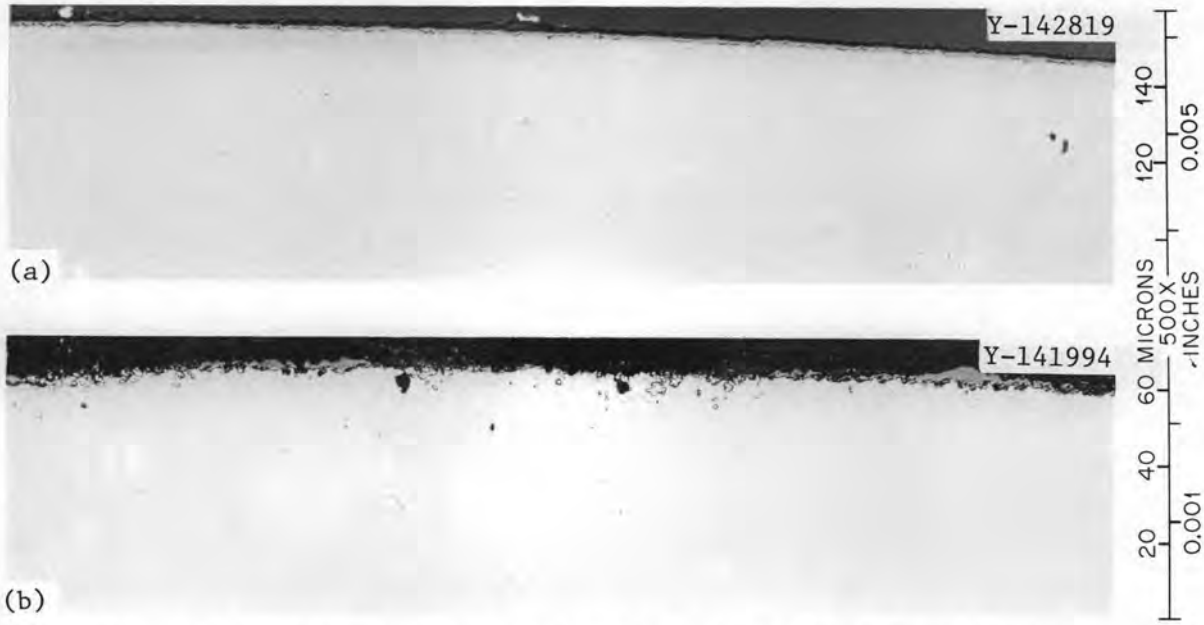

Fig. 2.12. Edge of Cross Section of Shoulders of Hastelloy X Creep Specimens. (a) Test 17332, HTGR helium exposed for 2790 hr at 816°C (1500°F). (b) Test 17375, air exposed for 1905 hr at 816°C (1500°F).

2.2.3 Low-Cycle Fatigue — J. P. Strizak

The objective of this task is to characterize the fatigue and creep-fatigue behavior of selected materials operating in prototypic HTGR helium environments to determine design-basis correlations. Current ASME code elevated-temperature design allowables are based on properties measured in air, but the impact of HTGR prototypic environments on these properties must be defined for design and safety purposes. Towards this end, facilities for determining strain-controlled fatigue behavior in prototypic environments are currently being developed. During the interim, tests have been conducted in air on 2 1/4 Cr-1 Mo Steel and Hastelloy X to establish a firm data base for later comparisons.

An environmental chamber and specimen grip assembly have been designed. The assembly (Fig. 2.13) was received in mid-September 1976, and has been installed in the fatigue testing machine previously used to conduct tests in air. The chamber has been connected to the gas analysis and supply system currently being employed for creep tests

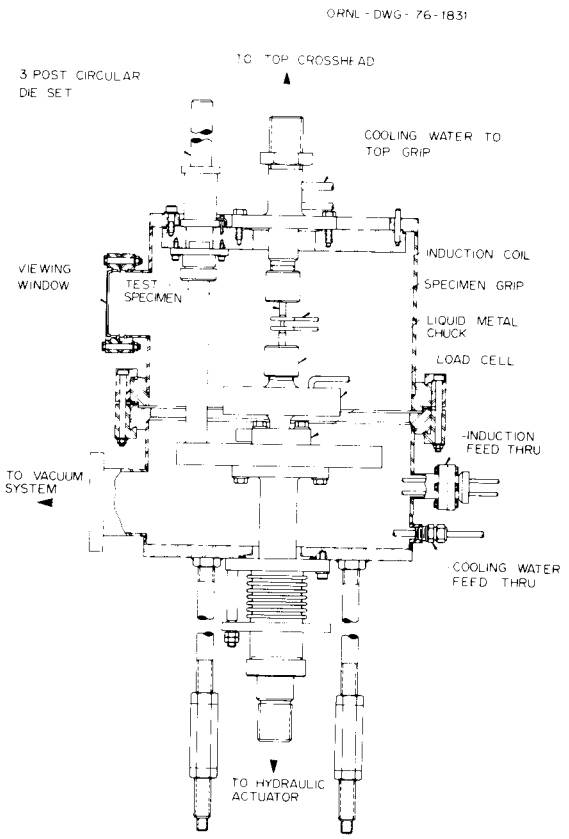

Fig. 2.13. Schematic of Environmental Fatigue Test Chamber.

in prototypic helium environments. Upon completion of an operational checkout of the environmental fatigue testing facility and establishment of operating procedures, tests will be initiated to study the fatigue and creep-fatigue behavior of 2 1/4 Cr-1 Mo Steel and Hastelloy X in simulated HTGR helium.

2.2.3.1 Description of 2 1/4 Cr-1 Mo Steel Tested

Fatigue and creep-fatigue testing of 2 1/4 Cr-1 Mo steel has continued. Three commercial heats of material have been tested. Two heats (20017 and 3P5601) are 25-mm-thick (1-in.) plate obtained from Babcock and Wilcox Company. In addition, some tests were performed on a 25-mm-thick (1-in.) plate of low-carbon material, heat 50557 obtained from Sumitomo Metals. Chemical analyses of representative material from the plates are compared in Table 2.7.

Table 2.7. Chemical Composition, Grain Size, and Product Form of 2 1/4 Cr-1 Mo Steel

Heat Number	Product Form	Grain Size		Analysis	Chemical Composition, wt %								
		ASTM	(μm)		C	Mn	Si	Cr	Mo	Ni	S	P	N
20017	Plate, ASME SA-387, Grade D	4–5	55–80	Vendor	0.11	0.55	0.29	2.13	0.90		0.014	0.012	0.012
				ORNL[a]	0.135	0.57	0.37	2.2	0.92	0.16	0.016	0.012	
3P5601	Plate, ASME SA-387, Grade D	5	55	Vendor	0.12	0.35	0.27	2.3	0.96	0.20	0.022	0.009	0.0135
50557	Plate, ASTM A 387, Grade D	8	20	Vendor	0.026	0.50	0.27	2.45	1.0		0.009	0.012	0.0125
M5691 (No. 2)	Pipe, ASME SA-335,[b] Grade P22	4–5	55–80	BCL[c]	0.11	0.47	0.35	2.39	0.96	0.26	0.009	0.013	0.011
MC7409 (No. 3)	Pipe, ASME SA-335,[b] Grade P22	7–8	20–27	BCL[c]	0.12	0.35	0.23	2.42	0.92	0.04	0.025	0.008	0.0111

[a]Oak Ridge National Laboratory.

[b]Data reported in ref. 13.

[c]Battelle Columbus Laboratories.

Sections of the plates were isothermally annealed as follows: austenitized at 927°C ± 14°C (1700 ± 25°F) for 1 hr, cooled to 704 ± 14°C (1300 ± 25°F) at a maximum rate of 56°C/hr (100°F/hr), held at 704 ± 14°C (1300 ± 25°F) for 2 hr, and cooled at room temperature at a rate not to exceed 6°C/min (10°F/min).

Tensile and fatigue specimens were generally machined with their longitudinal axes parallel to the plate rolling direction. Tensile specimens had a 6.35-mm-diam by 31.75-mm-long (0.25 by 1.25-in.) gage section, while the fatigue specimens had an hourglass-shaped gage arc configuration with a radius-to-diameter ratio (R/D) of 6. The minimum diameter of the fatigue specimens was either 6.35 or 5.08 mm (0.25 or 0.20 in.)

Fully reversed strain-controlled axial push-pull cyclic testing was done with closed-loop electrohydraulic fatigue test machines. Axial strain control was maintained by employing a diametral extensometer, a load cell, and a simple diametral-to-axial strain computer. A triangular wave form (Fig. 2.14) was employed for all continuous cycling tests with and without tensile or compressive hold times at peak strain values. The fatigue specimens were heated in air by induction, and thermocouples attached to the specimens measured the temperature near the point of minimum diameter.

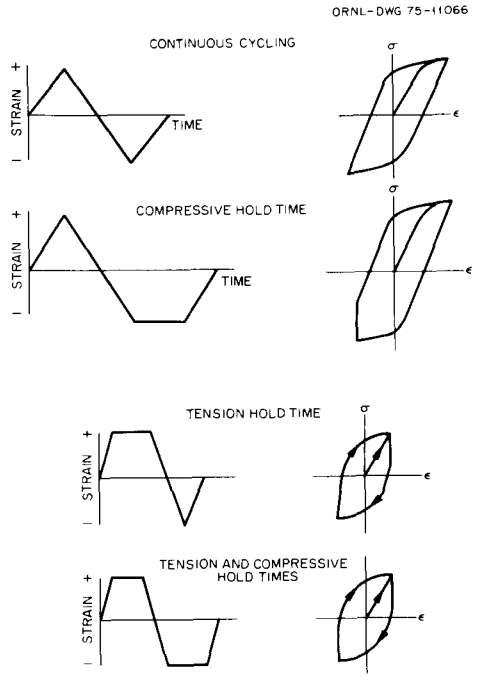

Fig. 2.14. Cyclic Wave Forms for Strain-Controlled Hourglass-Shaped-Specimen Fatigue Tests.

The tensile properties for the three heats of material in either the isothermally annealed or annealed (furnace cooled) condition are compared in Fig. 2.15. The higher carbon heats were stronger and less ductile (as measured by reduction of area) than the low-carbon heat. Isothermally annealed heat 3P5601 had slightly lower strength than the annealed (furnace-cooled) material.

The data for ultimate strength and reduction of area are plotted in Fig. 2.16 as functions of temperature and strain rate for annealed heat 20017. Strain rate ranged from 2.7×10^{-6} to 144/s and temperature from 23 to 566°C (75 to 1050°F). Increasing the temperature decreased the ultimate strength, generally with a corresponding increase in reduction of area from room temperature to about 200°C (400°F); however, above this temperature the effect of dynamic strain aging is apparent over the range from about 200 to 430°C (400 to 750°F). Above this temperature range strength decreases and ductility increases; however, the properties show strain rate sensitivity over the entire temperature range.

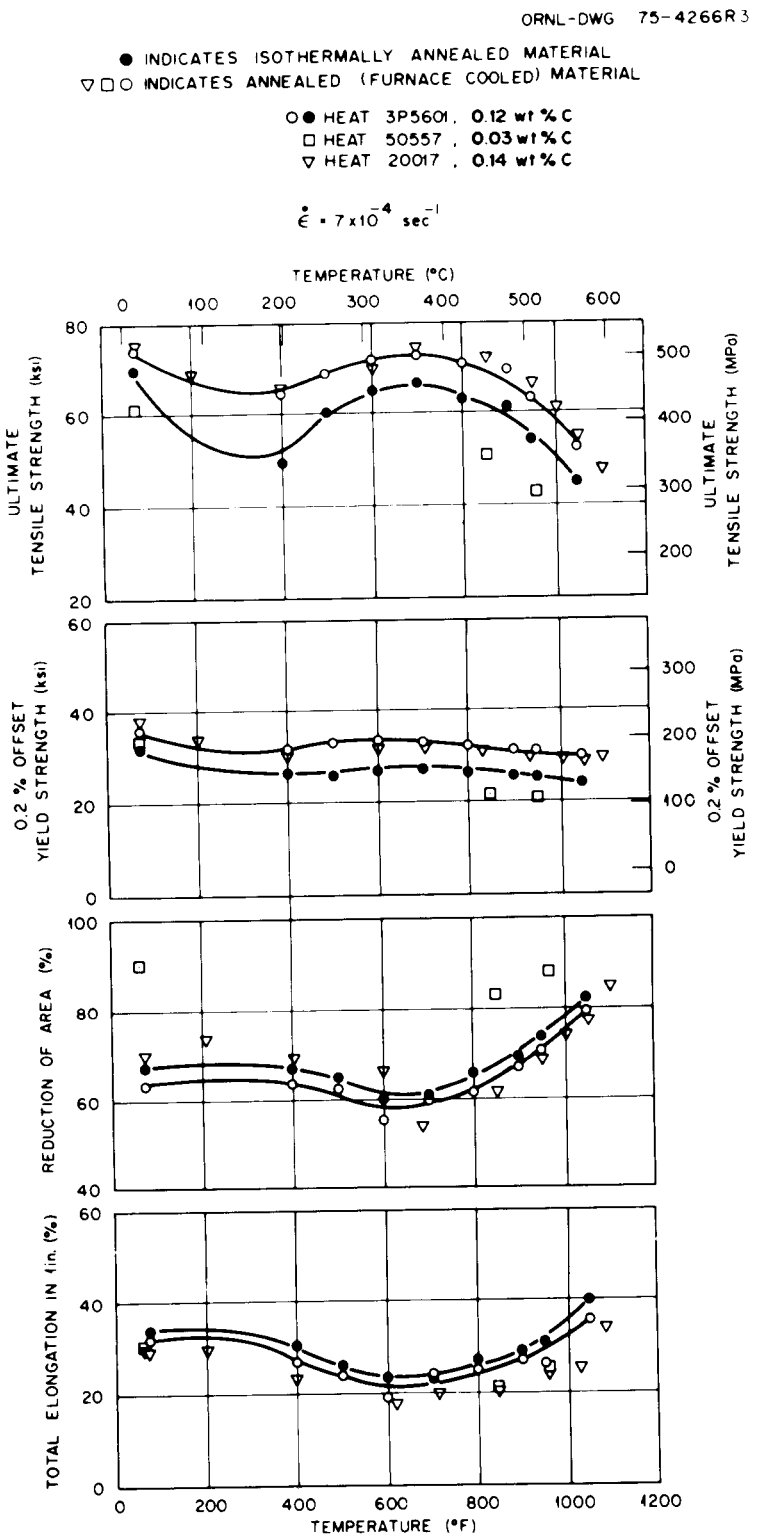

Fig. 2. 15. Comparison of Tensile Properties for Three Heats of 2 1/4 Cr-1 Mo Steel.

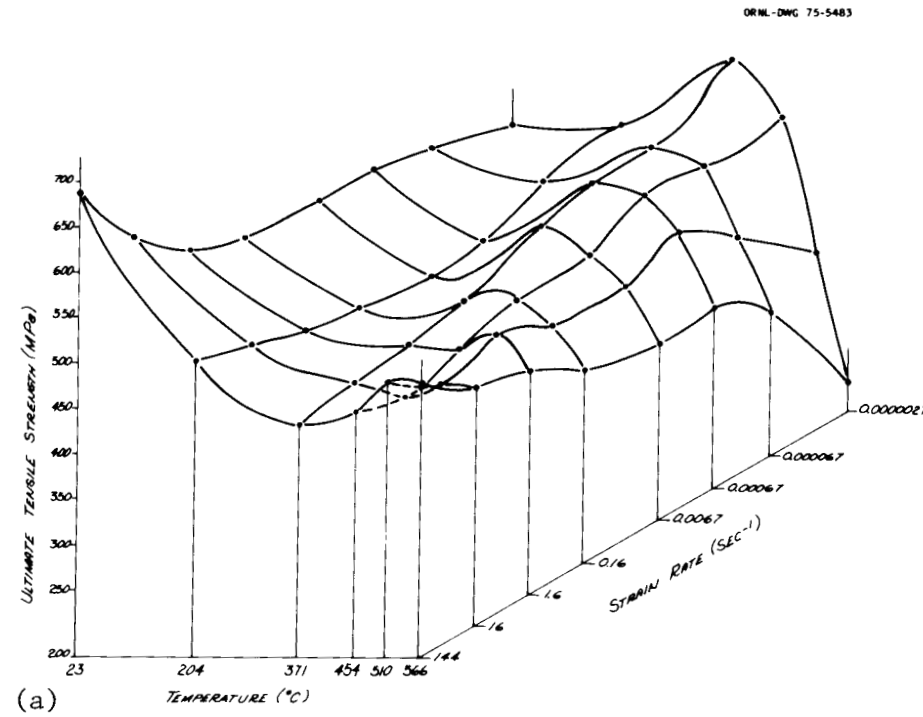

(a)

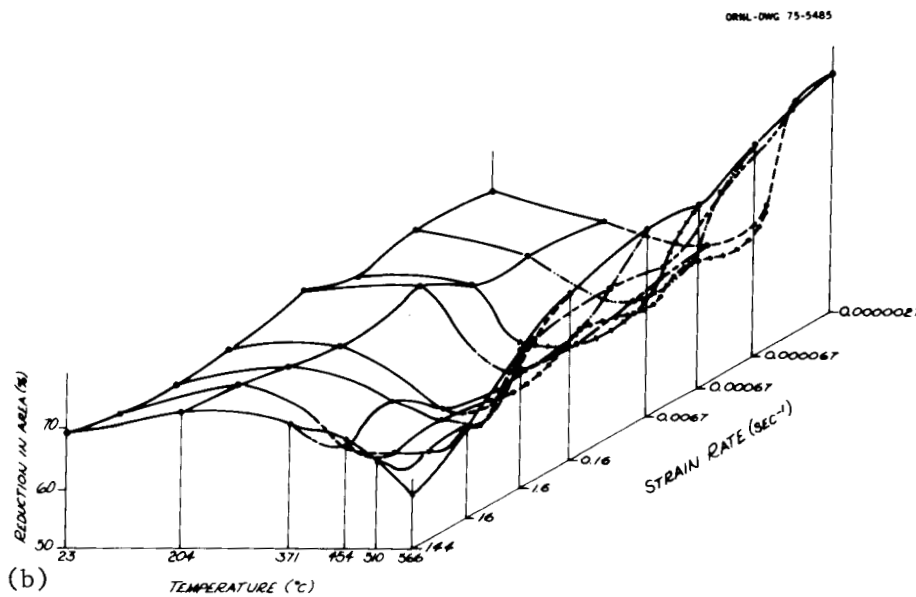

(b)

Fig. 2.16. Tensile Properties of Annealed 2 1/4 Cr-1 Mo Steel as Functions of Temperature and Strain Rate. (a) Ultimate strength. (b) Reduction of area.

2.2.3.2 Continuous Cycling Fatigue Behavior of 2 1/4 Cr-1 Mo Steel

In uniaxial, fully reversed, continuous-cycling strain-controlled fatigue tests conducted at a strain rate of 4×10^{-3}/s, we showed previously that components of the total strain range, $\Delta\varepsilon_t$ — namely, the plastic component, $\Delta\varepsilon_p$, and elastic component, $\Delta\varepsilon_e$, can be expressed as a simple power-law relationship of N_f, the cycles to failure. Thus:

$$\Delta\varepsilon_t = \Delta\varepsilon_p + \Delta\varepsilon_e \ , \tag{1}$$

and

$$\Delta\varepsilon_t = AN_f^{-a} + BN_f^{-b} \tag{2}$$

Best fit values of the coefficients and exponents in this equation were determined by linear least-squares regression analysis and are given in Table 2.8.

Table 2.8. Elastic and Plastic Strain Range Constants for Strain-Controlled Tests Conducted at a Strain Rate of 4×10^{-3}/s

Heat	Temperature (°C)	N_f Range (cycles)	Values of constants[a] in $\Delta\varepsilon_t = AN_f^{-a} + BN_f^{-b}$				Approximate Cyclic Transition Point[b] (cycles)
			A	a	B	b	
20017	Room	$<6 \times 10^5$	112	0.585	0.684	0.082	
20017	315	$<6 \times 10^4$	112	0.585	0.684	0.082	24000
		$>6 \times 10^4$	1.03	0.164	0.684	0.082	
20017 and 3P5601	371	$<10^5$	102	0.602	1.713	0.081	
		$>10^5$	0.214	0.063	0.713	0.081	14000
20017	427	$<1.8 \times 10^4$	166	0.661	0.753	0.0967	
20017		$>1.8 \times 10^4$	8.23	0.349	0.407	0.031	
3P5601	427	$<1 \times 10^4$	166	0.661	0.396	0.037	16000
3P5601		$>1 \times 10^4$	3.755	0.232	0.396	0.037	
20017	539	$<1 \times 10^4$	263	0.756	0.440	0.048	
		$>1 \times 10^4$	16.3	0.439	0.440	0.048	10000
1,2,3[c]	593	$<7.5 \times 10^3$	210.6	0.744	0.445	0.064	
		$>7.5 \times 10^3$	3.768	0.284	0.445	0.064	16000

[a]Strain in percent.

[b]Life where the elastic and plastic strains are equal.

[c]See Table 2.7 and ref. 13.

Log-log plots of the plastic strain range vs cycles to failure from 10^3 to 10^7 cycles indicated that the data could be approximated by two straight lines. Characteristically, in the intermediate-to-high-cycle region the slope of the $\Delta\varepsilon_p$ vs N_f plot becomes less negative (Fig. 2.17). The intersection of the low-cycle $\Delta\varepsilon_p$ line with the high-cycle $\Delta\varepsilon_p$ line is referred to here as the "break point" (N_b). The number of cycles at the break point (N_b) depended on temperature and perhaps heat. Over the temperature range from 25 to 593°C (75–1100°F) N_b can be approximated by the relationship

$$N_b = 1.138 \times 10^7 \, e^{-0.009T} ,$$

where

T = temperature in Kelvins.

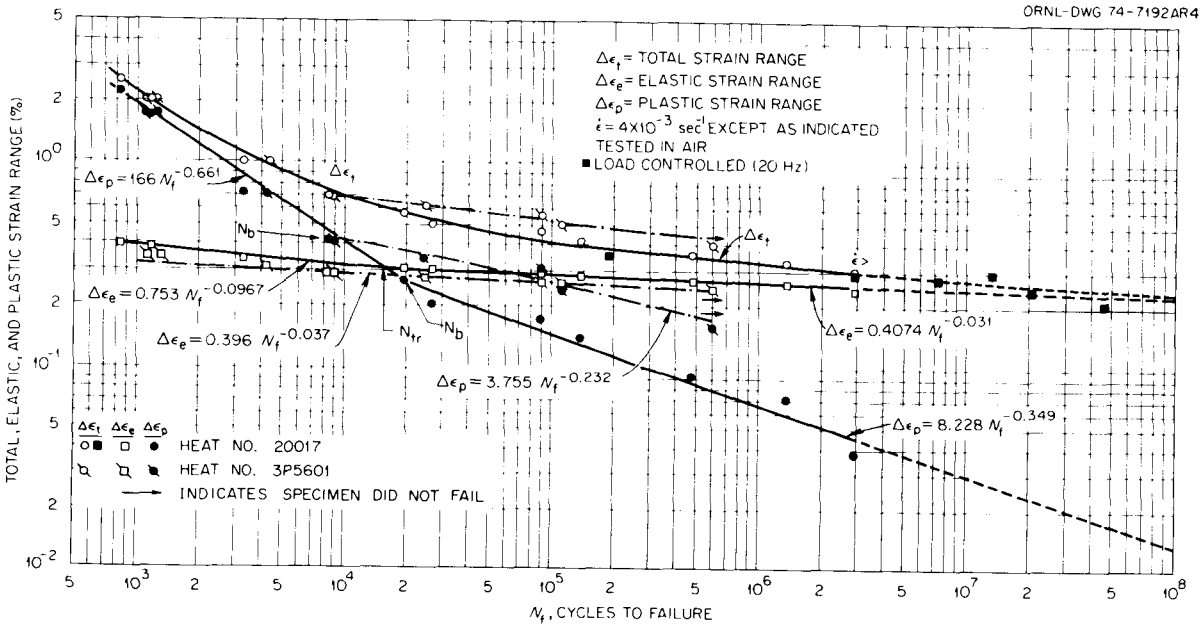

Fig. 2.17. Total, Elastic, and Plastic Strain Range vs Cycles to Failure for 2 1/4 Cr-1 Mo Steel (Isothermally Annealed) at 427°C, Showing Transition Fatigue Life, N_{tr}, and Break Points, N_b.

Figure 2.17 shows differences between the fatigue life of heats 20017 and 3P5601 in the region of 10^4 to 10^6 cycles to failure, with heat 3P5601 having the greater fatigue resistance. This heat-to-heat variation was not apparent for the limited data at 371°C (700°F) (Table 2.8) and was apparently not as significant at 538°C (1000°F) as shown in Fig. 2.18 by the data plotted along the zero hold time line. However, the difference in long-life fatigue behavior between these heats was again indicated at 482°C (900°F), as shown by the two points for 0.4% strain range on the zero hold time line in Fig. 2.19. The continuous cycling fatigue behavior of the three heats was investigated at 427°C (800°F). Only total strain ranges are plotted in Fig. 2.20 for clarity. As indicated in the figure the fatigue life of the low-carbon heat (50557) is less than that of the other two heats.

The observed heat-to-heat variations in fatigue behavior suggest that dynamic strain aging is an important consideration. Therefore, a three-dimensional diagram (Fig. 2.21) of cyclic life as a function of temperature and strain rate was constructed from the available continuous cycling data for a single strain range of 0.5%. A maximum or peak in cyclic lifetime, particularly for heat 3P5601, is apparent at the continuous strain rate of 4×10^{-3}/s. Heat 20017, within the scatter of the data, showed a nearly constant cycle life over the range from room temperature to 427°C (800°F) but the cycle life decreases at temperatures above 482°C (900°F).

The stress to maintain a constant strain range is generally constant except at the beginning and near the end of life testing. For this reason comparisons are often made as a function of the half-life stress (σ at $N_f/2$). Values of the half-life stress for various strain ranges are plotted as a function of temperature in Fig. 2.22. The indication of a peak strength over the range 316 to 427°C (600–800°F) is apparent. Also, heat 20017 consistently hardened to higher strength levels than heat 3P5601, and the difference was maintained even at the lower strain ranges, except possibly at 593°C (1100°F). Data from the literature[13] for material in both the isothermal and the annealed (furnace-cooled) conditions are also plotted from the results of tests conducted at or near the same strain range (Fig. 2.22).

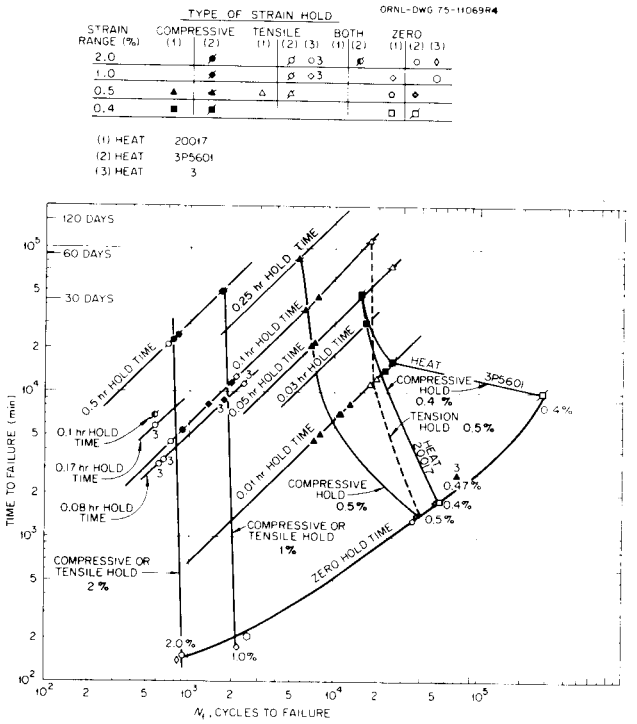

Fig. 2.18. Time-to-Failure vs Cycles-to-Failure Diagram Showing the Influence of Hold Periods on the Strain-Controlled Cyclic Life of Annealed 2 1/4 Cr-1 Mo Steel Tested at 538°C (1000°F).

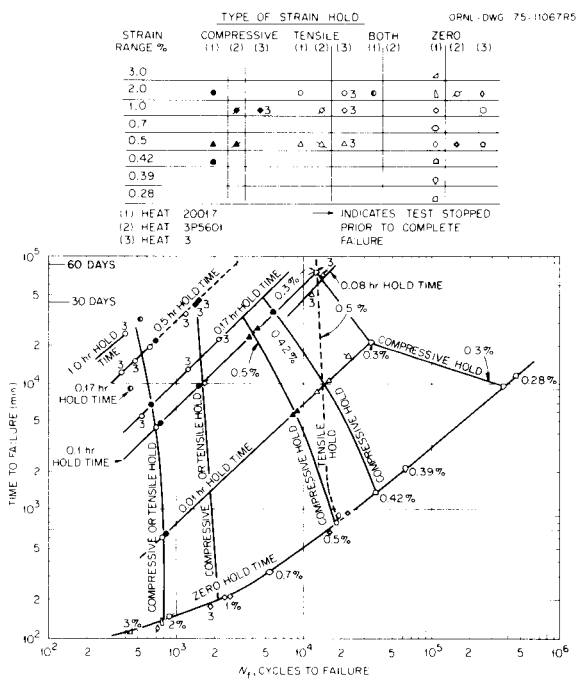

Fig. 2.19. Time to Failure vs Cycles to Failure Diagram Showing the Influence of Various Hold Periods on the Strain-Controlled Cycle Life of Isothermally Annealed 2 1/4 Cr-1 Mo Steel Tested at 482°C (900°F).

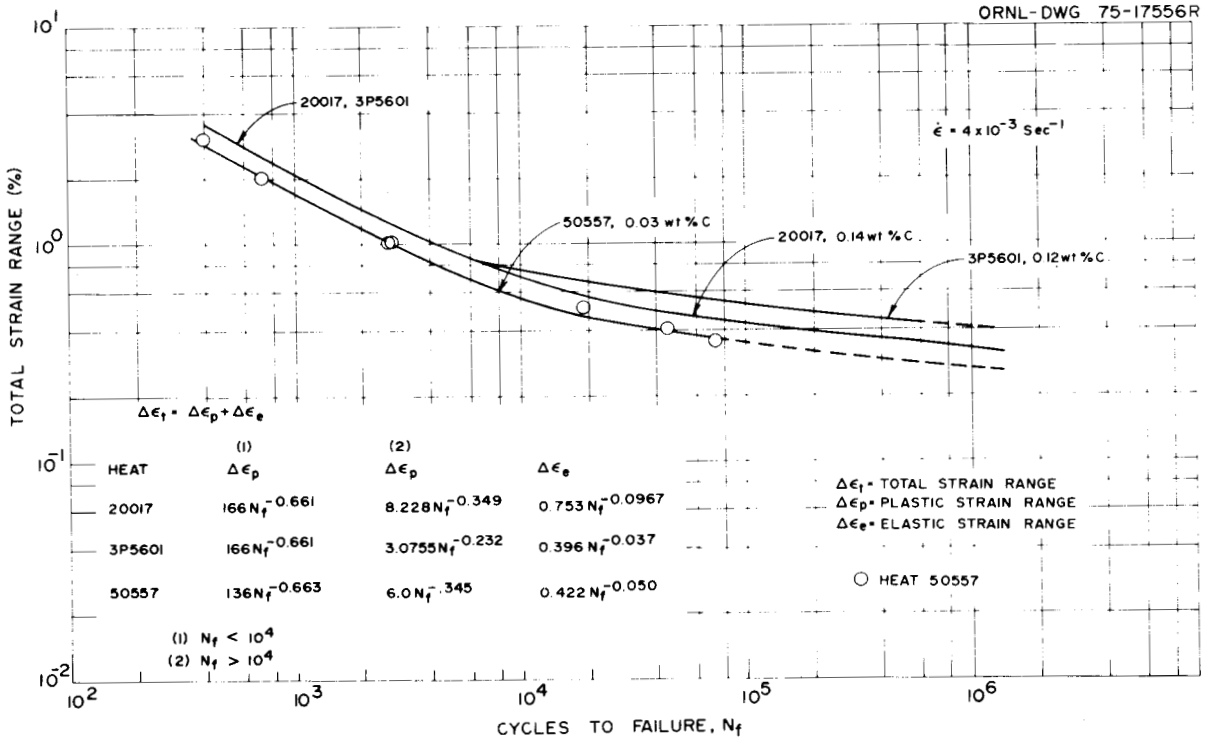

Fig. 2.20. Comparison of the Strain-Controlled Fatigue Behavior of Three Heats of Isothermally Annealed 2 1/4 Cr-1 Mo Steel Tested at 427°C (800°F) at a Single Strain Rate. Carbon contents were as indicated.

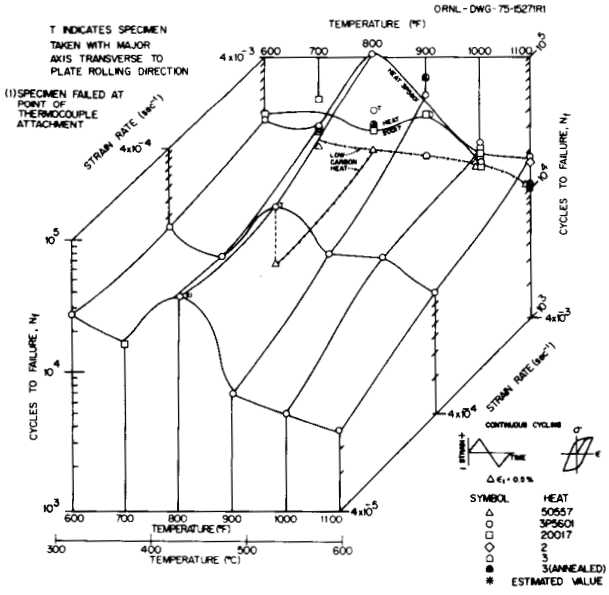

Fig. 2.21. Cycles to Failure as a Function of Temperature and Strain Rate for 2 1/4 Cr-1 Mo Steel in the Annealed (a) or Isothermally Annealed Condition.

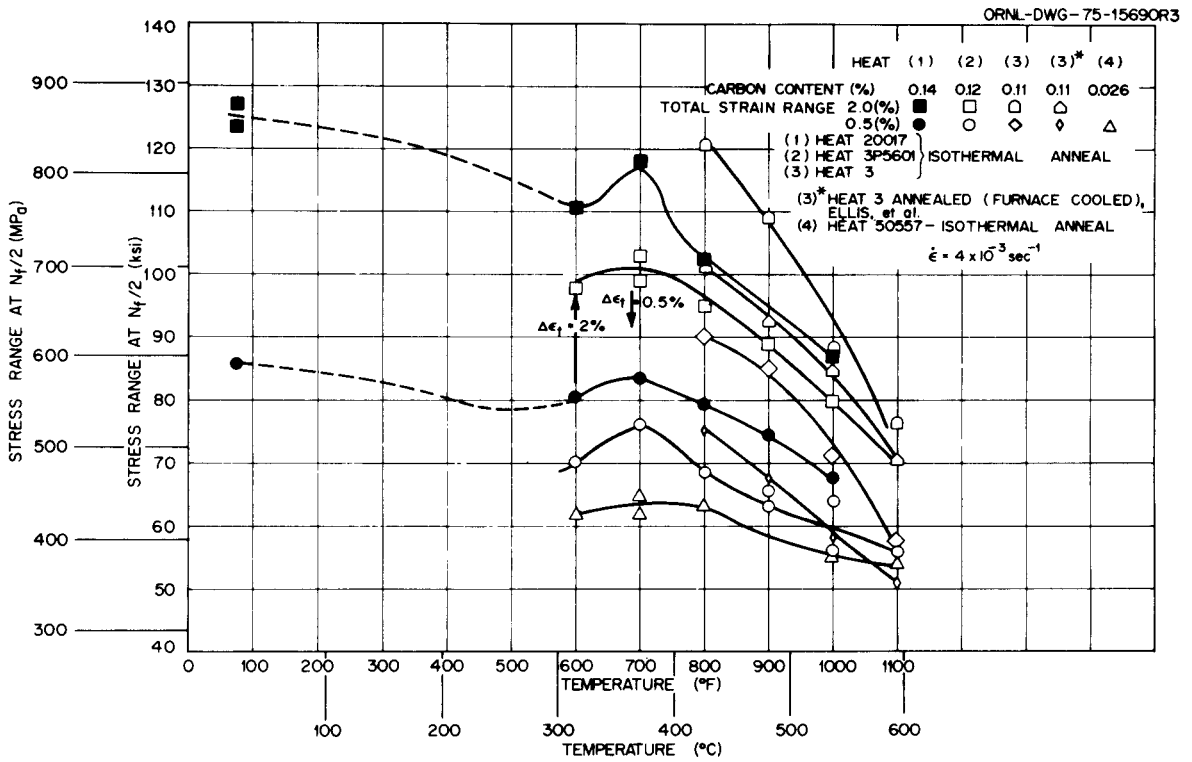

Fig. 2.22. Stress Range at $N_f/2$ as a Function of Temperature at Several Total Strain ranges ($\Delta\varepsilon_t$) for Four Heats of 2 1/4 Cr-1 Mo Steel.

2.2.3.3 Creep-Fatigue Behavior of 2 1/4 Cr-1 Mo Steel

The results of strain-controlled fatigue tests conducted at a rate of 4×10^{-3}/s (zero hold time) are compared with the results of tests that contained a hold time or period (tensile, compressive, or both) at peak strain during each cycle in Figs. 2.18, 2.19, and 2.23. These figures are isothermal plots of time to failure as a function of cycles to failure (t-N diagrams). These plots allow observation of the overall effect of hold time at the various strain ranges employed (i.e., 2, 1, 0.5, and 0.4%). Limited extrapolation is also possible by treatment of the individual isostrain range lines where they are linear.[14] The main value of the t-N diagram is that it clearly shows that, while hold times may reduce the fatigue life (cycles), there is an overall increase in test time. The nearly vertical lines in Figs. 2.18, 2.19, and 2.23 are iso-strain-range trend lines (i.e., 2, 1, 0.5, and 0.4%), which are intersected by iso-hold-time trend

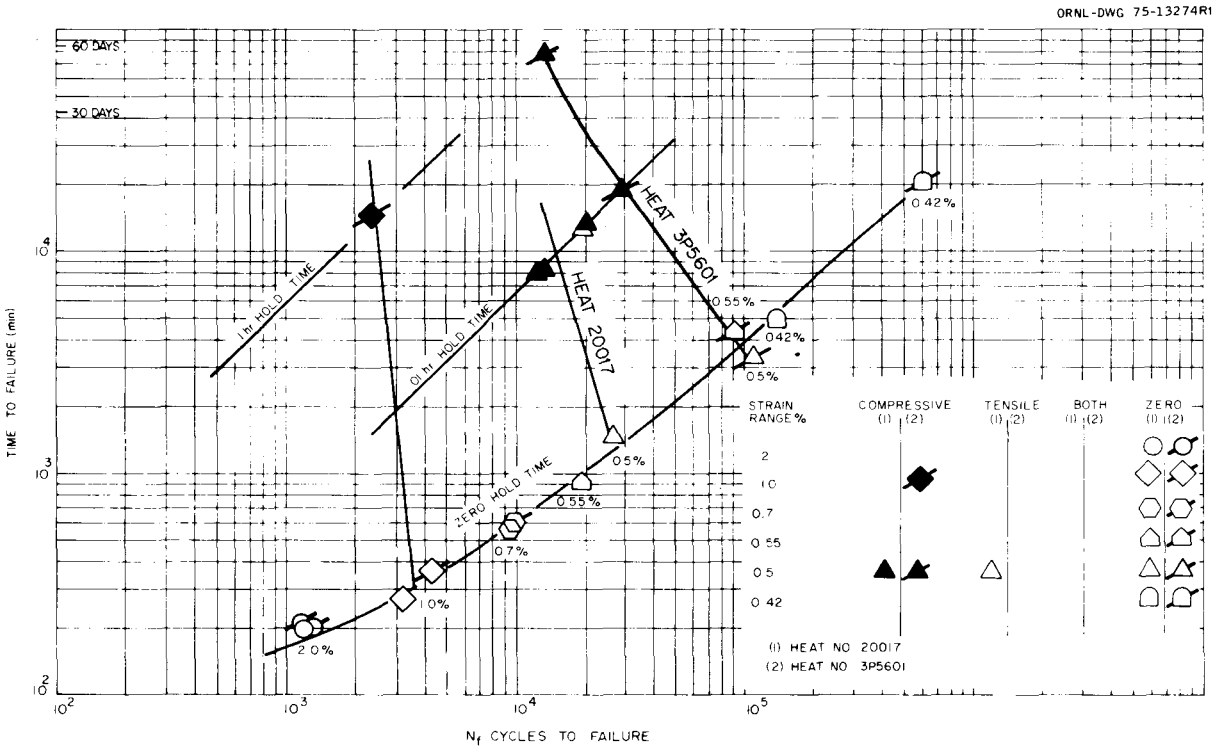

Fig. 2.23. Time-to-Failure vs Cycles-to-Failure Diagram Showing the Influence of Various Hold Periods on the Strain-Controlled Cycle Lifetime of 2 1/4 Cr-1 Mo Steel Tested at 427°C.

lines. Thus, one can observe overall behavior, as demonstrated by the trend lines, or compare the behavior of individual heats by noting the positions of individual data points. For high strain ranges the amount of degradation in fatigue life due to the introduction of a hold period at the peak strain amplitude in the tensile and/or compressive halves of the cycle is small. However, as the strain range is reduced, the influence of hold time becomes more significant. Compressive hold times are more damaging to fatigue life than tensile hold times (Figs. 2.18 and 2.19). Figure 2.18 shows that for strain ranges of about 0.5%, there is a heat-to-heat effect on fatigue life when compressive holds are introduced into each cycle, heat 3P5601 showing the greater lifetimes at this temperature. However, differences between the cycle life of the two heats tend to become smaller when the temperature is raised to 482 or 538°C and the hold times exceed 0.01 hr (Figs. 2.18 and 2.19).

Again, compressive hold times are more deleterious to fatigue life than tensile hold times, as shown in the three-dimensional diagram of cyclic life as a function of temperature and hold time for a single strain range of 0.5% (Fig. 2.24). The deleterious influence of increasing hold time on cycle lifetimes becomes more pronounced with increasing temperature.

Cyclic hardening behavior at 482°C (900°F) is compared in Fig. 2.25 for specimens from heat 3P5601 fatigued at a strain range of 0.5% with and without tensile or compression hold times. Hold times decreased the cyclic stress range.

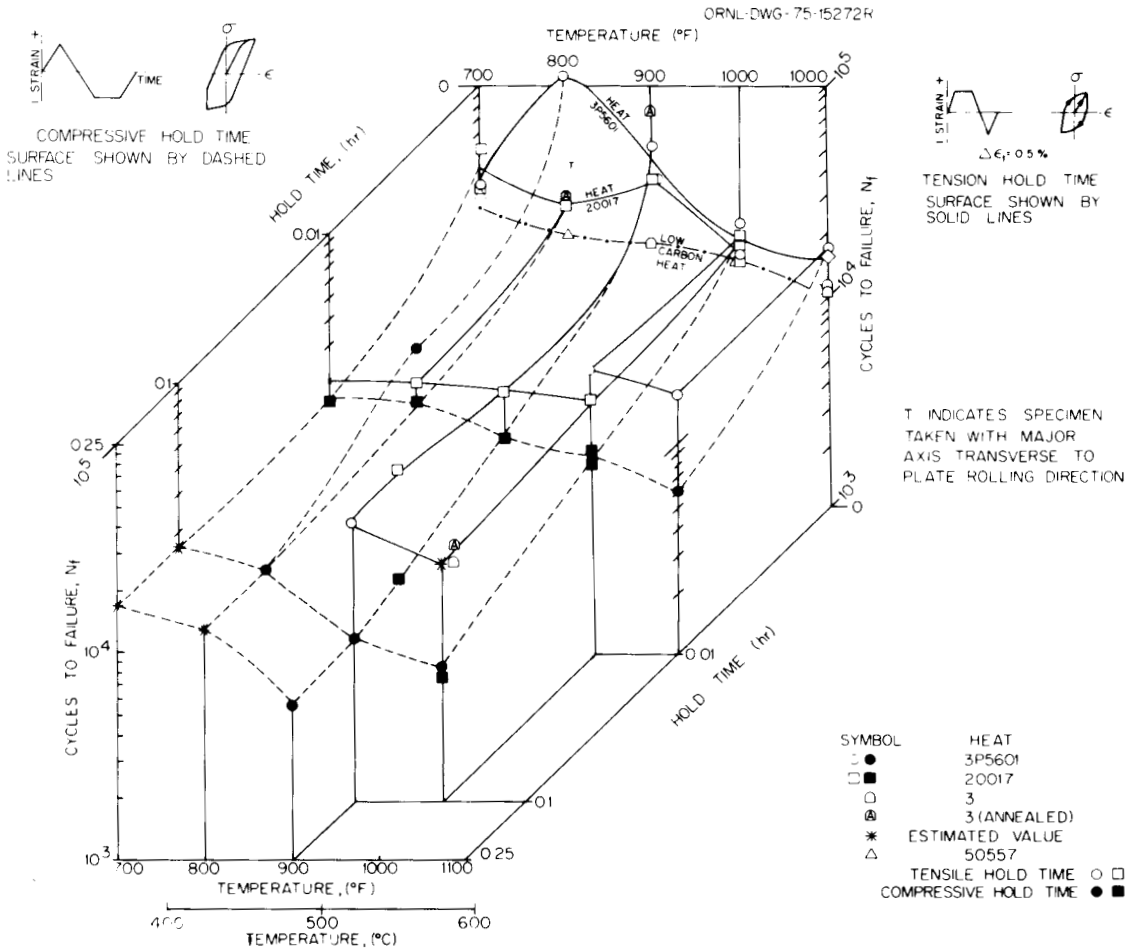

Fig. 2.24. Cycles to Failure as a Function of Temperature and Either a Tensile of Compressive Hold Time Introduced Each Cycle for 2 1/4 Cr-1 Mo Steel in the Annealed (A) or Isothermally Annealed Condition.

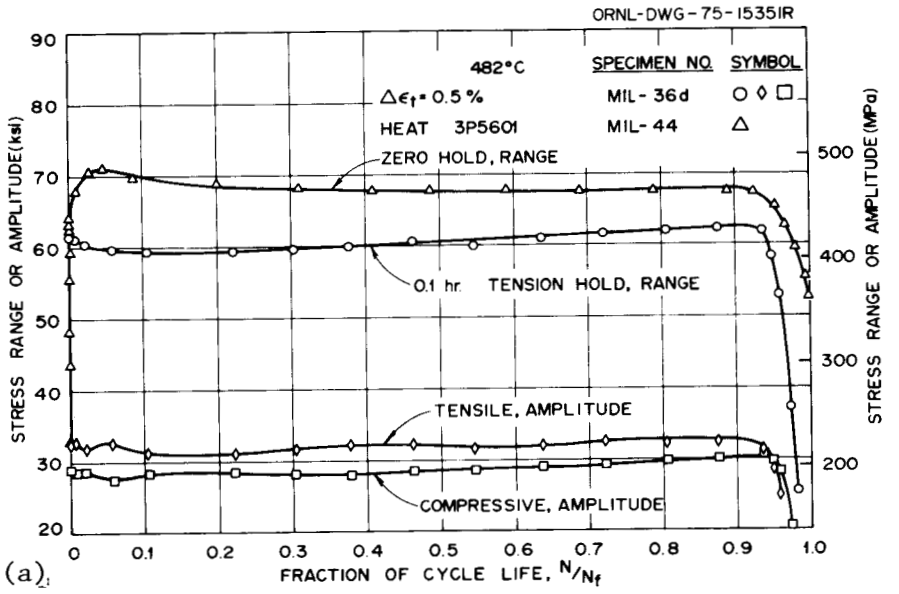

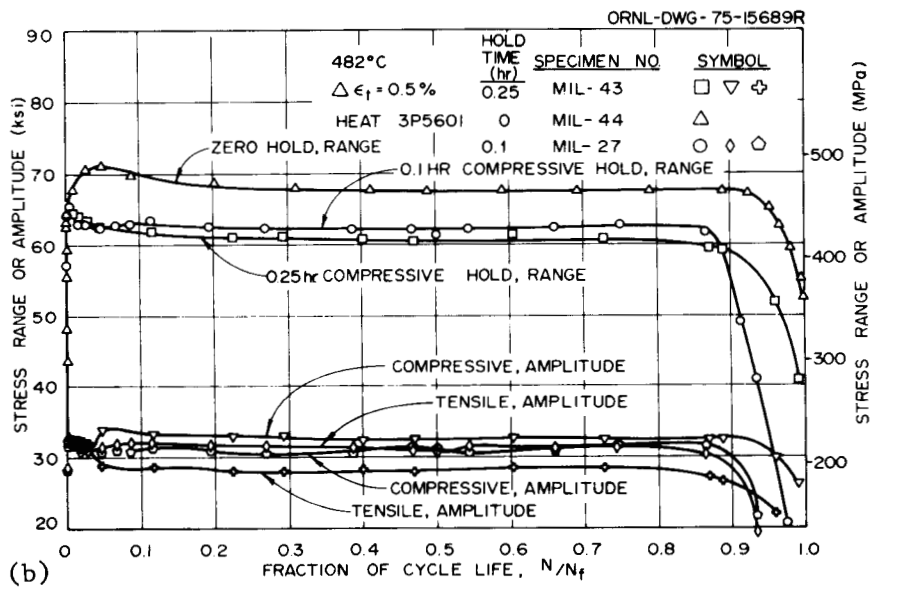

Fig. 2.25. Stress Range or Amplitude as a Function of Fraction of Cycle Life for One Heat of 2 1/4 Cr-1 Mo Steel, Showing the Influence Hold Time. (a) Tensile hold. (b) Compressive hold.

Lord and Coffin[15] characterized the low-cycle fatigue and hold time behavior of cast René 80 and found that compressive hold times were more damaging than tensile hold times. This behavior was qualitatively explained in terms of the ability of the material to sustain a mean stress at cycle lives beyond the transition fatigue life; that is, the elastic strain range was greater than the plastic strain range. These workers postulated that in this material compressive hold times were particularly deleterious at low strain ranges because tensile mean stresses that enhanced crack growth rates could be maintained. For 2 1/4 Cr-1 Mo steel tested at 482°C the cyclic transition life was around 10,000 cycles, such that specimens tested at a strain range of 0.5% or less clearly had elastic strain ranges in excess of the plastic strain ranges. On the other hand, compressive hold-time tests did not consistently result in the development of tensile mean stresses; nor as a consequence of tensile hold time tests did a compressive mean stress develop. Indeed the opposite was often found to be the case. Figure 2.25(a) shows an example where for a tensile hold, the tensile stress amplitude exceeded the compressive amplitude throughout the test. Figure 2.25(b) compares stress amplitudes developed during compressive hold time tests conducted at about 482°C and at a strain range of 0.5%. Comparison of the stress amplitude shows that for the 0.1-hr hold time test, the tensile amplitude was slightly greater than or equal to the compressive amplitude throughout the test. However, for the test conducted with a 0.25-hr hold time, the compressive amplitude maintained was consistently greater than the tensile amplitude. In the case of the 0.01-hr compressive hold time test conducted at a strain range of 0.4% (Fig. 2.19), the tensile amplitude was equivalent to the compressive amplitude. Thus, no consistent trends in mean stress were noted and no explanation as to why compressive hold times are more deleterious than tensile hold times is offered at this time.

Several methods for the analysis of creep-fatigue data have been proposed, including the strain range partitioning approach,[16] the linear summation of damage approach,[17] the frequency modification approach,[18]

the ductility exhaustion approach,[19] and others. Most methods require a complete spectrum of data, including a range of hold times, strain ranges, etc. However, data obtained in the current program are as yet incomplete, making analysis by these latter methods difficult. Interim results by the strain range partitioning concept are reported here.

The strain range partitioning approach involves partitioning the inelastic strain range traversed by a cycling specimen into four parts:

$\Delta\varepsilon_{pp}$ = tensile plastic strain reversed by compressive plastic strain, and obtained in this work from the zero hold time tests conducted at a strain rate of 4×10^{-3}/s;

$\Delta\varepsilon_{cc}$ = tensile creep strain reversed by compressive creep strain, and obtained in this work as a consequence of imposing both a tensile and compressive hold time each cycle;

$\Delta\varepsilon_{cp}$ = tensile creep strain reversed by compressive plastic strain, and obtained in this work as a consequence of the tensile hold time imposed each cycle;

$\Delta\varepsilon_{pc}$ = tensile plastic strain reversed by compressive creep strain, and obtained in this work as a consequence of the compressive hold time imposed each cycle.

Here, "plastic" strain is defined as time-independent inelastic strain, while "creep" strain is defined as time-dependent inelastic strain. Figure 2.26 illustrates the "life relationships" determined for these four types of strain, whereby $\Delta\varepsilon_{pp}$, $\Delta\varepsilon_{cp}$, $\Delta\varepsilon_{pc}$, and $\Delta\varepsilon_{cc}$ are related respectively to N_{pp}, N_{cp}, N_{pc}, and N_{cc}, where N_i is the expected cycle life of a specimen cycled in pure $\Delta\varepsilon_i$ strain. Shown in the figure are the lines previously determined by Manson et al.[16] compared with data obtained in this program as well as with data reported previously.[13]

It should be noted that both the lines and points in Fig. 2.26 were calculated by the linear damage rule:

$$\frac{1}{N_{cp}} + \frac{1}{N_{pc}} + \frac{1}{N_{cc}} + \frac{1}{N_{pp}} = \frac{1}{N_f} \, . \tag{3}$$

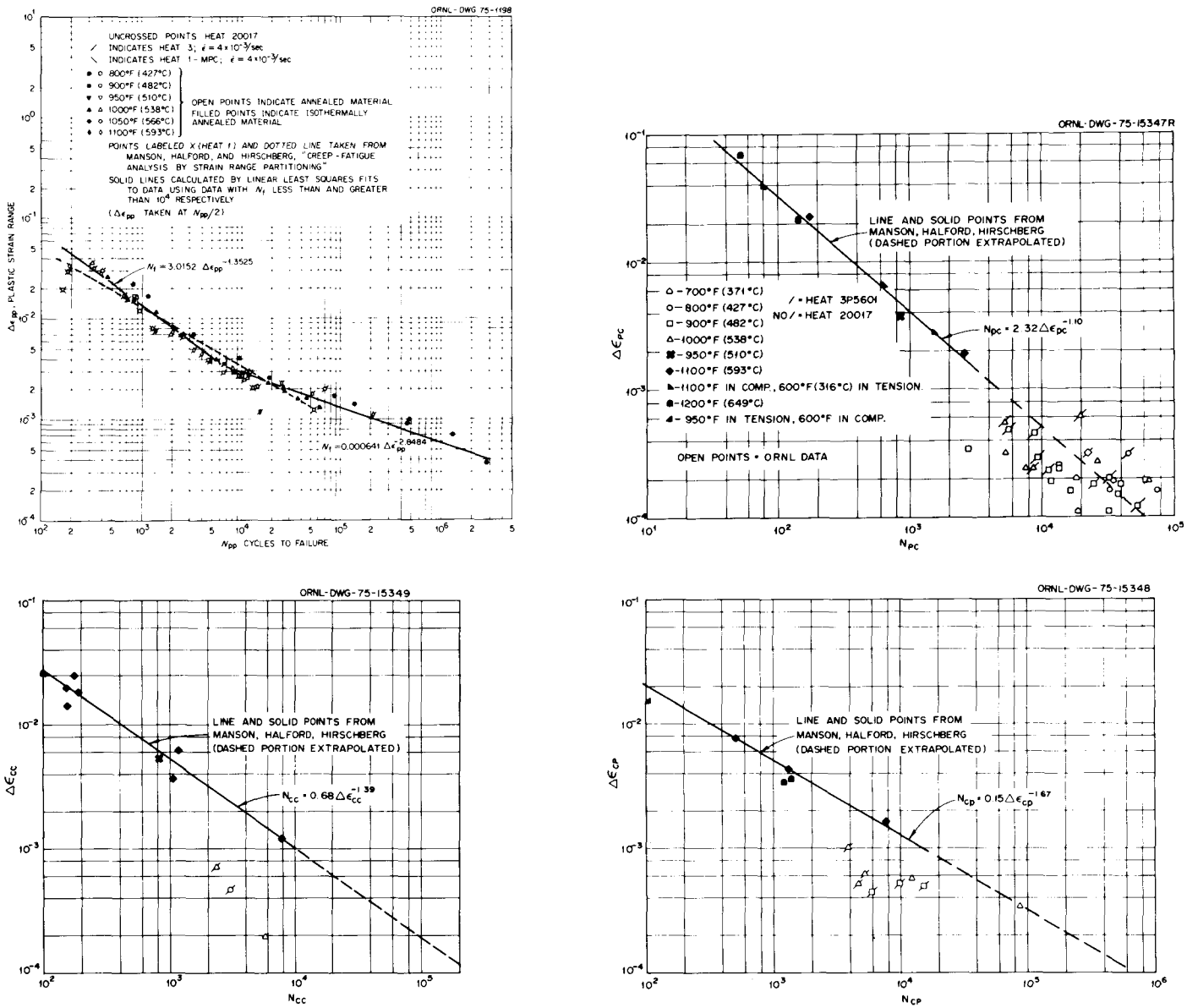

Fig. 2.26. Partitioned Plastic Strain Range Relationships for 2 1/4 Cr-1 Mo Steel.

Thus, if the type and magnitude of the inelastic strain involved can be estimated the cyclic life of a component can be determined.

Comparing the data obtained in this program (Fig. 2.26) with the line drawn through the data reported by Manson et al.[16] for the $\Delta\varepsilon_{pc}$, $\Delta\varepsilon_{cc}$, and $\Delta\varepsilon_{cp}$ plots indicates considerable scatter and some divergence from the extrapolated lines. The apparent bilinearity of the $\Delta\varepsilon_{pp}$ vs N_{pp} line on log-log coordinates is also apparent in Fig. 2.26. The data used to establish the dashed $\Delta\varepsilon_{pp}$ vs N_{pp} line by Manson et al.[16] were obtained at frequencies of 0.03 to 0.8 Hz, while the data reported in this investigation were obtained at frequencies of 0.1 to 0.7 Hz. The high degree of scatter and the deviation from the extrapolated lines (dashed) at low levels of inelastic strain may be due to a number of factors, including temperature and strain rate effects, heat-to-heat variations, inability to measure the inelastic strain components accurately, the assumption of incorrect power law relationships between the inelastic strain components and the associated cycles to failure, and the inaccuracy of Eq. (3) at low inelastic strain ranges. Most tests were conducted at strain ranges, temperatures, and hold periods such that the reduction in fatigue life attributable to hold periods was not large. Therefore, final judgment as to the applicability of the method for use with this material for most nuclear design applications (low total strain ranges) must be withheld pending the availability of long-term low total strain range test results, where the reduction in fatigue life is most pronounced.

2.2.3.4 Description of Hastelloy X

Fully reversed isothermal uniaxial strain-controlled fatigue tests have been conducted in air on a single heat and product form of Hastelloy X. Background and composition of this material are given in Table 2.9.

Fatigue specimens were made from the solution annealed material. The specimens were generally machined with their longitudinal axes parallel to the plate rolling direction. The specimens had an hourglass-shaped gage area with a radius-to-diameter ratio (R/D) of 6 and a minimum diameter of 5.08 mm (0.20 in.).

Table 2.9. Characterization of Hastelloy X

Product form:	13-mm (1/2-in.) plate
Heat	2600-3-4936
Source	Cabot-Stellite
Specification	ASME SB-435 (N06002)
Heat treatment	Solution annealed at 1177°C (2150°F) followed by a rapid cool
Grain size	78 μm (ASTM 4)
Hardness	DPH 190
Content, wt %	
Ni	Bal
Cr	21.82
Fe	19.09
Mo	9.42
Co	1.68
W	0.63
Mn	0.58
Si	0.44
C	0.07
P	0.016
S	<0.005
B	<0.002

Continuous cycling tests were completed over the range from 22 to 871°C (72–1600°F). These tests were conducted at a continuous cycling strain rate of 4×10^{-3}/s except as noted, using a ramp wave form of the type shown in Fig. 2.14. In addition, a limited number of tests have been conducted at 871°C (1600°F) to investigate creep-fatigue interaction at elevated temperatures. Figure 2.14 also shows wave forms for those tests in which a strain dwell or hold period was introduced in either or both the tensile and compressive halves of the cycle. Fatigue data obtained to date are given in Tables 2.10 and 2.11.

2.2.3.5 Continuous Cycling Fatigue Behavior of Hastelloy X

Total strain range, $\Delta\varepsilon_t$; plastic strain range, $\Delta\varepsilon_p$; and elastic strain range, $\Delta\varepsilon_e$ are plotted in Figs. 2.27 through 2.31 against cycles to failure, N_f, for tests conducted at a continuous cycling strain rate of 4×10^{-3}/s except as noted. The data of Jaske and Porfilio[20]

Table 2.10. Results of Strain-Controlled Fatigue Tests on Hastelloy X [Heat 2600-3-4936 13-mm (1/2 in.) Plate] Tested in Air[a]

Specimen[b]	Poisson's Ratio, ν	Total Strain Range, $\Delta\varepsilon_t$	Strain Range at $N_f/2$, %				Cycles to Failure, N_f	Time to Failure, t_f	Stress Range at 10th Cycle, $\Delta\sigma_{10}$		Properties of $N_f/2$, MPa (ksi)		
			Elastic, $\Delta\varepsilon_e$		Inelastic, $\Delta\varepsilon_{in}$								
			Measured	Calculated[c]	Measured	Calculated[d]			(MPa)	(ksi)	Stress Range[c]	Tensile Stress Amplitude, σ_t	Compressive Stress Amplitude, σ_c
Tested at 22°C (72°F) (Young's Modulus E = 199 GPa = 28.87 × 10^6 psi)													
HXL-51	0.315	4.10	0.79	0.72	3.31	3.38	439	146	1292	187.4	1425 (206.7)	698 (101.3)	727 (105.4)
HXL-29	0.265	3.04	0.76	0.70	2.28	2.34	591	148	1237	179.5	1392 (201.9)	681 (98.8)	711 (103.1)
HXL-28	0.285	2.11	0.62	0.59	1.49	1.51	1,494	249	1087	157.7	1177 (170.8)	584 (84.8)	593 (86.0)
HXL-27	0.280	1.50	0.49	0.49	1.02	1.02	6,101	763	956	138.6	968 (140.4)	478 (69.3)	490 (71.1)
HXL-23	0.278	0.99	0.46	0.43	0.53	0.56	10,245	854			862 (125.0)	427 (62.0)	435 (63.1)
HXL-47	0.261	0.89	0.48	0.42	0.41	0.47	15,796	1,185	815	118.1	829 (120.3)	407 (59.1)	422 (61.2)
HXL-22	0.269	0.80	0.46	0.42	0.33	0.38	49,664	3,311			837 (121.4)	406 (58.9)	431 (62.5)
Tested at 538°C (1000°F) (Young's Modulus E = 162 GPa = 23.54 × 10^6 psi)													
HXL-46	0.299	4.06	0.89	0.94	3.18	3.12	177	59	1084	157.2	1530 (221.9)	748 (108.4)	782 (113.5)
HXL-16	0.306	3.02	0.73	0.83	2.94	2.19	418	104	847	122.8	1353 (196.3)	665 (96.5)	688 (99.8)
HXL-20	0.274	1.56	0.65	0.70	0.91	0.86	1,181	148	764	110.8	1141 (165.5)	562 (81.6)	579 (83.9)
HXL-30	0.302	0.99	0.62	0.63	0.37	0.36	5,182	432	666	96.6	1015 (147.3)	494 (71.7)	521 (75.6)
HXL-3	0.268	0.79	0.73	0.67	0.06	0.12	7,596	501			1084 (157.2)	493 (71.5)	591 (85.8)
HXT-2	0.290	0.71	0.57	0.53	0.13	0.18	14,240	831	577	83.7	855 (124.0)	405 (58.7)	450 (65.3)
HXT-4	0.320	0.65	0.48	0.56	0.17	0.08	13,675	741	542	78.6	917 (133.0)	446 (64.7)	471 (68.3)
HXL-19	0.341	0.60	0.56	0.54	0.04	0.06	225,000	11,250			877 (127.2)	444 (64.4)	433 (62.8)
Tested at 649°C (1200°F) (Young's Modulus E = 154 GPa = 22.4 × 10^6 psi)													
HXL-6	0.312	4.17	0.80	0.96	3.37	3.21	94	31	1118	162.3	1476 (214.0)	719 (104.2)	757 (109.8)
HXL-14	0.323	3.00	0.76	0.91	2.24	2.09	133	33	1059	153.6	1412 (204.8)	693 (100.6)	719 (104.2)
HXL-42	0.316	2.03	0.72	0.82	1.31	1.21	318	53	872	126.5	1258 (182.5)	611 (88.6)	647 (93.8)
HXL-44	0.334	1.52	0.63	0.72	0.89	0.80	713	89	711	103.1	1119 (162.3)	547 (79.3)	572 (83.0)
HXL-8	0.305	1.00	0.63	0.63	0.38	0.37	1,617	135			972 (141.0)	478 (69.3)	494 (71.7)
HXT-3	0.270	0.80	0.64	0.59	0.16	0.22	5,147	343	628	91.1	909 (131.8)	438 (63.5)	471 (68.3)
HXL-10	0.308	0.70	0.55	0.54	0.15	0.16	11,764	686			831 (120.5)	406 (58.9)	425 (61.6)
HXL-7	0.325	0.50	0.45	0.47	0.05	0.03	19,262	802			731 (106.2)	371 (53.9)	360 (52.3)
HXL-1	0.258	0.50	0.46	0.46	0.04	0.04	17,820	742			715 (103.8)	382 (55.5)	333 (48.3)
HXL-15	0.381	0.44	0.42	0.45	0.02		148,497	5,445	454	65.9	700 (101.6)	351 (51.0)	349 (50.6)
Tested at 760°C (1400°F) (Young's Modulus E = 146 GPa = 21.16 × 10^6 psi)													
HXL-13	0.321	4.48	0.54	0.70	3.94	3.78	56	21	966	140.1	1016 (147.4)	494 (71.7)	522 (75.7)
HXL-11	0.305	3.00	0.55	0.64	2.45	2.36	154	38	848	123.0	935 (135.7)	465 (67.4)	470 (68.2)
HXL-48	0.282	2.07	0.55	0.62	1.52	1.45	280	46	725	105.2	902 (130.8)	449 (65.2)	453 (65.6)
HXL-50	0.316	1.50	0.50	0.55	1.00	0.95	598	75	663	96.2	800 (116.1)	396 (57.4)	404 (58.7)
HXL-2	0.294	1.0	0.48	0.47	0.52	0.53	1,582	132			684 (99.2)	339 (49.2)	345 (50.0)
HXL-17	0.320	0.70	0.42	0.45	0.28	0.25	3,351	195			655 (95.0)	323 (46.9)	332 (48.1)
HXL-18	0.369	0.51	0.37	0.40	0.14	0.11	8,362	348	434	63.0	586 (85.0)	293 (42.5)	293 (42.5)
HXT-5	0.267	0.45	0.38	0.35	0.07	0.10	102,168	3,831	460	66.7	518 (75.1)	256 (37.2)	262 (38.0)
HXL-5	0.308	0.35	0.34	0.32	0.02	0.03	215,747	6,293	363	52.7	476 (69.0)	213 (30.9)	263 (38.1)
Tested at 871°C (1600°F) (Young's Modulus E = 137 GPa = 19.86 × 10^6 psi)													
HXL-41	0.311	4.00	0.42	0.53	3.58	3.47	96	32	702	101.8	720 (104.7)	347 (50.4)	373 (54.0)
HXL-40	0.326	3.01	0.41	0.52	2.60	2.49	138	34	690	100.1	715 (103.7)	343 (49.7)	372 (54.0)
HXL-33	0.337	2.01	0.34	0.44	1.67	1.57	312	52	536	77.8	610 (88.5)	298 (43.2)	312 (45.3)
HXL-53[e]	0.319	2.00	0.35	0.44	1.65	1.56	280	19	609	88.4	682 (99.0)	333 (48.3)	349 (50.7)
HXL-34[f]	0.298	2.00		0.47		1.53	216	1,332	566	82.0	638 (92.6)	318 (46.1)	320 (46.4)
HXL-35[g]	0.329	2.00		0.48		1.52	185	1,141	536	77.7	655 (95.0)	333 (48.2)	322 (46.8)
HXL-37[f,g]	0.320	2.00		0.47		1.53	196	2,384	521	75.6	644 (93.4)	319 (46.3)	325 (47.1)
HXT-7	0.307	1.50	0.34	0.44	1.16	1.06	466	58	542	78.6	604 (87.5)	297 (43.1)	307 (44.5)
HXL-36	0.305	1.00	0.38	0.38	0.62	0.62	1,156	96	486	70.4	523 (75.8)	257 (37.2)	266 (38.6)
HXL-54[h]	0.274	0.99		0.389		0.601	618	9,322	417	60.5	533 (77.3)	275 (39.8)	258 (37.4)
HXL-43	0.307	0.80	0.32	0.35	0.48	0.45	2,002	133			479 (69.5)	236 (34.2)	243 (35.2)
HXL-21	0.270	0.59	0.34	0.33	0.25	0.26	3,433	172	408	59.2	452 (65.6)	229 (33.2)	223 (32.4)
HXL-24[e]	0.279	0.59	0.34	0.34	0.25	0.25	3,494	70			460 (66.8)	232 (33.6)	228 (33.2)
HXL-26[f,i]	0.253	0.60		0.37		0.23	2,191	13,255	385	55.8	509 (73.8)	219 (31.8)	290 (42.1)
HXL-32[g,i]	0.315	0.60		0.37		0.23	1,084	6,558	383	55.5	510 (74.1)	274 (39.8)	236 (34.3)
HXL-38[f,g]	0.283	0.60		0.36		0.24	984	11,857	394	57.2	495 (71.8)	247 (35.9)	248 (35.9)
HXT-6	0.255	0.50	0.34	0.28	0.16	0.22	13,234	551	374	54.3	392 (56.9)	195 (28.3)	197 (28.6)

[a]Strain rate 4 × 10^{-3}/sec unless otherwise noted.

[b]L in specimen number implies specimen axis parallel to rolling direction; T transverse.

[c]$\Delta\sigma/E$.

[d]$\Delta\varepsilon_t - \Delta\sigma/E$.

[e]Strain rate 10 × 10^{-3}/sec.

[f]0.1-hr tensile hold period.

[g]0.1-hr compressive hold period.

[h]0.25-hr compressive hold period.

[i]Strain rate 9 × 10^{-3}/sec.

Table 2.11. Creep-Fatigue Data on Hastelloy X in Air at 871°C

Specimen	Strain Rate (sec^{-1})	Hold Period, hr		Relaxed Stress, MPa (ksi)		Partitioned Inelastic Strain Range,[a] %		Associated Cycle Lifetimes, hr	
		Tensile	Compressive	Tensile, σt_r	Compressive, σ_c	$\Delta\varepsilon_{pp}$	Other	N_{pp}	Other
HXL-34	4×10^{-3}	0.1		48 (7.0)		1.34	$\Delta\varepsilon_{cp} = 0.20$	312	$N_{cp} = 70$
HXL-35	4		0.1		38 (5.6)	1.31	$\Delta\varepsilon_{pc} = 0.21$	320	$N_{pc} = 50$
HXL-37	4	0.1	0.1	33 (4.8)	33 (4.8)	1.32	$\Delta\varepsilon_{cc} = 0.21$	318	$N_{cc} = 58$
HXL-54	4		0.25		38 (5.6)	0.44	$\Delta\varepsilon_{pc} = 0.16$	1,746	$N_{pc} = 222$
HXL-26	9	0.1		57 (8.3)		0.11	$\Delta\varepsilon_{cp} = 0.11$	15,039	$N_{cp} = 1221$
HXL-32	9		0.1		49 (7.1)	0.090	$\Delta\varepsilon_{pc} = 0.14$	20,604	$N_{pc} = 669$
HXL-38	4	0.1	0.1	26 (3.9)	30 (4.3)	0.079	$\Delta\varepsilon_{cc} = 0.16$	25,228	$N_{cc} = 667$

[a]Based on the strain-range partitioning technique for creep-fatigue data analysis.

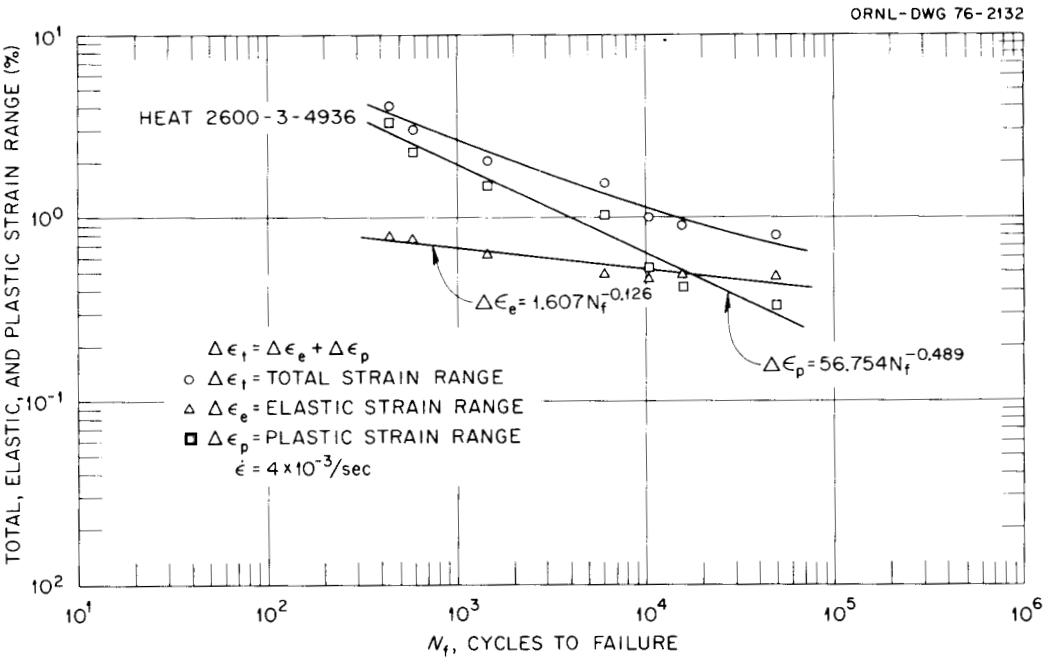

Fig. 2.27. Total, Elastic, and Plastic Strain Range vs Cycles to Failure at Room Temperature for Hastelloy X Tested in Air.

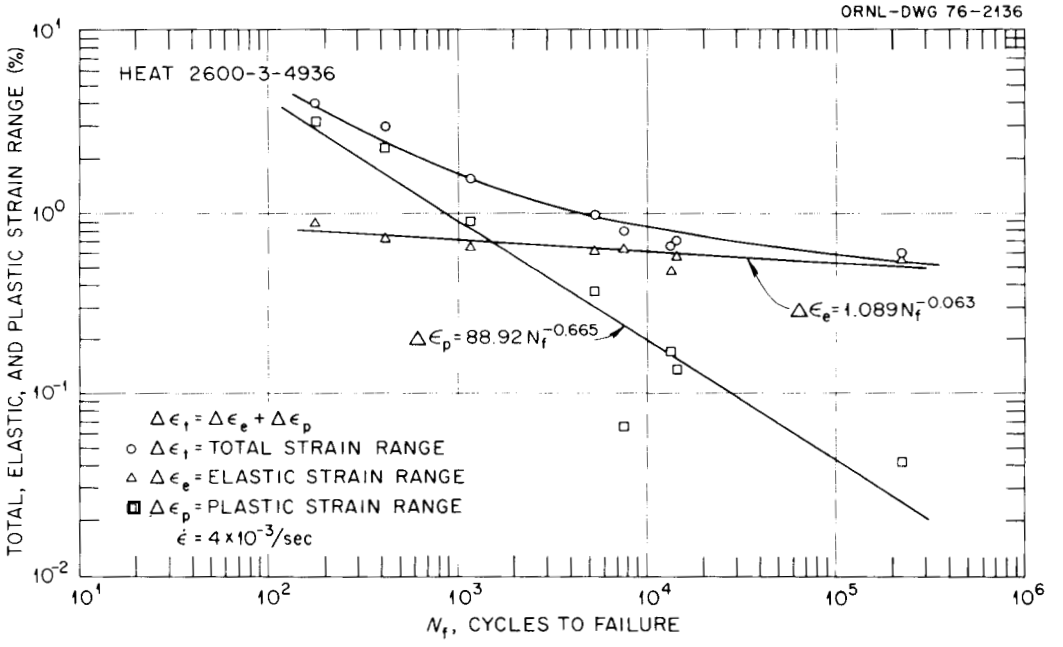

Fig. 2.28. Total, Elastic, and Plastic Strain Range vs Cycles to Failure at 538°C (1000°F) for Hastelloy X Tested in Air.

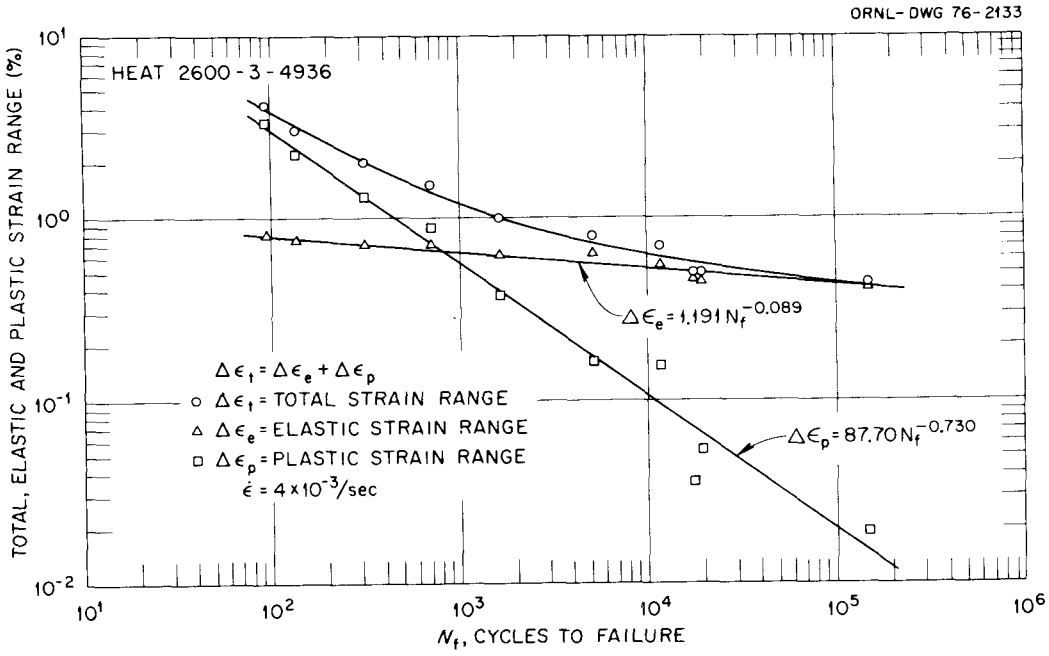

Fig. 2.29. Total, Elastic, and Plastic Strain Range vs Cycles to Failure at 649°C (1200°F) for Hastelloy X Tested in Air.

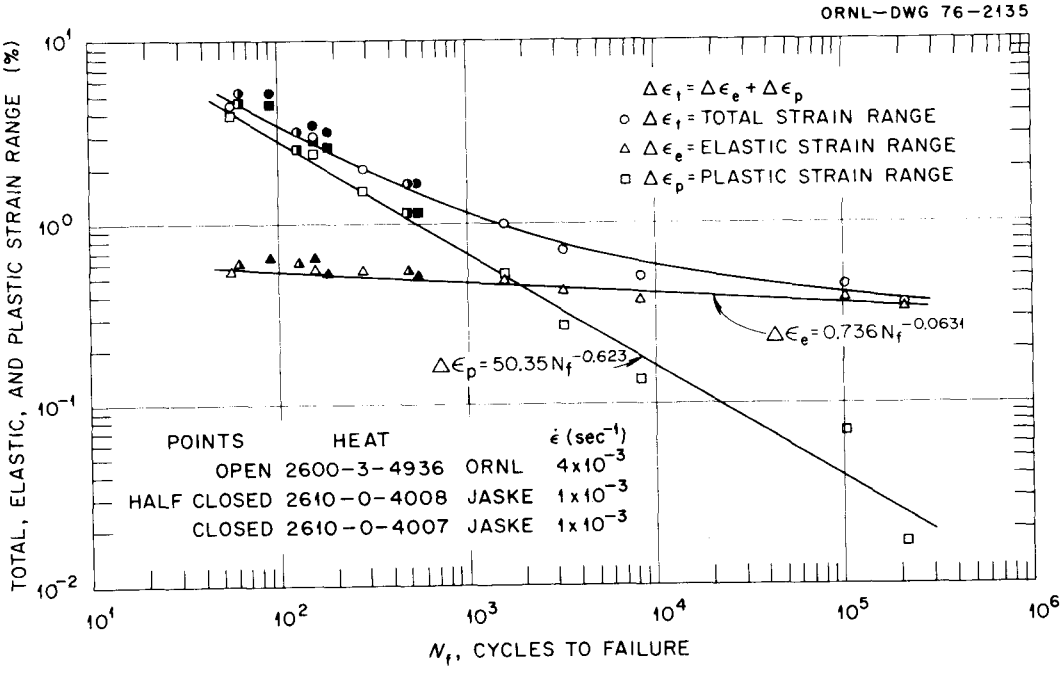

Fig. 2.30. Total, Elastic, and Plastic Strain Range vs Cycles to Failure at 760°C (1400°F) for Hastelloy X Tested in Air.

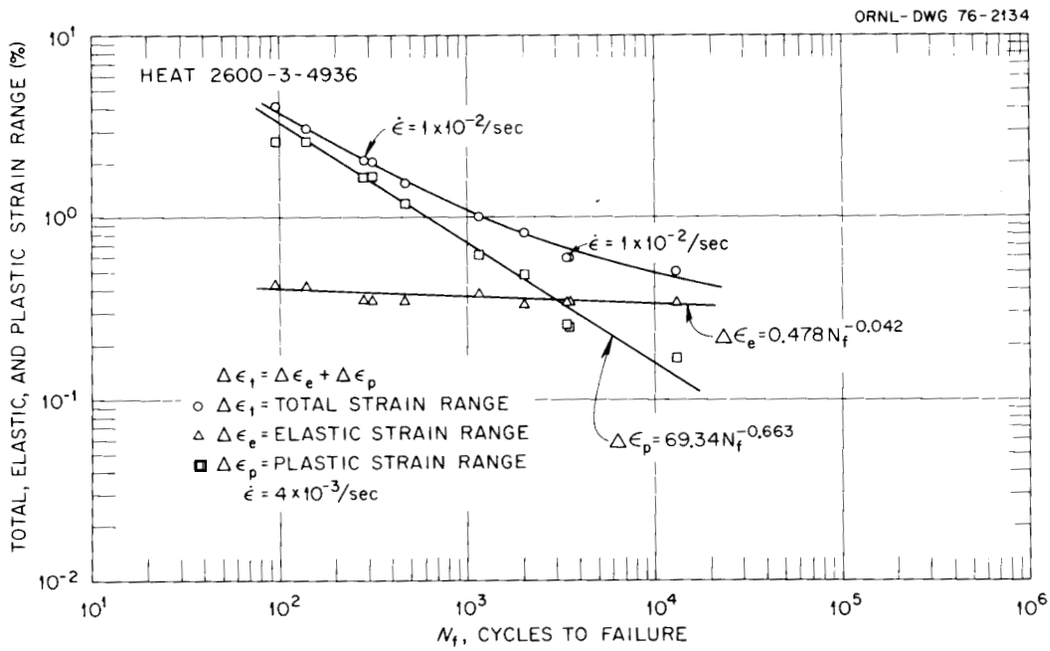

Fig. 2.31. Total, Elastic, and Plastic Strain Range vs Cycles to Failure at 871°C (1600°F) for Hastelloy X Tested in Air.

were included in the plot of 760°C (1400°F) data (Fig. 2.30). Figures 2.27 through 2.31 demonstrate that the components of the total strain range, $\Delta\varepsilon_t$, namely the plastic, $\Delta\varepsilon_p$, and elastic, $\Delta\varepsilon_e$, strain ranges, can be expressed as simple power law relationships; thus

$$\Delta\varepsilon_t = \Delta\varepsilon_p + \Delta\varepsilon_e ,$$

$$\Delta\varepsilon_t \quad AN_f^{-a} \quad BN_f^{-b} .$$

Values of the coefficients and exponents in the above equation have been determined by linear least squares analysis and are summarized in Table 2.12.

Figure 2.32 compares the best fit plot with the isothermal total strain range vs cycles to failure data. Increasing the temperature generally decreases the continuous-cycling fatigue life of Hastelloy X, as shown. Several tests were conducted at a strain rate of 0.01/s at 871°C (1600°F) to determine if fatigue life depended on strain rate within the creep range at strain rates in excess of 4×10^{-3}/s.

Table 2.12. Values for the Elastic and Plastic Strain Range Constants for Strain-Controlled Tests Conducted on Hastelloy X Heat 2600-3-4936 at a Strain Rate of 4×10^{-3}/s

Temperature		Values of Constants in $\Delta\varepsilon_t = AN_f^{-a} + BN_f^{-b}$			
(°C)	(°F)	A	a	B	b
Room	Room	56.75	0.489	1.607	0.126
538	1000	88.92	0.665	1.089	0.0633
649	1200	87.70	0.730	1.191	0.0890
700	1400	50.35	0.623	0.736	0.0631
871	1600	69.34	0.663	0.478	0.0420

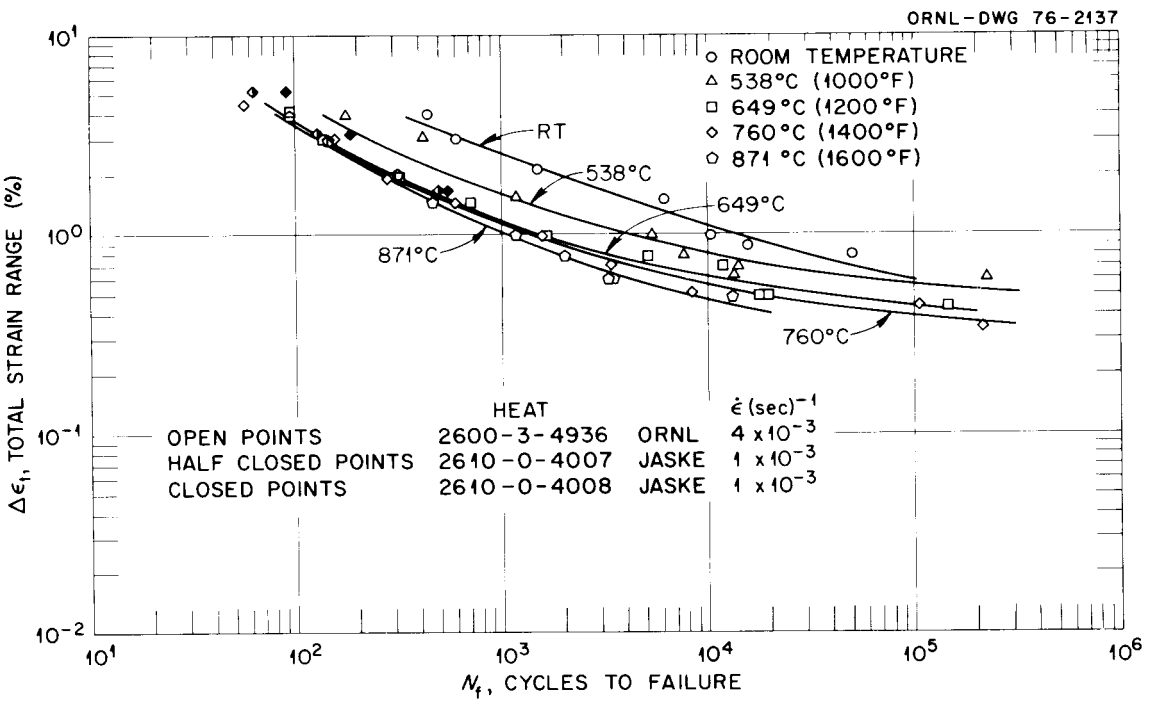

Fig. 2.32. Total Strain Range vs Cycles to Failure for Hastelloy X Tested in Air.

The results of the higher strain rate tests gave essentially identical cyclic lives, indicating strain-rate independence in that range.

Since other structural materials[21,22] will be used for various components within HTGR systems, the continuous-cycling fatigue properties of Hastelloy X and a number of these materials were compared. These materials include Inconel alloy 718, Incoloy alloy 800,[23—27] 2 1/4 Cr-1 Mo steel,[28] type 304 stainless steel, [24—27,29,30] type 316 stainless steel,[24,26,31] and AISI 1010 steel.[32] Product forms from which the data were generated, along with several tensile properties of interest in fatigue analysis at temperatures where comparisons can be made, are given in Table 2.13. All data were taken in air at a continuous-cycling strain rate of 4×10^{-3}/s. Comparative plots are given in Figs. 2.33 through 2.35.

Comparing the continuous-cycling fatigue of these materials in Figs. 2.33 through 2.35 indicates similar behavior in the low-cycle range, even though they show wide differences in ductility, particularly at room temperature. However, as the total strain range is reduced, marked differences in fatigue life occur and are accentuated by increasing the temperature. High-cycle fatigue resistance is a function of the ultimate tensile strength, and, therefore, Inconel alloy 718 shows the best high-cycle fatigue resistance, with Hastelloy X second best.

2.2.3.6 Creep-Fatigue Behavior of Hastelloy X

To determine the influence of creep-fatigue interactions on the flow and failure behavior of Hastelloy X, tests involving constant strain (see Fig. 2.14) and load hold periods introduced during each fully reversed strain cycle are being conducted. At this time, only a few hold-time tests, all with constant-strain hold periods, have been conducted at 871°C (1600°F), and the interim data are reported in Table 2.11. Hysteresis loops at roughly half the cycle life for

Table 2.13. Comparison of Several Tensile Properties (Average Values) of Several Structural Materials Used in Nuclear Reactor Construction

Material and Heat Treatment	20°C (70°F)	538°C (1000°F)	649°C (1200°F)
Inconel Alloy 718 (Plate), Solution Annealed at 954°C (1750°F); Duplex Aged at 718/621°C (1325/1150°F)			
Ultimate Tensile Strength, MPa (ksi)	1372 (199)	1193 (173)	1069 (155)
Yield Strength, MPa (ksi)	1034 (150)	965 (140)	903 (131)
Reduction of Area (%)	28	27	23
Hastelloy Alloy X (Plate), Solution Annealed at 1176°C (2150°F) followed by rapid air cool or water quench			
Ultimate Tensile Strength, MPa (ksi)	758 (110)	593 (86)	510 (74)
Yield Strength, MPa (ksi)	358 (52)	227 (33)	221 (32)
Reduction of Area (%)	60	38	38
Incoloy Alloy 800, Grades 2 (Bar), and H, Solution Annealed at 1148°C (2100°F)			
Ultimate Tensile Strength, MPa (ksi)	545 (79)	448 (65)	379 (55)
Yield Strength, MPa (ksi)	228 (33)	131 (19)	117 (17)
Reduction of Area (%)	73	55	53
Type 316 Stainless Steel (Bar), Solution Annealed			
Ultimate Tensile Strength, MPa (ksi)	593 (86)	455 (66)	365 (53)
Yield Strength, MPa (ksi)	250 (37)	172 (25)	165 (24)
Reduction of Area (%)	72	66	69
Type 304 Stainless Steel (Bar), Solution Annealed			
Ultimate Tensile Strength, MPa (ksi)	593 (86)	393 (57)	290 (42)
Yield Strength, MPa (ksi)	248 (36)	131 (19)	117 (17)
Reduction of Area (%)	81	69	58
2 1/4 Cr-1 Mo Steel, Plate and Pipe, Annealed or Isothermally Annealed			
Ultimate Tensile Strength, MPa (ksi)	500 (73)	380 (55)	
Yield Strength, MPa (ksi)	260 (37)	195 (28)	
Reduction of Area (%)	70	75	
AISI 1010 Steel, Hot-Rolled 3/4-in.-diam (1.91-cm) bar			
Ultimate Tensile Strength, MPa (ksi)	369 (54)	153 (22)	
Yield Strength, MPa (ksi)	261 (38)	92 (13)	
Reduction of Area (%)	74	90	

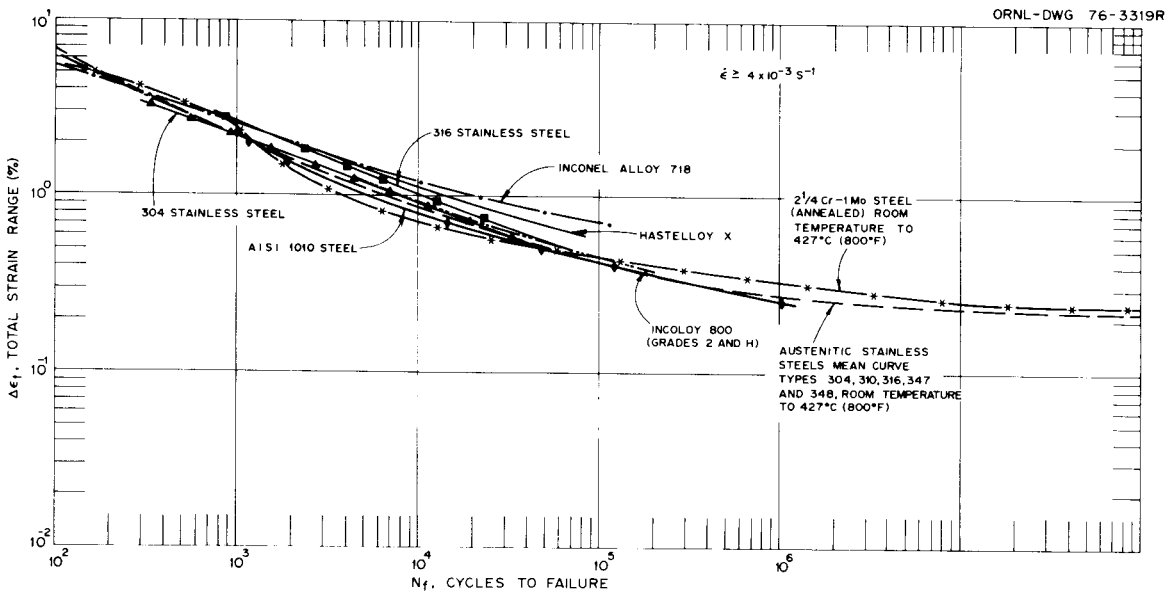

Fig. 2.33. Comparison of the Fatigue Behavior of Several Materials at Room Temperature (Except as Indicated). Lines represent best fit values of actual data.

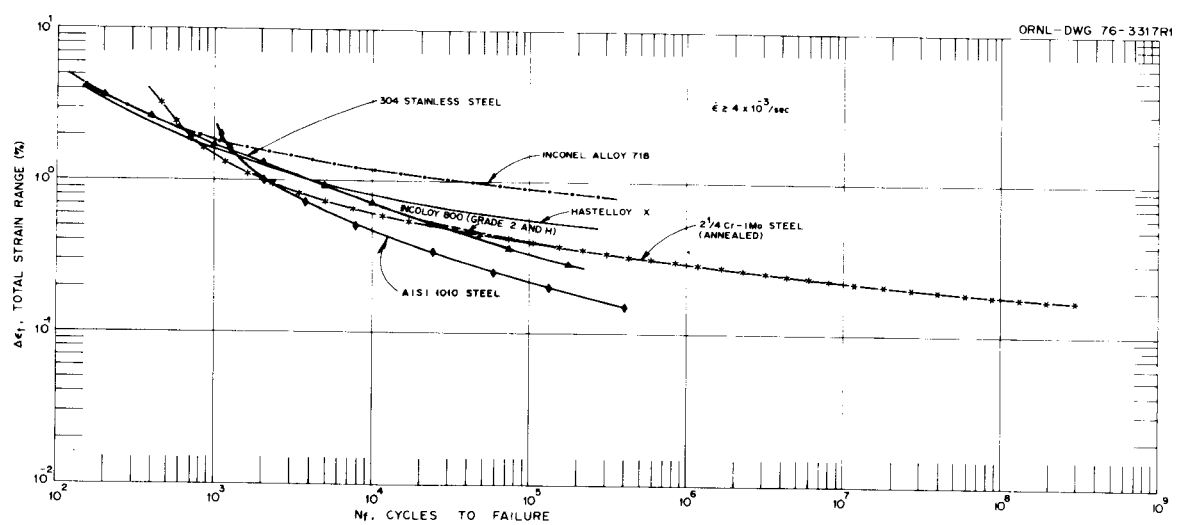

Fig. 2.34. Comparison of the Fatigue Behavior of Several Materials at 538°C (1000°F). Lines represent best fit values of actual data. Data for type 304 stainless steel include tests conducted at 538°C (1000°F) and 566°C (1050°F).

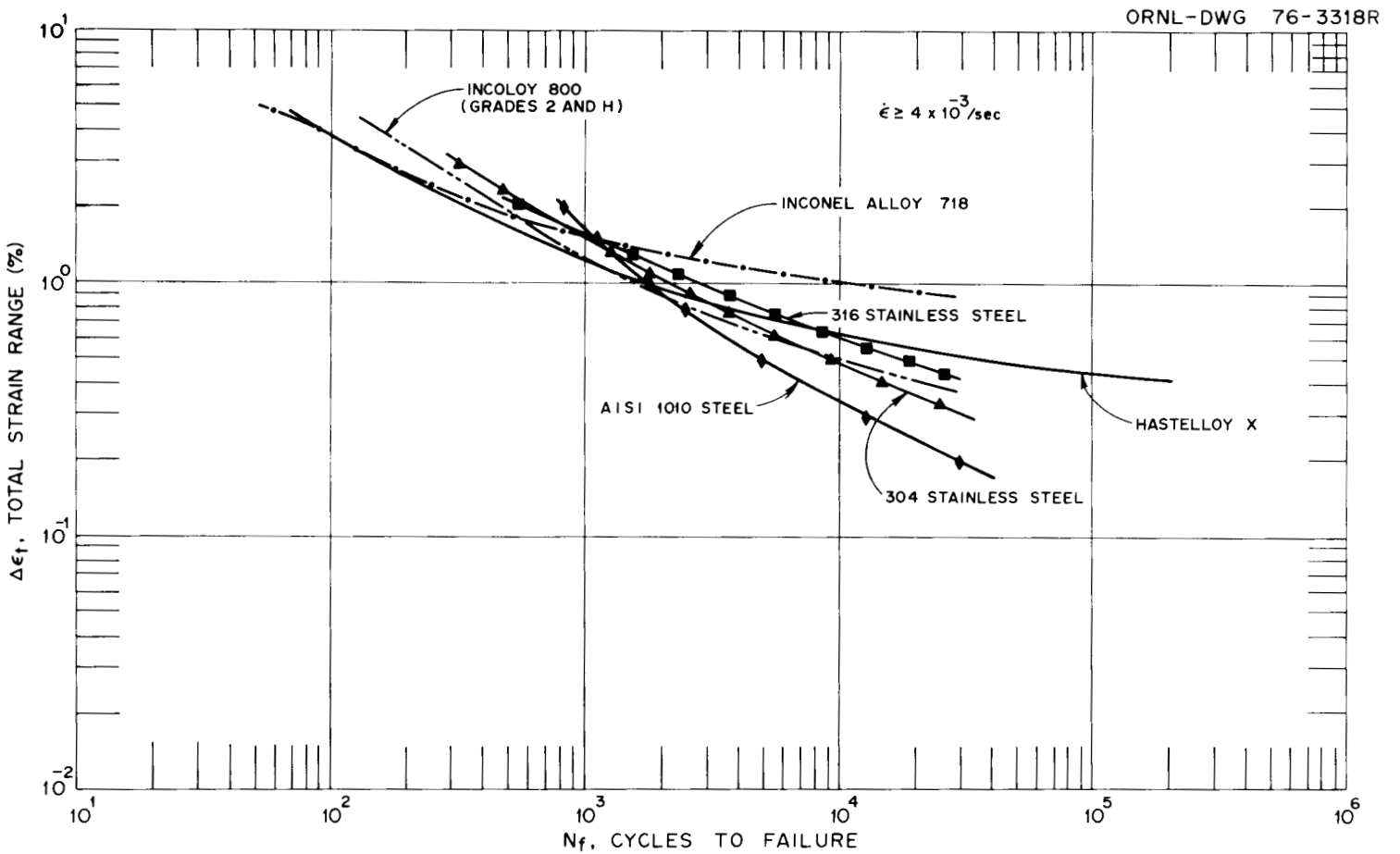

Fig. 2.35. Comparison of the Fatigue Behavior of Several Materials at 649°C (1200°F). Lines represent best fit values of actual data.

two strain ranges (i.e., 2 and 0.6%) are compared in Fig. 2.36, which shows that (1) the number of cycles to failure is generally reduced when hold periods are introduced, and (2) compressive hold times tend to be the more damaging. Further, the hysteresis loops for the 0.6% total strain range tests show that the test conducted with only a tensile hold time developed a mean compressive stress and that the test conducted with a compressive hold period developed a mean tensile stress. The test with both tensile and compressive holds developed little or no mean stress.

As discussed previously, for cast René 80 compressive hold times were more damaging than tensile hold times.[15] Compressive hold times were particularly deleterious at low strain ranges, because it was postulated that tensile mean stresses that enhanced crack growth rates could be maintained. For Hastelloy X tested at 871°C (1600°F), the cycle life of a continuously cycled specimen tested at 0.6% total strain

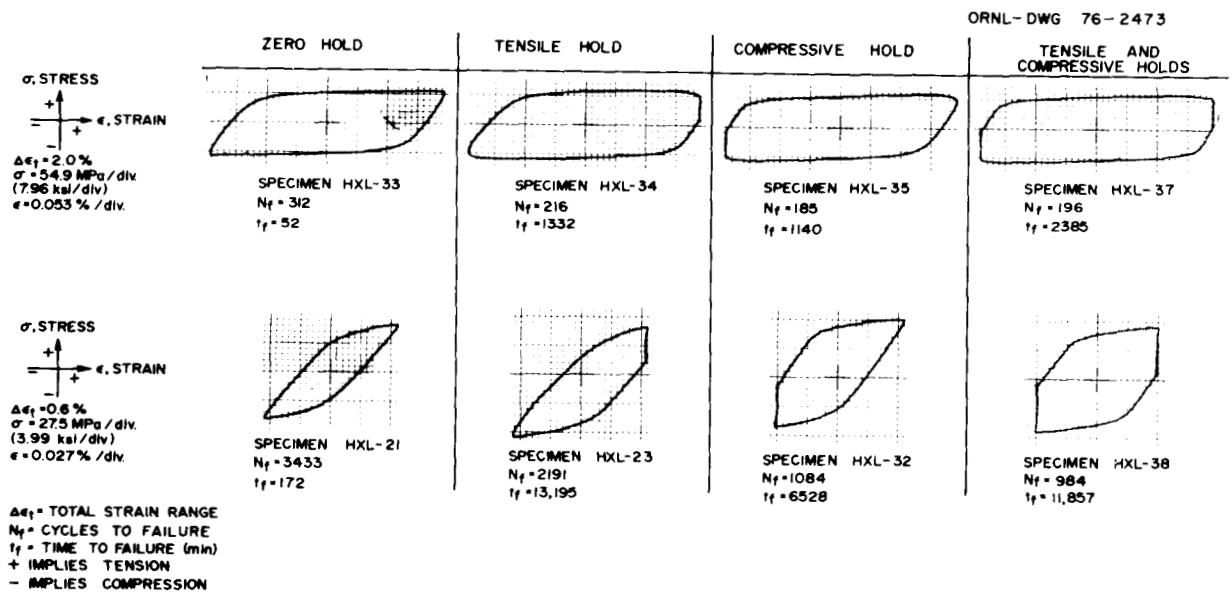

Fig. 2.36. Comparison of Actual Hysteresis Loops from Strain-Controlled Low-Cycle Fatigue Tests Involving Zero Hold Periods or 0.1-hr Hold Periods at Peak (Maximum, Minimum, or Both) Strain Amplitudes. Tests were conducted on Hastelloy X (Heat 2600-3-4936) at 871°C (1600°F) in air.

range is greater than the transition fatigue life. Therefore, the above explanation as to why compressive hold times are more damaging than tensile hold times is plausible.

The technique of strain range partitioning[33,34] is being used as a guide in developing the necessary data to determine the influence of creep-fatigue and environmental interaction on the flow and failure behavior of Hastelloy X. The inelastic strain components ($\Delta\varepsilon_{pp}$, $\Delta\varepsilon_{cp}$, $\Delta\varepsilon_{pc}$, and $\Delta\varepsilon_{cc}$, refer to Sect. 2.2.3.3) from the tests conducted to date are plotted in Fig. 2.37. Only data in the range 649°C (1200°F) to 871°C (1600°F) are included in this plot. The $\Delta\varepsilon_{pp}$ plastic strain data obtained from tests conducted at temperatures of 538°C (1000°F) and lower were excluded from the plot, since values clearly fell above the high-temperature data.

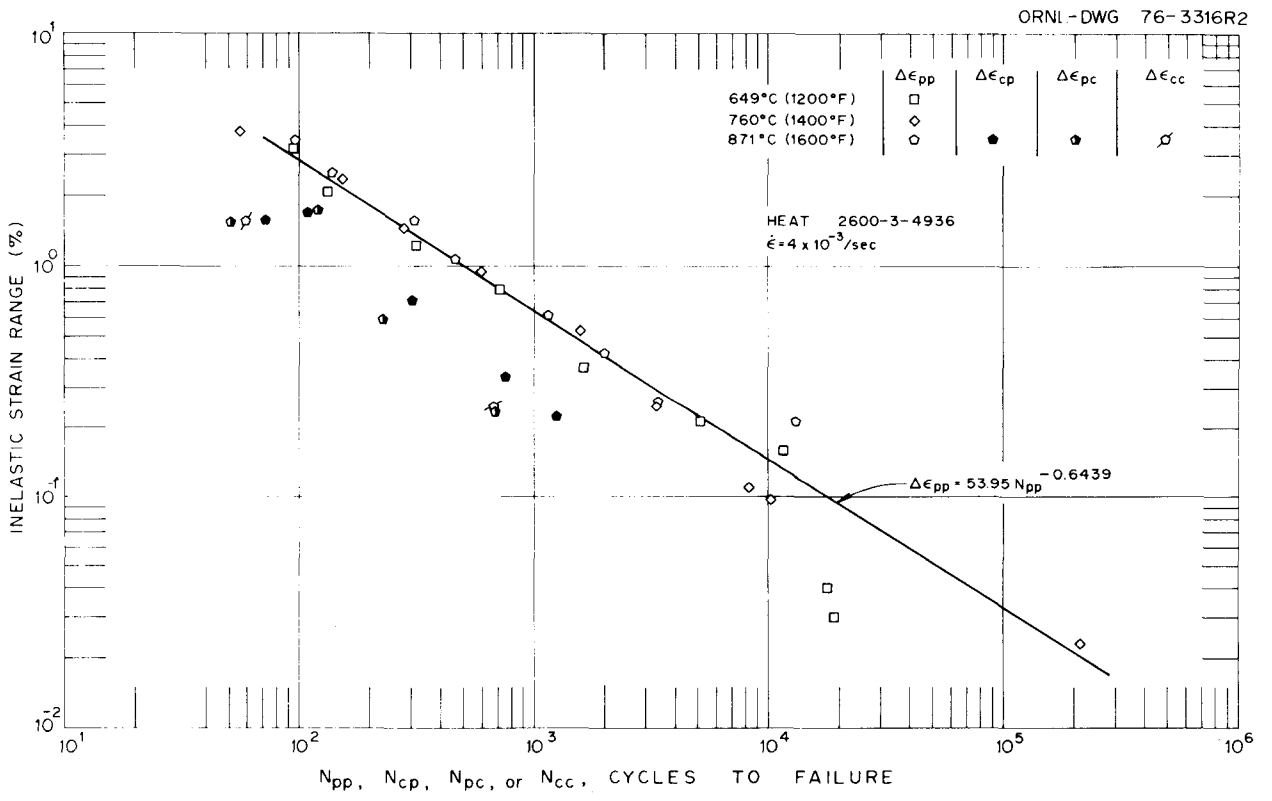

Fig. 2.37. Partitioned Inelastic Strain Components vs Associated Figure Lifetimes for Hastelloy X.

Cyclic lines associated with the various components of time-dependent inelastic strain, that is, N_{cp}, N_{pc}, and N_{cc}, were calculated with the interaction damage rule:

$$\frac{F_{pp}}{N_{pp}} + \frac{F_{pc}}{N_{pc}} + \frac{F_{cp}}{N_{cp}} + \frac{F_{cc}}{N_{cc}} = \frac{1}{N_f} ,$$

where $F_i = \Delta\varepsilon_i/\Delta\varepsilon_{in}$, and $\Delta\varepsilon_{in}$ = total inelastic strain range associated with the particular cycle being analyzed.

Tests in air are continuing, and tests in helium will begin soon.

2.2.4 Crack Growth Studies — W. R. Corwin

Subcritical fatigue crack growth has been studied on Hastelloy X and 2 1/4 Cr-1 Mo steel. One heat of Hastelloy X, Cabot 2600-3-4936, was tested in the solution annealed condition. Two heats of 2 1/4 Cr-1 Mo steel, Babcock and Wilcox heats 20017 and 3P5601, were tested in the isothermally annealed condition and one heat, 50557 from Sumitomo Metal, Japan, was tested in the annealed condition. Background and chemical composition of these materials are shown in Tables 2.7 and 2.9. Details concerning the mechanical properties of the test materials as well as the testing procedures employed in this study have been reported previously.[35–38]

2.2.4.1 Hastelloy X

A limited study to determine effects of simulated HTGR primary coolant on the fatigue crack propagation (FCP) behavior of Hastelloy X was performed by first testing in air at 25, 538, and 649°C (77, 1000, and 1200°F) and then running comparative tests in HTGR helium at the elevated temperatures. The simulated HTGR helium contains 250–300 μatm H_2, 25–30 μatm CH_4, 15–25 μatm CO, and 1–3 μatm H_2O (1 μatm = 0.10132 Pa). All tests had an R value (ratio of minimum to maximum load) of 0.05 and were run at a frequency of 1 Hz (60 cpm) at the elevated temperatures and 40 Hz (2400 cpm) at room temperature, where thermal processes are largely inactive. The results are shown in

Figs. 2.38 and 2.39. No difference in crack growth rate, da/dN, was observed in simulated HTGR helium at either of the elevated test temperatures when compared with results obtained in air on specimens of similar geometry. However, a systematic, reproducible difference was observed at all temperatures between the CT (compact tension) and WOL (wedge opening load) geometries. This has since been traced to a specimen geometry effect that affects calculations of the crack stress intensity factor. The CT specimens were used primarily for experimental convenience in the HTGR helium environmental chamber. It appears that the planar dimensions of the CT specimen, 25 by 24 mm (0.98 by 0.95 in.) are too small when compared with crack length, remaining ligament width, and plastic zone size to allow a valid calculation of the stress intensity factor, ΔK. The crack growth rate, which is experimentally measured during the test, is nonetheless valid, and comparative effects obtained with the CT geometry are

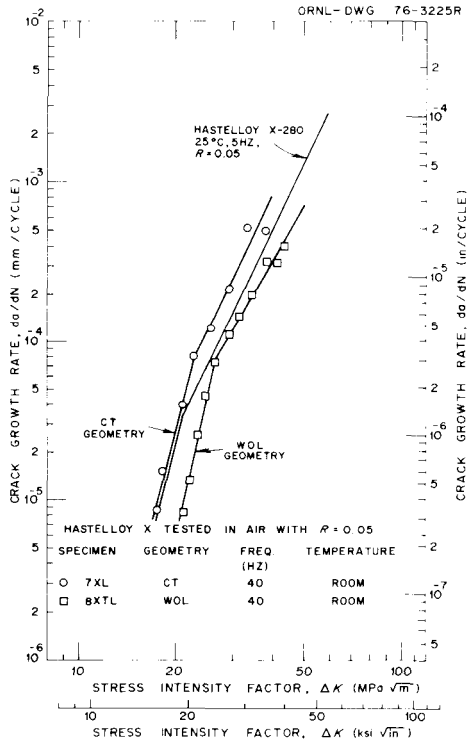

Fig. 2.38. Effect of Specimen Geometry on Fatigue Crack Growth Rate at Room Temperature.

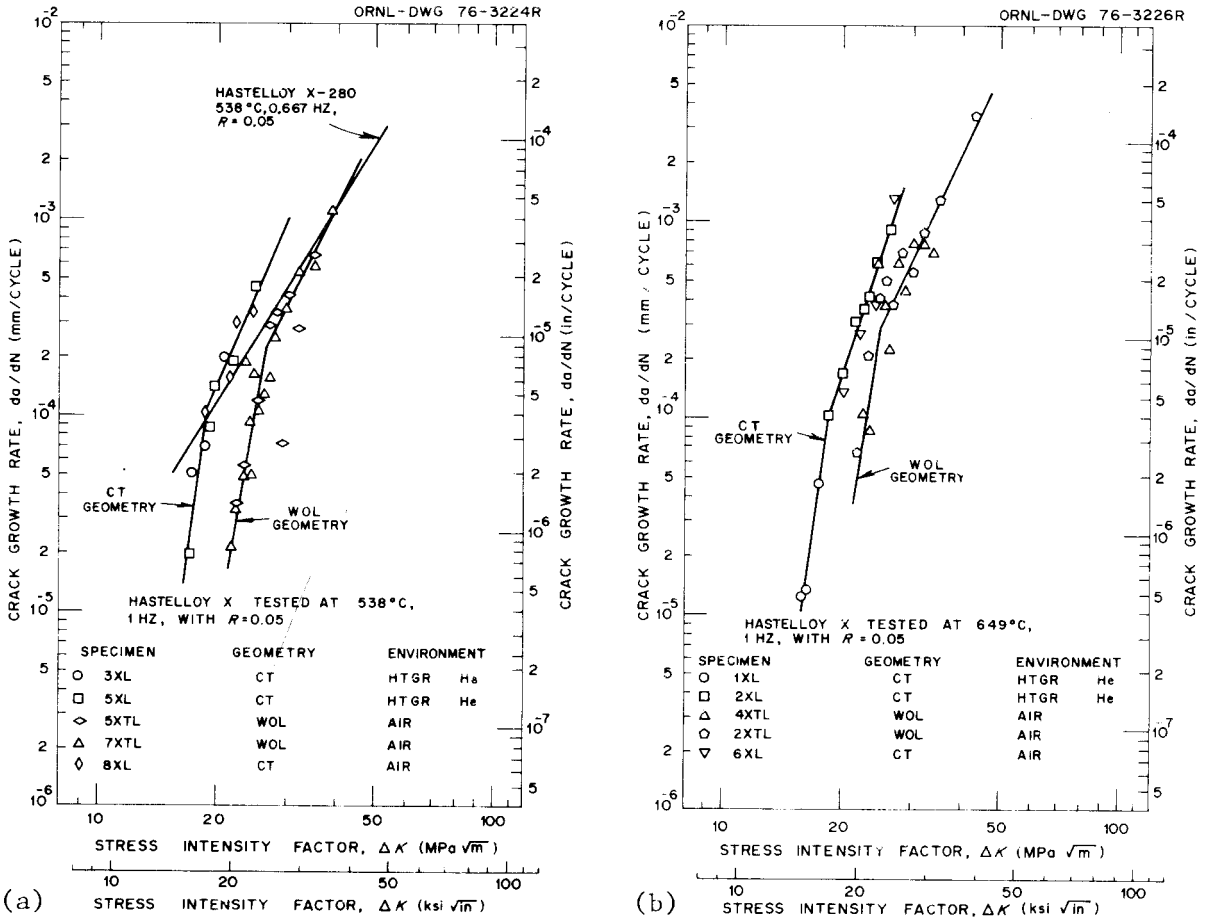

Fig. 2.39. Effect of Simulated HTGR Primary Coolant and Specimen Geometry on Fatigue Crack Growth Rate at (a) 538°C (1000°F) and (b) 649°C (1200°F).

quite real. Only the value of ΔK is inaccurate for the CT specimen. To eliminate this problem in future testing, a single-edge-notched (SEN) specimen with significantly larger planar dimensions will be used. However, to reduce ambiguity in reporting environmental effects of HTGR helium all comparisons of crack growth rates made in this report will be between specimens of similar geometry.

The effect of temperature on the crack growth rate is shown in Fig. 2.40. Crack growth rate clearly increases with increasing temperature at a constant level of ΔK.

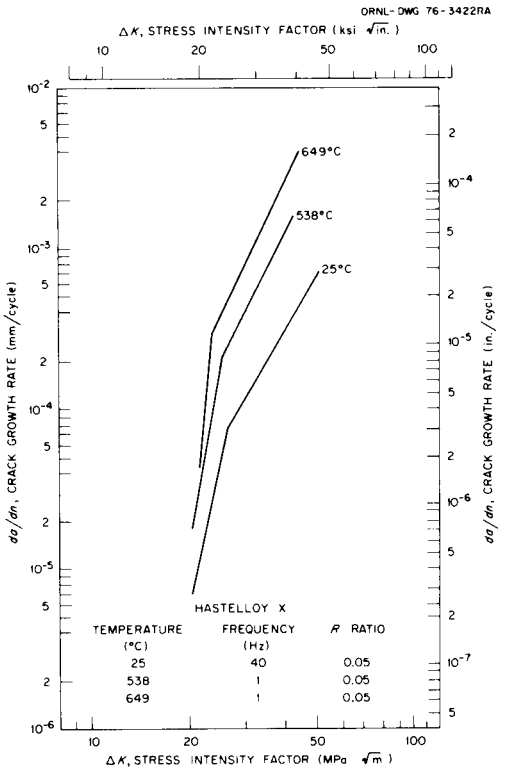

Fig. 2.40. Effect of Temperature on the Fatigue Crack Growth Behavior of Hastelloy X.

2.2.4.2 2 1/4 Cr-1 Mo Steel

In a significantly more extensive test program on 2 1/4 Cr-1 Mo steel we have investigated effects of: stress intensity, ΔK; temperature; frequency, ν; carbon content; heat-to-heat variations; and environments of air, steam, vacuum, and HTGR helium.

Increasing the temperature increased the FCP rate of 2 1/4 Cr-1 Mo steel at a given ΔK level and frequency over the range from −46 to 593°C (−50–1100°F), as shown in Fig. 2.41. The only exception to this behavior was at 371°C (700°F), which is in the temperature range in which dynamic strain aging occurs in this material. Increased fatigue resistance in uniaxial strain-controlled tests[37] and increased tensile strength [36] have also been observed around this temperature in related studies.

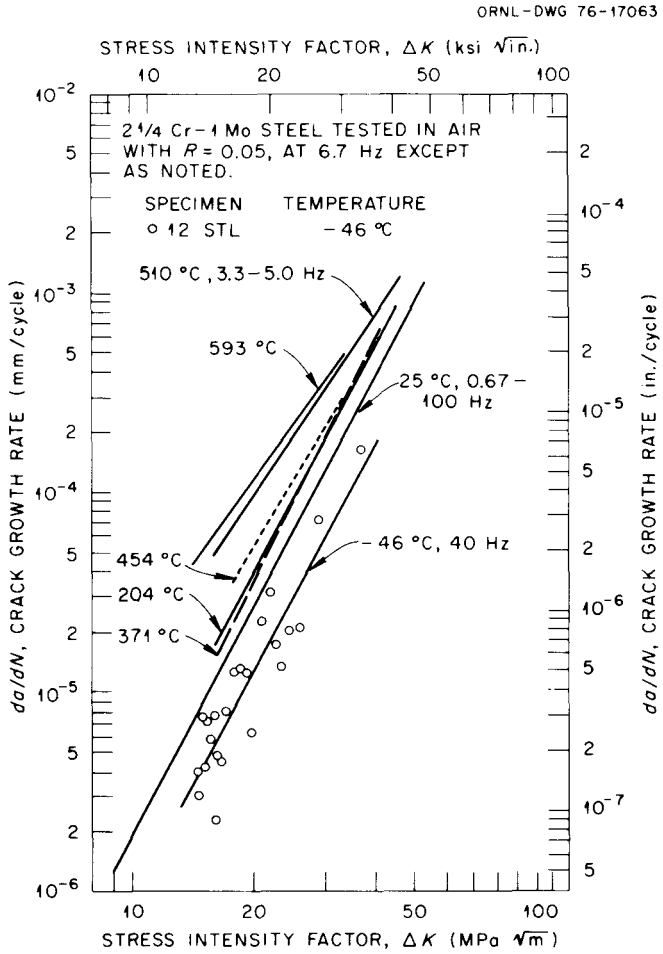

Fig. 2.41. Effect of Temperature on Crack Growth Rate.

Effects of frequency have been examined at four temperatures: 25, 371, 510, and 593°C (78, 700, 950, and 1100°F). As reported,[35] no effect was noted on da/dN over the range 0.67 to 6000 Hz at room temperature. Similarly no significant effect was noticed at 371°C (700°F) in samples from heat 3P5601 at 6.7 and 0.067 Hz as shown in Figure 2.42. However, at this temperature the apparent lack of effect may be the result of competing and offsetting factors. Lower frequencies require longer testing times, and environmental corrosion would tend to increase da/dN. However, a decrease in da/dN would be expected with an increase in strength due to greater dynamic strain hardening at the lower test frequencies. At the higher temperatures the effect is far better defined. As shown in Fig. 2.43 at 510 and 593°C (950 and

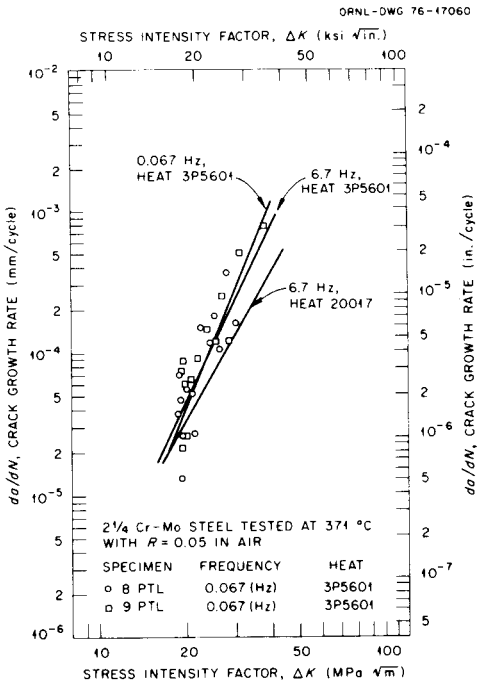

Fig. 2.42. Frequency and Heat-to-Heat Effects on Crack Growth Rate.

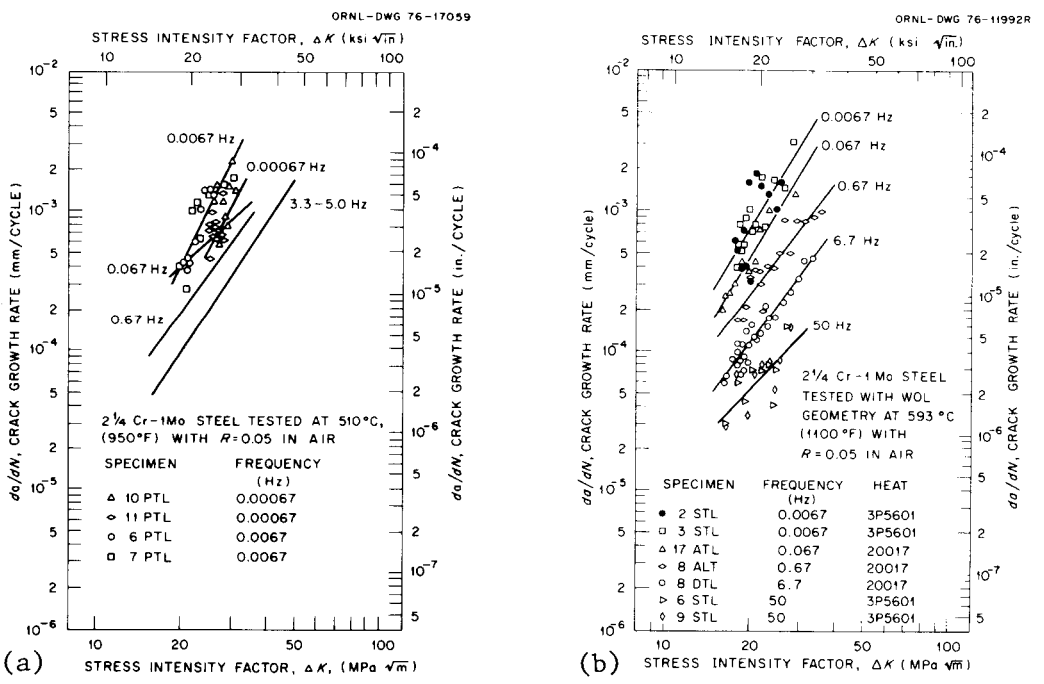

Fig. 2.43. Effect of Test Frequency on Fatigue Crack Growth Rate. (a) 510°C. (b) 593°C.

1100°F) the crack growth rate increases with decreasing test frequency down to 0.0067 Hz. Two tests were conducted at the lower frequency of 0.00067 Hz at 510°C (950°F). However, the results at this frequency showed a lower crack growth rate than at 0.0067 Hz, which indicated that significant crack blunting and crack tip stress relaxation occurred during testing. This means that calculation of the stress intensity factor was inaccurate under these conditions, and further testing at such frequencies was suspended.

Heat-to-heat effects were compared at three temperatures: 25, 371, and 510°C (77, 700, and 950°F) between heats 3P5601 and 20017. Tests at room temperature in air indicate a small difference in crack growth rate with values for 3P5601 approximately 20% higher than for 20017, as shown in Figure 2.44. While this difference appears genuine it is

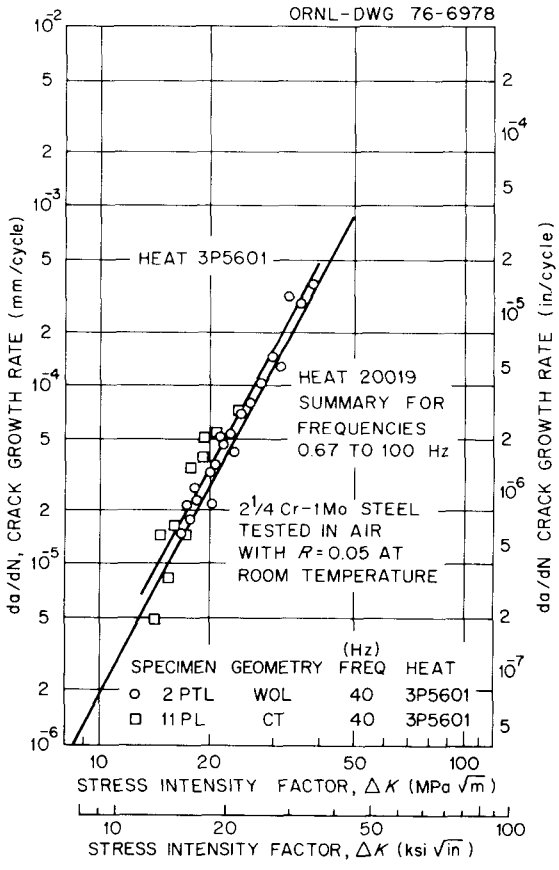

Fig. 2.44. Heat-to-Heat Variation in Fatigue Crack Growth Rate of 2 1/4 Cr-1 Mo Steel.

well within the standard experimental error factor of 2 which exists in this type of testing even in ASTM round robin conditions.[14] Only at 371°C (700°F) were appreciable heat-to-heat effects noticed. As shown in Fig. 2.45 heat 20017 was noticeably more resistant to cracking, particularly at the higher ΔK levels. This is attributed to a greater amount of dynamic strain aging in heat 20017 because of its higher carbon content (0.135% vs 0.119% for heat 3P5601). In the same figure are the results obtained at 510°C (950°F), which show virtually identical trend lines for both heats, but with more scatter seen for heat 3P5601. To determine the effect of decarburization comparative testing on a special low-carbon heat of 2 1/4 Cr-1 Mo steel (Heat 50057, 0.026% C) was performed. The results obtained at 510°C (950°F) and ν = 0.67 Hz in air are compared in Fig. 2.46 with those obtained under identical testing conditions on heats 3P5601 and 20017 with carbon

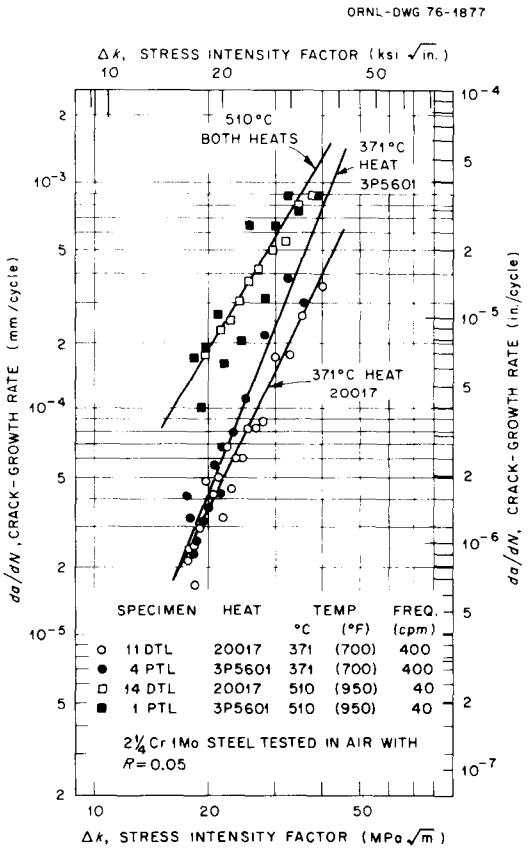

Fig. 2.45. Heat-to-Heat Effects on Fatigue Crack Growth.

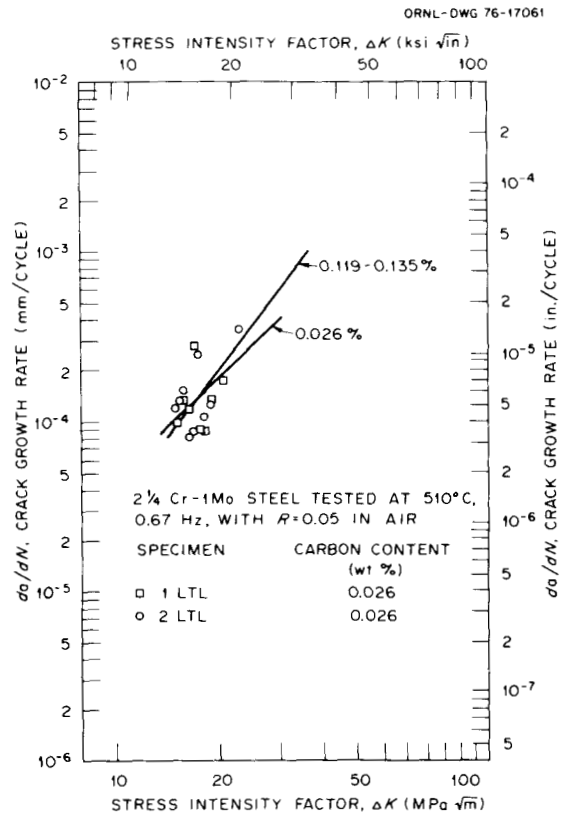

Fig. 2.46. Effect of Carbon Content on Fatigue Crack Growth Rate.

contents of 0.119 and 0.135%, respectively. Very little difference was observed on the FCP rate as a function of carbon content. A small effect was evident at the higher levels of ΔK. The tests on heat 50057 had to be terminated at shorter crack lengths and lower stress intensity factors than tests on the other heats because of excessive plasticity. This presumably was due to the lower tensile strength of the low-carbon material. The difference in slope of the da/dN vs ΔK plot is not particularly significant inasmuch as the range of ΔK is so small that the scatter in the data could very easily have affected the slope of a least squares fit.

The effect of aging on the FCP behavior of 2 1/4 Cr-1 Mo steel was also examined. Specimen blocks from heat 20017 were aged for 10,000 hr at both 482 and 538°C (900 and 1000°F) in argon. Specimens were then fabricated and tested at 510°C (950°F), ν = 0.67 Hz in air, and the results were compared with identical tests on isothermally

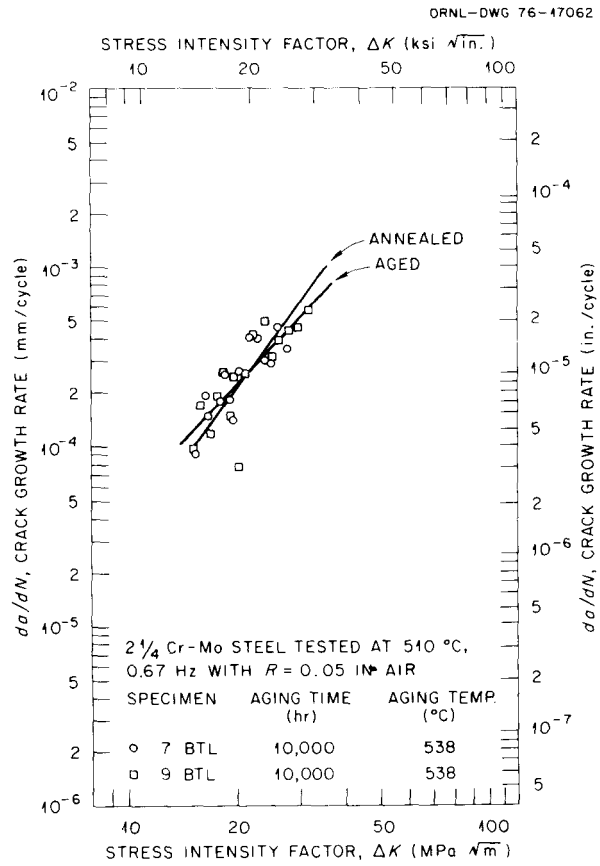

Fig. 2.47. Effect of Aging on Fatigue Crack Growth Rate.

annealed, nonaged material. As seen in Fig. 2.47 there was no appreciable effect of aging for 10,000 hr at 538°C (1000°F) on the subsequent crack growth behavior at 510°C under the conditions examined. The specimens aged at 482°C will be tested soon.

Examination of the comparative behavior of 2 1/4 Cr-1 Mo steel in air and simulated HTGR helium environment showed marked differences from that observed for Hastelloy X. Figures 2.48 and 2.49 show that the crack growth rate is reduced by factors of 2 to 6 at 510°C (950°F) and 8 at 593°C (1100°F) from that obtained in air. This result agrees with the findings of other investigators,[39] who have found that the fatigue resistance of 2 1/4 Cr-1 Mo steel at 593°C is significantly greater in helium, liquid sodium, and vacuum than in air. This effect has been attributed to the exclusion of oxygen from the crack tip and is believed to be the dominant factor in this study.

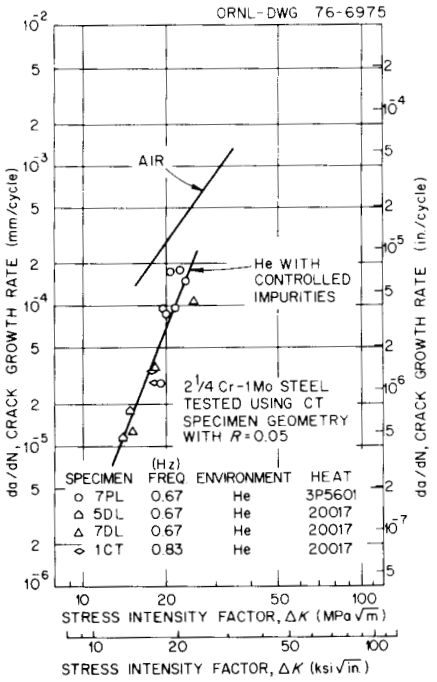

Fig. 2.48. Comparison of Crack Growth Rates in Air and Helium with Controlled Impurity Levels at 510°C.

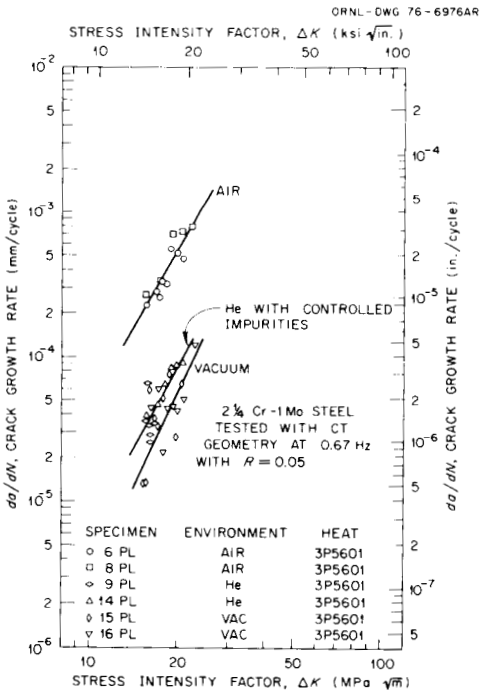

Fig. 2.49. Comparison of Crack Growth Rates in Air, Helium with Controlled Impurity Levels, and Vacuum at 593°C (1100°F).

That HTGR helium is not a completely inert environment for crack growth is also shown in Fig. 2.49 where results obtained in vacuum at 593°C (1100°F) are compared with those in air and HTGR helium. The crack growth rate is evidently still reduced slightly further in vacuum of 0.1 mPa (10^{-6} torr) from that in HTGR helium under otherwise identical conditions, showing that some small amount of environmental interaction is occurring in the HTGR helium.

Crack growth was also studied in steam, and compared with results in air at 510 and 593°C in Figs. 2.50 through 2.52. We did not expect crack growth rates in steam to be less than those observed in air since the detrimental effect of moisture on FCP has been repeatedly demonstrated. However, in all conditions examined here, the crack growth rate in steam was slightly less than in air.

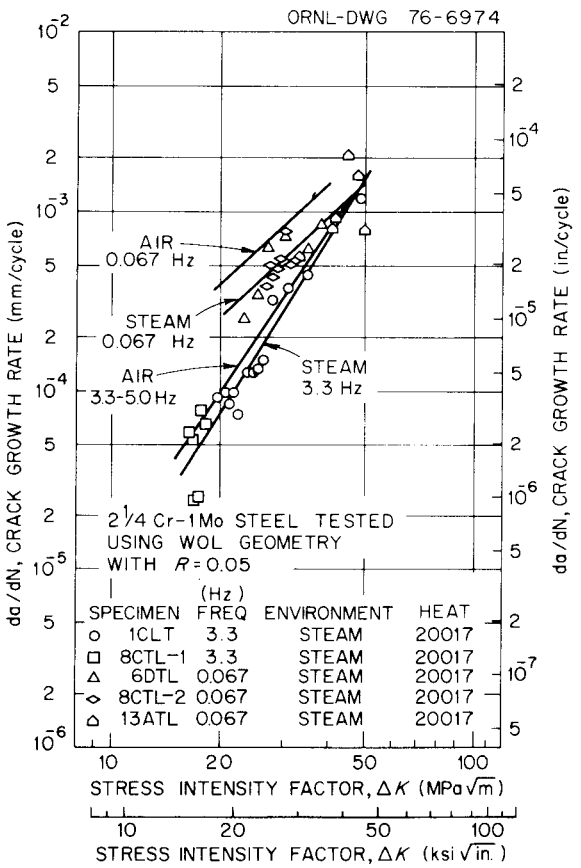

Fig. 2.50. Comparison of Crack Growth Rates in Air and Steam at 510°C.

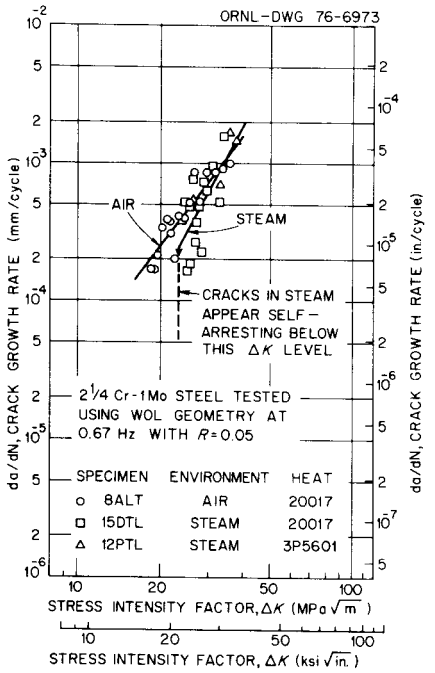

Fig. 2.51. Comparison of Crack Growth Rates in Air and Steam at 593°C and 0.67 Hz.

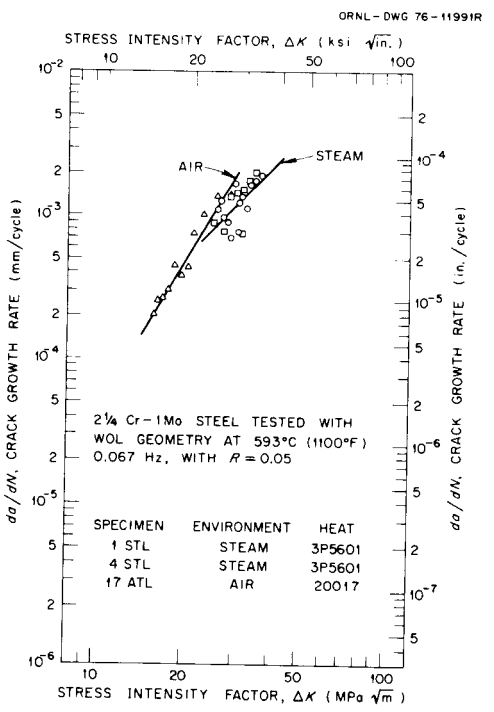

Fig. 2.52. Comparison of Crack Growth Rates in Air and Steam (Supersaturated in Air) at 0.067 Hz.

Steam is clearly not an inert environment for the fatigue crack propagation of 2 1/4 Cr-1 Mo steel, as is shown by comparison of crack growth rates in steam and helium. Further, the strong frequency effect in steam is not indicative of an inert environment. Yet it is apparent that steam is less aggressive than air. Recent corrosion studies[40] on 2 1/4 Cr-1 Mo steel in air and steam appear to offer an explanation. In the temperature regime examined here, similar corrosion products were produced in both steam and air environments, indicating similar corrosion processes, but there was less attack in steam, apparently because of a lower effective oxygen potential. This lower oxygen potential in steam is believed responsible for the lower observed crack growth rates in this study.

2.3 WELDING DEVELOPMENT — J. F. King

Hastelloy X has been chosen for fabrication of several components in various gas-cooled reactor system designs. During the reporting period this program has concentrated on investigating the weldability and metallurgical stability of welds joining Hastelloy X to itself and to other materials. These studies have included determining (1) the effect of heat-to-heat variation of the Hastelloy X base material on hot cracking behavior, (2) the selection of filler metals for dissimilar-metal welds, and (3) the thermal aging response of similar- and dissimilar-metal welds involving Hastelloy X.

2.3.1. Hot Cracking Tests

We examined the heat-to-heat variation of the susceptibility of Hastelloy X base metal to hot cracking. Two heats of Hastelloy X in the form of 12.7-mm (1/2-in.) plate were used in this study. The chemical analysis of each heat is given in Table 2.14. Both heats of Hastelloy X were tested in the mill solution annealed condition.

The test used to compare the hot cracking susceptibility of these two heats of Hastelloy X was the "modified-Varestraint test" or also known as "Tigamajig." Goodwin[41] has described the features of this test and used it in studying hot cracking in Inconel 600. This test evaluates the hot cracking tendency of a specimen prepared from either

Table 2.14. Chemical Analysis of Hastelloy X

Heat	Content, wt %[a]								
	Cr	W	Fe	C	Si	Co	Mn	Mo	P
2600-4-4284	21.79	0.63	19.06	0.06	0.35	2.40	0.59	8.82	0.018
2600-3-4936	21.82	0.63	19.09	0.07	0.44	1.68	0.58	9.42	0.016

[a]Balance nickel. <0.005% S and <0.002% B.

previously deposited weld metal or base metal. The specimen is subjected to an arc spot-welding thermal cycle, and the hot zone is strained a predetermined amount while the spot fusion zone is still molten. The augmented strain of successive specimens is varied in incremental amounts. Cracking data is obtained by measuring cracks on the specimen surface. In this study, as in most investigations, the only cracks considered were those that touched the fusion boundary outside the arc-spot weld nugget. Figure 2.53 illustrates the equipment and method used in this type of hot cracking test. The usual

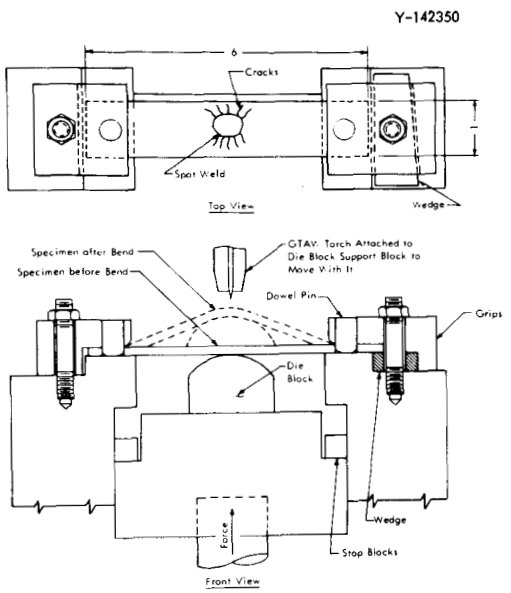

Fig. 2.53. "Tigamajig" Test Device Showing the Way in Which a Specimen is Tested.

method of expressing Varestraint test results is to plot one of the crack measurement criteria, normally the total crack length, against augmented strain. Figure 2.54 is a plot of the cracking data obtained from two heats of Hastelloy X. As shown, the two heats did exhibit different susceptibility to hot cracking. Heat 2600-4-4284 would be expected to exhibit more problems with heat-affected zone hot cracking during welding than the other heat tested.

The theory of hot cracking in metals has received extensive study. Specific work in this area has been performed on Hastelloy X by use of other hot cracking tests. W. F. Savage and B. M. Krantz[42,43] have reported the results of their work on Hastelloy X in detail, including the study of the macro- and microsegregation in the original base metals, which have a deterimental influence on the hot cracking tendency of the alloy. Further investigation into the elements and microconstituents that produce hot cracking in Hastelloy X was beyond the scope of this study. The present work was performed to establish the suitability of using the modified-Varestraint test as a tool to rate the relative weldability of various heats of Hastelloy X and establish a base with which future heats can be prepared. Work in this area will continue.

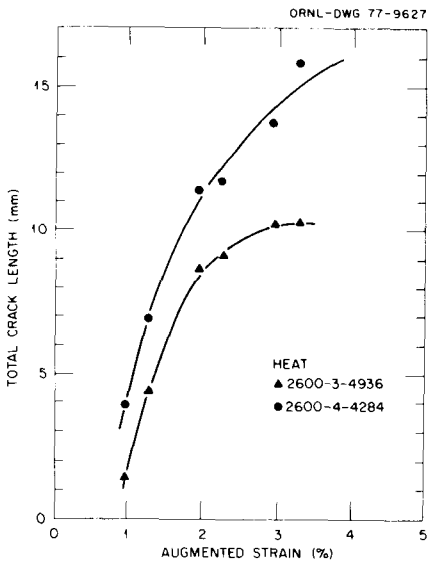

Fig. 2.54. Total Crack Length vs Augmented Strain for Commercial Heats of Hastelloy X.

2.3.2 Hastelloy X and Dissimilar-Metal Weldment Studies

The objective of this study was to evaluate the weldability, select filler metals, and determine tensile properties and metallurgical stability of aged similar- and dissimilar-metal joints involving Hastelloy X. All weldments in this study were made in 12.7-mm (0.5-in.) plate using the automatic gas tungsten-arc welding process with cold-wire filler addition. Material combinations included: Hastelloy X to itself, Hastelloy X to alloy 800H, and Hastelloy X to A 537 Class 1 steel. Base metal combinations and filler metals used are listed in Table 2.15. All completed weldments were inspected radiographically before thermal aging and testing. No defects were revealed in any of the weldments. The weldments of Hastelloy X to itself and to alloy 800H were thermally aged for all filler metal combinations. The aging matrix is presented in Table 2.16. The aged weldments were evaluated by tensile testing, metallography, and microhardness measurements.

Table 2.15. HTGR Transition Joint Welds Involving Hastelloy X

Weld Type	Second Base Metal[a]	Filler Metal
I	Hastelloy X	Hastelloy X
II	Incoloy 800H	Hastelloy X
III	Incoloy 800H	Hastelloy S
IV	Incoloy 800H	Hastelloy W
V	Incoloy 800H	Inconel 82
VI	A 537 Class 1	Hastelloy X
VII	A 537 Class 1	Hastelloy S
VIII	A 537 Class 1	Hastelloy W
IX	A 537 Class 1	Inconel 82

[a]Welded to Hastelloy X.

Table 2.16. Thermal Aging Matrix for Similar- and Dissimilar-Metal Weldments of Hastelloy X

Time (hr)	Weld Types[a] Tested at Each Temperature, °C (°F)				
	427 (800)	538 (1000)	649 (1200)	760 (1400)	871 (1600)
100	II III IV V	II III IV V	I II III IV V	I	I
500	II III IV V	II III IV V	I II III IV V	I	I
1000	II III IV V	II III IV V	I II III IV V	I	I
2000	II III IV V	II III IV V	I II III IV V	I	I

[a]Roman numerals refer to weld type listed in Table 2.15.

Room-temperature tensile tests were performed on specimens taken transverse to the weld in Hastelloy X weldments. These tensile specimens contained weld metal, heat-affected zone, and base metal in the gage length. The results of these tests are presented in Table 2.17. All ruptures occurred in the weld metal except in specimens aged at 649°C (1200°F). Elongation and reduction of area decreased with aging time for all three aging temperatures. These decreases occurred rapidly at 700 and 871°C (1400 and 1600°F). Aging at 649°C (1200°F) produced a slower decrease in ductility, but it ultimately reached the same level as that of the material aged at 760 and 871°C. This is shown

Table 2.17. Room-Temperature Tensile Data for Weldments of Hastelloy X to Hastelloy X with Hastelloy X Filler Metal[a]

Specimen Type	Aging Condition			Ultimate Strength		0.2% Offset Yield Strength		Elongation (%)	Reduction of Area (%)
	Temperature As Welded		Time						
	(°C)	(°F)	(hr)	(MPa)	(ksi)	(MPa)	(ksi)		
T1-0-0				766	111.1	446	64.7	47.6	38.25
T1-1-12	649	1200	100	778	112.8	448	65.0	43.2	39.1
T1-5-12	649	1200	500	905	131.2	531	77.1	25	36
T1-10-12	649	1200	1000	958	138.9	582	84.5	19.4	29.2
T1-20-12	649	1200	2000	1152	167.0	744	108.0	14.9	11
T1-1-14	760	1400	100	927	134.4	563	81.6	16.7	15.5
T1-5-14	760	1400	500	943	136.8	555	80.5	17	11
T1-10-14	760	1400	1000	955	138.5	555	80.5	18	13
T1-20-14	760	1400	2000	965	140.0	578	83.9	13	9.5
T1-1-16	871	1600	100	812	117.8	457	66.3	17.6	12.7
T1-5-16	871	1600	500	760	110.3	432	62.7	15	11
T1-10-16	871	1600	1000	782	113.5	410	59.4	19	13
T1-20-16	871	1600	2000	712	103.2	426	61.8	10	8.7

[a]Each value average for three tests. Failures all occurred in weld metal except in material aged at 649°C (1200°F). All welds made with GTAW process.

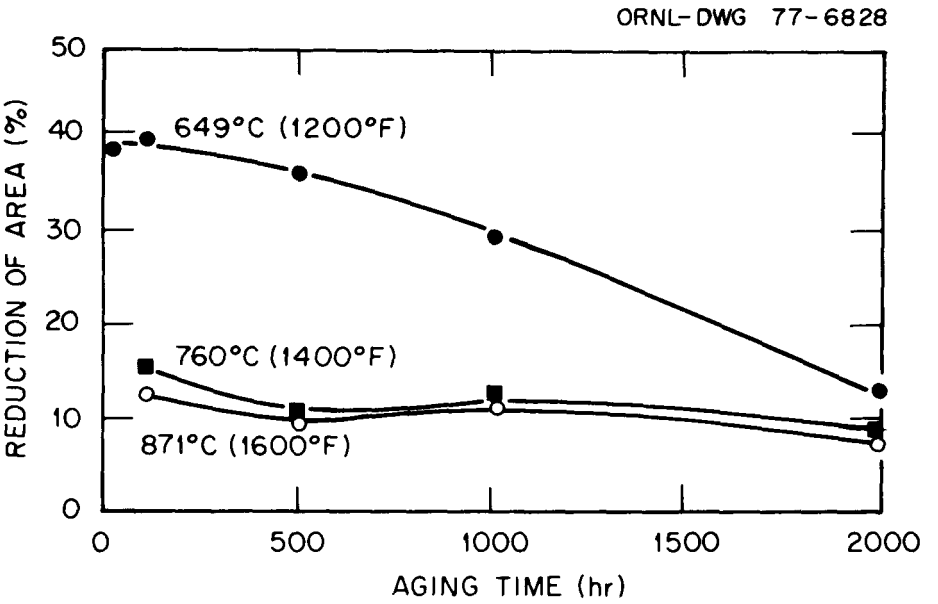

Fig. 2.55. Effects on Hastelloy X Weldment Ductility.

graphically in Fig. 2.55. The change in properties of Hastelloy X weldments is also demonstrated by microhardness measurements, as shown in Fig. 2.56. These microhardness traverse data show that the weld metal response to thermal aging is very similar to that of the base material.

Room-temperature tensile testing was conducted on transverse specimens from weldments between A 537 Class 1 steel and Hastelloy X joined with Hastelloy X, Hastelloy S, Hastelloy W, and Inconel 82 filler metals. Defect-free welds were produced with all four filler metals. As discussed previously under Hastelloy X weldment testing, the tensile specimens contained base metal, heat affected zone, and weld metal in the gage length. All specimens failed in the steel outside the heat-affected zone. Therefore, the tensile tests indicated only that A 537 Class 1 steel is the weak link in the joint, and all four weld filler metals have adequate tensile strength. Other testing methods will be needed to determine the optimum filler metal for this material combination.

Dissimilar-metal weldments of Hastelloy X to alloy 800H were aged, and tensile tests were conducted on the aged joints. No degradation of joint integrity was seen from the tensile data, and metallographic examination showed that all the tensile specimens failed in the alloy 800H portion of the transverse tensile specimen. We concluded that

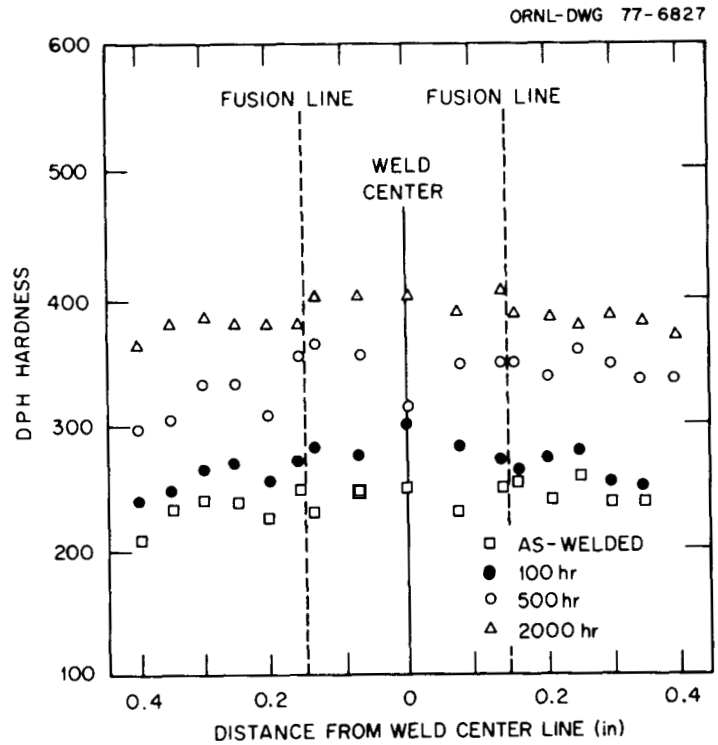

Fig. 2.56. Room-Temperature Hardness Profiles of Aged and Unaged Hastelloy X Weldments. 1 in. = 25.4 mm.

other testing techniques, such as creep testing, will be needed to screen the various weld filler metals.

2.4 STEAM CORROSION — J. C. Griess, J. H. DeVan, W. A. Maxwell,* and J. R. DiStefano

The purpose of this program is to determine the corrosion behavior of selected materials that are planned or being considered for use in nuclear steam supply systems in both pure steam and in steam under faulted conditions. The actual testing of materials is performed by the Southern Nuclear Department of the NUS Corporation under subcontract to Oak Ridge National Laboratory. The test facilities are located at the Bartow Plant of the Florida Power Corporation in St. Petersburg, Florida, and the steam supply comes directly from the fossil-fuel electrical generating plant. Since the results from this program are

---

*NUS Corp., Clearwater, Fla.

useful to high-temperature reactors in general, funding is provided by both the HTGR and LMFBR projects.

2.4.1. Injection Loops

As indicated in the last report[44] two loops were operated in which chloride solutions were injected into the incoming steam to determine the effect of chloride on the corrosion of different materials. In one loop the test environment was superheated steam at 482°C (900°F) and 11.2 MPa (1625 psi) containing 2 ppm dissolved chloride as sodium chloride. For the first 4626 hr the steam contained no oxygen (<0.007 ppm) but for the final 5958 hr oxygen was maintained at 8 ppm. In the other loop the pressure and oxygen concentration were constant at 11.2 MPa (1625 psi) and 8 ppm, respectively, but the temperature was alternated every 24 hr between superheated steam at 385°C (725°F) and saturated steam at 318°C (605°F). During the superheated part of the cycle a dilute calcium chloride solution was injected into the incoming steam to give a chloride concentration of 2.7 ppm; during the saturated part of the cycle the injection rate was increased to yield a concentration of 10 ppm. In both loops constant-stress corrosion specimens were exposed, and in the constant-temperature loop some weight-change specimens were also included.

Both tests are completed and the detailed results have been reported.[45] The results are only briefly summarized here.

Constant-stress specimens of 2 1/4 Cr-1 Mo and 9 Cr-1 Mo steels, Incoloy alloy 800, types 304 and 304L stainless steel, Inconel 600, and Inconel 625 exposed in either of the chloride-containing environments showed no tendency toward stress-corrosion cracking. The only failures of the stressed specimens occurred in 2 1/4 Cr-1 Mo steel specimens exposed to alternate wet-dry environments, in which excessive general corrosion led to failure by wall thinning, and in the superheated environment, where abnormally high temperatures during two loop excursions resulted in stress rupture of some of the more highly stressed specimens.

In superheated steam containing 2.7 ppm chloride many small pits developed on 2 1/4 Cr-1 Mo steel specimens, but these did not appear to grow

beyond 25 to 38 μm (1.0 to 1.5 mils) deep. With oxygen in the steam, pits did not develop. In neither case were pits found on 2 1/4 Cr-1 Mo steel that had been stabilized with 1% Nb.

2.4.2 Inconel 617 Test Loop

Fabrication of the Inconel 617 test loop was completed and the first test was begun. The loop has the same basic features as the injection loops, including two autoclaves for specimen exposure. In the present test only pure superheated steam (no impurities added) from the Bartow power plant passes through the loop at a rate of 45 kg/hr (100 lb/hr). Duplicate sets of specimens — coupons and U-bends, both welded and unwelded — are in the two autoclaves. The temperature of the steam in the top autoclave is 482°C (900°F) and in the lower, 538°C (1000°F). The steam pressure is 10.5 MPa (1525 psi), and the steam velocity past the specimens is 1.5 m/s (5 fps).

The present test has been in progress for slightly more than 5000 hr, and the test specimens have been examined four times. The weight gains observed on coupons of the wrought material, their initial surface condition, and the average penetrations calculated from weight gains are shown in Table 2.18 for the 482 and 538°C exposures. In all cases the corrosion products appear to be totally adherent, and as expected, a log-log plot of the data in the table yields straight lines with slopes of 0.4 to 0.5 with the following exceptions: HF9 at 538°C and type 304 stainless steel at both temperatures. Also the weight gains on the Inconel 617 and the alloy 800 specimens with ground surfaces are so low that the kinetics of the oxidation process cannot be established at this time.

Welded specimens exposed in the loop include autogenous welds of 2 1/4 Cr-1 Mo steel and alloy 800, specimens cut from thick plates of alloy 800 welded to alloy 800 and to 2 1/4 Cr-1 Mo steel with Inconel 82 filler metal, and specimens of Inconel 617 welded to itself with Inconel 617 filler metal. In addition to flat weight-change coupons of the above, U-bends with the welds on the outer radius are also being exposed in the loop. Weight changes on the welded specimens

Table 2.18. Corrosion of Materials in Superheated Steam at 10.5 MPa

Alloy	Surface Condition[a]	Average Weight Gain, mg/cm^2				Av Metal Penetration[b] (μm)
		504 hr	1621 hr	3051 hr	5073 hr	
		Exposed at 482°C				
2 1/4 Cr-1 Mo Steel	ground	1.92	3.24	4.21	5.13	17.0
	annealed	1.58	2.74	3.68	4.62	15.2
	pickled	1.97	3.27	4.36	5.39	17.8
Alloy 800	ground	0.03	0.03	0.03	0.04	0.25
	pickled	0.83	1.33	1.86	2.35	8.4
Inconel 617	ground	0.01	0.02	0.02	0.02	<0.25
304 Stainless Steel	ground	0.01	0.04	0.10	0.28	1.0
9 Cr-1 Mo Steel	ground	1.38	2.29	3.12	3.92	12.7
Sandvik HT-9	ground	1.39	2.21	2.85	3.55	11.9
		Exposed at 538°C				
2 1/4 Cr-1 Mo Steel	ground	2.98	4.69	6.32	7.90	26.2
	annealed	2.92	4.82	6.13	7.99	26.4
	pickled	3.12	5.15	6.65	8.64	28.7
Alloy 800	ground	0.05	0.06	0.06	0.07	0.25
	pickled	1.59	2.78	3.68	4.79	16.8
Inconel 617	ground	0.04	0.04	0.04	0.05	0.25
304 Stainless Steel	ground	0.06	1.29	2.23	3.10	10.2
9 Cr-1 Mo Steel	ground	2.47	4.23	5.61	7.20	23.6
Sandvik HT-9	ground	2.19	3.51	4.22	4.85	15.8

[a]Ground on 100-mesh belt grinder, annealed in argon after grinding — light film on surface, or pickled after annealing.

[b]Calculated from weight gain after 5073 hr.

have been very similar to the weight gains shown in Table 2.18 for base material. Examination of the U-bend specimens has shown no evidence of cracking in any material.

The present test is continuing, with the next examination of the specimens scheduled after a total exposure of 8000 hr. Plans call for continuing the test for a total of 30,000 hr with specimen examination at intermediate times.

2.4.3 The Heat-Transfer Corrosion Test Loop

In the last report[44] the corrosion results obtained from tests in which 2 1/4 Cr-1 Mo steel was subjected to a heat flux of 126 kW/m^2 and cooled by superheated steam were presented. Since that time a detailed description of the procedures and results has been issued in a formal report.[46] In this series of tests the specimens were made from standard air-melted 2 1/4 Cr-1 Mo steel and specimen-steam interfacial temperatures along the 0.61-m (24-in.) heated length were 510 to 541°C (950 to 1005°F). Cracking and porosity in the oxide were noted after exposures as short as 500 hr, and exfoliation of the oxide began after about 2000 hr. Once exfoliation began the average corrosion rate was constant at 45 μm/year (1.8 mils/year).

A second series of tests at the same heat flux is in progress, but in this case the material is vacuum-arc-remelted 2 1/4 Cr-1 Mo steel, and the sufrace temperatures of the specimens are lower — 502 to 522°C (935—972°F). Tests of 1000- and 3000-hr duration have been completed and 6000- and 10,000-hr tests are in progress. The results presently in hand indicate lower corrosion than in the first series of tests, probably because of the lower temperature rather than because of basic corrosion differences in the two grades of steel. Cracks and porosity in the oxides were noted on the 1000-hr specimen, and oxide exfoliation had occurred on the 3000-hr specimen. It appears that with increased exposure time the extent of exfoliation will increase and a constant corrosion rate will result, as was the case with the air-melted material.

2.5 REFERENCES

1. P. L. Rittenhouse, "Tensile Testing," *HTGR Base-Technology Program Prog. Rep. Jan. 1, 1974–June 30, 1975,* ORNL-5108, pp. 67–73.
2. R. J. Wolwowicz, *Creep-Rupture Properties of Incoloy 800H, 2 2/4 Cr-1 Mo Steel, and Hastelloy X Alloys in Simulated HTGR Environment. Interim Report,* GA-A-13876 (June 1976).
3. H.G.A. Bates et al., *The Influence of Impure Helium on Properties of Some Austenitic Steels,* Dragon Project Report 934 (May 1975).
4. R. J. Pearce, R.A.U. Huddle, and P. Kofstad, *Fundamental Aspects of the Interaction of the HTR Helium with Metals and Alloys,* Central Electricity Generating Board Report RD/B/R2866 — RPC/CM-P(74)4-DPTN/522 (Modified, January 1974).
5. S. Quaranta and H. Walther, *Initial Tests on the Environmental Creep Rigs at FIAT,* Dragon Project Report 931 (May 1975).
6. W. J. Scheffel, N. L. Baldwin, R. W. Tomlin, *Operating History Report for the Peach Bottom HTGR,* GA-A-13907, Vol. 1 (Aug. 31, 1976).
7. General Atomic, *Public Service Company of Colorado 330-MW(e), High-Temperature Gas-Cooled Reactor Research and Development Program,* GA-A-13997 (Oct. 31, 1976).
8. M. R. Everett, *Helium Impurity Levels for Compatibility Testing of HTGR Primary Circuit Materials,* Dragon Project Report 932 (May 1975).
9. R. J. Pearce and R. K. Wild, *Oxygen Partial Pressures in Helium Cooled and in Experimental Helium Loops,* Central Electricity Generating Board Report, RD/B/R2059 — RPC/CM/P(71)67 (August 1971).
10. R. C. Cavenan, Beckman Instruments, Inc., Fullerton, California, W. A. Hilchey, La Fleur Corporation, Fardena, California, "A Sensitive System for Analyzing Permanent Gases," unpublished manuscript.
11. M. K. Booker, T. L. Hebble, D. O. Hobson, and C. R. Brinkman, *Mechanical Properties Correlations for 2 1/4 Cr-1 Mo Steel in Support of Nuclear Reactor Systems Design,* ORNL/TM-5329 (June 1976).
12. J. W. Tackett, *The Creep Rupture Properties of Hastelloy Alloy S Sheet,* Tech. Dept. Report 8745, Stellite Division, Cabot Corporation, Kokomo, Indiana, 1975.

13. J. R. Ellis et al., "Elevated-Temperature Fatigue and Creep-Fatigue Properties of Annealed 2 1/4 Cr-1 Mo Steel," pp. 213–46 in *Symposium on Structural Materials for Service at Elevated Temperature in Nuclear Power Generation,* MPC-1, American Society of Mechanical Engineers, New York, 1975.

14. J. R. Ellis and E. P. Esztergar, "Creep-Fatigue Interaction in Design Analysis," pp. 29–33 in *Symposium on Design for Elevated Temperature Environment,* American Society of Mechanical Engineers, New York, May 1971.

15. D. C. Lord and L. F. Coffin, Jr., "Low-Cycle Fatigue Hold Time Behavior of Cast René 80," *Metall. Trans.* 4: 1647 (1973).

16. S. S. Manson, G. R. Halford, and M. H. Hirschberg, *Creep-Fatigue Analysis by Strain-Range Partitioning,* NASA-TM-X-67838 (1971).

17. R. D. Campbell, "Creep Fatigue Interaction Correlation for 304 Stainless Steel Subjected to Strain-Controlled Cycling with Hold Times at Peak Strain," *J. Eng. Ind.* 93: 887–92 (1971).

18. L. F. Coffin, Jr., "Predictive Parameters and Their Applications to High Temperature, Low Cycle Fatigue," pp. 643–54 in *Proc. Int. Conf. Fract. 2nd, 1969,* Chapman and Hall, London.

19. J. F. Polhemus, C. E. Spaeth, and W. H. Vogel, "Ductility Exhaustion Model for Prediction of Thermal Fatigue and Creep Interaction," pp. 625–35 in *Fatigue at Elevated Temperatures, ASTM Spec. Tech. Publ.* 520, American Society for Testing and Materials, Philadelphia, 1972.

20. C. E. Jaske and T. L. Porfilio, *Low-Cycle Fatigue of Type 347 Stainless Steel and Hastelloy X in Hydrogen Gas Environment,* TID/SNA-2047 (1971).

21. P. L. Rittenhouse, *Initial Assessment of the Status of HTGR Metallic Structural Materials Technology,* ORNL-TM-4760 (December 1974).

22. P. L. Rittenhouse and C. S. Morgan, *Status Report on Structural Materials of HTGR Primary System Components,* ORNL/TM-5136 (January 1976).

23. C. R. Brinkman and G. E. Korth, "Strain Fatigue and Tensile Behavior of Inconel 718 from Room Temperature to 650°C," *J. Test. Eval.* 2(4): 249–59 (July 1974).

24. J. B. Conway, R. H. Stentz, and J. T. Berling, *Fatigue, Tensile and Relaxation Behavior of Stainless Steels,* TID-26135 (1975).

25. D. L. Keller, *Progress on LMFBR Cladding, Structural, and Component Material Studies During July 1971 Through June 1972 — Final Report Task 32,* BMI-1928.

26. D. L. Keller, *Progress on LMFBR Cladding, Structural, and Component Materials Studies During July 1970 Through June 1971 — Annual Report, Task 32, Final Report, Task 14,* BMI-1914.

27. General Atomic Company, *Component and Systems Development Program, Quart. Prog. Rep. June 30, 1975,* GA-A-13512.

28. C. R. Brinkman, M. K. Booker, J. P. Strizak, W. R. Corwin, J. L. Frazier, and J. M. Leitnaker, *Interim Report on the Continuous Cycling Elevated Temperature Fatigue and Subcritical Crack Behavior of 2 1/4 Cr-1 Mo Steel,* ORNL-TM-4993 (December 1975).

29. Personal communication with D. R. Diercks, January 1976.

30. C. R. Brinkman and G. E. Korth, *Heat-to-Heat Variations in the Fatigue and Creep-Fatigue Behavior of AISI Type 304 Stainless Steel, and the Fatigue Behavior of Type 308 Stainless Steel Weld Metals,* ANCR-1097 (May 1973).

31. C. R. Brinkman, G. E. Korth, and R. R. Hobbins, "Estimates of Creep-Fatigue Interaction in Irradiated and Unirradiated Austenitic Stainless Steels," *Nucl. Technol.* 16: 297–307 (October 1972).

32. C. E. Jaske, "Low Cycle Fatigue of AISI 1010 Steel at Temperatures up to 1200°F (649°C)," presented at American Society of Mechanical Engineers International Joint Pressure Vessels and Piping and Petroleum Mechanical Engineering Conference, September 19–24, 1976, Mexico City, Mexico.

33. S. S. Manson, G. R. Halford, and M. H. Firshberg, "Creep-Fatigue Analysis by Strain-Range Partitioning," pp. 12–28 in *Symposium on Design for Elevated Temperature Environments,* ed. by S. Y. Zamrik, American Society of Mechanical Engineers, New York, 1971.

34. M. H. Hirshberg and G. R. Halford, "Use of Strain-Range Partitioning to Predict High-Temperature Low-Cycle Fatigue Life," NASA Lewis Research Center, Cleveland, Ohio (to be published).

35. W. R. Corwin, Subcritical Crack Growth Studies," *HTGR Base-Technology Program Prog. Rep. Jan. 1, 1974–June 30, 1975*, ORNL-5108, pp. 81–95.

36. P. L. Rittenhouse, "Tensile Testing," *HTGR Base-Technology Program Prog. Rep. Jan. 1, 1974–June 30, 1975*, ORNL-5108, pp. 67–73.

37. J. P. Strizak, "Low-Cycle Fatigue Life Testing," *HTGR Base-Technology Program Prog. Rep. Jan. 1, 1974–June 30, 1975*, ORNL-5108, pp. 95–128.

38. J. P. Strizak, "Fatigue Life Testing," *Mechanical Properties Test Data for Structural Materials Quart. Prog. Rep. Jan. 1, 1976*, ORNL-5112, pp. 162–68.

39. R. C. Andrews and L. H. Kirschler, *Design Properties of One Heat of 2 1/4 Cr-1 Mo Steel and 316 Stainless Steel in High Temperature Air, Helium and Sodium Environments*, MSAR-66-174 (Sept. 14–16, 1966).

40. H. E. McCoy and B. McNabb, *Corrosion of Several Iron- and Nickel-Base Alloys in Supercritical Steam at 1000°F*, ORNL-TM-4552 (August 1974).

41. G. M. Goodwin, *The Effect of Minor Elements on the Hot Cracking of Inconel 600*, Ph.D. Thesis, Rensselaer Polytechnic Institute (June 1968).

42. W. F. Savage and B. M. Krantz, "An Investigation of Hot Cracking in Hastelloy X," *Weld. J. (N.Y.)* 45(1): 13-s–25-s (1966).

43. W. F. Savage and B. M. Krantz, "Microsegregation in Autogenous Hastelloy X Welds," *Weld. J. (N.Y.)* 50(7): 292-s-303-s (1971).

44. J. C. Griess, J. H. DeVan, W. A. Maxwell, and P. L. Rittenhouse, "Corrosion of Steam Generator Materials," *HTGR Base-Technology Program Prog. Rep. Jan. 1, 1974–June 30, 1975*, ORNL-5108, pp. 128–39.

45. J. C. Griess, J. H. DeVan, J. P. Hammond, and W. A. Maxwell, *The Corrosion of 2 1/4 Cr-1 Mo Steel and Other Alloys in Chloride Contaminated Steam*, ORNL-5268 (July 1977).

46. J. C. Griess, J. H. DeVan, and W. A. Maxwell, *Effect of a High Heat Flux on the Corrosion of 2 1/4 Cr-1 Mo Steel in Superheated Steam,* ORNL/TM-5551 (October 1976).

3. FISSION PRODUCT TECHNOLOGY

A. P. Malinauskas

3.1 INTRODUCTION

Major emphasis in the fission product technology effort has involved release measurements from bare kernels and intact fuel particles, and postirradiation examinations of Peach Bottom HTGR fuel elements. The data derived from these investigations serve several purposes; these range from providing input data to computational programs that are developed for systems response analyses to providing a data base for the validation of such computer codes.

3.2 FISSION PRODUCT RELEASE FROM COATED PARTICLE FUELS — M. T. Morgan and R. L. Towns

Much of the work involving fission product release has focused on releases from Biso-coated ThO_2 particles that had been irradiated in the HT-12 through -15 capsules. This section summarizes the coating failure and fission product release studies, which are described in greater detail in a more general report[1] of these capsule irradiation and postirradiation activities.

3.2.1 Coated Failure Determinations

Gas pressure measurements on particles irradiated in the HT capsule series indicated that some of the particles retained neither the CO nor the fission product gases, even though visual examination adjudged the coatings on these particles to be intact. A study was therefore undertaken to compare the methods currently employed to detect coating failure — vis., visual inspection, gas pressure measurement, and hot chlorine leaching — and the results were reported previously.[2]

Those results indicated that in some instances the leaching and pressure measurements showed failure of virtually all of the particles in the sample although no failures had been detected visually. Also, the fraction of failures determined by radioactivity measurements after leaching agreed reasonably with that determined by thorium

collection during leaching, but the thorium data consistently yield lower values. A comparison of the fraction of failures for each batch in the same irradiation capsule indicates that the higher number of failures occurred at the lower conditions of temperature, burnup, and fast fluence.

Particles from two batches were individually analyzed by gamma spectroscopy before and after the hot chlorine leaching at 1000°C to determine fission product loss due to the leaching process. The leach was generally performed for a minimum of 17 hr if no thorium was collected or, ir thorium was collected, until accumulation of the thorium in the leachant ceased. The maximum total time required was about 60 hr.

Table 3.1 compares the fraction of fission products collected during leaching with the fraction of coating failures and the fraction of thorium collected. The fractions of fission products and thorium collected are based on the corresponding total amounts as analyzed in the particles before leaching. The ^{144}Ce and ^{137}Cs results agree more closely with the actual failure fraction than the ^{232}Th results; however, the ^{232}Th results are more uniform.

Table 3.1. Fission Products and Thorium Collected During Chlorine Leaching at 1000°C

Sample	Number of Particles Tested	Collected Amount (% of total)					Number of Particles Failed	Failures (%)
		^{106}Ru	^{125}Sb	^{137}Cs	^{144}Ce	^{232}Th		
HT-12-8	16	≤0.02	≤0.01	≤0.004	≤0.002	<0.02	0	0.0
HT-12-13	16	ND[a]	0.18	0.040	0.028	0.33	0	0.0
HT-12-21	16	0.24	0.097	0.015	0.32	<0.02	0	0.0
HT-12-26	16	4.8	ND	5.2	4.8	4.8	1	6.2
HT-13-8	16	5.9	ND	5.2	5.5	4.9	1	6.2
HT-13-13	12	ND	ND	0.007	0.002	<0.014	0	0.0
HT-13-21	16	≤0.011	≤0.022	0.037	0.005	0.021	0	0.0
HT-13-26	16	0.035	0.060	0.004	0.014	<0.01	0	0.0
HT-14-8	16	110	ND	82	103	80	15	93.8
HT-14-13	8	57	ND	62	76	58	6	75.0
HT-14-21	16	16	≤14	6.9	17	14	3	18.8
HT-15-8	6	106	81	109	114	76	6	100.0
HT-15-13	8	28	≤40	77	95	70	7	87.5
HT-15-26	8	0.32	2.4	3.1	0.085	<0.047	0	0.0

[a]Not determined.

Several defective and nondefective coated particles, both irradiated and urirradiated, were examined by the scanning electron microscope before and after leaching. No evidence of cracks or porosity was observed at magnifications up to 1000×. Also, no differences between leached and unleached surfaces were evident.

The coating failure studies led to the following conclusions:

1. visual inspection is not sufficient to determine coating stability;
2. hot chlorine leaching is a sensitive method for determining coating failure;
3. hot chlorine leaching has no effect on intact pyrocarbon-coated particles at 1000°C, but the chlorine can react with the carbon if thoria is present;
4. the fractions of cesium, cerium, or thorium released during leaching are closely equivalent to the fraction of coating failures;
5. some of the coated particles developed permeability during irradiation, particularly at lower irradiation temperatures.

3.2.2 Fission Product Release During Irradiation

Fission product losses during irradiation were determined by comparing the average amounts of fission products in the coated particles as measured by gamma-ray spectroscopy after irradiation with the corresponding calculated inventories. For the low-temperature, low-burnup capsule irradiations, the measured inventories were higher than the calculated results. Assuming that the differences were due to discrepancies in the burnup or reaction rate, a correction factor was applied. The results showed no significant loss of ^{95}Zr, ^{106}Ru, or ^{144}Ce even at the higher burnups and temperatures or from defective coated particles.

The fractional releases of ^{137}Cs and ^{125}Sb are presented graphically as a function of burnup in Figs. 3.1 and 3.2. The data in Fig. 3.1 show no significant loss of cesium to a burnup of about 2% FIMA at either 1200 or 1500°C. At 1200°C, no loss is apparent until a burnup of 4.5% FIMA is exceeded. At 1500°C, the release of up to 20% cesium at 6% FIMA indicates that losses occur earlier at the higher temperature and increase with burnup, as would be expected. The effects of coating

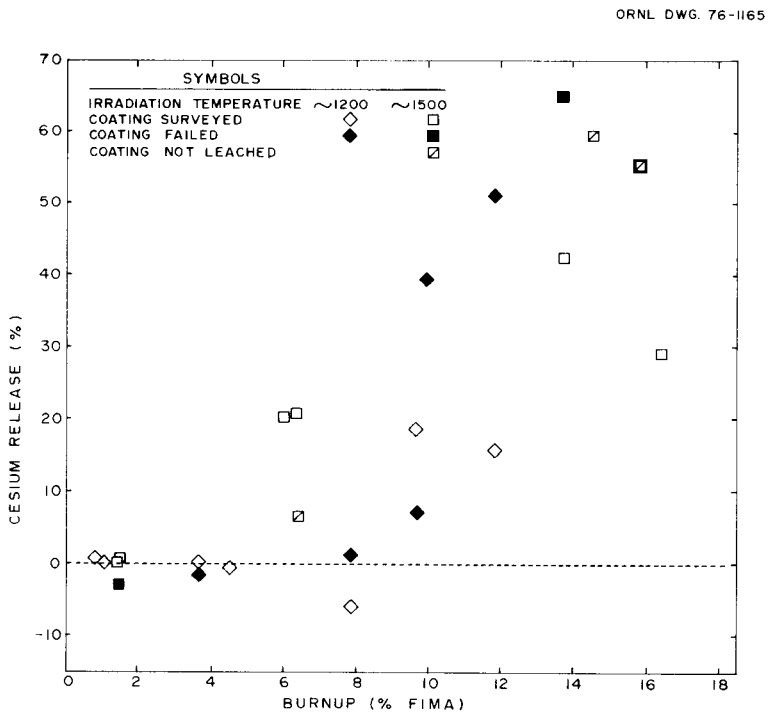

Fig. 3.1. Release of ^{137}Cs from Biso-Coated ThO_2 Particles During Irradiation in Capsules HT-12 Through -15.

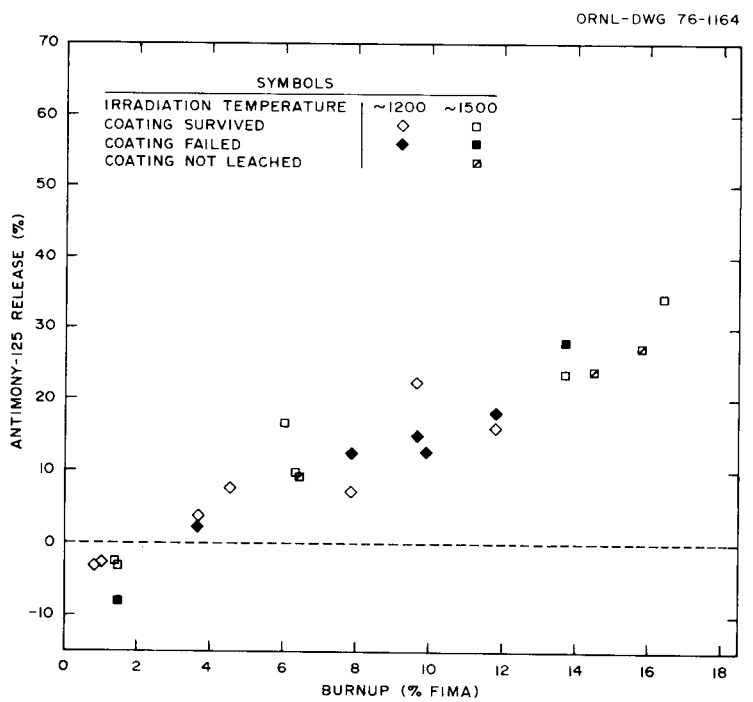

Fig. 3.2. Release of ^{125}Sb from Biso-Coated ThO_2 Particles During Irradiation in Capsules HT-12 Through -15.

failures are difficult to assess. In most samples, all or nearly all the coatings either survived or failed; thus direct comparisons are limited. Also, the time of failure cannot be determined accurately. The data show no effect of coating failure at lower burnups, but suggest a possibly higher release at the higher burnups. The data in Fig. 3.2 show an increase in ^{125}Sb release with burnup but, within the scatter of the data, no definite effects of temperature or coating failure.

3.2.3 Cesium, Antimony, and Europium Release from Bare Kernels During Postirradiation Anneal Experiments

The experiments described in this section were conducted primarily to determine the rate of release of cesium from bare ThO_2 kernels and to obtain an estimate of the diffusion coefficient. Kernels were separated from coated particles and annealed at 1400°C. The annealing system consisted of eight tungsten tubes, which were inserted in holes in a graphite crucible and heated by induction. Each tube contained one kernel. The tubes were removed at various intervals, the kernels removed, and the tubes and kernels analyzed for fission products with a sodium iodide gamma-ray detector. The kernels were then replaced in the tubes and the anneal continued. Peaks for ^{125}Sb and ^{134}Cs were found and subtracted to obtain accurate ^{137}Cs analyses, but the ^{125}Sb and ^{154}Eu peaks were not distinct enough for accurate analyses of these fission products. However, the kernels and tubes were analyzed on another system with a germanium detector after the annealing series ended to obtain the fractions of ^{125}Sb and ^{154}Eu released and to verify the ^{137}Cs release values.

A typical plot of cesium release as a function of annealing time is shown in Fig. 3.3. The line on the graph represents a least squares fit of the data. From the slope of the line and the average radius of the kernel, the diffusion coefficient (D) was obtained by the equation

$$D = F^2 a^2 / 36 t^{1/2} \ , \qquad (1)$$

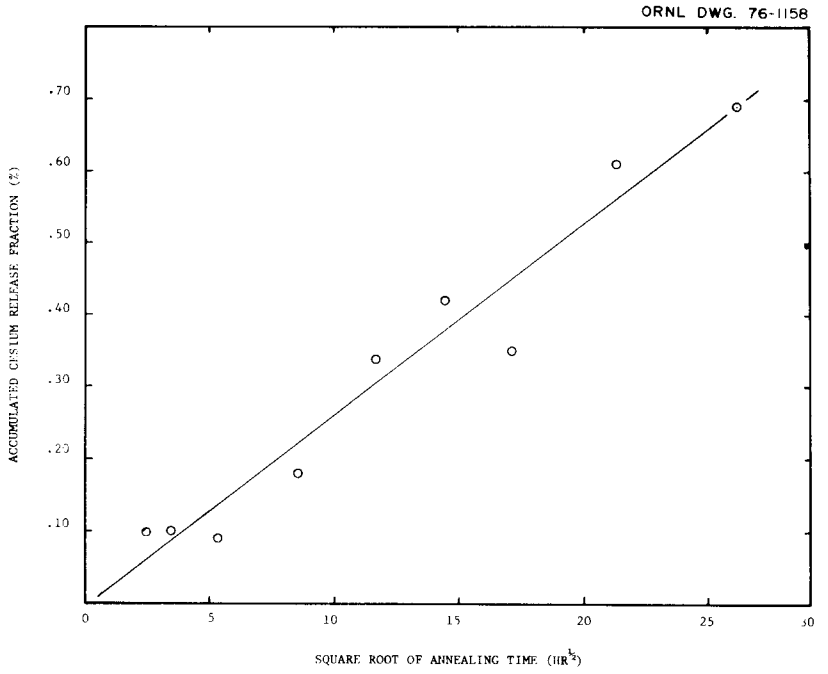

Fig. 3.3. Cesium Release from Bare ThO_2 Kernel During Postirradiation Anneal at 1400°C.

where F is the fraction of cesium released in time t, and a is the radius of the kernel. This equation, which is adapted from Booth and Rymer,[3] is a valid approximation up to a release of 20%. The use of the kernel radius rather than the unknown radius of the grains making up the kernel introduces some error, so that the calculated values for D are larger than would be determined if grain radii were employed. Diffusion coefficients determined in this way for cesium are presented in Table 3.2 for eight kernels; also tabulated are the total cesium, antimony, and europium releases at 684 hr.

3.2.4 Cesium Concentration Profiles in Pyrocarbon Coatings

Cesium concentration profiles in coatings of particles from the HT-12 and -13 capsules have been obtained by a grinding technique as described in a previous report.[4] A typical profile of cesium concentration in the coating of a particle from HT-13-8 is shown in Fig. 3.4. A corresponding profile for a coated UO_2 particle, which had

Table 3.2. Cesium Diffusion Coefficients and Final Fractions for Cesium, Antimony, and Europium Release in Bare Kernels of Capsules HT-12 Through -15 During Postirradiation Anneals at 1400°C

Coated Particle	Fraction Released in 684 hr, %			Cesium Diffusion Coefficient (m^2/s)
	^{137}Cs	^{125}Sb	^{154}Eu	
HT-12-8-1	0.27	1.20	0.0	1.5×10^{-21}
HT-12-8-2	0.047	0.76	0.0	9.1×10^{-23}
HT-12-13-1	0.130	5.21	1.4	2.6×10^{-21}
HT-12-13-2	0.17	0.49	0.0	2.7×10^{-21}
HT-13-8-1	0.69	17.35	11.4	7.0×10^{-20}
HT-13-8-2	0.66	16.35	9.4	7.9×10^{-20}
HT-13-13-1	0.92	19.26	15.6	1.9×10^{-19}
HT-13-13-2	0.67	20.89	20.5	8.3×10^{-20}

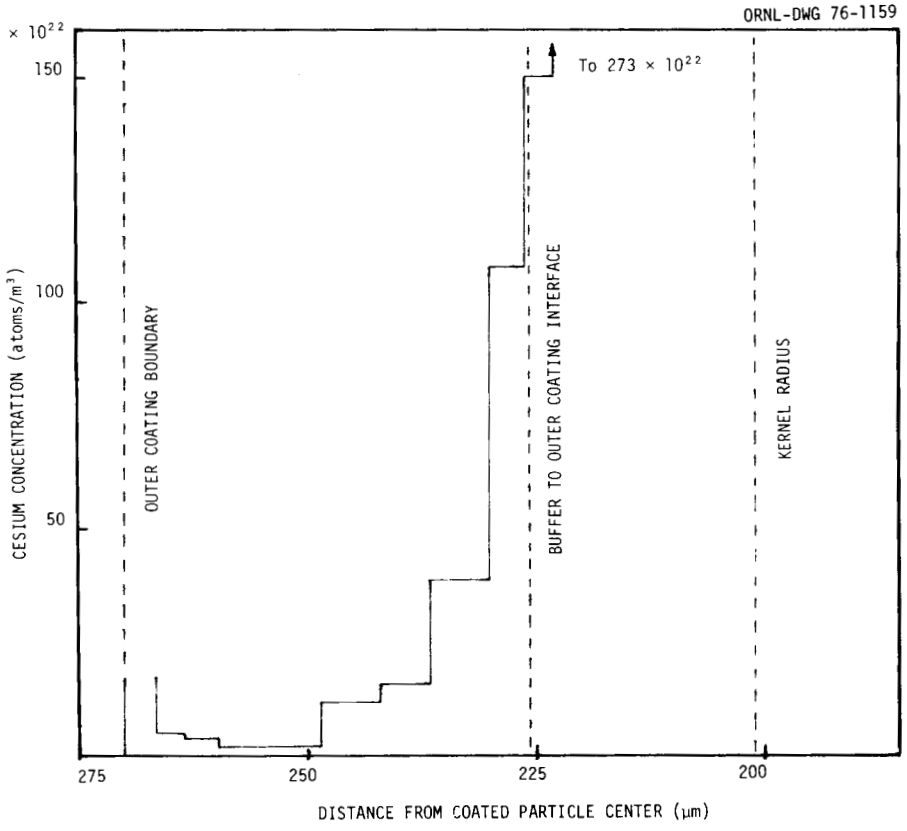

Fig. 3.4. Cesium Concentration in Coating of Particle from HT-13-8.

been irradiated to a higher burnup and which demonstrated constant-potential cesium transport, is shown in Fig. 3.5 for comparison. The lower concentrations shown in Fig. 3.4 reflect the low cesium release from this particle.

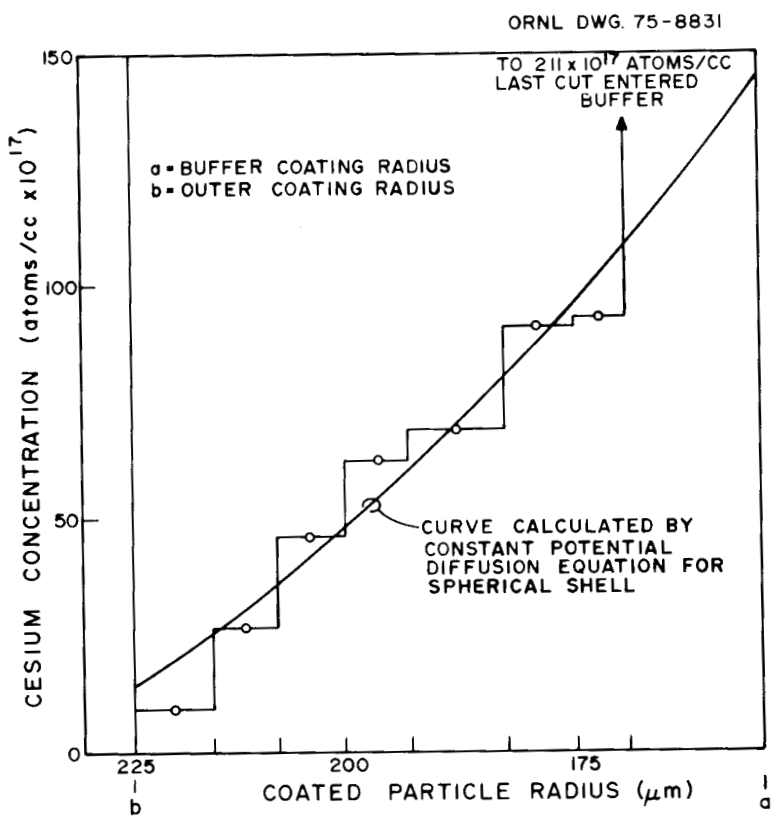

Fig. 3.5. Cesium Concentration Profile in Pyrocarbon Coating of UO_2 Particle Irradiated to 11% FIMA and Annealed 30 hr at 1400°C.

3.3 FEASIBILITY STUDY OF THE DESIGN OF FUEL STABILITY AND FISSION PRODUCT RELEASE IN REACTOR EXPERIMENTS — M. T. Morgan and J. G. Morgan

Preliminary studies were conducted for the design of irradiation experiments to determine the limits of coating stability of reference fuel, to investigate fission product release from failed fuel, and to obtain data on fission product release from fuel with intact Biso coatings. The fuel stability and failed fuel release studies are intended to provide information on the extent of fission product release during local temperature excursions, whereas the results of

studies of release from intact coated particle fuels during irradiation are intended for comparison with results from postirradiation anneal experiments, to determine the validity of the latter. The fuel stability experiments differ from other coated particle irradiation studies performed in the past in that reference fuel is to be irradiated over a range of burnups at temperatures necessary to induce failure, and the fission products released are collected quantitatively for postirradiation analysis.

3.3.1 High-Temperature Materials

Both the fuel stability and the release from intact particle experiments impose severe demands on high-temperature technology. A literature search was conducted to determine the best materials to be used, the compatibility of materials at high temperatures, methods of determining temperatures, and methods of heating the coated particles. As a guide to this preliminary study, elements with melting points above 1400°C were selected and rearranged in decreasing order of melting points. These are given in Table 3.3 together with physical properties and neutron cross sections. (Additional information is needed on compatibility, cost, high-temperature stability, workability, and mass transport.) Many of the elements listed can be eliminated because of high neutron cross sections or difficulty in forming. Although carbon or graphite could be used to support the fuel, the containment must be of metal. Niobium is most attractive for this purpose because of its high melting point and ease of machining compared with other high-temperature materials. To avoid the reaction of graphite with the container, the use of a molybdenum or a tungsten foil separator is envisaged.

3.3.2 Temperature Measurement

No methods of temperature measurement in current use can give fuel temperatures within 50°C consistently. The sensors themselves are subject to irradiation damage, and thermal conductivity and dimensional changes of components during irradiation further complicate the measurements.

Table 3.3. Physical Properties of High-Temperature Elements[a]

Atomic Number	Atomic Weight	Element	M.P. (°C)	B.P. (°C)	Density (g/cm³)	Coefficient of Linear Expansion (× 10⁻⁶/°C)	Thermal Conductivity Near 20°C (J/m K)	Thermal Conductivity Near 20°C (cal/m s K)	Total Neutron Cross Section[b]
6	12.011	Carbon	3727[c]	4830	2.25	0.6-4.3	24	5.7	0.01
74	183.86	Tungsten	3410	5930	19.3	4.6	166	39.7	54
75	186.22	Ruthenium	3180 ± 20	5900	21.04	6.7	71	17	174
73	180.95	Tantalum	2996 ± 50	5425 ± 90	16.6	6.5	54	13.0	91.0
76	190.2	Osmium	2700 ± 200	5500	22.57	4.6			22.0
42	95.95	Molybdenum	2610	5560	10.22	4.9	142	34	5.2
44	101.1	Ruthenium	2500 ± 100	4900	12.2	9.1			7.1
41	92.91	Niobium	2468 ± 10	4927	8.57	7.31	52	12.5	2.0
77	192.2	Iridium	2454 ± 3	5300	22.5	6.8	59	14	660
72	178.58	Hafnium	2222 ± 30	5400	13.09	519	22	5.3	250
5	10.82	Boron	∿2030		2.34	8.3			794
45	102.91	Rhodium	1966 ± 3	4500	12.44	8.3	88	21	263
23	50.95	Vanadium	1900 ± 25	3400	6.1	8.3	31	7.4	5.1
24	52.01	Chromium	1875	2665	7.19	6.2	67	16	3.2
40	91.22	Zirconium	1852	3580	6.489	5.85	21	5.0	0.3
78	195.09	Platinum	1769	4530	21.45	8.9	69	16.5	23.4
90	232.05	Thorium	1750	3850 ± 350	11.66	12.5	38	9	15.9
22	47.90	Titanium	1668	3260	4.507	8.41	11.3	2.7	6.4
71	174.99	Lutetium	1652	1930	9.85				174
46	106.7	Palladium	1552	3980	12.02	11.76	70	16.8	11.0
69	168.94	Thulium	1545	1720	9.31				276
21	44.96	Scandium	1539	2730	2.99				27
26	55.85	Iron	1536 ± 1	3000 ± 150	7.87	11.76	75	18	2.7
39	88.92	Yttrium	1509	2020	4.47		14.6	3.5	62.0
68	167.27	Erbium	1497	2630	9.15	9.0	9.6	2.3	231
27	58.94	Cobalt	1495 ± 1	2900	8.85	13.8	69	16.5	44.0
67	164.94	Holmium	1461	2330	6.79				135
28	58.71	Nickel	1453	2730	8.902	13.3	92	22	4.7
14	28.09	Silicon	1410	2680	2.33	2.8-7.3	84	20	0.2
66	162.51	Dysprosium	1407	2330	8.55	9.0	10.0	2.4	1103

[a]Data condensed from *Metals Handbook*, 8th ed., vol 1; "Properties and Selection of Metals," T. Layman, ed., American Society for Metals, Metals Park, Ohio, 1961.

[b]The total neutron cross section values are based on the assumption that the resonant neutron flux is 10% of the thermal flux and are not valid for reactor calculations where other conditions may apply. These were obtained by

$$\sigma_T = \sum_{i=1}^{n} A_i(\sigma_0 + RI/10)_i ,$$

where A_i = isotopic abundance of the ith isotope of a particular element, σ_0 is the thermal cross section, (RI is the resonance integral, and n is the number of stable isotopes from N. E. Holden and F. W. Walker, *Chart of Nuclides, 11th ed.*, Knolls Atomic Power Laboratory, operated by General Electric Co., April 1972.

[c]Sublimes.

The Johnson noise thermometer[5,6] seems to be the best sensing device since it is not subject to change with irradiation dose and has an accuracy within ±20°C at 1250°C. However, it is still under development and has not been proven for use over long periods of irradiation. If thermocouples must be employed, tungsten-rhenium alloy thermocouples appear to be best suited for temperatures of 1250°C or above.

3.3.3 Fuel Stability Irradiation Experiment

A preliminary conceptual design for an irradiation experiment to determine fuel stability is shown in Fig. 3.6. The central thermometer is normally withdrawn and inserted only at periodic intervals to limit irradiation damage. Moreover, this thermocouple can be replaced without removing the capsule from the reactor. Temperature control can involve either vertical positioning of the capsule in-reactor to control the neutron flux, or providing a tapered heat source. These techniques would permit operation under nearly isothermal conditions.

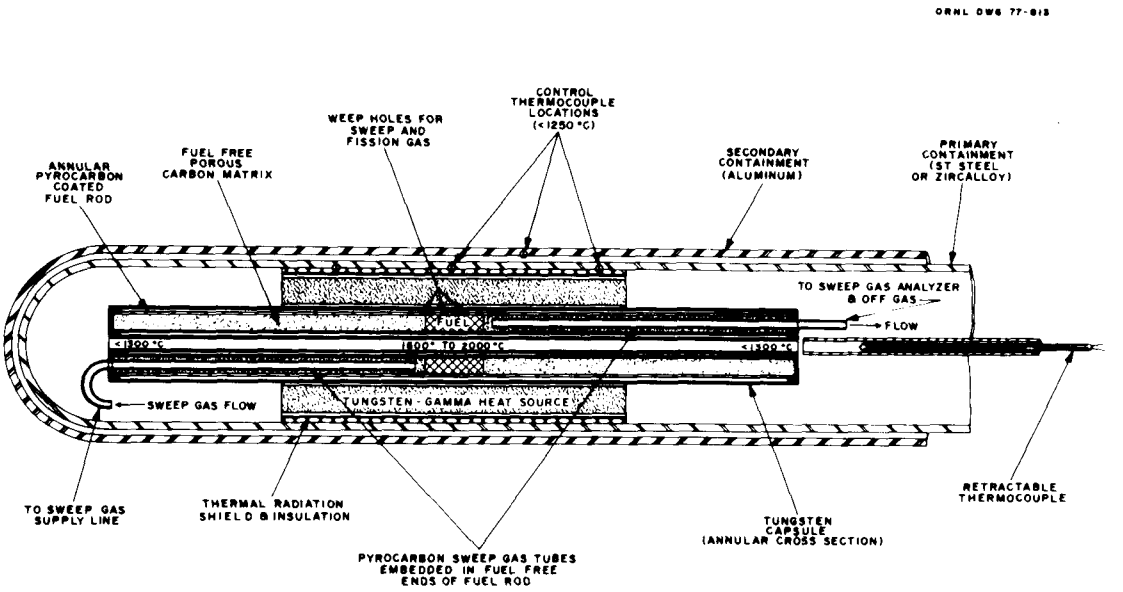

Fig. 3.6. Conceptual Design for Isothermal Irradiation Experiment.

An alternate design is to use fission heat as the heat source. A similar arrangement to that shown could be used, with a graphite- or pyrocarbon-enclosed coated-particle-fueled heat source being substituted for the massive tungsten. This design would provide a much higher fast-to-thermal neutron ratio, and the central retractable thermocouple would fail more rapidly. Also, constant conditions could not be maintained over long periods because of burnup. Although this type of experiment would be more difficult to analyze, it provides better simulation of actual reactor operation.

3.3.4 In-Reactor Studies of Fission Product Release from Intact Fuel Particles

The fraction of fission products released from fertile fuel particles over the fuel lifetime is expected to be less than 5% at an irradiation temperature of 1400°C, as determined from postirradiation annealing experiments on ThO_2 kernels. However, it remains to be demonstrated that this postirradiation result is applicable to in-reactor conditions. Moreover, this small release cannot be determined accurately as a difference between measured and calculated inventories of irradiated coated particles. Temperature measurement and control become extremely important in the release studies, since the rate of release varies exponentially with temperature. For example, calculations of coating-controlled release of cesium from Biso-coated particles indicate typically that an error of 50°C in temperature at 1250°C causes a change in the fractional release by a factor of 2.

3.4 FISSION PRODUCT SURVEILLANCE OF THE PEACH BOTTOM HTGR PRIMARY CIRCUIT — F. F. Dyer, W. J. Martin. L. L. Fairchild, and R. P. Wichner

A series of measurements regarding the distribution and levels of radioactivity in the primary circuit of the Peach Bottom HTGR was undertaken throughout the course of Core 2 operation, from July 1970 to final shutdown in October 1974. Four types of observation were conducted in this phase of the Peach Bottom Surveillance Program: (1) the cold duct of the primary circuit was scanned axially for gamma-emitting nuclides on four occasions, the last soon after final shutdown; (2) the primary

coolant was sampled upstream and downstream from the steam generator through diffusion tubes and filters to differentiate between gaseous and particulate-borne activity; (3) the primary coolant and fuel element purge flow were sampled for fission gas measurement; and (4) dust samples collected by use of the cyclone separators in the primary loops were examined for size distribution, chemical makeup, and contained activity. These activities have been described in detail elsewhere.[7]

3.4.1 Surveillance of the Primary Duct

Primary circuit gamma scans were obtained on four occasions, following 252, 385, 701, and 900 equivalent full-power days (EFPDs) of Core 2 operation. The last scan was acquired soon after final reactor shutdown; the first three scans were taken during scheduled maintenance intervals. The major observed surface activity was due to the nuclides ^{134}Cs and ^{137}Cs. Initially, approximately 4.2 Ci of ^{137}Cs was found to be deposited on the cold ducts, representing about 0.0045% of total core inventory. The observed surface activity due to ^{137}Cs fell between the first and the second primary circuit scans to about half the initial value. Subsequently, it rose slightly between the second and third scans and then sharply between the third and fourth scans to a final value of about 10 Ci. The initial high value may be attributed to residue left from Core 1 operation, during which substantially higher fuel failure fractions were experienced, whereas the sharp rise in deposited activity in the final year of operation is attributed to diffusive breakthrough of cesium generated during Core 2 operation. This view is supported by the observed decline in the isotopic ratio $^{137}Cs/^{134}Cs$ during this period.

Other nuclides generally observed on the primary circuit cold ducts were ^{54}Mn, ^{59}Fe, ^{60}Fe, ^{65}Zn, ^{110m}Ag, ^{140}Ba, and ^{144}Ce. On the occasion of the third gamma scan, when conditions were most advantageous, the distribution of ^{131}I along the cold duct was measured; at other times only upper limit values of iodine plateout activity could be ascertained. Other nuclides occasionally identified on the cold duct were ^{103}Ru, ^{106}Ru, ^{154}Eu, and ^{233}Pa.

3.4.2 The Coolant Sampler Experiment

Six coolant sampling experiments were performed; moreover, the last four were in pairs run simultaneously at locations upstream and downstream from the steam generator. Each of these experiments was conducted over periods ranging from 1700 to 6600 hr of reactor operating time while coolant was continuously drawn isokinetically through a set of diffusion tubes, filters, and iodine absorbers to determine the nature of the transported species. The amount of dust collected during each of the coolant sampler experiments per unit mass of coolant throughput is summarized in Table 3.4.

Table 3.4. Summary of the Dust Concentration in the Peach Bottom HTGR Coolant as Determined by Coolant Samplers

Sampler Designation	Operating Dates	Location Relative to Steam Generator	Dust Collected per Unit Mass of Coolant Throughput (mg/kg coolant)
CG		Upstream	0.16
C1	7/71–12/71	Downstream	0.041
CA-1	9/72–11/72	Upstream	0.039
CA-2	1/73–5/73	Upstream	0.070
CB	1/73–5/73	Downstream	0.087
CC	3/74–5/74	Upstream	0.029
CD	3/74–5/74	Downstream	<0.002

Two of the coolant samplers were equipped with impactor plates for classifying particulates according to size. Analysis of the dust collected on these plates revealed it to be composed primarily of graphite, Fe_3C, and an unknown iron-silicon compound, which yielded no x-ray diffraction pattern.

All the coolant samplers were equipped with diffusion tubes for distinguishing between molecular and particulate-borne activity. In theory, an observed steep axial gradient of deposited activity along the tube signifies molecular transport, whereas a flat profile would result from deposition of particulates. A number of cesium profiles

(but not all) do indeed conform to this theoretical model; however, most of the observed profiles for ^{110m}Ag, ^{131}I, and ^{54}Mn appear to be more complex than can be accounted for by the available simple deposition model.

3.4.3 Measurement of Xenon and Krypton Levels

Levels of fission gases (isotopes of krypton and xenon) in the primary coolant were determined on three occasions during Core 2 operation — December 1970, February 1973, and September 1973. Fission gas levels in the fuel element purge gas were also determined in the last series of experiments, and the release-to-birth rate ratios presented in Table 3.5 were obtained.

Table 3.5. Release-to-Birth Ratios of Noble-Gas Fission Products as Determined in the Peach Bottom HTGR September 1973

Nuclide	Half-Life	Release to Birth Rate Ratios Observed, September 1973[a]	
		To Purge Gas	To Primary Coolant
^{85m}Kr	4.48 h	7.2 E−4	6.5 E−8
^{85}Kr	10.7 y		
^{87}Kr	76 m	6.8 E−4	4.7 E−8
^{88}Kr	2.8 h	5.5 E−4	4.4 E−8
^{89}Kr	3.16 m	2.9 E−5	1.9 E−8
^{90}Kr	32 s		
^{131m}Xe	12.0 d		
^{133m}Xe	2.23 d		1.0 E−6
^{133}Xe	5.29 d		4.0 E−8
^{135m}Xe	15.3 m	2.2 E−4	2.0 E−8
^{135}Xe	9.17 h	3.4 E−4	2.5 E−8
^{137}Xe	3.84 m	1.7 E−5	1.6 E−8
^{138}Xe	12.2 m	5.4 E−5	1.5 E−8
^{139}Xe	39.7 s		2.2 E−7
^{140}Xe	13.6 s		2.1 E−6

[a]Read 7.2 E−4 as 7.2×10^{-4}.

Four different methods for obtaining fission gas levels in the primary coolant and purge gas were employed. These have been described in detail.[7] Short-lived nuclides, such as ^{90}Kr, ^{139}Xe, and ^{140}Xe, were best detected with a high-pressure flow-through system, whereas long-lived nuclides were best measured by collection on charcoal cooled to liquid-nitrogen temperature.

3.4.4 Primary System Dust Levels

The dust collected by the loop-1 cyclone separator was acquired on three occasions. The observed sample masses and estimated dust concentrations and dust production rates are presented in Table 3.6. Since the efficiency of collection of the cyclone separator departs significantly from unity for particle sizes below about 0.1 or 0.3 μm, the data apply to the particulate levels in the primary circuit above this size range.

Table 3.6. Dust Concentrations in the Peach Bottom HTGR as Inferred from Loop-1 Cyclone Separator Data

Collection Period	Sample Mass, Loop 1 (g)	Dust Concentration in Primary Loop During Operating Period ($\mu g/m^3$)	Rate of Dust Production During Operating Period ($\mu g/s$)
July 1970—April 1971	80.0	21	8.2
June 1971—Sept. 1973	110.0	15	5.8
Jan. 1973—Oct. 1974	15.3	4.3	1.7

Scanning electron micrographs of the dust collected beneath the cyclone separators indicate that the most frequently observed particles are iron rich (metallic iron and both oxide and carbide were detected) in the size range 10 to 40 μm. Frequently these particles appeared as tightly held agglomerates, achieving sizes up to a few millimeters. A

second major constituent of the dust appears to be carbon, both amorphous and graphite. Twice, pieces of metallic foil up to 13 mm in length, evidently from the hot-duct insulation, were found in the dust collection bottle.

About 200 mg of "soot" was collected from each of two fuel elements removed from the core. This black, fine powdery material appeared as a deposit in the exterior region above the fueled zone, and is believed to be one of the sources for circulating particulates in the primary system. Scanning electron micrographs revealed it to be composed of filaments 0.1 to 0.5 μm in width and flakes up to 4 μm. The major constituents of this material are amorphous carbon, graphite, and iron.

3.5 POSTIRRADIATION EXAMINATION OF PEACH BOTTOM HTGR FUEL ELEMENTS — R. P. Wichner, F. F. Dyer, W. J. Martin, L. L. Fairchild, and L. C. Bate

A series of six driver fuel elements are being examined; these include one 384-EFPD element, one irradiated to 700 EFPDs, and four end-of-life elements experiencing 900 EFPDs service in the Peach Bottom HTGR second core. Of these, the examinations of first two elements and one end-of-life element are complete and have been reported elsewhere,[8—10] whereas examination of the remaining three end-of-life fuel elements continues.

The examination procedures include: (1) photographic documentation of the appearance of all critical parts of the fuel elements; (2) measurement of the inner and outer diameters of about ten fuel compacts and the sleeve at the same axial locations; (3) measurement of the length of each fuel compact and the length and diameter of each spine piece; (4) gamma-ray spectroscopic determinations of the axial distributions of gamma- and beta-emitting nuclides in the graphite portions of the fuel element (these are primarily the sleeve and spine, but also include the upper, lower reflector, and fission product trap regions); and (6) determinations of the radial distributions of gamma- and beta-emitting radionuclides at six axial locations in both the sleeve and the spine graphite.

3.5.1 Physical Appearance and Dimensional Change of Fuel Element Components

The appearance of Compacts 23 to 26 and associated graphite spine of fuel element E11-07 are shown in Fig. 3.7. The well-worn appearance of Compacts 23 and 24 may be noted, while Compact 26, which experienced only slightly lower temperatures, appears to have maintained its original surface condition. Machining grooves may be seen on the right portion of Compact 25. The spalled zone on the spine opposite Compact 24 occurred at no other location in this fuel element.

Figure 3.8 illustrates the axial distribution of the compact-to-sleeve gap in elements E11-07 and E14-01. The nominal preirradiation range is indicated at bottom right in the figure, and indeed the preirradiation gaps measured for E14-01 largely fall in the nominal range. The figure shows that the gap increases with irradiation service to a maximum value of about 0.76 mm (30 mils) for E14-01 and a maximum range of from about 0.76 to 1.4 mm (30 to 55 mils) for E11-07. While both fuel and graphite radial dimensions were decreased by irradiation, the dimensional change experienced by the fuel was the larger, and hence the gap increased.

3.5.2 Nuclide Inventories in Fuel Compacts

Inventories of the radionuclides ^{95}Zr, ^{103}Ru, ^{106}Ru, ^{110m}Ag, ^{125}Sb, ^{134}Cs, ^{137}Cs, ^{141}Ce, ^{144}Ce, ^{154}Eu, and ^{233}Pa in each of the 30 fuel compacts at end of life are obtained as a part of the postirradiation examination.[8–10] Inspection of these inventory distributions indicates that some nuclides, such as cesium and europium, may show gross shifts in axial location, while others, such as zirconium and cerium seem fixed in location. Therefore, it is useful to view the axial inventory distributions relative to either zirconium or cesium, since so doing largely negates the effect of the axial variation in production rates due to the flux profile. An example of one such plot for $^{137}Cs/^{95}Zr$ and $^{134}Cs/^{95}Zr$ ratios is shown in Fig. 3.9 for element E14-01, which received 900 EFPDs irradiation. The smooth curves shown in Fig. 3.9 indicate no gross cesium movement in this element. The slight curvature

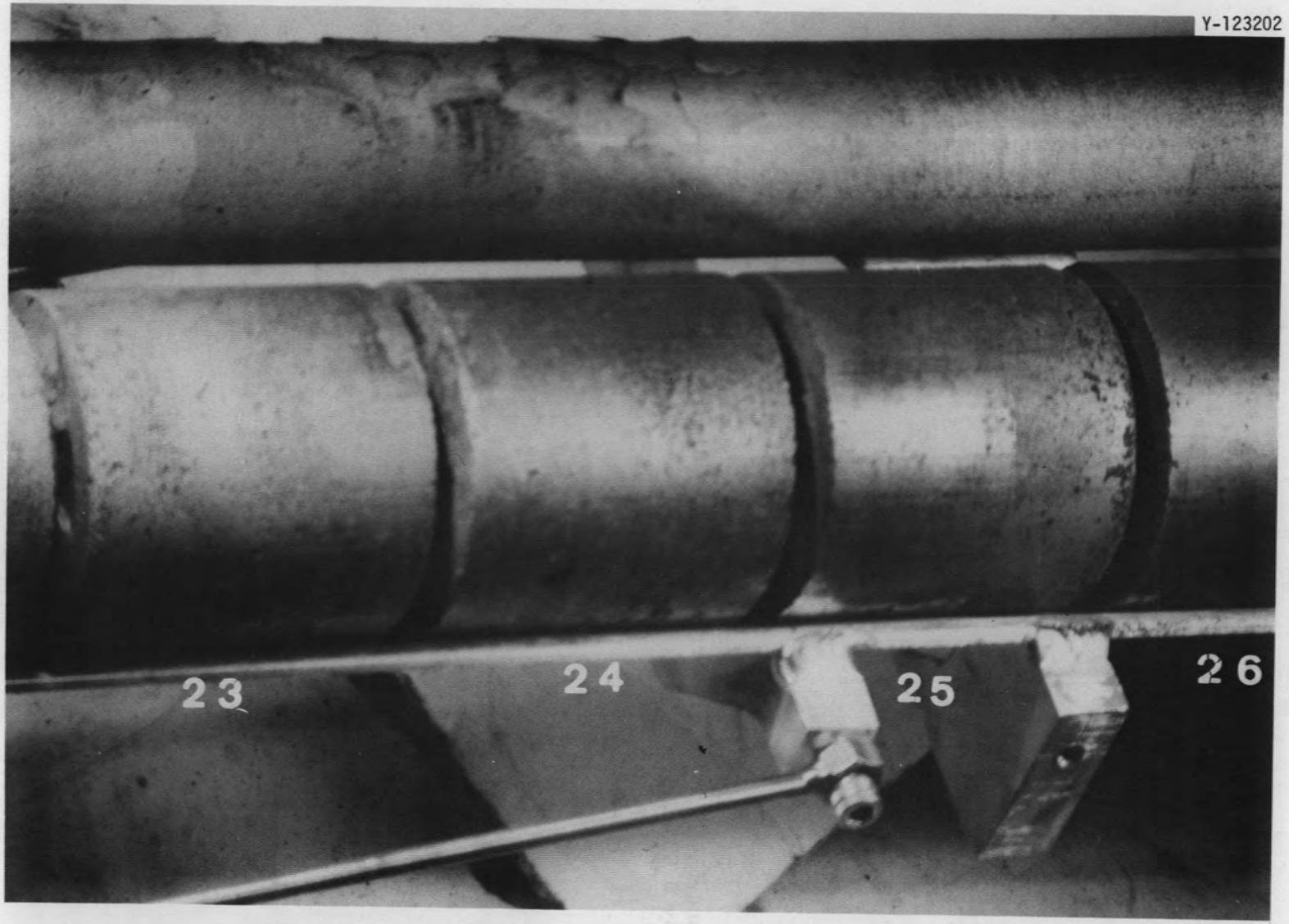

Fig. 3.7. Appearance of Compacts 23 to 26 and Associated Spine of Element E11-07.

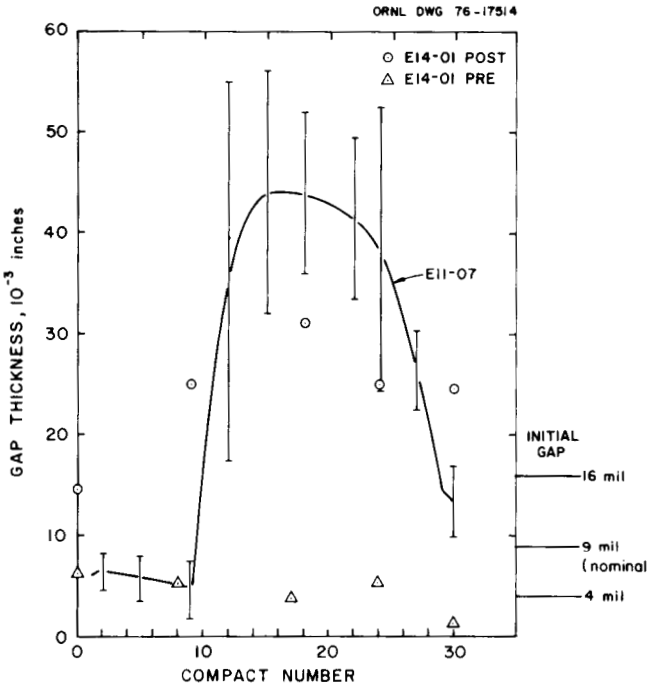

Fig. 3.8. Gap Between Fuel Compacts and Sleeve for Elements E11-07 and E14-01. To convert values on ordinate scale to millimeters, multiply by 0.0254.

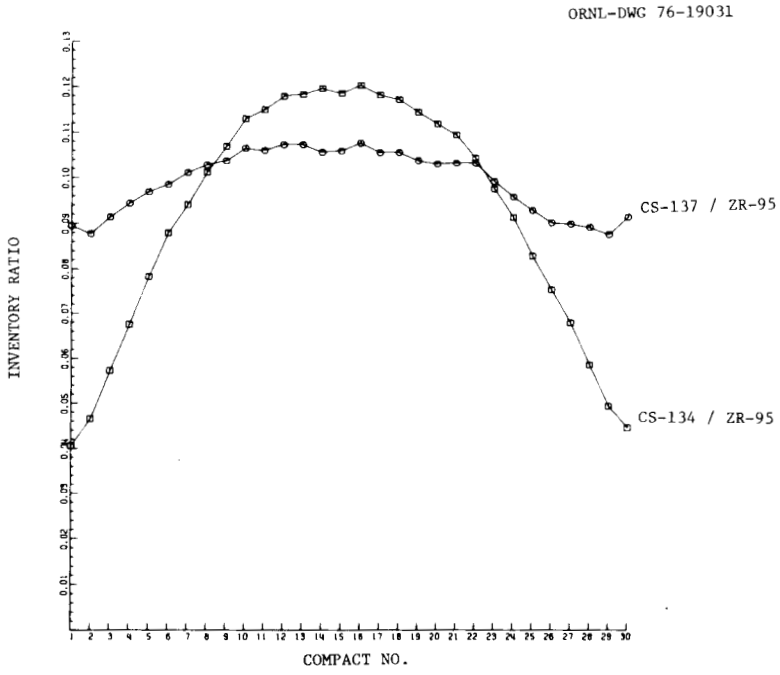

Fig. 3.9. Inventory Ratios $^{137}Cs/^{95}Zr$ and $^{134}Cs/^{95}Zr$ in Peach Bottom HTGR Fuel Element E14-01 Compacts at End of Life.

displayed in the $^{137}Cs/^{95}Zr$ profile is due to variations in fission product yield between ^{233}U and ^{235}U fissions. The greater curvature shown by the $^{134}Cs/^{95}Zr$ profile is caused by the production of ^{134}Cs by activation of fission product ^{133}Cs, which distributes it in the fuel as the square of the neutron flux; therefore, the indicated $^{134}Cs/^{95}Zr$ profile, to a first approximation, varies as the neutron flux.

Figure 3.10 shows a similar pair of curves for element E11-07 in which, evidently, significant shifts in cesium inventory occurred. The dip in the value of the ratio $^{137}Cs/^{95}Zr$ between compacts 14 and 25 indicates loss of cesium, whereas the elevated values of this ratio for compacts 1 through 14 indicates that the shift occurred towards the lower compacts. Approximately 16% of the ^{137}Cs fuel inventory moved in this fuel element.

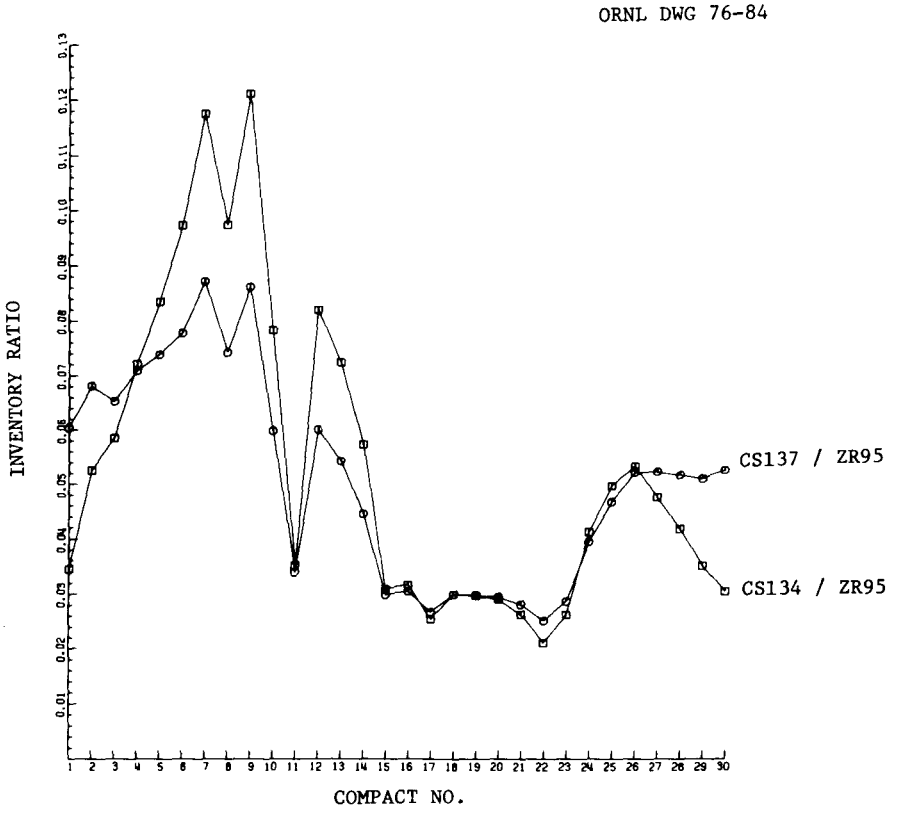

Fig. 3.10. Ratios of $^{137}Cs/^{95}Zr$ and $^{134}Cs/^{95}Zr$ in Peach Bottom HTGR Fuel Compacts in Element E11-07.

A preliminary estimate of the maximum fuel temperature in element E11-07 is 1350°C, compared with approximately 1280°C for element E14-01, in which no gross cesium shift was observed. In general, shifts in ^{154}Eu inventory closely resemble those observed for cesium. In Peach Bottom HTGR fuel, ^{110m}Ag showed the greatest tendency to move whereas Ru and Sb (as well as Zr and Ce) displayed little tendency to be transported.

3.5.3 Axial Distribution of Fission Products in the Graphite Sleeve and Spine

The facility for obtaining axial distributions in the graphite portions of the Peach Bottom fuel elements is depicted in Fig. 3.11. A cylindrical lead shield is situated directly above a hot cell. An opening in the hot cell roof enables the graphite components to be conveniently transferred into a scanning cask by means of a motor and pulley, which are situated at the top of the cask. Timers, shown at right in the figure, may be programmed for either continuous or intermittent operation of the motor that moves the specimen in the cask. The Ge(Li) detector assembly is shown at the left in the figure.

Axial distributions of ^{137}Cs in the sleeve and spine of element E11-07 are shown in Fig. 3.12. It should be noted that the fuel element purge flow proceeds from right to left in the figure, and the zones of depletion and accretion of ^{137}Cs in the fuel are denoted by the dashed lines, which represent the ^{137}Cs/^{95}Zr ratios in the fuel. The locations of the cesium deposits in the sleeve and spine relative to the zones of depletion in the fuel strongly suggest that the purge flow transports cesium to the graphite portions of the fuel element.

Similar axial profiles in the sleeve and spine of element E11-07 are shown in Fig. 3.13 for ^{110m}Ag and in Fig. 3.14 for the nuclides ^{154}Eu and ^{60}Co. Table 3.7 summarizes the total inventories of the the indicated six radionuclides found in the graphite portions of four Peach Bottom fuel elements. We may note that relatively large amounts of cesium were deposited on the graphite parts of elements E11-07 and F03-01 compared with that observed for elements E06-01 and E14-01.

Fig. 3.11. Axial Gamma Scanning System for Sleeve and Spine.

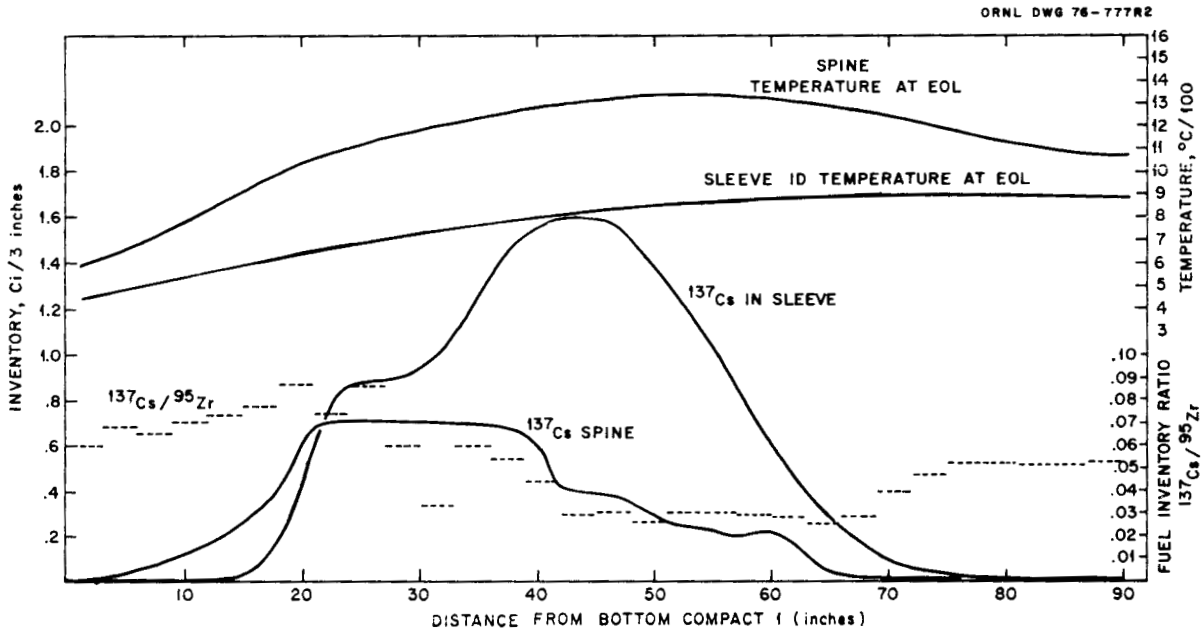

Fig. 3.12. Axial Distribution of ^{137}Cs in Sleeve and Spine of Element E11-07. Inventory scale is in curies per 76 mm. Multiply distance scale by 0.0254 to convert to meters.

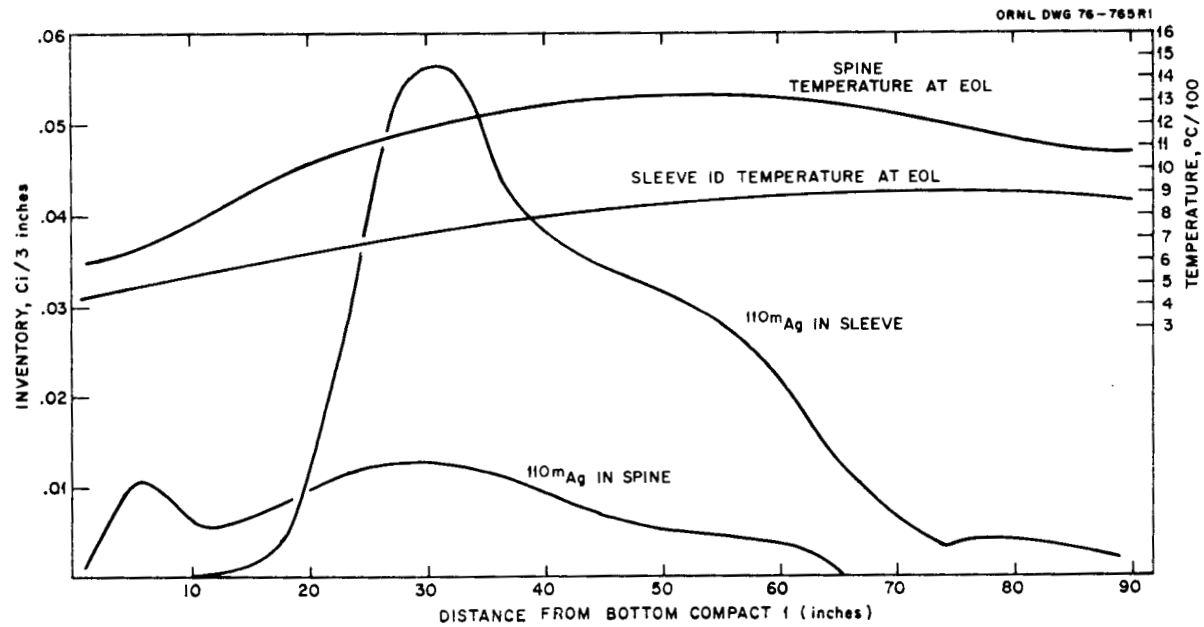

Fig. 3.13. Axial Distribution of ^{110m}Ag in Element E11-07 Sleeve and Spine of September 14, 1973. Inventory scale is in curies per 76 mm. Multiply distance scale by 0.0254 to convert to meters.

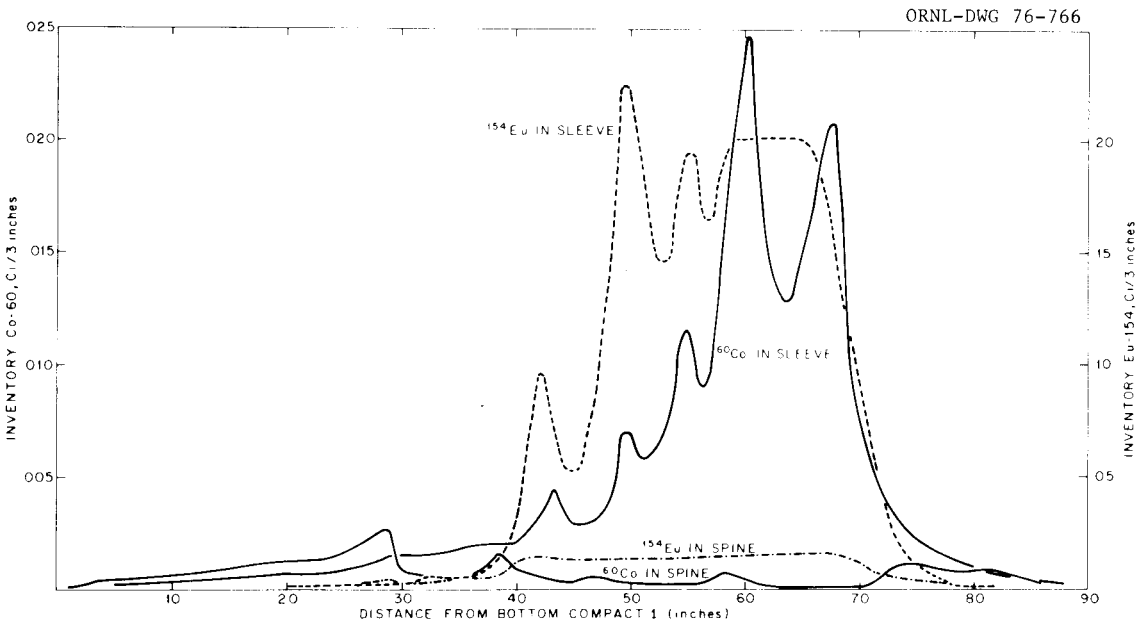

Fig. 3.14. Axial Distribution of ^{60}Co and ^{154}Eu in Sleeve and Spine of Peach Bottom Element E11-07. Inventory scales are in curies per 76 mm. Multiply distance scale by 0.0254 to convert to meters.

Table 3.7. Total Nuclide Inventories on Sleeve and Spine of Four Peach Bottom Driver Elements

Element	Exposure (EFPD)	Part Examined	Inventory, Ci					
			^{60}Co	^{110m}Ag	^{134}Cs	^{137}Cs	^{144}Ce	^{154}Eu
E06-01	384	Sleeve	0.01	0.05	0.024	0.035	0.36	0.004
		Spine	0.004	0.02	0.011	0.012	0.05	0.004
E11-07	701	Sleeve	0.13	0.56	30.0	17.2		1.60
		Spine	0.02	0.17	14.6	8.24		0.15
E14-01	900	Sleeve	0.021	0.21	0.31	0.24	0.12	0.0087
		Spine	0.91	0.085	0.058	0.047	0.23	0.010
F03-01	900	Sleeve	0.11	0.66	63.7	36.0	5.42	1.44
		Spine	0.047	0.17	17.6	9.76	1.68	0.24

3.5.4 Radial Distributions of Radionuclides in Graphite Fuel Element Components

A lathe adapted for remote operation in a hot cell and collection of graphite samples is shown in Fig. 3.15. This facility is used for radial sectioning of sleeve and spine pieces. Shown at right is the steel pan that, when situated beneath the cutting tool, collects the radial sample. The dial gage for centering the specimen in the collet is shown in place, and the hinged Lucite dust cover is shown in the open position. The dial gage in the foreground is used to determine the tool crossfeed location. Best results were obtained at cutting speeds below 200 rpm.

Figure 3.16 illustrates radial profiles of ^{137}Cs, ^{134}Cs, ^{54}Mn, ^{60}Co, ^{106}Ru, and ^{110m}Ag in the sleeve and spine of element E11-07 at compact location 18. The dashed lines signify that only upper limit values were obtained for ^{110m}Ag throughout most of the sleeve and all of the spine. The upward bend of the profiles at the outside of the sleeve signifies an external source of radionuclides in addition to the source coming directly from the fuel.

An interesting feature of the radial profiles obtained from element E11-07 is illustrated in Fig. 3.17, in which ratios $^{137}Cs/^{134}Cs$ are plotted as a function of radial distance in the sleeve and spine for samples drawn from various compact locations. The significance of this nuclide ratio is that the xenon precursor of ^{137}Cs has a half-life of only 3.8 min, compared with 5.3 days for the precursor of ^{134}Cs. One may note however from Fig. 3.17 that these significantly different life-spans for the noble gas precursors do not greatly affect the relative distributions in the higher temperature locations, as indicated by the rather level values of the isotopic ratio at compact locations 12 and 18. For the cooler locations at compacts 5 and 28, on the other hand, transport of the xenon precursors evidently does affect the cesium profiles. Here we note an enhanced ability for ^{134}Cs penetration to the central portions of the spine. The more complex dependence of the $^{137}Cs/^{134}Cs$ ratio at compact 28 in the sleeve is not understood at this time.

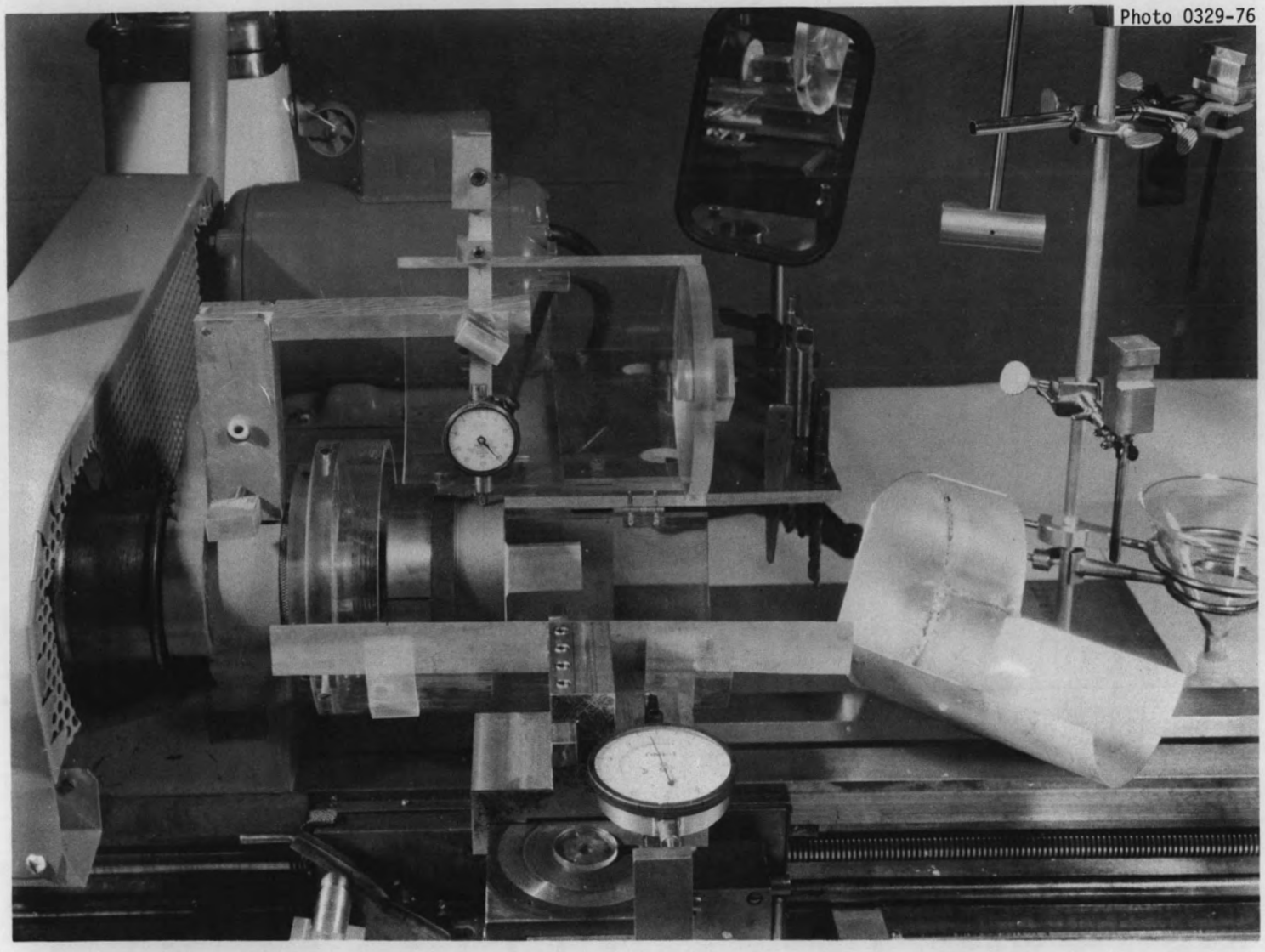

Fig. 3.15. Lathe Adapted for Remote Operation Used for Radial Sectioning of Peach Bottom Fuel Elements.

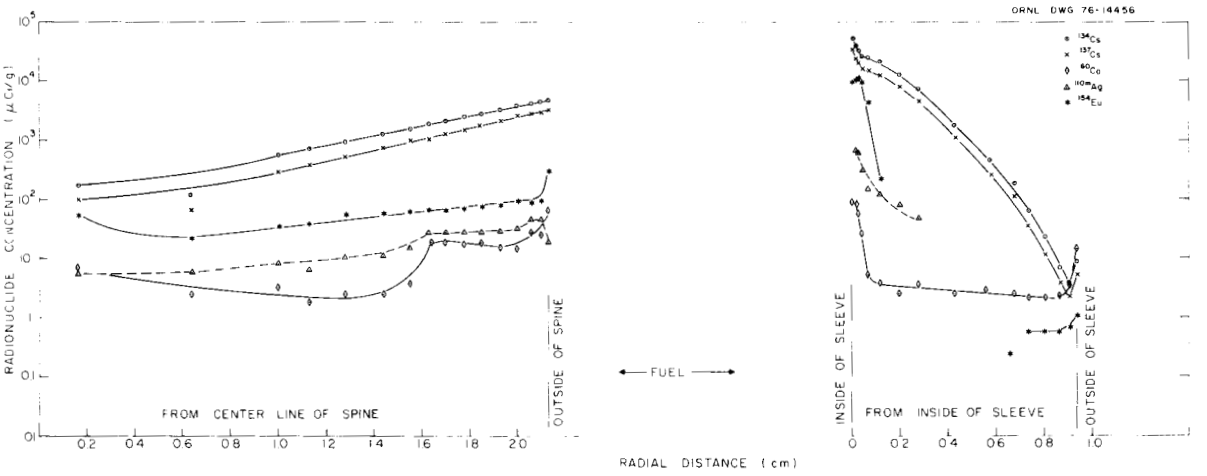

Fig. 3.16. Radial Distribution of Gamma-Emitters at Compact 18 of Peach Bottom Element E11-07.

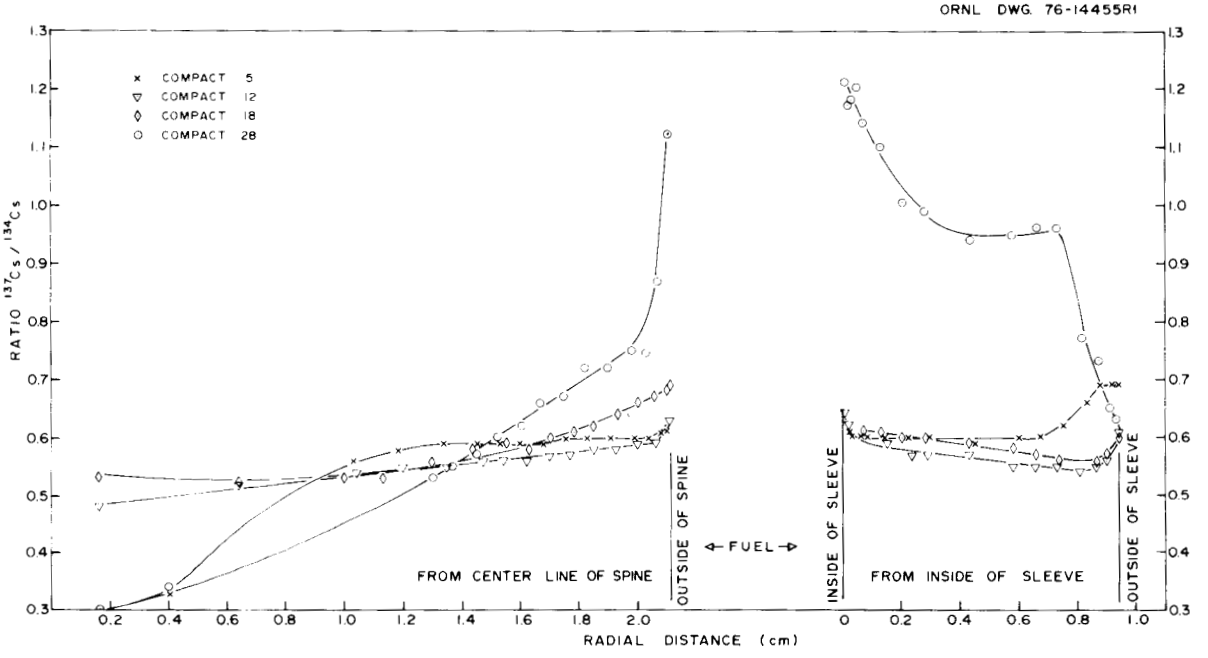

Fig. 3.17. Radial Distribution of Ratio of ^{137}Cs to ^{134}Cs for Element E11-07 (Corrected to Sept. 14, 1973).

3.6 REFERENCES

1. M. J. Kania, T. B. Lindemer, M. T. Morgan, and J M Robbins, *Irradiation Performance of HTGR Fertile Fuel in HFIR Target Capsules HT-12 through HT-15: Part I — Experimental Description and Fission Product Behavior*, ORNL-TM-5305 (February 1977).
2. M. T. Morgan, R. B. Evans III, R. L. Towns, and L. L. Fairchild, "Fission Product Release from Coated Particle Fuels," *HTGR Base-Technology Program Prog. Rep. Jan. 1, 1974–June 30, 1975*, ORNL-5108, pp. 143–54; note especially Table 3.2, p. 152.
3. A. H. Booth and G. T. Rymer, *Determination of the Diffusion Constant of Fission Xenon in UO_2 Crystals and Sintered Compacts*, CRDC-721 (September 1957).
4. R. B. Evans III and M. T. Morgan, *Mathematical Description of Fission Product Transport in Coated Particles During Postirradiation Anneals*, ORNL-4969 (June 1974).
5. R. L. Shepard, C. J. Borkowski, J. K. East, R. J. Fox, J. L. Horton, and T. V. Blalock, "Ultrasonic and Johnson Noise, Fuel Centerline Thermometry," pp. 737–74 in *International Colloquium on High-Temperature In-Pile Thermometry*, (held at JRC, Patten, Netherlands, Dec. 12–13, 1974), EUR-5395 (1975).
6. R. L. Shepard, C. J. Borkowski, T. B. Blalock, J. K. East, R. J. Fox, and J. L. Horton, "Johnson Noise Thermometer Development," *HTGR Base-Technology Program Progress Report Jan. 1, 1974–June 30, 1975*, ORNL-5108: pp. 414–16.
7. F. F. Dyer, R. P. Wichner, W. J. Martin, and H. J. deNordwall, *Distribution of Radionuclides in the Peach Bottom HTGR Primary Circuit During Core 2 Operation*, ORNL-5188 (January 1977).
8. F. F. Dyer, R. P. Wichner, W. J. Martin, L. L. Fairchild, R. J. Kedl, and H. J. deNordwall, *Post-Irradiation Examination of Peach Bottom HTGR Driver Fuel Element E06-01*, ORNL-5126 (April 1976).
9. R. P. Wichner, F. F. Dyer, W. J. Martin, and L. C. Bate, *Distribution of Fission Products in Peach Bottom HTGR Fuel Element E11-07*, ORNL-5214 (April 1977).
10. R. P. Wichner, F. F. Dyer, and W. J. Martin, *Distribution of Fission Products in Peach Bottom Fuel Element E14-01*, ORNL/TM-5730 (to be issued).

4. HTGR KERNEL MIGRATION AND IRRADIATED FUEL CHEMISTRY

A. P. Malinauskas

4.1 INTRODUCTION

The main objective of this program is an understanding of the kinetic processes and thermodynamics of the fuel, fission product, coating system to a degree that permits identification and quantitative description of failure mechanisms and improved fuel performance by means of kernel chemistry modification.

4.2 KERNEL MIGRATION STUDIES — R. L. Pearson and T. B. Lindemer

In this activity quantitative data on fuel kernel migration rates are obtained out-of-reactor on unirradiated HTGR fuels. Similar in-reactor data are obtained on irradiated fuels during postirradiation examination of irradiation capsules. A report of this work has been published elsewhere;[1] an abstract of this report follows:

> Nuclear fuels for the high-temperature gas-cooled reactor (HTGR) consist of spherical kernels of actinide compounds contained in gastight pyrolytic carbon and SiC. The fuel kernels migrate up the temperature gradient and into the coating layers. A theoretical analysis of in-reactor migration data indicates that a solid-state diffusion process controls the migration rate in fissioned $Th_{0.84}U_{0.16}C_2$, UO_2, ThO_2, PuO_{2-x}, and $Th_{0.8}U_{0.2}O_2$ particles. The theoretically based kernel migration coefficient (KMC), measured in units (cm/s) K^2 $(K/cm)^{-1}$, is thus used to correlate the laboratory and in-reactor data. The KMC values for Pu containing particles may be dependent on the extent of fission, the fission of either ^{233}U or ^{235}U, or the presence of an SiC coating layer. Laboratory KMC values were obtained for unirradiated ThO_2, $UO_{1.65}N_{0.25}$, UC_2, ThC_2, and $Th_{0.84}U_{0.16}C_2$ particles and generally appeared to be consistent with in-reactor data.

4.3 GAS PRESSURE MEASUREMENTS — T. B. Lindemer

This study involves the measurement and interpretation of the dependence of in-particle Kr + Xe and CO contents on burnup and temperature in HTGR ThO_2 particles. Final results of this work are being published,[2,3] an abstract of one of these reports[2] is presented below:

> Microspheres of ThO_2 and $Th_{0.81}U_{0.19}O_2$ have been irradiated in the form of High-Temperature Gas-Cooled Reactor (HTGR) particles. This resulted in the buildup of CO, as well as Kr + Xe, within the particle. The particles were later equilibrated at a temperature of $1325 \leqslant T \leqslant 2270$ K, crushed, and the CO and Kr + Xe were measured. Oxygen release as CO can be represented by the expression $O/f = 74.6\ F \exp(-7400/T)$, where O/f is the moles of oxygen released per mole of fissioned actinide, F is fractional fissions per initial heavy-metal atom, and, T is the equilibration temperature. This oxygen release is reasonably consistent with that predicted from thermodynamic data for the oxides of the fuel and fission products. Release of Kr and Xe to the void space within the particle was consistent with published data and approached the theoretical value of $\sim$0.32 moles per mole of fissioned actinide.

4.4 THE CHEMICAL BEHAVIOR OF HTGR FISSILE FUELS — T. B. Lindemer

This work has been concerned primarily with the thermodynamic interpretation of the irradiation behavior of HTGR fissile fuel, particularly the weak-acid-resin-derived (WAR) UO_2-UC_2 particle. The results of this analysis are incorporated in a report[4] whose abstract appears below:

> Two fuel failure mechanisms have been identified for coated particle fuels which are directly related to fuel kernel stoichiometry. These mechanisms are thermal migration of the kernel through the coating layers and chemical interaction between rare-earth fission products and the SiC layer (the primary barrier to diffusion of metal fission products out of the particle) leading to failure of the SiC layer. Thermal migration appears to be most severe for oxide fuels, while chemical interaction is most severe with carbide systems.
>
> Thermodynamic calculations have indicated that oxide-carbide fuel kernels may permit a stoichiometry that will reduce both problems to manageable levels for the currently planned High-Temperature Gas-Cooled Reactors. Such stoichiometry adjustment is possible over the complete

spectrum from UO_2 to UC_2 for the present recycle fuel, a weak-acid-resin-derived (WAR) fissile kernel. The thermodynamic calculations indicate that WAR kernels containing <15% UC_2 (>85% UO_2) will develop excessive CO overpressures within the particle during irradiation; in 100% UO_2 particles thermal migration and oxidation of the SiC layer have been observed after irradiation. The calculations also indicate that WAR kernels containing >70% UC_2 (<30% UC_2) will contain insufficient oxygen to oxidize the rare-earth fission products formed in fuel operated to the maximum burnup levels of 75% fissions per initial metal atom (75% FIMA). Instead, the rare earths are present in part or completely as dicarbides. As such they have been observed to segregate from the kernel and collect at the SiC interface on the cold side of the particle, react with the SiC, and eventually fail this coating.

Five WAR kernel stoichiometries have been irradiated. These are either UO_2 kernels, UO_2 plus 15, 50, or 75% UC_2, or 100% UC_2. The results of these tests are consistent with the thermodynamic calculations. Additional tests are in progress to establish the optimum stoichiometry; preliminary indications suggest an optimum value of about 35% conversion with a permissible range of ±20%.

4.5 LOSS OF UC_2 FROM WAR KERNELS — R. L. Pearson and T. B. Lindemer

A report[5] describes the results of an investigation of the loss of UC_2 from Biso particles containing UC_2. The abstract of this report[5] follows:

Recycle fuel for the High-Temperature Gas-Cooled Reactor (HTGR) contains a weak-acid-resin (WAR) kernel, which consists of a mixture of UC_2, UO_2, and free carbon. At 1900°C, Biso-coated WAR UC_2 or UC_2-UO_2 kernels lose a significant portion of their uranium in several hundred hours. The UC_2 decomposes and uranium diffuses through the pyrolytic carbon coating. The rate of escape of the uranium is dependent on the temperature and the surface area of the UC_2, but not on a temperature gradient. The apparent activation energy for uranium loss, ΔH, is ~90 kcal/mole. Calculations indicate that uranium loss from the kernel would be insignificant under conditions to be expected in an HTGR.

4.6 INTERACTION OF SiC WITH LANTHANIDE DICARBIDES — R. L. Pearson and T. B. Lindemer

Extensive irradiation experiments have demonstrated the presence of Nd, La, Ce, and Pr at chemical reaction interfaces involving SiC in carbide-fueled Triso particles.[4,6] Irradiation of the WAR UO_2-UC_2 fuels initially containing <75% UC_2 also reveals the presence of these same fission-product elements, in apparently lower concentrations, at the pyrocarbon-SiC interface, but reaction with SiC is apparently absent or not as prevalent as with the carbide fuels.[4] (In Triso oxide fuels no such interactions are observed.) Laboratory investigations with irradiated Triso fuels are being conducted elsewhere;[7] these studies are to be complemented by experiments conducted at ORNL with as-coated Triso particles containing kernels of specific fission-product systems. The proposed ORNL experiments will establish quantitative reaction rate data under known thermodynamic conditions.

Correlation of irradiation results with an extensive analysis of the relevant thermodynamic literature suggests two primary considerations for ORNL experiments. These are the partial pressures of the fission-product metals (P_{Me}) and the oxygen pressure (P_{O_2}) in the system. The element is the most predominant gaseous species over the fission-product metal dicarbides, with P_{Me} at a given temperature differing by many orders of magnitude for different species (e.g., La vs Sm). In turn, P_{O_2} determines whether the fission-product dicarbide or oxide will be present and also influences P_{Me}. Consideration of all these factors suggests that the experimental program should initially consider four kernel compositions that will bracket the extremes of P_{Me} and P_{O_2}. These are La_2O_3-LaC_2, Sm_2O_3-SmC_2, Nd_2O_3-UO_2-UC_2, and SrO-SrC_2. (The strontium system is included because strontium is known to diffuse through pyrolytic carbon coatings, and P_{Sr} is significant, about 0.1 kPa (10^{-3} atm) at 1500°C, although no Sr-SiC interaction has as yet been observed.) Many of these kernels have been synthesized with the WAR process. Additionally, dicarbides of Sr, Nd, and La have been obtained either by arc melting or from commercial vendors and have been used to prepare dicarbide kernels. All these systems exist at some time during irradiation of the range of WAR UO_2-UC_2 kernel compositions.

Laboratory experiments on the Triso-coated kernels are being performed over the temperature range 1000 to 2100°C. Two types of tests are involved; one of these employs isothermal conditions, whereas in the second a thermal gradient is maintained across the particles. Quantitative reaction rates are being determined from metallographic measurements, while reaction products and other phases present are being studied by metallographic, crystallographic, and microprobe techniques.

4.7 REFERENCES

1. T. B. Lindemer and R. L. Pearson, "Kernel Migration for HTGR Fuels from the System Th-U-Pu-C-O-N," *J. Am. Ceram. Soc.* 60: 5–14 (January–February 1977).
2. T. B. Lindemer, "Measurement and Interpretation of CO and Kr + Xe in Irradiated ThO_2-Containing HTGR Fuel Particles," submitted to *Journal of the American Ceramic Society*.
3. M. J. Kania, T. B. Lindemer, M. T. Morgan, and J M Robbins, *Irradiation Performance of HTGR Fertile Fuel in HFIR Target Capsules HT-12 to -15, Part I — Experiment Description and Fission Product Behavior*, ORNL/TM-5305 (February 1977).
4. F. J. Homan, T. B. Lindemer, F. L. Long, Jr., T. N. Tiegs, and R. L. Beatty, "Stoichiometric Effects on Performance of HTGR Fuels from the U-C-O System," submitted to *Nuclear Technology*.
5. R. L. Pearson and T. B. Lindemer, *Uranium Loss from Biso-Coated Weak-Acid-Resin HTGR Fuel*, ORNL/TM-5552 (February 1977).
6. C. B. Scott, *Thermochemical Stability of Irradiated HTGR Fuel Particles*, Gulf-GA-B-12409 (1973).
7. *HTGR Fuels and Core Development Program, Quarterly Progress Report for Period Ending February 29, 1976*, GA-A-13804, (1976) pp. 9–85.

5. COOLANT CHEMISTRY: THE STEAM-GRAPHITE REACTION

A. P. Malinauskas

5.1 INTRODUCTION

The graphite core and core support members are readily corroded by steam at normal operating temperatures. Moreover, hydrogen, carbon monoxide, and carbon dioxide are produced by the corrosion process. Radiation-induced reactions are also likely, and these reactions can produce methane in addition to the corrosion products already mentioned. The purpose of the coolant chemistry studies is to assess the consequences of the introduction of these species into the coolant circuit, primarily to identify those factors that limit acceptable steam inleakages in terms of both the magnitude of the steam ingress and its duration.

Two aspects of the coolant chemistry studies were pursued during this period; one of these concerned an examination of gaseous impurities in the Fort St. Vrain HTGR coolant during start-up to assess the significance of radiation-induced reactions in determining the coolant composition, whereas the second investigation, which was partially supported by the Division of Physical Research, involved determinations of the internal geometries of candidate core support post graphites using gas transport characterization techniques.

5.2 ANALYSIS OF COOLANT IMPURITY COMPOSITION DATA OBTAINED DURING FORT ST. VRAIN HTGR START-UP — G. L. Tingey and W. C. Morgan (Battelle, Pacific Northwest Laboratories)

Considerable reaction kinetics data have been collected over the past decade, and computational programs developed, to assist HTGR designers in setting realistic standards on helium coolant purity. The present effort seeks to verify the computer codes that have been developed and to examine the adequacy of the code input data. Information being obtained during start-up testing of the Fort St. Vrain HTGR provides a particularly unique opportunity for this purpose, because the amount of water in the primary coolant circuit has been sufficiently large to

yield measurable reaction effects, and the lower power testing has been conducted at temperatures sufficiently low that an examination of the effects of radiation-induced reactions could be made without the complexities that are introduced by the thermal reactions.

In this study, the measured gas compositions are compared with those calculated using the Graphite Oxidation Program (GOP).[1,2] These comparisons are then used to evaluate the validity of the reaction parameters used in GOP. Revisions are made where necessary to improve the accuracy of the code.

An evaluation of the rate constants used for the reaction of steam with graphite pointed out the need for more thorough measurements at higher steam pressures, where the reaction is predicted to become zero order in steam concentration. Presently, the code predicts higher rates than observed[3] in the pressure range up to 3 kPa (0.03 atm), but no data are available above that pressure. No information at high steam pressures is expected to be acquired through this program, and it therefore remains an area where further experimental work should be considered.

Initial start-up tests were conducted in April and May 1975. During these tests the power was limited to 2% of full power. Although the data were very limited, and to some extent uncertain, a comparison could be made with calculated gas compositions, and inferences drawn from the results.[4]

Start-up tests were again resumed in July 1976, and operation continued until early August. During these tests the reactor was operated at various power levels up to 27% of full power. Gas compositions were analyzed by gas chromatography sensitive to concentrations of less than 0.1 ppm. Table 5.1 lists the results of the analysis at five power levels. These levels were chosen because the power was held relatively constant for a period long enough to have a reasonable chance of nearing the steady-state gas compositions. Preliminary comparisons were made with calculations using the GOP code. The code and the input data are being adjusted to give a better fit to the experimental data. Although our analyses are not yet complete, several meaningful observations can be

Table 5.1. Measured Gas Compositions in Fort St. Vrain HTGR Coolant, July—August, 1976

Power (%)	Outlet Temperature (°C)	Content, ppm				
		H_2O	CO	CO_2	H_2	CH_4
2	240	30	0.2	0.7	22	0.3
7.5	330	50	1	3	25	1.2
11.4	390	34	1.5	2.5	33	2
19.5	450	100	2	6	80	3.5
27	500	80	3	7	30	3

made. It should be recognized that the model treats a system where the only source of impurity is leakage from outside the core. During the early stages of start-up this is certainly not true, since gases are being desorbed from the core components. One could argue that the gas compositions are entirely dictated by outgassing rates, and it is indeed true that the product ratios fall within the widely varying product ratios reported from outgassing of various grades of graphite. However, the almost steady source of gases observed at constant temperature is not consistent with the exponentially decreasing rate observed in outgassing studies. In addition, outgassing should be very slow or nonexistent when the temperature is decreased during the test below the maximum temperature to which the core has been exposed. For these reasons we tend to reject the theory that the gases observed are solely a result of outgassing. Rather it appears that chemical reactions are occurring between the graphite and the water vapor or other reactive gases. Also, reactions are expected to occur between the various gaseous components in the coolant.

Estimates using GOP predict that thermally induced reactions contribute almost insignificantly to the reaction rates at the temperatures of interest (up to 500°C). Therefore, radiolytic processes appear to be controlling the system. We are encouraged by the fact that gas product ratios appear to be reasonably close to predicted values in most cases. However, the data at 19.5 and 27% power indicate that the code is overestimating the rates of the radiolytic processes. The code will therefore

be changed to bring the prediction closer to the measured values. Studies are under way to evaluate the parameters that appear to be causing the errors. Future tests are expected to resolve some of the problems in interpretation of the data because outgassing should continue to decrease and problems in the purification system will be corrected.

5.3 GAS TRANSPORT PROPERTIES OF HTGR GRAPHITES* — R. B. Evans III, A. L. Sutton, and R. L. Towns

The major emphasis of these studies has previously focused on the diffusion of cesium either as a noble-gas precursor or as an adsorbed species in or about graphite components associated with fueled regions.[5] Experimental activities concerned the Fort St. Vrain and "reference design" reactors (which involved Great Lakes Carbon Company H-327 and H-451 graphites). A portion of the theoretical studies concerned analyses of cesium diffusion profiles in Peach Bottom HTGR surveillance specimens (involving Great Lakes HLM-85 and Speer 711 graphites). Both facets of the work have been based on attempts to approach the problem logically and systematically; this demands some knowledge of the pore structure and gas transport properties of all the material involved to resolve all the widely variable responses arising from radioactive decay, complex adsorption phenomena, and transverse forced flow. Thus, pursuing the primary objectives has forced us to expend considerable effort regarding the gas-flow characterization of various graphites, and we have now extended this effort to include core-support graphites. The two prime candidates for core support material are National Carbon ATJ graphite and Stackpole 2020 graphite.

It is of importance to note that the core support materials will never be "changed out" during a reactor lifetime. Although the fission product adsorption characteristics are of interest, the major consideration concerning core-support graphites is their long-term structural integrity, which might be undermined by possible gas-flow-controlled oxidation

---

*Supported in part by the Division of Physical Research.

reactions resulting from inleakage of trace quantities of steam. An analysis of the resulting oxidation corrosion reaction could, under certain conditions, be based on a model that states that the overall corrosion depends on the relative rates at which gaseous reactants (H_2O) and products (CO, CO_2, and H_2) can enter and exit the bulk of the material via the interconnected pores, which exist in all structural graphites.

A statement of such a model is usually given in a modified form of Fick's second law, which, for unidirectional flow along the x coordinate, takes the form

$$D_i \frac{\partial^2 C_i}{\partial x^2} - v \frac{\partial C_i}{\partial x} = \varepsilon \frac{\partial C_i}{\partial t} \pm \varepsilon S_i C_i \ . \tag{1}$$

Under the conditions of interest, interactions between reactants and products are unimportant at points removed from the actual reaction sites; thus the overall mathematical system comprises a series of binary mixtures of dilute gases denoted by subscripts i in an environment that is predominately helium, denoted by subscript 2. Terms in Eq. (1) are defined as follows:

D_i = the effective diffusion coefficient characteristic of the species i;

C_i = the concentration or density of dilute gas i;

v = the relative velocity of helium induced by transverse flow through the graphite; since helium predominates, the subscript 2 is not required;

ε = the effective total porosity of the graphite;

S_i = a source or sink term for component i, which is based on a pseudo first-order reaction.

Also note that $J_v = vC$, where $C = p/RT$ is the overall gas (helium) density and J_v is the forced flow flux due to viscous transport, p is the total pressure, and T the absolute temperature.

The system of equations denoted by Eq. (1) clearly can be applied only to discrete time intervals unless a means for predicting corrosive increases in ε as a function of time can be worked out (D and v increases may be directly proportional to some power of the ε increases). A model of this sort has been described by Malinauskas;[6] synthetic collations and/or relations have been presented by Wichner.[7] Nonetheless, Eq. (1) demonstrates the importance of the parameters pertinent to the present evaluations. Our objective, stated precisely, has been to determine structural parameters that can be used to obtain high-temperature, high-pressure extrapolations of the initial D_i and v values as well as the initial ε, which is relatively temperature insensitive. The kinetic term with the S_i is often expressed in terms of surface area rather than pore volumes; thus, associated results of surface area measurements have been included.

5.3.1 Description of the Bulk Source Graphites

Both National Carbon ATJ and Stackpole 2020 graphites can be classified as high-quality very fine-grained structural graphites. These materials exhibit a fair degree of uniformity, with the absence of flaws or vugs. Both have good machining properties and high strengths when compared with other graphites. The compressive strengths of 2020 and ATJ range about 76 and 59 MPa (11,000 and 8500 psi), respectively. Although the bulk density and open porosity of the two materials are comparable, the corresponding forced-flow parameters are quite different. For example, the permeability for helium flow parallel to the grain structure ranges about 1.0 cm^2/s for ATJ at 23°C and 0.1 MPa (1 atm) pressure compared with 0.10 cm^2/s for Stackpole 2020.

The Stackpole 2020 specimens were fabricated from four source plugs; two each of these plugs were removed from two monolithic cylindrical structures (1.81 m long by 0.27 m OD) labeled I and II.* The plugs

---

*We acknowledge the efforts of W. C. Morgan, Battelle Pacific Northwest Laboratories, Richland, Washington, regarding the acquisition and selection of the Stackpole 2020 source plugs used in these studies.

labeled I were removed at the same axial position (0.25 m from one end), but at radial locations corresponding to the outer edge and near the center. The plugs labeled II were removed at the same radial location in the second monolith, but at different axial positions (near one end and at the center). Thus we could determine 2020 parameters as a function of axial and radial position and different monoliths as well. The three ATJ specimens, on the other hand, were obtained at a common axial position at mean radial positions adjacent to one another in the same block, which measured 0.5 × 0.6 × 0.2 m. Flow specimens in each case were oriented such that flow would occur normal to the molding axis (i.e., parallel to the grain structure). Proper orientation was verified by electrical resistivity measurements.

5.3.2 Procedures and Results

5.3.2.1 Porosity and Surface Area

Both these determinations are based on equilibrium measurements; flow measurements are not involved. For the porosity determination, one first measures the bulk volume of a cylindrical specimen with calibrated micrometers, and then the solid volume in a helium pycnometer.[8] For the surface area determination, known volumes of an inert gas (usually krypton for structural graphites) are condensed on pore surfaces at a low temperature (~78 K) at several different known pressures. Correlation of the pressure-volume data in terms of the Brunauer-Emmett-Teller isotherm yields a coverage volume that can be converted to a surface area.* Porosity (ε) and surface area (SA) results obtained for the Stackpole 2020 graphite specimens are presented in Table 5.2.

Variations in the observed porosity and density values are acceptable in view of the relative positions of the specimens in the original monoliths. However, differences between surface areas for specimens I and II are somewhat surprising. We discovered that residual outgassing

---

*Surface area determinations were carried out by Mary Klipple under supervision of J. A. Cochran at ORGDP. Complete descriptions of the methodology and theory are given by: D. O. Hayward and B.M.W. Trapnell, *Chemisorption*, Butterworths, Washington, D.C., 1964.

Table 5.2. Equilibrium Gas Characterization Factors for Stackpole 2020 Graphite Specimens

Specimen	ε, Total Porosity (vol %)	ρ, Bulk Density (g/cm^3)	ρ_{He}, Solid Density (g/cm^3)	Surface Area (m^2/g)
I-A-5[a]	13.05	1.798	2.07	0.441
I-A-45[b]	12.52	1.795	2.05	0.227
II-B-4	13.60	1.789	2.07	0.707
II-E-2	13.41	1.780	2.06	0.714

[a]Center specimen.

[b]Edge specimen.

had intruded the SA experiments with the specimens I; this suggests some sort of site poisoning effect. We should note that all four specimens were outgassed together under vacuum at 1000°C for 6 hr. We plan to repeat these determinations after outgassing at 2800°C.

Equilibrium gas characterization parameters, as determined for the NCC-ATJ graphite specimens, were: ε = 15.52%, ρ = 1.738 g/cm^3, ρ_{He} = 2.06 g/cm^3, and SA = 0.14 m^2/g.

5.3.2.2 Gas Transport Characterization

Two rather basic experiments are conducted in this regard. First we subject specimens to a forced helium flow induced by a known pressure drop, Δp, to produce measured standard flow rates at various mean pressures $\langle p \rangle$. These data are combined to give a set of K versus $\langle p \rangle$ values, where K is a flow admittance called a permeability coefficient. The permeability coefficient comprises two separate coefficients, a Knudsen coefficient, related to gas-wall diffusive interactions, and a viscous-flow coefficient, which increases directly with $\langle p \rangle$ since gases exhibit marked compressive effects. Secondly, we subject the same specimens to a Graham's law determination carried out under quasi-steady-state conditions in helium-air mixtures. Since $\Delta p = 0$ in this case, viscous flow is eliminated and the results depend entirely on

diffusive effects expressed in terms of the Knudsen coefficient, D_{HeK}, again, and a mutual or normal coefficient, D_{He-air}, which depends on helium-air interactions.

Typical results for helium forced flow (permeability) experiments are displayed in Fig. 5.1. We see that K varies linearly with the mean pressure $\langle p \rangle$; this dependence is generally expressed mathematically by the equation

$$K = D_{HeK} + \Delta K \langle p \rangle / \Delta \langle p \rangle \ , \tag{2}$$

$$K = \frac{4}{3}\bar{v}K_0 + \frac{(1.013 \times 10^6)B_0}{\eta_{He}}\langle p \rangle \ . \tag{3}$$

Gas related properties are the mean thermal speed, $\bar{v}$, and the viscosity, η. Parameters reflecting the nature of the graphite structure are K_0 and B_0. The intercepts of the lines in Fig. 5.1 give D_{HeK}, whereas the slopes give viscous flow information.

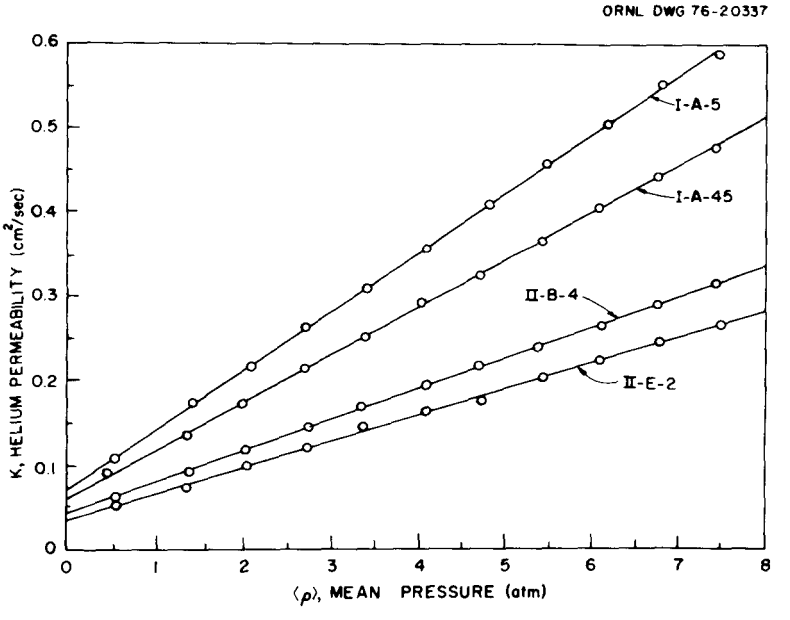

Fig. 5.1. Helium Permeability (Forced Flow) as a Function of Pressure at 24°C for Four Stackpole 2020 Graphite Specimens. Flow was perpendicular to the molding axis. 1 atm = 0.101 MPa.

Typical results for a Graham's law diffusive-flow experiment are displayed in Fig. 5.2. In this experiment the graphite specimen is attached to one end of a buret and the other end is submerged under water. After filling the buret with helium, one measures the rise of water inside the buret while maintaining equal water levels inside and outside the buret ($\Delta p = 0$). The rise occurs because helium diffuses out of the system (through the specimen at top) faster than the air can diffuse in. Thus one measures the *net* integrated volume change as a function of time.[9] If v_{He} represents the volume of helium in the buret at the beginning of the test and v_{air} the corresponding volume at the end of the experiment, then

$$v_{He}/v_{air} = (M_{air}/M_{He})^{1/2} , \tag{4}$$

where M refers to molecular mass. The theoretical ratio is 2.69: a value of 2.70 was obtained from the data in Fig. 5.2.

Correlation of the early-time portions of data curves such as that presented in Fig. 5.2 in terms of the equation for binary diffusion in porous media[10] permits extraction of a value of D'_{He-air}, where

$$D'_{He-air} = (\varepsilon'/q)D_{He-air} . \tag{5}$$

The structure-related parameter we seek is ε'/q, which is the ratio of the experimental coefficient for mutual diffusion of a gas pair through a given graphite to the free-space coefficient. With this ratio, effective coefficients for other gas mixtures can be readily computed.

Summaries of all of the gas-flow parameters obtained for Stackpole 2020 and NCC-ATJ are presented in Table 5.3. Comparisons of the forced flow parameters for these materials reveal that the permeability of Stackpole 2020 is much lower than that of ATJ. In contrast, the ε'/q values are quite similar. This type of behavior is not at all unusual; it merely reflects the different dependences of the transport coefficients on pore size.

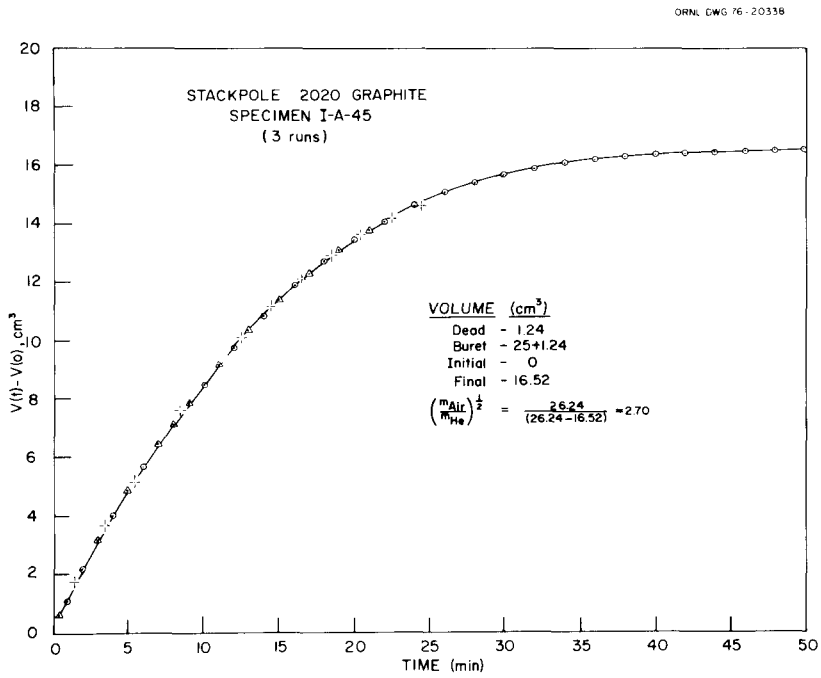

Fig. 5.2. Typical Volumetric Buildup Curves as a Function of Time at 24°C Resulting from Diffusive Flow (No Forced Flow) in a Graham's Law Experiment.

Table 5.3. Gas Flow Parameters for Graphite Specimens at 24°C

Specimen	D_{HeK}, Knudsen Coefficient (cm^2/s)	K_0 (cm)	$\Delta K/\Delta\langle p\rangle$, Viscous Flow Term ($cm^2/s$ atm)	B_0 (cm^2)	ε'/q
		Stackpole 2020			
I-A-5[a]	0.0700	4.20×10^{-7}	0.0705	1.37×10^{-11}	5.94×10^{-3}
I-A-45[b]	0.0603	3.62	0.0568	1.11	6.04
II-B-4	0.0450	2.70	0.0367	0.711	3.71
II-E-2	0.0375	2.55	0.0309	0.600	3.47
		National Carbon ATJ			
II-1[c]	0.239	1.43×10^{-6}	0.799	1.56×10^{-10}	5.51×10^{-3}
II-2	0.253	1.51	0.872	1.70	6.41
II-3	0.270	1.62	0.937	1.83	6.80

[a]Center specimen.

[b]Edge specimen.

[c]Adjacent plugs I and II had porosites 15.50 and 15.54 vol % and densities 1.743 and 1.732 g/cm^3, respectively.

5.4 REFERENCES

1. R. G. Giberson and C. A. Oster, *Computer Calculation of Reactor Graphite Oxidation*, BNWL-331 (April 1967).
2. R. C. Giberson and G. L. Tingey, *Reaction of Gaseous Impurities in a High Temperature Gas-Cooled Reactor*, BNWL-974 (December 1968).
3. *HTGR Fuels and Core Development Quarterly Progress Report for the Period Ending August 31, 1975*, GA-A-13592, Sept. 20, 1975, pp. 64–69.
4. G. L. Tingey and W. C. Morgan, "Radiolytic Reactions in the Coolant of Helium-Cooled Reactors," pp. 309–17 in *Transactions of the Symposium on Gas-Cooled Reactors with Emphasis on Advanced Systems*, Vol. 1, International Atomic Energy Agency, Vienna, 1976.
5. R. B. Evans III and A. L. Sutton, Jr., "Transport of Strongly Adsorbed Species in Porous Media," *HTGR Base-Technology Program Prog. Rep. Jan. 1, 1974– June 30, 1975*, ORNL-5108 (November 1976), p. 154.
6. A. P. Malinauskas, D. S. Joy, and S. C. Stem, "Computer Simulation of Laboratory-Scale Steam-Graphite Reaction Experiments," *HTGR Base-Technology Program Prog. Rep. Jan. 1, 1974–June 30, 1975*, ORNL-5108, pp. 227–28.
7. R. P. Wichner, *Effect of Steam Corrosion on Core Post Strength Loss: 1. Low Chronic Steam Ingress Rates*, ORNL/TM-5534 (October 1976).
8. C. G. Rall, H. C. Hamontre, and D. B. Taliaferro, *Determination of Porosity by a Bureau of Mines Method*, BMRI-5025 (February 1954).
9. T. Graham, *Phil. Mag.* 2: 175, 269, 351 (1933).
10. R. B. Evans III, L. D. Love, and E. A. Mason, *J. Chem. Educ.* 46: 423 (1969).

6. HTGR FUEL QUALIFICATION

F. J. Homan

6.1 INTRODUCTION

The National Steam Cycle HTGR Fuel Development Program is organized around four goals. They are: (1) qualification of reference initial and makeup (IM) fuel and processes, (2) qualification of reference recycle fuel and processes, (3) qualification of backup fuels and processes to the developmental references, and (4) characterization, testing, and development in support of irradiation performance evaluations. The ORNL Program also supports work on a service basis for General Atomic Company (GA) and Los Alamos Scientific Laboratory (LASL) in the areas of specimen preparation and characterization, irradiation, and postirradiation examination. The GA Program emphasizes goal 1, the ORNL Program emphasizes goal 2, and the LASL Program emphasizes advanced HTGR fuel development. The LASL Program was concluded at the end of FY 1976.

Portions of the fuel qualification work at ORNL are funded by the Thorium Utilization Program (ThU), and are reported in its Annual Report (ORNL-5266). The ThU-supported work includes the Peach Bottom Recycle Test Element Examinations and the Fort St. Vrain Test Elements. Some of the fuel qualification work is jointly supported by the HTGR Base-Technology Program and the ThU Program. This work (OF-1 and OF-2 capsules) is reported in this chapter. Some of the characterization work reported in Sect. 6.4 is also partially funded by the ThU Program.

6.2 FUEL PARTICLE PROCESS DEVELOPMENT AND QUALIFICATION — W. P. Eatherly

The work described in this section is relevant to and supported by both the HTGR Base Program and the Thorium Utilization Program. The studies on resin kernel conversion and the control of stoichiometry for the uranium oxycarbide have been completed and a topical report issued.[1] More recently, the effect of oxygen and chloride ions has been investigated, since both species are known to alter the course of polymer carbonization. In the present case, neither appears useful.

The coating process is being reviewed in the light of increased fuel densities in the reactor core for higher conversion ratios. The sensitive particle is the Biso thorium oxide. In particular, the acetylene-produced buffers are difficult to handle (soot formation) and have large standard deviations of thickness. The intent is to lay down high-density, highly reproducible buffers from MAPP gas, and subsequently react the ThO_2 with the buffer to produce both the required void volume and a reduced oxygen potential. The approach appears to be very promising.

6.2.1 Resin Kernel Property Control — J M Robbins and W. P. Eatherly

A comprehensive study of problem areas in the carbonization and conversion of weak-acid-resin-derived (WAR) fuels dominated this report period. The problems to be discussed in this report are:

1. resolution of the temperature and specific gas flow effect on conversion level,
2. possible improved carbonization procedure for WAR fuel by HCl and air additions during certain stages of carbonization.

The ratio of argon volume to the product of uranium mass and percent conversion is plotted against $1/T$ in Fig. 6.1. The predicted behavior for the two primary projected conversion reactions is shown together with the regression line fit for the experimental data. The material is apparently converting somewhat faster than is predicted by classical bulk thermodynamics for apparent measured temperature. This behavior may be attributed to effective bed temperatures somewhat above the measured temperatures and/or to a surface tension contribution from the very small radius of curvature of the pores in the kernel. Another possibility is that two conversion reactions are proceeding simultaneously. One, $UO_2 \rightarrow UC_2$, converts the UO_2 to UC_2 directly; the other, $UO_2 \rightarrow UC_{1-x}O_x \rightarrow UC_2$, goes through an intermediate oxycarbide phase. Debye-Scherrer diffraction patterns indicate the presence of the intermediate oxycarbide phase, and the divergence of the experimental data curve at the higher temperatures could be explained if the relative rates of the two reactions vary with temperature.

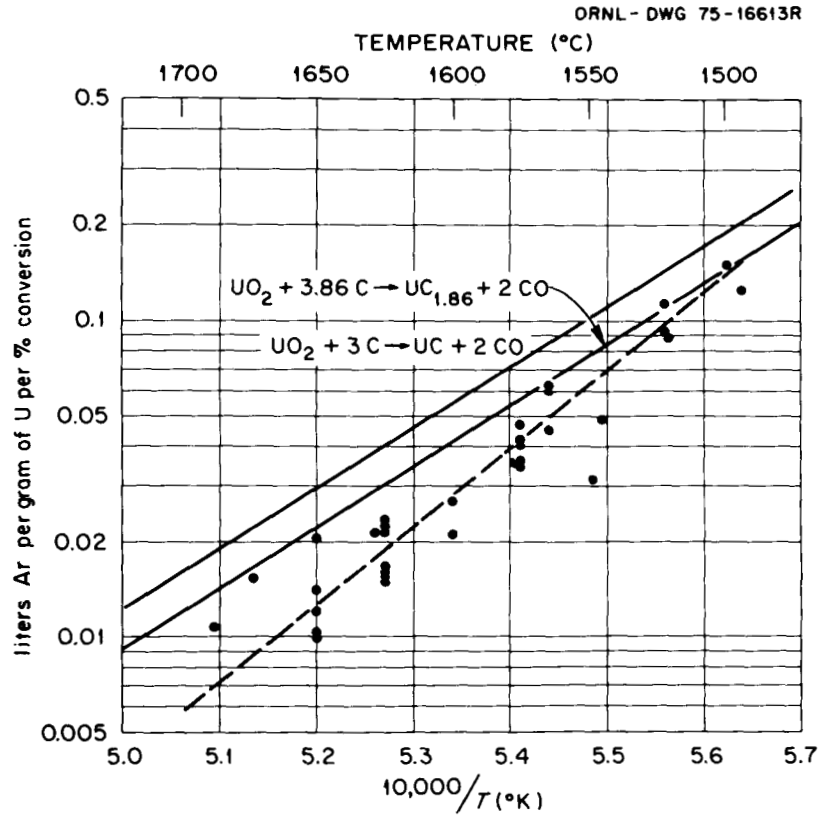

Fig. 6.1. Sweep Gas Requirement for Conversion of Weak-Acid-Resin-Derived Fuel.

We investigated the possibility of improving the carbonization procedure for weak-acid-resin-derived fuels by the introduction of HCl and air at certain stages of the carbonization cycle. The carbonization of the resin is similar to pyrolysis reactions in other hydrocarbons, so alternative approaches suggested by other work were explored. Bacon[2] has shown that substituting HCl for N_2 significantly decreases the weight loss and widens the reaction region for the pyrolysis of rayon. Similarly, substituting oxygen for argon up to the critical reaction temperature decreased the weight loss observed in pyrolysis of Villwyte rayon. To investigate the possibility of applying this information to the current resin carbonization process, air was substituted for argon during the first stages of a 1200°C carbonization process with a 40-g batch of material. The material was heated at 2°C/min in air up to 270°C, which is the approximate

temperature at which the first significant reaction occurs. At 270°C the air was replaced by argon, and the particles changed color in the manner expected when air exposure is prevented. The 270°C temperature was identified as the maximum feasible temperature for exposure to air because higher temperatures produced rapid oxidation.

Similarly, the effect of HCl was explored by installing a bubbler with concentrated HCl in the fluidizing gas line. The HCl was introduced up to 500°C in runs otherwise identical with those made with argon only and with the low-temperature air exposure. Observable bed changes were delayed by about 50 to 60°C. A yellowish film formed on the sight glass and furnace lid at approximately 1100°C. This film disappeared when exposed to air. Subsequent examination with an alpha counter showed the residue to have a significant contamination level, indicating that uranium had transferred. Adjustment of the heating procedure from 800 to 1200°C did not eliminate this problem. The normally carbonized resin is compared with those exposed to air and HCl is shown in Table 6.1.

The behavior of the HCl-exposed material was attributed to the HCl carrying considerable amounts of uranium. The substitution of air for argon in the initial stage of carbonization does not appear to produce a significantly different material. Although the carbon-to-uranium ratio was not increased, the economics of replacing the argon with air up to 270°C may be very favorable.

Table 6.1. Effect of Air and HCl Atmospheres on Carbonization of Uranium-Loaded Ion-Exchange Resin

Process	Carbon-to-Uranium Ratio	Loss, %	
		Weight	Volume
Normal	5.57	37	67
Air substituted for argon up to 270°C	5.62	37	67
HCl added up to 500°C	6.03	38	66

6.2.2 Carbon Coating Development — J M Robbins and W. P. Eatherly

Future high-temperature reactors will require fuel with increased heavy metal loadings to achieve higher ^{232}Th to ^{233}U conversions to attain more efficient fuel utilization. Minimizing coating thicknesses and complete deletion of some coatings, together with partial carbothermic reduction of the ThO_2 to create void volume tailored to metal content, are possible means of fabricating fuels with increased heavy metal loadings.

We have started studies directed toward application of buffer coatings with gases other than acetylene. The goal is twofold. Alternative coating gases would avoid the handling problems associated with acetylene; more importantly, lower standard deviations in coating thickness might be achieved in coatings with acceptable density and irradiation stability. The large standard deviation in present buffer thicknesses requires application of approximately 85-μm-mean buffer coating to meet the requirement of a minimum 50-μm thickness on the fertile particle. By lowering the standard deviation, a significant increase in heavy metal loading and potential core conversion ratio may be obtained.

Initial experiments are being performed with MAPP gas, a commercially available mixture of methylacetylene and propadiene with alkanes as stabilizers. A few runs have been made at a density of approximately 1.4 g/cm^3. Indications are that standard deviations of about one-half those obtained with acetylene are achievable; however, many more runs are necessary to statistically prove the early results.

With 1.4-g/cm^3-dense buffers, additional void volume must be provided to at least equal that in a buffer of 1.2 g/cm^3 or less in density. The first efforts to supply the additional void volume were by partial carbothermic reduction of the ThO_2 kernel. The MAPP buffer was applied and then heated to temperatures as high as 1975°C for times as long as 2.5 hr to achieve reduction. In the initial runs, conversion to ThC_2 was erratic between particles, indicating a lack of process control or some inconsistency inherent in the system. Again, this work is in its infancy and much additional work is required.

6.3 FUEL ROD FABRICATION DEVELOPMENT AND QUALIFICATION — W. P. Eatherly

Early in this report period, a development effort was undertaken to find and establish a thermosetting resin as a fuel rod binder. The objective was to avoid the in-block carbonization process, with its attendant changes in coke yield and difficulty of inspection for completed fuel rods. This program was terminated in July 1976, largely as a result of funding limitations and changes in program guidance.

At the time the work was terminated, only partial success had been obtained. Two problems, both probably surmountable, had been identified — namely, incomplete curing of the resins in the fast cycle times required and extensive cracking of the carbonized matrix due to high shrinkages of the thermosetting resins during pyrolysis.

Also reported herein is the development of a low-level technique for determining lithium in graphite. With a mass spectrometer, normal lithium is compared with a ^{6}Li spike to detect sub-parts-per-billion levels. Apparently lithium exists in nuclear graphite at levels below 5 ppb and thus is not a significant contributor of tritium to the reactor system.

6.3.1 Studies of Quick-Cure Resin Materials — J M Robbins

Most fabrication of fuel rods for irradiation testing of coated particles employs slug injection of a thermoplastic material to bond the particles together. Certain advantages would result if a suitable thermosetting binder were available.[3] Work thus far has been with the Hercules H-type resins, but this did not produce satisfactory rods.[3] New resins were procured for experimental analysis during this report period.

Seven phenolic resins from five vendors were evaluated for possible use as thermosetting binders for fabricating fuel rods. All resins were solid at room temperature and became liquid upon heating. Prolonged heating resolidified the liquid. The resins used oxalic acid, salicylic acid, or hexamethylenetetramine as the catalyst. Resin evaluation included experimental determination of coking yield, solubility in various solvents, melting or use temperature, and effect of temperature

on polymerization rate. Finally, bodies of the resins mixed with graphite flour were prepared and evaluated for use in the standard slug-injection technique for fabricating bonded fuel rods. Table 6.2 lists the coking values and the solubility of the various resins. As noted, the solvent of choice is acetone except for SP-7480, and alcohol must be used to dissolve this resin.

Table 6.2. Characteristics of Experimental Thermosetting Resins

Resin	Source	Coking Value (wt %)	Solubility				
			Acetone	Benzene	Toluene	Trichloro-ethylene	Ethyl Alcohol
PA-60-179	Polymer Applications, Inc.	42	VG	VS	VS	S	G
PA-80-219	Polymer Applications, Inc.	40	VG	I	I	VS	G
Type 518	Plastic Engineering Company	59	VG	I	I	I	F
Durez 22352	Hooker Chemical Co.	60	G	I	I	I	F
Polyrez 3827	Polyrez, Inc.	66	F	I	I	I	F
SG-3173	Schenectady Chemical Company	66	G	I	I	I	F
SP-7480	Schenectady Chemical Company	63	I	I	I	I	G

[a]Very good (VG), Good (G), Fair (F), Slight (S), Very slight (VS), Insoluble (I).

Experimental matrices were formulated with these resins by dissolving the resin in acetone (alcohol in the case of SP-7480), then adding 40 wt % −200 mesh-GLCC1074 graphite flour. The graphite flour was slurried with the resin and kept agitated until the mixture was too viscous to separate. This mix was then dried overnight in a vacuum oven at room temperature. The mixes appeared dry after being in the vacuum oven overnight, so they were powdered and placed in a sealed container. After about 24 hr the powdered mix had consolidated and bonded together, indicating that some of the solvent had been retained. A second set of mixes was made, and after drying in the vacuum oven they were powdered and spread thinly on aluminum foil and placed in the vacuum oven, again for approximately 16 hr. This time the powdered bodies did not slump and bond after being bottled. The dried powdered matrix materials were formed into pellets or slugs for use in making

slug-injected rods. All specimens were fabricated at an injection temperature and pressure of 125°C and 3.4 MPa (700 psi), respectively. Four pellets were made with each of the resins. Fabrication of the pellets was identical except for the time that each pellet was maintained at the injection temperature to promote polymerization of the resin. One pellet from each resin was held at the injection temperature for 4, 6, 8, or 10 min. At the end of the specified time interval the pressure was released, the mold cooled, and the pellet ejected. At this point all pellets looked good; they were then carbonized, unsupported, in a graphite tray. After carbonization at 900°C the pellets did not look good. Slumping on the diameter from 0.64 mm (0.025 in.) to complete puddling had occurred, depending on the particular resin. Most intact rods were badly cracked, and the particles were easily debonded. Pellets made with resin PA-80-219 were the best of the lot. However, slumping and expansion were still present, and the matrix was not as strong as required.

A redirection of funds prohibited any further work on these resins at this time. Possible ways for improving the quality of the thermosetting matrix includes the addition of higher percentages of graphite flour, using higher curing temperatures, and evaluating other resins, including the ones that are liquid at room temperature.

6.3.2 Determination of Low-Level Lithium in Graphite by Isotope Dilution Mass Spectrometry — J. R. Walton, R. L. Walker, and J. A. Carter

A method for the analysis of low-level (ppb) quantities of lithium in graphite has been developed. The lithium content of the graphite used in gas-cooled reactors should be as low as possible since the resulting tritium and helium from the $^{6}Li(n,\alpha)T$ reaction would cause serious problems from the buildup of gas and tritium activity. This study was begun to evaluate the contribution of lithium as an impurity to the possible buildup of tritium activity for HTGR-type graphite. Previous attempts to evaluate the impact of lithium, employing measurements of both atomic absorption and emission techniques, were inconclusive.

The method of analysis involves ashing the graphite in a low-temperature asher followed by isotope dilution mass spectrometry, using a spike of ^{6}Li enriched to 99.99%. A 5-g sample of graphite requires about 12 hr to ash, depending on its physical character. The ashed residue is dissolved in the spike solution, transferred to a small centrifuge cone, and evaporated to dryness. The final residue is dissolved and is loaded on prebaked, precertified lithium-free filaments and analyzed in a 0.15-m-radius (6-in.) 60° solids mass spectrometer equipped with an electron multiplier for ion detection for increased sensitivity. Only 10 ng Li gives sufficient signal for analysis.

Graphite standards have been analyzed by isotope dilution mass spectrometry and cross-checked by flame emission with the standard addition method. Satisfactory agreement (±10%) with the stated values was obtained; certified values for the standards are not expected to be better than ±5%. When highly enriched ^{6}Li (99.99%) is used as a spike, the limit of detectability has been in the sub-parts-per-billion level for 5-g samples. However, even with this sensitivity, we have chosen a reporting limit of <5 ppb, because variable levels of contamination and losses in the low-temperature asher are possible. These parameters were checked with ppm-level standards but cannot be studied fully in the low ppb concentration, because standards in this range are unavailable. After analyzing six samples of HTGR graphite for General Atomic Company in which the sample results were <5 ppb Li, we now consider that the impact of lithium as a contributor to the possible tritium activity is negligible.

6.4 CHARACTERIZATION OF PYROCARBON COATINGS — W. P. Eatherly

The work on coating characterization is of interest and is supported by both the HTGR Base Program and the Thorium Utilization Program. During the present reporting period, many of the previous techniques being investigated have been abandoned because of funding limitations and the increase in interest of coating permeability measurements.

The ORNL OPTAF equipment has been abandoned because of the rapid progress made at General Atomic with the Synchronous Micro-Polarimeter. This device utilizes the same technique of measurement as the ORNL

system but avoids the problem of sample rotation by rotating the plane of polarization of the incident light ray. The most significant accomplishment of the present report period is the recognition of sample polishing as a large source of error, which always leads to too high a value of the anisotropy. Work has continued with evaluation of a direct x-ray determination of the anisotropy (BAF) as a potential means of avoiding entirely the polishing of specimens.

The recent awareness that Biso-coated particles can become permeable during irradiation, now observed at both KFA and ORNL, has prompted a considerable effort to determine permeabilities of coatings and their relationship to microstructure. The technique being evaluated at ORNL is to compare the flow of helium and neon through the LTI and into the buffer and kernel at high temperatures and fixed times. The most intriguing result to date is that the flow does not obey gas laws but is an activated process with relatively high activation energies. Work is continuing not only to evaluate coatings before and after irradiation, but also to elucidate the mechanism involved.

6.4.1 OPTAF Techniques — W. P. Eatherly

During 1976, a comparative analysis of various means of measuring optical anisotropy was completed with the objective of determining which system or systems would be installed at ORNL. This included using ORNL personnel to operate both the Seibersdorf and General Atomic equipment. The dominant requirement is to measure equivalent Bacon Anisotropy Factors (BAF_o) of magnitude less than 1.07 with well-determined variances of about 0.006 or less.

The most severe problem encountered has been the lack of flatness of the polished particles. The flatness can be determined by observing the particle sample mount in an interferometer at a slight angle off the surface normal. Curvature of the surface is apparent by the fringe pattern changing both direction and spacing. Unless considerable care is taken in polishing, the surface normals can vary by several degrees. A 0.5° error will increase the BAF_o by about 0.001 unit.

This lack of flatness of the mount can be easily compensated for by use of a gimballed stage on the microscope. Such a stage is used on the GA-developed Synchronous Micro-Polarimeter (SMP), and Dennis Stevens of GA currently rotates the sample surface at the point under observation into normality by observing the reflected image of the source illumination and bringing this image into juxtaposition with the optical axis of the microscope. A similar technique could be employed in the Seibersdorf unit if it were also equipped with a tiltable stage.

The main difference between the Seibersdorf and SMP systems is that the Seibersdorf unit examines the reflected ray directly, whereas the SMP unit as now operated analyzes the reflected ray with a second polarizing plate. The measurements are the same in principle, but the use of an analyzer yields greater sensitivity at the cost of total light intensity. Further, the Seibersdorf design involves polarizing the light source before reflecting into the microscope axis, whereas the SMP polarizes the incident ray after reflectance. Thus, the Seibersdorf unit requires standards to measure the relative reflected intensities, while the SMP unit should be an absolute device.

The main advantages to the Seibersdorf system at this time is that it is fully engineered, is semiautomatic, and has been used extensively at a number of sites. We and GA are currently studying the SMP system to determine the means for automating it to the same degree as the Seibersdorf equipment. If no difficulties are foreseen, we intended to procure one or both units at ORNL during the next fiscal year.

6.4.2 X-Ray Diffraction Determination of BAF — C. S. Morgan, C. J. Sparks, and O. B. Cavin

A fuel particle holder that will permit determination of x-ray diffraction from the (0002) planes of a small volume of the pyrocarbon coating has been designed and constructed. The device, the Spark's anisotropy device (SAD), can then be turned 90°, and the diffraction from (0002) planes orthogonal to the first set is obtained from the

same volume of coating. To obtain sufficient intensity, more than 100 fuel particles are used. These are held in 0.89-mm (35-mil) holes in a 0.30-mm-thick (12-mil) niobium plate. Correspondingly positioned 0.1-mm (4-mil) holes are located in 0.1-mm-thick niobium sheets on each side of the center plate holding the fuel particles. The center holder can be moved in both directions so as to properly locate the fuel particles with respect to the 0.1-mm holes, allowing admission of incident x-rays and exit of the diffracted beam. The ratio of the diffracted intensities from orthogonal planes is a measure of structural anisotropy in the pyrocarbon layer.

Testing of the SAD is continuing, and sufficient intensity of the diffracted beam is readily obtainable. Several small modifications to improve performance are being made. Use of the SAD to determine anisotropy in the outer pyrocarbon coating will obviate the need for mechanical polishing. It will give a measurement representing an average value within a 0.1-mm-diam volume within the thickness of the pyrocarbon layer.

6.4.3 Permeability of Pyrocarbon Coatings — C. S. Morgan and G. L. Powell*

The permeability of pyrocarbon coatings for light inert gases has been investigated by subjecting fuel particles to high-temperature anneal in an inert gas. The amount of gas diffusing through the coating into the buffer layer is then determined by breaking the LTI in a mass spectrometer and measuring the quantity of the gas released. Where necessary, particles were preannealed 1 hr in vacuum at 1800°C to remove gases entrapped during preparation. Figure 6.2 shows the mass spectrometer response on breaking a typical fuel particle that had been annealed sufficiently to fill it with helium at 98 kPa. Fuel particles were broken one at a time, and normally emission from 14 particles was determined and results reported are the average.

Figure 6.3 shows the helium content of fuel particles from batch OR-2261-HT as a function of temperature after annealing until saturated in 98 kPa (~1 atm) of helium. Results for helium diffusion into OR-2261-HT fuel particles are also given in Table 6.3 as a function of temperature and heat treatment time.

---

*Development Division, Oak Ridge Y-12 Plant.

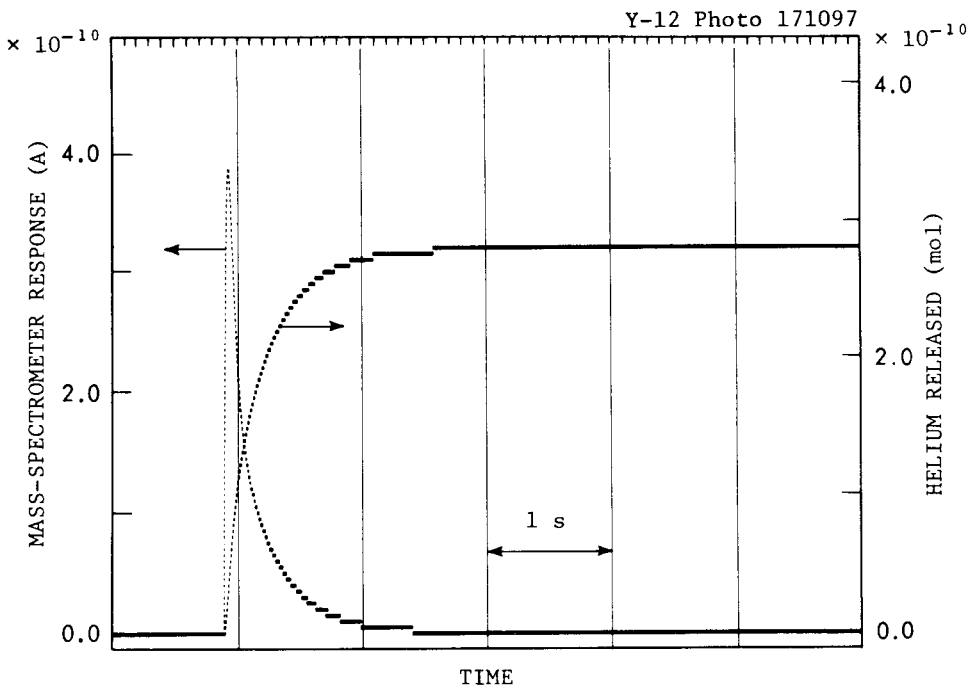

Fig. 6.2. Release of Helium Upon Crushing a Fuel Particle.

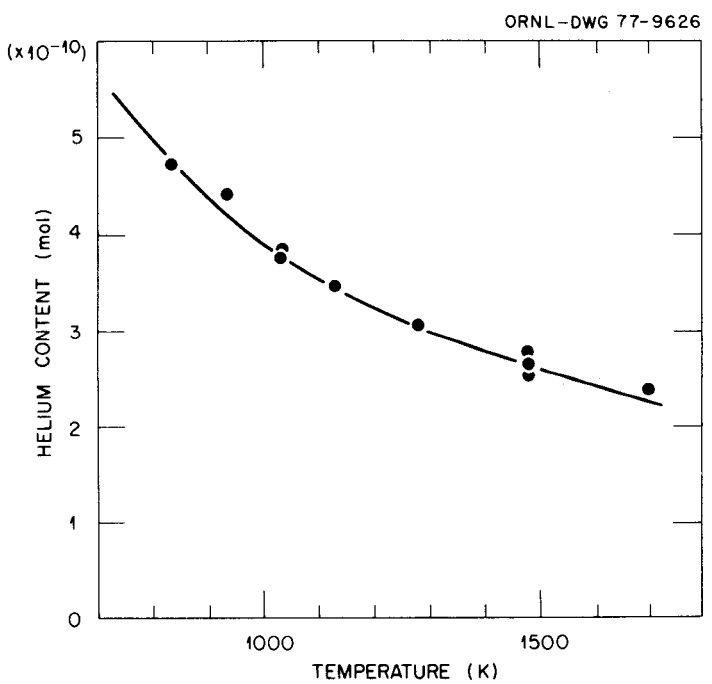

Fig. 6.3. Helium Content of Fuel Particles from Batch OR-2261-HT After Annealing in 98 kPa (∿1 atm) Helium Until Saturated.

Table 6.3. Helium Content of OR-2261-HT Fuel Particles Annealed in Helium

Temperature (°C)	Time (hr)	Helium Content, mol × 10^{-10}			Number of Particles Tested
		As Measured	Corrected to 20°C, 98 kPa	Standard Deviation	
750	1	0.11	0.39	0.02	10
840	1	0.66	2.58	0.19	11
970	1	2.3	10.04	0.3	10
1100	1	2.11	10.15	0.77	16
1200	1	3.00	15.49	0.80	10
1400	1	2.1	12.31	0.3	10
1800	0.5	2.2	15.99	0.38	6
1800	2	2.3	16.71	0.49	8
1800	4	2.2	15.97	0.31	10

On breaking the pyrocarbon coating of a fuel particle nearly all the gas is released. Small additional amounts are evolved if the broken particles are ground. This indicates that the bulk of void volume in the buffer layer is in the form of connected porosity. The additional gas released on grinding comes from small pores in the LTI and in the buffer layer structure. The standard deviation is included in Table 6.3 to indicate the variation of results among fuel particles. A substantial part of this variation is thought to be due to variations in size of the particles. The results in Table 6.3 indicate that helium pressure in the fuel particles reaches equilibrium after 1 hr at about 1200°C.

Response of the rate of helium permeation of the pyrocarbon coatings to temperature change indicates that the process is thermally activated. The activation energy for helium permeation of batch OR-2261-HT, which has a typical pyrocarbon coating, is 118 kJ/mol (28 kcal/mol).

A standard procedure to measure permeability has been developed. It consists of annealing the specimens in 50 kPa (0.5 atm) Ne and 50 kPa (0.5 atm) He at 1375°C for 1 hr. The ratio of moles of the two gases in the particles then represents a sensitive measure of the permeability. The use of two gases in the standard procedure for

determining permeability takes advantage of the sensitivity of a slower diffusing gas while the lighter, faster diffusing gas prevents mistaking the absence of gas release on breaking the pyrocarbon coating for very low permeability. It was necessary to base the neon determination on ^{22}Ne as doubly ionized argon interferes with ^{20}Ne measurement. Table 6.4 gives the Ne/He ratio for a selection of fuel particle batches. The Ne/He ratio at 1500°C is also included for some batches to show the sensitivity of the measurement to temperature. The deposition conditions are included and indicate that in general the permeability increases with increasing deposition rate. It has a less pronounced increase with increasing MAPP gas content and increasing temperature.

Table 6.4. Measurement of Permeability of Pyrocarbon Coatings[a]

Specimen	Neon/Helium Ratio		Deposition Conditions		
	1375°C	1500°C	Temperature (°C)	MAPP Gas (%)	Coating Rate (μm/min)
OR-1978-HT	0.03	0.054			0.8
OR-2263-HT	0.13	0.32	1325	25	3.6
OR-2276-HT	0.13	0.30	1275	15	3.1
OR-2273-HT	0.14		1275	25	5.2
OR-2294-HT	0.15		1275	50	3.6
OR-2299-HT	0.19		1275	50	2.3
OR-2262-HT	0.20	0.45	1275	50	6.5
OR-2261-HT	0.23	0.49	1325	50	7.4
OR-2271-HT	0.23		1275	50	10.7
OR-2293-HT	0.23		1325	50	3.9
OR-2298-HT	0.24		1325	50	2.5
OR-2297-HT	0.27		1275	100	4.9
J-489	0.28	0.59			
J-490	0.29	0.72			
OR-2265-HT	0.32	0.66	1325	100	15.7
OR-2269-HT	0.40		1325	50	12.5
OR-2531-HT	0.40				
OR-2275-HT	0.41	0.82	1275	100	23.0
OR-2296-HT	0.44		1325	100	5.6
OR-2274-HT	0.50	0.89	1325	100	28.0
OR-2537-HT	0.59				

[a]Neon/helium ratios at 1375 and 1500°C.

The argon permeability of pyrocarbon coatings was examined, and results for a few batches are given in Table 6.5. The second column gives argon content after the fuel particles were annealed under vacuum at 1800°C. The particles still retain process argon. The fourth column indicates argon content after a second 1800°C anneal, this time in an atmosphere of argon. Only fuel particle batch OR-2274-HT was sufficiently permeable to show an increase in argon content. We presume that this means that the pyrocarbon coatings of unirradiated fuel particles are impermeable to krypton and xenon.

Table 6.5. Argon Permeability Tests of LTI Coatings

Specimen	Moles Ar × 10^{10} for Each Treatment			
	1800°C Vacuum, 1 hr		1800°C Vacuum, then 1800°C Argon, 1 hr	
	Amount	Standard Deviation[a]	Amount	Standard Deviation[a]
OR-2261-HT	0.99	0.23	1.01	0.21
OR-2264-HT	1.62	0.33	1.51	0.23
OR-2265-HT	0.28	0.10	0.38	0.10
OR-2274-HT	0.25	0.09	0.51	0.08

[a]14 fuel particles tested in each case.

The effect of irradiation on the permeability of fuel particle coatings has been tested on particles with inert cores. Data on permeability of inert particles from HT-30 and -31 are given in Table 6.6 along with design fluences and temperatures. The increase in permeability indicated (i.e., higher Ne/He ratios) for particles irradiated at the higher temperatures in HT-30 is misleading, as the capsule in HT-30 was backfilled with neon. The high Ne/He ratios simply indicate that neon diffused into the particles during irradiation. The low-temperature data from HT-30 and the data from HT-31 indicate that the permeability of the pyrocarbon coatings decreased during irradiation. Whether this occurs in coatings with fissile material

Table 6.6. Permeability of Irradiated Fuel Particles

Batch	Fluence (n/m^2)	Temperature (°C)	Content per Fuel Particle, 10^{-10} mol		Ne/He
			Helium	Neon	
		HT-30			
OR-2291-HT (Blank)	0×10^{25}		1.53	0.41	0.27
OR-2291-HT (ES1)	3.5	900	1.01	0.23	0.23
OR-2291-HT (EL1)	7.2	900	1.16	0.23	0.20
OR-2291-HT (MS1)	7.5	1250	1.01	0.90	0.89
OR-2291-HT (ML1)	8.6	1250	1.12	1.41	1.26
		HT-31			
OR-2294-HT (inerts)	0×10^{25}		1.07	0.24	0.22
OR-2294-HT (inerts)	4.0	950	1.10	0.13	0.12
OR-2261-HT (included for comparison)	0		1.42	0.30	0.21

in the cores will have to be determined, but it indicates than neutron damage in the pyrocarbon does not cause an increase in the permeability.

The quantity of gas diffusing into the fuel particles can be used to calculate the void volume of the buffer layer. The void volume determined by gas content and the buffer volume determined by geometric measurements of radiographs for several fuel particle batches are given in Table 6.7. The void volumes determined agreed very well with those determined by mercury porosimetry. However, it is not certain that all void volume is included. Gas in very small pores may not be released. High-temperature annealing tests are planned to determine this.

Table 6.7. Fuel Particle Void Volume Determined by Helium Content After 1 hr at 1800°C in Helium at 97 kPa (730 torr)

Specimen	Helium Content, (mol) particle		Volume per Particle, cm^3		Buffer Volume Filled at 1800°C (%)
	Av 15 particles	Standard Deviation	Void	Buffer from Radiograph	
OR-1849	1.8×10^{-10}	0.2×10^{-10}	2.42×10^{-5}	8.0×10^{-5}	30.3
OR-1967-HT	0	0.12	1.42	6.61	21.5
OR-1972-HT	0.87	0.11	1.54	7.15	21.5
OR-1975-HT	0.88	0.12	1.56	7.05	22.1
OR-1978-HT	0.89	0.10	1.58	7.19	22.0
OR-1985-HT	0.77	0.12	1.36	7.35	18.5
OR-1986-HT	0.82	0.14	1.45	7.12	20.4
OR-1987-HT	0.75	0.14	1.33	7.53	17.7
OR-2010-HT	2.4	0.17	4.25	18.34	23.2
OR-2013-HT	0.96	0.10	1.70	8.57	19.8
OR-2261-HT	2.2		3.89	10.99	35.4

6.5 IRRADIATION TESTS IN THE HFIR TARGET FACILITY — F. J. Homan

Work during the reporting period on HT capsules included data analysis on capsules HT-17 through -19 and postirradiation examination (PIE) on capsules HT-20 through -23. The HT-20 through -23 series contained specimens for physical property measurements after irradiation (containing unfueled coated particles), and several of the specimens were broken during disassembly of the capsules. Replacement specimens were irradiated in capsules HT-31 and -32. Capsule HT-33 contained only General Atomic fuel, although some ORNL experiments were conducted in the driver rods. Irradiated capsules HT-28 through -30 were examined during the reporting period.

At the end of the reporting period capsule HT-32 was in reactor. All others were either being examined or the data were being analyzed and reports prepared.

6.5.1 Postirradiation Examination of HT-17, -18, -19 — W. P. Eatherly

Preliminary results for this capsule series were presented in the previous progress report,[4] at which time the results were ambiguous. Further data and analysis have now begun to elucidate consistent explanations for the particle behavior.

Considerable variability of the buffer coating thicknesses was observed in the final heat-treated coated particles. This was surprising in that the individual particle batches were all derived from the same seal-coat run (A-242) and buffer run (A-240) performed in a 0.13-m coater by W. J. Lackey. The data are presented in Table 6.8. The pertinent statistical variable is k, the non-central t-variable, here calculated against a minimum acceptable buffer thickness of 52 μm, 80% of the nominal minimum 65 μm buffer desired. It is noted immediately that the seal coat penetrated about 7 μm into the buffer, yielding a total thickness of about 10 μm, sufficient to be impermeable to the LTI coating gases. A varience analysis on the nine batches with presumably identical buffers yielded a within-batch variance of 6.98 μm and a between-batch variance of 2.15 μm. This latter value is just significantly different from zero at the 95% confidence level. Moreover, there is no pattern to the batch means or variances as contrasted to the coating conditions. We conclude all buffer coatings are in fact the same, and the sample size of 25 particles per batch is too small for a reliable estimate of the distribution tails. Hence, differences in failure of the irradiated particles cannot be attributed to differing buffer coatings.

Table 6.8. Statistical Analysis of Buffer Coatings on Particles for HT-17 Through -19

Batch	Description	Buffer Thickness		Degrees of Freedom	k
		Mean (μm)	Std. dev. (μm)		
A-240	Buffer only	86.86	9.73	24	
A-242	Buffer plus sealer	89.05	13.49	49	
A-242	Sized	77.98	7.99	24	
OR-1978-T	LTI Coating rate 0.8 μm/min	69.84	4.10	24	4.35
OR-1987-T	1.7	72.43	9.75	24	2.10
OR-1972-T	2.0	69.37	6.23	24	2.79
OR-1986-T	2.1	69.23	7.24	24	2.38
OR-1985-T	2.9	71.03	7.60	24	2.50
OR-1967-T	5.2	75.64	5.23	24	4.52
OR-2013-T	11.5	71.68	8.69	24	2.26
OR-1975-T	11.8	68.51	7.84	24	2.11
OR-2012-T	(3.7)	74.09	6.34	24	3.48
	Between Batches		2.15	8	
	Within Batches		6.98	216	
	Total	71.27	7.61	224	2.53

The geometrical characteristics of the LTI coatings are given in Table 6.9. Again considerable variation is observed in the k-values, calculated against a minimum acceptable thickness of 67.5 μm, 90% of the nominal minimum 75-μm coating desired. Values of k as low as 2.28 permit 5.1% of the distribution to lay below 67.5 μm at the 95% level, and even k = 3.17 yields 1.0% below 67.5 μm. Batches OR-1972 and OR-1986 would be expected to fail before full life because of anistropy; however, batches OR-1985 and OR-1967 can be considered suspect from possible pressure-vessel failure. For those batches to have obtained k-values of the order of 4.0 would require standard deviations below 2.3 and 2.7 μm, respectively, well below any value expected from the laboratory coaters.

Table 6.9. Statistical Analysis of Pyrocarbon LTI Coatings on Particles for HT-17 Through -19

Batch	LTI Coating Rate (μm/min)	LTI Thickness,[a] μm		k
		Mean	Std. Dev.	
OR-1978-T	0.8	83.9	3.6	4.556
1987	1.7	84.9	4.3	4.046
1972	2.0	78.7	4.3	2.605
1986	2.1	78.6	3.5	3.171
1985	2.9	76.4	3.9	2.282
1967	5.2	78.4	3.7	2.946
2013	11.5	84.5	3.9	4.359
1975	11.8	83.0	3.5	4.428
2012	(3.7)	100.4	3.0	10.967

[a]24 degrees of freedom for all analyses.

OPTAF (BAF_o) values for the above particle batches are summarized in Table 6.10. Also presented are the fluences at which the particles were still intact by visual examination and the fluence at which failures were observed. The entry zero in the intact rows simply indicates the particles failed before the lowest fluence at which they were observed.

Table 6.10. Anisotropy and Failure Data for Particles in HT-17 Through -19

Batch	Coating Rate (μm/min)	BAF				Results in 900°C Magazine			Results in 1250°C Magazine			Hypothesized Reason for Failure
		ORNL	KFA	Seibers-dorf	GA	Fluence, 10^{24} n/m^2		Temper-ature of Coating (°C)	Fluence, 10^{24} n/m^2		Temper-ature of Coating (°C)	
						Particles Still Intact	Particle Failure Observed		Particles Still Intact	Particle Failure Observed		
OR-1978-T	0.8	1.51		1.38	1.44	2.37	4.74	1275	0	4.73	1525	Anisotropy
OR-1987-T	1.7			1.15		3.07	6.14	1350	0	4.47	1550	Anisotropy
OR-1972-T	2.0			1.08		3.21	6.44	1350	0	4.55	1550	Anisotropy, thin LTI
OR-1986-T	2.1			1.14		0	3.42	1300	4.58	9.19	1550	Anisotropy, thin LTI?
OR-1985-T	2.9	1.03	1.026	1.065		0	3.56	1300	0	4.67	1575	Thin LTI
OR-1967-T	5.2	1.02	1.014	1.045		3.74	7.49	1375	0	4.70	1550	Thin LTI?
OR-2013-T	11.5	1.02	1.014	1.027	1.02		not tested		14.2		1575	
OR-1975-T	11.8	1.02	1.029	1.06			not tested			12.8	1500	

Reasonably good agreement on OPTAF-BAF between the various laboratories is noted, especially if one remembers that no attempt was generally made to measure the same particles and/or locations. The failure for batches with coating rates equal to or less than 2.1 μm/min can be clearly ascribed to too large a degree of anisotropy.

Temperatures of the particle surface have been computed by M. J. Kania, and are also tabulated in Table 6.10 at the terminal time for the irradiation to failure.

At the present time, batch OR-1975-T cannot be said to have failed during its design fluence of 9×10^{24} n/m^2, since it was observed only in a single irradiation well beyond design life. Failures observed otherwise can be attributed to anisotropy or LTI coating thickness, with the possible exception of batch OR-1967-T, where the coating thickness is marginal. The surprise is the outstanding behavior of batch OR-2013-T. T. B. Lindemer has measured the gas content of these particles after irradiation and found for those from HT-18 (7.67% FIMA) a 24% loss of ^{137}Cs and expected CO, Kr, and Xe contents. For those from HT-19 (13.5% FIMA) he found 28% loss of ^{137}Cs and again the expected CO, Kr, and Xe contents. The ^{137}Cs loss is that anticipated for solid-state diffusion and also implies that the coatings were impermeable. Hence the apparent success of this batch is real and cannot be attributed to permeable coatings.

The examination of micropore texture by small-angle x-ray scattering has been completed by P. Krautwasser and is shown in Fig. 6.4. Values of pore volume are relative to a standard pyrolytic. Of interest are the relatively large pore volumes and peaking at aroung 4.0 nm pore diameter exhibited by OR-2013-T. This is in sharp contrast to the other three batches with coating rates equal to or greater than 2.9 μm/min and BAFs below 1.07. Clearly OR-2013-T is unique in both microstructure and resistance to radiation-induced failure. It is also unique in that it was fabricated with CO_2 rather than argon as a diluent!

A final report is in preparation. Further data on helium and neon permeability will be obtained before the experiment will be considered complete.

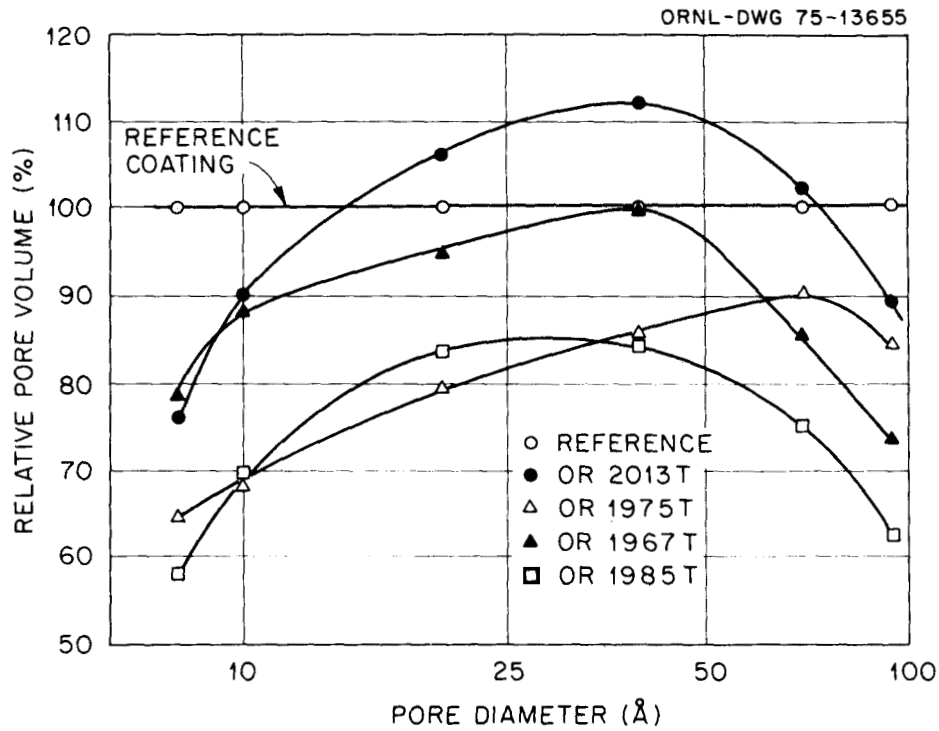

Fig. 6.4. Relative Pore Volumes of Several LTI Coatings as Measured by Small-Angle X-ray Scattering.

6.5.2 Capsules HT-20 Through -23 — J. P. Moore and T. G. Godfrey

The goal of this effort is the determination of thermal conductivity, λ; coefficient of thermal expansion, CTE; electrical resistivity, ρ; and absolute Seebeck coefficient, S, of simulated bonded fuel sticks as a function of particle volume loading, temperature, and neutron fluence. This experiment has been described in detail.[6,7]

Numerous cylindrical specimens were fabricated with nominal OD, ID, and length of 10.16, 3.175, and 50.8 mm, respectively. These specimen batches included extruded material with nominal particle volume loadings of 0, 13, 25, and 35% in addition to a batch of slug-injected (intrusion bonded) material with loadings near 60%. Fuel particles were simulated with Biso carbon-coated carbon kernels. The λ measurements required attachment of a heater and a heat sink to opposite ends of each specimen. These attachments prevented irradiation in HFIR after λ measurements.

For this reason, the five most uniform and homogeneous specimens of each loading were selected for the measurement series on the premise that neutron fluence would have the same effect in all specimens with the same particle loading.

Values of the ρ, λ, and CTE of all unirradiated specimens were reported previously,[7] and most effort this year was devoted to measurements on irradiated specimens. All CTE data are presented in Table 6.11, and values calculated from the equations at 298 and 973 K are also given. Before irradiation, the CTE at a given temperature increased approximately linearly with particle loading. However, the expansion becomes insensitive to particle loading after irradiation.

Table 6.11. Coefficient of Thermal Expansion of Simulated Fuel Elements

Particle Loading (vol %)	Neutron Fluence (n/m^2)	10^6CTE, K^{-1}				
		Constants for CTE = $A + BT + CT^2$			Calculated Values	
		A	B	10^6C	298 K	973 K
0	0×10^{25}	0.273	0.00628	−2.58	1.92	3.95
0	2.02	−1.051	0.01306	−15.82	1.48	
0	4.02	0.029	0.00502	−0.78	1.45	4.17
0	8.05	−0.545	0.00790	−3.36	1.51	3.96
0	12.1	−0.221	0.00744	−3.31	1.70	3.88
13	0	0.746	0.00627	−2.59	2.38	4.39
13	2.02[a]					
13	4.03	0.076	0.00502	−0.96	1.49	4.00
13	8.05	−0.549	0.00736	−2.97	1.38	3.80
13	12.1	−0.573	0.00763	−3.43	1.40	3.60
23	0	0.762	0.00736	−3.41	2.66	4.69
23	2.26	0.451	0.00496	−1.34	1.81	5.81
23	4.5[a]	−0.387	0.00675	−2.60	1.395	3.72
23	9.0	−0.687	0.00704	−2.70	1.17	3.60
35	0	1.189	0.00708	−3.11	3.02	5.13
35	2.26	0.155	0.00650	−2.66	1.86	3.96
35	4.5					
35	9.0	0.145	0.00469	−0.96	1.46	3.81
58	0	2.027	0.00658	−2.94	3.74	5.66

[a]Results not yet available.

Although the thermal and electrical conductivities of carbons and graphites are not related directly, both depend on some of the same structural conditions within the material. Therefore, the electrical resistivity often indicates expected values for λ. Therefore, ρ was measured on all specimens studied. These results are presented in Table 6.12 and room-temperature values are shown in Fig. 6.5 as a function of neutron fluence. The extruded specimens have much lower ρ values than do the slug-injected materials at all fluences. The resistivities of the extruded specimens increase with fluence initially, saturate above about 4×10^{25} to 6×10^{25} n/m^2, and then begin to

Table 6.12. Smoothed Values of the Electrical Resistivity of Simulated Fuel Elements

Particle Loading (vol %)	Neutron Fluence (n/m^2)	Resistivity, $\mu\Omega$ m, at Each Temperature K							
		300	400	500	600	700	800	900	1000
0	0×10^{25}	17.04	16.05	15.21	14.52	13.99	13.60	13.36	13.27
0	2.02	26.60	24.15	22.00	20.17	18.65	17.43	16.52	15.92
0	4.03[a]	28.80							
0	8.05	39.25	36.20	33.40	31.00	29.00	27.20	25.60	24.20
0	12.09	67.20	63.00	59.60	56.25	53.00	50.15	47.40	45.00
13	0[a]	22.18							
13	2.02	32.06	29.21	26.70	24.53	22.72	21.25	20.13	19.36
13	4.03	34.58	31.40	28.70	26.40	24.60	23.10	22.00	
13	8.05	43.74	40.30	37.40	34.80	32.40	30.20	28.50	26.90
13	12.09	67.04	61.60	57.00	52.80	49.20	46.00	43.00	40.40
23	0	26.34	24.98	23.79	22.76	21.90	21.22	20.69	20.33
23	2.26	36.86	33.40	30.40	28.05	26.00	24.20	22.90	21.80
23	4.50	39.60	35.80	32.60	29.80	27.50	25.60	23.80	22.50
23	9.0	51.08	46.75	43.00	39.85	36.95	34.35	32.00	29.80
23	13.5[a]	90.76							
35	0	30.05	28.46	27.09	25.93	24.99	24.26	23.74	23.44
35	2.26	38.75							
35	4.50	40.15	36.60	33.60	30.80	28.40	26.35	24.60	23.50
35	9.0	51.24	46.30	42.40	39.30	36.60	34.60	33.40	32.70
35	13.5[b]								
58	0	78.52	74.12	70.08	66.40	63.09	60.14	57.55	55.32

[a]Results not yet complete.

[b]Specimen broken.

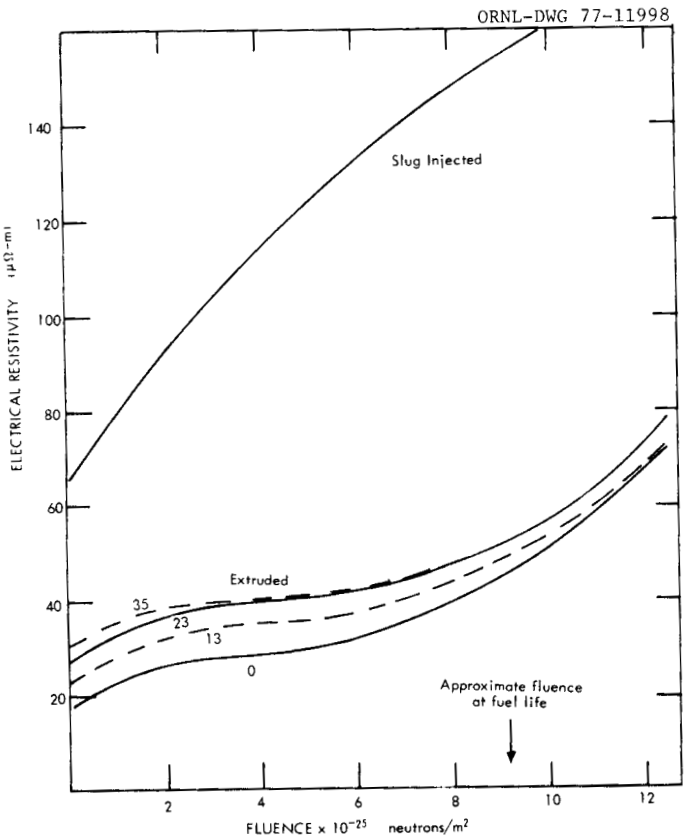

Fig. 6.5. Electrical Resistivity Versus Neutron Fluence for Extruded Specimens of Different Volume Percent Particle Loading and for Several Specimens Fabricated with a Slug-Injected Process.

increase slowly above 6×10^{25} to 9×10^{25} n/m^2. The ρ of the slug-injected specimens increases with fluence, and on the basis of the limited available data does not appear to saturate. The ρ values of several slug-injected specimens from the Fuel Cycle Technology Group were also measured at room temperature. These specimen contained ThO_2 particles with 0, 23, and 36 vol % shim and had average electrical resistivities of 91.00, 77.91, and 84.96 μΩ m, respectively. These ρ values are essentially the same as those of the slug-injected specimens used in this study.

Results given in Table 6.13 indicate that the λ of unirradiated extruded material decreases with increasing particle content, but all extruded materials have a higher λ than does the slug-injected material with 58 vol % inert particles. Johnson[8] measured λ of slug-injected

Table 6.13. Smoothed Values for the Thermal Conductivity of Simulated Fuel Elements

Particle Loading (vol %)	Neutron Fluence (n/m^2)	Thermal Conductivity, W/m K, at Each Temperature, K						
		400	500	600	700	800	900	1000
0	0×10^{25}	47.5	47.2	46.2	44.6	42.1	39.0	35.3
0	2.02	40.4	42.3	43.3	43.3	42.4	40.6	38.0
0	4.03[a]							
0	8.05[a]							
0	12.09	9.6	10.1	10.5	10.6	10.6	10.6	10.5
13	0	33.0	34.6	35.2	34.9	34.0	32.2	30.6
13	2.02	32.8	34.1	34.5	34.2	33.6	32.3	30.4
13	4.03[a]							
13	8.05	18.8	19.8	20.5	21.0	21.0	20.6	19.7
13	12.09	11.2	12.0	12.5	12.7	12.5	12.0	11.0
23	0	29.5	30.0	30.2	30.4	30.2	29.6	29.2
23	2.26	28.6	30.0	30.8	30.5	29.6	28.1	26.0
23	4.50	28.1	28.7	28.8	28.6	28.0	27.1	26.0
23	9.0	18.0	18.8	19.2	19.2	18.9	18.3	17.6
23	13.5[a]							
35	0	24.2	24.6	24.7	24.2	23.3	22.0	
35	2.26	27.6	29.0	30.0	30.2	29.6	28.0	26.0
35	4.50	22.2	24.0	25.6	26.7	27.8	28.5	28.5
35	9.0	12.5	13.4	14.2	14.4	14.0	13.0	11.5
35	13.5[b]							
58	0	10.2	10.8	11.2	11.3	11.2	10.8	10.4
58	2.34	11.8	12.0					

[a]Results not yet complete.

[b]Specimen broken.

fuel from 1223 to 1573 K and tabulated linearly extrapolated values at 873, 1073, and 1673 K. Since λ is so low, a more realistic guess would be that λ is nearly constant with temperature at 10 and 7 W/m K for the 23 and 0 vol % shim, respectively. This 23 vol % shim slug-injected specimen would contain 37 vol % fuel particles, so we compare it with the 35 vol % extruded material. In the unirradiated condition the λ ratio of extruded 35 vol % to the slug-injected specimen with 23 vol % shim would be about 2.2.

The results of Table 6.13 indicate that neutron irradiation lowers λ of matrix material (containing no inert particles) at all radiation levels. The λ of extruded material containing 35 vol % fuel particles increases with initial neutron irradiation and then decreases with irradiation above 3×10^{25} or 4×10^{25} n/m^2. The 58 vol % slug-injected material also shows an initial slight increase in λ, but data obtained on small specimens, which were not an initial part of this experiment, indicate that λ of the slug-injected material decreases with neutron fluence beyond 2×10^{25} n/m^2. According to data obtained to date, the thermal conductivity of extruded and slug-injected fuel sticks should have the approximate values listed in Table 6.14. This table indicates that the ratio of λ (extruded) to λ (slug injected) would be at least 2 at all fluences (with the one exception) and possibly higher than 4 during some irradiation stages. All subtleties of this effect may be of little consequence when we consider that the ratio of electrical resistivities varies from about 2.2 to 3.2 and that the matrix density ratio of the extruded to slug-injected material is midway between the two values (1.60/0.6 = 2.7).

Table 6.14. Thermal Conductivity of Slug-Injected and Extruded Fuel Sticks as Functions of Fluence and Temperature

Fluence (n/m^2)	Thermal Conductivity Measurements at Each Temperature					
	900 K			1400 K		
	Value, W/m K		Ratio	Value, W/m K		Ratio
	35 vol % Extruded	Slug Injected		35 vol % Extruded	Slug Injected	
0×10^{25}	23	10.5[a]	2.2	17.5	9.0[a]	1.9
2.2	30	12.4[b]	2.4	26.5	10.5[b]	2.5
4.5	29	6.4[c]	4.7	26.5	6.4[c]	4.1
9.0	14	5.0[d]	2.8	12.0	5.0[d]	2.4

[a]Measured at ORNL on a specimen with 60 vol % Biso-coated inert particles.

[b]Measured at ORNL on a specimen with 60 vol % Biso-coated inert particles and then extrapolated beyond 400 K.

[c]Estimated from ρ; a specimen exists for later measurement of λ.

[d]Extrapolated from low-temperature measurements on sample containing 20.2% shim + 36.7% particles.

6.5.3 Irradiation Experiments HT-28, -29, and -30 — R. L. Hamner

The HFIR irradiation test capsules HT-28, -29, and -30 were designed primarily to study relative fast-neutron damage resistance of pyrolytic carbon coatings on fertile and inert carbon kernels. Capsules HT-28 and -29 contained unbonded specimens of ORNL and GA fertile particles and LASL inert particles with ZrC coatings as well as hot-pressed ZrC and extruded graphite prepared by LASL. Capsule HT-30 was designed to test bonded beds (slug-injected) containing ORNL fertile particles as well as loose inert particles with ORNL coatings. Nearly all the preirradiation information relative to these experiments was previously reported.[9] However, some of this information is repeated herein for ready reference along with complementary information received since that time.

All three capsules were inserted in the HFIR on February 4, 1975. HT-28 and -30 were removed from the reactor as scheduled after four cycles on May 9, 1975. HT-29 was removed on June 3, 1975, after five cycles.

6.5.3.1 Operating History

Irradiation history for all three experiments is given in Table 6.15. Thermal and fast fluences for these experiments are given in Table 6.16; burnups for uranium (in the driver particles) and thorium are given in Table 6.17.

Table 6.15. Operating History for Capsules HT-28, -29, and -30[a]

Cycle	Begin		End		Irradiation Time, hr	
	Time	Date	Time	Date	During Cycle	Accumulated
117	1700	2/4/75	1800	2/26/75	527.76	527.76
118 A	1732	2/28/75	1726	3/6/75	143.28	671.04
119	1524	3/7/75	0233	3/30/75	539.04	1210.08
118 B	1821	3/30/75	0639	4/16/75	396.00	1606.08
120	0153	4/17/75	0400	5/9/75	529.92	2136.00
121[b]	2125	5/11/75	0918	6/3/75	539.28	2675.28

[a]HT-28, -29, and -30 were irradiated in target positions A-3, E-2, and F-7, respectively.

[b]Only HT-29 was irradiated during Cycle 121.

Table 6.16. Thermal and Fast Fluences for HT-28, -29, and -30

Specimen	Distance from HMP to Specimen Centerline		Flux, n/m^2 s		Fluence, n/m^2			
					HT-28 and -30		HT-29	
	(mm)	(in.)	Thermal <0.414 eV	Fast >0.18 MeV	Thermal	Fast	Thermal	Fast
1, 52	233.65	9.199	1.44×10^{19}	0.560×10^{19}	1.11×10^{26}	4.31×10^{25}	1.39×10^{26}	5.39×10^{25}
2, 51	226.29	8.909	1.50	0.595	1.15	4.58	1.44	5.73
3, 50	219.10	8.626	1.56	0.640	1.20	4.92	1.50	6.16
4. 49	211.94	8.344	1.62	0.665	1.25	5.11	1.56	6.40
5, 48	204.75	8.061	1.68	0.695	1.29	5.34	1.62	6.69
6, 47	197.59	7.779	1.74	0.730	1.34	5.61	1.67	7.03
7, 46	190.40	7.496	1.80	0.760	1.38	5.84	1.73	7.32
8, 45	183.24	7.214	1.86	0.790	1.43	6.07	1.79	7.61
9, 44	176.05	6.931	1.90	0.820	1.46	6.31	1.83	7.90
10, 43	168.88	6.649	1.94	0.850	1.49	6.54	1.87	8.19
11, 42	161.70	6.366	2.00	0.880	1.54	6.77	1.93	8.48
12, 41	154.53	6.084	2.06	0.909	1.58	6.99	1.98	8.75
13, 40	147.35	5.801	2.10	0.930	1.61	7.15	2.02	8.96
14, 39	106.65	4.199	2.36	1.040	1.81	8.00	2.27	10.02
15, 38	99.29	3.909	2.41	1.060	1.85	8.15	2.32	10.21
16, 37	92.10	3.626	2.46	1.075	1.89	8.27	2.37	10.35
17, 36	84.94	3.344	2.50	1.095	1.92	8.42	2.41	10.55
18, 35	77.75	3.061	2.55	1.108	1.96	8.52	2.46	10.67
19, 34	70.59	2.779	2.58	1.120	1.98	8.61	2.48	10.79
20, 33	63.40	2.496	2.62	1.130	2.01	8.69	2.52	10.88
21, 32	56.24	2.214	2.65	1.140	2.04	8.77	2.55	10.98
22, 31	49.05	1.931	2.68	1.150	2.06	8.84	2.58	11.07
23, 30	41.88	1.649	2.72	1.155	2.09	8.88	2.62	11.12
24, 29	34.70	1.366	2.75	1.160	2.11	8.92	2.65	11.17
25, 28	27.53	1.084	2.77	1.165	2.13	8.96	2.67	11.22
26, 27	20.35	0.801	2.80	1.170	2.15	9.00	2.70	11.27

Table 6.17. Burnups for HT-28, -29, and -30

Specimen	Burnup, % FIMA						
	HT-28			HT-29			HT-30
	^{235}U	^{238}U	^{232}Th	^{235}U	^{238}U	^{232}Th	^{232}Th
1, 52	84.16	10.60		84.33	13.60		4.61
2, 51			4.90			7.15	4.90
3, 50	84.22	11.50		84.37	14.70		5.12
4, 49			5.40			7.85	5.40
5, 48			5.62			8.20	5.62
6, 47	84.32	12.90		84.44	16.40		5.85
7, 46			6.10			8.80	6.10
8, 45			6.30			9.09	6.30
9, 44	84.41	14.10		84.51	17.70		6.50
10, 43			6.70			9.60	6.70
11, 42			6.90			9.89	6.90
12, 41	84.50	15.19		84.58	19.00		7.10
13, 40			7.21			10.30	7.21
14, 39	84.67	17.00		84.70	21.10		8.09
15, 38			8.21			11.40	8.21
16, 37	84.71	17.40		84.73	21.60		8.30
17, 36			8.40			11.70	8.40
18, 35			8.49			11.80	8.49
19, 34	84.77	18.00		84.78	22.20		8.59
20, 33			8.62			12.00	8.62
21, 32			8.69			12.10	8.69
22, 31	84.80	18.30		84.81	22.60		8.75
23, 30			8.80			12.20	8.80
24, 29			8.85			12.30	8.85
25, 28	84.83	18.50		84.83	22.90		8.88
26, 27			8.91			12.40	8.91

6.5.3.2 Postirradiation Examination

There was some difficulty in disassembling HT-29 because of the reaction between graphite crucibles and zirconium getters, which bonded them together. No difficulties were encountered with HT-28 and -30.

A visual inspection of the loose fertile particles tested in HT-28 and -29 is summarized in Tables 6.18 and 6.19. Practically all particles have been accounted for, but in a few instances some particles were lost during disassembly.

Stereoscopic examination of the bonded fuel rods from HT-30 revealed no unusual features or broken particles. Every rod looked to be in excellent condition. Dimensional measurements of these rods after irradiation are summarized in Table 6.20.

Table 6.18. Results of Stereoexamination of Loose Coated Particles from HT-28

Capsule Position	Specimen Lot	Design Temperature (°C)	Number of Particles			Failed (%)	Fast Fluence, >0.18 MeV (n/m^2)	Burnup (% FIMA)
			Irradiated	Intact	Failed			
2	6252-04[a]	900	34	34	0	0	4.58×10^{25}	4.90
4	6252-03[a]	900	36	35	1	2.8	5.11	5.40
5	6542-28	900	41	37	2	5.1	5.34	5.62
7	6252-05[a]	900	36	34	2	5.6	5.84	6.10
8	OR-2294-HT	900	39	37	0	0	6.07	6.30
10	OR-2266-HT	900	39	39	1	2.5	6.54	6.70
11	6542-22	900	41	31	7	18.4	6.77	6.90
13	6542-01	900	41	37	5	11.9	7.15	7.21
15	6542-28	1250	57	56	0	0	8.15	8.21
17	6542-30	1250	51	51	0	0	8.42	8.40
18	6252-04[a]	1250	47	40	3–4[b]	7–9[b]	8.52	8.49
20	6252-03[a]	1250	51	29	6–7[b]	17–19[b]	8.69	8.62
21	OR-2294-HT	1250	55	54	0	0	8.77	8.69
23	OR-2266-HT	1250	55	56	0	0	8.88	8.80
24	6542-22	1250	58	58	0	0	8.92	8.85
26	6542-01	1250	58	58	0	0	9.00	8.91
27	6542-24	1250	54	54	0	0	9.00	8.91
29	OR-2273-HT	1250	55	25	7–9[b]	22–26[b]	8.92	8.85
30	OR-2297-AHT	1250	55	55	1–2[b]	1.8–3.5[b]	8.88	8.80
32	OR-2262-HT	1250	55	53	0	0	8.77	8.69
33	6542-35	1250	57	57	0	0	8.69	8.62
35	6542-29	1250	58	58	0	0	8.52	8.49
36	6542-34	1250	58	51	0	0	8.42	8.40
38	6542-27	1250	53	53	0	0	8.15	8.21
40	6542-24	900	38	38	0	0	7.15	7.21
42	OR-2273-HT	900	39	39	0	0	6.77	6.90
43	OR-2297-AHT	900	39	39	0	0	6.54	6.70
45	OR-2262-HT	900	39	38	0	0	6.07	6.30
46	6542-35	900	40	38	2	5.0	5.84	6.10
48	6542-29	900	41	41	0	0	5.34	5.62
49	6542-34	900	41	41	0	0	5.11	5.40
51	6542-27	900	37	37	0	0	4.58	4.90

[a]Triso-coated GA particles; all others Biso coated.

[b]Estimated from coating fragments; conservative coating failure fraction.

Table 6.19. Results of Stereoexamination of Loose Coated Particles from HT-29 (Design Temperature 900°C)

Capsule Position	Specimen Lot	Number of Particles			Percent Failed	Fast Fluence, >0.18 MeV (n/m^2)	Burnup (% FIMA)
		Irradiated	Intact	Failed			
2	OR-2264	100	90	0	0	5.73×10^{25}	7.15
4	OR-2294	100	100	0	0	6.40	7.85
5	6542-22	106	102	1–2		6.69	8.20
7	6542-01	105	103	0	0	7.32	8.80
8[a]	6252-04	86	86	0	0	7.61	9.09
10[a]	6252-03	93	93	0	0	8.19	9.60
11	6542-28	104	104	0–1[b]	0–0.95	8.48	9.89
13	6542-30	93	93	0	0	8.96	10.30
15	OR-2291	59	59	0	0	10.21	11.40
17[a]	6252-04	50	50	0	0	10.55	11.70
18[a]	6252-03	54	53	0	0	10.67	11.80
20[a]	6252-05	54	53	0	0	10.88	12.00
21	6542-30	54	53	1	1.85	10.98	12.10
23	OR-2262	59	59	1[b]	1.67	11.12	12.20
24	6542-22	58	54	3–4[b]	5.36–6.9	11.17	12.30
26	6542-01	62	63	0	0	11.27	12.40
27	6542-24	54	54	0	0	11.27	12.40
29	OR-2299	59	59	0	0	11.17	12.30
30	OR-2261	59	58	0	0	11.12	12.20
32	6542-35	60	79[c]	0	0	10.98	12.10
33	6542-29	62	41[c]	0	0	10.88	12.00
35	6542-34	62	57	0	0	10.67	11.30
36	6542-27	56	54	0	0	10.55	11.70
38	OR-2290	59	59	0	0	10.21	11.40
40	6542-34	106	106	0	0	8.96	10.30
42[d]	6542-29	106	198[d]	0	0	8.48	9.89
43[a,d]	6252-05	92		0	0	8.19	9.60
45	6542-27	96	90	0	0	7.61	9.09
46	6542-24	99	99	0	0	7.32	8.80
48	OR-2298	100	23–24	0	0	6.69	8.20
49	OR-2293	100	99	0	0	6.40	7.85
51	OR-2263	100	100	0	0	5.73	7.15

[a]Triso-coated GA particles; all others Biso-coated.

[b]Estimated from coating fragments; conservative coating failure fraction.

[c]Some particles from crucible 33 mixed with 32.

[d]Particles from crucibles 42 and 43 mixed together.

Table 3.20. Summary of Results of Dimensional Measurements from HT-30

Capsule Position	Postirradiation Diameter (mm)	Postirradiation Diameter (in.)	$\Delta D/D$ (%)	Postirradiation Length (mm)	Postirradiation Length (in.)	$\Delta L/L$ (%)	Design Temperature (°C)	Fast Fluence, >0.18 MeV (n/m^2)
1	9.322	0.3670	−2.86	7.028	0.2767	−1.95	900	4.31×10^{25}
2	9.291	0.3658	−2.97	6.502	0.2560	−2.51	900	4.58
3	9.301	0.3662	−3.02	6.520	0.2567	−2.43	900	4.92
4	9.225	0.3632	−3.61	6.642	0.2615	−1.88	900	5.11
5	9.228	0.3633	−3.61	6.546	0.2577	−2.83	900	5.34
6	9.223	0.3631	−3.71	6.571	0.2587	−2.96	900	5.61
7	9.192	0.3619	−3.75	6.543	0.2576	−3.34	900	5.84
8	9.205	0.3624	−3.87	6.500	0.2559	−3.69	900	6.07
9	9.202	0.3623	−4.23	6.472	0.2548	−3.56	900	6.31
10	9.190	0.3618	−3.98	6.492	0.2556	−3.73	900	6.54
11	9.180	0.3614	−3.99	6.576	0.2589	−2.85	900	6.77
12	9.197	0.3621	−3.88	6.513	0.2564	−3.68	900	6.99
13	8.195	0.3620	−3.77	6.363	0.2505	−3.13	900	7.15
14	8.994	0.3541	−5.97	6.568	0.2586	−3.00	1250	8.00
15	8.992	0.3540	−6.10	6.533	0.2572	−5.48	1250	8.15
16	9.027	0.3554	−5.50	6.624	0.2608	−2.47	1250	8.27
17	9.007	0.3546	−6.19	6.436	0.2534	−5.90	1250	8.42
18	9.017	0.3550	−5.86	6.421	0.2528	−7.70	1250	8.52
19	9.007	0.3546	−5.67	6.464	0.2545	−5.46	1250	8.61
20	9.002	0.3544	−6.04	6.452	0.2540	−5.79	1250	8.69
21	9.027	0.3554	−5.75	6.774	0.2667	−2.31	1250	8.77
22	9.032	0.3556	−5.25	6.566	0.2585	−6.20	1250	8.84
23	9.017	0.3550	−5.46	6.591	0.2595	−6.15	1250	8.88
24	8.979	0.3535	−6.58	6.436	0.2534	−8.19	1250	8.92
25	9.014	0.3549	−5.51	6.472	0.2548	−6.43	1250	8.96
26	9.022	0.3552	−5.66	6.533	0.2572	−4.28	1250	9.00
27	9.032	0.3556	−5.63	6.452	0.2540	−6.03	1250	9.00
28	9.017	0.3550	−5.81	6.480	0.2551	−5.87	1250	8.96
29	9.007	0.3546	−6.12	6.480	0.2551	−4.28	1250	8.92
30	9.004	0.3545	−5.92	6.444	0.2537	−6.52	1250	8.88
31	9.022	0.3552	−5.68	6.627	0.2609	−3.51	1250	8.84
32	8.989	0.3539	−6.03	6.444	0.2537	−6.42	1250	8.77
33	8.984	0.3537	−6.16	6.515	0.2565	−5.73	1250	8.69
34	8.997	0.3542	−5.97	6.490	0.2555	−5.27	1250	8.61
35	9.002	0.3544	−5.69	6.525	0.2569	−4.00	1250	8.52
36	8.979	0.3535	−5.30	6.485	0.2553	−7.26	1250	8.42
37	9.025	0.3553	−5.58	6.403	0.2521	−6.32	1250	8.27
38	9.002	0.3544	−5.84	6.528	0.2570	−3.75	1250	8.15
39	9.032	0.3556	−5.58	6.528	0.2570	−4.43	1250	8.00
40	9.180	0.3614	−4.11	6.467	0.2546	−2.97	900	7.15
41	9.195	0.3620	−4.00	6.462	0.2544	−3.53	900	6.99
42	9.208	0.3625	−3.69	6.447	0.2538	−3.53	900	6.77
43	9.195	0.3620	−3.80	6.528	0.2570	−6.51	900	6.54
44	9.197	0.3621	−3.95	6.756	0.2660	−3.90	900	6.31
45	9.202	0.3623	−3.72	6.637	0.2613	−3.61	900	6.07
46	9.205	0.3624	−3.69	6.528	0.2570	−6.51	900	5.84
47	9.230	0.3634	−3.61	6.538	0.2574	−5.61	900	5.61
48	9.246	0.3640	−3.55	6.449	0.2539	−3.39	900	5.34
49	9.241	0.3638	−3.45	6.614	0.2604	−3.05	900	5.11
50	9.279	0.3653	−2.95	6.513	0.2564	−2.55	900	4.92
51	9.317	0.3668	−2.89	6.657	0.2621	−2.96	900	4.58
52	9.327	0.3672	−2.70	6.612	0.2603	−1.77	900	4.31

6.5.3.3 Chlorine Leach Analyses

Irradiated fuel rods from the high-temperature magazines of capsule HT-30 — rods 14 through 39 — and archive Biso-coated thoria particle samples from the various particle lots used to load the rods were heated with chlorine at 1000°C to determine the particle failure fraction. Five of the irradiated rods (Nos. 14, 25, 32, 36, and 39) were sent to GA for release-to-birth rate ratio (*R/B*) analysis in TRIGA before leach analysis. The *R/B* data combined with chlorine leach analyses for archive fuel rods for the five capsule portions will also be used to determine post-irradiation particle failure fraction and compared with the chlorine leach results. Chlorine leach analysis of the fuel rods from the low-temperature magazine — rods 1 through 13 and 40 through 52 — was delayed until the chlorine leach analyses of the high-temperature rods had been completed, the results reviewed, and the failure fraction obtained by *R/B* measurement compared with the chlorine leach data.

All the chlorine leach analyses were completed on the specimens from the high-temperature magazines. The data for the irradiated rods and corresponding archive particles are presented in Table 6.21. With only two exceptions, the rod and particle samples contained no defective or failed particles and, in general, the thorium recovered by chlorine leach corresponds to precision of the calorimetric thorium measurement, ±1 μg. The chlorine leach data for the archive particle sample and irradiated fuel that contained defective particles are presented in Tables 6.22 and 6.23, respectively. For both cases the sample was repeatedly chlorinated for approximately 20 hr and after each chlorination interval the thorium removed and measured.

A radiograph of a 57 archive particle sample from lot OR-2274-HT after the final chlorination showed five particles with kernels completely removed and eight particles with 5 to 90% of the kernel removed. The chlorination data and the radiograph indicate that the particle failures are due to permeable coatings. However, the corresponding irradiated rod, HT-30-24, yielded only about 1-μg Th (i.e., zero failure fraction). This disparity may be due to the rod binder infiltration sealing the particle coating in the irradiated specimen.

Table 6.21. Capsule HT-30 Chlorine Leach Analyses for Irradiated Rods and Archive Particles

Irradiated Rods[a]			Archive Particles[a]		
Capsule Position	Chlorination Time (hr)	Thorium Recovered (μg)	Specimen Lot	Chlorination Time (hr)	Thorium Recovered (μg)
14[b]	20	0.6[c]	J-489	18	0.5
15[d]	d	d	OR-2276-HT	19	0.5
16	24	1.6	OR-2298-HT	18	0.5
17	18	1.6	OR-2299-HT	18	0.5
18	18	1.6	OR-2290-HT	18	1.6
19	18	0.5	OR-2291-HT	18	1.6
20	18	1.1	OR-2293-HT	18	0.0
21	18	4.7	OR-2294-HT	20	1.1
22	18	2.1	OR-2265-HT	20	1.1
23	18	4.7	OR-2266-HT	18	0.0
24	18	1.1	OR-2274-HT	134	4504[e]
25[b]	20	0.6[c]	OR-2275-AHT	16	1.6
26	18	1.6	J-488	19	0.0
27	20	1.1	J-490	20	1.1
28	19	1.6	OR-2272-HT	20	1.1
29	19	1.1	OR-2273-HT	20	0.5
30	19	1.1	OR-2297-HT	20	1.6
31	148	919[e]	OR-2296-HT	20	0.5
32[b]	20	0.6[c]	OR-2262-HT	16	0.5
33	20	1.1	OR-2261-HT	20	0.0
34	20	1.6	OR-2271-HT	16	0.0
35	60	393	OR-2269-HT	20	0.0
36[b]	20	0.6[c]	OR-2264-HT	20	1.1
37	16	4.2	OR-2263-HT	19	0.0
38	20	2.1	OR-2295-HT	20	1.6
39[b]	20	0.6[c]	J-491	22	0.5

[a]All irradiated rods and archive particle samples contain 57 Biso-coated thoria particles equal to a thorium loading of 33.9 mg.

[b]Irradiated HT-30 rods from capsule positions 14, 25, 32, 36, and 39 sent to GA for *R/B* analyses in TRIGA prior to chlorine leach analyses.

[c]Chlorinated under extremely controlled conditions. Limit of detection — 0.4 to 0.6 μg.

[d]Irradiated HT-30 rod from capsule position 15 was destroyed during analyses due to oxygen leach in system.

[e]The thorium content of a particle is equal to 596 μg. See Tables 6.22 and 6.23.

Table 6.22. Chlorine Leach of OR-2274-HT Archive Particles

Time Interval (hr)		Thorium Recovered (μg)
19		410
19		135
19		1020
19		1115
19		760
19		472
20		592
134	Total	4504

Table 6.23. Chlorine Leach of HT-30 Irradiated Rod[a] 31

Time Interval (hr)		Thorium Recovered (μg)
19		420
19		16
22		5
20		9
20		21
20		86
28		362
148	Total	919

[a]OR-2296-HT.

The chlorine leach of irradiated rod HT-30-31 detected one defective particle with a cracked coating in the initial chlorination interval, and then permeability of the coatings developed with successive chlorination intervals. The corresponding archive particle sample, however, contained no defective particles (< 1 μg Th recovered).

6.5.3.4 Fission-Gas Release Measurements on HT-30 Fuel Compacts

Five high-temperature fuel rod specimens were selected from the HT-30 capsule for failure fraction determinations by postirradiation fission-gas release measurement. The specimens were shipped to GA for reirradiation in the TRIGA reactor. A summary describing the fertile particles contained in the fuel rod specimens is given in Table 6.24. Each fuel rod contained 57 Biso-coated ThO_2 particles, reached a burnup level of 8% FIMA, accumulated a fast fluence exposure of 8×10^{21} n/cm^2 (>0.18 MeV), and had been irradiated in the high-temperature region of the capsule (1250°C design).

To determine the *R/B* of fission gas, the amount of fissionable material present in each compact at the time the measurements are made has to be known. The ^{233}U and ^{235}U inventory for each compact is given

Table 6.24. Summary of Dimensions of Fertile Particles Used in Fuel Rod Specimens from HT-30 That Were Submitted for Fission-Gas Release Measurements

Specimen	Batch	Kernel Diameter (μm)	Buffer		Outer Isotropic Coating			
			Thickness (μm)	Density (g/cm^3)	Thickness (μm)	Density (g/cm^3)	Deposition Rate (μm/min)	OPTAF[a]
14	J-489[b]	496.8	74.7	1.17	76.9	1.904	5.8	1.01
25	OR-2275-AHT[c]	507	93.0	1.15	87.4	2.053	23.0	1.02
32	OR-2262-HT[c]	507	98.0	1.15	85.1	2.009	6.5	1.01
36	OR-2265-HT[c]	507	96.5	1.16	91.6	1.986	3.2	1.02
39	J-491[b]	495.6	83.8	1.23	75.6	2.004	9.1	1.01

[a]Measured in twofold symmetry (without analyzer) after heat treatment.

[b]Coating deposited in 5-in. (0.13-m) coating furnace.

[c]Coating deposited in 2.5-in. (65-mm) coating furnace.

in Table 6.25. The contribution from the ^{239}Pu and ^{241}Pu isotopes to the fission gas inventory is negligible because of their low concentrations; consequently, all fission gas was assumed to have resulted from uranium fissions.

The computer program used to calculate the R/B levels assumes that all the fission gas released results from fissions of ^{235}U. To account for the contribution from ^{233}U fissions, the fissile inventory was normalized to ^{235}U, and an equivalent weight of ^{235}U was calculated for each compact. This equivalent weight of ^{235}U is the amount of ^{235}U that would produce the same yield of ^{85m}Kr as all the fissionable material (^{235}U + ^{233}U) in the compacts. The thermal fission yields of ^{85m}Kr are 1.33 and 2.21% for ^{235}U and ^{233}U, respectively. The equivalent weight of ^{235}U was calculated for each compact by:

$$\text{Eq wt } ^{235}U = (\text{wt } ^{235}U) + (\text{wt } ^{233}U)\,\frac{2.21}{1.33}\,, \qquad (1)$$

and the results are given in Table 6.25.

Table 6.25. Fuel Compact Fissile Inventory

Compact Number	Fissile Inventory[a] (atom/barn-cm)		Fissile Inventory[a] (mg)[b]		Equivalent Weight of ^{235}U[c] (mg)
	^{233}U	^{235}U	^{233}U	^{235}U	
	$\times 10^{-5}$	$\times 10^{-6}$			
14	0.8088	0.6625	1.375	0.114	2.399
25	0.8268	0.7362	1.406	0.126	2.462
32	0.8122	0.6980	1.381	0.120	2.415
36	0.7843	0.6501	1.333	0.111	2.326
39	0.7923	0.6320	1.347	0.108	2.346

[a]Calculated at end of life + 120 days.

[b]Each compact assumed to have a volume of 0.4395 cm^3.

[c]The amount of ^{235}U that would produce the equivalent ^{85m}Kr yield of all fissionable material (^{233}U and ^{235}U) in the fuel compact.

Fission-gas release was measured on each compact at 1100°C in the TRIGA King furnace. The compacts were irradiated at an appropriate power level for 0.5 hr to produce approximately 10^{14} fissions. During irradiation, the released fission gases were swept with helium into a nitrogen-cooled charcoal trap. The trapped gases were assayed for fission product isotopes with a Ge(Li) detector and a 4096-channel analyzer.

To calculate the level of fuel failure in the compacts, the measured R/B data have to be corrected for fission gases released from heavy-metal contamination. The thorium contamination levels for each compact are given in Table 6.26. The gaseous release from the contamination $[R/B_{C(Th)}]$ was calculated by assuming a fractional release for contamination of 0.30. The R/B from failed fuel was determined by subtracting the $[R/B_{C(Th)}]$ from the measured EOL R/B. Particle failure levels were then calculated by using Eq. (2)

$$X = \frac{R/B_{\text{Failed Fuel}}}{r/b_f} \tag{2}$$

and assuming a fractional release for failed fuel in a constrained configuration (r/b_f) of 5×10^{-3}.

The results of these calculations are given in Table 6.26. The data indicated that no particle failure occurred during irradiation in any of the compacts. The $R/B_{C(Th)}$ was slightly higher than the measured R/B_{EOL} in four of the five compacts. This is not considered unusual in view of the low levels of fission gas release and since the thorium contamination levels were determined on companion archive compacts with an uncertainty of ±0.5 μg.

Table 6.26. Fission-Gas Release Data

Compact	Thorium Contamination[a]	$R/B_{C(Th)}$[b]	R/B_{EOL}[c]	R/B[d] Failed Fuel	Particle Failure Level[e] (%)
14	4.7×10^{-5}	14×10^{-6}	3.9×10^{-6}	0	0
25	3.2	9.6	2.2	0	0
32	1.5	4.5	12	7.5×10^{-6}	0
36	1.5	4.5	2.5	0	0
39	3.2	9.6	4.2	0	0

[a]Fraction of thorium not sealed inside the coating, as determined by chlorine leaching of archive compacts.

[b]Calculated assuming a fractional release for contamination of 0.30.

[c]R/B ^{85m}Kr measured at 1100°C.

[d]$R/B_{\text{Failed Fuel}} = R/B_{EOL} - R/B_{C(Th)}$.

[e]Calculated assuming a fractional release of 5×10^{-3} for failed fuel in a constrained geometry. Since each compact contains 57 fuel particles the calculated failure level (or level of exposed fuel) would have to be greater than 1.8% if a failed particle was present.

6.5.3.5 Permeability of LTI Coatings in HT-30

The inert particles from HT-30 that had been placed in the magazine end plugs were submitted for permeability measurements. The permeability of pyrocarbon coatings for light inert gases was found by measuring the helium and neon contents of fuel particles after annealing at 1375°C in an atmosphere of equal amounts of these gases. The neon-to-helium ratio then represents a measure of permeability and has been found to range from 0.13 to 0.60 for recently prepared unirradiated fuel particles.

The results of the permeability measurements are presented in Table 6.27. The first specimen, OR-2291-HT (Blank), represents the unirradiated results of this Biso fuel. The Ne/He ratio (0.27) observed is in the expected range based on past observations for fuel particles annealed at 1375°C for 1 hr. The ES 1 and EL 1 Ne/He ratios of 0.23 and 0.20, respectively, are essentially the same as for the unirradiated particles. These results indicate that little change in permeability was observed in the low-temperature (900°C) and low-fluence regions. For samples irradiated to higher fluences and higher temperatures (MS 1 and ML 1) the postirradiation permeability was decisively higher, indicating that the atomic disordering produced by neutron fluence increases the ease of inert gas diffusion. However, it should be noted that only about ten particles were available for each gas measurement in the mass spectrograph, and that number is inadequate for precise measurements.

Table 6.27. Permeability of Irradiated Coated Inert Particles

Batch	Fluence	Irradiation Temperature (°C)	Content Per Fuel Particle, mol[a]		Neon/Helium
			Helium	Neon	
OR-2291-HT[b] (Blank)	0×10^{-21}		1.53×10^{-10}	0.41×10^{-10}	0.27
OR-2291-HT (ES 1)	3.6	900	1.01	0.23	0.23
OR-2291-HT (EL 1)	7.2	900	1.16	0.23	0.20
OR-2291-HT (MS 1)	7.5	1250	1.01	0.90	0.89
OR-2291-HT (ML 1)	8.6	1250	1.12	1.41	1.26

[a]Gas measurement made on ten particles.

[b]Coated in same furnace run with fertile particles (also designated OR-2291-HT) then separated by density gradient column.

6.5.3.6 Other Materials

The material belonging to LASL in HT-28 and -29 was recovered and examined for LASL. The extruded graphite specimens in HT-28 and the ZrC wafers in HT-29 were dimensionally measured and photographed. No outstanding features were observed in either case. The inert particles contained in the end plugs of both experiments were retrieved, visually examined and photographed. This information and materials were shipped to LASL. The GA particles in the experiments were photographed and shipped to GA for further examination.

6.5.4 Irradiation of Capsule HT-31 — J M Robbins, R. L. Hamner, and B. H. Montgomery

Irradiation capsule HT-31 was a cooperative effort between GA, LASL, and ORNL and was designed as a four-cycle experiment operating at graphite sleeve temperatures of 950 and 1250°C. The top half of the capsule contained loose coated inert particles and loose coated normal UO_2 particles from ORNL and bonded rods from LASL and ORNL. The lower half contained loose coated fertile particles from GA and low-enriched driver particles from ORNL. Since LASL and GA submitted their own plans for the experiment, only the rationale for the ORNL portion of the experiment will be discussed here.

The ORNL objectives were as follows:

1. The primary objective of the ORNL bonded rods was to furnish supplemental data to replace that information lost when certain specimens from previous experiments (HT-20, -21, -22, and -23) were broken during disassembly. The purpose of these rods was to provide measurements of changes in thermal conductivity, electrical resistivity, thermal expansion, and dimensions as a function of particle volume loading and fast neutron fluence.

2. A secondary objective of the experiment involved furnishing coated $^{238}UO_2$ particles to more accurately determine the internal gas pressure of irradiated particles. We intended to provide particles that had 20 to 25% FIMA burnup. This information is important to the design of HTGR fuel particles. Normal UO_2 particles were used instead of $^{235}UO_2$ particles because a larger supply could be irradiated in an HT capsule.

6.5.4.1 Description of Experiment

The design of this capsule was identical to that[9] of capsule HT-28. A schematic of the capsule design is shown in Fig. 6.6.

Crucible 1 contained loose coated inert particles for coating studies and 1.024 g Re as an additional gamma heat source to obtain the 950°C graphite sleeve temperature.

Bonded rods ORNL-1 and -2 had nominal dimensions of 10.2 mm OD by 3.3 mm ID by 51 mm long (0.40 by 0.13 by 2.0 in.). Slug-injected rod ORNL-1 was unirradiated and contained about 58 vol % inert coated particles. Extruded rod ORNL-2 containing 35 vol % inert coated particles had been irradiated in experiment HT-23 for two cycles.

Small graphite holders designated U_n-16 and U_n-17 contained 0.010 g each of natural uranium as loose coated UO_2 particles. Particles in U_n-16 were Biso coated; in U_n-17 they were Triso coated. Both were derived by the sol-gel process.

The three specimens from LASL are extrusions and are described in LASL Procedure MOP-CPE-EP-1 dated September 29, 1975. Each of these bonded rods contained 0.0139 g/cm^3 of 6.5%-enriched uranium and 0.0413 g/cm^3 of thorium and had maximum dimensions of 9.78 mm diam by 21.34 mm long (0.385 by 0.840 in.). The 6.5%-enriched uranium was for heat generation early in the irradiation.

The fertile particle space in the lower half of the capsule occupied by GA is described in GA's Document HT-31-101.

Tables 6.28 through 6.30 show the properties and coating conditions for the ORNL-coated particles. All these particles were annealed at 1800°C for 10 min before insertion into the capsule. Table 6.31 shows the major properties of the ORNL bonded rods. Tables 6.32 and 6.33 show the loading scheme and heavy metal loadings, respectively, for Capsule HT-31.

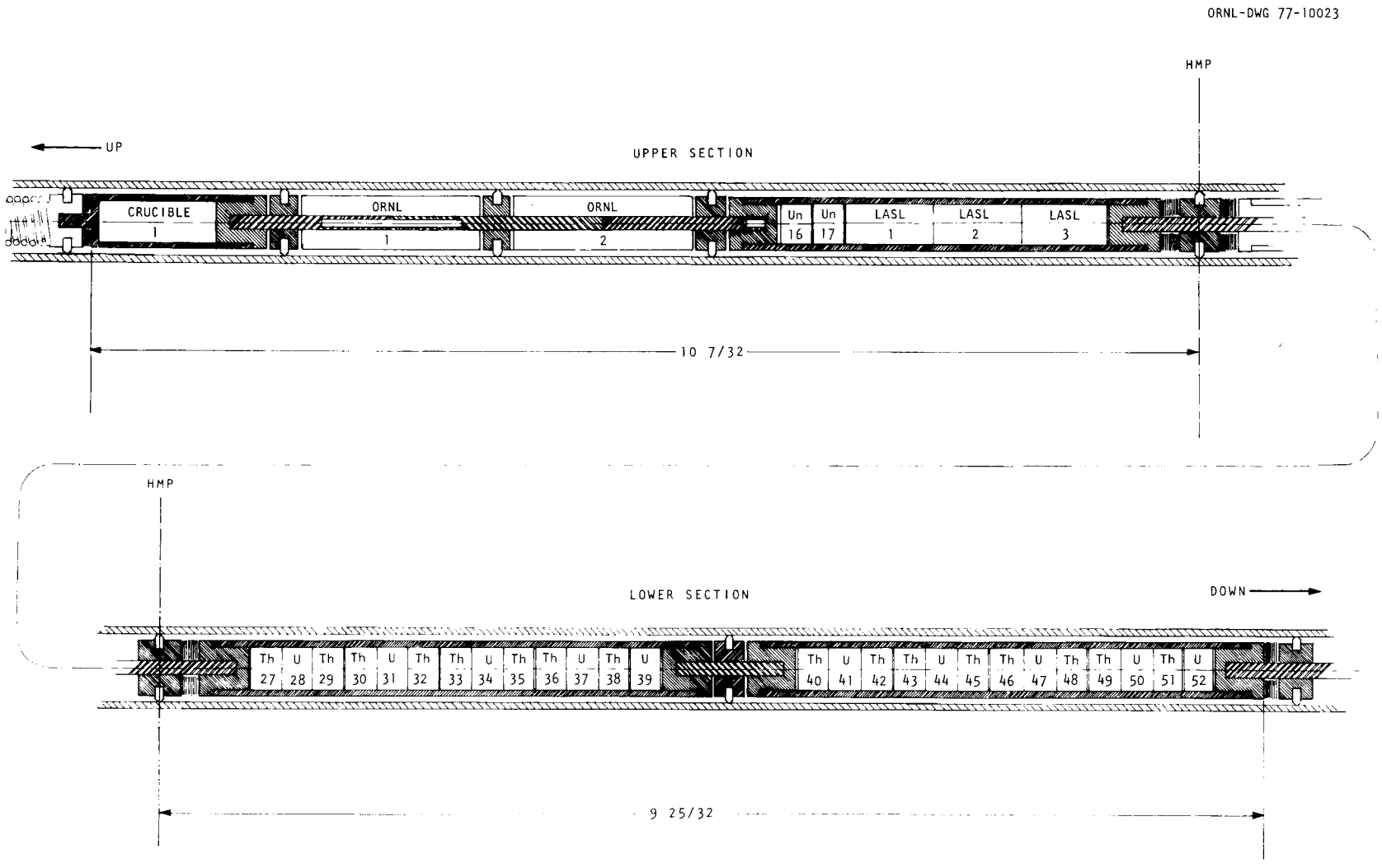

Fig. 6.6. Schematic Diagram of Sample Placement in HFIR Irradiation Capsules HT-31 and HT-32. Lengths shown are in inches. They correspond to 259.6 and 248.4 mm.

Table 6.28. Compositional Characterization of Coated Particles for HT-31[a]

Batch	Kernel Material	Uranium Content (wt %)	^{235}U Enrichment (at. %)	Positions in Capsule
OR-2305-FH	SAR carbon[b]			ORNL-1
OR-2086-H	SAR carbon			ORNL-2
OR-2511-H	sol-gel UO_2	29.10	normal	17
OR-2533-H	sol-gel UO_2	25.17	normal	16
OR-2248-H[c]	$UC_{4.86}O_{1.22}$	21.31	6.53	28, 31, 34, 37, 39 41, 44, 47, 50, 52
OR-2248-H	$UC_{4.86}O_{1.22}$	15.67	6.53	Top end plug magazines 14, 15
OR-2294-HT	SAR carbon			Crucible 1

[a]Coated at ORNL.

[b]Desulfurized strong-acid resin.

[c]With outer LTI burned off.

Table 6.29. Conditions for Coating Particles for HT-31

Batch	Buffer Coating[a] Temperature (°C)	Deposition Rate, μm/min			
		Buffer	Inner LTI[b]	SiC[c]	Outer LTI[b]
OR-2305-FH	1250	5.77			8.16
OR-2086-H	1300	5.29			5.95
OR-2511-H	1125	21.24			32.50
OR-2533-H	1125	21.24	33.03	0.25	24.33
OR-2248-H	1125	9.18	6.26	0.26	9.85
OR-2294-H	1250	5.09			3.34

[a]Deposited from C_2H_2.

[b]Deposited from MAPP gas at 1275°C.

[c]Deposited from CH_3SiCl_3 at 1550°C.

Table 6.30. Mean Dimensions and Densities[a] of Coated Particles for HT-31 Coated at ORNL

Batch	Kernel Diameter (μm)	Thickness, μm				Density, g/cm³				
		Buffer	Inner C	SiC	Outer C	Kernel	Buffer	Inner C	SiC	Outer C
OR-2305-FH	324 (18.1)	92.3 (12.7)			114.3 (7.2)	1.428	1.20			2.14
OR-2086-H	471.5 (24.6)	74			83.3 (5.5)	1.37	0.94			1.958 (0.011)
OR-2511-H	308.8 (2.9)	182.7 (16.5)			96.6 (4.3)	10.65	1.19			2.037
OR-2533-H	398.9 (2.3)	196.3 (18.2)	46.9 (3.0)	41.8 (3.7)	42.4 (2.4)	10.65	1.19	2.045 (0.016)	3.203	2.107 (0.006)
OR-2248-H	422.6 (33.9)	55.1 (11.1)	40.7 (4.8)	38.9 (1.7)	burned off	2.87	1.12	1.934 (0.008)	3.184 (0.011)	
OR-2248-H	422.6 (33.9)	55.1 (11.1)	40.7 (4.8)	38.9 (1.7)	46.8 (3.3)	2.87	1.12	1.934 (0.008)	3.184 (0.011)	2.02 (0.005)
OR-2294-HT	459.8 (29.3)	81.4 (9.6)			86.9 (4.3)	1.33	1.13			

[a]Numbers in parentheses are standard deviations.

Table 6.31. Properties of ORNL Bonded Rods for HT-31

Property	Slug-Injected ORNL-1 (2-5)	Extruded ORNL-2 (JI-179-4)	
		Before HT-23	After HT-23[a]
Dimensions, mm (in.)			
Average OD	10.155 (0.3998)	10.165 (0.4002)	9.835 (0.3872)
Average ID	3.30 (0.130)	3.33 (0.131)	3.23 (0.127)
Average length	50.084 (1.9718)	50.813 (2.0005)	48.618 (1.9141)
Matrix density, g/cm³	0.41	1.62	
Particle loading, vol %	57.4	34.8	
Electrical resistivity at 295 K, Ω-m	79.26	29.46	40.15

[a]After two cycles in HFIR capsule HT-23 and after graphite fixtures had been machined from bottom and top of specimen.

Table 6.32. Loading Scheme — Capsule HT-31

Position[a]	Type Specimen	Fuel (HM)[b]	Batch[c]	Type Coating
		Low-Temperature Zone — Upper Half		
Crucible 1	Loose particles	Carbon	OR-2294-HT	Biso
ORNL-1	Slug-injected rod; 58 vol % coated particles	Carbon	OR-2305-FH	Biso
ORNL-2	Extrusion; 35 vol % coated particles	Carbon	OR-2081-H	Biso
			OR-2084-H	Biso
			OR-2085-H	Biso
			OR-2086-H	Biso
		Magazine 16 — High-Temperature Zone — Upper Half		
16	Loose particles	Sol-gel UO_2	OR-2533-H	Triso
17	Loose particles	Sol-gel UO_2	OR-2511-H	Biso
LASL-1		Uranium	OR-2257-H	Triso
		Thorium	GA-6291 — composite 3	Biso
LASL-2	Extrusions	Carbon	LASL 76-53HT	Triso (ZrC)
LASL-3		Carbon	LASL 76-54HT	Triso (ZrC)
		Magazine 15 — High-Temperature Zone — Lower Half		
Top end plug	Loose particles	Uranium	OR-2248-H	Triso
27		Thorium	6252-05-0160-006	
28		Uranium	OR-2248-H[d]	
29		Thorium	6252-08-0161-002	
30		Thorium	6252-10-0161-002	
31		Uranium	OR-2248-H[d]	
32		Thorium	6252-09-0161-002	
33		Thorium	6252-07-0261-002	
34		Uranium	OR-2248-H[d]	
35		Thorium	6252-07-0161-002	
36		Thorium	6252-06-0261-002	
37		Uranium	OR-2248-H[d]	
38		Thorium	6252-06-0161-002	
39		Uranium	OR-2248-H[d]	
		Magazine 14 — Low-Temperature Zone — Lower Half		
Top end plug	Loose particles	Uranium	OR-2248-H	Triso
40		Thorium	6252-10-0161-001	
41		Uranium	OR-2248-H[d]	
42		Thorium	6252-09-0161-001	
43		Thorium	6252-05-0160-005	
44		Uranium	OR-2248-H[d]	
45		Thorium	6252-07-0261-001	
46		Thorium	6252-07-0161-001	
47		Uranium	OR-2248-H[d]	
48		Thorium	6252-06-0261-001	
49		Thorium	6252-06-0161-001	
50		Uranium	OR-2248-H[d]	
51		Thorium	6252-08-0161-001	
52		Uranium	OR-2248-H[d]	

[a]Refer to Fig. 6.6.

[b]All heavy metal is in combined form; the thorium is $^{232}ThO_2$ from GA.

[c]Kernel in OR-2257-H is (WAR) $UC_{5.01}O_{1.26}$; kernel in OR-2248-H is WAR $UC_{4.86}O_{1.22}$

[d]Outer LTI burned off.

Table 6.33. Heavy Metal Loadings — Capsule HT-31

Position	Loading, g			Enrichment (at. %)	Number of Particles
	Uranium	^{235}U	Thorium		
Magazine 16 — High-Temperature Zone — Upper Half					
16	0.01	<0.0001		0.7	
17	0.01	<0.0001		0.7	
LASL-1	0.0192	<0.0012	0.0396	6.36	
LASL-2	0.0180	<0.0011	0.0587	6.36	
LASL-3	0.0187	<0.0012	0.0541	6.36	
Magazine 15 — High-Temperature Zone — Lower Half					
Top end plug	0.0223	0.0014		6.5	
27			0.0334		51
28	0.0223	0.0014		6.5	
29			0.0331		80
30			0.0333		79
31	0.0223	0.0014		6.5	
32			0.0332		78
33			0.0330		78
34	0.0223	0.0014		6.5	
35			0.0332		80
36			0.0326		77
37	0.0223	0.0014		6.5	
38			0.0334		78
39	0.0223	0.0014		6.5	
Magazine 14 — Low-Temperature Zone — Lower Half					
Top end plug	0.0159	0.0010		6.5	
40			0.0223		53
41	0.0159	0.0010		6.5	
42			0.0226		53
43			0.0222		34
44	0.0159	0.0010		6.5	
45			0.0224		53
46			0.0224		54
47	0.0159	0.0010		6.5	
48			0.0220		52
49			0.0227		53
50	0.0159			6.5	
51			0.0224		54
52	0.0159	0.0010		6.5	

6.5.4.2 Operating Conditions

Capsule HT-31 was inserted into HFIR target position G-5 on March 14, 1976, and removed on June 16, 1976, after 2146.56 hr at 100-MW reactor power and delivered to the hot cells for postirradiation examination June 18, 1976. The thermal and fast fluences, irradiation history, and burnups for the capsule are presented in Tables 6.34, 6.35, and 6.36, respectively.

Table 6.34. Thermal and Fast Fluences for HT-31

Specimen	Distance From HMP to Specimen Centerline		Flux, n/m^2 s		Fluence, n/m^2	
	(mm)	(in.)	Thermal <0.414 eV	Fast >0.18 MeV	Thermal	Fast
			$\times 10^{19}$	$\times 10^{19}$	$\times 10^{26}$	$\times 10^{25}$
Crucible-1	246.38	9.700	1.33	0.482	1.03	3.72
ORNL-1	196.85	7.750	1.76	0.733	1.36	5.66
ORNL-2	139.70	5.500	2.15	0.950	1.66	7.34
U-16	92.10	3.626	2.46	1.075	1.90	8.31
U-17	84.94	3.344	2.50	1.095	1.93	8.46
LASL-1	70.59	2.779	2.58	1.120	1.99	8.65
LASL-2	49.05	1.931	2.68	1.150	2.07	8.89
LASL-3	27.53	1.084	2.77	1.165	2.14	9.00
27	−20.35	−0.801	2.80	1.170	2.16	9.04
28	−27.53	−1.084	2.77	1.165	2.14	9.00
29	−34.70	−1.366	2.75	1.160	2.13	8.96
30	−41.88	−1.649	2.72	1.155	2.10	8.93
31	−49.05	−1.931	2.68	1.150	2.07	8.89
32	−56.24	−2.214	2.65	1.140	2.05	8.81
33	−63.40	−2.496	2.62	1.130	2.02	8.73
34	−70.59	−2.779	2.58	1.120	1.99	8.65
35	−77.75	−3.061	2.55	1.108	1.97	8.56
36	−84.94	−3.344	2.50	1.095	1.93	8.46
37	−92.10	−3.626	2.46	1.075	1.90	8.31
38	−99.29	−3.909	2.41	1.060	1.86	8.19
39	−106.65	−4.199	2.36	1.040	1.82	8.04
40	−147.35	−5.801	2.10	0.930	1.62	7.19
41	−154.53	−6.084	2.06	0.909	1.59	7.02
42	−161.70	−6.366	2.00	0.880	1.55	6.80
43	−168.88	−6.649	1.94	0.850	1.50	6.57
44	−176.05	−6.931	1.90	0.820	1.47	6.34
45	−183.24	−7.214	1.86	0.790	1.44	6.10
46	−190.40	−7.496	1.80	0.760	1.39	5.87
47	−197.59	−7.779	1.74	0.730	1.34	5.64
48	−204.75	−8.061	1.68	0.695	1.30	5.37
49	−211.94	−8.344	1.62	0.665	1.25	5.14
50	−219.10	−8.626	1.56	0.640	1.21	4.95
51	−226.29	−8.909	1.50	0.595	1.16	4.60
52	−233.65	−9.199	1.44	0.560	1.11	4.33

Table 6.35. Irradiation History of HT-31

Cycle	Begin		End		Irradiation Time[a] (hr)	
	Time	Date	Time	Date	During Cycle	Accumulated
130	1732	3/14/76	2354	4/6/76	557.76	557.76
131	2124	4/7/76	2312	4/30/76	552.48	1110.24
132	2142	5/1/76	0800	5/22/76	489.60	1599.84
133	2211	5/23/76	1240	6/16/76	546.72	2146.56

[a]At 100 MW Reactor Power.

Table 6.36. Capsule HT-31 Fuel Specimens Burnups (FIMA)

Specimen	Burnups (% FIMA)		
	^{235}U	^{238}U	^{232}Th
U-16	84.71	17.40	
U-17	84.73	17.60	
LASL-1	84.77	18.00	8.59
LASL-2	84.80	18.30	8.75
LASL-3	84.83	18.50	8.88
27			8.91
28	84.83	18.50	
29			8.85
30			8.80
31	84.80	18.30	
32			8.69
33			8.62
34	84.77	18.00	
35			8.49
36			8.40
37	84.71	17.40	
38			8.21
39	84.67	17.00	
40			7.21
41	84.50	15.19	
42			6.90
43			6.70
44	84.41	14.10	
45			6.30
46			6.10
47	84.32	12.90	
48			5.62
49			5.40
50	84.22	11.50	
51			4.90
52	84.16	10.60	

6.5.4.3 Postirradiation Examination

The bonded rods as referred to above under ORNL objective 1 have been visually examined and their dimensions measured. The data are summarized in Table 6.37. The rods have been transmitted to the Physical Properties Group, who will measure and report thermal expansivities and conductivities.

The $^{238}UO_2$ particles for objective 2 appeared intact under visual examination and have been submitted for the gas pressure measurements.

The driver particles were cursorily examined to confirm previous results. These were from batch OR-2248-H with the oLTI removed in crucibles U-31, -34, -37, and -39 in the high-temperature zone and U-41, -50, and -52 in the low-temperature zone. The particles in the high-temperature zone exhibited extensive fission-product migration, as observed previously, with many broken coatings and fragments, due to the high heat generation in the loose particles combined with plutonium generation. Virtually all particles in the low-temperature crucibles survived, with the exception of a few coating fragments observed in U-41.

Inert particles (Batch OR-2294-HT) were placed in an end plug, crucible 1, for measurement of He/Ne gas permeability. This measurement is as yet qualitative but indicative of preferential diffusion of helium over neon. Large values of the ratio of neon to helium content indicate high diffusion of helium, and hence a relatively

Table 6.37. Dimensional Changes in Rods Irradiated for Thermal Property Measurement

Dimension	Average Value, mm (in.)		Change, %[a]	
	ORNL 1	ORNL 2	ORNL 1	ORNL 2[b]
Average OD	9.774 (0.3848)	10.053 (0.3958)	−3.88	−1.10
Average ID	3.250 (0.128)	3.230 (0.127)	−1.5	−3.0
Average length	48.077 (1.8928)	48.951 (1.9272)	−4.01	−3.52

[a]Changes given for OD and ID are radial.

[b]Total change from preirradiated values.

porous coating. These results are given in Table 6.38. For this low fast fluence (3.72×10^{25} n/m^2, >0.18 MeV) during which the pyrolytic coating is still tending to densify, the results indicate a significant decrease in permeability.

Table 6.38. Permeability of Irradiated Inert Fuel Particles from HT-31

Batch	Fluence (n/m^2)	Temperature (°C)	Content, mol/fuel particle		Ne/He
			Helium	Neon	
OR-2294-HT (inerts)	0		1.07×10^{-10}	0.24×10^{-10}	0.22
OR-2294-HT (inerts)	4.0×10^{25}	950	1.10	0.13	0.12
OR-2261-HT (included for comparison)	0		1.42	0.30	0.21

6.5.5 Irradiation Experiment HT-32 — J M Robbins

Irradiation capsule HT-32 is a cooperative effort between LASL and ORNL, funded by the ERDA-sponsored HTGR Fuel Development Program. The capsule is scheduled for a four-cycle HFIR irradiation beginning in mid-November, 1976. The upper half of the capsule has both loose coated particles and bonded rod specimens. The lower half of the capsule contain 16 positions for test specimens, 6 positions for driver particles, and 4 positions for heater rods containing these same driver particles, which are 7%-enriched ^{235}U, to produce fission heat during the early part of the irradiation. Also, these heater rods contain particles and matrices designed to meet certain experimental objectives. In addition to LASL and ORNL specimens, two particle batches from KFA, Jülich, West Germany, are being irradiated. Peripheral experiments involve irradiation of small, high-purity, recrystallized alumina rods placed in two of the end caps of the magazines and inert particles placed in two other end caps. The capsule was designed to explore the following objectives.

1. It is to furnish supplemental thermal conductivity data on specimens to replace information that was lost when certain specimens from previous experiments (HT-20, -21, -22, -23) were broken. Data at higher fluences are needed so that the analysis of the information obtained from HT-20, -21, -22, -23 can be completed. Two specimens were included here for that purpose.

2. It is to test fertile kernels doped with 10 at. % Al and Si as oxides and to evaluate their ability to entrap fission products such as cesium and strontium. The doped particles for this objective were supplied by KFA under the ORNL/KFA exchange agreement. These are dense thoria kernels approximately 525 μm doped with about 10 at. % alumina and silica. The purpose of the additive is to tie up cesium and strontium as aluminosilicates. This is also of interest to the HTGR Programs in the USA. KFA considers HT-32 to be a very important irradiation experiment for the further development of doped fertile particles in Germany. It plans to start a large test with spheres that will contain Triso fissile and Biso doped fertile particles. This is to be accomplished in the Spring of 1977. The information gained from the HT-32 experiment may essentially influence the decision for insertion of these spheres. German data suggest that the holdup does occur, whereas GA fails to see a holdup. It is tentatively believed that the two experiments may not be in disagreement, as the GA irradiation was at a relatively low temperature where the silicate would not be mobile. In any event, the present experiment should settle the question.

3. It is to study and evaluate the stability and permeability of LTI coatings under irradiation. It is well known that subtle differences in the microstructure of carbon coatings influence resistance to fast-neutron irradiation damage. Preferred orientation or OPTAF and the amount and type of porosity are such variables. The carbon-coated inert particles are being irradiated in this experiment to supply a large quantity of nonradioactive but neutron-damaged particles for these coating studies.

4. It is to test Biso- and Triso-coated ThO_2 particles that were prepared in a 0.24-m-diam coating furnace with a multi-inlet porous plate gas distributor. For at least three reasons the particles coated in the 0.24-m-diam coating furnace should be tested. First is the recent concern over whether commercial-size equipment can be used to deposit LTI coatings that are both impermeable and low enough in BAF value to resist neutron damage. Recent experiments show that the multi-inlet porous plate gas distributor used to coat the particles for this portion of the irradiation test is superior to conical gas distributors as far as yielding impermeable coatings with low BAF values. However, to confirm that the particles are acceptable, they must be irradiated. A second justification for irradiating these particles is to learn whether silicon carbide deposited with the 0.24-m-diam frit performs successfully. Finally, design of the 0.24-m-diam remote coater can proceed with greater confidence if this test demonstrates that coatings deposited with the large frit have satisfactory irradiation performance.

5. To further test Triso- and SiC-coated (no outer LTI) particles in warm-mold (WM) specimens with a resin binder and as loose particles. This objective will be met with specimens in the heater rod positions. Four types of coated particles are contained in the heater rods. These are (1) low-enriched, weak-acid-resin-derived (WAR) of standard Triso-coated design, (2) standard WAR Triso minus the outer LTI, (3) Triso-coated inerts, and (4) Triso inerts minus the outer LTI. The test matrix for these rods is shown in Table 6.39. The fissile particles described above are used in the driver particle holders. These types of coatings are also being irradiated in Experiment HT-33. The test matrix shown in Table 6.39 simulates some higher estimated loadings for equilibrium recycle fuel elements in a large HTGR. This experiment seeks direct comparison between Triso- and SiC-coated particles bonded by warm molding using a resin binder. The SiC-coated particles are of interest because the application and characterization of an outer LTI coating would be eliminated, higher fuel loadings could be

Table 6.39. Test Matrix for Heater Rod Specimens in HT-32[a]

Particle Type	Approximate Loading, vol %	
	950°C	1250°C
Triso fissile	12	17
Triso inert	28	23
	40	40
SiC fissile	8	12
SiC inert	32	28
	40	40

[a]These specimens are spares prepared for the previously irradidiated experiment HT-33. All are warm molded with resin binder.

incorporated in continuous-matrix fuel rods, and the problem of matrix-particle interaction would be minimized. It is also desirable to determine fuel rod integrity when no outer LTI is applied to the particles. The thermosetting resin is being used because specimens formed with such resins can be carbonized without mechanical support and without the deformation associated with pitch-type binders.

6. To evaluate high-density alumina as a potential sheathing material for thermocouples that measure centerline temperatures in irradiation experiments. There is a continuing effort to measure fuel centerline temperatures in irradiation experiments. One problem has been that the sheathing material for the thermocouple reacts under certain conditions of temperature with the fueled specimens. High-density alumina rods were placed in holes in one magazine end cap in the low-temperature region and in one magazine end cap in the high-temperature region to test this material under irradiation to determine its suitability as a thermocouple sheathing material.

6.5.5.1 Description of Experiment and Operating Conditions

Target capsule HT-32 is identical in design to HT-31. This design is shown graphically in Fig. 6.6. Each LASL bonded rod in the upper half of the capsule will contain 13.9 kg/m^3 of 6.36%-enriched uranium and 414 kg/m^3 of thorium and have maximum dimensions of 9.8 mm diam by 21.3 mm long. The enriched uranium is for heat generation in the early part of the irradiation. Specimens Th-16 and -17 are small graphite holders containing 0.0331 g Th each as coated particles. These two specimens are contained in the LASL magazine, which is designed to operate at a surface temperature of 1250°C.

The ORNL-1 and -2 bonded rod specimens are designed for an operating temperature of 950°C at each midpoint. ORNL-1 will have approximately 2.03 g W inside the Poco graphite spine as an additional gamma heat source. Crucible 1 will house inert loose particles and will need 1.024 g Re as an additional gamma heat source to obtain the 950°C surface temperature. The rhenium will be in the form of foil disks located inside the crucible, evenly distributed through the length, with layers of loose particles separating the disks. Table 6.40 shows the arrangement and the design operating temperature of the specimens in the upper half of HT-32.

The lower half of HT-32 consists of two graphite magazines, each containing 13 positions (see Fig. 6.6). The magazine adjacent to the reactor midplane was designed to operate at a specimen surface temperature of 1250°C. The lower magazine will operate at 950°C. Eight of the 13 positions in each magazine is occupied by a thorium-containing bonded rod or a Poco graphite holder housing thorium-containing loose coated particles. The remaining five positions in each magazine contain 7%-enriched coated particles either loose or in bonded rods. Table 6.41 shows the arrangement and the design operating conditions of the specimens in the lower half of HT-32.

Capsule HT-32 was inserted into HFIR on November 15, 1976, for a four-cycle irradiation. It is scheduled for removal in the middle of February 1977.

Table 6.40. Arrangement and Design Operating Conditions for the Upper Half of HT-32

Specimen Designation	Specimen Origin	Average Estimated Fast Fluence, >0.18 MeV (n/m^2)	Design Surface Temperature (°C)
Top of Capsule (T.P.)			
Crucible 1[a]	ORNL	5.0×10^{25}	950
ORNL-1[b]	ORNL	6.7	950
ORNL-2[c]	ORNL	8.6	950
Th-16[d]	ORNL	9.8	1250
Th-17[e]	ORNL	10.1	1250
LASL-1[f]	LASL	10.2	1250
LASL-2[f]	LASL	10.5	1250
LASL-3[f]	LASL	10.7	1250
Horizontal midplane			

[a]Loose inert particles with rhenium foil.

[b]Unirradiated slug-injected specimen for thermal conductivity measurements.

[c]Irradiated extruded rod for thermal conductivity measurements.

[d]Loose Triso-coated ThO_2 particles from 0.24-m-diam coater.

[e]Loose Biso-coated ThO_2 particles from 0.24-m-diam coater.

[f]Extruded rods containing coated UO_2, ThO_2, and carbon particles.

Table 6.41. Specimen Position and Design Operating Conditions for the Lower Half of HT-32

Specimen Position	Heavy-Metal Loading, g		Estimated Fast Fluence,[a] >0.18 MeV (n/m^2)	Estimated Burnup (% FIMA)			Design Surface Temperature (°C)
	U	Th		^{235}U	^{238}U	^{232}Th	
27[b]		0.0331	9.00×10^{25}			8.91	1250
28[c]	0.0268		8.96	84.83	18.50		1250
29[d]		0.0331	8.92			8.85	1250
30[e]		0.0331	8.88			8.80	1250
31[c]	0.0268		8.84	84.80	18.30		1250
32[f]		0.0331	8.77			8.69	1250
33[g]		0.0331	8.69			8.62	1250
34[c]	0.0268		8.61	84.77	18.00		1250
35[h]		0.0331	8.52			8.49	1250
36[i]		0.0331	8.42			8.40	1250
37[j]	0.0268		8.27	84.71	17.40		1250
38[k]		0.0331	8.15			8.21	1250
39[j]	0.0268		8.00	84.67	17.00		1250
40[b]		0.0234	7.15			7.21	950
41[c]	0.0191		6.99	84.50	15.19		950
42[d]		0.0234	6.77			6.90	950
43[e]		0.0234	6.54			6.70	950
44[c]	0.0191		6.31	84.41	14.10		950
45[f]		0.0234	6.07			6.30	950
46[g]		0.0234	5.84			6.10	950
47[c]	0.0191		5.61	84.32	12.90		950
48[h]		0.0234	5.34			5.62	950
49[i]		0.0234	5.11			5.40	950
50[j]	0.0191		4.92	84.22	11.50		950
51[k]		0.0234	4.58			4.90	950
52[j]	0.0191		4.31	84.16	10.60		950

[a]Estimated from HT-28 values.
[b]Rod — KFA kernel and coating; heat-treated at 1800°C.
[c]Driver particles.
[d]Rod — KFA kernel and coating; heat-treated at 1500°C.
[e]Rod — KFA kernel, ORNL coating; heat-treated at 1800°C.
[f]Rod — KFA kernel, ORNL coating; heat-treated at 1500°C.
[g]Rod with reference Biso-coated ThO_2 particle.
[h]Loose particles; KFA kernel and coating; heat-treated at 1800°C.
[i]Loose particles; KFA kernel and coating; heat-treated at 1500°C.
[j]Heater rods.
[k]Loose particles; KFA kernel, ORNL coating; heat-treated at 1800°C.

6.5.6 Capsule HT-33 — R. L. Hamner

The primary objective of HFIR capsule HT-33 was to test fertile fuel particles fabricated by GA. Both Biso and Triso particles were included, and the test plan for the experiment was prepared by General Atomic. The HT-33 capsule was designed like the HT-28 capsule,[9] with 32 loose particle holders containing thoria. The GA experiment used all 32 holders. HT-33 also employed 20 driver rods containing 7%-enriched ^{235}U to produce heat during the early part of the irradiation. In the HT-28 and other earlier experiments the driver rods or loose particles were discarded after irradiation. However, in HT-33, experimental objectives were identified that could be met by use of these nonreference fissile driver particles. This was done with no loss of fertile particle test space and in no way interfered with the GA test objectives.

The objectives for the driver rods were:

1. comparison of a slug-injected (SI) matrix having a pitch binder and a warm-molded (WM) matrix having a thermosetting resin binder,
2. comparison of two shim types in SI rods,
3. comparison of Triso-coated and SiC-coated (no outer LTI) particles in WM specimens and Triso-coated particles in SI specimens.

The test matrix for the driver fuel is given in Table 6.42. Four types of coated particles were used: (1) low-enriched weak-acid resin (WAR) with the standard Triso coating, (2) standard WAR Triso minus the outer LTI coating, (3) Triso-coated inerts, and (4) Triso inerts minus the outer LTI. The inert particles were included in the specimens to simulate large HTGR fuel particle loadings.

The test matrix shown in Table 6.42 was selected to simulate the maximum loading estimated for equilibrium recycle fuel elements in a large HTGR. Many other loadings will be required for the entire fuel cycle scheme, but for this experiment we desired to directly compare shimmed slug-injected matrices and warm-molded continuous matrices with identical "metal" loadings. The SiC-coated particles were of interest because the application and characterization of an outer LTI

Table 6.42. Test Matrix for Driver Fuel in Irradiation Experiment HT-33

Item	Fabrication Method (Binder)	Particle Type	Loading, vol %	
			1250°C	900°C
1,5	Slug injection (pitch)	Triso fissile	17	12
		Triso inert	23	28
		Shim (GL H-451)	18	18
Total			58	58
2,6	Slug injection (pitch)	Triso fissile	17	12
		Triso inert	23	28
		Shim (Speer fluid coke)	18	18
Total			58	58
3,7	Warm molding (resin)	Triso fissile	17	12
		Triso inert	23	28
Total			40	40
4,8	Warm molding (resin)	SiC fissile	12	8
		SiC inert	28	32
Total			40	40

coating would be eliminated, higher fuel loadings could be incorporated in continuous-matrix fuel rods, and the problem of matrix-particle interaction would be eliminated. It was also desired to determine the fuel rod stability when no outer LTI was present for bonding.

The thermosetting resin binder was included because specimens formed by use of such materials can be carbonized without mechanical support and without the deformation that is associated with pitch-type binders.

The shim particles and filler prepared from Great Lakes Carbon Corporation (GLCC) H-451 graphite were selected because in GA's previous reference fabrication scheme, the slabs obtained during machining of the H-451 fuel blocks were to be ground to make shims and the fines resulting from the grinding were to be used as filler material for forming the fuel rods. The Speer fluid coke shim was selected for comparison with the H-451 shim because it is nearly spherical as it comes from the coking oven and only requires screening to obtain the desired size fraction, then calcining and heat-treating for densification.

6.5.6.1 Operating Conditions

Experiment HT-33 was designed to be a five-cycle experiment with fuel surface temperatures of 900 and 1250°C. Fuel loading for thorium-bearing specimens in the low-temperature regions was 0.0234 g; in the high-temperature regions it was 0.0331 g per specimen. Uranium loading in the low-temperature regions was 0.0191 g of 7%-enriched uranium per specimen; in the high-temperature regions it was 0.0268 g per specimen. Table 6.43 shows the loading scheme for the capsule. Not shown are the inert particles placed in magazine end plugs for permeability studies.

6.5.6.2 Fabrication of Specimens

Tables 6.44 and 6.45 give the properties of the fissile particles in the driver rods and the conditions for coating them. The two batches used were identical throughout the deposition of the SiC coating; batch OR-2576-H was given the outer LTI coat, while Batch SC-375 was not coated further. Table 6.46 gives the properties of the two types of shim particles used in the slug-injected driver rods; these particles are shown in Fig. 6.7.

The Triso-coated particles were annealed at 1800°C for 10 min before incorporation in the fuel rods. The SiC-coated particles were used as coated. The matrix materials for the slug-injected specimens were 32 wt % −325 mesh H-451 graphite and 68 wt % Ashland grade 240 pitch. Injection was at 185°C and 4.8 MPa (700 psi). The matrix materials for the warm-molded specimens were 58.74 wt % −200 mesh H-451 graphite, 10.49 wt % Thermax, 27.97 wt % Varcum, and 2.80 wt % maleic anhydride. These specimens were prepared by slurry blending then pressing at 150°C and 4.8 MPa (700 psi). The slug-injected rods were packed in graphite powder for carbonizing; the resin-bonded, warm-molded rods were carbonized free-standing. Both were carbonized at 900°C, then heat-treated at 1800°C for 30 min. The specimens were nominally 9.78 mm (0.385 in.) diam, 6.98 mm (0.275 in.) long. Major properties of specimens are given in Table 6.47.

Table 6.43. Loading Scheme — Capsule HT-33

Position[a]		Type Specimen[b]	Item[c]	Heavy Metal	Batch	Type Coating
1		SI	5	Uranium	OR-2576-H	Triso
2		GA		Thorium	6542-39-0161-001	Biso
3		SI	6	Uranium	OR-2576-H	Triso
4		GA		Thorium	6542-40-0161-001	Biso
5		GA		Thorium	6542-40-0261-001	Biso
6		WM	7	Uranium	OR-2576-H	Triso
7	900°C	GA		Thorium	6542-40-0260-001	Biso
8		GA		Thorium	6542-27-0161-001	Biso
9		WM	8	Uranium	SC-375	SiC
10		GA		Thorium	6542-29-0261-001	Biso
11		GA		Thorium	6542-41-0161-001	Biso
12		SI	5	Uranium	OR-2576-H	Triso
13		GA		Thorium	6542-41-0160-001	Biso
14		SI	1	Uranium	OR-2576-H	Triso
15		GA		Thorium	6542-29-0261-002	Biso
16		WM	4	Uranium	SC-375	SiC
17		GA		Thorium	6542-27-0161-002	Biso
18		GA		Thorium	6542-41-0161-002	Biso
19		WM	3	Uranium	OR-2576-H	Triso
20	1250°C	GA		Thorium	6542-41-0160-002	Biso
21		GA		Thorium	6542-39-0161-002	Biso
22		SI	2	Uranium	OR-2576-H	Triso
23		GA		Thorium	6542-40-0161-002	Biso
24		GA		Thorium	6542-40-0261-002	Biso
25		SI	1	Uranium	OR-2576-H	Triso
26		GA		Thorium	6542-40-0260-002	Biso
HMP						
27		GA		Thorium	6252-08-0161-004	Triso
28		WM	3	Uranium	OR-2576-H	Triso
29		GA		Thorium	6252-10-0161-004	Triso
30		GA		Thorium	6252-05-0160-008	Triso
31		WM	3	Uranium	OR-2576-H	Triso
32		GA		Thorium	6252-06-0261-004	Triso
33	1250°C	GA		Thorium	6252-06-0161-004	Triso
34		SI	2	Uranium	OR-2576-H	Triso
35		GA		Thorium	6252-07-0261-004	Triso
36		GA		Thorium	6252-07-0161-004	Triso
37		SI	1	Uranium	OR-2576-H	Triso
38		GA		Thorium	6252-09-0161-004	Triso
39		WM	4	Uranium	SC-375	SiC
40		GA		Thorium	6252-09-0161-003	Triso
41		SI	6	Uranium	OR-2576-H	Triso
42		GA		Thorium	6252-07-0161-003	Triso
43		GA		Thorium	6252-07-0161-003	Triso
44		WM	7	Uranium	OR-2576-H	Triso
45		GA		Thorium	6252-05-0160-007	Triso
46	900°C	GA		Thorium	6252-06-0261-003	Triso
47		WM	8	Uranium	SC-375	SiC
48		GA		Thorium	6252-06-0161-003	Triso
49		GA		Thorium	6252-08-0161-003	Triso
50		SI	5	Uranium	OR-2576-H	Triso
51		GA		Thorium	6252-10-0161-003	Triso
52		WM	7	Uranium	OR-2576-H	Triso

[a]Starting from top of capsule.

[b]SI = slug injected; WM = warm molded. All GA specimens are loose particles.

[c]Identified in Table 6.42.

Table 6.44. Selected Properties of Fissile Particles Used in Driver Rods for HT-33

Property	Value
Kernel material	$UC_{4.40}O_{1.43}$
Particle uranium content, wt %	
Batch OR-2576-H	15.99
Batch SC-375	21.54
^{235}U enrichment, at. %	7.09
Kernel diameter, μm	376.1
Standard deviation	10.10
Kernel density, g/cm^3	3.26

Table 6.45. Properties and Deposition Conditions for Coatings on Fissile Particles from Batches OR-2576-H and SC-375 Used in Driver Rods for HT-33

Property	Buffer	Inner LTI	SiC	Outer LTI[a]
Coating gas	C_2H_2	MAPP[b]	CH_3SiCl_3	MAPP
Coating temperature, °C	1125	1275	1550	1275
Deposition rate, μm/min	8.80	2.37	0.19	3.78
Thickness, μm[c]	53.7 (7.02)	34.57 (3.20)	35.6 (1.50)	37.18 (2.60)
Density, g/cm^3[c]	1.12	1.939 (0.007)	3.200 (0.0007)	2.020 (0.0046)

[a]Batch OR-2576-H only; not applied to batch SC-375.

[b]Mixture of methylacetylene and propadiene with lesser amounts of propane, butane, isobutane, propylene, and butadiene.

[c]Numbers in parentheses are standard deviations.

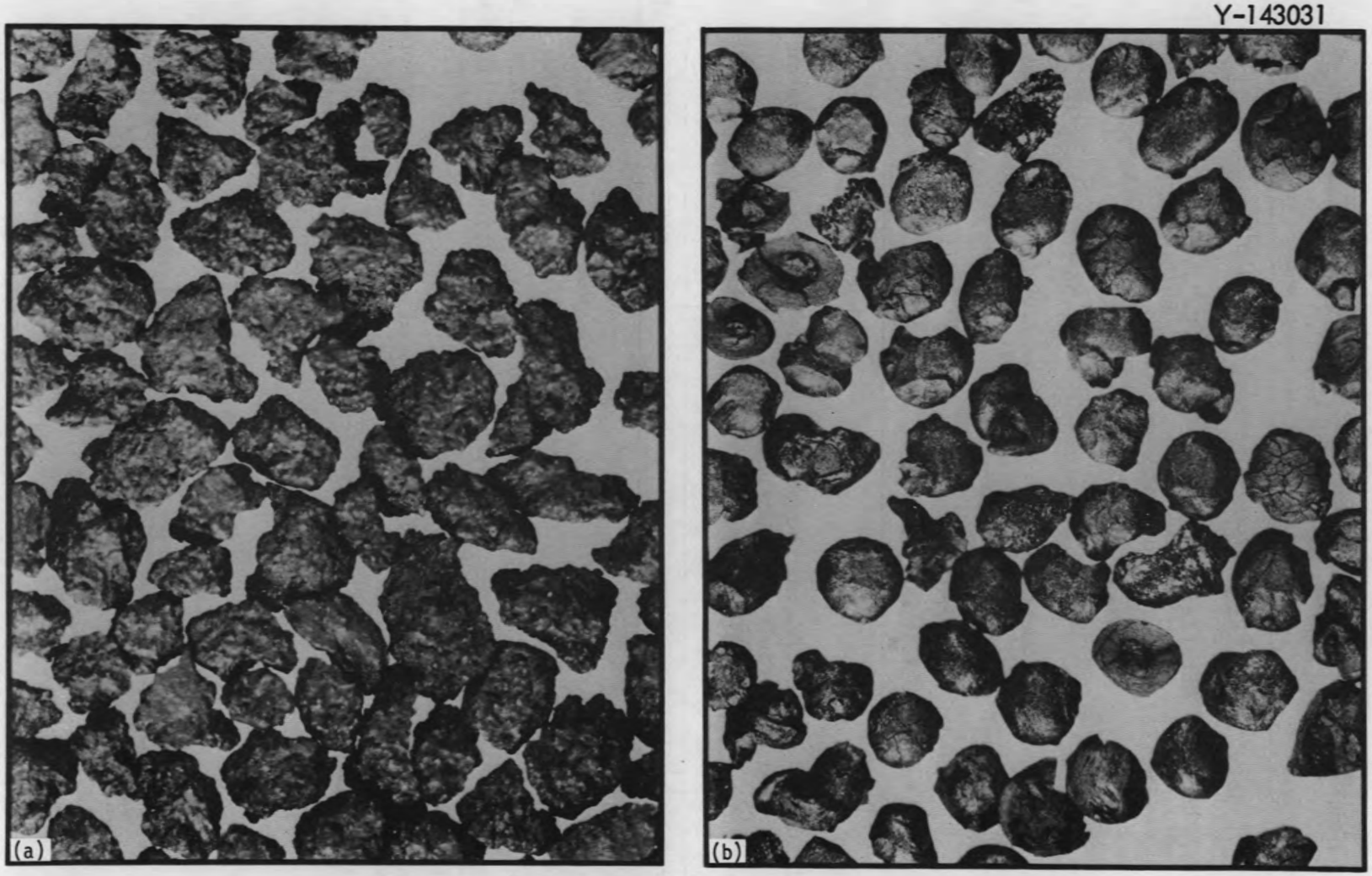

Fig. 6.7. Shim Particles Used in Irradiation Experiment HT-33. (a) GLCC H-451. (b) Speer fluid coke.

Table 6.46. Characteristics of Shim Particles for HT-33

Material	Size Range (μm)	Bulk Density[a] (g/cm^3)	Open Porosity[b] (%)
Speer fluid coke[c]	840–1000	1.92	10.54
GLCC H-451[d]	710–1190	1.94	8.99

[a]Determined by mercury porosimetry at 0.52 MPa (75 psi).

[b]Determined by mercury porosimetry at 103 MPa (15,000 psi).

[c]From Speer Carbon Company; heat-treated at 2800°C for 1 hr.

[d]Ground H-451 graphite from Great Lakes Carbon Corporation; heat-treated at 2800°C for 1 hr; impregnated at ORNL with MAPP gas.

Table 6.47. Nominal Properties of Driver Rods for HT-33

Fabrication	Matrix Density (g/cm^3)	Particle Loading, vol %		Coke Yield (%)
		Fuel	Shim	
Slug Injected	0.60	40	14	20
Warm Molded	1.35	40	0	41

6.5.6.3 Postirradiation Examination

Capsule HT-33 was removed from the HFIR on October 21, 1976. Tables 6.48 and 6.49 give the operating history and related calculations (fluences and burnups) for the capsule. The capsule appeared to be in excellent condition on receipt at the hot cells. The gas atmosphere in the capsule was sampled and appeared to be largely argon, with other gases present in the following descending order: He, Xe, Kr, and H_2. A small amount, about 0.23 mol %, of water vapor was also detected.

No difficulty was encountered on opening the capsule and removing the four graphite magazines. The end plugs, which contained inert coated particles for permeability measurements, were removed and the particles retrieved. However, the particles were too active to be handled in the permeability equipment and are in storage until their activity has decayed to a workable level. Postirradiation examination was initiated but is as yet largely incomplete. The following results are tentative.

Table 6.48. Reactor Operating History During Irradiation of HT-33

Cycle	Begin		End		Irradiation Time, hr	
	Time	Date	Time	Date	During Cycle	Accumulated
134	0152	6-17-76	0800	7-9-76	534	534
135	0355	7-10-76	2350	8-1-76	547	1081
136	1655	8-2-76	0400	8-25-76	540	1621
137	1223	9-2-76	2400	9-25-76	564	2185
138	0645	9-27-76	0400	10-21-76	574	2759

Table 6.49. Estimated Neutron Fluences and Heavy Metal Burnup for Capsule HT-33

Capsule Position	Estimated Fluence, n/m^2		Estimated Burnup, % FIMA		
	<0.414 eV	>0.18 MeV	^{235}U	^{238}U	^{232}Th
1, 52	1.43×10^{26}	5.56×10^{25}	84.7	10.4	
2, 51	1.49	5.91			5.6
3, 50	1.55	6.36	84.7	11.7	
4, 49	1.61	6.61			6.2
5, 48	1.67	6.90			6.5
6, 47	1.73	7.25	84.7	13.7	
7, 46	1.79	7.55			7.1
8, 45	1.85	7.85			7.5
9, 44	1.89	8.14	84.7	15.4	
10, 43	1.93	8.44			8.1
11, 42	1.99	8.74			8.5
12, 41	2.05	9.03	84.7	17.0	
13, 40	2.09	9.24			9.1
14, 39	2.34	10.3	84.7	20.3	
15, 38	2.39	10.5			11.0
16, 37	2.44	10.7	84.7	21.0	
17, 36	2.48	10.9			11.5
18, 35	2.53	11.0			11.7
19, 34	2.56	11.1	84.7	21.9	
20, 33	2.60	11.2			12.1
21, 32	2.63	11.3			12.2
22, 31	2.66	11.4	84.7	22.5	
23, 30	2.70	11.5			12.5
24, 29	2.73	11.5			
25, 28	2.75	11.6	84.7	23.0	
26, 27	2.78	11.6			12.8

The low-temperature magazines, 1 and 4, yielded their contents of fuel rods and graphite crucibles with no difficulty. Considerable difficulty was encountered with the high-temperature magazines, 2 and 3, and eventually it was necessary to slit magazine 2 to recover the specimens. This difficulty is not reflected in the dimensional data (to be presented below) but must be attributable to debonding of heater rods 14, 22, and 25 (see Table 6.50).

The results of stereoexamination of the fuel rods are summarized in Table 6.50. These observations indicate that the warm-molded specimens that contained Triso-coated particles performed better than

Table 6.50. Stereoexamination of Heater Rods from HT-33

Position[a]	Fabrication[b] Process	Type Shim	Shim Loading (vol %)	Appearance
1	SI	H-451	14.08	Good
3	SI	Speer	14.55	Few cracked particles
6	WM(Triso coated)	None		Some matrix cracking
9	WM(SiC coated)	None		Some debonding
12	SI	H-451	14.82	Good
14	SI	H-451	13.69	Complete debonding
16	WM(SiC coated)	None		Slight debonding
19	WM(Triso coated)	None		Good
22	SI	Speer	13.55	Complete debonding
25	SI	H-451	13.66	Complete debonding
28	WM(Triso coated)	None		Some debonding
31	WM(Triso coated)	None		Good
34	SI	Speer	13.91	Some debonding
37	SI	H-451	13.68	Good
39	WM(SiC coated)	None		Few cracked particles
41	SI	Speer	14.65	Some debonding
44	WM(Triso coated)	None		Good
47	WM(SiC coated)	None		Some debonding
50	SI	H-451	14.69	Good
52	WM(Triso coated)	None		Good

[a]Positions 1 through 12 — magazine 1, 900°C; positions 14 through 25 — magazine 2, 1250°C; positions 28 through 39 — magazine 3, 1250°C; positions 41 through 52 — magazine 4, 900°C.

[b]WM — warm molded; SI — slug-injected.

those that contained SiC-coated particles. The slug-injected specimens containing the H-451 shim performed better than those with the Speer shim. Except for specimens in Magazine 2 (1250°C), where much debonding occurred, the slug-injected and warm-molded specimens performed about the same. Some of the specimens are shown in Figs. 6.8 through 6.10.

Only two specimens, both from the high-temperature zone, have been examined metallographically — U-16 (warm molded with SiC-coated particles), and U-19 (warm molded with Triso-coated particles). The SiC-coated driver particles had all failed. The SiC coating had apparently been attacked from the outside, as shown in Fig. 6.11. The SiC coating on the inert particles seemed to be attacked only when they were in close proximity to the driver particles. By comparison, the Triso-coated

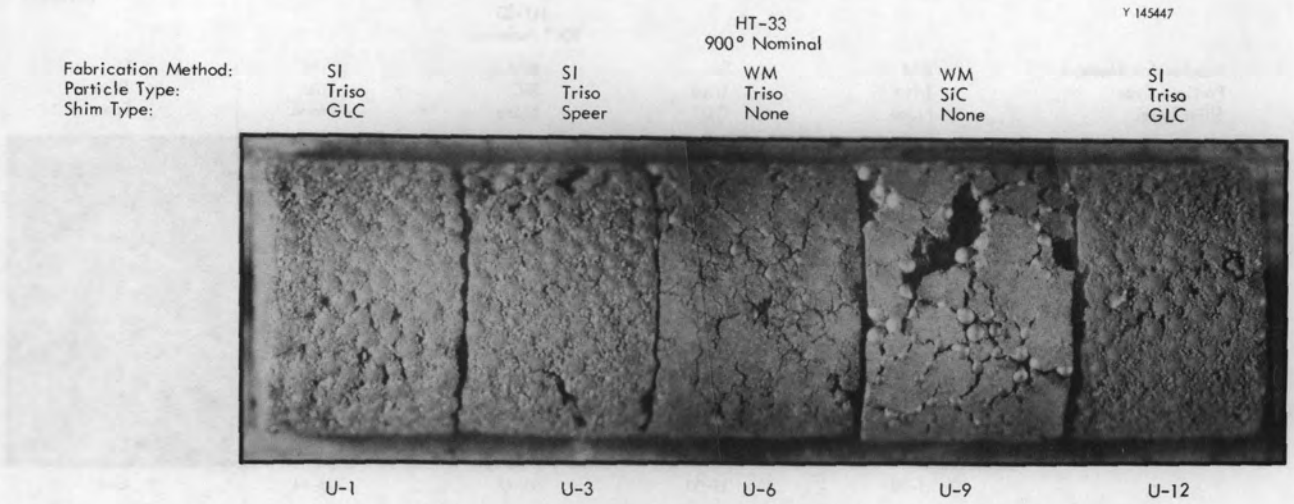

Fig. 6.8. Irradiated Heater Rod Specimens from Low-Temperature Magazine 1 in HT-33.

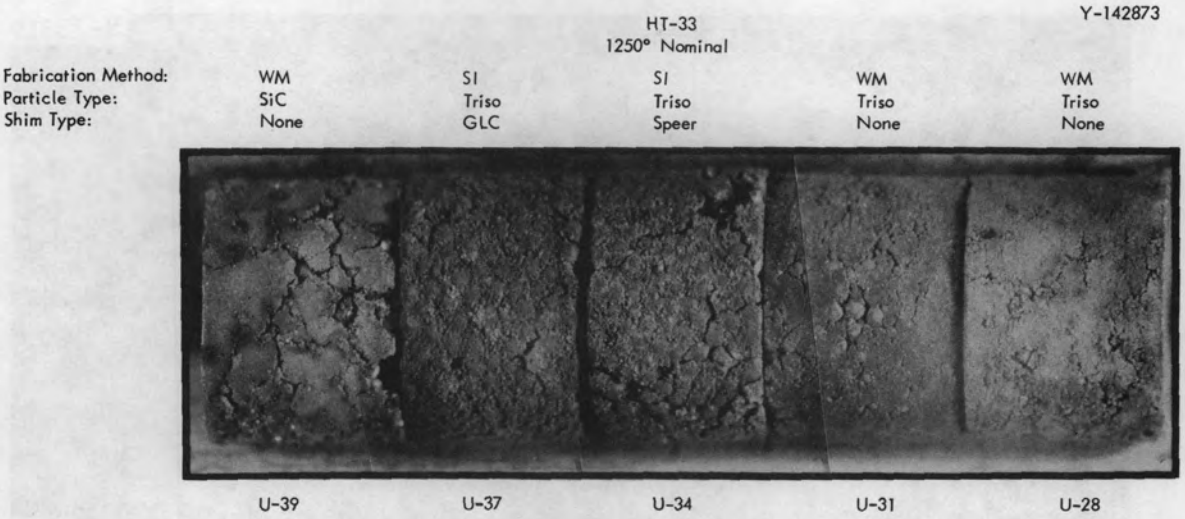

Fig. 6.9. Irradiated Heater Rod Specimens from High-Temperature Magazine 3 in HT-33.

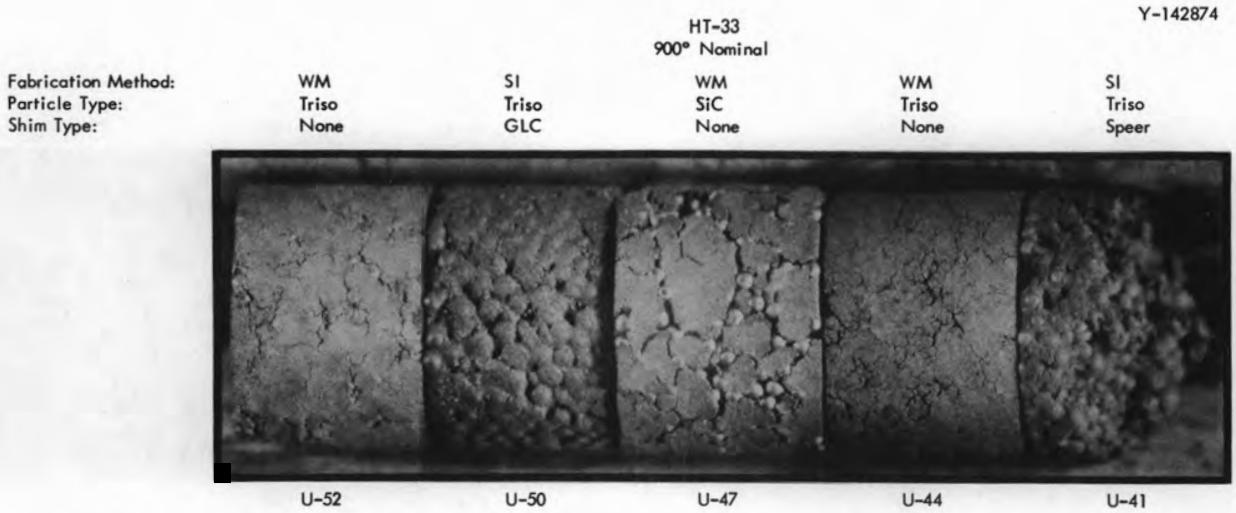

Fig. 6.10. Irradiated Heater Rod Specimens from Low-Temperature Magazine 4 in HT-33.

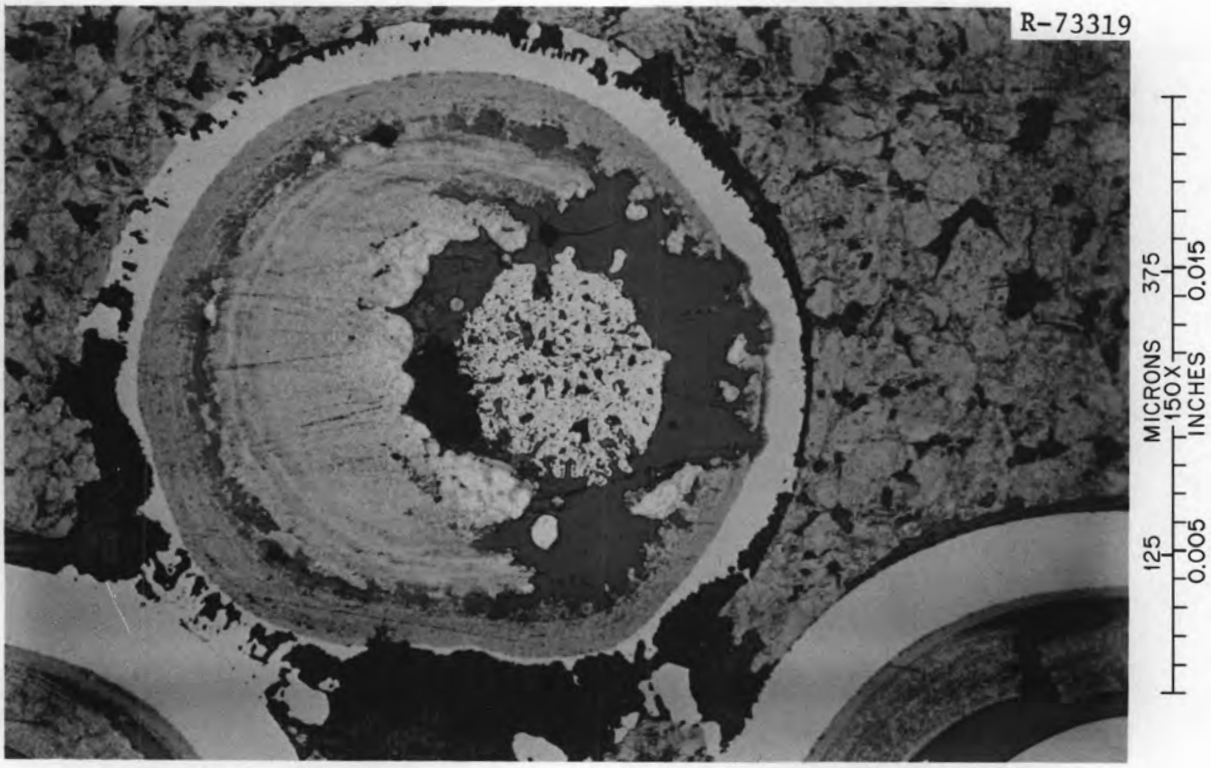

Fig. 6.11. Polished Section of SiC-Coated Fissile Particle in High-Temperature Irradiated Heater Rod Specimen in HT-33 Showing Attack on Outside Surface of the SiC.

particles in the warm molded specimens appeared to have operated well. No failures were observed but some fission product corrosion of the SiC coating was observed as shown in Fig. 6.12. Metallographic examination of other specimens from both the high-temperature and the low-temperature zones is in progress.

Dimensional changes of the heater rods are shown in Table 6.51. The diameters of all specimens measured shrank. Generally a shrinkage in length occurred, but some specimens expanded slightly. It should be kept in mind, however, that the lengths of the unirradiated specimens are generally more difficult to measure accurately than the diameters because more irregularities occur on the specimen ends than on the sides and fewer measurements are taken.

The crucibles containing the GA fertile particles were removed intact and opened in the presence of GA personnel. The particles were repackaged and shipped to GA for detailed examination.

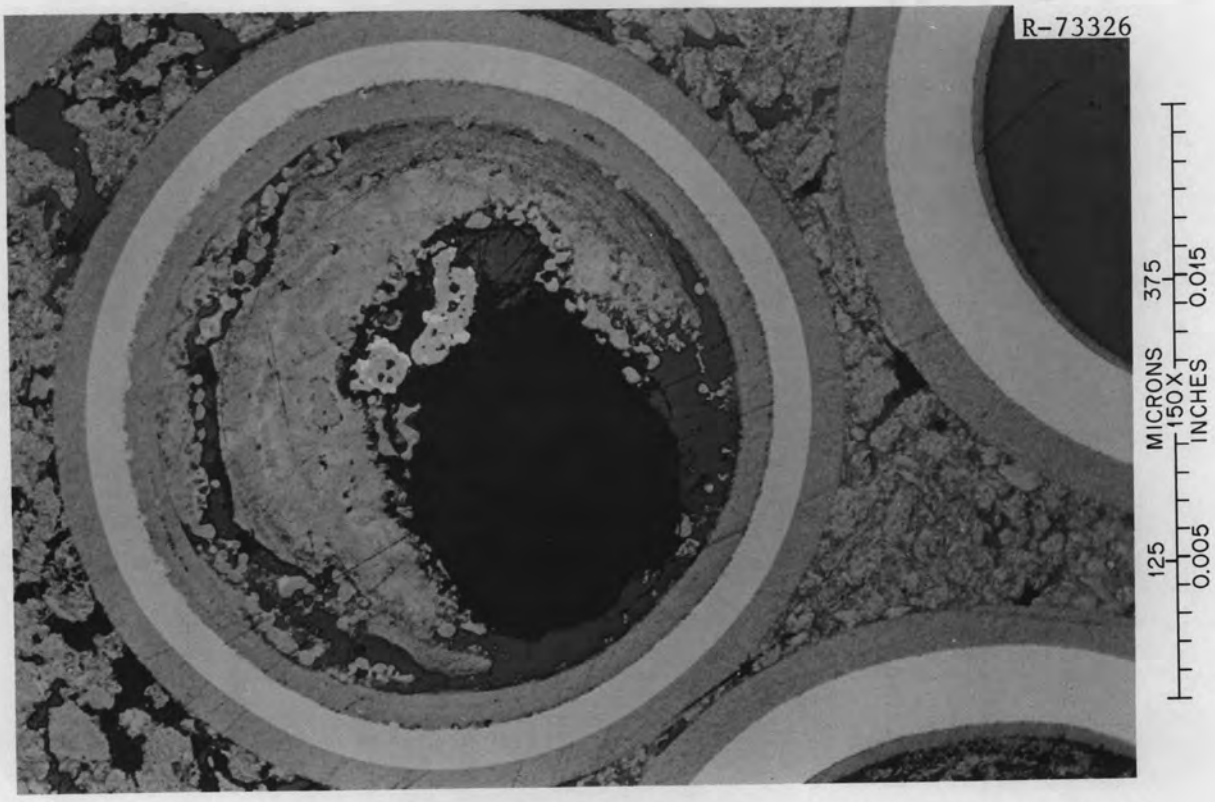

Fig. 6.12. Polished Section of Triso-Coated Fissile Particle in High-Temperature Irradiated Heater Rod Specimen in HT-33. Only attack on the inner surface of the SiC by fission products shows.

Table 6.51. Dimensional Changes in Heater Rods for HT-33

Position	Type Specimen[a]	Dimension Change, %		Temperature (°C)	Estimated Fast (>0.18 MeV) Neutron Fluence[b] (n/m^2)
		Diameter	Length		
1	SI(H-451 shim)	−1.44	+1.45	900	5.56×10^{25}
3	SI(Speer shim)	−1.07	−1.99	900	6.36
6	WM(Triso-coated particles)	−1.38	−3.90	900	7.25
9	WM(SiC-coated particles)	−0.57	−5.76	900	8.14
12	SI(H-451 shim)	−0.57		900	9.03
16	WM(SiC-coated particles)	−1.51	−6.03	1250	10.7
19	WM(Triso-coated particles)	−1.04	−0.59	1250	11.1
28	WM(Triso-coated particles)	−1.82	+0.45	1250	11.6
31	WM(Triso-coated particles)	−2.24	−2.97	1250	11.4
34	SI(Speer shim)	−1.23		1250	11.1
37	SI(H-451 shim)	−1.12	−1.92	1250	10.7
39	WM(SiC-coated particles)	−0.99	+0.16	1250	10.3
44	WM(Triso-coated particles)	−0.92	+0.33	900	8.14
47	WM(SiC-coated particles)	−0.10	+0.48	900	7.25
50	SI(H-451 shim)	−1.41	−3.30	900	6.36
52	WM(Triso-coated particles)	−1.85	−2.12	900	5.56

[a]SI — slug-injected; WM — warm molded.

[b]Based on operating history of capsule.

6.6 IRRADIATION TESTS IN HFIR REMOVABLE BERYLLIUM FACILITY — F. J. Homan

Six HFIR Removable Beryllium (HRB) experiments had been completed before this reporting period. Documentation on four additional experiments was completed during the reporting period.[10,11] The HRB-11 capsule completed irradiation during the reporting period; HRB-12 and HRB-13 were still in the reactor at the end of the reporting period. HRB Capsules through HRB-6 have been covered in previous annual progress reports and will not be discussed here. Abstracts from the HRB-7 and -8 and HRB-9 and -10 reports are included. Complete reportings of the objectives and execution of the HRB-11, -12, -13 capsules are also included.

6.6.1 Capsules HRB-7 and -8 — F. J. Homan

The abstract of the report[10] on these experiments follows.

The HRB-7 and -8 experiments were designed as a comprehensive test of mixed thorium-uranium oxide fissile particles with Th:U ratios from 0 to 8 for HTGR recycle application. In addition, fissile particles derived from Weak-Acid Resin (WAR) were tested as a potential backup type of fissile particle for HTGR recycle. Several other minor objectives were also accomplished in these experiments, which were conducted at two temperatures (1250 and 1500°C) to determine the influence of operating temperature on the performance parameters studied. The minor objectives were comparison of advanced coating designs where ZrC replaced SiC in the Triso design, testing of fuel coated in laboratory-scale equipment with fuel coated in production-scale coaters, comparison of the performance of ^{233}U-bearing particles with that of ^{235}U-bearing particles, comparison of the performance of Biso coatings with Triso coatings for particles containing the same type of kernel, and testing of multijunction tungsten-rhenium thermocouples. All objectives were accomplished, although the performance of the tungsten-rhenium thermocouples was disappointing. As a result of these experiments the mixed thorium-uranium oxide fissile kernel was replaced by a WAR-derived particle in the reference recycle design. A tentative decision to make this change had been reached before the HRB-7 and -8 capsules were examined, and the results of the examination confirmed the accuracy of the previous decision. Even maximum dilution (Th/U $\cong$ 8) of the mixed thorium-uranium oxide kernel was insufficient to prevent amoeba of the

kernels at rates that are unacceptable in a large HTGR. Other results showed the performance of ^{233}U-bearing particles to be identical to that of ^{235}U-bearing particles, the performance of fuel coated in production-scale equipment to be at least as good as that of fuel coated in laboratory-scale coaters, the performance of ZrC coatings to be very promising, and Biso coatings to be inferior to Triso coatings relative to fission product retention.

6.6.2 Capsules HRB-9 and -10 — F. J. Homan

The abstract of the report[11] on these experiments follows.

The HRB-9 and -10 experiments were primarily a test of the influence of initial oxygen-to-uranium ratio on the performance of weak-acid-resin-derived (WAR) fissile kernels. The performance of 15, 50, and 75%-converted WAR fissile kernels was superior to that of 0 and 100%-converted WAR kernels. The partially converted kernels tested also performed superiorly to the dense UC_2 and $(4Th,U)O_2$ kernels also tested in the HRB-9 and -10 capsules. A WAR UC_xN_y kernel performed poorly. All fissile particles tested in this experiment were Triso coated. The WAR UO_2 kernels (0% converted) migrated up the temperature gradient, as has been observed in dense UO_2 and mixed-oxide coated particle fuels. In WAR UC_2 (100% converted) fuel particles, fission products interacted extensively with the inner pyrocarbon coating and SiC layer on the cold side of the particle, as has been observed with dense UC_2 fuel particles.

6.6.3 Capsules HRB-11 and -12 — M. J. Kania, R. L. Hamner, and J M Robbins

The HFIR irradiation capsules HRB-11 and -12 were primarily designed to compare the performance of candidate recycle fuel prepared by ORNL as well as test GA alternative matrices and LASL advanced coatings. The specific objectives of these capsules are described below.

1. To determine the effects of WAR kernel oxygen content on irradiation performance. This is to supplement data obtained[11] from HRB-9 and -10 and to provide design limits and optimization of kernel composition.

2. To obtain performance data on a second source resin, Diamond Shamrock's Duolite C-464. All experience thus far has been with Rohm and Haas' Amberlite IRC-72. The Duolite C-464 has a lower density than IRC-72.

3. To determine whether the minimum 20-μm buffer, currently specified for fission fragment recoil shielding, can be reduced or eliminated for the very porous Duolite C-464 based resin kernel. This is important because a reduction in buffer thickness or elimination of the buffer would increase fuel loading capability and reduce fuel fabrication costs.

4. To test the influence of SiC deposition rate on fission product retention.

5. To test fuel produced in the 0.13-m coating furnace with a frit gas distributor and with a cone distributor. This test would supplement data from the OF-2 experiment.

6. To test GA fuel fabricated with thermosetting matrices.

7. To further test ZrC coatings provided by LASL. This would provide a direct comparison of ZrC and SiC for fission product retention.

6.6.3.1 Capsule Design

Capsules HRB-11 and -12 were instrumented and swept with inert gases (helium and neon) to monitor fuel performance and control temperatures. Each capsule contained 25 fuel rods plus one graphite crucible containing loose particles in a graphite sleeve for gamma spectroscopy standards. The sleeve and specimens were encapsulated in a dual-wall stainless steel containment vessel. Each of the capsules was instrumented with eight Chromel vs Alumel thermocouples located in the graphite sleeve, as shown in Fig. 6.13. In addition, each capsule contained one centerline temperature monitoring device. In HRB-11 a Pt—5% Mo vs Pt—0.1% Mo thermocouple was installed, and in HRB-12 a dual-element Johnson noise power thermometer was installed. Both capsules were designed with identical fissile and fertile loadings and a single design operating temperature, 1350°C. Basic capsule design features are outlined below:

ORNL-DWG 75-9493R2A

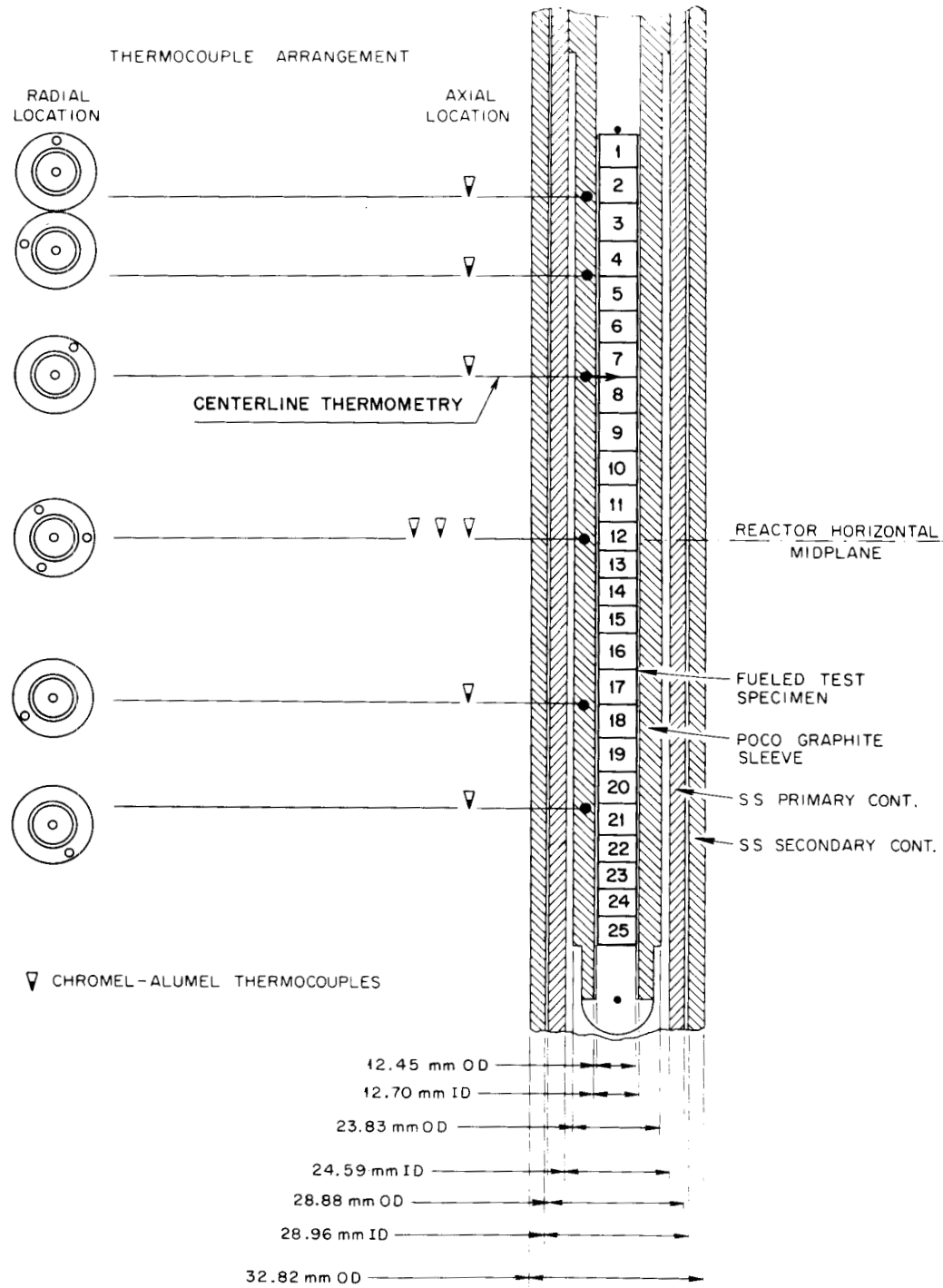

Fig. 6.13. Configuration for HRB-11 and -12.

1. Capsule loading comprises the equivalent of 23 rods, each nominally 16.92 mm (0.666 in.) long, plus one 5.33-mm (0.210-in.) crucible containing the gamma spectroscopy standards. This crucible was placed at the bottom of the fuel stack. Previous HRB fuel rods were nominally 20 mm (0.8 in.) long. Rod diameter was 12.45 mm (0.490 in.).

2. The GA portion of each capsule was 100 mm (4 in.). In this space GA irradiated eight 13-mm (0.5-in.) rather than six 17.92-mm-long (0.666-in.) rods. Thus each capsule contained a total of 25 fuel rods.

3. The irradiation time for each capsule was three cycles in the permanent beryllium (PB) facility and nine cycles in the removable beryllium (RB) facility. This was an increased exposure from two PB cycles plus either six or eight RB cycles used in previous experiments. This increase in PB time allowed increased ^{235}U loading. Compared with HRB-7 through -10 (ref. 10, 11), this increase was about 40 to 50% at the top of the fuel stack, zero near the reactor horizontal midplane, and about 20% at the lower end of the fuel stack. Thus, the number of fissile particles incorporated in a 16.92-mm (0.666-in.) rod was nearly the same as previously loaded in a 20-mm (0.8-in.) rod. The increased RB irradiation time was to accumulate damage fluence approximately equivalent to large HTGR design values.

4. Fuel rods 1 through 9 had axial holes nominally 3.5 mm (0.137 in.) diam to accommodate the centerline thermometry; rods below 9 did not have center holes.

5. The maximum fuel design temperature was 1350°C for all specimens. This resulted in rods near the ends of the capsule operating at lower temperatures than 1350°C for much of each HFIR cycle. Each fuel specimen had a heavy-metal loading calculated for the maximum temperature, rather than the zoned loadings used previously.

6. Heavy-metal loadings were made up of 93%-enriched ^{235}U (approximately 5.5% ^{238}U) and ^{232}Th.

7. In addition to the test fissile particles, each fuel rod contained Biso-coated fertile particles and Triso-coated inert particles. Since the inert particles occupied a large volume of each specimen, the Triso coatings were included to minimize irradiation-induced shrinkage and improve temperature control.

6.6.3.2 Preparation of Test Specimens

In HRB-11 and -12, 19 types of fully enriched fissile particles and 22 types of fertile particles were tested in bonded-bed specimens. In addition, 24 Triso-coated fissile particles, batch OR-2211-H, and 24 Triso-coated fertile particles, batch OR-2233-H, were placed in a graphite crucible in each capsule for use as gamma spectroscopy standards. Each rod specimen contained one fissile particle type, one Biso-coated fertile particle type, and Triso-coated inert particles. In HRB-11 the inert particles were from batch OR-2323-DH, and in HRB-12 inert particles were from batches OR-2323-BH and OR-2323-DH. Particle batch numbers, their respective positions in capsule, and their specific objectives are shown in Table 6.52 for HRB-11 and Table 6.53 for HRB-12. Each of the GA bonded-bed specimens contained Triso-coated UC_2 fissile particles, Biso-coated ThO_2 fertile particles, and Triso-coated inert particles. All the particles coated at ORNL were heat-treated at 1800°C to stabilize the coatings. The characteristics of the ORNL fissile particle test set are described in Table 6.54, and the characteristics of the fertile particle test set is described in Table 6.55. Coating rates for each particle type are described for HRB-11 in Table 6.56 and for HRB-12 in Table 6.57.

All fuel rod specimens in both capsules were fabricated by the slug-injection method. The matrix materials for the ORNL specimens were the same: 29 wt % Ashbury Natural Flake 6353 graphite filler in Ashland 240 petroleum pitch. The particles were blended in an air blender. The matrix was injected through the particle bed at 180°C and 5.5 MPa (800 psi) in a metal mold. For specimens 1 through 9 a small metal rod 3.48 mm (0.137 in.) diam was placed in the center

Table 6.52. Coated Particles and Positions in HRB-11

Position in Capsule	Fissile Batch	Fertile Batch	Objective
1	OR-2466-H	J-488	WAR kernel oxygen content Second source resin
2	OR-2460-H	J-489	Buffer reduction
3	OR-2459-H	J-490	Buffer reduction
4	A-615	J-491	Frit vs cone gas distributor
5	A-601	J-488	WAR kernel oxygen content Frit vs cone gas distributor
6	A-611	J-489	WAR kernel oxygen content Frit vs cone gas distributor
7	OR-2463-H	J-490	WAR kernel oxygen content Second source resin
8	OR-2460-H	J-491	Buffer reduction
9	OR-2459-H	OR-2275-AHT	Buffer reduction
10	OR-2463-H	OR-2266-HT	WAR kernel oxygen content Second source resin
11	OR-2456-H	OR-2291-HT	WAR kernel oxygen content Second source resin
12	6151-17-020	6542-27-015	GA Thermosetting Matrix 4
13	6151-17-020	6542-27-015	GA Thermosetting Matrix 3
14	6151-17-020	6542-27-015	GA Thermosetting Matrix 2
15	6151-17-020	6542-27-015	GA Thermosetting Matrix 1
16	OR-2458-H	OR-2297-AHT	WAR kernel oxygen content Second source resin
17	OR-2471-H	OR-2271-HT	WAR kernel oxygen content Second source resin
18	OR-2466-H	OR-2262-HT	WAR kernel oxygen content Second source resin
19	OR-2456-H	OR-2294-HT	WAR kernel oxygen content Second source resin
20	OR-2458-H	OR-2299-HT	WAR kernel oxygen content Second source resin
21	OR-2471	OR-2273-HT	WAR kernel oxygen content Second source resin
22	6151-17-020	6542-27-015	GA Thermosetting Matrix 4
23	6151-17-020	6542-27-015	GA Thermosetting Matrix 3
24	6151-17-020	6542-27-015	GA Thermosetting Matrix 2
25	6151-17-020	6542-27-015	GA Thermosetting Matrix 1

Table 6.53. Coated Particles and Positions in HRB-12

Position in Capsule	Fissile Batch	Fertile Batch	Objective
1	8-HT	OR-2266-HT	ZrC vs SiC performance
2	9-HT	OR-2265-HT	ZrC vs SiC performance
3	10-HT	OR-2262-HT	ZrC vs SiC performance
4	OR-2486-H	OR-2261-HT	SiC deposition rate
5	OR-2494-H	OR-2266-HT	SiC deposition rate
6	OR-2480-H	OR-2265-HT	ZrC vs SiC performance SiC deposition rate
7	8-HT	OR-2262-HT	ZrC vs SiC performance
8	9-HT	OR-2261-HT	ZrC vs SiC performance
9	10-HT	OR-2274-HT	ZrC vs SiC performance
10	OR-2493-H	OR-2265-HT	SiC deposition rate
11	OR-2497-H	OR-2290-HT	SiC deposition rate
12	6151-17-020	6542-27-015	GA Reference Matrix 1
13	6151-17-020	6542-27-015	GA Thermosetting Matrix 5
14	6151-17-020	6542-27-015	GA Thermosetting Matrix 6
15	6151-17-020	6542-27-015	GA Thermosetting Matrix 7
16	OR-2458-H	OR-2296-AHT	SiC deposition rate
17	OR-2486-H	OR-2269-HT	SiC deposition rate
18	OR-2497-H	OR-2261-HT	SiC deposition rate
19	OR-2320-H	OR-2293-HT	WAR kernel oxygen content
20	OR-2493-H	OR-2298-HT	SiC deposition rate
21	OR-2320-H	OR-2272-HT	SiC deposition rate
22	6151-17-020	6542-27-015	GA Reference Matrix 1
23	6151-17-020	6542-27-015	GA Thermosetting Matrix 5
24	6151-17-020	6542-27-015	GA Thermosetting Matrix 6
25	6151-17-020	6542-27-015	GA Thermosetting Matrix 7

Table 6.54. Fissile Particle Test Set for HRB-11 and -12

Batch	Kernel[a] Composition	Kernel[b] Diameter (μm)	Thickness,[b] μm				Density[b,c] (Mg/m³)					Capsule HRB-
			Buffer	iLTI	SiC	oLTI	Kernel	Buffer	iLTI	SiC	oLTI	
A-601	WAR-A	354.2(15.0)	58.8(10.1)	35.4(3.1)	30.0(1.4)	35.8(3.4)	3.034	1.217[d]	1.713[e](0.012)	3.206(0.0009)	1.724[e](0.008)	11
A-611	WAR-A	366.5(15.0)	47.6(10.2)	36.8(3.0)	30.5(1.4)	35.5(3.9)	3.102	1.159[d]	1.753[e](0.020)	3.204(0.0003)	1.696[e](0.006)	11
A-615	WAR-A	354.1(15.7)	51.0(12.3)	30.7(3.3)	29.5(1.5)	32.4(4.2)	3.076	1.040 1.330[d]	1.857[e](0.009)	3.200(0.0008)	1.910[e](0.004)	11
OR-2320-H	WAR-A, $UC_{5.12}O_{1.54}$	374.0(20.6)	43.8(5.0)	36.8(3.4)	34.3(2.0)	38.6(3.1)	3.17	1.30[f]	1.953(0.007)	3.205(0.002)	1.995(0.008)	12
OR-2456-H	WAR-D, $UC_{5.16}O_{1.36}$	414.4(26.0)	42.8(4.0)	38.4(2.7)	34.1(1.8)	39.0(3.1)	2.43	1.23	1.964(0.006)	3.204(0.008)	2.011(0.004)	11
OR-2458-H	WAR-D, $UC_{4.83}O_{1.09}$	413.4(21.7)	45.9(4.9)	34.3(2.4)	36.0(2.0)	38.4(2.8)	2.47	1.25	1.962(0.008)	3.203(0.007)	2.005(0.005)	11,12
OR-2459-H	WAR-D, $UC_{4.83}O_{1.09}$	407.9(23.9)	20.5(2.8)	35.2(3.4)	33.9(2.0)	26.5(2.6)	2.47	1.35	1.950(0.009)	3.199(0.009)	2.026(0.007)	11
OR-2460-H	WAR-D, $UC_{4.80}O_{1.06}$	396.1(20.7)		36.3(3.4)	35.3(2.4)	33.8(2.5)	2.45		1.950	3.159(0.004)	2.008(0.010)	11
OR-2463-H	WAR-D, $UC_{5.32}O_{1.65}$	415.7(23.1)	47.0(6.6)	39.8(3.6)	33.9(1.9)	36.2(2.1)	2.41	1.16	1.941(0.013)	3.200(0.006)	2.019(0.005)	11
OR-2466-H	WAR-D, $UC_{4.45}O_{0.73}$	406.1(26.7)	50.6(4.9)	34.3(2.4)	34.9(1.8)	34.3(3.1)	2.38	1.24	1.952(0.007)	3.197(0.007)	2.024(0.006)	11
OR-2471-H	WAR-D, $UC_{4.48}O_{0.62}$	391.4(20.0)	47.6(5.6)	34.7(2.6)	34.4(1.3)	33.9(3.8)	2.53	1.25	1.956(0.009)	3.194(0.008)	1.992(0.007)	11
OR-2480-H[g]	WAR-A, $UC_{4.58}O_{1.13}$	362.8(20.2)	49.9(7.1)			72.1(3.8)	3.186	1.27			2.01(0.005)	12
OR-2486-H	WAR-A, $UC_{4.58}O_{1.13}$	361.4(22.2)	48.2(6.5)	40.2(3.37)	30.7(1.5)	40.4(2.9)	3.186	1.27	2.004(0.008)	3.190(0.004)	2.020(0.006)	12
OR-2493-H	WAR-A, $UC_{4.60}O_{1.10}$	363.3(23.1)	43.3(6.6)	36.6(3.9)	32.2(1.6)	36.1(3.0)	3.203	1.304	2.010(0.007)	3.190(0.007)	2.038(0.007)	12
OR-2494-H	WAR-A, $UC_{4.60}O_{1.10}$	363.3(23.1)	43.3(6.6)	36.6(3.9)	32.2(1.3)	36.4(3.0)	3.203	1.304	2.010(0.007)	3.197(0.004)	2.027(0.006)	12
OR-2497-H	WAR-A, $UC_{4.58}O_{1.13}$	361.4(22.2)	48.2(6.5)	40.2(3.37)	36.4(1.4)	38.5(3.7)	3.186	1.27	2.004(0.008)	<3.15	2.011(0.010)	12
8-HT	WAR-A, $UC_{4.60}O_{1.10}$	363.3(23.1)	43.3(6.6)	36.6(3.9)	30.0(1.88)	37.6(4.15)	3.203	1.304	2.010(0.007)			12
9-HT	WAR-A, $UC_{4.60}O_{1.10}$	363.3(23.1)	43.3(6.6)	36.6(3.9)	30.0(1.88)	33.7(3.11)	3.203	1.304	2.010(0.007)			12
10-HT	WAR-A, $UC_{4.60}O_{1.10}$	363.3(23.1)	43.3(6.6)	36.6(3.9)	14.5(1.0)	23.7(2.3)	3.203	1.304	2.010(0.007)	25.9(2.6)		12

[a]WAR-A is Amberlite weak-acid resin; WAR-D is Duolite weak-acid resin.

[b]Numbers in parentheses are standard deviations.

[c]Gradient column densities unless otherwise noted.

[d]Density after depositing iLTI.

[e]Corrected gradient density.

[f]Tap density.

[g]Biso-coated fissile particle.

Table 6.55. Fertile Particle Test Set for HRB-11 and -12

Batch	Kernel[a] Diameter (μm)	Thickness[a] (μm)		Gradient Column Density,[a] Mg/m^3				Capsule HRB-
		Buffer	LTI	Kernel	Buffer	LTI[b] Observed	LTI[b] Corrected	
J-488	497.2(2.7)	87.4(18.2)	78.7(6.6)	9.95	1.285	1.976(0.008)	1.873(0.007)	11
J-489	496.8(2.2)	74.7(13.8)	76.9(5.3)	9.95	1.168	1.904(0.009)	1.793(0.009)	11
J-490	495.6(2.8)	81.7(15.0)	74.8(5.4)	9.95	1.238	1.992(0.010)	1.858(0.009)	11
J-491	495.6(3.1)	83.8(13.8)	75.6(5.9)	9.95	1.232	2.004(0.006)	1.858(0.006)	11
OR-2261-HT	506(2.5)	95.8(10.8)	88.9(6.5)	10.0	1.15	1.886(0.005)		12
OR-2262-HT	507(2.5)	98.0(13.5)	85.1(5.6)	10.0	1.15	2.009(0.007)		11, 12
OR-2265-HT	508(2.6)	96.1(13.1)	94.2(8.1)	10.0	1.15	1.949(0.008)		12
OR-2266-HT	506(2.6)	94.8(15.8)	91.3(6.8)	10.0	1.15	2.019(0.013)		11, 12
OR-2269-HT	507(2.4)	88.8(10.8)	81.4(6.8)	10.0	1.17	1.908(0.007)		12
OR-2271-HT	507(3.1)	88.6(14.6)	80.3(5.8)	10.0	1.17	2.015(0.010)		11
OR-2272-HT	506(2.2)	86.8(13.2)	83.0(4.8)	10.0	1.17	1.860(0.006)		12
OR-2273-HT	507(2.3)	89.2(7.6)	83.5(4.8)	10.0	1.17	2.009(0.006)		11
OR-2274-HT	507(2.5)	99.7(12.3)	90.8(8.1)	10.0	1.15	1.957(0.012)		12
OR-2275-AHT	507(2.3)	93.0(11.1)	87.4(8.4)	10.0	1.15	2.053(0.009)		11
OR-2290-HT	507(2.2)	95.3(12.4)	94.4(6.4)	10.0	1.12	1.882(0.008)		12
OR-2291-HT	507(2.3)	95.1(14.9)	87.6(5.7)	10.0	1.12	1.982(0.007)		11
OR-2293-HT	506(2.7)	97.6(13.9)	89.0(5.1)	10.0	1.12	1.832(0.004)		12
OR-2294-HT	506(2.3)	90.0(15.6)	92.7(7.0)	10.0	1.12	1.961(0.007)		11
OR-2296-AHT	506(2.5)	97.1(14.6)	89.3(7.5)	10.0	1.12	1.898(0.007)		12
OR-2297-AHT	505(2.6)	96.5(12.3)	90.2(7.3)	10.0	1.12	1.975(0.011)		11
OR-2298-HT	506(2.5)	94.5(14.3)	84.4(5.8)	10.0	1.12	1.823(0.012)		12
OR-2299-HT	508(2.4)	94.5(13.1)	91.6(5.6)	10.0	1.12	1.910(0.005)		11

[a]Numbers in parenthesis are standard deviations.

[b]After heat treatment of 1800°C for 30 min.

Table 6.56. Deposition Rates for Fissile and Fertile Particles in HRB-11

Batch	Rate, μm/min			
	Buffer[a]	iLTI[b]	SiC[c]	oLTI[b]
		Fissiles		
A-601	29.40	4.72	not given	4.84
A-611	26.74	4.72	0.15	5.14
A-615	17.70	3.99	not given	4.00
OR-2456-H	10.07	6.59	0.38	6.84
OR-2458-H	3.96	6.53	0.40	7.46
OR-2459-H	11.38	7.04	0.39	7.77
OR-2460-H	None	7.44	0.41	8.45
OR-2463-H	10.06	6.05	0.38	6.73
OR-2466-H	12.65	7.54	0.40	8.11
OR-2471-H	10.19	6.72	0.40	7.37
		Fertiles		
J-488	25.56			7.22
J-489	22.98			5.83
J-490	25.14			6.18
J-491	24.29			9.10
OR-2262-HT	24.50			6.55
OR-2266-HT	23.70			14.04
OR-2271-HT	22.15			10.71
OR-2273-HT	22.30			5.22
OR-2275-AHT	23.25			23.00
OR-2291-HT	23.78			7.30
OR-2294-HT	22.50			3.57
OR-2297-AHT	24.13			4.88
OR-2299-HT	23.53			2.35

[a] C_2H_2 used as coating gas; all A- and J- particle batches at 1350°C; all OR batches at 1125°C.

[b] C_3H_6 used as coating for all A- and J- particle batches at 1350°C; MAPP gas used for OR- particle batches at 1275°C.

[c] CH_3SiCl_3 used as coating gas; all A- particle batches at 1575°C; all OR- particle batches at 1550°C.

Table 6.57. Deposition Rates for Fissile and Fertile Particles in HRB-12

Batch	Rate, μm/min			
	Buffer[a]	iLTI[b]	SiC[c]	oLTI[b]
		Fissiles		
8-HT	4.77	4.18	d	e
9-HT	4.77	4.18	d	e
10-HT	4.77	4.18	d	e
OR-2486-H	5.67	4.68	0.90	11.22
OR-2494-H	Mixture of OR-2465-H—OR-2478-H		0.52	9.71
OR-2480-H	5.87	8.48	None	None
OR-2493-H	Mixture of OR-2465-H—OR-2478-H		0.21	9.23
OR-2497-H	5.67	4.68	0.24	8.56
OR-2320-H	7.30	6.90	0.22	7.02
OR-2465-H	4.76	4.18		
OR-2478-H	5.67	4.68		
OR-2458-H	3.96	6.53	0.40	7.46
		Fertiles		
OR-2266-HT	23.70			14.04
OR-2265-HT	24.03			15.70
OR-2262-HT	24.50			6.55
OR-2261-HT	23.91			7.41
OR-2274-HT	24.93			27.94
OR-2290-HT	23.83			8.58
OR-2296-AHT	24.28			5.58
OR-2269-HT	22.20			12.52
OR-2293-HT	24.40			3.87
OR-2298-HT	23.63			2.48
OR-2272-HT	21.70			6.15

[a] C_2H_2 used as coating gas at 1125°C.

[b] MAPP gas used as coating gas for all coatings. Coatings on fissile particles and fertile batches OR-2262-HT and OR-2266-HT were deposited at 1275°C. Outer LTI on other fertile batches was deposited at 1325°C.

[c] CH_3SiCl_3 used as coating gas on all OR- particle batches at 1550°C.

[d] ZrC in place of SiC was applied by LASL.

[e] Outer LTI applied by LASL.

of the mold to form the hole for placement of the centerline thermometry. Specimens were then carbonized at 900°C vertically in a packed bed of alumina at a heating rate of 60°C/hr. They were then heat-treated at 1800°C for 30 min for dimensional stability.

Particles to be used for the gamma spectroscopy standards were individually chosen from x radiographs, and each was carefully analyzed for its respective heavy metal content and dimensions. Two particles, one fissile and one fertile, were then chosen and placed in each of the 24 holes drilled into the graphite crucible. The positions and characteristics of each particle set in the graphite holder were then recorded. Two graphite crucibles were loaded, one for each capsule.

The specimens were characterized by dimensional measurements, weight, radiography, metallography, and photography. The specimens were all nominally 12.5 mm (0.49 in.) OD and 17.0 mm (0.67 in.) long, with specimens 1 through 9 having a 3.48-mm (0.137-in.) hole for placement of centerline thermometry. An identification mark was formed on one end of each specimen for orientation, so that the specimen dimensions could be measured at the same location both before and after irradiation. The heavy metal loadings and dimensions for each specimen are shown in Table 6.58.

6.6.3.3 Capsule Operation

The operating schedules for HRB-11 and through December 1976 for HRB-12 are shown in Table 6.59. Both capsules were irradiated for three cycles in the PB-13 (VXF-13) facility before going into the RB facility. This was done to burn out sufficient ^{235}U to avoid overpowering the particles in the RB facility. The PB facility is located farther from the HFIR core (0.39 m from the center compared with 0.27 m for the RB-5 facility).[12] The thermal flux in the PB facility is about 60% of the RB flux, and the fast flux is about 11%. Using the PB facility for preirradiations permits irradiation of fully enriched fissile particles, which could not be done otherwise because of very high power production rates at the beginning of the test. Capsule HRB-11 was irradiated for three cycles in PB-13, and then moved to

Table 6.58. Dimensions and Heavy Metal Loadings for ORNL Specimens in HRB-11 and -12

Rod[a]	Average Diameter		Average Length		Loading, Mg/m^3		
	(mm)	(in.)	(mm)	(in.)	^{235}U	^{238}U	^{232}Th
			HRB-11				
1	12.443	0.4899	16.774	0.6604	0.0275	0.0016	0.4594
2	12.426	0.4892	16.612	0.6540	0.0261	0.0015	0.4073
3	12.441	0.4898	16.977	0.6684	0.0254	0.0014	0.3552
4	12.441	0.4898	17.059	0.6716	0.0224	0.0013	0.3252
5	12.438	0.4897	16.731	0.6587	0.0221	0.0013	0.3207
6	12.436	0.4896	16.985	0.6687	0.0217	0.0012	0.3037
7	12.433	0.4895	16.998	0.6692	0.0201	0.0011	0.2915
8	12.446	0.4900	16.876	0.6644	0.0181	0.0011	0.2854
9	12.441	0.4898	17.107	0.6735	0.0187	0.0010	0.2770
10	12.443	0.4899	16.665	0.6561	0.0141	0.0008	0.2323
11	12.449	0.4901	16.883	0.6647	0.0111	0.0007	0.2264
16	12.456	0.4904	16.810	0.6619	0.0140	0.0008	0.2314
17	12.471	0.4910	16.640	0.6551	0.0145	0.0009	0.2429
18	12.443	0.4899	17.003	0.6694	0.0142	0.0008	0.2422
19	12.423	0.4891	17.015	0.6699	0.0155	0.0009	0.2489
20	12.423	0.4891	16.871	0.6642	0.0177	0.0010	0.2660
21	12.408	0.4885	16.919	0.6661	0.0170	0.0010	0.2743
			HRB-12				
1	12.454	0.4903	16.673	0.6564	0.0277	0.0016	0.4614
2	12.451	0.4902	16.825	0.6624	0.0256	0.0015	0.4002
3	12.479	0.4913	17.059	0.6716	0.0234	0.0014	0.3511
4	12.449	0.4901	16.744	0.6592	0.0227	0.0013	0.3308
5	12.441	0.4898	16.876	0.6644	0.0219	0.0013	0.3178
6	12.461	0.4906	17.320	0.6819	0.0198	0.0012	0.2970
7	12.471	0.4910	16.634	0.6549	0.0190	0.0011	0.2960
8	12.469	0.4909	16.678	0.6566	0.0183	0.0011	0.2876
9	12.426	0.4892	16.690	0.6571	0.0179	0.0011	0.2846
10	12.456	0.4904	16.840	0.6630	0.0140	0.0008	0.2295
11	12.459	0.4905	16.911	0.6658	0.0137	0.0008	0.2256
16	12.466	0.4908	16.881	0.6646	0.0139	0.0008	0.2301
17	12.464	0.4907	16.868	0.6641	0.0143	0.0008	0.2399
18	12.451	0.4902	16.800	0.6614	0.0144	0.0008	0.2440
19	12.451	0.4902	16.904	0.6655	0.0155	0.0009	0.2493
20	12.449	0.4901	16.848	0.6633	0.0164	0.0010	0.2652
21	12.449	0.4901	16.640	0.6551	0.0172	0.0010	0.2770

[a]Specimens 1 through 9 have inside diameters of 3.48 mm (0.137 in.).

Table 6.59. Capsules HRB-11 and -12 Reactor Power and Irradiation History

HFIR Fuel Cycle	Operating Facility	Cycle Dates		Irradiation Time, hr	
		Begin	End	In Cycle	Total Accumulated
		Capsule HRB-11			
126	PB-13	12/7/75	12/30/75	559	559
127	PB-13	12/31/75	1/23/76	558	1117
128	PB-13	1/24/76	2/16/76	556	1673
129	RB-7	2/19/76	3/13/76	554	2227
130	RB-7	3/14/76	4/6/76	558	2785
131	RB-7	4/7/76	4/30/76	552	3337
132	RB-7	5/1/76	5/22/76	490	3827
133	RB-7	5/23/76	6/16/76	547	4374
134	RB-7	6/17/76	7/9/76	534	4908
135	RB-7	7/10/76	8/1/76	547	5455
136	RB-7	8/2/76	8/25/76	540	5995
137	RB-7	9/2/76	9/25/76	564	6559
		Capsule HRB-12			
129	PB-13	2/19/76	3/13/76	554	554
130	PB-13	3/14/76	4/6/76	558	1112
131	PB-13	4/7/76	4/30/76	552	1664
132	RB-5	5/1/76	5/22/76	490	2154
133	RB-5	5/23/76	6/16/76	547	2701
134	RB-5	6/17/76	7/9/76	534	3235
135	RB-5	7/10/76	8/1/76	547	3782
136	RB-5	8/2/76	8/25/76	540	4322
137	RB-5	9/2/76	9/25/76	564	4886
138	RB-5	9/27/76	10/21/76	574	5460
139	RB-5	10/21/76	11/14/76	574	6034
140[a]		11/15/76	12/14/76		
141[b]	RB-5	12/15/76	11/10/77	568	6602

[a]Capsule was removed from facility during cycle 140.

[b]Projected.

RB-7 for an additional nine cycles at a design temperature of 1350°C (for the fuel centerline). Capsule HRB-12 was inserted into the PB-13 at the beginning of HFIR cycle 129 (when HRB-11 was moved out) for three cycles, and then moved to RB-5 for the remainder of its irradiation. Capsule HRB-12 was irradiated in the RB-5 facility for eight cycles and then removed from the reactor at the beginning of cycle 140. The capsule was reinserted into RB-5 at the beginning of cycle 141 in December 1976. This capsule was also irradiated at a design temperature of 1350°C (for the fuel centerline).

Calculated burnups for capsule HRB-11 are shown in Table 6.60; neutron fluxes and fluences are tabulated in Table 6.61.

Table 6.60. Calculated Specimen Burnup in Capsule HRB-11

Specimen	Calculated Burnup, % FIMA								
	^{235}U			^{238}U			^{232}Th		
	PB-13	RB-7	Total	PB-13	RB-7	Total	PB-13	RB-7	Total
1	52.5	31.9	84.4	0.89	15.0	15.9	0.24	5.96	6.20
2	54.6	30.3	84.9	0.99	16.8	17.8	0.27	6.80	7.07
3	56.9	28.4	85.3	1.11	19.0	20.1	0.30	7.80	8.10
4	58.8	26.9	85.7	1.22	20.6	21.8	0.34	8.60	8.94
5	60.1	25.8	85.9	1.30	22.2	23.5	0.36	9.39	9.75
6	61.3	24.9	86.2	1.38	23.5	24.9	0.39	10.0	10.4
7	62.3	24.1	86.4	1.45	24.7	26.1	0.41	10.6	11.0
8	63.2	23.4	86.6	1.52	25.6	27.1	0.43	11.1	11.5
9	63.7	23.1	86.8	1.56	26.2	27.8	0.45	11.4	11.9
10	64.3	22.5	86.8	1.60	26.7	28.3	0.46	11.7	12.2
11	64.6	22.2	86.8	1.63	27.2	28.8	0.47	11.9	12.4
12[a]	64.7	22.2	86.9	1.64	27.4	29.0	0.47	12.0	12.5
13[a]	64.6	22.3	86.9	1.63	27.3	28.9	0.47	12.0	12.5
14[a]	64.3	22.5	86.8	1.60	27.0	28.6	0.46	11.8	12.3
15[a]	63.9	22.8	86.7	1.57	26.5	28.1	0.45	11.5	12.0
16	63.2	23.4	86.6	1.52	26.0	27.5	0.43	11.3	11.7
17	62.1	24.3	86.4	1.43	25.2	26.6	0.41	10.8	11.2
18	60.9	25.4	86.3	1.35	24.1	25.5	0.38	10.3	10.7
19	59.4	26.7	86.1	1.26	23.1	24.4	0.35	9.75	10.1
20	57.9	27.9	85.8	1.16	21.6	22.8	0.32	9.03	9.35
21	56.0	29.5	85.5	1.06	20.2	21.3	0.29	8.31	8.60
22[a]	53.9	31.3	85.2	0.95	18.6	19.6	0.26	7.56	7.82
23[a]	52.1	32.8	84.9	0.87	17.1	18.0	0.23	6.85	7.08
24[a]	49.6	34.9	84.5	0.76	15.4	16.2	0.20	6.07	6.27
25[a]	47.4	36.7	84.1	0.68	14.2	14.9	0.18	5.50	5.68

[a]GA specimens.

Table 6.61. Calculated Thermal and Fast Fluences for HRB-11 Specimens

Specimen	Fluence in PB-13, n/m^2		Fluence in RB-7, n/m^2		Total Fluence, n/m^2	
	Thermal, <1.86 eV	Fast, >0.18 MeV	Thermal, <1.86 eV	Fast, >0.18 MeV	Thermal, <1.86 eV	Fast, >0.18 MeV
1	2.37×10^{25}	2.68×10^{24}	1.04×10^{26}	4.68×10^{25}	1.27×10^{26}	4.95×10^{25}
2	2.54	2.87	1.16	5.24	1.41	5.53
3	2.70	3.05	1.30	5.84	1.57	6.15
4	2.89	3.24	1.41	6.35	1.70	6.67
5	3.00	3.38	1.49	6.68	1.79	7.02
6	3.12	3.54	1.60	7.17	1.91	7.52
7	3.23	3.64	1.71	7.68	2.03	8.04
8	3.33	3.76	1.79	8.02	2.12	8.40
9	3.36	3.83	1.83	8.25	2.17	8.63
10	3.46	3.90	1.88	8.42	2.23	8.81
11	3.50	3.95	1.92	8.58	2.27	8.98
12[a]	3.51	3.95	1.93	8.65	2.28	9.05
13[a]	3.51	3.95	1.92	8.62	2.27	9.02
14[a]	3.46	3.90	1.90	8.53	2.25	8.92
15[a]	3.42	3.85	1.86	8.35	2.20	8.74
16	3.33	3.76	1.83	8.25	2.16	8.63
17	3.21	3.62	1.74	7.86	2.06	8.22
18	3.08	3.48	1.69	7.58	2.00	7.93
19	2.93	3.32	1.60	7.19	1.89	7.52
20	2.79	3.15	1.49	6.68	1.77	7.00
21	2.62	2.96	1.41	6.35	1.67	6.65
22[a]	2.45	2.78	1.28	5.75	1.53	6.03
23[a]	2.33	2.63	1.20	5.42	1.43	5.68
24[a]	2.17	2.43	1.07	4.85	1.29	5.09
25[a]	2.00	2.25	0.985	4.45	1.18	4.68

[a]GA specimens.

6.6.3.4 Postirradiation Examination

Disassembly and a partial physical examination of irradiation capsule HRB-11 was completed during this report period. The capsule was disassembled without incident. A GA representative was present for removal of the GA specimens. Visual examination of the fuel rods showed that all rods were in good condition, with little debonding at the edges. Very few broken particles were noted on the rod surfaces. However, when the central platinum-molybdenum thermocouple was removed, five individual particles were bonded to the rhenium sheath, which was wrapped around the thermocouple. This fuel-sheath interaction is discussed further in Sect. 6.8 of this report.

The dimensional analysis of the ORNL fuel rods has been completed and is presented in Table 6.62.

Table 6.62. Dimensional Changes of ORNL Fuel Rods in HRB-11[a]

Specimen	Diameter, mm (in.)		Change (%)	Length, mm (in.)		Change (%)
	Preirradiation	Postirradiation		Preirradiation	Postirradiation	
HRB-11-1	12.443(0.4899)	12.248(0.4822)	−1.57	16.774(0.6604)	16.469(0.6484)	−1.82
-2	12.426(0.4892)	12.301(0.4843)	−1.00	16.612(0.6540)	16.215(0.6384)	−2.39
-3	12.441(0.4898)	12.289(0.4838)	−1.22	16.977(0.6684)	16.571(0.6524)	−2.39
-4	12.441(0.4898)	12.324(0.4852)	−0.94	17.059(0.6716)	16.812(0.6619)	−1.44
-5	12.438(0.4897)	12.286(0.4837)	−1.23	16.731(0.6587)	16.513(0.6501)	−1.31
-6	12.436(0.4896)	12.261(0.4827)	−1.41	16.985(0.6687)	16.805(0.6616)	−1.06
-7	12.433(0.4895)	12.281(0.4835)	−1.23	16.998(0.6692)	16.998(0.6692)	0.00
-8	12.446(0.4900)	12.324(0.4852)	−0.98	16.876(0.6644)	16.647(0.6554)	−1.35
-9	12.441(0.4898)	12.291(0.4839)	−1.20	17.107(0.6735)	16.782(0.6607)	−1.90
-10	12.443(0.4899)	12.283(0.4836)	−1.29	16.665(0.6561)	16.464(0.6482)	−1.20
-11	12.449(0.4901)	12.205(0.4805)	−1.96	16.883(0.6647)	16.695(0.6573)	−1.11
-16	12.456(0.4904)	12.375(0.4872)	−0.65	16.810(0.6619)	16.761(0.6599)	−0.30
-17	12.471(0.4910)	12.375(0.4872)	−0.77	16.640(0.6551)	16.538(0.6511)	−0.61
-18	12.443(0.4899)	12.233(0.4816)	−1.69	17.003(0.6694)	16.718(0.6582)	−1.67
-19	12.423(0.4891)	12.240(0.4819)	−1.47	17.015(0.6699)	16.673(0.6564)	−2.02
-20	12.423(0.4891)	12.238(0.4818)	−1.49	16.891(0.6642)	16.673(0.6564)	−1.17
-21	12.408(0.4885)	12.212(0.4808)	−1.58	16.919(0.6661)	16.485(0.6490)	−2.57

[a]GA rods were Nos. 12–15, 22–25.

6.6.4 Capsule HRB-13 — M. J. Kania, R. L. Hamner, E. L. Long, Jr., and J. M. Robbins

Capsule HRB-13 was designed to provide input for the HTGR recycle fuel product specification as well as provide irradiation space for advanced fuels for Very High-Temperature Reactors (VHTRs). The fuel product specification specimens were provided by ORNL, and the advanced fuel specimens were provided by LASL. The ORNL specimens were designed to provide definitive results on how variously misshapen kernels affect the irradiation performance of the weak-acid-resin-derived (WAR) particle. Specific objectives for the experiment are listed below:

1. to determine the extent to which small satellites attached to the fuel kernels derived from the Amberlite IRC-72 resin, manufactured by Rohm and Haas, affect irradiation performance;
2. to determine the extent to which numerous satellites attached to fuel kernels derived from the IRC-72 resin affect irradiation performance;
3. to obtain irradiation performance data on irregularly shaped fuel kernels or clusters of small fuel particles derived from the IRC-72 resin;
4. to evaluate the importance of slight eccentricity of fuel kernels derived from the Duolite C-464 resin, manufactured by Diamond Shamrock Company, on irradiation performance;
5. to evaluate the importance of gross eccentricity of fuel kernels derived from the C-464 resin on irradiation performance;
6. to test the effect of very irregular shapes on the irradiation performance of the C-464 resin.

The currently planned loading process for resin-derived kernels requires that the first step be to screen and shape separate the as-received resin to a suitable size fraction before loading. The reject level of the as-received resin is about 80%. However, on a production basis it is very difficult to remove all the nonspherical particles, so that after loading with uranium and drying, some irregularly shaped and nonspherical particles are present. In the fuel irradiated to date the loaded resins are further upgraded to

remove essentially all the irregularly shaped or nonspherical particles before carbonization and conversion. Thus, to date we have irradiated only "perfect" particles and have no experience concerning the performance of particles that do not meet the current kernel specifications (The current HTGR Fuel Product Specification, Issue B, requires that "no more than 10% of the kernels shall have a ratio of maximum diameter/ minimum diameter $\geqslant$ 1.2.") These specifications are based on experience obtained with sol-gel and VSM kernels. The HRB-13 irradiation capsule will address this problem directly and study the extent to which the irregularly shaped kernels affect irradiation performance.

6.6.4.1 Capsule Design

Capsule HRB-13 is instrumented and swept with inert gases (helium and neon) to monitor fuel performance and control temperatures. This capsule contained 40 fuel rod specimens in a graphite sleeve, encapsulated in a dual-wall stainless steel containment vessel. The capsule was instrumented with eight Chromel vs Alumel thermocouples located in the graphite sleeve as shown in Fig. 6.14. Basic design features of HRB-13 are described below:

1. Capsule loading comprised the equivalent of 40 fuel rods each 9.84 mm (0.388 in.) long and 12.45 mm (0.490 in.) in diameter (LASL specimens occupied a space equivalent to eight rods — or 20% of the stack length.

2. The irradiation time will be three cycles in the PB facility and nine cycles in the RB facility. The three cycles in the PB are to allow a ^{235}U loading increase of approximately 15% over the HRB-7 through -10 capsules.[13,14] Thus, more fissile particles can be incorporated in a rod to increase the significance of the survival statistics.

3. Conversion level, the nominal UC_2 content, was maintained at 30 to 40%, with the balance UO_2 throughout. Previous irradiation experience[15] indicates that this is near the optimum kernel stoichiometry.

4. Heavy-metal loadings included 93%-enriched ^{235}U (approximately 5.5% ^{238}U) and ^{232}Th.

ORNL-DWG 75-9493R2

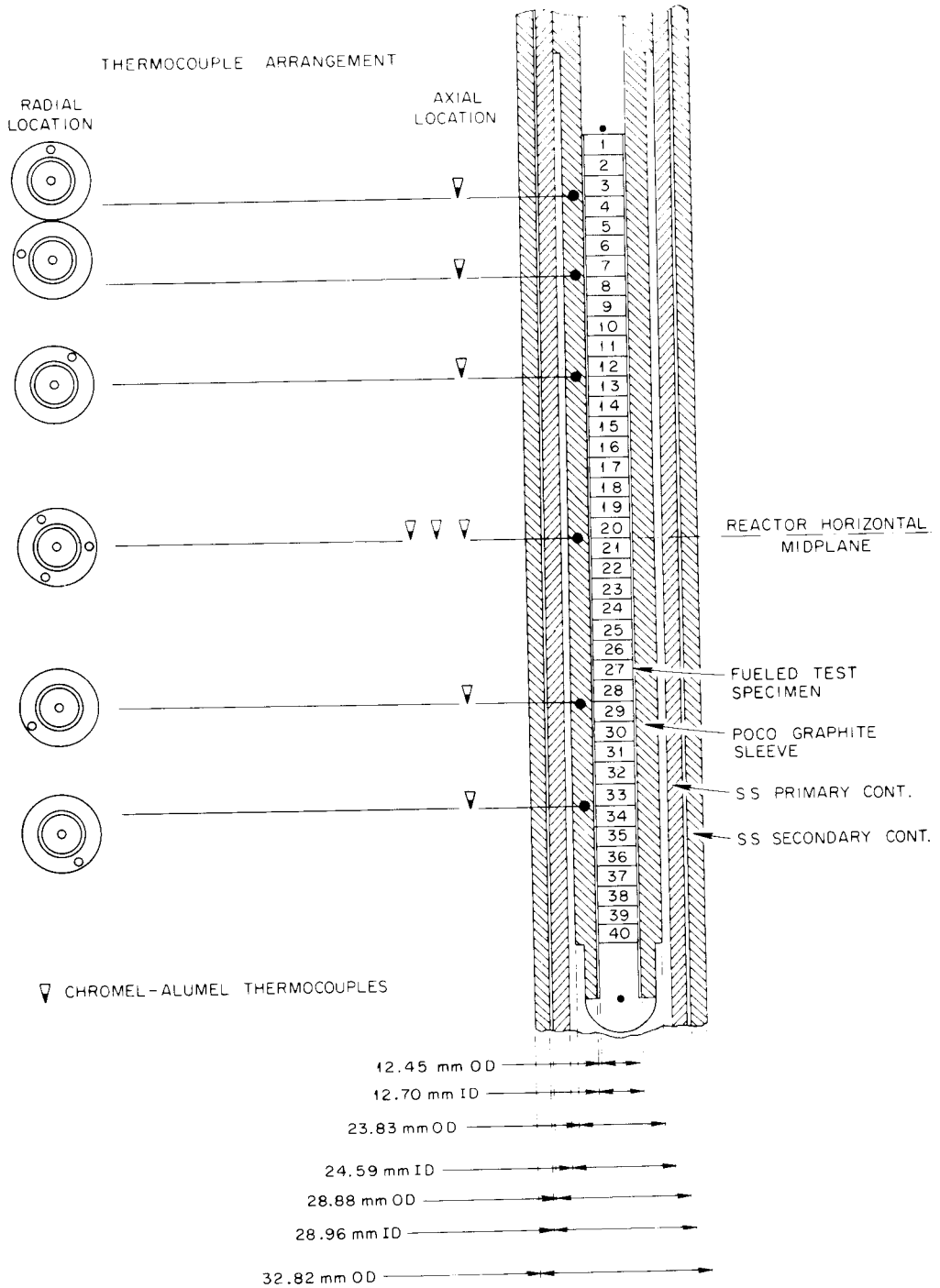

Fig. 6.14. Configuration for HRB-13.

5. In addition to the test fissile particles, each fuel rod contained Biso-coated fertile particles and Triso-coated inert particles. Since inert particles occupy a large volume fraction of each specimen, the Triso coatings will minimize irradiation-induced shrinkage and improve temperature control.

6.6.4.2 Preparation of Test Specimens

Two batches of Triso-coated fissile particles, one having a WAR Amberlite (IRC-72 resin) kernel and the other having a WAR Duolite (C-464) kernel, were prepared and each separated into four fractions varying from near spherical to large deviations from a perfect sphere. Quantitative image analysis performed on all types showed that the deviations of the Amberlite particle type ranged from 9.6 to 29.7% and the Duolite from 9.6 to 15.8%. Table 6.63 presents the various shape characteristics of the fissile particles selected. Figure 6.15 shows radiographs of particles representing three significantly different shapes. The positions in the capsule, kernel composition and resin type, and their specific objectives are described in Table 6.64. Each fuel rod specimen contained one of the two Triso-coated fissile particle types, Biso-coated particles from batch J-489, and Triso-coated inert particles. All the ORNL-coated particles were heat-treated at 1800°C to stabilize the coatings. The physical characteristics of the ORNL-coated particle test set is described in Table 6.65. Deposition conditions for the fissile and fertile particles of HRB-13 are described in Table 6.66.

All ORNL fuel rod specimens were warm-molded. This technique provides a continuous matrix surrounding the fuel particles in a bonded-bed specimen. The matrix materials for all specimens were the same: 55 wt % Great Lakes Carbon Corporation (GLCC) 1074 graphite filler, 15 wt % Thermax, and 30 wt % Ashland grade 240 pitch. The particles were slurry blended with the matrix materials after which the mix was granulated, poured into a steel mold, and pressed at 135°C and 4.1 MPa (600 psi). Specimens were fabricated with a central hole

Table 6.63. Particle Shape Characteristics of Fissile Particles in Irradiation Capsule HRB-13

	Diameter, mm		Ratio	Area (mm^2)	Parimeter (mm)	Shape Factor[b]	Ratio[c]	Deviation from Sphere (%)
	Minimum	Maximum						
		Sample NXE OR-2549-H-3G (101 kernels, 99 particles)						
Kernel	0.368	0.379	1.030	0.108	1.221	0.072	0.905[c]	9.6
Coated Particle	0.580	0.593	1.024	0.272	1.938	0.072	0.905	
		Sample NXA OR-2549-H-2R (104 kernels, 101 particles)						
Kernel	0.332	0.371	1.112	0.094	1.152	0.069	0.867	13.3
Coated Particle	0.584	0.588	1.073	0.251	1.869	0.071	0.892	
		Sample NWW OR-2549-H-1RG (117 kernels, 112 particles)						
Kernel	0.284	0.324	1.121	0.072	0.991	0.068	0.854	14.6
Coated Particle	0.511	0.559	1.089	0.223	0.761	0.071	0.892	
		Sample NWX OR-2549-H-1RR (108 kernels, 102 particles)						
Kernel	0.391	0.503	1.294	0.134	1.540	0.056	0.704	29.7
Coated Particle	0.563	0.697	1.243	0.295	2.100	0.066	0.829	
		Sample NPG OR-2565-H-1GG (101 kernels, 98 particles)						
Kernel	0.412	0.431	1.045	0.138	1.383	0.072	0.905	9.6
Coated Particle	0.637	0.664	1.043	0.334	2.149	0.072	0.905	
		Sample NPE OR-2565-H-1GR (115 kernels, 111 particles)						
Kernel	0.422	0.479	1.133	0.154	1.476	0.070	0.880	12.1
Coated Particle	0.631	0.705	1.119	0.348	2.206	0.071	0.892	
		Sample NPF OR-2565-H-1RG (108 kernels, 102 particles)						
Kernel	0.423	0.503	1.190	0.160	1.518	0.069	0.867	13.3
Coated Particle	0.626	0.727	1.165	0.355	2.244	0.070	0.880	
		Sample NPD OR-2565-H-1RR (106 kernels, 106 particles)						
Kernel	0.426	0.511	1.202	0.161	1.537	0.067	0.842	15.8
Coated Particle	0.626	0.721	1.155	0.350	2.233	0.070	0.880	

[a]All values are based on average measurements.

[b]Shape factor formula = area/parimeter^2; for perfectly spherical particles, this value = $\pi r^2/(2\pi r)^2$ = 0.0796.

[c]Ratio = calculated shape factor/0.0796.

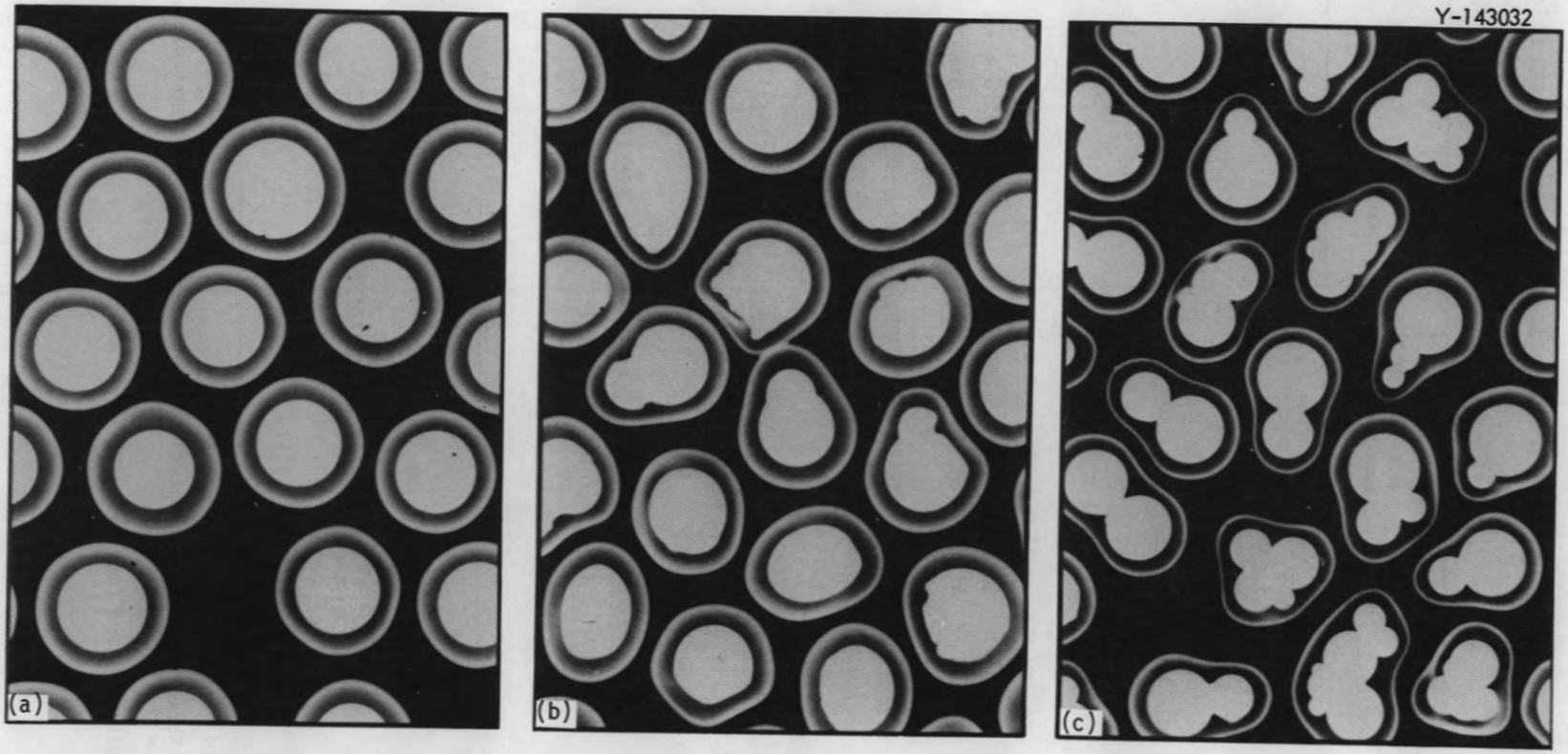

Fig. 6.15. Radiographs of Particles with Significantly Different Shapes. 24×. (a) OR-2565-A-1GG. (b) OR-2565-H-1RR. (c) OR-2549-1RR. Reduced 16%.

Table 6.64. Capsule Position, Kernel Compositions and Type, and Objective of HRB-13 Fuel Rod Specimens

Position in Capsule	Kernel Composition and Type[a]	Batch	Objective
1,2	WAR-A ($UC_{4.64}O_{1.36}$)	OR-2549-H-2R	Single satellite peaks attached to kernels
3,4	WAR-D ($UC_{5.04}O_{1.31}$)	OR-2565-H-1GR	Primarily slightly eccentric kernel
5,6	WAR-A ($UC_{4.64}O_{1.36}$)	OR-2549-H-1RG	Multiple and single satellites attached to kernels
7,8	WAR-A ($UC_{4.64}O_{1.36}$)	OR-2549-H-1RR	Clusters of small spheres and irregularly shaped kernel
9,10	WAR-A ($UC_{4.64}O_{1.36}$)	OR-2549-H-1RG	Multiple and single satellites attached to kernels
11,12	WAR-A ($UC_{4.64}O_{1.36}$)	OR-2549-H-2R	Single satellite peaks attached to kernels
13,14	WAR-D ($UC_{5.04}O_{1.31}$)	OR-2565-H-1GR	Primarily slightly eccentric kernel
15,16	WAR-A ($UC_{4.64}O_{1.36}$)	OR-2549-H-3G	Kernel meets or exceeds reference specification
17,18	WAR-A ($UC_{4.64}O_{1.36}$)	OR-2549-H-1RR	Clusters of small spheres and irregularly shaped kernel
19,20	WAR-A ($UC_{4.64}O_{1.36}$)	OR-2549-H-2R	Single satellite peaks attached to kernels
21,22	WAR-D ($UC_{5.04}O_{1.31}$)	OR-2565-H-1GR	Primarily slightly eccentric kernel
23,24	WAR-D ($UC_{5.04}O_{1.31}$)	OR-2565-H-1RR	Irregularly shaped kernel
25,26	WAR-D ($UC_{5.04}O_{1.31}$)	OR-2565-H-1GG	Kernel meets or exceeds specification
27–30	LASL Experiment		Advanced fuels
31,32	WAR-D ($UC_{5.04}O_{1.31}$)	OR-2565-H-1RG	Primarily grossly eccentric kernel
33,34	WAR-D ($UC_{5.04}O_{1.31}$)	OR-2565-H-1RR	Irregularly shaped kernel
35,36	WAR-D ($UC_{5.04}O_{1.31}$)	OR-2565-H-1RG	Primarily grossly eccentric kernel
37–40	LASL Experiment		Advanced fuels

[a]WAR-A from Amberlite weak-acid resin; WAR-D from Duolite weak-acid resin.

Table 6.65. Characteristics of the ORNL Coated Particle Test Set for HRB-13

Batch Number	Position	Kernel Type	Conversion (%)	Kernel		Coating Thickness, μm, and Coating Density (Mg/m^2)			
				Diameter (μm)	Density (Mg/m^2)	Buffer	iLTI	SiC	oLTI
OR-2549-H (Fissile)	1, 2, 5, 6, 7, 8, 9, 10, 11, 12, 15, 16, 17, 18, 19, 20	WAR-A	30–40	360	3.2	50 (<1.2)	35 (1.95)	30 (>3.18)	35 2.00
OR-2565-H (Fissile)	3, 4, 13, 14, 21, 22, 23, 24, 25, 26, 31, 32, 33, 34, 35, 36	WAR-D	30–40	410	2.5	50 (<1.2)	35 (1.95)	32 (>3.18)	35 2.00
J-489 (Fertile)	All ORNL specimens	ThO_2 (sol-gel)		500	10	85 (1.1)	none	none	75 (1.9)

2.29 mm (0.90 in.) in diameter. (Original plans called for a platinum-molybdenum centerline thermocouple; however, because of the chemical interaction observed in HRB-11 it was removed before irradiation.) Specimens were then carbonized vertically in a packed bed of natural flake graphite at 900°C at a heating rate of 90°C/hr. They were then heat-treated at 1800°C for 30 min for dimensional stability.

The specimens were characterized by dimensional measurements, weight, radiography, metallography, and photography. The specimens were all nominally 12.5 diam and 10 mm long (0.49 by 0.39 in.). All specimens had a 2.29-mm-diam (0.090-in.) central hole. An identification mark was formed on one end of each specimen for orientation so that the specimen dimensions could be measured at the same location both before and after irradiation. The dimensions along with the heavy-metal loadings for each specimen are shown in Table 6.67.

Table 6.66. Deposition Conditions for Fissile and Fertile Particles for HRB-13

Layer	Coating Gas	Temperature, °C		Deposition Rate, μm/min		
		Fissile	J-489	OR-2549-H	OR-2565-H	J-489
Buffer	C_2H_2	1125	1350	6.67	6.25	22.98
iLTI	MAPP	1275		2.19	2.00	
SiC	CH_3SiCl_3	1550		0.20	0.20	
oLTI	MAPP	1275		3.12	3.02	
	C_3H_6		1350			5.83

Table 6.67. Dimensions and Heavy-Metal Loadings for ORNL Fuel Specimens in Irradiation Capsule HRB-13

Specimen Location[a]	Average Diameter[b]		Average Length		U per Specimen (g)	Loading, Mg/m^3	
	(mm)	(in.)	(mm)	(in.)		^{235}U	Th
1	12.410	0.4886	9.934	0.3911	0.0526	0.0421	0.5666
2	12.395	0.4880	9.837	0.3873	0.0526	0.0426	0.5736
3	12.423	0.4891	9.842	0.3875	0.0472	0.0381	0.5365
4	12.436	0.4896	9.756	0.3841	0.0472	0.0383	0.5401
5	12.413	0.4887	9.733	0.3832	0.0431	0.0352	0.5125
6	12.418	0.4889	9.764	0.3844	0.0431	0.0351	0.5105
7	12.398	0.4881	9.761	0.3843	0.0396	0.0323	0.4897
8	12.426	0.4892	9.804	0.3860	0.0396	0.0320	0.4853
9	12.421	0.4890	10.020	0.3945	0.0361	0.0286	0.4566
10	12.428	0.4893	9.695	0.3817	0.0361	0.0296	0.4713
11	12.416	0.4888	9.931	0.3910	0.0337	0.0269	0.4445
12	12.403	0.4883	9.820	0.3866	0.0337	0.0273	0.4505
13	12.416	0.4888	9.749	0.3838	0.0323	0.0264	0.4383
14	12.413	0.4887	9.929	0.3909	0.0323	0.0259	0.4306
15	12.431	0.4894	9.830	0.3870	0.0313	0.0252	0.4217
16	12.426	0.4892	9.815	0.3864	0.0313	0.0253	0.4227
17	12.428	0.4893	9.820	0.3866	0.0301	0.0243	0.4114
18	12.408	0.4885	9.982	0.3930	0.0301	0.0240	0.4061
19	12.451	0.4902	9.947	0.3916	0.0300	0.0238	0.3939
20	12.428	0.4893	9.807	0.3861	0.0300	0.0243	0.4011
21	12.433	0.4895	9.771	0.3847	0.0300	0.0243	0.4022
22	12.431	0.4894	9.680	0.3811	0.0300	0.0246	0.4062
23	12.443	0.4899	9.718	0.3826	0.0301	0.0245	0.4147
24	12.433	0.4895	9.710	0.3823	0.0301	0.0246	0.4157
25	12.403	0.4883	9.985	0.3931	0.0313	0.0250	0.4171
26	12.416	0.4888	9.746	0.3837	0.0313	0.0255	0.4264
31	12.441	0.4898	9.764	0.3844	0.0361	0.0295	0.4697
32	12.405	0.4884	9.888	0.3893	0.0361	0.0289	0.4611
33	12.408	0.4885	9.870	0.3886	0.0396	0.0319	0.4834
34	12.403	0.4883	9.967	0.3924	0.0396	0.0316	0.4792
35	12.405	0.4884	9.776	0.3849	0.0431	0.0351	0.5109
36	12.416	0.4888	9.977	0.3928	0.0431	0.0344	0.4998

[a]Specimens 27 through 30 and 37 through 40 were LASLs advanced fuels.

[b]Inside diameter for all specimens is 2.29 mm (0.090 in.).

6.6.4.3 Capsule Operation

Irradiation capsule HRB-13 was installed into the PB-13 (VXF-13) facility of HFIR on November 15, 1976, at the beginning of cycle 140. (The PB-13 facility is described in Sect. 6.6.3.3 of this report.) The reactor was started up slowly during cycle 140 to minimize the impact of the high fission heat rates, which usually occur in fully enriched fissile particles at the beginning of an HRB experiment. The reactor power began at 68 MW and gradually increased to 100 MW after 24 days, at which time sufficient reactivity was left in the HFIR core to operate for three days at 100 MW. During this initial irradiation cycle the capsule sweep gas was maintained at 100% He.

To date the HRB-13 capsule is in its second irradiation cycle in the PB-13 facility, and has operated at 100 MW reactor power and a temperature of 1250°C for approximately 900 hr. The planned schedule calls for HRB-13 to be irradiated for three cycles in the PB facility and nine cycles in the RB facility.

6.7 IRRADIATION TESTS IN THE ORR — T. N. Tiegs

The irradiation test series in the Oak Ridge Research Reactor (ORR) includes two capsules to date: OF-1 and OF-2. The OF-1 capsule was irradiated for more than 9300 hr at reactor full power and achieved a peak fluence of 1.08×10^{26} n/m^2 (>0.18 MeV). The irradiation of capsule OF-2 was terminated on August 1, 1976, following 8440 hr of full power irradiation.

6.7.1 OF-1 Capsule

The OF-1 Irradiation Experiment was the first in the series of HTGR fuel irradiations in the ORR. It was a joint experiment between GA and ORNL. Detailed descriptions of the design, fabrication, operation and postirradiation examination have been previously reported.[16–19] A final report[20] on the OF-1 experiment was completed during this reporting period.

6.7.2 Capsule OF-2

The OF-2 Irradiation Experiment was the second in a series of HTGR fuel irradiations in the ORR. It was irradiated to approximately 80% of HTGR burnup and fast (>0.18 MeV) neutron exposure. The experiment consisted of three graphite magazines, each containing four fuel holes with fuel rods. Details of the OF-2 capsule have been reported previously.[19,21]

6.7.2.1 Capsule Operation

Capsule OF-2 began irradiation in the E-7 position of the ORR core on June 21, 1975 and terminated irradiation on August 1, 1976 following 8440 hr at reactor full power.

During initial operation it was discovered that the total reaction rates were higher in the ends of the capsule because of a change in the neutron spectrum. The result was an increase of approximately 20% in heat generation rate for fuel rods located at the top of magazine A and at the bottom of magazine C (i.e., at the ends of the capsule). The major temperature changes were for fuel rods in the top 50 mm (2 in.) in magazine A, which operated approximately 100°C above the design temperature of 1150°C, and the maximum temperature in magazine C (1350°C) occurred in the fuel rods at the bottom. Details of these results are presented in ref. 21.

A complete history of fission gas release-to-birth rate ratios (R/B) for cells 1 and 2 is presented in Fig. 6.16. Cell 1 was occupied by magazine C, while magazines A and B were in cell 2. The fuel contained in magazines A, B, and C is described in detail in ref. 19.

Neutron radiographs of capsule OF-2 were taken. Although detailed examinations of the radiographs have not been completed, it was quite apparent that magazines B and C were not centered in their respective cells. Postirradiation dimensional analysis showed that magazines B and C were both bowed in excess of 1.0 mm (0.04 in.).

Preliminary estimates of fast neutron fluence and fuel burnup have been made and are presented in Figs. 6.17 through 6.19. It should be emphasized that these are preliminary values and will be revised when the dosimetry analysis is completed.

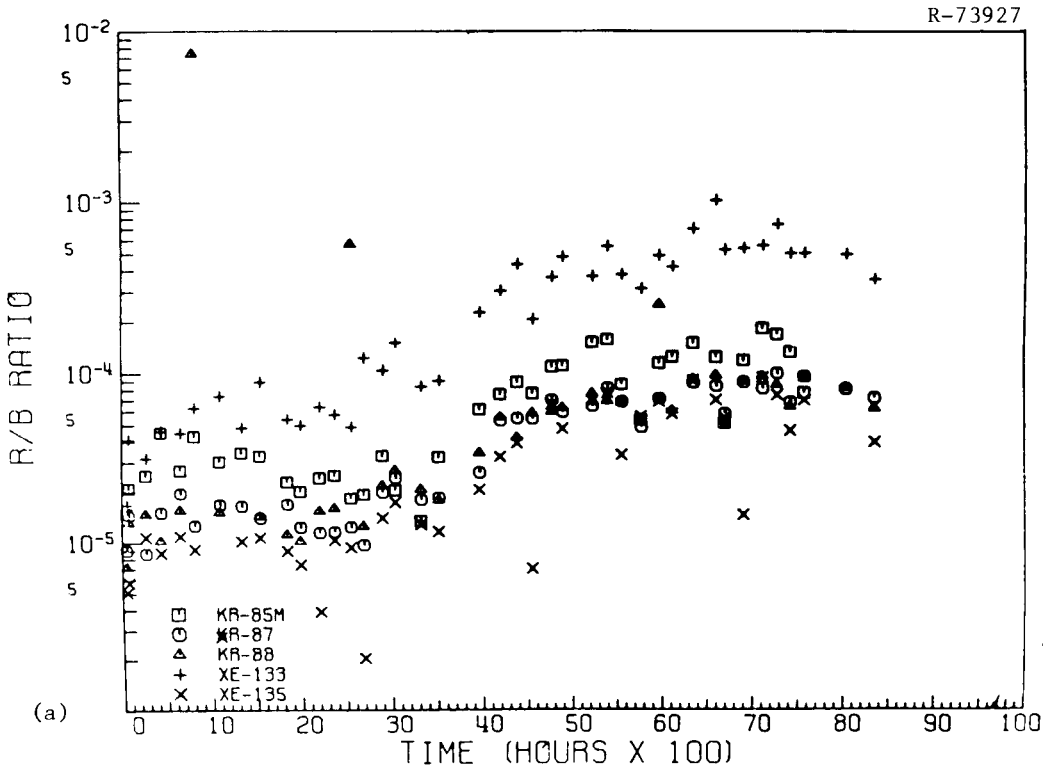

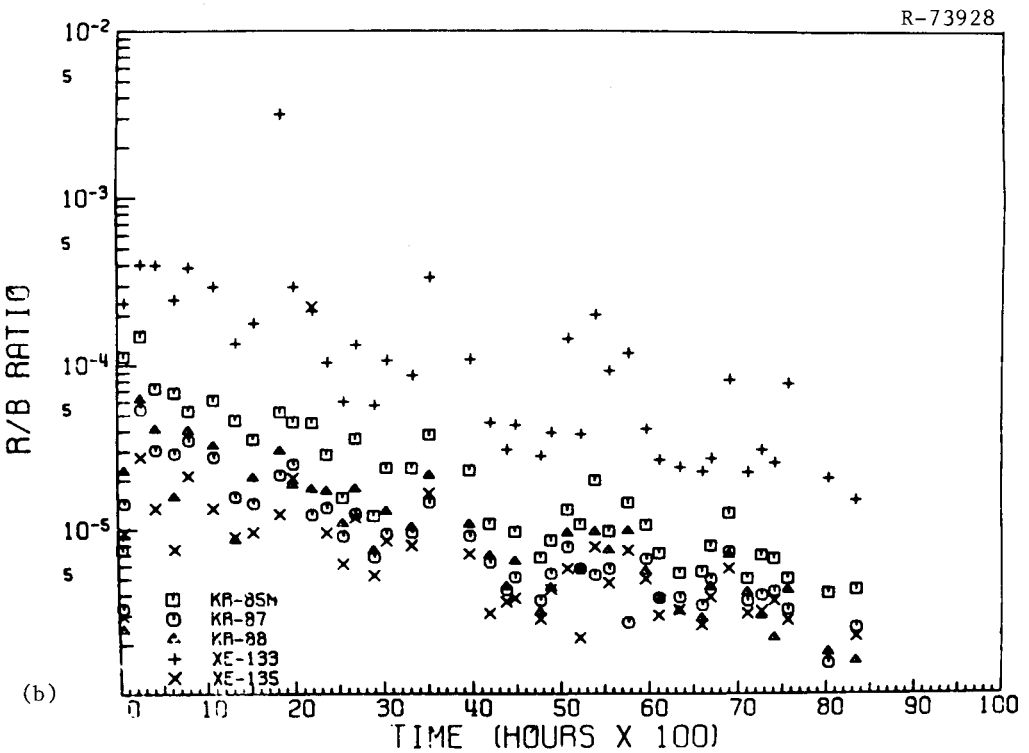

Fig. 6.16. Fission Gas Release-to-Birth Ratios for OF-2 During Irradiation. (a) Cell 1. (b) Cell 2.

R-73931

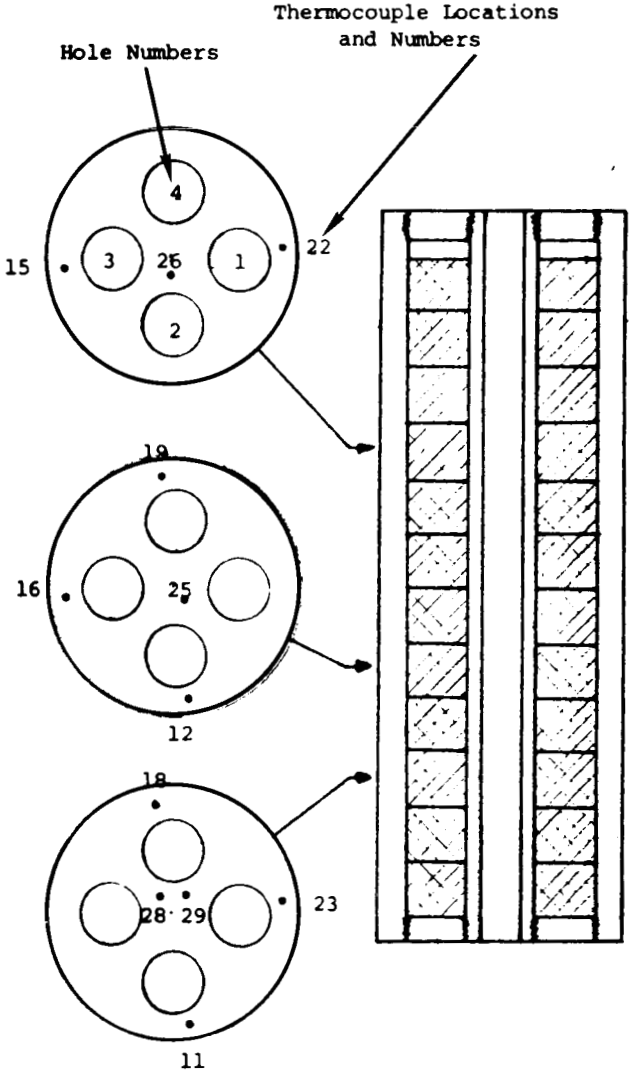

Distance Above HMP (mm)	Distance Above HMP (in.)	Estimated Average Fast Fluence, >0.18 MeV (n/m^2)	Estimated Average Burnup (% FIMA) ^{235}U	^{238}U	^{232}Th
266.7	10.50	1.94×10^{25}	50.0	2.29	0.59
254.0	10.00	2.25	54.1	2.83	0.74
241.3	9.50	2.55	58.3	3.48	0.94
228.6	9.00	2.83	61.7	4.14	1.13
215.9	8.50	3.19	59.9	4.20	1.14
203.2	8.00	3.57	63.0	4.89	1.35
190.5	7.50	3.92	65.2	5.46	1.53
177.8	7.00	4.24	67.1	6.01	1.71
165.1	6.50	4.56	69.0	6.63	1.91
152.4	6.00	4.88	70.4	7.15	2.08
139.7	5.50	5.23	71.2	7.74	2.28
127.0	5.00	5.58	73.0	8.31	2.48

Fig. 6.17. Preliminary Estimates of Neutron Fluence and Fuel Burnup in Specimen Holder A of Capsule OF-2.

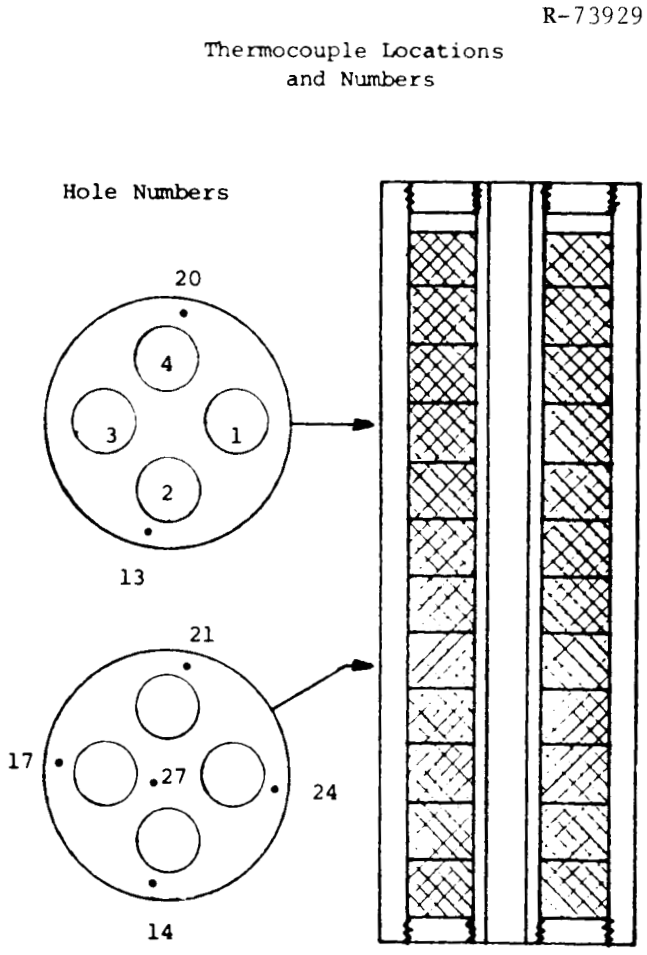

Distance Above HMP (mm)	Distance Above HMP (in.)	Estimated Average Fast Fluence, >0.18 MeV (n/m^2)	Estimated Average Burnup (% FIMA) ^{235}U	^{238}U	^{232}Th
92.08	3.625	6.38×10^{25}	75.5	9.69	2.96
79.38	3.125	6.64	76.1	10.1	3.13
66.68	2.625	6.86	76.7	10.6	3.29
53.98	2.125	7.11	77.3	11.0	3.44
41.28	1.625	7.31	77.8	11.4	3.60
28.58	1.125	7.56	78.1	11.7	3.71
15.88	0.625	7.75	78.4	12.1	3.84
13.18	0.125	7.91	78.7	12.4	3.94
−9.52	−0.375	8.01	79.0	12.7	4.07
−22.22	−0.875	8.20	79.2	12.9	4.15
−34.92	−1.375	8.26	79.4	13.1	4.22
−47.62	−1.875	8.36	79.5	13.2	4.28

Fig. 6.18. Preliminary Estimates of Neutron Fluence and Fuel Burnup in Specimen Holder B of Capsule OF-2.

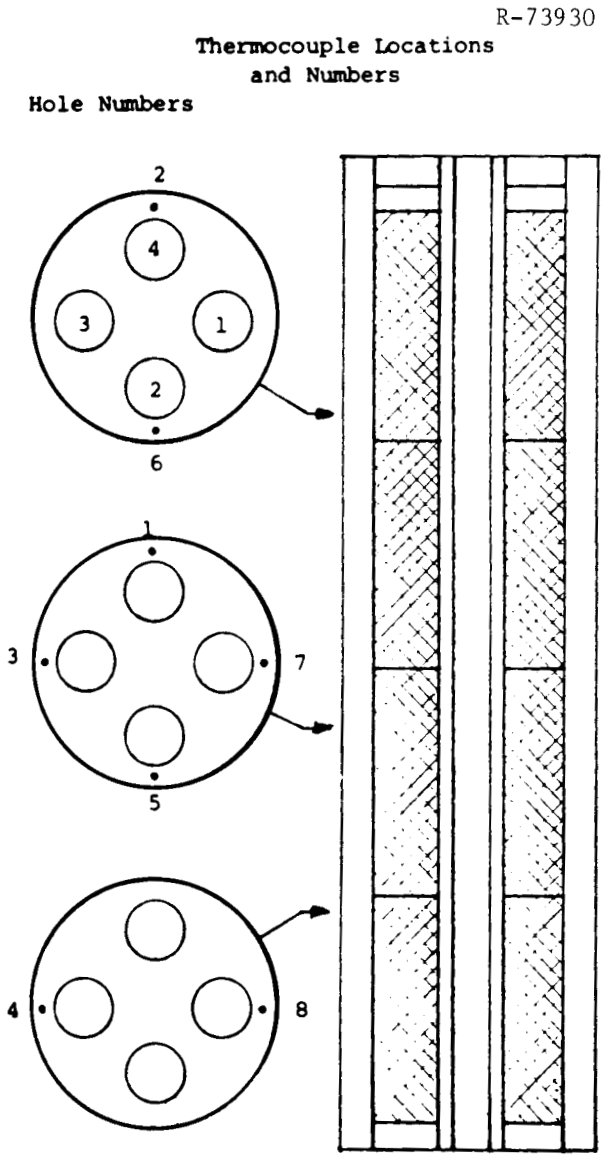

Distance Above HMP (mm)	Distance Above HMP (in.)	Estimated Average Fast Fluence, >0.18 MeV (n/m^2)	Estimated Average Burnup (% FIMA) ^{235}U	^{238}U	^{232}Th
−123.8	−4.875	8.91×10^{25}	79.6	13.4	4.34
−174.6	−6.875	8.50	79.0	12.7	4.07
−225.4	−8.875	7.62	77.5	11.2	3.50
−276.2	−10.875	5.86	75.9	9.15	2.77

Fig. 6.19. Preliminary Estimates of Neutron Fluence and Fuel Burnup in Specimen Holder C of Capsule OF-2.

6.7.2.2 Postirradiation Examination

The OF-2 capsule was sectioned, and the bulkheads along with accompanying thermocouples were removed. All three graphite magazines were retrieved in excellent condition.

Gross gamma scans (0.55–0.75 MeV) along the magazines indicated some fuel rod inhomogeneity. The burnup profiles along the magazines were fairly constant except for the bottom portion of magazine C. Fuel rods located at this position had been fabricated with much higher fuel loadings to compensate for the expected lower neutron reaction rates at this axial position of the ORR core. This problem is discussed in detail in ref. 21. The gamma scans showed that the loadings were too high, as the burnup profiles were much higher than those of adjoining fuel rods.

The fuel rods were removed from the graphite magazines and visually examined. The results are given below:

Magazine A — Fuel rods from this magazine were in good condition, with only slight debonding. This magazine contained 36 fuel rods located in four fuel holes. Fuel holes 1 and 2 each contained six 25-mm-long (1-in.) rods, and fuel holes 3 and 4 each contained twelve 13-mm-long (0.5-in.) rods. Visual inspection of the surface of each of the fuel rods indicated that ten rods had from 1 to 12 failed particles visible. The remaining 26 rods indicated no visible failures on the fuel rod surface.

Magazine B — This magazine also contained 36 fuel rods located in four fuel holes in a similar arrangement to that described above for magazine A. Fuel rods from holes 1 and 2 were in good condition, with only slight debonding at their edges. Fuel rods from holes 3 and 4 were in much worse condition. Eight fuel rods had completely debonded, having no apparent structure. These rods were located in positions B-3-1, -2, -6, -7, -8, B-4-1, -2, and -11. All the rods from holes 3 and 4 were fabricated with the same matrix characterized by low pitch-coke yields (12–19%), which may have resulted in weak fuel rods. The

eight completely debonded rods were not visually examined for particle failures. Of the remaining 28 fuel rods, eight had from 1 to 12 failed particles visible on the fuel rod surface and 20 had no visible failures on the fuel rod surface.

Magazine C — This magazine contained sixteen 50-mm-long (2-in.) fuel rods located in four fuel holes. The fuel rods from this magazine were in good condition, with only moderate debonding on a few rods. Visual examination at high magnification revealed a large number of outer pyrocarbon coating failures on the surfaces of several of the fuel rods. Failures were most prevalent on the surface of rods containing fissile particle batch A-615. This particle batch is 75% converted and was coated with a cone gas distributor in the 0.13-m (5-in.) coating furnace. Those fuel rods with high loadings located at the bottom of the magazine also had a high number of failures located on their surfaces.

The results of the dimensional analysis of the fuel rods are given in Fig. 6.20. The fuel rods from magazines A and B exhibited shrinkage up to a fast fluence of 7×10^{25} n/m^2 (>0.18 MeV), at which point a

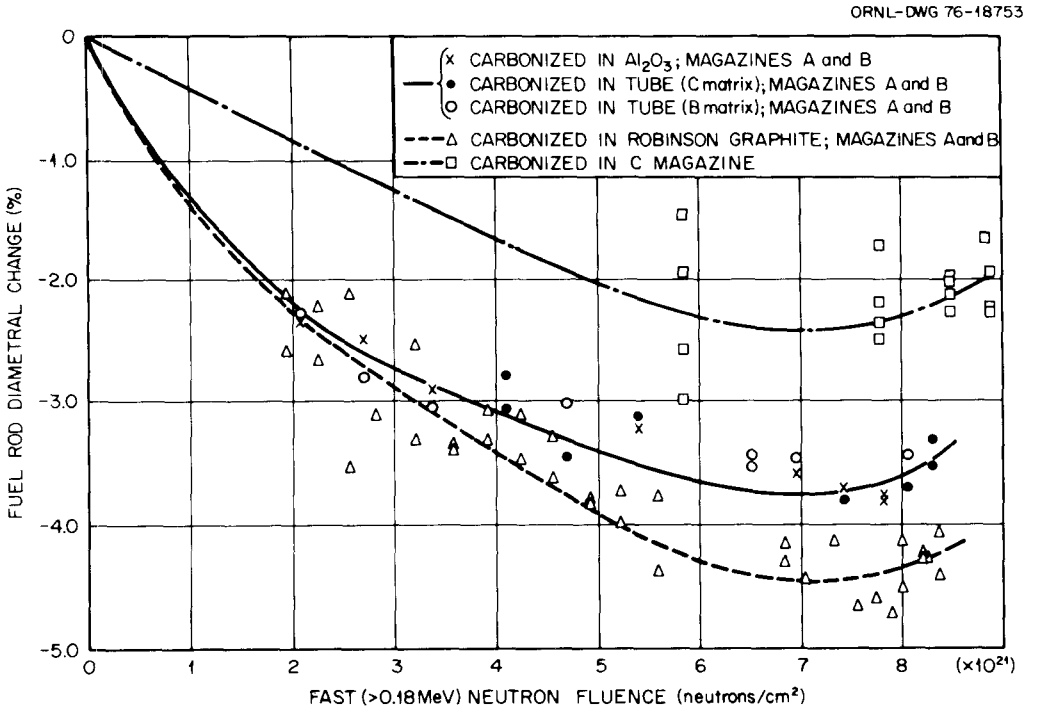

Fig. 6.20. OF-2 Fuel Rod Dimensional Changes vs Estimated Fast Fluences.

turnaround was encountered and the rods began to swell. The rods carbonized in Robinson graphite showed greater shrinkages than those rods carbonized in packed Al_2O_3 or in-tube. Because the rods in magazine C were carbonized in-block, the diametral changes were calculated by use of preirradiation dimensions of rods fabricated and processed exactly like the ones irradiated. These rods showed lower shrinkages than rods carbonized in any other modes. It should be noted that the rods in C magazine contained many more Triso-coated particles (in the form of inerts and fissiles) than rods irradiated in the other two magazines. The increase in Triso-particle packing fractions apparently resulted in less irradiation-induced shrinkage.

Selected fuel rods from magazine C were examined metallographically to determine the cause of the coating failures observed during the visual examination. Representative particles from each fissile particle batch included in magazine C are shown in Fig. 6.21. As shown, particles from batches A-601 and A-611 appeared in relatively good condition, whereas particles from batch A-615 showed failure of the outer LTI in every particle examined. The outer LTI failures in batch A-615 are attributable to anisotropy of the coating, which causes differential shrinkage during irradiation. Coating failures of this type have been observed in previous experiments.[20,22] In addition to outer LTI failures due to irradiation-induced shrinkage, outer LTI failures caused by matrix-particle interaction were also observed in the metallographic examination.

Other than the outer LTI failures, the fissile particles from the three batches in magazine C, the fuel appeared to have performed very well. No broken SiC coatings were observed and only slight fission product attack ($\leqslant 5$ μm) was noted. No amoeba-type kernel migration or other thermal gradient effects were seen.

The postirradiation examination of capsule OF-2 is continuing and will be completed during the next reporting period.

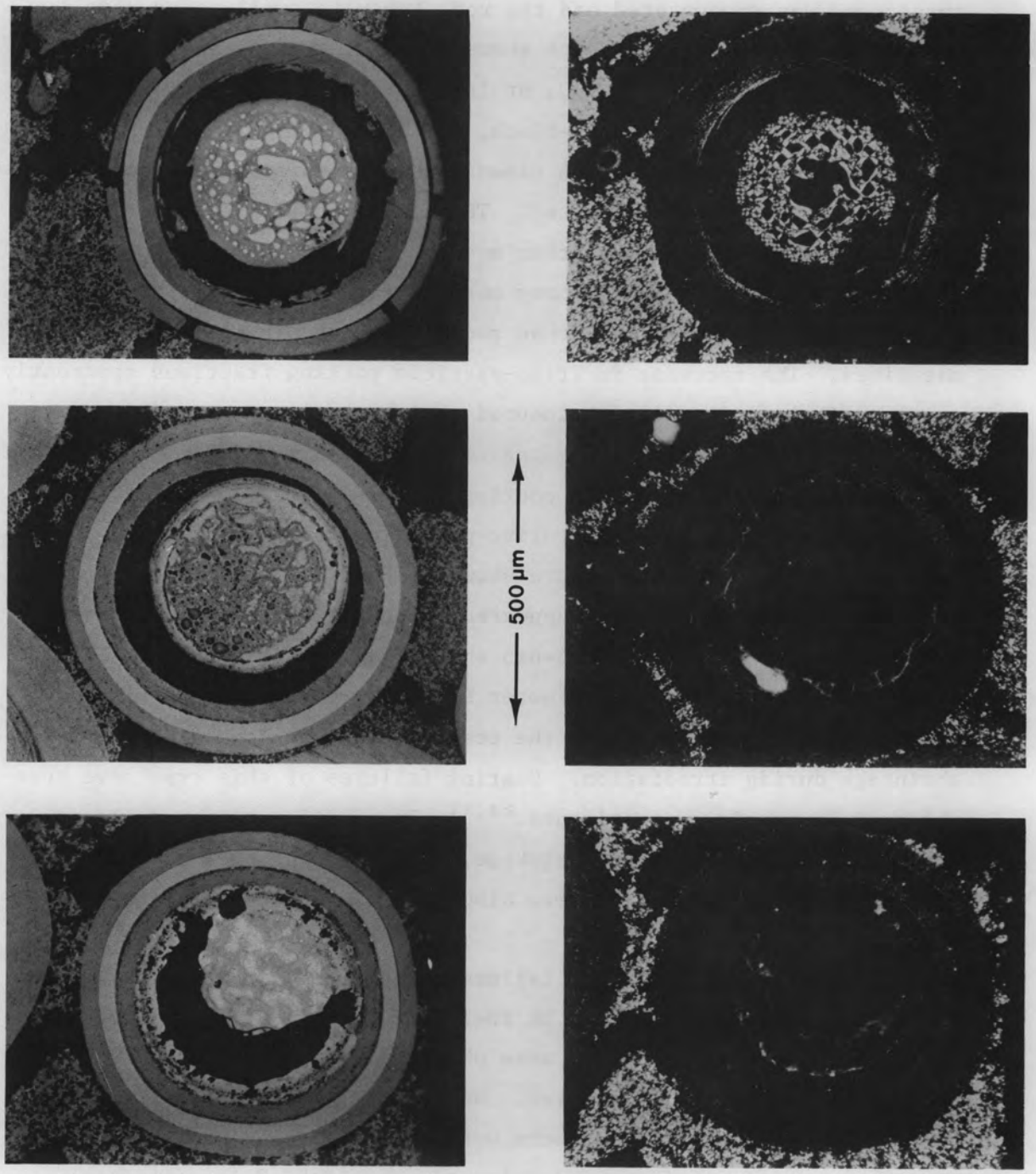

Fig. 6.21. Comparison of Batches Made with Different Gas Distributors in the 0.13-m Coater. Frit distributor (middle, batch 611, and bottom, batch 601) gives better irradiation behavior than cone (top, batch 615). Left: bright field. Right: polarized light.

6.8 CAPSULE THERMOMETRY — R. L. Shepard, K. R. Thoms, and R. K. Williams

Thermometers with improved accuracy, reliability, and chemical compatibility are being developed for instrumented irradiation capsules for HTGR fuel qualification and graphite creep tests. Fuel irradiation experiments conducted in the HRB series capsules in the HFIR require centerline thermometers less than 3 mm OD that can measure temperatures to at least 1350°C with an accuracy of ±10°C during irradiations as long as 6000 hr, during which the thermometers accumulate a neutron fluence of as much as 3×10^{26} n/m^2 (thermal) and 8×10^{25} n/m^2 (fast). A specific problem in this application is graphite-sensor compatibility: both preventing carbon contamination of the thermometer and also preventing the attack on fuel particle coating by sensor sheath materials. Graphite creep irradiation tests in the OC series in the ORR require thermometers that can measure temperatures from 600°C to 1250°C with an accuracy of 1% during irradiations as long as 4700 hr (four reactor cycles), accumulating a neutron fluence of about 2×10^{25} n/m^2 (total fast and thermal). In the creep tests, the thermometers are not in contact with coated fuel particles, but the thermometer must be protected from contamination by the surrrounding graphite holder.

During this reporting period, development and testing of three thermometers were continued: (1) the Johnson noise power thermometer (JNPT), (2) platinum-alloy thermocouples with low neutron cross sections, and (3) the tungsten-rhenium (W-Re) thermocouples.

6.8.1 Thermometer Development

6.8.1.1 Johnson Noise Power Thermometer Development — R. L. Shepard, T. V. Blalock,* R. J. Fox, and J. L. Horton

The Johnson noise power thermometer (JNPT) utilizes the electrical noise spontaneously produced by a passive resistor to provide an absolute measurement of temperature that is independent of composition,

---

*Professor of Electrical Engineering, University of Tennessee, Knoxville.

irradiation, or past history of the sensor.[23] Fuel centerline JNPTs were built and used in the HRB-9 and -10 irradiation capsules at temperatures of 1350 to 1500°C during 4500-hr irradiations to demonstrate the feasibility of the use of these thermometers in irradiation capsule thermometry.[24] These JNPTs employed sensors with a single rhenium 20-Ω resistor and an electronic system that alternately measured the noise voltage and the noise current from the resistor. The two measurements were combined by a digital processor to calculate noise power and absolute temperature.

A serious deficiency in the sensor design was revealed in the HRB-10 experiment. The coated fuel particles and the rhenium-foil-wrapped Mo-Re sensor sheath chemically interacted, as shown in Fig. 6.22 at an irradiation temperature of about 1500°C. To improve the

Fig. 6.22. Interaction Between Coated Fuel Particle and Rhenium-Foil-Wrapped Mo-Re Sensor Sheath in HRB-10 Experiment. 150×.

compatibility of the sensor-fuel system, short sections of rhenium, tungsten, and Mo—48% Re tubing were coated with a 76-μm thickness of ZrC, applied by chemical vapor deposition (CVD). These sections were heated in contact with graphite at 1700°C for 500 hr in an inert atmosphere and then examined. The ZrC coating provided an adequate carbon barrier, as shown in Fig. 6.23. Sheaths were then prepared for the JNPT sensors for the HRB-12 experiment by coating closed-end rhenium tubes with 0.08 to 0.15-mm-thick CVD ZrC coatings.

The sensors for the HRB-12 experiment were made with two 18-Ω rhenium resistors, insulated with hard-fired BeO, contained within the 3.2-mm-OD (0.125-in.) ZrC-coated rhenium sheath. This sensor design, shown in Fig. 6.24 with the appropriate electronics, permits measurement of noise voltage on one resistor simultaneously with

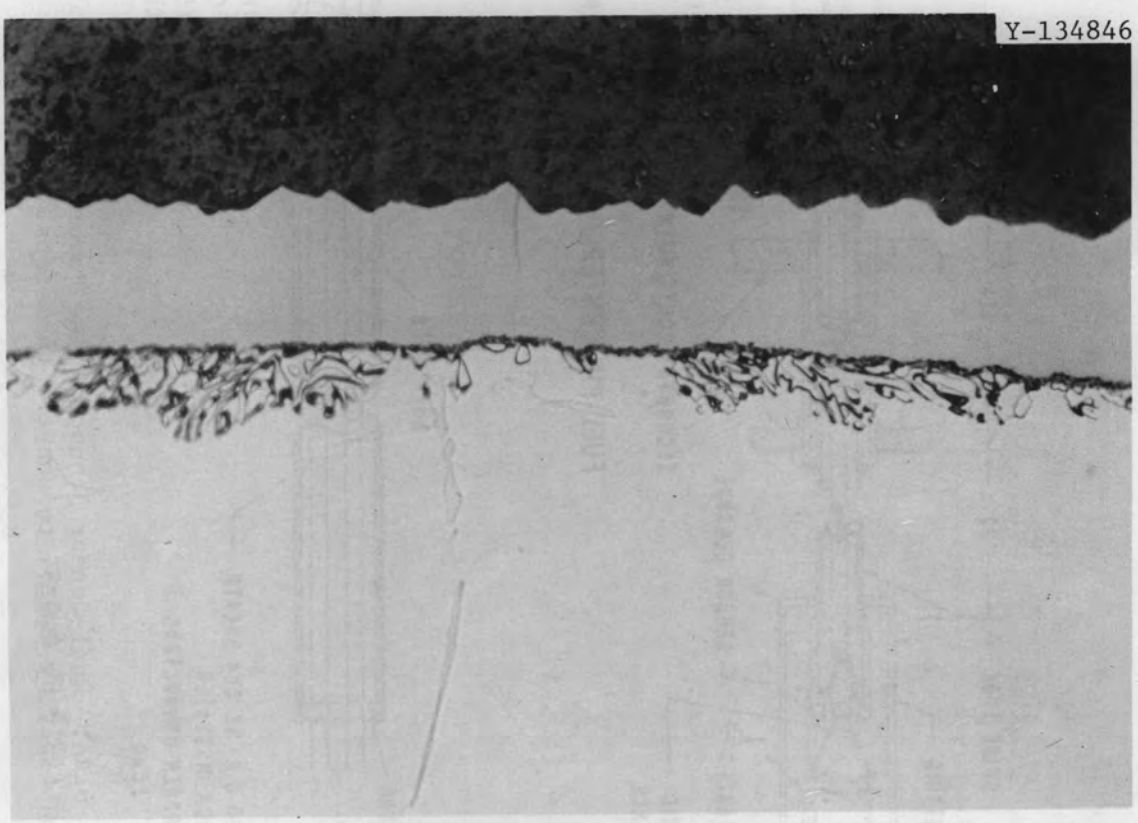

Fig. 6.23. ZrC Coating on Mo-Re Tubing Provided an Adequate Carbon Barrier. Note carbide formed at interface during 500-hr bake at 1700°C. 500×.

ORNL-DWG 75-18071

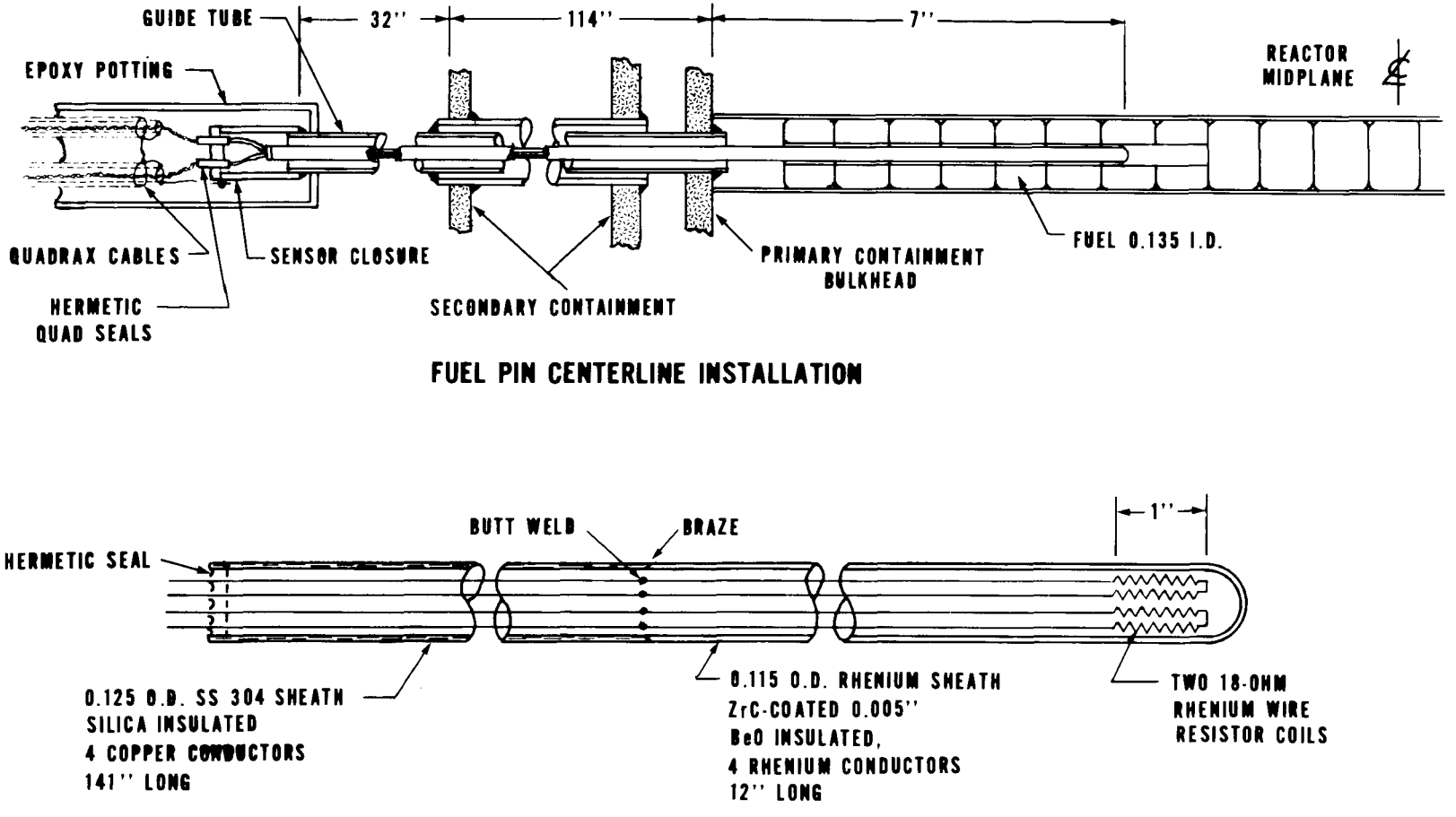

Fig. 6.24. Dual-Sensor Johnson Noise Power Thermometer for Capsule HRB-12. Dimensions are in inches; multiply by 0.0254 to convert to meters.

noise current on the other, reducing the signal acquisition time from about 40 s to 10 s, and providing sensor redundancy when operated in the commutating mode used in HRB-9 and -10.

This dual sensor was installed in the HRB-12 capsule and irradiated. At the beginning of irradiation, with the reactor at 100 MW power, the HRB-12 JNPT indicated 1145°C as compared with a temperature of 1170°C indicated by the Pt-Mo thermocouple in the nearly identical HRB-11 capsule under the same conditions. After four days irradiation, the JNPT indicated temperatures 100 to 200°C higher than the Pt-Mo thermocouple had indicated, and became then progressively higher and unstable. During the reactor shutdown after the first irradiation cycle, the JNPT-indicated temperature was observed to be affected by the main water pump, dropping from 305 to 105°C when the pump was turned off and then increasing 200°C when the pump was turned on. This behavior was examined by vibrating a similar sensor at 60 to 80 Hz with a 0.25 *g* acceleration. This produced an increased electrical noise (at the 80 kHz measuring frequency) corresponding to a 50% increase in absolute temperature, or approximately 150°C at room temperature. This microphonic behavior was found in other sensors with loose-fitting, hard-fired insulators, and was eliminated in a later design by swaging the sensor sheath and compacting the insulator. Following seven reactor cycles of generally unsuccessful behavior, the HRB-12 JNPT failed with both resistors open circuit at the start of the eighth cycle.

6.8.1.2 Development of Platinum-Base Thermocouples — R. K. Williams, D. L. McElroy, and R. L. Shepard

The goals of this work are to develop improved platinum-base thermoelements and define the factors that limit their application at higher temperatures. Some drift test and compatibility results were obtained during the last year. The drift test included eight different platinum-sheathed, Al_2O_3-insulated, low-cross-section thermocouples, and data were obtained for 1000 hr at 1400°C plus a final 24 hr at 1500°C. The nominal thermocouple compositions and drift data are shown in Table 6.68. The post-test examination of these thermocouples is incomplete, but results obtained to date indicate:

Table 6.68. Drift Test[a] Results on Some Low-Cross-Section Thermocouples[b]

Number	Thermocouple Elements		Decalibration, °C, at 1400°C After		Remarks
	+	−	200 hr	1000 hr	
1	Pt–5% Mo	Pt	Failed open circuit at 44 hr		No Pt sheath
2	Pt–5% Mo	Pt	−7	−26	
3	Pt–5% Mo	Pt–0.1% Mo	−4	−20	
4	Pt–5% Mo	Pt–0.1% Mo	−22	−66	Swaged construction from construction vendor
5	Pt–5% Mo	Pt–1% Mo	−1	−18	Survived 24 hr at 1500°C
6	Pt–8% Ru	Pt	−11	−69	
7	Pt–8% Ru	Pt	−23	−61	Damaged during assembly; small He leak detected
8	Pt–8% Ru	Pt–1% Ru	−12	−31	
9	Pt–5% Mo	Pt–8% Ru	−3	−18	Survived 24 hr at 1500°C
10	Pt–3% Cr	Pt	−14	−38	Pt–3% Cr alloy produced at ORNL
11	Pt–0.5% Nb	Pt	−4	−14	Pt–0.5% Nb alloy produced at ORNL
12	Pt–30% Rh	Pt–6% Rh	−5	−32	Calibrated thermocouple included for initial calibration and comparison

[a]Graphite-argon environment.

[b]All thermocouples had insulated junctions and, except as noted above, were Pt sheathed and insulated with high-purity hard-fired Al_2O_3. These thermocouples were baked out under vacuum at about 950°C for 24 hr and backfilled with 34 kPa (0.33 atm) He.

1. the Pt–5% Mo vs Pt–8% Ru and Pt–5% Mo vs Pt–1% Mo thermocouples showed the best performance over the whole test period,
2. platinum-base thermocouples are more stable when both thermoelements are alloyed, and
3. the carbon-platinum-alumina system is not compatible at 1400°C.

Metallographic examination (Fig. 6.25) of interaction between platinum sheath and hard-fired alumina insulators showed a reaction layer at this boundary. Apparently the reaction involves solution of the alumina in platinum, and this drastically lowers the solidus temperature of the platinum-alumina alloy reaction products.

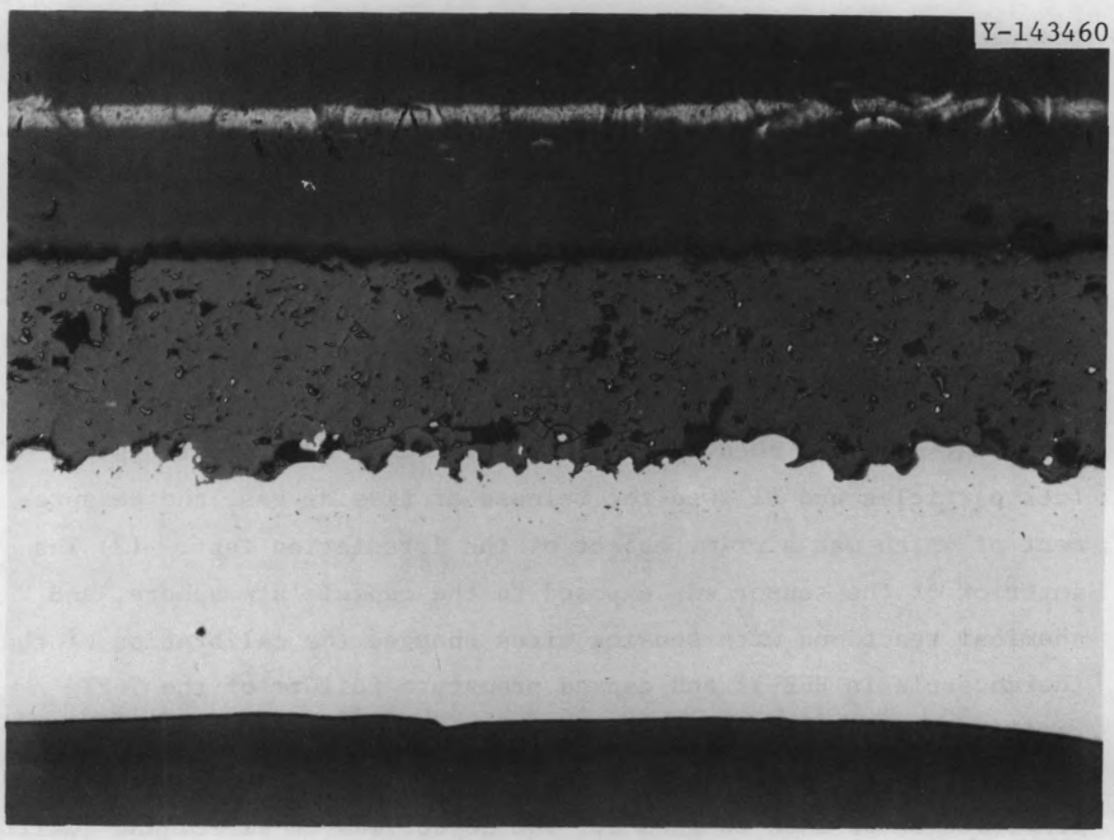

Fig. 6.25. Interaction Between Platinum Sheath and Alumina Insulator in the Presence of Carbon at 1400°C. 100×.

A 1500°C 110-hr test in argon and graphite was also conducted to aid in interpreting the long-term drift results. These samples showed that:

1. Carbon and platinum do not interact very much. A platinum tube that did not contain Al_2O_3 showed minimal grain growth, dimensional stability, and unchanged ductility.

2. Carbon and Al_2O_3 react in the absence of platinum, but platinum enhances the reaction, probably by dissolving aluminum.

3. Tests on evacuated platinum capsules containing high-purity oxide powders showed that MgO should be much superior to Y_2O_3 and Al_2O_3 as a thermocouple insulator.

These studies indicate that the two principal problems limiting the usefulness of the low-cross-section platinum thermocouples are (1) compatibility of the sheath-insulator system in a reducing environment and (2) mechanical degradation of the wires due to excessive grain growth. Some possible solutions to these problems are now being investigated.

6.8.1.3 Sensor Sheath Compatibility with Coated Fuel Particles — R. L. Shepard, R. L. Beatty, C. S. Morgan, and G. W. Weber*

Failures of sensor sheaths in HRB-10 and -11 caused two major problems: (1) The sheath materials reacted with the coatings of fuel particles and allowed the release of fission gas, the measurement of which was a prime object of the irradiation test. (2) The interior of the sensor was exposed to the capsule atmosphere, and chemical reactions with sensing wires changed the calibration of the thermocouple in HRB-11 and caused premature failure of the JNPT resistors in HRB-10. A series of 500-hr compatibility tests was conducted in a graphite tube furnace with an inert atmosphere at temperatures of 1300 to 1500°C. The object was to select and qualify sensor sheath materials for JNPTs and platinum-alloy thermocouples to measure fuel centerline temperatures up to 1300°C in HRB capsules for periods up to 6000 hr.

---

*Present address, Oak Ridge Y-12 Plant.

Coatings of ZrC, about 0.1 mm thick, applied to rhenium or molybdenum-rhenium tubes, prevented carbon diffusion from the coated fuel particles into the refractory metal in a 500-hr 1700°C test described in Sect. 6.8.1.1. Pending results of the postirradiation examination of HRB-12, this coated structure now appears to be satisfactory for the JNPT sensors.

Protective sheaths for the platinum-alloy thermocouples present a more difficult problem, since the thermocouple calibration is significantly affected by contamination of the wires, whereas the calibration of the JNPT is not. In these thermocouples, the sheath must both prevent interactions with the coated particles to protect their integrity and also maintain a static, clean interior chemical environment for the platinum-alloy thermoelements. A first choice for interior compatibility for platinum-alloy thermocouples would be a platinum sheath containing magnesia or alumina insulation with a slightly oxidizing interior atmosphere. Platinum, however, above 1000°C absorbs carbon as much as 0.1% by weight,[25] removing coating from fuel particles and reducing the oxide insulators. The internal reaction frees aluminum or magnesium, which contaminates the platinum-alloy thermoelements, changing their calibration, and generates CO, which expands and ruptures the sheath. In addition, the platinum sheaths at temperatures above 1000°C undergo grain growth, lose mechanical strength, and rupture at grain boundaries. This behavior was shown (Fig. 6.26) in a compatibility test conducted at 1500°C for 500 hr with a platinum-sheathed thermocouple in contact with a graphite block in an inert atmosphere.

An attempt to inhibit the carbon-platinum reaction by wrapping the sheath with two layers of 38-μm-thick rhenium foil failed in the same test because platinum dissolved in rhenium at 1500°C, as shown in Fig. 6.27. All tests have shown that rhenium is virtually transparent to carbon at these temperatures, and its use in fuel centerline sensor installations cannot be recommended other than to provide a spacer between sheath and fuel.

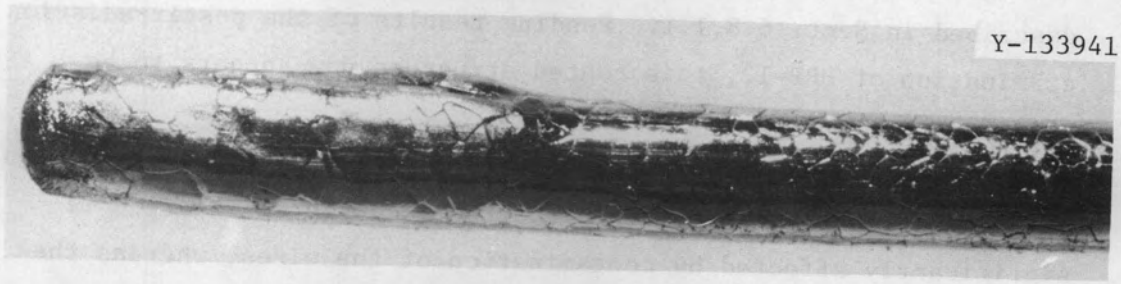

Fig. 6.26. Grain Growth and Swelling of Platinum Thermocouple Sheath in Contact with Graphite for 500 hr at 1500°C.

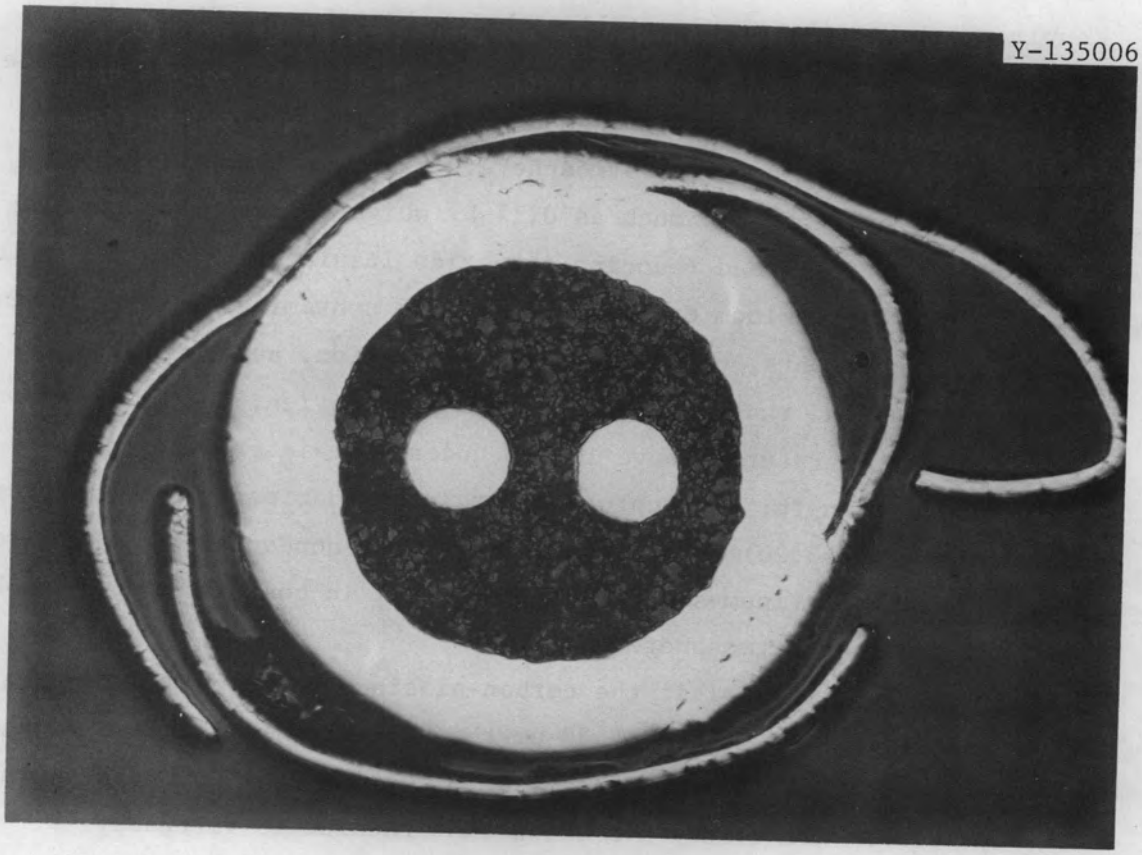

Fig. 6.27. Interaction Between Rhenium Foil and Platinum Thermocouple Sheath in the Presence of Carbon at 1500°C. 50×.

The grain growth in the platinum sheath and platinum-alloy wires could be reduced by the use of oxide dispersion, which has been shown[26] to reduce grain growth and increase strength of platinum, or by heavily (more than 5%) alloying the platinum with a low-cross-section element, such as Mo, Ru, Cr, or Nb. This program will pursue these possibilities in future work.

Another approach to protecting the platinum sheath from carbon interaction was based on the successful use of ZrC coatings on refractory metals. Coatings of ZrC about 0.1 mm thick applied by CVD on platinum and on platinum with an intermediate barrier coating of 30-μm-thick CVD tungsten and rhenium were tested for compatibility in a 500-hr, 1450°C test in contact with dummy coated fuel particles. These tests showed that the platinum reacted with ZrC in contact with it, and that the ZrC coatings were not protected from the platinum by the intermediate refractory films. The ZrC coatings split and broke, and platinum inclusions were found in the coated fuel compacts. Results are shown in Fig. 6.28.

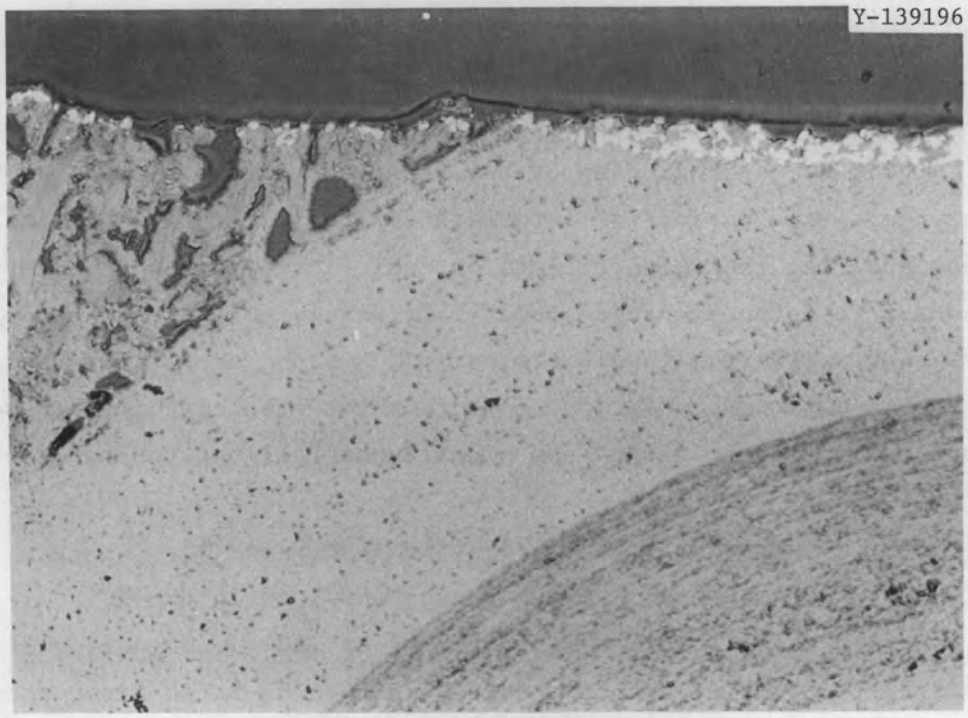

Fig. 6.28. Platinum Found in Dummy Fuel Particle Coating from ZrC-Coated Platinum Thermocouple Sheath after 500 hr at 1450°C. 500×. Reduced 13%.

To date, we have found no satisfactory protective sheath system that is compatible with carbon-coated fuel particles at 1500°C, even for out-of-reactor furnace tests, when platinum is chosen for the sheath. Alternatives being investigated include a refractory sheath with ZrC coating and the possible use of fused, hard-fired alumina protective tubes, possibly with exterior ZrC or other carbide coatings.

6.8.2 Thermometry in HRB Capsules — R. L. Shepard, R. J. Fox, J. L. Horton, and B. H. Montgomery

Irradiation tests of the JNPT and W-Re thermocouples in HRB-series HFIR irradiation capsules are summarized:

HRB-9 (Oct. 6, 1974 to June 3, 1975)

Centerline Sensor. — A Johnson noise power thermometer, containing a single 18-Ω rhenium resistor contained in a 2.5-mm-OD Mo—48% Re sheath, wrapped with 40-μm-thick Re foil.

Conditions. — Irradiated for 5400 hr at 1250—1500°C two cycles in the HFIR PB-13 facility and eight cycles in the HFIR RB-7 facility, accumulating a neutron fluence of 2.8×10^{26} n/m^2 (thermal) and 8×10^{25} n/m^2 (fast).

Performance. — The JNPT indicated fuel centerline temperatures of 1350 to 1400°C during most of the irradiation until the sensor failed open circuit at the beginning of the last reactor cycle after 4500 hr of service. Some periods of interference from external electrical noise sources and from radiation effects on cable insulators were observed. The sensor resistance changed about 15%, partly because of an estimated 80% transmutation from rhenium to osmium.

Postirradiation Condition. — Thermometer open circuit near sensing resistor end; sheath intact. No significant fuel-sheath-insulator interaction.

HRB-10 (Nov. 25, 1974 to June 9, 1975)

Centerline Sensor. — Rhenium sensor JNPT, as in HRB-9.

Conditions. — Irradiated for 3738 hr at 1500°C nominal, two cycles in HFIR PB-13 facility and five cycles in HFIR RB-5 facility, accumulating a neutron fluence of 1×10^{26} n/m^2 (thermal) and 4×10^{25} n/m^2 (fast).

Performance. — The JNPT indicated temperatures as high as 1650°C during the first irradiation cycle in PB-13. More typical readings were 1400—1550°C. The thermometer became erratic in the RB-5 facility and then failed open circuit after 1300 hr irradiation.

Postirradiation Condition. — The Mo-Re sheath had reacted with fuel particle coatings by carbon diffusing through the Re foil barrier where the sheath pressed against the fuel. The fuel shrank about 6% and the Mo-Re sheath expanded about 10% from carbon absorption, and fuel particles adhered to and were partially absorbed by the Re foil and Mo-Re sheath. This catastrophic failure caused high fission gas activity in the experiment sweep gas and eliminates that choice of sensor sheath material from further consideration.

HRB-11 (Dec. 7, 1975 to Sept. 26, 1976)

Centerline Sensor. — A Pt—5% Mo vs Pt—0.1% Mo thermocouple, Al_2O_3 insulated, contained in a 1.6-mm-OD Pt sheath, and wrapped in 60-μm Re foil. The 1.5-m-long Pt thermocouple was connected to a stainless-steel-sheathed pair of Chromel vs Alumel thermocouples, used for extension wires for measuring the reference junction temperature of the Pt-Mo thermocouple and its loop resistance.

Conditions. — Irradiated for 6556 hr at 1100°C, including three cycles (1673 hr) in the PB-13 irradiation facility and nine cycles in an RB irradiation facility, accumulating a neutron fluence of 3.3×10^{26} n/m^2 (thermal) and 9.1×10^{25} n/m^2 (fast).

Performance. — The thermocouple exhibited a progressive degradation of loop resistance and indicated temperature, reading about 200°C low by the end of the irradiation. In-pool calibration tests conducted after 6000 hr irradiation showed the Pt-Mo thermocouple to be temperature gradient sensitive and predicted errors of as much as —245°C at 1100°C true temperature.

Postirradiation Condition. — The Re-foil-wrapped Pt sheath was severely affected by the 1100°C irradiation. Five coated fuel particles were stuck to the foil, and the foil had alloyed with the sheath where the two materials touched. Some fission gas release during irradiation

resulted from this interaction, and Pt metal was found in some coated particles. Melting of the sheath and foil apparently was caused by transmutation of Re to Os (estimated to be about 80%) and the formation of a Re-Os-Pt ternary compound.

HRB-12 (Feb. 19, 1976 to Jan. 10, 1977)

Centerline Sensor. — A dual, 18-Ω Re resistor JNPT, insulated with BeO and enclosed in a 3.33-mm-OD ZrC-coated Re sheath.

Conditions. — Irradiated for 6672 hr at 1100–1300°C (6602 hr at 100 MW), including three irradiation cycles totaling 1663 hr in the PB-13 HFIR irradiation facility, and 5009 hr in an RB facility during nine irradiation cycles, the last of which (Cycle 141) was at reduced reactor power. During this irradiation, a neutron fluence of 3.3×10^{26} n/m^2 (thermal) and 9.2×10^{25} n/m^2 (fast) was accumulated.

Performance. — During initial 100-MW operation, the JNPT indicated 1145°C, in close agreement with the Pt-Mo thermocouple at the start of the HRB-11 irradiation. The JNPT signal developed large nonthermal noise, identified as microphonics associated with the HFIR water pumps, and gave false temperature indications several hundred degrees Celsius above credible temperatures. Both Re resistors later failed open circuit at the start of the eighth irradiation cycle after 3780 hr irradiation.

Neutron fluences were calculated from the fluxes given in Table 6.69.

Table 6.69. Flux in HFIR HRB Irradiation Facilities

Facility	RB (Measured)	PB (Estimated)
Neutron Flux, n/m^2 s		
Thermal (<0.41 eV)	$1.4–1.8 \times 10^{19}$	$7–9 \times 10^{18}$
Epithermal	5×10^{18}	
Fast (>0.18 MeV)	5×10^{18}	5×10^{17}
Gamma Intensity		
R/hr	6.3×10^{9}	2×10^{9}
W/g graphite	14.7 (0.1–10 MeV)	5

6.8.3 Thermometry in ORR Capsules — R. L. Shepard and K. R. Thoms

In addition to the HRB experiments, a Pt-Mo thermocouple experiment was irradiated in the ORR. The observations are summarized:

OF-2 (June 1975 to August 3, 1976)

Spine Temperature Sensors. — Two Pt—5% Mo vs Pt—0.1% Mo thermocouples, Al_2O_3 insulated, sheathed in 1.6-mm-OD Pt, installed in the upper and middle canisters in the graphite spine.

Conditions. — Irradiated 8440 hr at 900—1250°C in the ORR. Using estimated neutron fluxes for these facilities, the thermocouples received fluences of 3—6 × 10^{25} n/m^2 (thermal) and 4—9 × 10^{25} n/m^2 (fast).

Performance. — Both thermocouples agreed with calculated graphite spine temperatures to within 1% during the irradiation.

Postirradiation Condition. — The Pt sheaths of both thermocouples showed moderate grain growth but no evidence of swelling, intergranular rupture, or reaction with graphite.

6.8.4 The Effect of Transmutation Alloying on the EMF of W-Re Thermocouples — M. W. Waddell, R. K. Williams, O. W. Hermann, and J. F. Mincey

The goal of this study is to develop a method for calculating the effect of transmutation alloying on the emf of W-Re thermocouples and compare the results with experimental data on in-reactor decalibration of the thermocouples. If these comparisons indicate that the calibration shifts can be predicted from composition changes alone, the method then could potentially be applied to improve the thermometry for irradiation tests.

The basis for the calculations was described previously.[27] The calculations require knowledge of the composition and temperature dependence of the Seebeck coefficients of both thermoelements and a calculation of the composition-distance profiles along each thermocouple wire. The emf of a transmuted thermocouple is given by:

$$\text{emf} = \int_{T_R}^{T} S_A(T,X)\, dT + \int_{T}^{T_R} S_B(T,X)\, dT \ ,$$

where

$S_A(T,X)$ = Seebeck coefficient of the positive thermoelement, which depends upon distance (composition) and temperature,

$S_B(T,X)$ = Seebeck coefficient of the negative thermoelement, which also depends upon composition and temperature,

T_R = reference temperature.

Then, if the form of the temperature gradient is known, the hot junction temperature, T, could be calculated by trial and error. A more direct test of the method can be obtained if all of the quantities in the equation are known, and this could be accomplished by calculating the out-of-reactor decalibration data obtained with the HRB-8 capsule[28] after the fourth irradiation cycle. Progress toward this goal includes:

1. experimental measurements of the S of nine W-Re and W-Re-Os alloys were completed and the compositions and crystal structures of the alloys were defined,
2. methods for interpolating and extrapolating the S data were developed, and
3. the composition calculations were checked by irradiating W and Re samples in the HFIR target region.

The S data seem to be satisfactory, although measurements on additional compositions would be desirable. The graphical interpolation and extrapolation scheme also yields reasonable results, but additional work on an analytical approach is required to shorten the calculation time. The irradiation experiment revealed serious discrepancies in W and Re cross-section values, and at present this difficulty limits the usefulness of this method. The experimental data were adequate to partially (±10%) resolve the W cross-section value, but the Re-to-Os transmutation rates still may be uncertain by as much as a factor of about 2. Additional experimental work is required to resolve this difficulty. Calculations for the presently anticipated maximum alloying decalibration of the centerline W—5% Re vs W—26% Re thermocouple are compared with experimental data obtained after the fourth irradiation cycle of the HRB-8 test in Table 6.70. These values show

Table 6.70. Comparison of Calculated and Experimental Decalibration of the HRB-8 Centerline W–5% Re vs W–26% Re Thermocouple

Temperature Gradient	Temperature Error, °C, at ~700°C	
	Experimental	Calculated
Low	–140	–90
Medium	–160	–135
High	–210	–180

that the method can predict the sign amd magnitude of the observed shifts in indicated temperature, but a final evaluation of the temperature correction due to alloying cannot be obtained until the transmutation composition calculations are experimentally improved.

6.9 NUCLEAR ANALYSIS IN SUPPORT OF IRRADIATIONS — E. J. Allen, H. T. Kerr, and J. F. Mincey

The design, operation, and interpretation of postirradiation examination (PIE) results for test capsules depend upon the availability of reliable neutronics information for the involved experimental facilities. To provide such information; the nuclear analysis effort during this period has included work in six identifiable areas.

1. A series of experimental flux mappings and a preliminary analysis of the data obtained with these mappings have been completed for the High Flux Isotope Reactor (HFIR) RB-3 and VXF-13 (PB-13) irradiation facilities. Investigations have been initiated to resolve anomalies identified by the preliminary data analysis.

2. A study of the neutronic parameters utilized in the calculation of linear fission heat rates for the HFIR Removable Beryllium (HRB) fuel irradiation program has been completed.

3. The design and operation of a calorimetric device, the GAFI (GAmma and FIssion) calorimeter, have been completed. Nuclear heating rates (including fission rates) have been measured for selected materials in the core of the ORR.

4. A coupled neutron-gamma cross-section library has been assembled. With this library, nuclear heating rates and other neutronic effects can be calculated with standard computer codes.

5. The development of a capsule designed to measure nuclear heating rates in the RB and VXF facilities of the HFIR has been initiated.

6. The retrieval of the OF-2 and OC-1 neutron flux dosimeters has been completed. The OF-2 dosimeter activities have been measured and are being analyzed. Summaries of these six topics follow.

6.9.1 HFIR Flux Map Experiment

The RB-5, RB-7, and VXF-13 facilities in the HFIR have been used for the irradiation of the HRB capsules. Unfortunately, the limited neutronics information available for the design of these capsules has resulted in poor agreement between calculated and observed capsule performances. Therefore a special dosimetry experiment was carried out to obtain accurate values for neutron-induced reaction rates for capsules in the HFIR reflector irradiation facilities. Neutron fluxes and isotopic reaction rates within the HFIR facilities have steep spatial gradients and vary with time during the 23-day fuel cycle. These spatial and time dependences are generally reproduced during each HFIR fuel cycle so that test capsule performance indices determined during any cycle are generally valid for similar capsules in other fuel cycles.

In addition to the above objective, a second and third objective existed. Dosimeter capsules were irradiated in the RB-3 and VXF-13 facilities both before and after the replacement of the HFIR permanent beryllium reflector. These irradiations were performed to determine what, if any, neutronic changes occurred in these two irradiation facilities as a consequence of replacing the reflector. These irradiations were based on the assumption that there is sufficient angular symmetry to apply measurements made in RB-3 to other RB

facilities in the HFIR; the RB-5 and RB-7 facilities were unavailable at the time the irradiations were performed. The third objective was to investigate the feasibility of using vanadium-encapsulated ^{232}Th and ^{235}U microspheres as neutron flux dosimeters.

6.9.1.1 Description of the Flux Capsules

One of the four flux map capsules is shown schematically in Fig. 6.29. The stainless steel pin located at the base of the capsule was used to orient the capsule such that the C dosimeter holes lay on a radius from the reactor centerline through the A dosimeter holes (the C dosimeter holes being closest to the HFIR's centerline).

6.9.1.2 Presentation of Results

Because of difficulties encountered in analyzing the ^{232}Th dosimeter data, the publication of a report on the flux mapping experiment has been delayed. Hence, a condensed summary of the mappings will be presented.

Figure 6.30 compares mappings of the total and >0.18 MeV fluxes for the RB-3 facility before and after replacement of the beryllium reflector. Figure 6.31 presents a similar comparison of the VXF-13 facility. A comparison of the RB-3 and VXF-13 facilities before and after replacement of the beryllium reflector has also been made with ^{235}U data in Fig. 6.32.

Though not shown, a similar set of comparisons was made with the ^{232}Th$(n,\gamma)^{233}$Pa reaction data. In order for the ^{232}Th results to agree with other dosimeters, the ^{232}Th radiative capture cross section had to be lowered by 30%.

6.9.1.3 Analysis of Results

Table 6.71 compares the RB-3 fluxes from the old and new beryllium flux mappings. In addition, average flux values generated from selected ^{235}U dosimeter fission product activities have been compared with the standard nonfissile dosimeter reactions.

ORNL-DWG 77-9647R

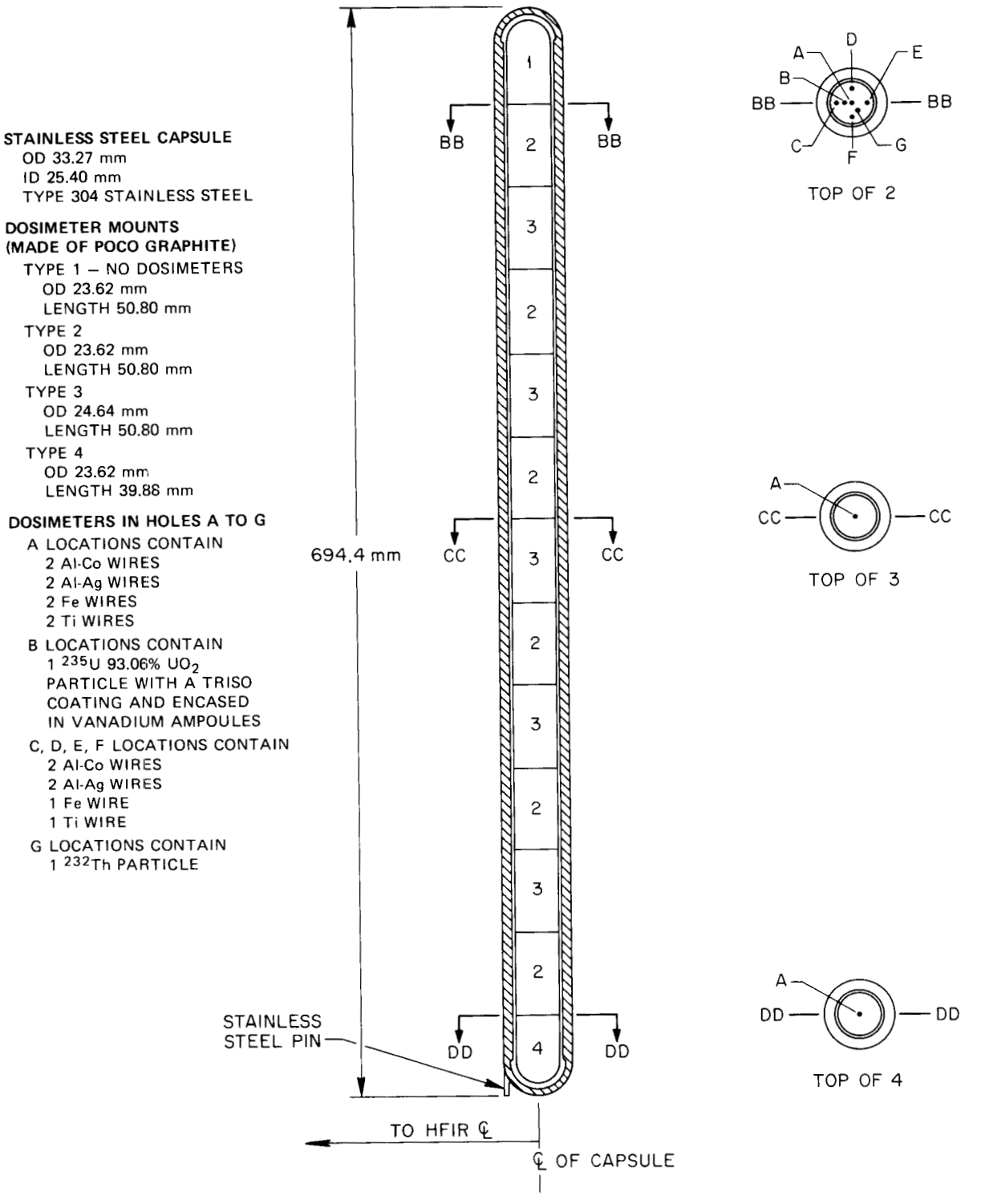

Fig. 6.29. Schematic of Stainless Steel Flux Map Capsule.

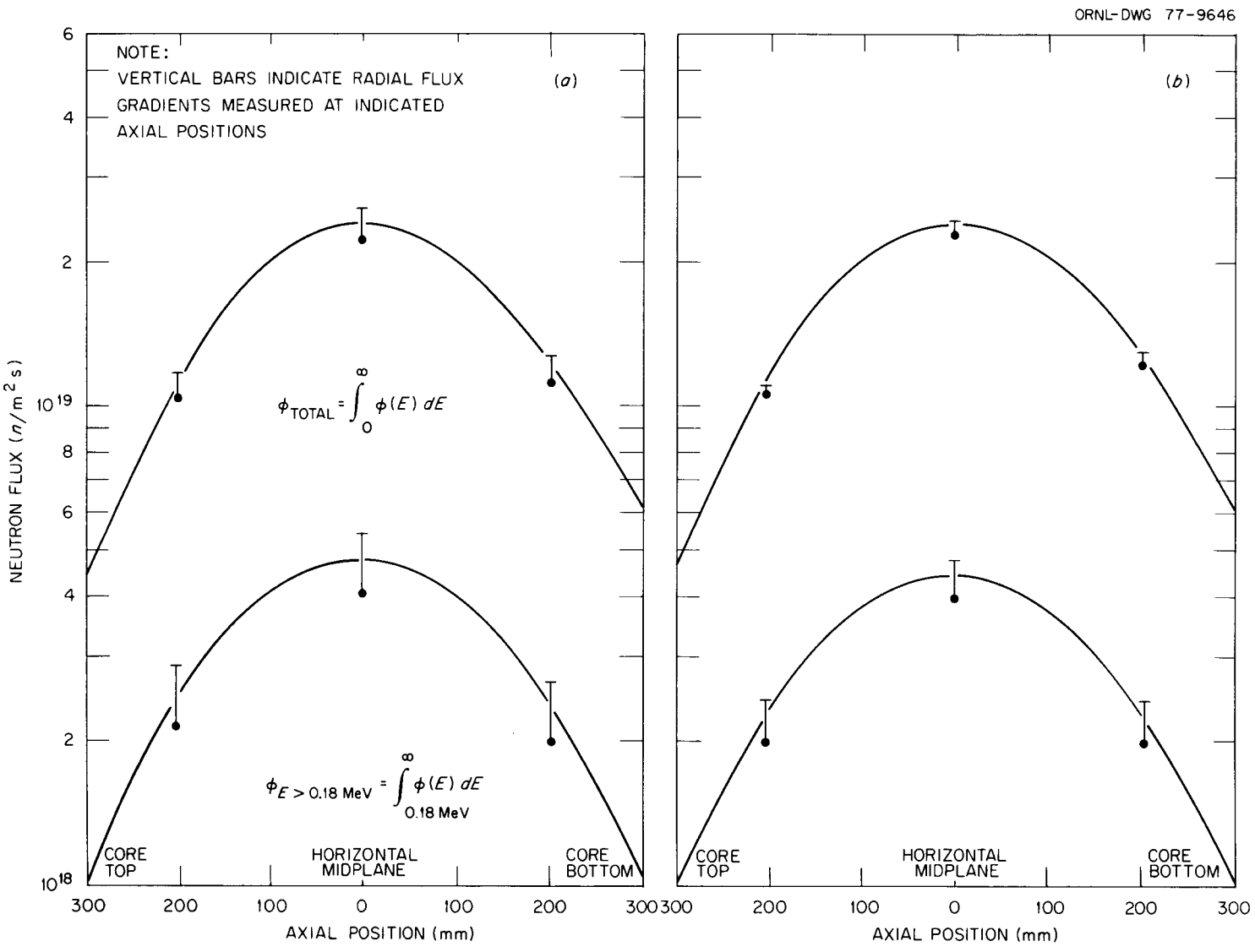

Fig. 6.30. Axial Flux Profiles in the RB-3 Flux Map. Total flux data based on ^{110m}Ag, ^{59}Fe, and ^{60}Co activities. Fast flux (>0.18 MeV) data based on ^{46}Sc and ^{54}Mn activities. For (a) old (b) new beryllium reflector.

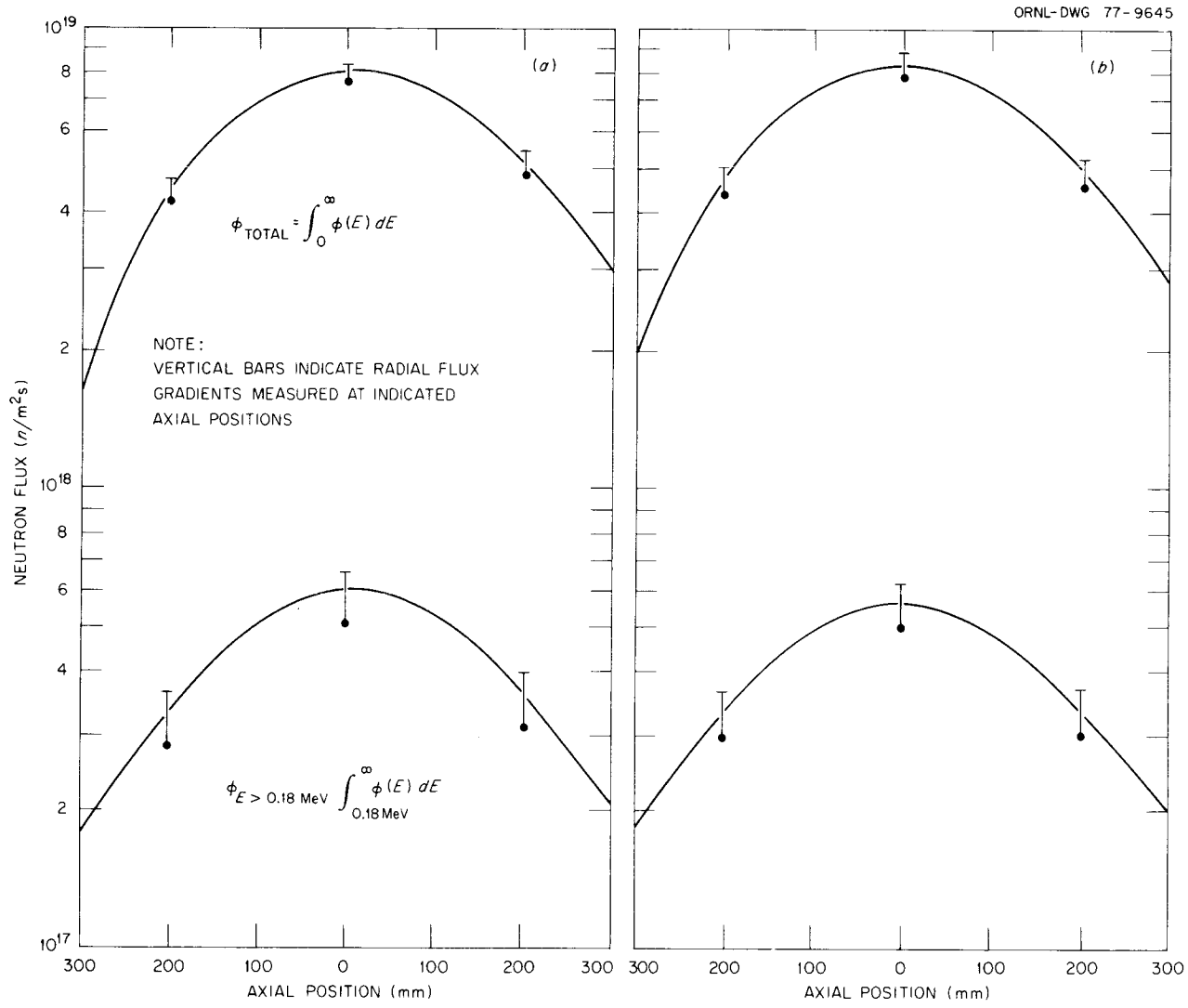

Fig. 6.31. Axial Flux Profiles in the VXF-13 Flux Map. Total flux data based on ^{110m}Ag, ^{59}Fe, and ^{60}Co activities. Fast flux (>0.18 MeV) data based on ^{46}Sc and ^{54}Mn activities. For (a) old and (b) new beryllium reflector.

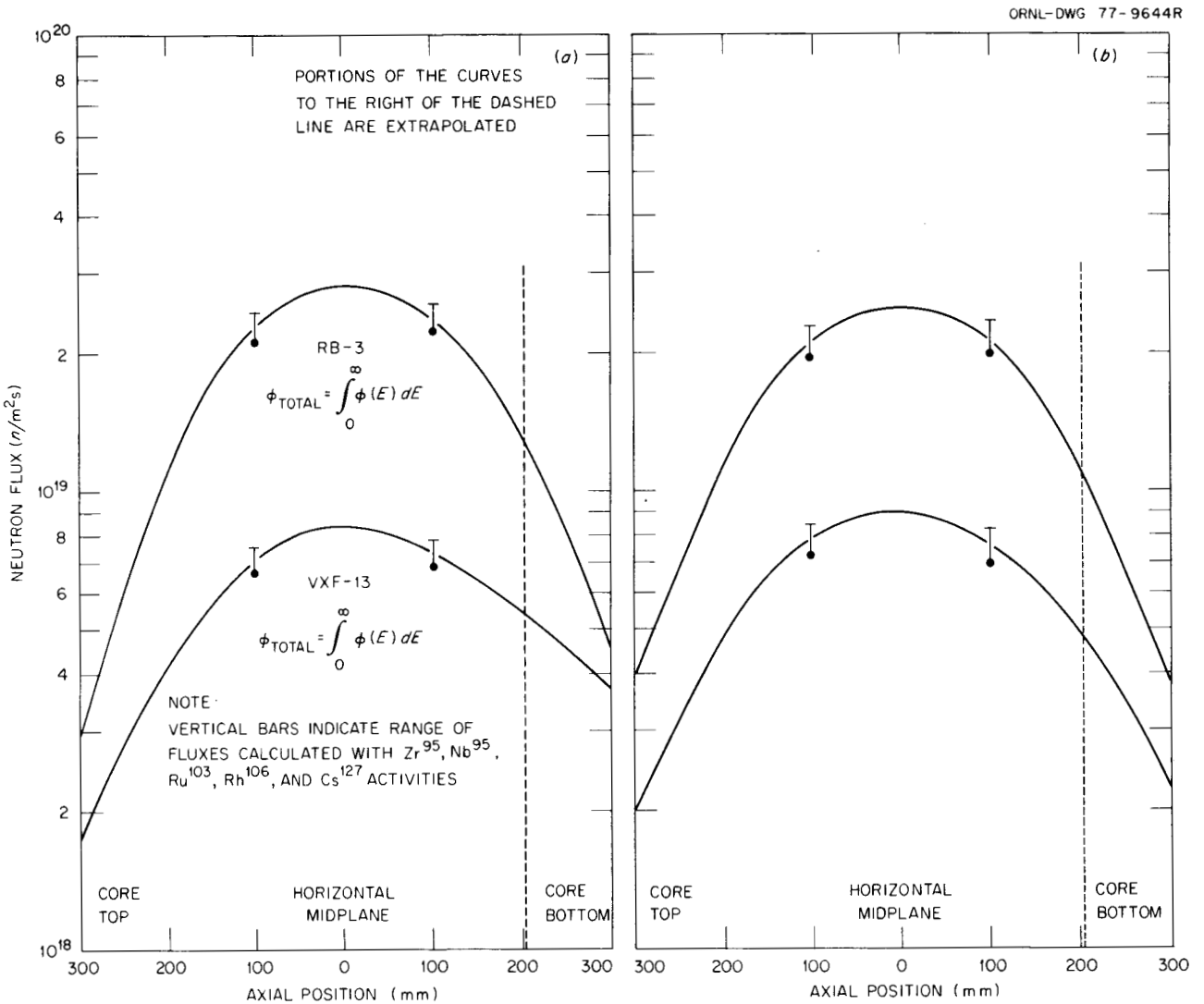

Fig. 6.32. Axial Flux Profiles in the RB-3 and VXF-13 Flux Maps. Curves reflect averages of fluxes calculated from ^{235}U dosimeter fission product activities. For (a) old and (b) new beryllium reflector.

Table 6.71. Comparison of Flux Mappings with the Old and New Beryllium Reflectors and with Different Dosimeters for HFIR Facilities

Distance Above HMP		Ratio, Old/New[a]			Ratio, ϕ_U/ϕ_T	
(m)	(in.)	ϕ_T	ϕ_F	ϕ_U	Old	New
		RB-3 Facility				
0.30	12	1.012	0.969	b	b	0.887
0.25	10	0.969	1.071	b	b	b
0.20	8	1.000	1.182	0.986	0.939	0.953
0.15	6	0.999	1.094	b	b	b
0.10	4	1.053	1.083	1.121	1.091	1.025
0.05	2	1.017	1.018[c]	b	b	b
0.00	0	1.024	1.079	1.097	1.165	1.088
−0.05	−2	1.012	1.045	b	b	b
−0.10	−4	b	b	1.098	b	1.058
−0.15	−6	0.990	1.067	b	b	b
−0.20	−8	0.954	1.059	b	1.080	b
−0.25	−10	0.964	1.056	b	b	b
		VXF-13 Facility				
0.30	12	0.777	0.992[c]	0.904	1.046	1.005
0.25	10	0.870	0.995	b	b	b
0.20	8	0.923	1.066[c]	0.925	0.964	0.962
0.15	6	0.934	0.976	b	b	b
0.10	4	0.943	0.920[c]	0.846	0.973	1.084
0.05	2	0.974	1.023	b	b	b
0.00	0	0.976	1.078	0.947	1.038	1.069
−0.05	−2	0.990	1.055	b	b	b
−0.10	−4	1.003	1.089	0.980	0.998	1.022
−0.15	−6	1.016	1.056	b	b	b
−0.20	−8	1.033	1.120	1.098	1.070	1.007
−0.25	−10	1.070[c]	1.050	b	b	b

[a] ϕ_T = total neutron flux, calculated from ^{60}Co, ^{59}Fe, and ^{110m}Ag activities; ϕ_F = neutron flux above 0.18 MeV, calculated from ^{54}Mn and ^{46}Sc activities: ϕ_U = total neutron flux calculated from ^{95}Zr, ^{95}Nb, ^{103}Ru, ^{106}Rh, and ^{137}Cs activities obtained from the fission products of the ^{235}U dosimeters.

[b] Comparison impossible; dosimeters were lost or nonexistent.

[c] One activity measurement missing; activity was too low to count accurately.

From these comparisons, two conclusions can be drawn. First, no significant change occurred in the neutronic properties of the RB-3 facility when the beryllium reflector was replaced. Second, the neutron fluxes calculated with the ^{235}U fission product activities are in good agreement with those calculated with conventional dosimeters.

Table 6.71 also contains a similar comparison for the VXF-13 facility. The study reveals a definite pattern not found in the corresponding comparison for RB-3 flux ratios. Fluxes determined with the old beryllium reflector present were higher than those with the new beryllium reflector at the bottom of the core and smaller at the top of the core. Since the RB-3 mappings have not shown this anomaly, evidence suggests that the VXF-13 capsule was improperly positioned when the old reflector was present. A small (approximately 13 mm) vertical displacement toward the top of the core seems to have existed. Appropriate corrections were made, assuming this displacement occurred, and the data are recompiled in Table 6.72. Since the pattern seen in Table 6.71 for the VXF-13 facility does not exist in Table 6.72, the conclusion was drawn that such a mispositioning error probably did occur. Then the asymmetry seen in Figs. 6.31(a) and 6.32(a) for the VXF-13 facility was not likely a characteristic of the facility before the replacement of the reflector.

The radial variations of the fluxes in the RB-3 new reflector flux map were significantly smaller than the corresponding variations in the old reflector flux map (see Fig. 6.30). This anomaly indicated that the capsule used in the RB-3 new beryllium map was also not properly positioned. Instead of the C dosimeter holes lying on a radius from the HFIR core centerline through hole A (see Fig. 6.29), the C dosimeter holes seem to have been at an angle with that radius line. This misalignment would cause the magnitudes of the radial flux gradients indicated by dosimeters in holes C and E to be smaller than if the capsule had been properly positioned.

Table 6.72. Comparison of VXF-13 Fluxes with the Old Beryllium Data Corrected for a 13-mm (0.5-in.) Axial Shift

Distance Above HMP		Ratio, Old/New[a]		
(m)	(in.)	ϕ_T	ϕ_F	ϕ_U
0.30	12	0.95	1.03	0.97
0.25	10	1.00	1.06	0.98
0.26	8	1.00	1.06	0.96
0.15	6	1.00	1.01	0.94
0.10	4	0.97	1.08	0.95
0.05	2	0.95	1.05	0.94
0.00	0	0.96	1.05	0.94
−0.05	−2	0.99	1.05	0.94
−0.10	−4	0.97	1.07	0.96
−0.15	−6	0.98	1.06	0.98
−0.20	−8	1.00	1.03	0.88
−0.25	−10	1.03	1.02	1.26

[a] ϕ_T = total neutron flux, calculated from ^{60}Co, ^{59}Fe, and ^{110m}Ag activities; ϕ_F = neutron flux above 0.18 MeV, calculated from ^{54}Mn and ^{46}Sc activities; ϕ_U = total neutron flux calculated from ^{95}Zr, ^{95}Nb, ^{103}Ru, ^{106}Rh, and ^{137}Cs activities obtained from the fission products of the ^{235}U dosimeters.

6.9.1.4 Conclusions

In answering the earlier stated objectives, four conclusions have been reached.

1. There has been no significant evidence compiled from this experiment suggesting that the replacement of the beryllium reflector significantly altered the neutronic properties of RB-3 and VXF-13.

2. The close agreement of fluxes obtained with ^{235}U dosimeter data and more conventional dosimeters established the feasibility of using ^{235}U microspheres as neutron flux dosimeters. A qualification must be added however. Care must be taken in using basic data (such as fission yields) and deciding which fission product activities to

use for reaction rate calculations. Ideally several fission product activities should be used for reaction rate calculations and an average value of flux computed.

3. The feasibility of using ^{232}Th microspheres as flux monitors has not yet been determined. At this time, the theoretical justification for lowering the ^{232}Th radiative capture cross section by 30% has not been satisfactorily explained. Three possible effects for this anomaly have been proposed: (a) inaccuracies exist in the resonance region of the neutron spectrum used in collapsing multigroup cross-section data into one-group form; (b) self-shielding corrections need to be made in the ^{232}Th capture cross sections for a microsphere; (c) a combination of the above effects.

4. Despite the problems associated with the ^{232}Th data, the averaged fluxes shown in Figs. 6.30 through 6.32 are within about ±10%: a reasonable accuracy for this type of experiment. Even though the cross sections used to calculate flux magnitudes will reflect any errors in the neutron energy spectrum, this effect has been minimized by computing average flux values from several different types of dosimeters, as some of the dosimeter reaction rates [like the ^{58}Fe$(n,\gamma)^{59}$Fe reaction] are relatively independent of resonance energy range effects.

6.9.1.5 Future Efforts

Work is continuing in order to resolve anomalies associated with the neutron resonance energy region and cross sections. A more intensive effort is needed to adequately resolve these problems.

While the reaction rates measured in this experiment are not directly applicable to the HRB capsule program; they represent some of the best neutronics data available concerning the HFIR RB and VXF facilities. In seeking to obtain agreement for flux magnitudes from compiled reaction rates, information can be gained about the validity of the neutron spectrum and cross-section data. This information is vital in computing HRB capsule cross sections.

6.9.2 Sensitivity Study of HRB Neutronics Parameters

Poor agreement between HRB capsule linear fission heat rates calculated from thermocouple data and heat rates calculated from neutronics data has existed for sometime. The large differences suggest that incorrect fluxes and/or cross sections were used in the neutronics calculations.

6.9.2.1 Results

Additional neutronics calculations (using CACA-2)[29] were done to find the perturbations in fluxes and cross sections necessary to achieve the fission heat rate profiles calculated from HRB capsule thermocouple data. The significant results are shown in Fig. 6.33.

6.9.2.2 Conclusions

According to the results of the HFIR flux map experiment, significant errors (>15%) do not exist in the magnitudes of HFIR RB and VXF fluxes used for HRB capsule calculations. The sensitivity study agrees with this conclusion; inadmissible perturbations of 40 to 50% in flux magnitudes were needed to explain the fission heat rate discrepancies if only the flux magnitudes were assumed to be in error.

The sensitivity study revealed that a more feasible 30 to 40% decrease in the ^{238}U and ^{232}Th radiative capture and fission cross sections could explain the heat rate discrepancies.

This finding agreed with the anomalies for ^{232}Th cross sections found in the analysis of the HFIR flux map experiment. The suspected causes for these anomalies are: inaccuracies in the neutron flux spectrum, especially in the resonance region; self-shielding effects, or a combination of these effects. Findings indicate that, while previously used cross sections for the HRB capsules are fairly accurate for weak resonance absorbers, significant errors seem to exist for strong resonance absorbers such as ^{238}U and ^{232}Th.

Based on these results, Table 6.73 has been compiled to reflect a 30% reduction in ^{232}Th and ^{238}U cross sections compared with previously used values. Note that the theoretical justification for these

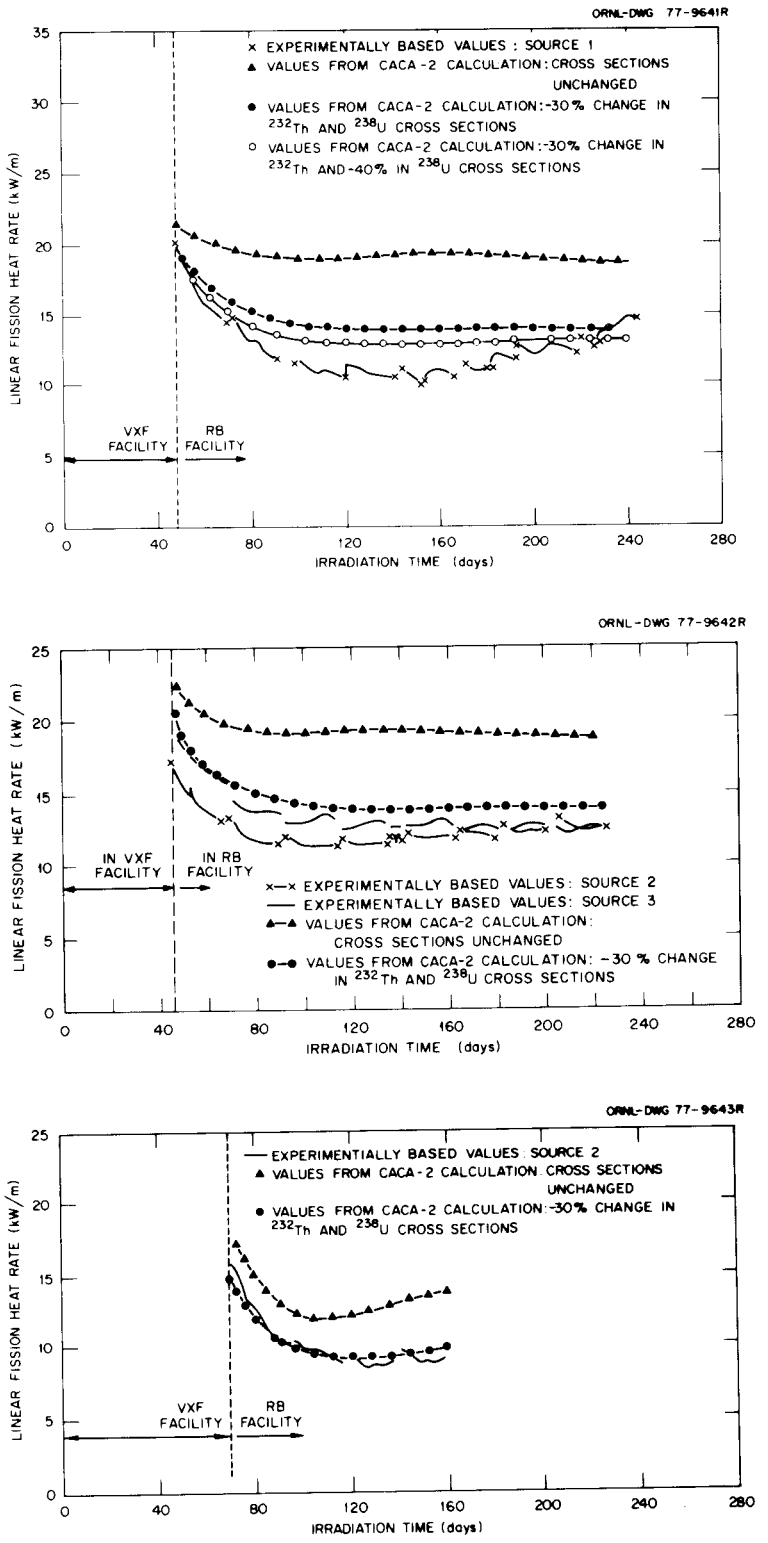

Fig. 6.33. CACA-2 Sensitivity Studies of HRB Capsules: Heat Rates at Horizontal Midplane. (a) HRB-8. (b) HRB-9. (c) HRB-11.

reductions has not yet been clearly established and further modification of these values may be necessary. Care should also be taken when these cross sections are applied to other capsule loadings, as the loading significantly affects the ^{232}Th and ^{238}U cross section values.

Table 6.73. Effective Total Fission and Capture Cross Sections in HFIR

Isotope	Reaction	Cross Section, b	
		RB Facility	VXF Facility
^{232}Th	(n,f)	0.006	0.001
^{234}Pa	(n,f)	1500.000	2500.000
^{233}U	(n,f)	151.000	243.000
^{235}U	(n,f)	144.000	241.000
^{238}U	(n,f)	0.023	0.006
^{238}Np	(n,f)	570.000	940.000
^{239}Pu	(n,f)	281.000	432.000
^{241}Pu	(n,f)	329.000	532.000
^{232}Th	(n,γ)	2.770	3.650
^{233}Pa	(n,γ)	32.200	37.100
^{234}Pa	(n,γ)	150.000	250.000
^{233}U	(n,γ)	16.100	24.300
^{234}U	(n,γ)	40.100	52.600
^{235}U	(n,γ)	27.900	44.000
^{236}U	(n,γ)	10.200	8.970
^{237}U	(n,γ)	110.000	180.000
^{238}U	(n,γ)	5.908	4.704
^{237}Np	(n,γ)	65.600	93.800
^{238}Np	(n,γ)	13.000	20.000
^{239}Np	(n,γ)	8.300	14.000
^{238}Pu	(n,γ)	130.000	220.000
^{239}Pu	(n,γ)	142.000	207.000
^{240}Pu	(n,γ)	287.000	342.000
^{241}Pu	(n,γ)	109.000	175.000
^{242}Pu	(n,γ)	36.500	35.500

6.9.2.3 Future Efforts

Efforts are being made to establish the theoretical basis for these modifications. Work will continue in identifying a computational technique to produce properly weighted cross sections.

6.9.3 Development of a Coupled Neutron-Gamma Cross Section Library for Calculation of Nuclear Heating Rates

Estimation of in-core nuclear heating rates requires experimentation and calculational techniques. Experimentation alone is time consuming, costly, and valid only for the particular experimental core conditions and materials used. Calculations, on the other hand, can be applied to any material or core configuration with relatively little expense. Further, calculations used in parallel with experimentation can greatly enhance the usefulness of an experiment. For these reasons, a coupled neutron-gamma cross section library has been compiled for the estimation of nuclear heating rates. With such a library, neutron and gamma fluxes can simultaneously be calculated and heating rates determined.

This coupled neutron-gamma multigroup cross section set has been constructed from ENDF/B-IV data. The group structure consists of 42 neutron energy groups and 18 gamma energy groups.

Nuclear heating calculations using this library have been made for the E-5 irradiation facility of the Oak Ridge Research Reactor (ORR). The calculation gave a gamma heating rate of 7.7 W/g in aluminum, while experimentation yielded values from 10 to 12 W/g. The discrepancy was expected and is attributed to the heating caused by fission product decay gammas, which have not yet been incorporated into the coupled neutron-gamma library.

The coupled neutron-gamma cross section library currently is being modified to include the contribution of gamma heating from fission products.

6.9.4 Performance of In-Core Nuclear Heating Instruments in the ORR

Determining nuclear heating rates by purely analytical means is difficult and subject to large uncertainties. Therefore, an experimental technique for accurately measuring nuclear heating rates in selected materials was developed. Calorimetric instruments have been designed and tested to permit accurate in-core measurements of nuclear heating rates in most structural materials. The instruments can also be used to measure fission rates in standard fissile foils.

Each instrument, as shown schematically in Fig. 6.34, consists essentially of three thermocouples and a central pedestal, which is welded at one end to a leaktight gas-filled can. The three thermocouples are embedded at specified positions in the pedestal and extend outside the irradiation facility to a reference system and a sensitive potentiometric voltmeter bridge. The temperatures of the thermocouples depend on the design and physical properties of the pedestal as well as the irradiation environment. The temperatures can be accurately measured, and the nuclear heating rates can be calculated from the measured temperature differences.

The calorimeters are designed to limit heat losses from the pedestal other than by conduction through the pedestal material. Heat transport calculations indicate that not more than about 5% of the total heat generated in the pedestal is lost by thermal radiation and heat transfer through the gas during normal operation.

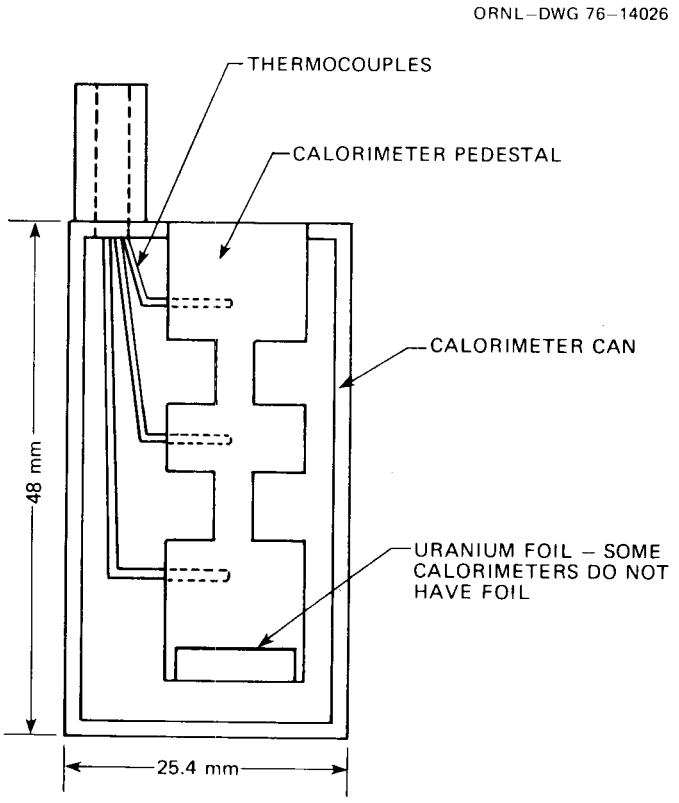

Fig. 6.34. Calorimeter.

Prototype calorimeters were fabricated with aluminum cans and pedestals because of the low cost and ease of fabrication. Three types of instruments were constructed. The first instrument had a solid cylindrical pedestal designed for high-intensity heating rates. The second instrument had a cylindrical pedestal with two constrictions designed to increase the axial temperature gradient in the pedestal. This instrument was suitable for low-intensity heating rates. The third instrument was of the same type as the second instrument but had a uranium foil (10%-enriched ^{235}U) attached to the free end of the pedestal. This instrument was used to determine the fission heating rate in the uranium foil.

The thermocouples in each of the three prototype instruments were calibrated at nine temperatures. In-core irradiation tests were then conducted in the E-5 facility of the Oak Ridge Research Reactor (ORR) at 1% of full power. The measured thermocouple responses at each of eight axial positions in E-5 were recorded, and an analysis was made to determine the fission and gamma heating rate profiles for the E-5 facility.

Nuclear heat rates were derived from the measured temperature distributions in the pedestal with the following calculational procedure. For any two positions (points a and b) in the pedestal, the following relationship was applicable:

$$Q = k\Delta T_{ab}/G_{ab} \ , \tag{1}$$

where

Q = heating rate,

k = thermal conductivity,

ΔT_{ab} = temperature difference between points a and b,

G_{ab} = geometry factor, which depends on location of points a and b and shape of pedestal.

The geometry factors for each pedestal were determined from HEATING[30] calculations. At each axial position, the three thermocouple responses provided two temperature differences for that pedestal. Each temperature difference was converted into a heating rate by use of Eq. (1); therefore, two values were obtained for each pedestal at each axial position. These results for two of the calorimeters are given in Table 6.74. The third calorimeter had a pedestal designed for higher nuclear heating rates (the ORR was operated at 1% power during the test) and gave lower accuracy.

Table 6.74. Full-Power Fission Rates and Nuclear Heating Rates in the E-5 Facility

Axial Position	Calorimeter with Uranium Foil Fission Rates, fissions/s		Calorimeter Without Uranium Foil, Nuclear Heating Rates in Aluminum, W/g	
	From ΔT_1	From ΔT_2	From ΔT_1	From ΔT_2
1	2.22×10^{-7}	2.17×10^{-7}	7.29	6.98
2	3.33	3.26	12.17	12.43
3	3.68	3.61	13.49	13.89
4	3.29	3.30	12.70	13.60
5	2.50	2.52	11.45	12.15
6	1.87	1.90	9.30	10.09
7	1.36	1.38	7.10	8.15
8	0.879	0.903	4.88	5.61

The two fission rates measured at each position agree to within 2%. The two nuclear heating rates in aluminum at each position agree on the average to within 8%; the difference is probably due to the axial gamma flux gradient in the pedestal.

The nuclear heating rate in aluminum is primarily due to core gammas, to fast neutrons, and to the 2.86-MeV beta released in ^{28}Al decay. The ^{28}Al is formed from the ^{27}Al(n,γ) reaction and has a half-life of 2.24 min. In the E-5 facility, the fast neutrons and the betas account for about 10% of the nuclear heating; the core gammas account for the remainder. Correcting the nuclear heating

in aluminum by this amount, the gamma heating is obtained. The gamma heating rate in aluminum and the fission rate in the E-5 facility are given in Fig. 6.35. Neutronic calculations were performed to determine the fission rate in the E-5 facility for this ORR core configuration. These calculations indicate that the maximum fission rate per atom is 3.63×10^{-7} fissions/s. The maximum measured fission rate per atom was 3.68×10^{-7} fissions/s.

Previous in-core gamma heat estimates have been based on measurement made with high-level gamma ionization chambers. Measurements recently made with this instrument indicate a peak gamma heat rate in graphite of 10 W/g in the E-5 facility.[31] The energy absorption mass attenuation coefficients for both aluminum and carbon are nearly equivalent over the energy range of most core gammas. Therefore, the heat rates in aluminum and carbon due to core gammas should be nearly equivalent.

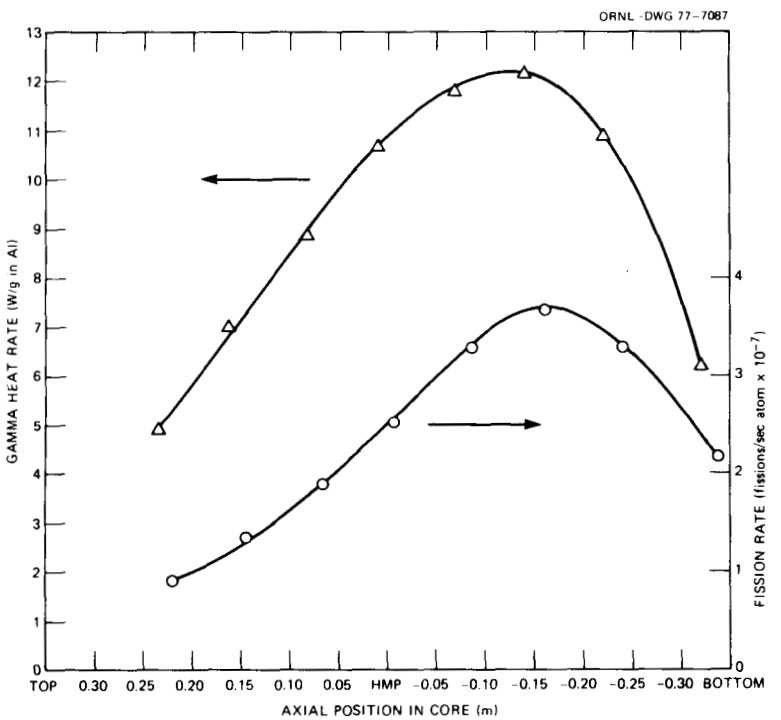

Fig. 6.35. Fission Rate and Gamma Heat Rate at Full Power in Aluminum-Water Experiment in the E-5 Facility.

The peak gamma heat rate measured with the calorimeter was 12 W/g. The 20% difference could be attributed to errors in the two techniques and/or to differences in the core configurations.

From the good agreement between independent temperature differences in each calorimeter and the agreement between calculated and experimental results, it appears that the instruments can measure nuclear heating rates to within 10%.

6.9.5 MONUHRIH Experiment (Measurement of Nuclear Heating Rates in the HFIR

6.9.5.1 Scope of the Experiment

A reliable nuclear heating rate computational model is needed along with a verifying experiment for the HFIR RB and VXF facilities. In particular, heating rate information is needed for structural materials such as graphite and stainless steel under the nuclear conditions imposed by a typical HRB capsule. To achieve this goal, the MONUHRIH experiment has been initiated.

6.9.5.2 Design Considerations

Based on the successful operation of the GAFI calorimeter, the proposed MONUHRIH experiment includes several such calorimeters enclosed in a single capsule physically resembling an HRB capsule. Three major limitations are placed on the design of this capsule.

1. The capsule wall material and geometry should nearly duplicate those of an HRB capsule. This restriction requires a dimensionally similar outer stainless steel capsule wall to ensure neutronic similarity with the HRB capsules.

2. The materials for which nuclear heating rates are measured should be (for optimum usefulness) stainless steel and Poco graphite. However, certain materials that have nuclear heating characteristics similar to these materials may also be used. Preliminary calculations

have shown that stainless steel calorimeters are unacceptable. Temperatures generated in stainless steel calorimeters will approach or exceed the melting point. This effect is primarily due to stainless steel's poor thermal conductivity. Copper, having nuclear properties similar to those of iron, is a good substitute and will replace stainless steel as a calorimeter material. Stainless steel heating rates will be estimated with the computational model.

Unfortunately, similar thermal-mechanical limitations prohibit a rapid mechanical design of the experiment. For copper and especially graphite, relatively large gaps will appear at interfaces with stainless steel at the capsule operating temperatures because of thermal expansion. Heat shrinking techniques or other similar techniques are required to prohibit such gaps from raising the capsule temperatures to the point that the success of the experiment might be jeopardized.

3. Chromel vs Alumel thermocouples have been chosen because of their availability and insensitivity to radiation damage.

6.9.6 Status of OC-1 and OF-2 Analysis

Most neutron flux dosimeters have been successfully removed from the OF-2 and OC-1 experiments. Some fusing of dosimeter wires to stainless steel spacers occurred in the center spline of the OF-2 experiment. According to a preliminary analysis of those data, this fusing involved the iron dosimeters. Steps have been taken to salvage information from those dosimeters.

The OC-1 dosimeter will have to be reweighed because of difficulty in distinguishing dosimeter position upon removal. Also, the titanium dosimeter wires were very embrittled and many were broken. Presently the activities of the OC-1 dosimeters are being measured.

6.10 POSTIRRADIATION PERFORMANCE ASSESSMENT — M. J. Kania, T. N. Tiegs, D. E. LaVelle, R. L. Walker, R. E. Eby, J. L. Botts, J. A. Carter, and D. A. Costanzo

Information gained through irradiation testing is interpreted and applied to process and equipment development and specification

writing. During this reporting period very little additional work was done to develop thermal analysis techniques for HT and HRB capsules. The work for these capsules is essentially complete, and the computer codes that have been developed are now operated routinely. Some work was done to develop more efficient models for thermal analysis of ORR capsules. Extensive work was done during the reporting period with the shielded electron microprobe. Fission product distributions within irradiated coated particles were determined as a function of the initial composition of the kernels. This work has been extremely useful in interpretating the irradiation behavior of weak-acid-resin-derived fissile fuels for the HTGR and in establishing a product specification on initial composition. Development work on the Irradiated Microsphere Gamma Analyzer (IMGA) system was completed during the reporting period. This device was developed to measure fission product inventories in individual coated particles, and to permit statistically accurate determinations of failed particle fractions. The system is now installed in the ORNL hot cells and will be routinely used as part of the postirradiation examination procedure for irradiation experiments. Work on chlorine leaching and burnup determinations continued during the reporting period. Development work in both areas is essentially complete, and the techniques developed are being applied routinely as part of the postirradiation examination procedures. Techniques for electrolytic disintegration of bonded HTGR fuel rods were developed during the reporting period. This step is necessary so that loose coated particles can be fed into the IMGA system for fission product inventory measurements and failed particle determination.

6.10.1 Thermal Analysis of Irradiation Capsules

During this past report period the computer codes developed and reported previously[32] have been routinely applied to irradiation capsules during postirradiation analysis. In particular, the HTCAP

code[33] is presently being used in the thermal analysis of HFIR target capsules HT-28, 29, and 30. It will also be used for the analysis of capsules HT-31 and 33. These analyses will be completed within the next year. The ENCTRK code[34] has been used for the thermal analysis of HRB capsules 9 and 10 and is reported in ref. 11. In addition, this code will be used for the thermal analyses of irradiation capsules HRB-11, 12, and 13 during the next year. The thermal analysis of the OF-1 capsule was completed during the past year by use of the HEATING3 code[35] and appropriate mathematical grid models, and is reported in ref. 20.

New code development work has centered around the analysis of the OF-type capsules, which are irradiated in the ORR. This work has been done by students in the MIT Practice School of Chemical Engineering here at ORNL. The primary emphasis has been on developing an automated thermal analysis code that will provide a two-dimensional time-temperature history for fuel rods irradiated in a cylindrical capsule arranged in a telephone dial pattern. This code has been written in FORTRAN IV for the IBM 360/91 and is still in early stage of application to the OF capsules. Use of this code is planned for the thermal analysis of the OF-2 capsule.

6.10.2 Microprobe Analysis of WAR Particles

HTGR fuel design requires retention of the fission products within the particle coatings. So an important part of performance assessment is a knowledge of the fission product behavior in the particles. A study was initiated[36] to determine fission product behavior in WAR particles irradiated in HRB-9. This study found that the level of kernel conversion (i.e., the ratio of UO_2 to UC_2) strongly affects the behavior of the fission products. Electron microprobe analyses were performed on WAR particles with nominal conversions of 0%, 15%, and 75%. Because of their corrosive attack of SiC, the behavior of the high-yield rare earth fission products (Nd, Ce, Pr, La)

was of prime importance. The results show that with increasing conversion levels (i.e., greater initial UC_2 content) there is a decrease in rare earth fission product retention in the kernels.

A study of the thermodynamics of the UO_2-UC_2 fission product system showed that the rare earth fission products would be present as oxides in irradiated particles with less than 70% initial conversion.[37] The rare earth oxides are expected to be stable and not migrate.

The rare earth fission product distributions in a 0%-converted WAR particle are shown in Fig. 6.36. Concentrations of these elements were found in the kernel, in separate kernel phases, along the inner surface of the iLTI, and at the iLTI-SiC interface. Obviously most are associated with the uranium (also shown in Fig. 6.36) in the kernel and the separate kernel phases. The presence of the rare earths along the inner surface of the iLTI and at the iLTI-SiC interface indicates that either the rare earths can migrate as oxides or thermodynamically they cannot hold the oxygen. There are conflicting results relating to the mobility of rare earth oxides.[10,38] Also the thermodynamic properties of irradiated fuel are not well known.

The rare earth fission product distributions in a 15%-converted WAR particle are shown in Fig. 6.37. The distributions are very similar to those in the 0% converted particle, except that the rare earths were not observed at the iLTI-SiC interface. As with the 0%-converted particle, the rare earth concentrations along the inner surface of the iLTI suggest some migration of rare earth oxides. Since no rare earths were observed at the iLTI-SiC interface, the iLTI coating appears to be a barrier for further migration. This is probably because no pathway through the iLTI coating was provided as with the 0%-converted particle, where migration of kernel through the iLTI was observed. Judging from the x-ray displays in Fig. 6.37, the concentrations of the rare earths along the inner surface of the iLTI appear higher in the 15%-converted particle than in the 0%-converted particle.

R-72498

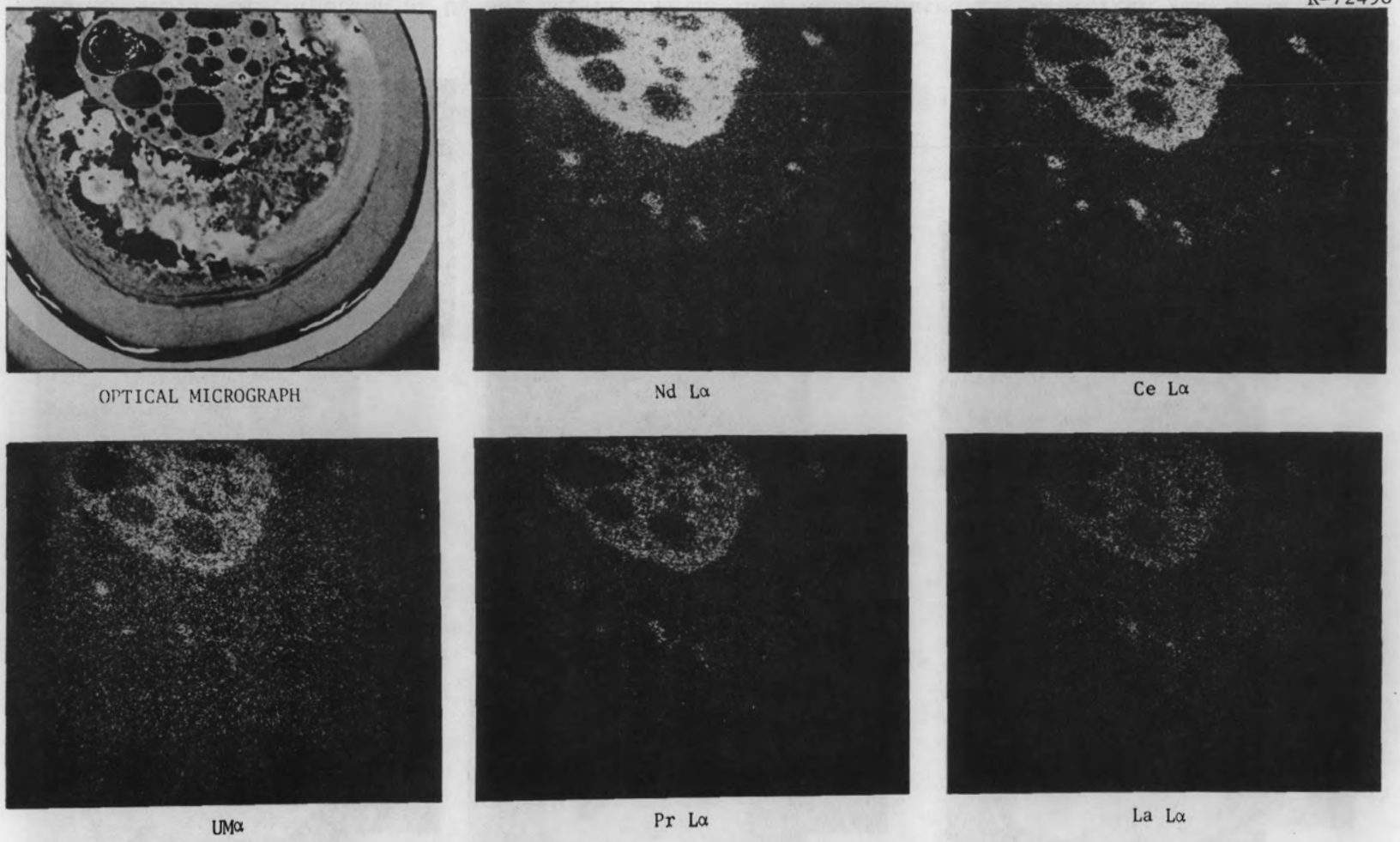

Fig. 6.36. Distribution of U, Nd, Ce, Pr, and La in a Triso-Coated 0%-Converted Weak-Acid-Resin-Derived Particle Irradiated in HRB-9. Average particle temperature was 960°C, burnup was 85% FIMA, average temperature gradient was 650°C/cm.

R-73933

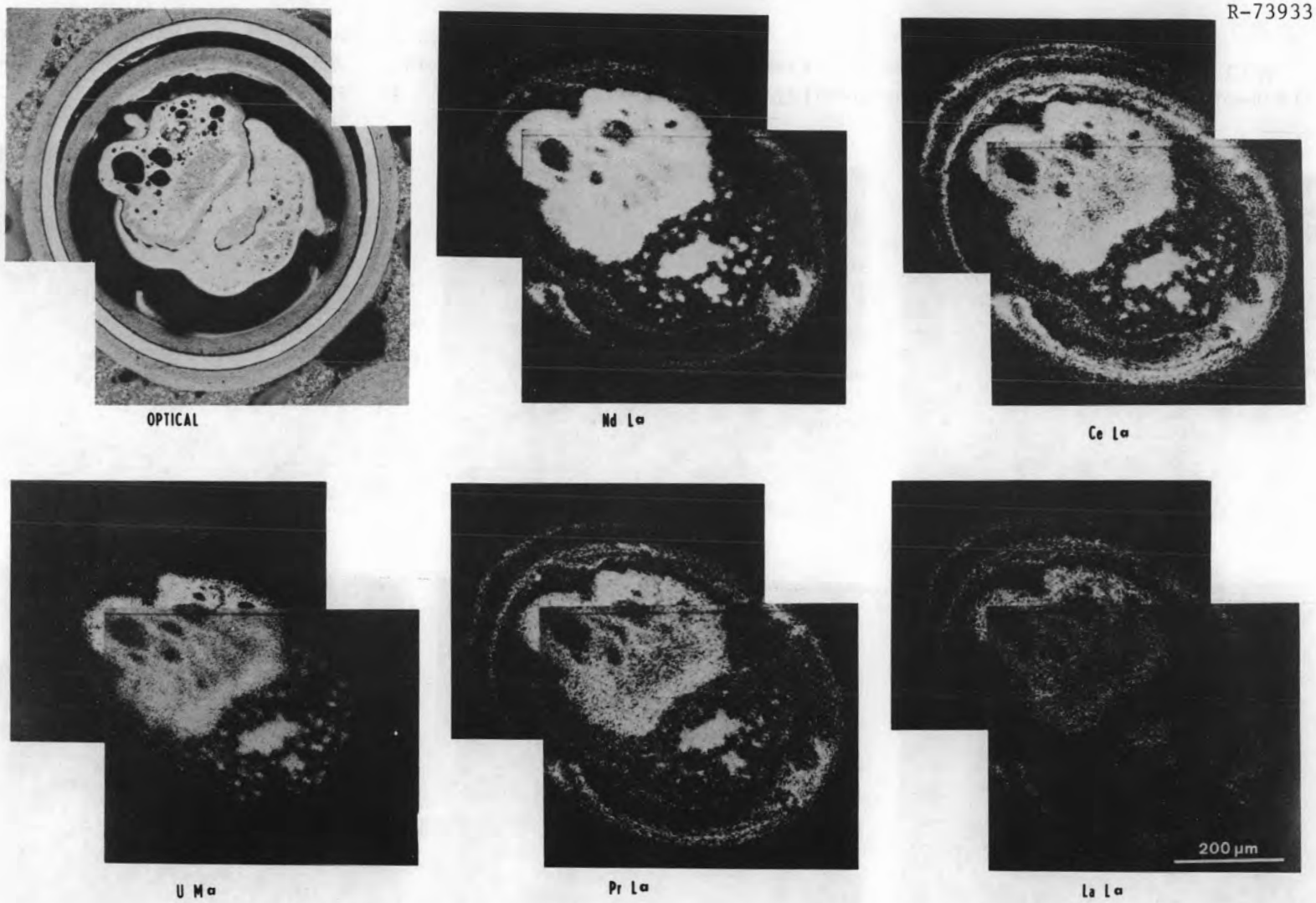

Fig. 6.37. Distribution of U, Nd, Ce, Pr and La in a Triso-Coated 15%-Converted Weak-Acid-Resin-Derived Particle Irradiated in HRB-9. Average particle temperature was 1050°C, burnup was 85% FIMA, average temperature gradient was 500°C/cm.

The rare earth fission product distributions in a 50%-converted particle are shown in Fig. 6.38. Concentrations were found in the two kernel phases, along the inner surface of the iLTI, and at the iLTI-SiC interface. Evidently more of the rare earths were present along the inner surface of the iLTI than with either the 0%-converted or 15%-converted particles. (Quantitative analysis showed this to be true.)[36]

The rare earth fission product distributions in a 75%-converted particle are shown in Fig. 6.39. The rare earths were present in the kernel (most of the kernel had fallen out but small fragments remained), in the densified buffer, along the inner surface of the iLTI and the iLTI-SiC interface. Obviously there appears to be less retention of the rare earths than with the 0%-, 15%-, and 50%-converted particles.

The results of the electron microprobe analysis show that the retention of the rare earths in the kernels is a function of the initial oxygen content (i.e., the conversion). As the conversion increases the retention of the rare earths decreases.

6.10.3 Irradiated-Microsphere Gamma Analyzer

The Irradiated-Microsphere Gamma Analyzer (IMGA)[39] System was designed to provide information concerning the types and amounts of fission products present in coated particle fuel after irradiation. This information is necessary to determine whether present fuel product specifications on irradiation performance are being met. The quantitative measurement of the fission product inventory is used to establish a statistically accurate measure of the failure fraction of irradiated coated particle fuel. Failure fraction is defined as that fraction of irradiated coated fuel particles that have lost a significant amount of their fission products through defective or broken coatings. Based on previous calculations,[40] an accurate failure fraction determination requires examination of several hundred to several thousand coated particles.

R-73932

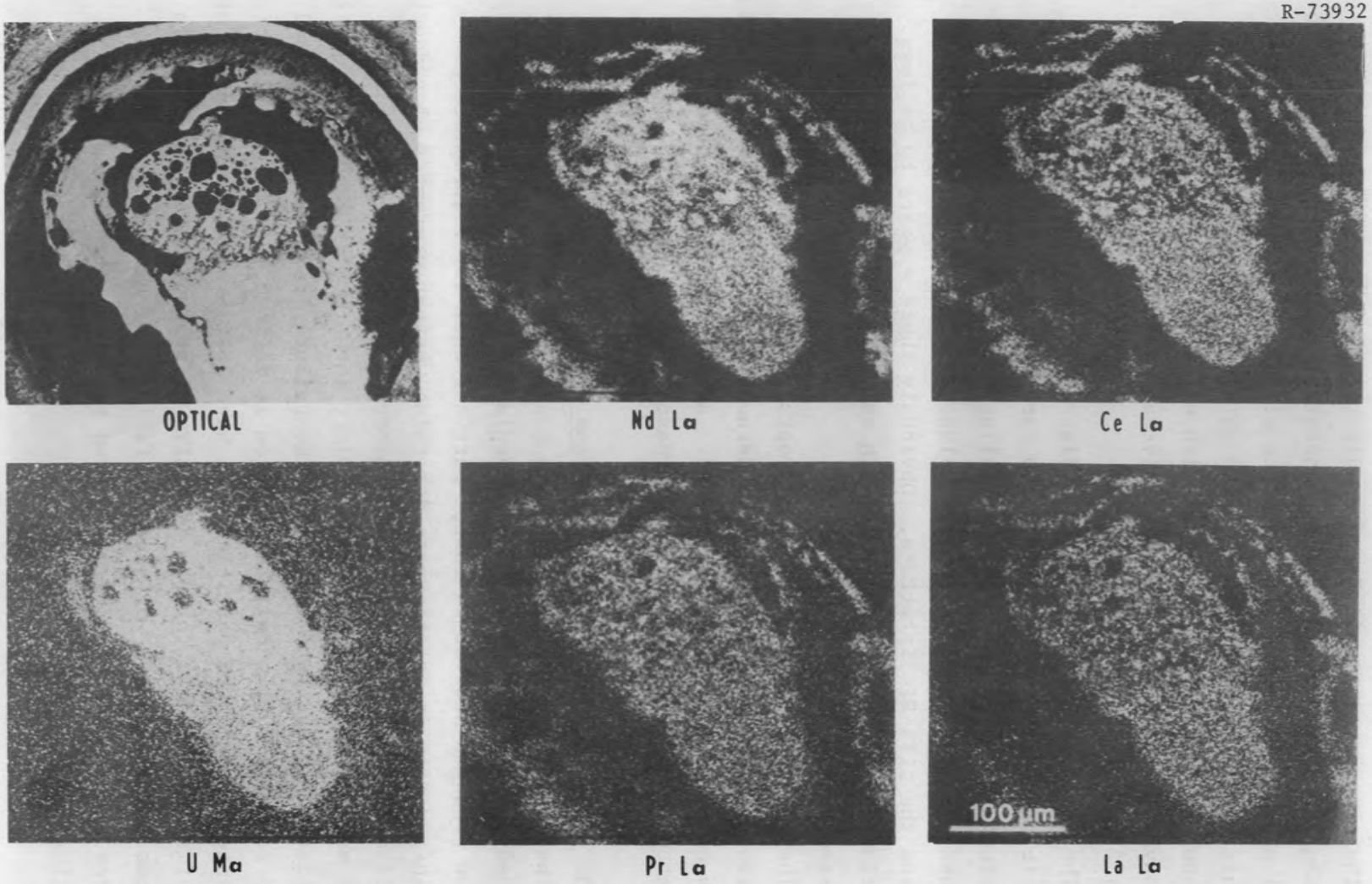

Fig. 6.38. Distribution of U, Nd, Ce, Pr, and La in a Triso-Coated 50%-Converted Weak-Acid-Resin-Derived Particle Irradiated in HRB-9. Average particle temperature was 1070°C, burnup was 85% FIMA, and average temperature gradient was 450°C/cm.

R-72499

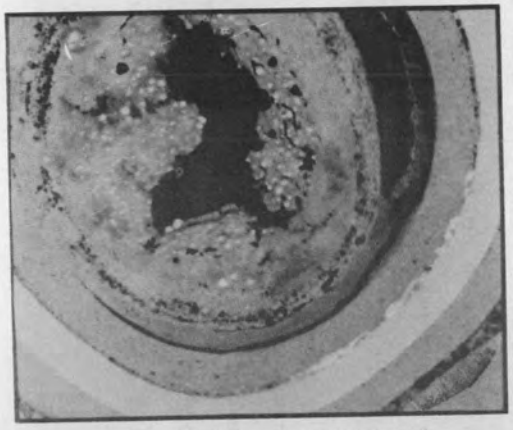

OPTICAL MICROGRAPH

Nd Lα

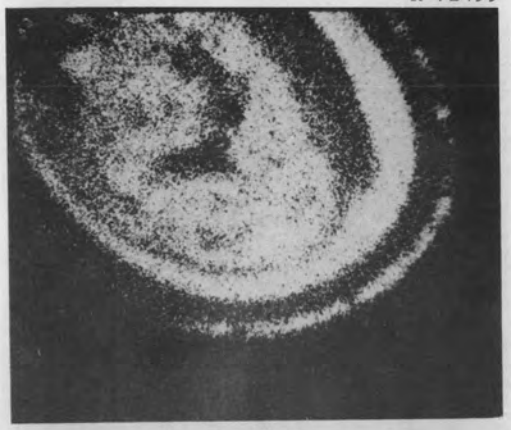

Ce Lα

BACK SCATTERED ELECTRON IMAGE

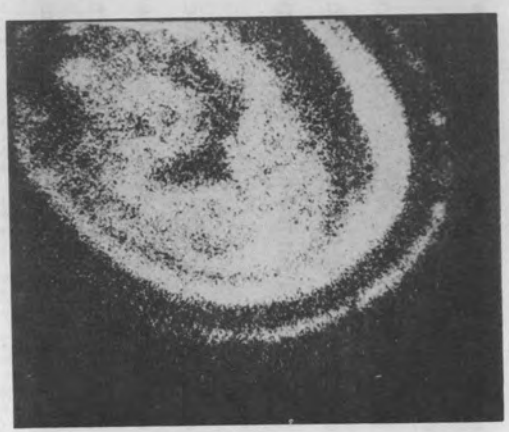

Pr Lα

La Lα

Fig. 6.39. Distribution of Nd, Ce, Pr and La in a Triso-Coated 75%-Converted Weak-Acid-Resin-Derived Particle Irradiated in HRB-9. Average particle temperature was 1080°C, burnup was 85% FIMA, average temperature gradient was 400°C/cm.

Basically IMGA consists of a high-resolution gamma-ray detector, a minicomputer-based pulse height analyzer, an automated particle handler, and appropriate interfaces to establish communication links between the three components. A description of each of the major components is outlined below:

Automated Particle Handler — The automated particle handler, designed and fabricated at ORNL, represents the unique component of the IMGA system. Figure 6.40 describes the automated handler with its lead shielding removed just before installation into the IMGA cubicle. The handler consists of three components: a particle singularizer, which can select one or several irradiated coated particles from a large population and load them into a sample holder; a sample changer, which contains three sample holders, 120° apart, and rotates them from the load position to the detector position and finally to the drop position; and a particle collector, which contains 20 bins in which particles can be classified according to their respective radioisotopic analyses. The operation of the handler under computer control has been described previously.[41]

Pulse Height Analyzer System — The pulse height analyzer system, which IMGA is structured about, is a Tennecomp Systems, Inc., model TP-5000, which is supplied with a Digital Equipment Corp. model PDP11/05 minicomputer. The 11/05 is a 16-bit machine with 4000 (4K) 14-bit words of memory in the main frame. Three additional 8K memory extension modules yield a total of 28K words of storage. This memory is used for storage of programming and variables and a histogram region. Two mass storage devices are also available: a Digital Equipment Corporation model RK05 disk unit, and a Tennecomp Systems, Inc. Datapacer with two four-track data cartridge transports.

Gamma-Ray Detector — The gamma-ray detector used with the IMGA system is an ORTEC high-resolution lithium-drifted germanium, Ge(Li), detector. Coupled with the detector are pulse processing units consisting of an ORTEC model 120-4 preamplifier, an ORTEC model 472 main

Y-140035

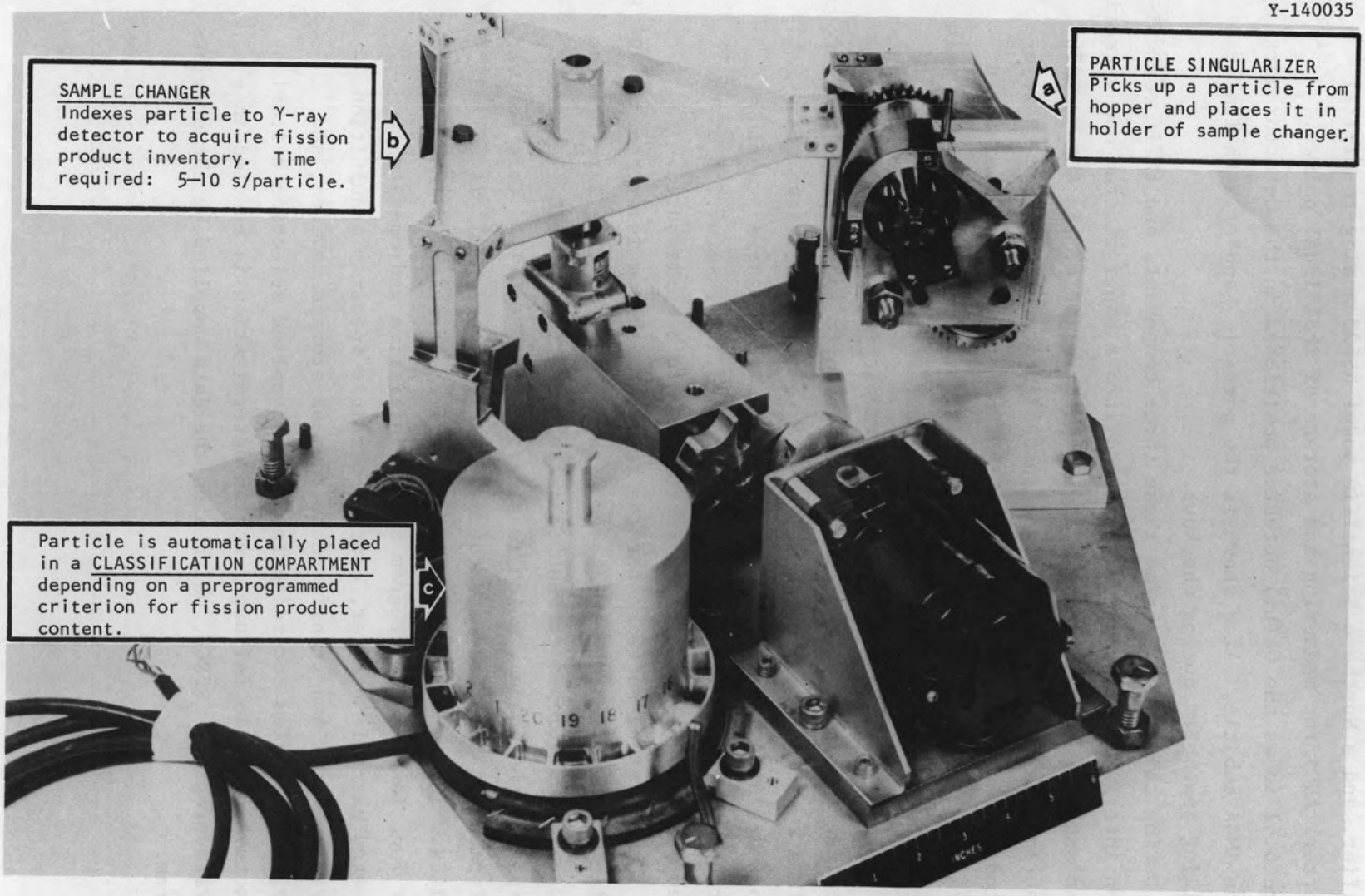

Fig. 6.40. Irradiated-Microsphere Gamma Analyzer, Including Particle Handling Mechanism. The system was developed to qualify the irradiation performance of recycle fuel particles.

amplifier, and a Northern Scientific model NS623 analog-to-digital converter (ADC) for measuring and storage of individual pulses. Figure 6.41 shows the Ge(Li) detector positioned in the detector port of the IMGA cubicle. Also shown is the particle handler with its lead shielding assembled during checkout.

During this report period these three components and their communication interfacing have been integrated into a sophisticated and versatile system and demonstrated to be efficient and reliable. In August 1976 the automated particle handler was installed into a shielded cubicle located on the second level of the High Radiation Level Examination Laboratory (HRLEL). The cubicle is positioned directly above the main hot cell area on the first level. A transfer device from the main cell area to the IMGA cubicle enables irradiated coated particle fuel to be inserted into the cubicle. In addition to the particle handler, the IMGA cubicle contains a shielded stereomicroscope stage with micromanipulators for single particle handling. Also a Scanning Electron Microscope (SEM) has been installed for examination of the coated particles after failure fractions have been measured.

The operating software for the Tennecomp system is written in PDP 11 machine language and was purchased with the system. The interpretive software was developed at ORNL in a language known as TIL (Tennecomp Interpretive Language), which is a version of FOCAL-11. This software development is complete, and the main analysis program[42] is called FALFRACK. This program controls the entire operation of IMGA. The major functions of the program are to initialize and operate the automated particle handler, control particle spectrum acquisition, analyze spectrum and transfer data to mass storage devices, and segregate particles according to a user-supplied selection criterion. The actual particle failure fraction determination is handled in a separate program, CRUNCH, which uses the data supplied by the previous program.

R-71356

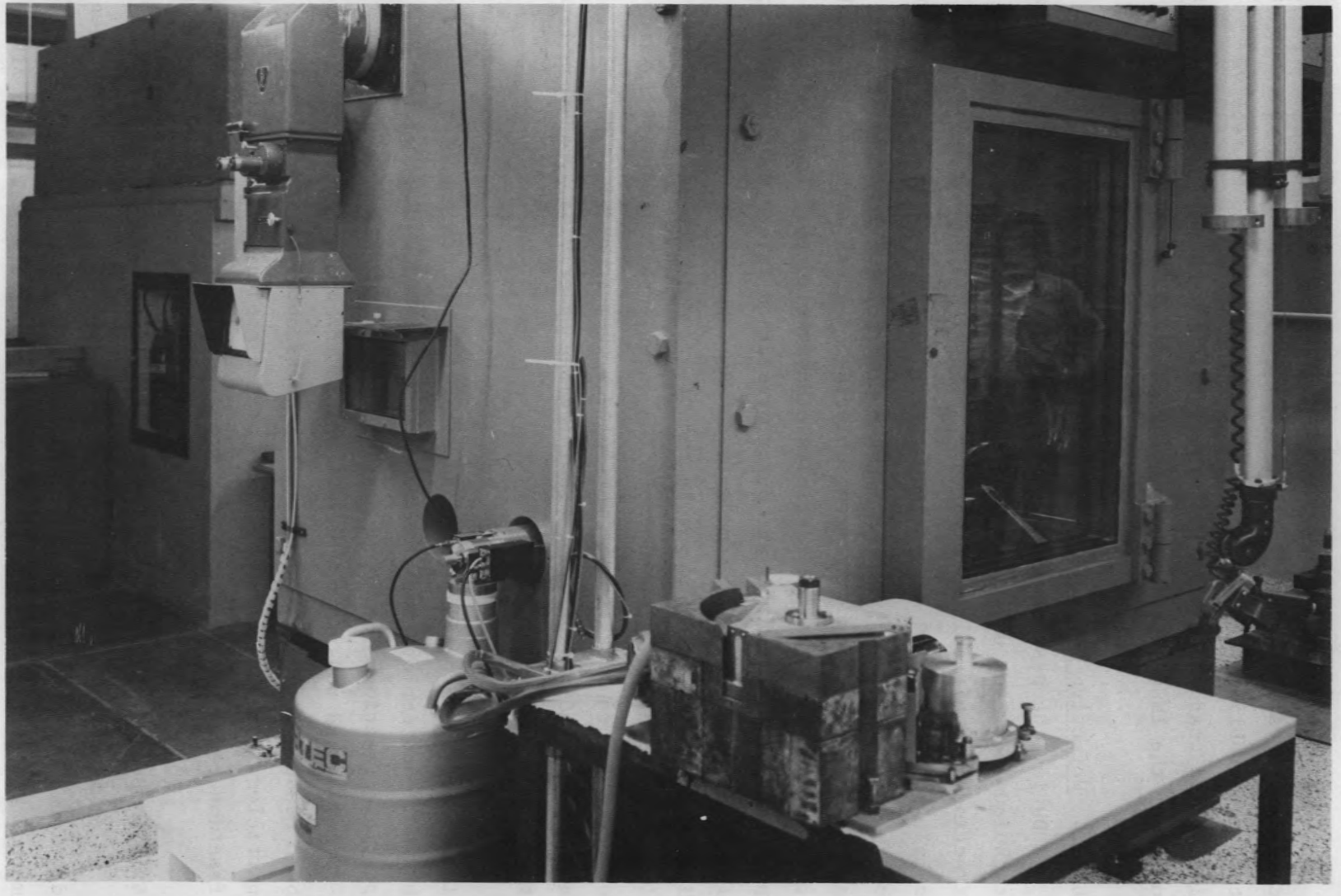

Fig. 6.41. IMGA Cubicle with Ge(Li) Detector Positioned in Detector Port and Automated Particle Handler, with Shielding Assembled, During System Checkout.

To date the IMGA system has been throughly checked out with cold particles and the reliability of all the components under computer control established. The IMGA system should be ready to receive irradiated coated particle fuel in early 1977. A manual for prospective users of the IMGA system is now being prepared.[42]

6.10.4 Defective Particle Fraction Measurement

During the past several years, the high-temperature chlorine leach technique has been used routinely to determine the particle failure fraction of nonirradiated HTGR fuel. In this method, a loose particle sample or fuel rod is heated inductively to 1500°C in a flowing steam of chlorine gas, and the fuel exposed by coating defects is volatilized and collected as the heavy metal chloride.[43] This method is applicable to Biso- and Triso-coated particles. However, with Triso-coated particles, both the inner and outer pyrocarbon layers must be defective for chlorine leaching to remove fuel. An exposed but otherwise intact SiC layer is destroyed by chlorine. A defect in a SiC layer itself is detected by burning off the outer pyrocarbon layer in air or oxygen, then treating the particles with mercury under pressure, and finally radiographically examining the underlying pyrocarbon layer for mercury incursion.[44]

The chlorine leach method has also been adopted for examination of irradiated fuel specimens, and an apparatus was designed for use in a hot cell and employs resistance heating at 1000°C. The defective particle fractions for loose particles in the HT-12 through -15 series and rods in the HT-30 capsule irradiation experiments have been measured. The chlorine leach results obtained for irradiated particles in the HT-12 through -15 are in good agreement with failure fraction results obtained by gas pressure and radioactivity measurements.[45]

6.10.5 Burnup Analysis of HTGR Fuel Particles

An isotope dilution mass spectrometry (IDMS) technique has been developed for the analysis of submicrogram amounts of zirconium. This method has sufficient sensitivity for the analysis of fission zirconium

produced in a single microspherical HTGR fuel particle and has been used for burnup analysis of particles at the 5% FIMA level. A paper that describes this method has been accepted for publication in Analytical Letters.[46] The abstract of this paper follows.

> A sensitive, isotope dilution technique has been developed for the analysis of sub-microgram amounts of zirconium. The analysis is based on the increased thermal ion emission for Zr adsorbed on a single anion resin bead. Zr is isolated from a solution containing the sample and a highly enriched ^{94}Zr (96%) spike. The determination is made possible by using a high-sensitivity pulse-counting 2-stage 30-cm radius mass spectrometer. The detection limit depends upon the amount of the isotope spike added and the desired precision. Fifty nanograms of zirconium (sample plus spike) produce sufficient ion signals for reliable isotopic analysis so that fission Zr can be measured with blank correction to a precision of 3%. By this method for fission Zr in spent reactor fuel particles, contamination from normal Zr and Mo can be corrected out by making isotopic measurements before and after spiking and scanning masses 90 and 95 during analysis. Since neither masses 90 nor 95 are stable fission products, their presence is due to sample contamination and can be used for correction based on their normal isotopic distributions. Zone-refined tantalum ribbon, essentially free of normal Zr and Mo was selected as the ionizing filament. This method can be adapted to a wide variety of samples.

The IDMS technique has also been applied to the analysis of thorium and uranium. In this method, after a particle is dissolved, an aliquot is first measured for isotopic composition, and then a second aliquot is equilibrated with a double spike containing enriched ^{230}Th and ^{238}U. The initial isotopic composition and the newly established ratios are used to calculate the uranium and thorium.

6.10.6 Fuel Rod Deconsolidation

Fuel rod deconsolidation is the process whereby fuel particles in an HTGR fuel rod are separated from the carbonaceous matrix by disintegrating it into fine graphite powder. Our incentive for developing the deconsolidation process is directly related to the operation of the IMGA system (Sect. 6.10.3), which requires that the

irradiated fuel be in the form of individual particles. Figure 6.42 describes the procedure necessary to make failure fraction measurements on irradiated HTGR fuel rods. The initial step is the electrolytic disintegration of the irradiated fuel rod.

Various methods[47] have been developed to remove the carbonaceous matrix in HTGR fuel rods. Each of these uses the formation of intercalation compounds of graphite with certain elements. This formation is accompanied by an enlargement of the *c*-spacing of the layer lattice, loosening the graphite matrix and causing it to disintegrate into a fine powder. The electrolytic disintegration reaction is based on the anodic oxidation of graphite in an electrolyte containing nitric acid.

During this report period emphasis has been on development of equipment and techniques necessary for use on irradiated material under remote handling operations. Figure 6.43 is a schematic of the irradiated fuel rod deconsolidation apparatus and Fig. 6.44 shows the actual

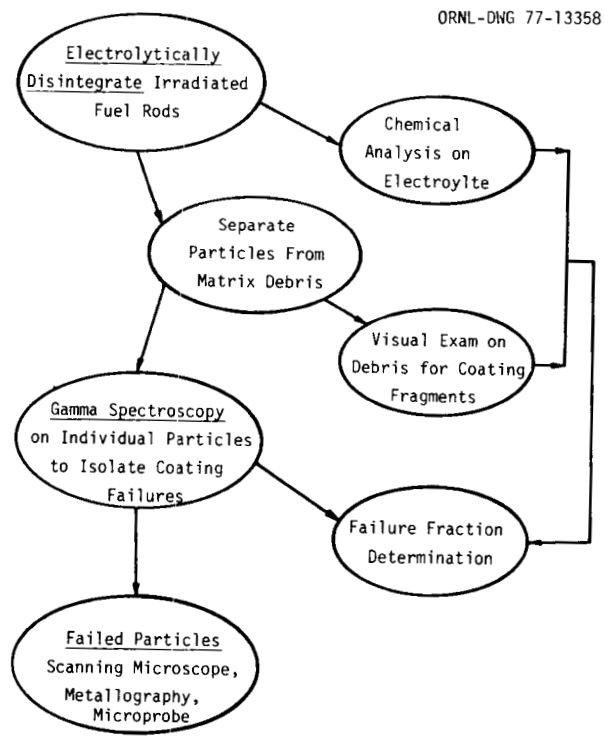

Fig. 6.42. Capabilities for Failure Fraction Measurements on Irradiated HTGR Fuel Rods.

ORNL-DWG 77-9640

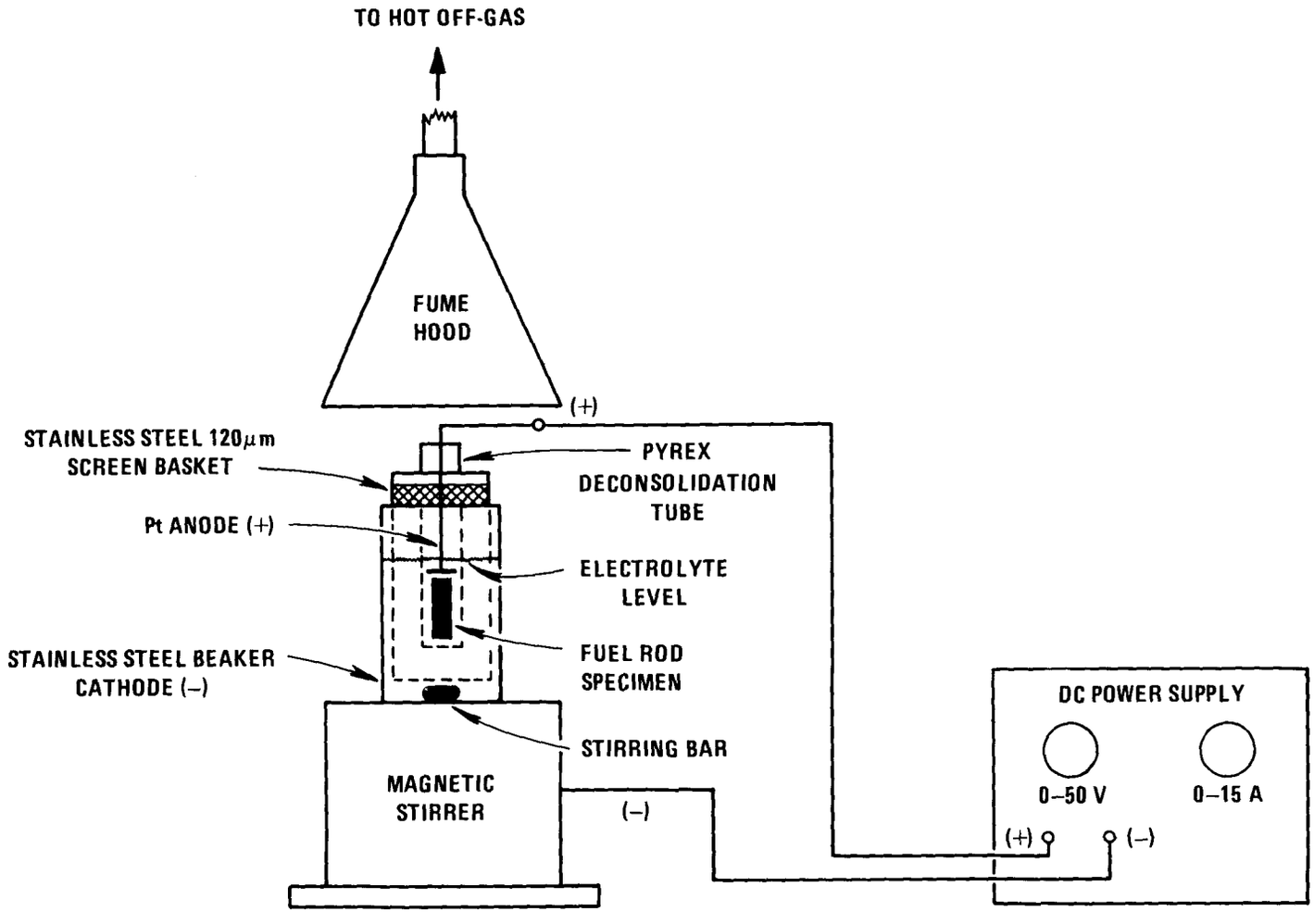

Fig. 6.43. Irradiated Fuel Rod Deconsolidation Apparatus.

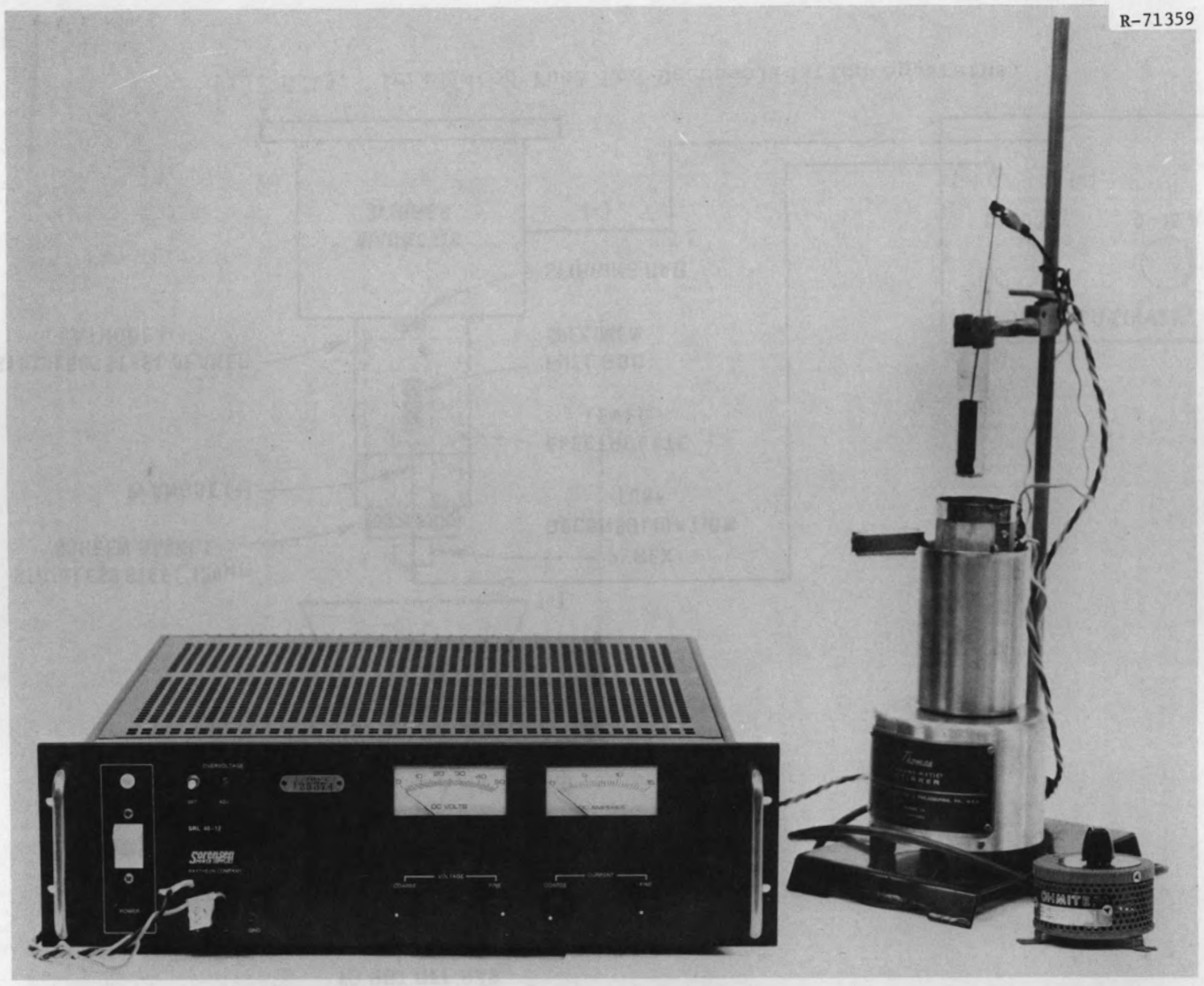

Fig. 6.44. Equipment for Deconsolidating HTGR Fuel Rods. Deconsolidation apparatus on right is operated remotely in the hot cell while power supply on left is operated from outside the cell.

equipment used here at ORNL. The apparatus basically consists of a glass deconsolidation tube with a 19-mm (0.75-in.) ID. This diameter is large enough to accommodate fuel rods (nominally 13 to 16 mm OD), yet small enough to prevent current from passing around the fuel rod in the electrolyte. The bottom of the glass tube is flat, with twenty 1.6-mm-diam (0.06-in.) holes. These openings allow debonded particles and fine matrix matter to fall into the screen basket. A platinum anode on top of the fuel rod during deconsolidation is the source of positive current. This electrode is a "churn dasher" type with a 1.3-mm-diam (0.05-in.) wire handle and a 0.6-mm-thick by 19.1-mm-diam (0.03 by 0.75 in.) disk as the dasher. This design provides good electrical contact with the fuel rod, and the churning action dislodges loose fuel particles during deconsolidation.

The deconsolidation tube sits in a stainless steel 120-μm screen basket, which is supported in a stainless steel beaker, which is also the cathode and contains 400 ml of the 8.0 *N* HNO_3 electrolyte. The screen basket receives the loose particles and also holds them during ultrasonic cleaning. The screen size allows the matrix powder to pass through during cleaning but retains the particles and any coating fragments. The beaker sits on a magnetic stirrer, which assures proper mixing of the electrolyte and also helps dislodge loose particles. A fume hood over the apparatus exhausts the nitric acid fumes generated during deconsolidation. A 0–15 A, 0–50 V dc power supply is used with the apparatus.

After the rod has been deconsolidated and cleaned, the remains — including particles, clusters, coating fragments, and matrix chunks — are shape separated to isolate completely debonded particles. The residue is then visually examined for particles not removed by the shape separator. The electrolyte is then submitted for chemical analysis of uranium and thorium that may have been leached out of broken particles.

A series of tests was conducted on unirradiated fuel rods to develop deconsolidation procedures and refine equipment. Rod characterization for the fuel rods used are described in Table 6.75. The Biso-coated

Table 6.75. Unirradiated Fuel Rods for Hot Cell Deconsolidation

Rod	Coated Particle[a] Weight (g)	Injection[b] Time (s)	Green Dimensions, mm		Weight, g		Coke Yield (%)
			Length	Diameter	Green	Fired	
M-152-109	12.402	50	50.52	12.45	15.642	14.130	22.61
M-152-110	12.400	50	51.05	12.45	15.703	14.176	23.33
M-152-111	12.398	55	50.52	12.45	15.653	14.144	23.12
M-152-112	12.400	40	51.82	12.45	15.808	14.239	23.65
M-152-113	12.388	45	51.36	12.45	15.751	14.196	23.32
M-152-115	12.380	50	51.05	12.45	15.684	14.140	22.50
M-152-116	12.399	50	51.26	12.45	15.697	14.171	23.27
M-152-117	12.385	45	51.00	12.45	15.718	14.135	21.46
M-152-119	12.393	50	51.56	12.45	15.746	14.138	20.47

[a]Particles from fertile particle batch A-642. Nominal particle dimensions are: kernel diameter, 496.9 μm; buffer thickness, 96.3 μm; LTI thickness, 79.1 μm.

[b]All rods were injected at a pressure of 4.14 MPa (600 psi) and at a temperature of 180°C (453 K) except rod M-152-109, which was injected at 175°C (448 K).

fertile batch A-652 was used in the fabrication of each rod. These particles were coated in the 0.13-m (5-in.) coating furnace with the fritted gas distribution system with undiluted propylene as the coating gas. Particles were then annealed at 1800°C (2073 K) for 1.8 ks (30 min). The failed fuel fractions of the as-coated particles, as determined by chlorine leach, were 6.9×10^{-5} and 8.9×10^{-5} for the two samples submitted for analysis. Fuel rods were formed by the slug injection process using the GA matrix M-152. Rods were carbonized in packed Al_2O_3 powder at a heating rate of 0.17 K/s (10°C/min) to a temperature of 1800°C (2073 K) and held at that temperature for 1.8 ks (30 min). Chlorine leach results of three representative fired fuel rods were $<1 \times 10^{-7}$, 2.4×10^{-5}, and $<1 \times 10^{-7}$.

Failure fraction results as determined on the deconsolidated particles and the operational data during the deconsolidation procedure are shown in Table 6.76. Fuel rods M-152-113 and -115 showed an increase

Table 6.76. Failure Fraction Determined by Chlorine Leach on Deconsolidated Biso-Coated ThO_2 Particles

Rod	Thorium Weight Per Rod[a] (g)	Chlorine Leach (mg)	Failure Fraction		Highest Voltage Obtained (V)	Power (W)	Time (min)
			Observed	Corrected[b]			
M-152-109	6.759	0.037	0.1×10^{-4}	0.0×10^{-4}	4	8	91
M-152-110	6.758	0.04	0.1	0.0	8	40	60
M-152-111	6.757	0.104	0.2	0.0	6	30	60
M-152-113	6.751	14.7	21.8	21.0	15	75	60
M-152-115	6.747	23.2	34.4	33.6	15	75	50
M-152-116	6.757	1.08	1.6	0.8	8	40	60
M-152-117	6.750	0.026	0.03	0.0	5	25	47
M-152-119	6.754	1.02	1.5	0.7	5	25	55

[a]Based on analytic chemistry results of 54.5% g Th/g particles.

[b]Observed failure fraction minus failed fuel fraction of as-coated particles.

in failure fraction after chlorine leach of the deconsolidated particles. Particles from each of these rods were radiographed after the chlorine leach. Rod-113 showed 31 particles with complete kernel removal and 3 particles with partial kernel removal. Rod-115 had 27 particles with missing kernels and 12 particles with partially missing kernels.

Rod M-152-112 was only partially deconsolidated and hence not included in Table 6.76. Figure 6.45 shows the partial deconsolidation of rod-112. Figure 6.46 shows the particles and matrix rubble after partial deconsolidation of rod 112. Both these figures are typical of rods formed by the slug-injection process. Upon completion of rod deconsolidation, particles were cleaned, dried, and shape separated.

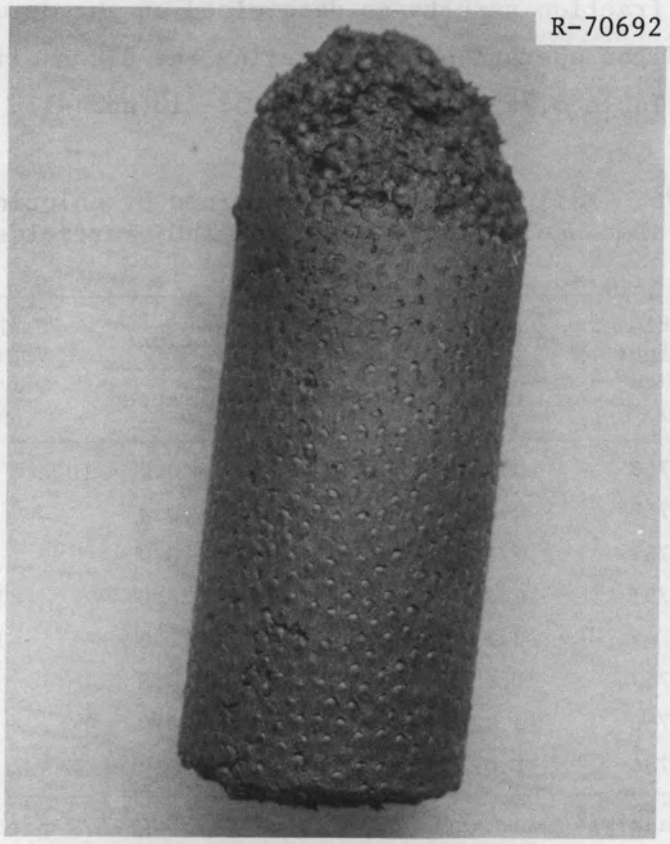

Fig. 6.45. Partially Deconsolidated Rod M-152-112.

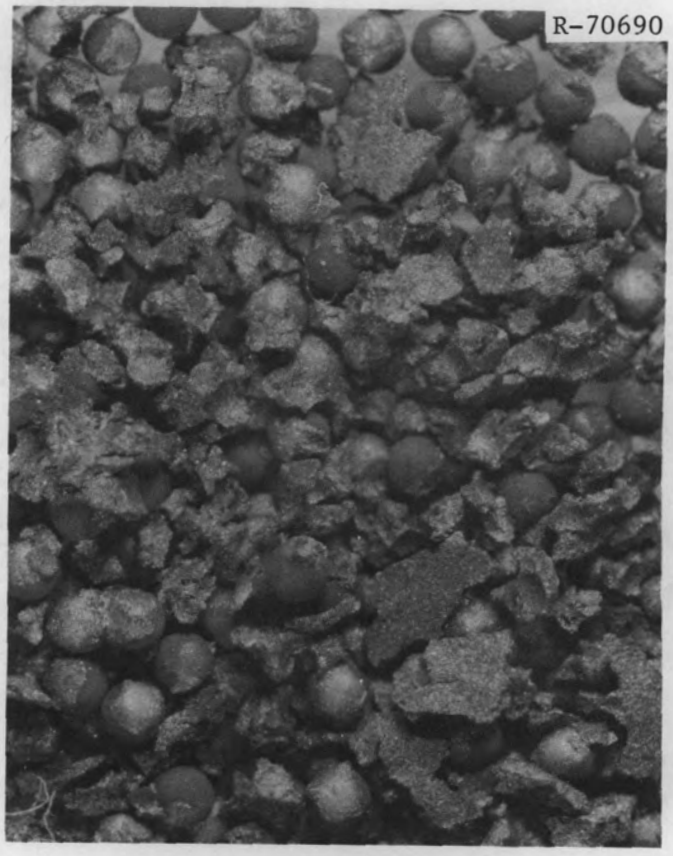

Fig. 6.46. Appearance of Fuel Rod After Deconsolidation But Before Ultrasonic Cleaning and Shape Separation.

The reject fraction contained small matrix debris, heavily faceted particles and eight doublets. Figure 6.47(a) shows the reject fraction obtained from shape separation on rod 117 (typical for a slug-injected rod). The remaining well-shaped particles were submitted for radiographs, chlorine leach, and post-chlorine-leach radiographs. Figure 6.47(b) shows a typical sample of particles after shape separation for rod 117. Chlorine leach results showed only surface contamination by thorium, and radiographs revealed no damage of particles.

The results of the test on unirradiated fired fuel rods indicate that low currents and voltages are necessary to prevent damage to the particles during deconsolidation.

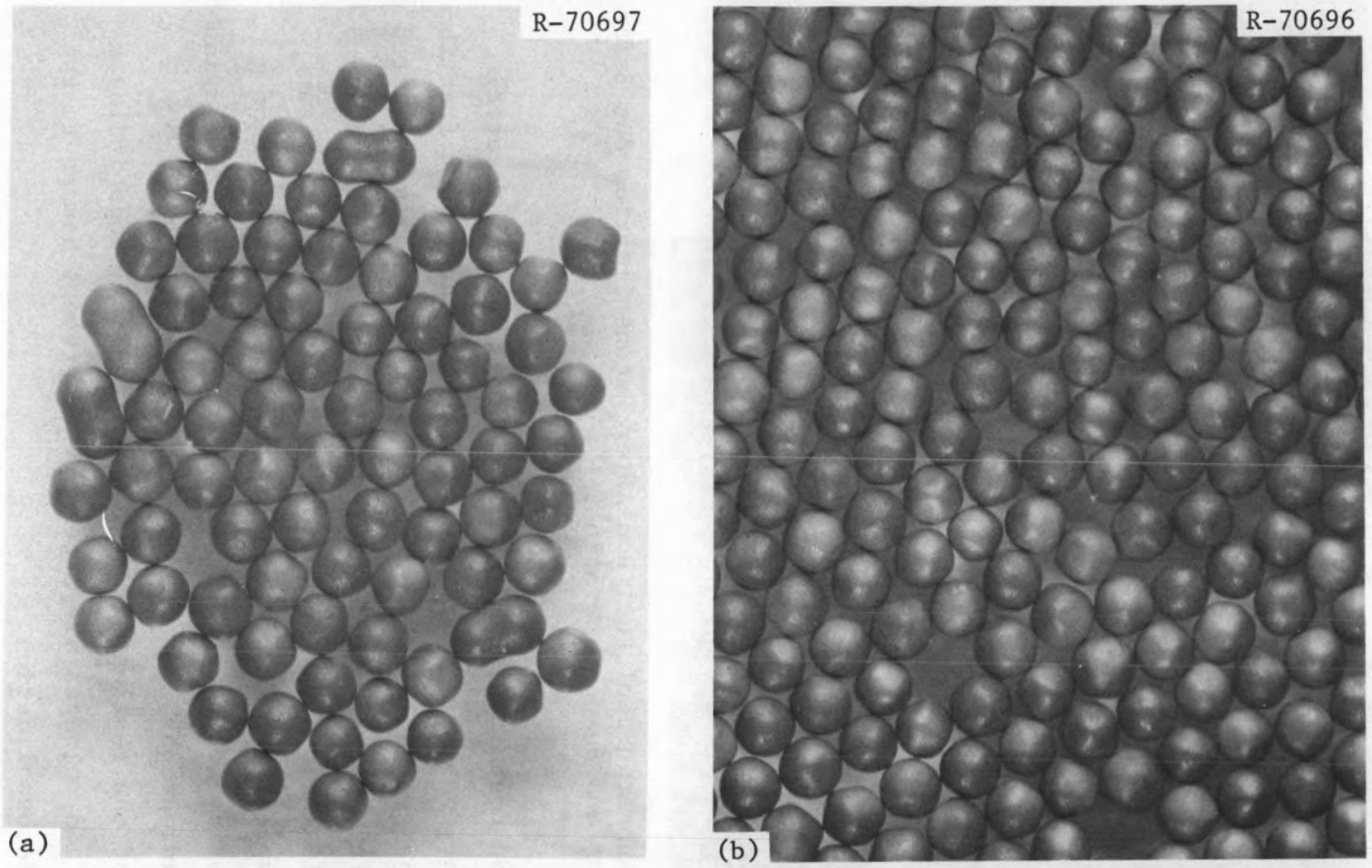

Fig. 6.47. Particles From Shape Separation From Rod M-152-117. (a) Rejected faceted particles and doublets. (b) Representative acceptable particles.

6.11 REFERENCES

1. G. W. Weber, R. L. Beatty, and V. J. Tennery, *Properties of Carbonized and Converted Uranium-Loaded Weak-Acid Resins*, ORNL-5201 (February 1977).
2. R. Bacon, "Carbon Fibers from Rayor Precursors," pp. 1–102, *Chemistry and Physics of Carbon*, vol. 9, P. L. Walker and P. R. Thrower eds., Dekker, New York, 1973; note p. 13.
3. R. L. Hamner and O. J. Horne, "Fuel Rod Fabrication Development and Qualification," *HTGR Base-Technology Program Prog. Rep. Jan. 1, 1974–July 1, 1975*, ORNL-5108, pp. 247–49.
4. R. L. Beatty, "Irradiation Test Capsules HT-17, -18, and -19," *HTGR Base-Technology Program Prog. Rep. Jan. 1, 1974–July 1, 1975*, ORNL-5108, pp. 269–76.
5. D. B. Owens, *Factors for One-Sided Tolerance Limits and for Variable Sampling Plans*, Sandia Corp., Albuquerque, N. M., March 1963.
6. W. P. Eatherly and J. M. Robbins, "Capsules HT-20 Through -23," *Gas-Cooled Reactor Program Ann. Prog. Rep. Dec. 31, 1973*, ORNL-4975, p. 138.
7. T. G. Godfrey, J. P. Moore, and J. M. Robbins, "Irradiation Tests HT-20 Through -23," *HTGR Base-Technology Program Prog. Rep. Jan. 1, 1974–June 30, 1975*, ORNL-5108, pp. 276–82.
8. W. R. Johnson, *Thermal Conductivity of Large HTGR Fuel Rods*, GA-A-12910 (GA-LTR-9) (March 1974).
9. R. L. Beatty, "Irradiation Test Capsules HT-28, -29, and -30," *HTGR Base-Technology Program Prog. Rep. Jan. 1, 1974–June 30, 1975*, ORNL-5108, pp. 286–95.
10. K. H. Valentine, F. J. Homan, E. L. Long, Jr., T. N. Tiegs, B. H. Montgomery, R. L. Hamner, and R. L. Beatty, *Irradiation Performance of HTGR Fuel Rods in HFIR Experiments HRB-7 and -8*, ORNL-5778 (May 1977).
11. F. J. Homan, E. L. Long, Jr., B. H. Montgomery, T. N. Tiegs, M. J. Kania, R. L. Hamner, R. L. Beatty, and B. A. Thiele, *Irradiation Performance of HTGR Fuel Rods in HFIR Experiments HRB-9 and -10*, ORNL-5254, in preparation.

12. R. T. Cheverton and T. M. Sims, *HFIR Core Nuclear Design*, ORNL-4621 (July 1971), p. 35.

13. K. H. Valentine, B. H. Montgomery, R. L. Hamner, E. L. Long, Jr., and T. N. Tiegs, "Capsules HRB-7 and -8," *HTGR Base-Technology Program Prog. Rep. Jan. 1, 1974–June 30, 1975*, ORNL-5108, pp. 303–35.

14. F. J. Homan, B. H. Montgomery, E. L. Long, Jr., R. L. Hamner, and T. N. Tiegs, "Capsules HRB-9 and -10," *HTGR Base-Technology Program Prog. Rep. Jan. 1, 1974–June 30, 1975*, ORNL-5108, pp. 336–59.

15. F. J. Homan, E. L. Long, Jr., T. B. Lindemer, R. L. Beatty, and T. N. Tiegs, *Development of a Fissile Particle for HTGR Fuel Recycle*, ORNL/TM-5602 (December 1976).

16. J. A. Conlin, K. R. Thoms, and R. B. Fitts, "Irradiations in ORR Core Facilities," *Gas-Cooled Reactor Programs Ann. Prog. Rep. Dec. 31, 1972*, ORNL-4911, pp. 115–16.

17. K. R. Thoms and A. W. Longest, "Irradiation Tests in ORR In-Core Facility," *Gas-Cooled Reactor Programs Ann. Prog. Rep. Dec. 31, 1973*, ORNL-4975, pp. 138–47.

18. C. C. Smith, *Preirradiation Report: Fuel Materials for Irradiation P13Q*, GA-A-13265 (June 1975).

19. M. J. Kania, K. R. Thoms, and T. N. Tiegs, "Irradiation Tests in the ORR," *HTGR Base-Technology Program Prog. Rep. Jan 1, 1974–June 30, 1975*, ORNL-5108, pp. 360–95.

20. T. N. Tiegs, E. J. Allen, M. J. Kania, E. L. Long, Jr., and K. R. Thoms, *Irradiation Experiment OF-1: Accelerated Testing of HTGR Fuel*, ORNL-5234 (August 1977).

21. K. R. Thoms and M. J. Kania, *Design, Fabrication, and Initial Operation of HTGR-ORR Capsule OF-2*, report in preparation.

22. F. J. Homan, E. L. Long, Jr., B. H. Montgomery, and R. L. Hamner, *Irradiation Performance of HTGR Fuel Rods in HFIR Experiment HRB-6*, ORNL-TM-5011 (December 1975).

23. C. J. Borkowski and T. V. Blalock, "A New Method of Johnson Noise Thermometry," *Rev. Sci. Instrum.* 45(2): 151–62 (February 1974).

24. R. L. Shepard, C. J. Borkowski, T. V. Blalock, J. K. East, R. J. Fox, and J. L. Horton, "Johnson Noise Thermometer Development," *HTGR Base-Technology Program Prog. Rep. Jan. 1, 1974–June 30, 1975*, ORNL-5108, pp. 414–416.

25. R. H. Siller et al., "The Solubility of Carbon in Palladium and Platinum." *J. Less-Common Metals* 16: 71–73 (1968).

26. H. J. Albert and J. S. Hill, *Development of a Platinum-Thorium Oxide Alloy for Resistojet Thruster Use*, NASA-CR-111959 (July 1971).

27. M. W. Waddell, R. K. Williams, O. W. Hermann, R. L. Shepard, and T. G. Kollie, "Correction of Tungsten-Rhenium Thermocouple Data," *HTGR Base-Technology Program Prog. Rep. Jan. 1, 1974–June 30, 1975*, ORNL-5108, pp. 428–35.

28. R. L. Shepard and T. G. Kollie, "Correction of Irradiation-Produced Drift in W-Re Fuel Centerline Thermocouples," pp. 237–68, vol. 1, in *International Colloquium on High-Temperature In-Pile Thermometry* (held at JRC, Petten, Netherlands, Dec. 12–13, 1974), EUR-5395 (1975).

29. E. J. Allen, *"CACA-2", Revised Version of CACA, A Heavy Isotope and Fission-Product Concentration Calculational Code for Experimental Irradiation Capsules*, ORNL/TM-5266 (February 1976).

30. W. D. Turner and J. S. Crowell, *Notes on HEATING — An IBM 360 Heat Conduction Program*, CTC-INF-980 (November 1969).

31. Private communications from K. R. Thoms to E. J. Allen, July 13, 1976.

32. F. J. Homan, "Thermal Analysis," *HTGR Base-Technology Program Prog. Rep. Jan. 1, 1974–June 30, 1975*, ORNL-5108, pp. 436–40.

33. M. J. Kania, *HTCAP, A FORTRAN IV Program for Calculating Coated Particle Operating Temperatures in HFIR Target Irradiation Experiments*, ORNL/TM-5332 (May 1976).

34. K. H. Valentine, *ENCTRK, A Computer Program to Model Heat Transfer Across Asymetric Gaps in Cylindrical Fuel Rods*, ONRL/TM report (in preparation).

35. W. D. Turner and M. Siman-Tov, *HEATING3: An IBM-360 Heat Conduction Program*, ORNL/TM-3208 (February 1971).

36. T. N. Tiegs and T. J. Henson, *Fission Product Behavior in Irradiated WAR Particles from HRB-9*, report in preparation.

37. F. J. Homan, T. B. Lindemer, E. L. Long, Jr., T. N. Tiegs, and R. L. Beatty, "Stoichiometric Effects on Performance of HTGR Fuels From the U-C-O System," accepted for publication in *Nuclear Technology*.

38. H. Kleykamp, *Microprobe Study of Fission Product Behavior in High-Burnup HTR Fuels*, KFK-2213 (September 1975).

39. K. H. Valentine and E. L. Long, Jr., "Fuel Particle Inspection with an Irradiated Microsphere Gamma Analyzer," *Trans. Am. Nucl. Soc.* 22: 213–14 (1975).

40. K. H. Valentine, "Statistical Basis for Failure Fraction Determinations," *HTGR Base-Technology Program Prog. Rep. Jan. 1, 1974–June 30, 1975*, ORNL-5108, pp. 450–56.

41. K. H. Valentine, "Irradiated Microsphere Gamma Analyzer System," *HTGR Base-Technology Program Prog. Rep. Jan. 1, 1974–June 30, 1975*, ORNL-5108, pp. 446–50.

42. K. H. Valentine and M. J. Kania, *Irradiated Microsphere Gamma Analyzer System Operating Manual*, report in preparation.

43. D. E. LaValle, D. A. Costanzo, W. J. Lackey, and A. J. Caputo, *The Determination of Defective Particle Fraction in HTGR Fuel*, ORNL/TM-5463 (November 1976).

44. D. M. Hewette II and W. R. Laing, "Detection of Defective SiC Layers in Coated Nuclear Fuel Particles," *Nucl. Technol.* 21: 149 (1974).

45. M. J. Kania, T. B. Lindemer, M. T. Morgan, and J. M. Robbins, *Irradiation Performance of HTGR Fertile Fuel in HFIR Target Capsules HT-12 Through HT-15: Part 1 — Experiment Description and Fission Product Behavior*, ORNL/TM-5305 (February 1977).

46. R. L. Walker, J. L. Botts, J. A. Carter, and D. A. Costanzo, "Mass Spectrometric Determination of Zirconium from a Resin Bead," accepted for publication in *Analytical Letters* 10(4): 251–62 (1977).

47. F. Hecht, "Chemical and Electrochemical Methods for the Disintegration of Graphitic Nuclear Fuel Elements," *Kerntechnik* 15: 554–61 Jahrgang (1973) Nr. 12.

7. CHARACTERIZATION AND STANDARDIZATION OF GRAPHITE

W. P. Eatherly and J. A. Conlin

7.1 INTRODUCTION

The various grades of graphite that are required in the cores of HTGRs and other reactor types must be characterized and standardized from both the safety and operational viewpoints. In particular, the fast-neutron radiation-induced creep must be investigated to provide a basis for the calculation of graphite stress loads caused by various thermal and fluence gradients throughout the core structure. As previously reported,[1] a series of irradiation tests was designed to obtain this information. The basic objective is to determine the primary and secondary coefficients for the neutron-induced creep at 600, 900, and 1250°C of various graphites of interest to HTGR designers for accumulated fluences of at least 8×10^{25} n/m^2 (>0.18 MeV), the full design fluence for the HTGR.

7.2 GRAPHITE CREEP EXPERIMENT OC-1 — R. L. Senn

Irradiation of capsule OC-1, the first of this series of 12 graphite creep irradiation experiments, has been completed. The capsule was operated at a nominal specimen temperature of 900°C in the Oak Ridge Research Reactor (ORR) E-5 core position for 1139 hr at 30 MW reactor power to a peak fluence of 1.3×10^{25} n/m^2 (equivalent fission fluence). A report covering capsule design, construction, and operation has been published.[2]

7.2.1 Experiment Design

Capsule OC-1 was designed to irradiate twenty-eight 15.24-mm-diam by 25-mm-long (0.6000 × 1.000-in.) compressively stressed graphite test specimens at 900°C to the first planned exposure level of 1×10^{25} n/m^2. A compressive stress of 13.8 MPa (2000 psi) was applied to 20 of the specimens in the test by precalibrated metal bellows expanded by gas pressure against the specimen columns. Eight of the specimens in the two columns had reduced diameters so as to increase the stress to 20.7 MPa (3000 psi). Each capsule also included 28 unstressed control specimens made of the same types of graphite.

A cross-sectional view showing the two stressed specimen columns in the in-core portion of the capsule is shown in Fig. 7.1. The specimens have shallow holes in each end to accommodate the graphite pins that pass through the spacers to serve as centering guides for the specimen column. The spacers center the column by means of longitudinal ridges protruding from their cylindrical surfaces. This centering is important to the proper loading and temperature control of the specimens. Typical specimens, spacers, and pins are shown in Figs. 7.2 and 7.3. The split graphite sleeve seen in Fig. 7.3 was used on the smaller diameter high-stressed specimens to provide the correct thermal resistance across the gas gap. A typical stressed specimen column is shown in Fig. 7.4.

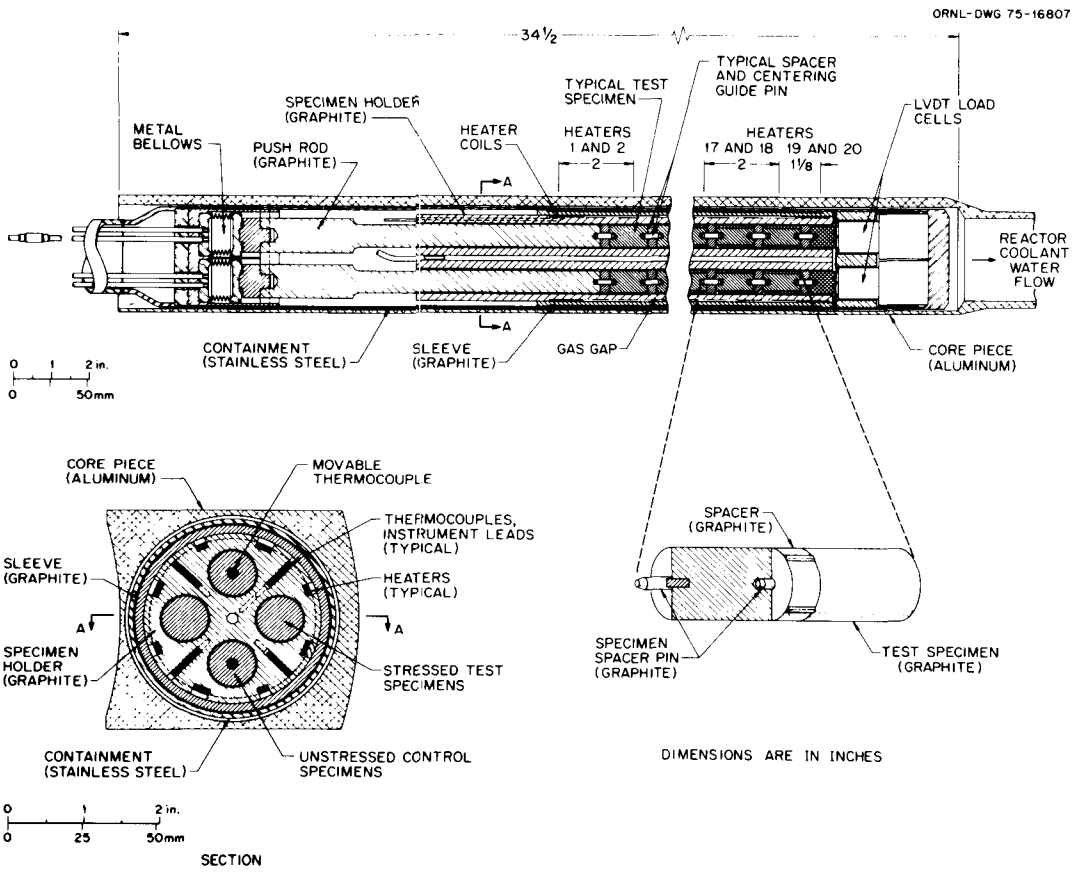

Fig. 7.1. Cross-Sectional View of the In-Core Portion of the ORR Capsule OC-1 Showing the Stressed Columns.

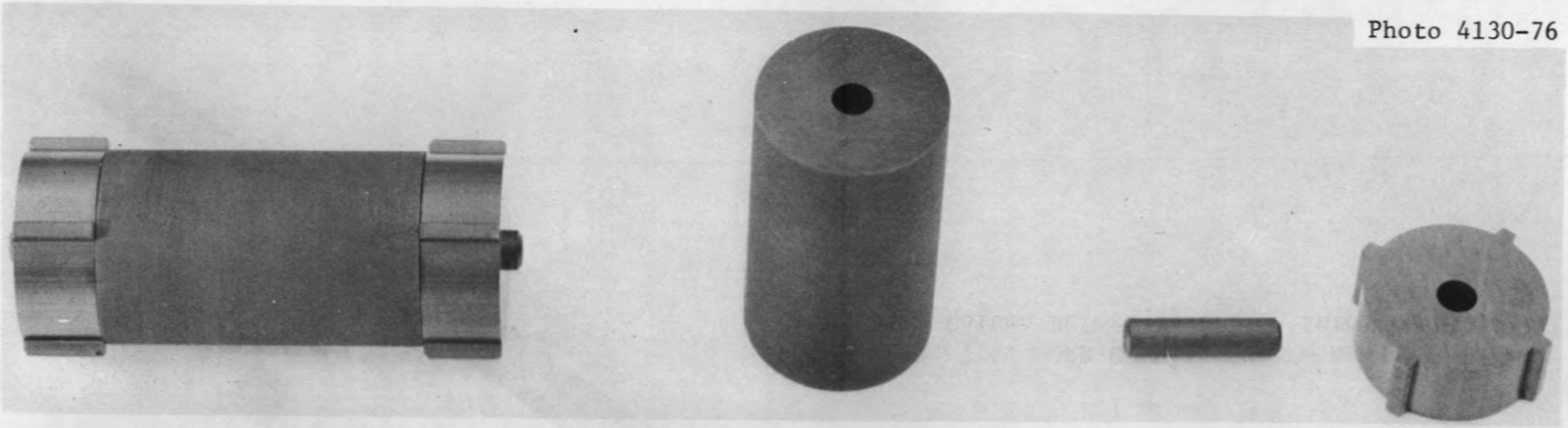

Fig. 7.2. ORR Capsule OC-1 — Typical Stressed Specimen with Spacers and Centering Pins. 1.9×.

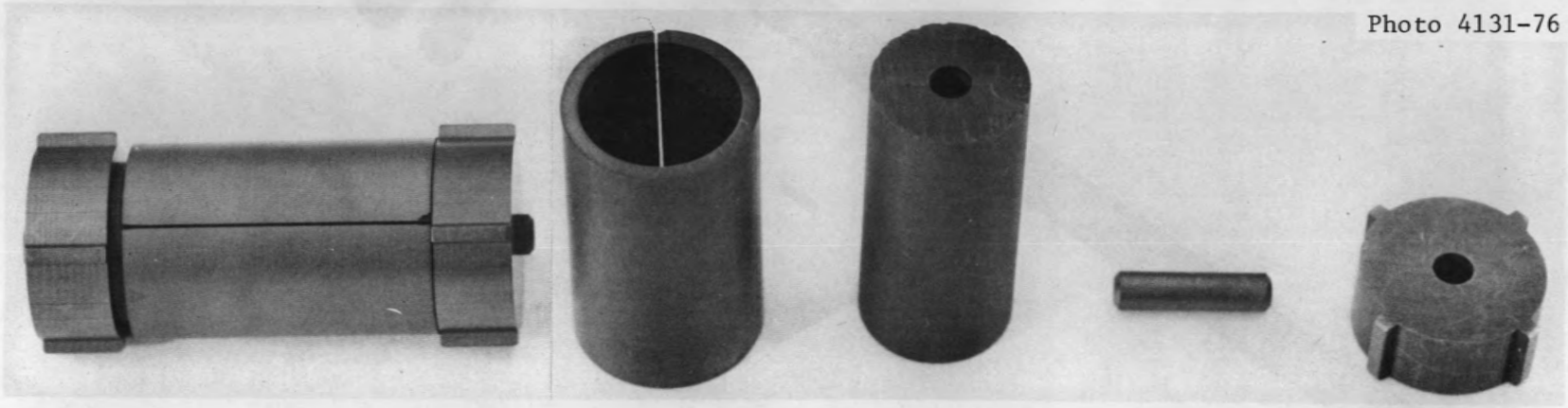

Fig. 7.3. ORR Capsule OC-1 — Typical High-Stressed Specimen with Spacers, Centering Pins, and Split Sleeve. 1.9×.

Photo 4129-76

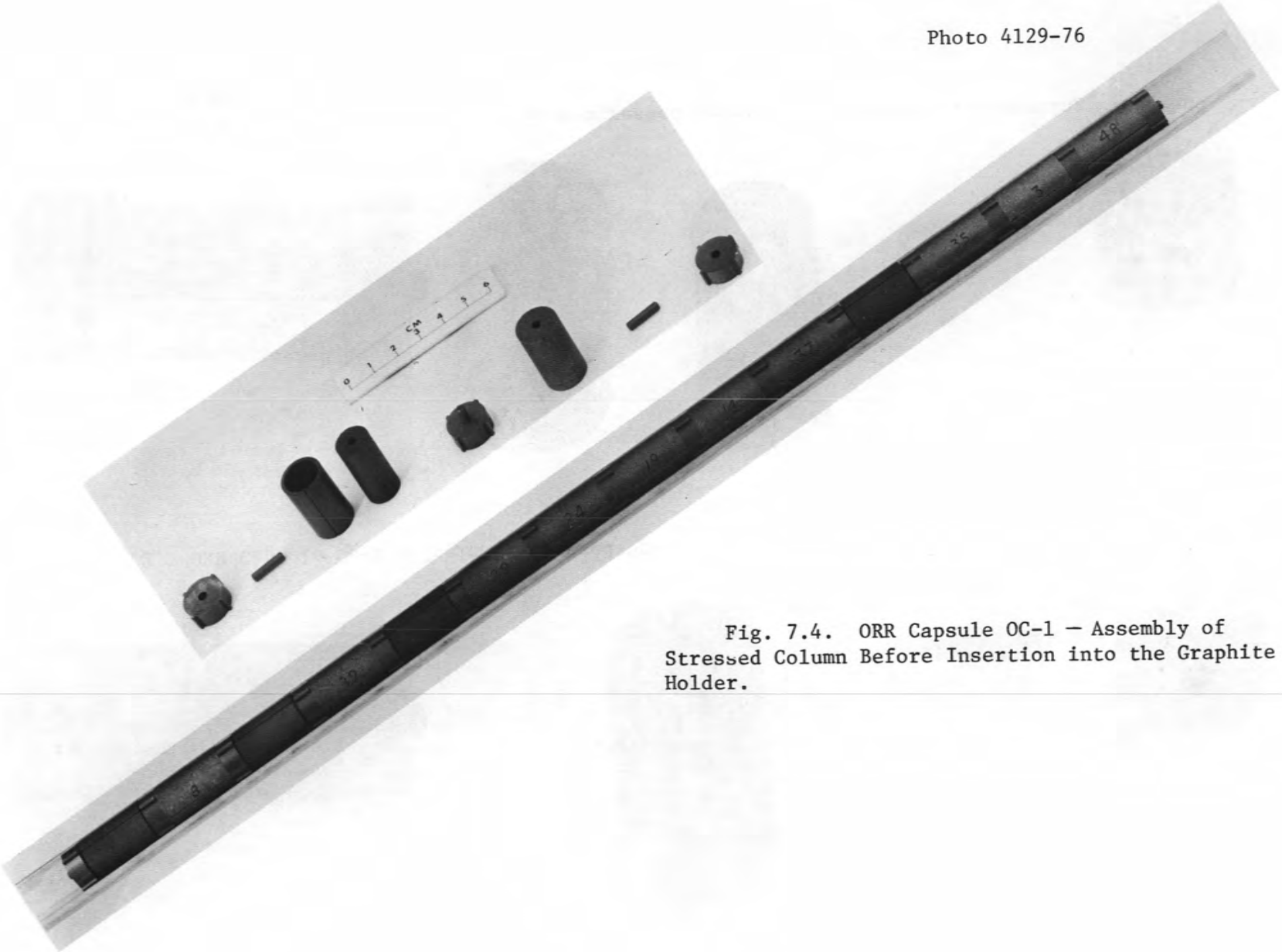

Fig. 7.4. ORR Capsule OC-1 — Assembly of Stressed Column Before Insertion into the Graphite Holder.

7.2.2 Capsule Operation and Initial Results

The irradiation of the OC-1 experiment was started on April 1, 1976. We had difficulty in maintaining the 900 ± 10°C uniform temperature along the specimen columns. There were two major reasons for this. The ORR core loading included some partially spent fuel elements, which skewed the flux patterns for the gamma and fast neutron radiations. The gamma heating rate failed to bring the specimen temperatures to within the 100°C of the desired operating temperature of 900°C. Consequently, we had to use helium-argon/neon sweep gas instead of just helium in the capsule and use more heater power than we had originally anticipated to bring the specimens to the design temperature.

The instrumentation of the capsule was generally a satisfying part of the experiment for the operational information that it supplied. For example, the two thermocouples that moved up or down through the central axes of the unstressed control specimens proved an invaluable aid in guiding our operation of the controls toward achieving the desired conditions. Overall, the ORR Data Acquisition and Control System (ORRDACS) with the computer as its principal component operated most successfully with data logging, data processing, and control and alarm functions.

Irradiation of capsule OC-1 was completed on May 22, 1976. In the following, the general operation of the experiment and some of its principal components are first summarized and then described in some detail.

7.2.3 Summary

Capsule OC-1 was successfully irradiated in the ORR E-5 core position for one ORR cycle with the following results:

1. The graphite specimens were irradiated for about 1139 hr at 30 MW reactor power at a nominal specimen temperature of 900°C to a peak fluence of 1.3×10^{25} n/m^2.

2. Temperatures of the specimens were high and off-design in the upper 16% of the specimen column. To maintain the lower part of the specimen column at or near the design temperature, the specimens in

the upper 0.1 m (4 in.) zones 1 and 2,* were permitted to operate at temperatures to 930°C. Also, the temperature profile along the specimen columns had a small dip approximately one-third of the way down from the top throughout the irradiation period. The dip could not be entirely eliminated by sweep-gas mixtures and/or heater power adjustments. Time-integrated temperatures for all specimens will be determined from the data to develop meaningful results.

3. The two movable thermocouple assemblies survived more than 61 and 65 cycles [two 381 mm (15 in.) traverses] before failing. The failures were apparently mechanical. The traverses cited were entered in the logbook during the experiment. Additional unrecorded traverses were known to have been made, both in pretest operation and during testing for temporary measurements.

4. Twenty-seven of twenty-eight 1.6-mm-diam fixed thermocouples survived the test period. The 24 thermocouples mounted in the graphite specimen holder operated at about 800°C during irradiation.

5. Seventeen of twenty heaters survived the test period, with some having operated to 1.26 kW/m (32 W/linear inch) of heater.

6. Both the 0.41 MPa gage (60 psig) gas mixture system used to sweep the capsule and to aid in the specimen temperature control and the gas system used to pressurize the bellows to apply the required loads to the specimens operated satisfactorily.

7. Operation of the LVDT load cell transducers was disappointing. The transducers did provide some evidence that the west bellows was probably binding and causing a ratchetting effect as the experiment was heated and cooled during reactor start-ups and shutdowns. Subsequent thermal expansion of the specimens and spacers at operating temperature in the west column caused a higher than anticipated stress to be applied to these specimens.

8. The computer control and data acquisition system (ORRDACS) for the capsule functioned well. The computer was capable of controlling experiment temperatures to within ±1°C of the set points. The automatic, periodic listing of all experiment parameters being monitored plus the

---

*Zones are longitudinal capsule sections, nominally 51 mm (2 in.) long except for zone 10 which is 28.6 mm (1 1/8 in.) long. These zones contain the heater pairs and are numbered 1 through 10 from the top toward the bottom of the capsule.

demand logs of any of the experiment parameters as required by the experiment operators provided valuable and essential data bases for the operation and monitoring records of the experiment.

7.2.4 Specimen Temperature Control

As is usually the case with the first experiment of a new series, some difficulties were experienced in attempting to bring the capsule to design conditions. It was necessary to add about 12 vol % Ar to the helium sweep gas to bring the specimen temperatures into a range where the heaters had the capacity to raise the specimens to design conditions. An unanticipated peak temperature along the capsule developed in zones 1 and 2, near the top 0.1 m (4 in.) of the specimen column. This peak temperature, which worsened as the reactor fuel was burned up and control rods were withdrawn, limited the temperatures that we could achieve in the rest of the specimen columns. These effects were attributed to the gamma heating profile being shifted by use of partially spent reactor fuel elements; therefore, the flux profile was different from that used for the thermal design of the experiment. This was corrected to some degree in the subsequent fuel loadings by loading the core with fresh fuel around the experiment. However, after approximately one week of irradiation, the peak near the top of the specimens again became the controlling factor in maintaining the capsule temperatures. By careful analysis of the data accumulated during the OC-1 irradiation, these temperature profile anomalies will be corrected for future experiments in this series by changing the gas gaps and other parameters that affect the specimen temperatures.

There was also a dip in the temperature profile along the capsule approximately in the middle of zone 4, about one-third down from the top of the four specimen columns.* The temperature peaking in zones 1 and 2 (see below) precluded the use of temperature trimming heaters there and inhibited the use of full operating power of the lower heaters in this vicinity in such a manner that the dip in the temperature profile could not be entirely eliminated during the test period.

---

*A specimen column is defined here as consisting of the 14 specimens plus the 15 spacers.

As discussed above, there was an unanticipated peak temperature in the top 16% of the specimen columns.* This effect worsened because of the reactor flux peak shifting toward the top of the experiment as the reactor fuel was burned up and the control rods were withdrawn. To keep the upper temperatures within a maximum limit set at 930°C and to maintain control of the temperatures in the lower portions of the capsule, five ORR refueling shutdowns were required during the irradiation.

Further analysis of the temperature increases resulting from the addition of mixed helium-argon versus pure helium sweep gas showed that the effects were as if an approximately 30 mol % Ar gas concentration were added to the experiment rather than the approximately 12 mol % mixture that was added according to the instrumentation. Analysis of gas samples taken from the exit sweep-gas line verified that we did, indeed, introduce an approximate 12 mol % Ar gas concentration to the experiment. These results tend to support a theory that some gas separation effect was occurring in the temperature control gas gaps such that there may have been zones of higher argon concentration in the capsule (especially the upper end), which were contributing to the higher than anticipated temperatures in the upper regions of the capsule.

A further test was conducted before a scheduled refueling shutdown on May 4, 1976. The sweep (control) gas, a He-Ar (88–12 mol %) mixture flowing at approximately 50 cm^3/min, was isolated within the capsule, and the capsule was operated for a few hours as a static system. The results showed an immediate rise in temperatures of the upper zones and slowly increasing temperatures in the lower zones. The test was terminated because the specimen temperatures in zone 2 were exceeding their limits. This test provided further evidence in support of the theory of gas separation occurring in the capsule gas gaps.

After the ORR refueling shutdown of May 4, the capsule was operated with a helium-neon sweep-gas mixture. Data were obtained with 100% Ne sweep gas and no heater power at 30-MW reactor power. Although there was still a temperature peak in the upper region of the capsule, the

---

*That portion of the specimens and their spacers within zones 1 and 2.

temperatures along the remainder of the capsule were much closer to the desired constant temperature profile predicted by earlier computations. We were unable to maintain the 100% Ne sweep gas except during initial reactor full-power operation before the gamma heat attained its full equilibrium value. The experiment was then operated with sweep gas mixtures ranging from 35—65 mol % (He-Ne) to 54—46 mol %. The neon concentration was slowly decreased as the flux profile changed during reactor fuel burnup. Zone 2 specimen temperatures were maintained at about 930°C with the above gas mixtures and no heater power. All zones below zone 2 were maintained at about 900°C specimen temperature by adding electric heat as required.

Specimen temperatures were maintained by requesting the appropriate graphite temperature set points via the computer control program. These set points were determined by comparing data taken while the movable thermocouples (Sect. 7.2.5) were operative with the corresponding graphite specimen holder temperatures. The computer-calculated specimen temperatures compared very well with the measured central specimen temperatures except for the anomalous regions in zones 1 and 2.

7.2.5 Movable Thermocouples Operation and Use

Two movable thermocouples, designated as TOON and TOOS, were used to determine the specimen temperatures, with each thermocouple traversing 0.38 m (15 in.) along holes drilled along the central axes of the control (unstressed) specimen columns. These temperature data were primarily sought for (1) direct monitoring of the temperatures along the specimen columns and (2) determining the specimen temperatures for comparison with the calculated specimen temperatures based on the graphite specimen holder temperatures. The latter temperatures were measured with fixed thermocouples mounted in the holder.

The movable thermocouples were used frequently to acquire such data. Normally, both movable thermocouples were simultaneously used whenever a temperature traverse was made. Results from a typical traverse are shown in Fig. 7.5.

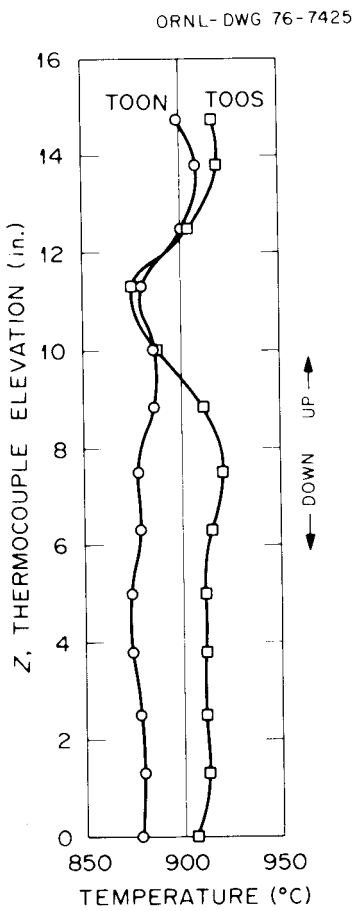

Fig. 7.5. Results from Typical Movable Thermocouple Traverse in ORR Capsule OC-1. Each point is the average of the down and up traverses. To convert elevation to meters, multiply by 0.0254.

After more than 33 cycles of TOON (April 19, 1976) (a cycle is a full 0.38-m traverse in both directions), the thermocouple circuit began to read open from the 208-mm to the 132-mm (8.2- to the 5.2-in.) levels above its lowest travel limit. Nevertheless, we continued to obtain useful data both above and below these points until the thermocouple had cycled more than 61 times. Finally, the TOON drive failed (April 26, 1976) with the thermocouple in the full down position, 0 mm, where it continued to respond, indicating the temperature in that region.

The south thermocouple, TOOS, operated satisfactorily through more than 53 cycles. At this time (April 19), it began to behave as an open thermocouple below the 127-mm (5-in.) level. This worsened after a total accumulation of about 57 cycles to show an open circuit below the 158-mm (6.2-in.) level. Finally, after more than 65 cycles (May 5), the TOOS circuit opened completely and no further temperature measurements

could be made. The evidence suggested that the spring-clip sliding contacts on a gold-plated contact strip that carried the signal from the thermocouple relaxed so as to cause the open thermocouple circuit.

By the time both the movable thermocouples failed, we had acquired sufficient data to make good correlations between specimen temperatures determined by the movable thermocouples and the calculated specimen temperatures based on the temperatures measured in the graphite specimen holder with the fixed thermocouples. Therefore, we continued the experiment confident that the desired specimen temperatures were being properly maintained.

7.2.6 Fixed Thermocouples

All the 28 fixed (permanently mounted) thermocouples operated satisfactorily throughout the test except one. A thermocouple (TE-T10A) positioned in the graphite specimen holder in zone 10 failed open (May 14). The probable mode of failure was a separation of the thermocouple wires at the hot junction.

The failed thermocouple (TE-T10A) was replaced by its companion thermocouple (TE-T10B) as the temperature sensor to its backup controller and the computer was instructed to ignore T10A in its control calculations.

7.2.7 Heaters

This experiment incorporated 20 sheathed heaters to augment the gamma heating of the capsule and its components so that the specimen temperatures could be trimmed to the desired operating temperature. Two heaters were mounted and wired in parallel in each of ten heated zones. For example, zone 1 contained heaters 1A and 1B.

We had to operate the heaters at higher power [up to 1.26 kW/linear meter (32 W/linear inch) of heater] than originally planned [0.79 kW/linear meter (<20 W/linear inch)] because the experiment generally operated at a lower temperature from gamma heating alone than anticipated.

During the experiment three heaters failed: 3B (April 7), 4B (April 12), and 7B (April 14). Since no two of the failures occurred in the same zone, we continued to have adequate power in all zones and were able to maintain the experiment temperatures.

The failure in heater 3B appeared to be located at its junction end where the heater wire is welded to the heater sheath because the circuit tended to close during a shutdown period while the experiment was cool and open again as the experiment heated up.

Near the end of the experiment, we carefully explored the performance of the heaters at higher power ranges. The neon concentration in the sweep gas was deliberately lowered to require more heater power to maintain the set-point temperatures. The heaters in zones 4, 7, and 10 were, respectively, operated at 0.79, 1.10, and 1.26 kW/linear meter (20, 28, and 32 W/linear inch) of heater for approximately 48 hr without indication of any incipient problems.

7.2.8 Pressure Systems

The bellows pressure systems used to load the test specimen columns were operated at their design point with less than 1% deviation throughout the test period.

The sweep-gas pressure system operating at 0.41 MPa (60 psig) was maintained by balancing the inlet and outlet flows of the sweep gas or gases. Manipulation of the various gas mixture concentrations caused minor variations in these pressures, and minor variations of ±14 kPa (±2 psig) were noted on heating or cooling the experiment.

7.2.9 Linear Variable Differential Transformer Load Cell Transducers

Operation of the two LVDT load cell transducers was less than satisfactory. The instrument zero point apparently shifted during transportation of the capsule to the reactor site. Attempts to calibrate the devices *in situ* before irradiation were largely unsatisfactory. The devices did respond to specimen loading bellows pressure changes, but large hysteresis effects in the load cell transducer responses were noted as the bellows pressures were changed. There was evidence, however, that the west bellows was binding and not contracting to relieve thermal expansion of the specimens and spacers in the column, as would be expected by the design. This ratchetting effect was indicated by an increasing reading on the west column (as compared with the east column) upon raising the experiment to operating temperature. This reading decayed somewhat

over the next few days of operation. Except for these rather gross indications, both LVDTs were erratic and quite temperature sensitive. A different type of load cell will be designed for future experiments in this series.

7.2.10 Computer Operation

The control and data acquisition by the computer worked very well during the entire experiment. The average temperature measured by two fixed thermocouples mounted in the graphite specimen holder in each zone was controlled by the computer to ±1°C from the requested set point as long as adequate heater power was available to the corresponding zones to permit the computer to maintain the requested temperature. As discussed above, these temperatures were also used to calculate the true specimen temperatures. The results agreed well with those directly measured by the movable thermocouples.

Periodic point logs (PPLs) were automatically taken every hour by the computer during the irradiation period. The PPLs were lists of the current values of all experimental parameters being monitored by the computer. These formed the data base for the experiment. In addition, demand logs were available to the experiment operator for examination of any of the experiment parameters as required. Both the PPLs and the demand logs provided the data bases essential for the operation and monitoring records for the experiment.

7.2.11 Postirradiation Examination

The first stage of the postirradiation examination of the graphite creep capsule OC-1 was completed with the retrieval of the test specimens, 28 from the unstressed columns and 28 from the stressed columns. The specimens were intact and have been identified and stored in sample bottles, ready for further examination. The flux monitors were retrieved, identified, and stored for analysis. The lower portion of the two movable thermocouples, the lower portion of the three pairs of heaters where failure occurred, and a pair of thermocouples located in the graphite holder were also saved.

Neutron radiographs of the capsule were taken at 0 and 90° at two elevations, thus providing complete coverage of the capsule. The radiographs were closely examined before the capsule was cut open to determine if any changes might have occurred during irradiation as compared with radiographs taken before irradiation. No obvious defects were noted. A space was seen between specimens in one of the unloaded columns as if the uppermost specimens in the column had moved up approximately 13 mm during retraction of one of the movable thermocouples. This should have no significant effect on the test results. We also noted that the bellows were extended from their original position (as expected). However, one was extended slightly farther than the other, indicating that the stack heights of the two stressed columns had changed differently, or that one of the bellows was wedged such that it could not return to its free state.

After the experiment lead tube was cut off just above the capsule proper in the ORR hot cell, the capsule was removed to a clean hot cell to prevent undue contamination of the specimens. The first cut was made approximately 25 mm below a weld just below the bellows region. This exposed the bottom side of the bellows. The interior of the region was bright and clean. We carefully pushed on each bellows and found them to be free to move within the copper chill block surrounding them. The bellows were removed from the assembly and examined. They were clean and without visible defects. We examined the interior of the holes in the copper block that served as guides for the bellows. Burnish marks were visible where the bottom plate on the bellows assembly moved against the wall of the closely fitted copper block, but there were no obvious indentations or scores to indicate that the bellows was askew and bound within the copper. Photographs were taken at each stage of this examination and throughout the disassembly of the capsule.

The lower portions of the two movable thermocouples were removed without difficulty and stored for further examination.

A second cut was made through the capsule just below the bottom end of the graphite specimen holder. This exposed the bottom end of the specimen columns and the top of the region holding the load cells. The stainless steel outer can was removed, exposing the graphite sleeve

surrounding the heaters and the graphite specimen holder. The sleeve was carefully examined and photographed in an effort to determine if there had been any cracking or discontinuity that might explain the anomalous temperature behavior. No defects were seen, and the sleeve appeared much the same as it did at installation.

The alumina insulators were removed from the bottom of the unstressed columns, and these columns of specimens were pushed out of the graphite sleeve into a "V" tray, examined, and stored in bottles labeled with the appropriate column identification and numbered 1 through 14 from the top to the bottom. Both unstressed columns were earily pushed out of the holder by pushing with a 13-mm-diam rod from the top.

Attempts to remove the stressed specimens similarly were unsuccessful. They were more tightly bound in the column, probably because of expansion of the graphite spacers between specimens. During irradiation, the spacers were under stress such that the lugs on the spacers would creep out against the inside of the hole in the graphite sleeve. There was a 25-μm (1-mil) diametral clearance between the spacer lugs and the inside of the holes originally. The specimens were ultimately removed by tapping against the push-rod, which was bearing against the uppermost spacer, with a 0.5-kg (1-lb) hammer, using approximately 0.15-m (6-in.) stroke. This permitted a 3 to 6 mm movement of the column of samples with each hammer stroke. Subsequent close examination of the spacers in these columns and the inside of the holes in the graphite sleeve revealed a burnishing effect on the outside of the spacer lugs and similar burnishing of the inside of the hole in the graphite where the spacers were forced along the hole as they were removed. There was no chipping and breaking of the lugs, and no obvious detents along the inside surface of the holes, which would have indicated a more severe interlocking of the spacers within the hole that might have interfered with the application of the loading stress from the bellows. We were unable to measure the force required to remove the specimens in the hot cell, but according to the evidence available so far, the spacers within the holes may have interfered somewhat with the loading applied to the specimen by the bellows assembly.

As described above, the stressed specimens were moved out of the graphite holder into a "V" tray, examined, and stored in bottles with appropriate column identification and numbered 1 through 14 from the top to the bottom. All specimens appeared to be intact and clean.

After successfully removing the specimens from the graphite holder subassembly, we removed the graphite sleeve surrounding the heaters. This piece was very close fitting during assembly and had to be forced in place. After irradiation it could not be slipped off the heaters and was removed by cracking with a screwdriver blade and hammer. The heaters were found to be in about the same condition as when installed. Heater pairs 3A and B, 4A and B, 7A and B were removed and saved for later inspection. Each of these pairs includes a heater that failed during testing. The thermocouples were removed from their grooves in the graphite holder. The thermocouples also had the same clean appearance as when installed. Thermocouples 10A and B were saved for future examination as discussed below.

Finally, the flux monitors were removed from their positions inside the thermocouple grooves, identified, and loaded into sample bottles. Induced radiation from the flux monitors ranged from 3.5 R at 51 mm (2 in.) [300 mR at 0.3 m (1 ft)] for those near the top of the capsule to a maximum of 10 R at 51 m (2 in.) [1 R at 0.3 m (1 ft)] for those near the midplane. The monitors are made of an approximately 25-mm-long segment of 1.6-mm-diam stainless steel tubing, each containing various monitor wires.

The induced activity of the test specimens ranged from 50 mR to 80 mR at 51 mm (2 in.) through the sample bottles. These samples were moved to the Metals and Ceramics Division laboratory for detailed dimensional analysis to determine their creep characteristics.

As discussed above, the lower ends of the two movable thermocouples, one pair of graphite thermocouples (TE-10A and -10B), and three pairs of heaters (3A and B, 4A and B, and 7A and B) were saved for further examination. Both movable thermocouples, one of the graphite thermocouples, and one of each pair of heaters failed during experiment operation. Continuity tests were made to determine which of the pairs were failed and to locate the discontinuity, if possible.

The test showed that the south movable thermocouple (TOOS) was open, probably at the junction. The measurements showed 6 MΩ resistance across the leads and 3.3 MΩ from each wire to the sheath. The north thermocouple (TOON) was intact, measuring 1.5 Ω resistance across the leads and 3.4 MΩ from each wire to sheath. All thermocouples in the experiment were built with ungrounded junctions, such that the wire-to-wire measurement should show a low resistance and the wire-to-sheath measurement should show a high resistance. These tests confirmed our previous indications that the north thermocouple failed because of a malfunction of the spring clip-slide wire assembly at the upper end of the thermocouple and that the south thermocouple failed at the welded junction on the sensing end of the thermocouple.

As expected, one of the graphite thermocouples from the TE-10 pair (TE-10A) was failed, probably at the welded junction. Measurements showed 1.6 MΩ resistance across the leads and 1.6 MΩ from each wire to sheath.

The three failed heaters were identified with the following measurements: heater 3B measured 33.6 Ω resistance wire to sheath; 4B measured 6.5 MΩ; and 7B measured 1.3 MΩ. These measurements corroborated our experience during experiment operation in that heater 3B tended to "close" during a shutdown period while the experiment was cool, and "open" again on return to power. This suggests that the weld of the heater wire to the sheath at the end of the heater was cracked such that thermal expansion of the materials would cause electrical discontinuity. This is consistent with the relatively high resistance of 33.6 Ω, compared with 6.94 Ω measured on heater 3A. On the other hand, heaters 4B and 7B failed completely and did not "remake" during operation. As one would expect, a completely open circuit as shown by very high resistance was measured on these two heaters. Because of the nature of the failures in 4B and 7B, we suspect that the faults could have been at either the junction of the copper lead wire to the heater lead wire just at the beginning of the heated section or at the weld of the heater wire to the sheath closure.

7.3 RESULTS FROM CAPSULE OC-1 — GRAPHITE SPECIMEN EVALUATION — C. R. Kennedy

7.3.1 Specimen Material Evaluation

Because of the variability in graphite, particularly in larger sizes, it is very important to clearly describe the sample material used in subsequent evaluations. Therefore, the graphite blocks for the OC-1 creep experiment were examined in detail to fully describe the material used to make the specimens. This study is limited, however, by the samples available from the parent logs of H-451 and H-327 graphites. Rather than receiving full sections of candidate materials, core drillings 15 mm (0.6 in.) in diameter from representative blocks in selected areas were received from General Atomic Company. The core drillings were furnished with the cutting plans giving the location of each piece in the parent block. The quantities and orientations of the sample materials are given in Table 7.1.

Each core drilling had the ends squared, was measured, and was weighed to determine the bulk density, and the electrical resistivity was measured by both a potentiometric and eddy-current methods. The

Table 7.1. HTGR Graphites Used in OC-1

Grade	Block	Number of Bars	Length (mm)	Length (in.)	Orientation	Remarks
H-451	6484-40-5B	50	150	6	Axial	Indicated to have uniform intermediate Young's modulus
H-451	6484-40-5B	28	71	2.8	Radial	
H-451	6484-41-5B	16	150	6	Axial	Eight of the bars were taken from the outer perimeter for high Young's modulus material and eight were taken from the center for low Young's modulus material
H-327	4974-3-2	24	38	1.5	Axial	All were from the outer perimeter
H-327	4794-3-2	8	130	5	Radial	Bars were taken from the outside in

actual specimens made from the bars were further tested by measuring the sonic velocities (both longitudinal and shear) and the 800°C coefficient of thermal expansion (CTE) as well as bulk density and conductivity. These measurements were adequate to yield a fair representation of the properties of each of the sample blocks and, in the case of block 6484-40-5B, an idea of the variation in properties across the block.

Virtually all physical properties have a first-order relationship with bulk density; therefore, it is very important to realize this variation within the block. A bulk density contour map, Fig. 7.6 shows density variations from 1.70 to 1.74 g/cm^3 across the section represented by the core drillings. Actually, the density is fairly uniform on one side of the block but appears to increase rapidly toward the side retained by GA. This side-to-side density variation is unexpected in that large extruded blocks generally have a high-density outer surface and a low-density core close to the block axis. This is indicated in Table 7.2, which compares the core drillings taken from the outer surface with those from the center.

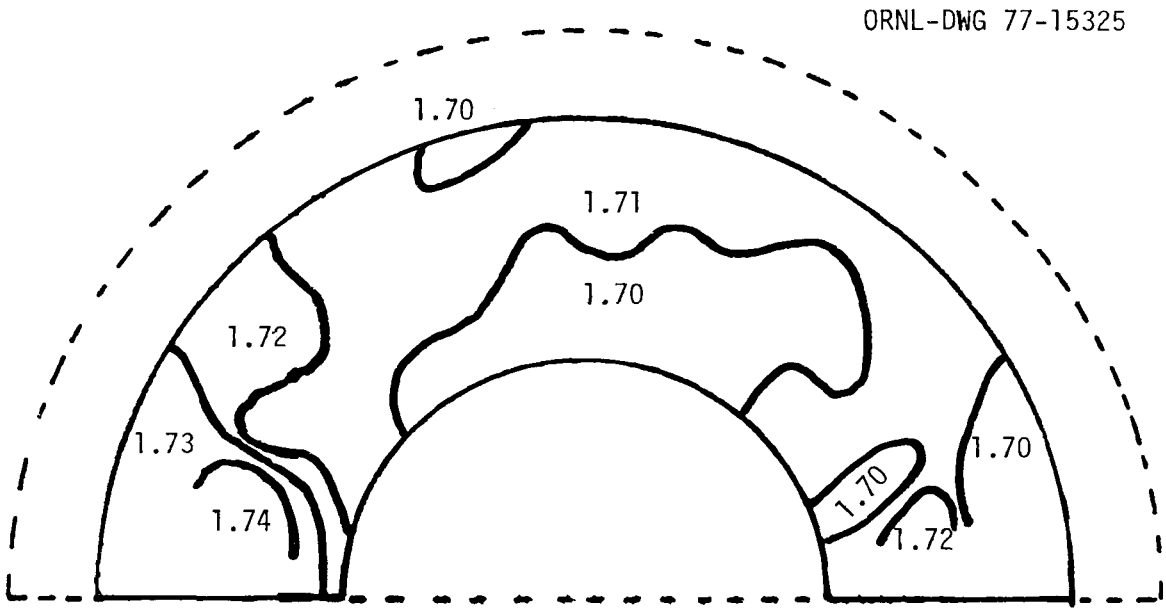

Fig. 7.6. Density (g/cm^3) Contour Map of Block 6484-40, Grade H-451. (Region within solid lines only material available.)

Table 7.2. Properties of Block 6484-41-5B

Axial Bars	Average Bulk Density (g/cm^3)	Average Modulus, GPa (10^6 psi)		Resistivity, μΩ-m	
		Young's	Shear	Axial[a]	In Plane[b]
25 mm (1 in.) from the outside surface	1.73	9.2 (1.30)	3.8 (0.55)	6.59	7.09
Within 50 mm (2 in.) of the block axis	1.71	8.7 (1.23)	3.6 (0.52)	6.92	7.34

[a]Measured by potential drop.

[b]Measured by eddy current.

The electrical resistivity of the bars in block 6484-40-5B was also measured. The results of eddy-current testing also yield a contour map, shown in Fig. 7.7, similar to the density map. In fact, the high density and low resistivity regions compare very well. The sonic velocities were also measured, but only on the machined specimens for the experiment. The results of this testing are given in Fig. 7.8 for both the longitudinal and shear velocities as given by the times to travel through the 25-mm-long (1-in.) sample. Again, these distributions demonstrated similar contours to the density map.

While the properties of the blocks appear to be consistent with one another and show gradual changes from one side to another, statistical studies of the graphite samples do indicate reasonable regions of like materials. Virtually all of 6484-40-5B is similar except those regions of density greater than 1.71 g/cm^3. The average properties of the uniform region are given in Table 7.3. The properties can be compared with those of 6484-41-5B in Table 7.2 and the properties are very similar to the inside samples. The major difference between the -40 and -41 blocks is that the electrical conductivity is somewhat better in the -41 block and the distribution of high-density material is different.

The third block of material was from a block of grade H-327 graphite. This material is highly aniostropic compared with grade H-451. Samples were removed from the block from only two directions, axial and radial.

ORNL-DWG 77-15326

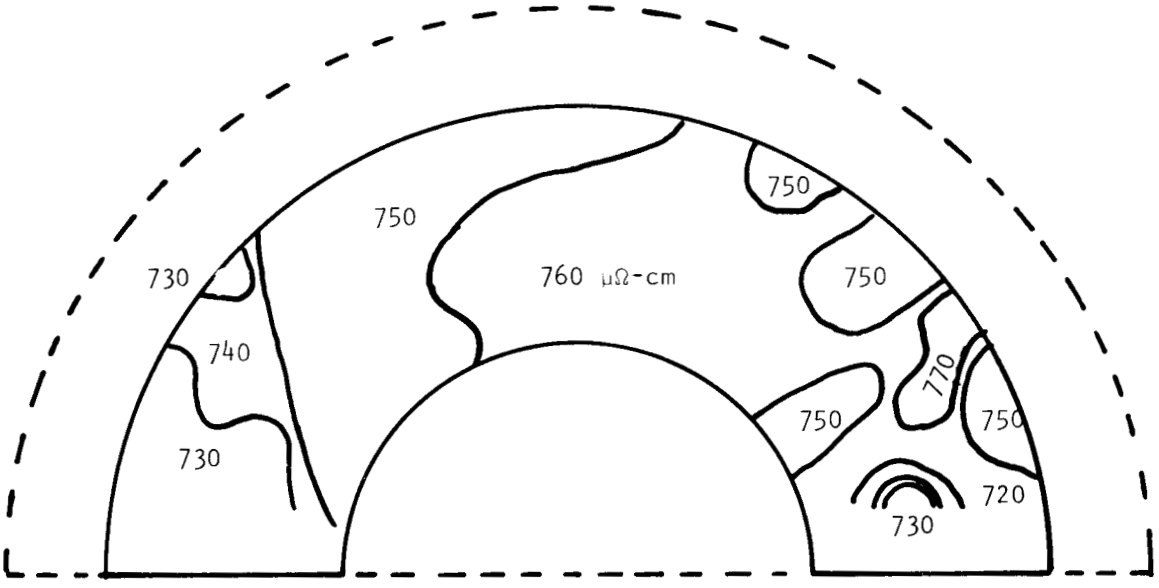

Fig. 7.7. Contour Map of In-Plane Resistivity Measured by Eddy Currents. Grade H-451, Block 6484-40.

ORNL-DWG 77-15327

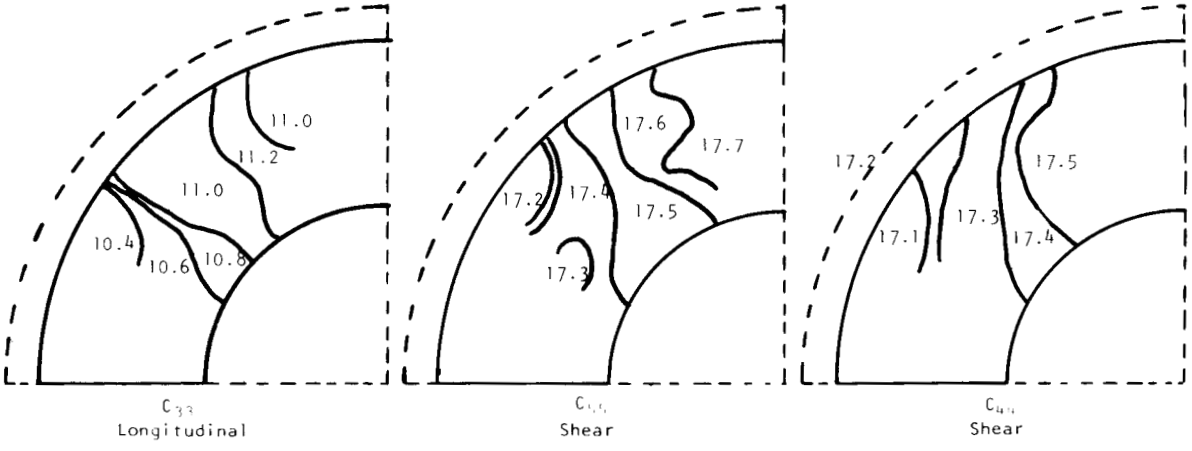

Fig. 7.8. Contour Maps of the Time (μs) to Travel 25 mm (1 in.) of Graphite with Sound. Grade H-451, Block 6484-40.

Table 7.3. Average Properties of Block 6484-40-5B

Density, g/cm^3		1.71
Electrical Resistivity, μΩ-m		
Potentiometric:	Axial	7.21
	Radial	8.33
Eddy Current:	Axial	7.24
	Radial	8.25
Elastic Properties (obtained from sonic velocities)		
Young's Modulus, GPa (psi)		
Axial $1/S_{33}$		8.6 (1.24×10^6)
Radial $1/S_{11}$		7.6 (1.10×10^6)
Shear Modulus, GPa, (psi)		
C_{44}		3.6 (0.52×10^6)
C_{66}		3.3 (0.48×10^6)
Poisson's Ratio		
$-S_{12}/S_{11}$		0.142
$-S_{13}/S_{11}$		0.124
$-S_{13}/S_{33}$		0.140
800°C CTE		
Axial		3.93×10^{-6}
Radial		4.56×10^{-6}

It is very clear from the data, however, that rotational symmetry does not exist and the block has a strong rod texture, with the circumferential direction containing more layer planes than the radial direction. The analysis of the data requires approximations, particularly since no circumferential samples are available. The problems of density variation, however, are very small in these blocks, although the average density is larger than generally observed for H-327 graphite. The average properties of the block are given in Table 7.4 and 7.5.

The physical property measurements made on the three blocks lead to several general conclusions:

1. Both graphites, H-327 and H-451, have very good conductivity compared with other grades of graphite.

Table 7.4. Physical Properties of Grade H-327 (Block 4974-3-2)

Density, g/cm^3	1.77
Elastic Properties (Obtained Sonically)	
Young's Modulus, GPa (psi)	
Axial $1/S_{33}$	11.4 (1.66 × 10^6)
Circumferential $1/S_{22}$	unknown
Radial $1/S_{11}$	5.8 (0.84 × 10^6)
Shear Modulus, GPa (psi)	
C_{44}	4.3 (0.63 × 10^6)
C_{55}	3.8 (0.55 × 10^6)
C_{66}	2.8 (0.40 × 10^6)
Poisson's Ratio (Assuming Rotational Symmetry $C_{44} = C_{55}$, $S_{11} = S_{22}$)	
$-S_{12}/S_{11}$	0.082
$-S_{13}/S_{11}$	0.009
$-S_{13}/S_{33}$	0.018
800°C CTE	
Axial	1.72 × 10^{-6}
Radial	3.32 × 10^{-6}
Circumferential	unknown

Table 7.5. Electrical Resistivity of Grade H-327 (Block 4974-3-2)

Measurement Method	Distance from Center		Electrical Resistivity, Ω-m		
	(m)	(in.)	Axial	Radial	Circumferential
Potentiometric	0.18	7		8.27	
	0.23	9	3.74		≈7.6
Eddy Current	0.18	7	3.81	8.45	7.70
	0.23	9	3.71	9.00	7.10

2. Both blocks of Grade H-451 have significant variations in density with the associated physical property variations. These variations are unpredictable.

3. The grade H-327 block had a higher-than-expected density with a low gradient over 0.13 m (5 in.) from the outside radius.

4. Grade H-451 was fairly isotropic and had a very slight loss in rotational symmetry (low enough to be ignored).

5. Grade H-327 was highly anisotropic and did not exhibit rotational symmetry. This type of preferred orientation would be expected to demonstrate a significant "size effect" in comparing dimensional stability of full blocks with radial samples. The full blocks may shrink 1% more than indicated by the radial sample measurements.

7.3.2 Examination of Creep Specimens

Measurement of the specimens creep tested in the OC-1 irradiation experiment has been completed. Dimensional changes, electrical resistivities, sonic velocities, and the CTE on each specimens have been measured. The results show significant effects of the creep deformation upon the physical properties of importance to the structural behavior of moderator columns. These properties will be discussed individually and then summarized in a final section.

7.3.3 Dimensional Changes

The dimensional measurements of the specimens clearly indicated ratchetting by the load cell readout during the experiment. It appears that each time the reactor shut down, the specimen column shrank, the loading system followed the shrinkage and jammed solid. Upon startup, the column expanded against the jammed load system to fairly high stresses, which then relaxed the irradiation creep. Thus, we have three sets of specimens, one set of controls under zero stress, one set of specimens under a constant 13.8 and 20.7 MPa, and one set experiencing creep relaxation of thermal stresses. The latter is an exaggerated condition similar to actual service requirements. The specimens subjected to the ratchetting exhibited deformation several times greater than those under constant stress.

The creep coefficients calculated from the constant-stress specimens are given in Fig. 7.9. These values include corrections for elastic modulus and CTE changes and assume the primary creep equal to the initial elastic strain. These corrections are confirmed by the H-451 axial data with a wide spread in fluence levels to allow an extrapolation back to zero flux. These results, shown in Fig. 7.9, are obviously in good agreement with the creep coefficient decreasing linearly with increasing modulus of elasticity. The value of the creep coefficient is also in good agreement with values given by Veringa and Blackstone[3] considering the flux level effect. The uncertainty in the load cell output by irradiation damage precludes accurate calculations of the creep coefficient by the relaxation behavior. However, the total strain introduced into the specimens indicates a creep coefficient of a similar value to the constant-stress specimens.

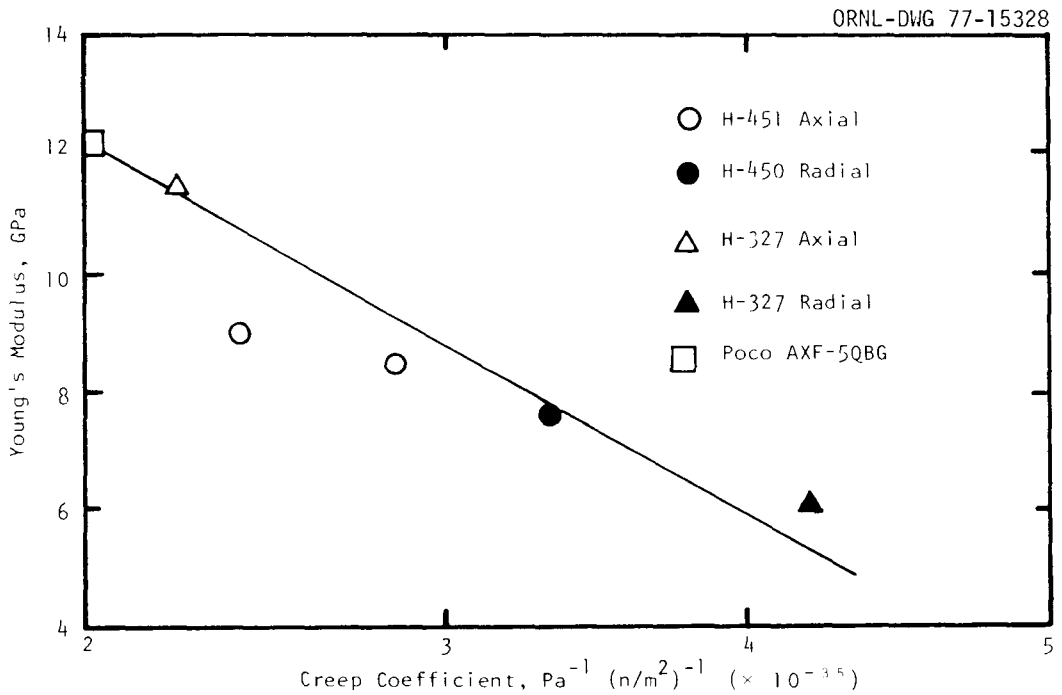

Fig. 7.9. The Creep Coefficient at 900°C Under Compression.

Diameter measurements of the stressed specimens indicate a significant reduction in volume by the compressive stresses. The ratio of the increase in diameter to the axial compressive strain varied from −0.1 to −0.2, significantly less than −0.5 required for no volume change. The decrease in volume was close to 2% for several of the higher strained specimens.

7.3.4 Elastic Properties

The elastic behavior was analyzed by use of sonic velocity measurements. Both longitudinal and shear wave velocities were measured. It should be remembered that the sonic velocities yield the C_{ij} values, which must be transformed into the S_{ij} values. This can accurately be done with graphites that are isotropic or have very low Poisson's ratios with longitudinal and shear velocities in only one direction. For anisotropic graphites with rotational symmetry and Poisson's ratios greater than 0.1, measurements in both the axis of symmetry and a normal direction must be made to accurately make the transformations. However, very close approximations can be made for measurements in the axis of symmetry assuming isotropy. Therefore, measurements of the irradiated samples will yield the shear moduli directly, a close approximation (<1%) of Young's modulus, and a reasonable approximation of Poisson's ratio (<10%).

The decrease in Young's modulus from the unstressed irradiated control samples by compressive deformation is given in Fig. 7.10. Apparently, like

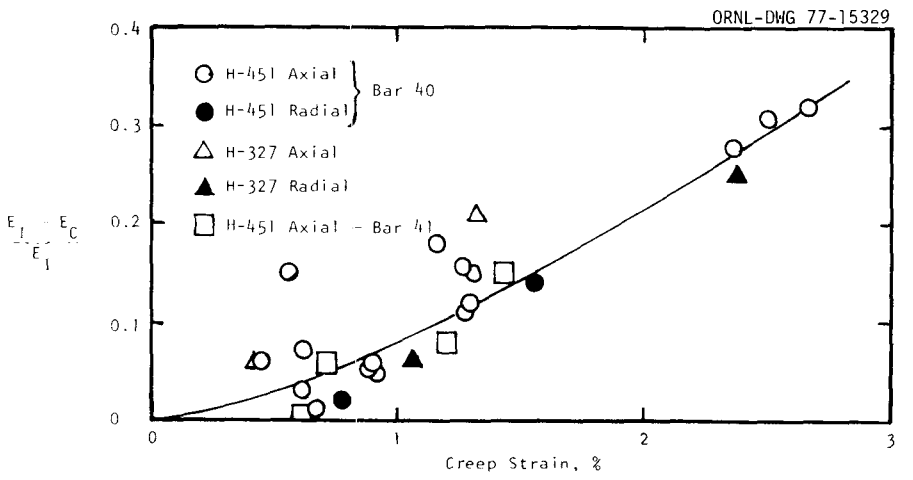

Fig. 7.10. The Reduction of Young's Modulus by Creep Strain.

the CTE, the alteration is independent of the fluence and dependent only upon the total deformation. Poisson's ratio, while virtually unchanged by irradiation without stress, is dramatically reduced to essentially zero by the compressive deformation. This is shown in Fig. 7.11 for grade H-451.

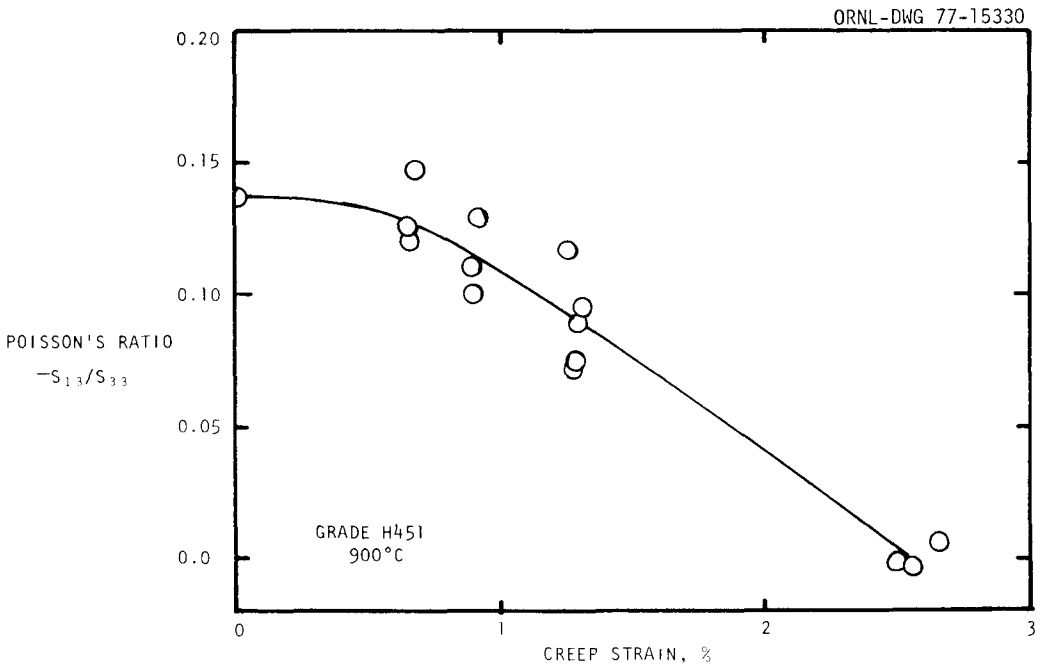

Fig. 7.11. The Reduction of Poisson's of Grade H-451 by Creep Strain.

7.3.5 Electrical Resistivity

The electrical resistivity of each sample was measured with a potentiometer to determine the specimen's axial resistance change. The normal plane resistance was found with eddy currents only on the stressed samples. The control samples had a large hole in each end, which precluded the eddy-current measurement. The results are given in Figs. 7.12 and 7.13. The increase in electrical resistance appears to be little affected by the creep deformation. There does seen to be a slight increase indicated by eddy-current measurements of the 3000-psi samples with the greatest deformation. This is not confirmed in the axial measurements using the potentiometric methods.

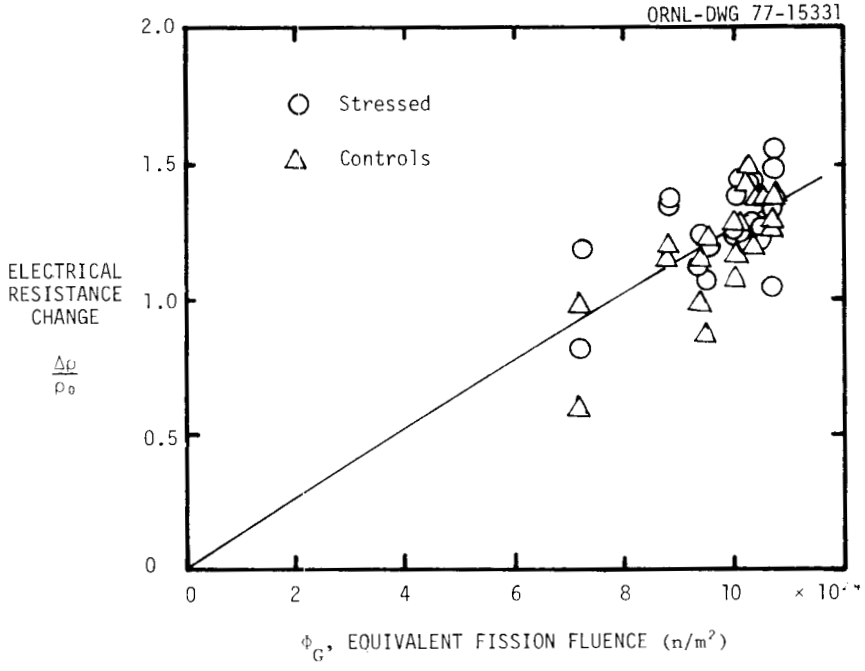

Fig. 7.12. Creep Strain has Virtually No Effect on the Conductivity (Measured by Voltage Drop).

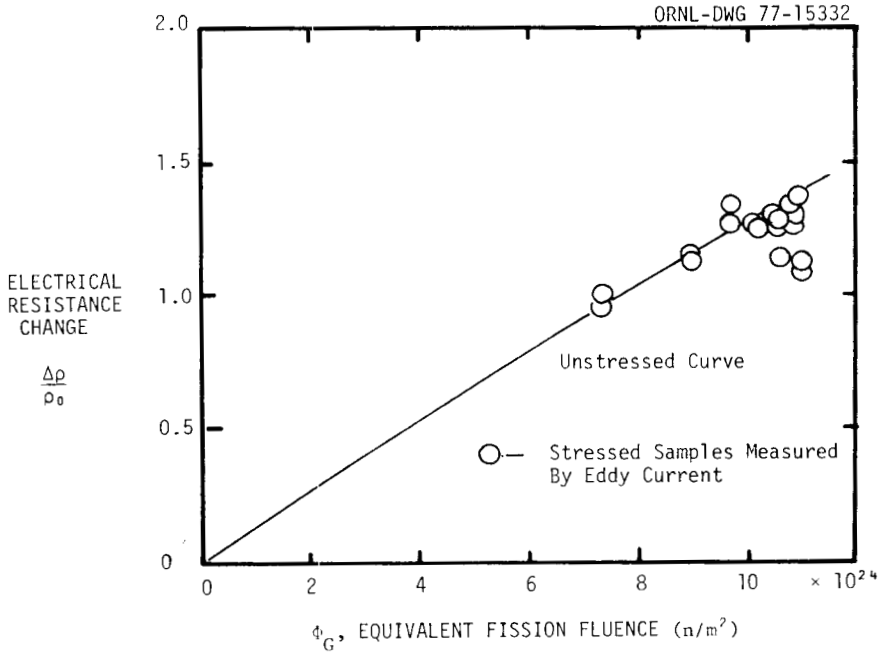

Fig. 7.13. The In-Plane Resistance Change is Similar to the Axial Change.

7.3.6 Coefficient of Thermal Expansion

The effect of compressive creep deformation did increase the CTE in a manner similar to the results of Brocklehurst and Brown.[4] The increase in the CTE appears to be linear with the creep deformation as shown in Fig. 7.14. The values of A and B in the figure are the constants of the equation

$$\text{mean CTE} = A + BT \ . \tag{1}$$

The values of B are generally similar for all graphites relatively independent of grade, method of fabrication, and preferred orientation. As seen in Fig. 7.14, the value of B retains this independence of grade and orientation but increases sharply with deformation. The value of A, of course, is a function of grade and preferred orientation. Therefore, the ratio A/A_0 is used for comparison rather than the actual value, as for B. As seen in Fig. 7.14, the values of A do not increase with deformation as significantly as the value of B.

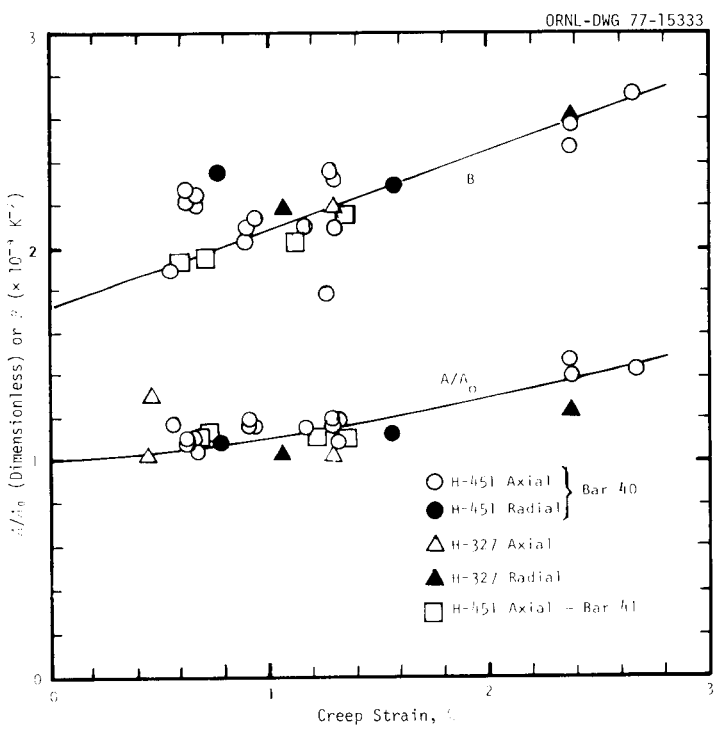

Fig. 7.14. Compressive Strain at 900°C Increases the Mean Coefficient of Thermal Expansion ($\overline{\alpha} = A + BT$).

7.3.7 Discussion

The mechanical deformation of graphite under irradiation is shown to be significant at 900°C. Strains of up to 2.5% in compression have been observed, which is clearly more than will have to be accommodated in most nuclear systems. This mechanism of the deformation is at least uncertain; however, it is clear that the deformation has altered the initial structure of the graphite. A significant part of the macroscopic strain is clearly a result of void closure or a reduction in volume. This is shown by direct measurement of diameter changes compared with the length changes. This does not imply that the voids have been healed but only that they have been closed. The apparent slowing of the deformation rate may indeed be real by virtue of eliminating the void volume. The degree of void volume reduction does, however, seem to depend on stress and modulus.

The reduction in Young's modulus can result from two causes. The first is a flattening of the void volume to reduce the overall spring constant of the structure, and the second is a reorientation to increase anisotropy and an intensification of the *c* axis in the axis of stress direction. Both the flattening of the voids and reorientation will also increase the CTE as observed. The result of significant losses in Poisson's ratio clearly describes an actual decrease in the continuity of structure. This is verification that the void volume has not been healed, but only reduced in size.

Verification of reorientation by deformation is seen in the rotational symmetry observed in the radial H-327 specimen. Therefore, the changes in physical properties by deformation appear to be a result of both reorientation and pore flattening.

It must be emphasized that all the physical properties except resistivity were measured in the stress axis direction. It would be expected that property changes in the normal direction would be considerably different. Young's modulus would be increased and the CTE decreased by the reorientation. The effect of void volume collapse would also increase the Young's modulus, but should only have a nominal effect on the CTE. Therefore, definitive measurements to separate the effects of reorientation and porosity collapse could be made in the normal directions.

The major implications of this study on the analysis of the moderator structure are as follows:

1. If the compressive strain increases the CTE, tensile strains will likely decrease the CTE. Therefore, moderator blocks in severe gradients to produce bending loads under irradiation will be subjected to greater thermal stresses upon shutdown. Those regions having high thermal stress should be reevaluated.

2. The effect of pore collapse and reorientation by compressive strains will undoubtedly reduce the tensile strength in the stress axis direction. This would be by both increasing the stress intensity factor of the void and reorientation of the graphite.

3. The accelerated reduction in volume by compressive straining may well lead to premature degradation of the structure. This is noted generally by a rapid volume expansion in unstressed material; however, this may not be the case for material under compressive loading. It is also noted by severe losses in both the elastic moduli, strength of the graphites, and significant increases in surface area. It would be prudent to consider including destructive testing as well as surface area measurements to more fully evaluate the extent of the damage produced by the deformation.

7.4 STATUS OF FUTURE GRAPHITE CREEP EXPERIMENTS — R. L. Senn

Design is complete on the second experiment of this series, capsule OC-2, to be operated at a nominal specimen temperature of 600°C. All other operating parameters will be the same as those for capsule OC-1.

A pnuematic electromechanical device, designated a PEM cell, has been designed to replace the LVDT-type load cells used in capsule OC-1. The new load cell uses metal bellows similar to those used to load the specimen columns. When the load is applied to the specimens, an insulated contact button located inside the PEM cell bellows is in electrical contact with the top flange of the bellows. The PEM cell bellows is then pressurized with helium to a pressure high enough to overcome the load on the specimens and open the electrical contact. By measuring the pressure required and detecting the resistance between the contact button and the grounded

bellows (infinite when open), the load being applied to the specimen column can be determined, thus ensuring that the load is indeed being applied to the column. By virtue of its all-metal construction, except for the alumina insulator required, we expect the PEM cell to be relatively insensitive to damage from high temperature and radiation. A bench test of a prototype PEM cell was conducted at room temperature with satisfactory results. Further testing at elevated temperatures also gave satisfactory results.

Assembly of capsule OC-2 has begun. We plan to complete construction of OC-2 this fiscal year, with irradiation of OC-2 to begin about February 1978.

Conceptual design and heat transfer calculations are in progress for the third temperature level (1250°C) capsule proposed for this series of tests. We plan to build and operate a bench test to determine the operating characteristics of the proposed design, using electric heaters to simulate gamma heating. One objective of the bench test is to determine sensitivity of the design to any changes of the radiant emissivity of an internal tungsten sleeve, which is required to achieve the 1250°C specimen temperature.

7.5 REFERENCES

1. W. P. Eatherly, J. A. Conlin, W. H. Cook, and R. L. Senn, "Characterization and Standardization of Graphite," *HTGR Base-Technology Program Prog. Rep. Jan. 1, 1974–June 30, 1975*, ORNL-5108, pp. 475–84.
2. R. L. Senn, W. H. Cook, J. A. Conlin, and W. P. Eatherly, *Design, Operation, and Initial Results from Capsule OC-1, The First of a Series of Graphite Creep Irradiation Experiments*, ORNL/TM-5798 (May 1977).
3. H. J. Veringa and R. Blackstone, *Carbon* 14: 279 (1976).
4. J. E. Brocklehurst and R. G. Brown, *Carbon* 7: 487 (1969).

ORNL-5274
Distribution
Category UC-77

INTERNAL DISTRIBUTION

1–2. Central Research Library
3. Document Reference Section
4–5. Laboratory Records Department
6. Laboratory Records, ORNL RC
7. ORNL Patent Office
8. E. J. Allen
9. S. J. Ball
10. D. E. Bartine
11. R. L. Beatty
12. R. A. Bradley
13. C. R. Brinkman
14. J. P. Callahan
15. D. A. Canonico
16. A. J. Caputo
17. J. A. Carpenter
18. J. A. Conlin
19. J. H. Coobs
20. D. A. Costanzo
21. F. L. Culler
22. F. C. Davis
23. J. R. DiStefano
24. W. G. Dodge
25. R. G. Donnelly
26. F. F. Dyer
27. W. P. Eatherly
28. D. N. Fanning
29. G. G. Fee
30. D. E. Ferguson
31. Uri Gat
32. J. C. Griess
33. P. A. Haas
34. R. F. Hibbs
35. M. R. Hill
36–48. F. J. Homan
49. J. A. Horak
50. J. D. Jenkins
51. D. R. Johnson
52. M. J. Kania
53–62. P. R. Kasten
63. C. R. Kennedy
64. H. T. Kerr
65. J. F. King
66. W. J. Lackey
67. K. H. Lin
68. T. B. Lindemer
69. E. L. Long, Jr.
70. A. L. Lotts
71. A. P. Malinauskas
72. H. E. McCoy, Jr.
73. D. L. McElroy
74. J. P. Moore
75. C. S. Morgan
76. R. K. Nanstad
77. D. J. Naus
78. F. H. Neill
79. K. J. Notz
80. A. R. Olsen
81. R. L. Pearson
82. S. Peterson
83. H. Postma
84. P. L. Rittenhouse
85. J M Robbins
86. R. L. Senn
87. J. H. Shaffer
88. R. L. Shepard
89. G. M. Slaughter
90. D. P. Stinton
91. J. P. Strizak
92. R. R. Suchomel
93. K. R. Thoms
94. T. N. Tiegs
95. D. B. Trauger
96. V.C.A. Vaughen
97. J. R. Weir
98. G. D. Whitman
99. R. P. Wichner
100. R. G. Wymer

EXTERNAL DISTRIBUTION

101–102. ERDA DIVISION OF REACTOR NUCLEAR RESEARCH AND APPLICATIONS, Washington, DC 20545

Director

103. ERDA IDAHO OPERATIONS OFFICE, P.O. Box 2108, Idaho Falls, ID 83401

Barry Smith

104. ERDA OFFICE PROGRAM MANAGEMENT, RESEARCH AND SPACE PROGRAMS, P.O. Box 81325, San Diego, CA 92138

J. B. Radcliffe

105. ERDA SAN FRANCISCO OPERATIONS OFFICE, 1333 Broadway, Wells Fargo Building, Oakland, CA 94612

Manager

106–108. ERDA DIVISION OF WASTE MANAGEMENT, PRODUCTION AND PROCESSING, Washington, DC 20545

Chief, Technology Branch
Chief, Projects Branch
Chief, Industrial Programs Branch

109–111. ERDA OAK RIDGE OPERATIONS DIVISION, P.O. Box E, Oak Ridge, TN 37830

Director, Research and Technical Support Division
Director, Reactor Division
F. E. Dearing, Reactor Division

112–288. ERDA TECHNICAL INFORMATION CENTER, P.O. Box 62, Oak Ridge, TN 37830

For distribution as shown in TID-4500 Distribution Category, UC-77 (Gas-Cooled Reactor Technology).

☆ U.S. GOVERNMENT PRINTING OFFICE: 1977-748-189/263